UNIVERSITÀ
DEGLI STUDI
DI PADOVA

Università degli Studi di Padova

Dipartimento di Scienze Chimiche

PhD course in Molecular Sciences

Curriculum: Chemistry Ciclo: XXXVIII

Advancing Synthetic Catalysis through Excited States and Strain-Release Strategies

Coordinatore: Prof. Stefano Corni

Supervisore: Prof. Luca Dell'Amico

Co-Supervisore: Prof. Sara Bonacchi

Ph.D. student: Lorenzo Rizzo

Abstract

The rapid development of photochemistry and transition-metal catalysis has profoundly expanded the repertoire of modern organic synthesis. Light has emerged not only as a sustainable energy source but also as a means to unlock new reactivity pathways, while palladium catalysis continues to play a central role in the construction of complex molecules. This Dissertation presents only the main projects developed during the PhD studies, each illustrating a different strategy to expand the scope of catalysis through excited-state processes and strain-release reactivity. The work begins with a project based on direct photochemistry, where π-extended iminium ions were designed to overcome intrinsic photophysical limitations and engage in stereoselective [2+2] photocycloadditions. It then moves to a study of energy-transfer photocatalysis combined with strain-release activation of azabicyclo[1.1.1]pentanes, leading to the radical construction of functionalized azetidines. Finally, the last chapter describes a project carried out during a visiting period abroad, centered on palladium catalysis. In this case, oxabicycles were employed as acetylene surrogates, and the strain-release event occurred at the end of the palladium-catalyzed cycle, enabling the enantioselective synthesis of spiroindenes.

Taken together, these studies illustrate how the rational combination of direct photochemistry, photocatalytic energy transfer, strain-release activation, and palladium catalysis can provide new avenues for molecular construction. Beyond the individual case studies, the methodologies developed in this work highlight broader principles for expanding the chemical space accessible through catalysis, offering general insights into the design of sustainable and stereoselective synthetic processes.

List of publications

Publications during my doctoral studies covered in this thesis

- Ricardo I. Rodríguez, Vasco Corti, Lorenzo Rizzo, Stefano Visentini, Marco Bortolus, Agnese Amati, Mirco Natali, Giorgio Pelosi, Paolo Costa, and Luca Dell'Amico
  Radical strain-release photocatalysis for the synthesis of azetidines.
  Nat Catal, **2024**, 7, 1223–1231 (2024).

- Vasco Corti, Gianluca Simionato, Lorenzo Rizzo, Stefano Serapian, Giorgio Pelosi, Mirco Natali, Luca Dell'Amico
  Triplet state reactivity of iminium ions in organocatalytic asymmetric [2 + 2] photocycloadditions
  Nat. Chemistry 2025 (https://doi.org/10.1038/s41557-025-01960-3)

- Clara Jans; Armaan Grewal; Xavier Abel-Snape; Lorenzo Rizzo; Gregory Hughes; Mark Lautens
  Synthesis of Spiroindenes via Palladium-Catalysis Using Oxabicycles as Acetylene Surrogates, accepted in Organic Letters (https://doi.org/10.1021/acs.orglett.5c04430)

Publications during my doctoral studies not covered in this thesis

- Simone Adorinni, Giulio Goti, Lorenzo Rizzo, Federica Grassi, Slavko Kralj, Fatima Matroodi, Mirco Natali, Rita De Zorzi, Silvia Marchesan, and Luca Dell'Amico
  Self-assembly of benzophenone-diphenylalanine conjugate into nanostructured photocatalyst
  Chem. Commun., **2023**, 59, 7619–7622.

Acknowledgments

It is difficult to realise that I have truly reached the end of this incredible journey, which has taught me so much both professionally and personally. These years have been challenging and far from straightforward, but also deeply formative and rewarding, largely thanks to the people who have stood by my side.

Per prima cosa desidero ringraziare i miei genitori: senza il vostro sostegno costante e i sacrifici che avete fatto, oggi non sarei qui. Ogni volta che qualcuno dice che io sono “in gamba” e che andrò lontano, ricordatevi che in realtà quelli in gamba siete voi, perché ho avuto la possibilità di arrivare dove sono solo grazie a voi.

Un pensiero speciale va a tutti i miei amici di Roma. Nonostante la distanza, il vostro affetto mi ha sempre accompagnato e non mi sono mai sentito solo. Non sarebbe stato lo stesso senza di voi. Grazie di cuore, Pera, Dario, Danilo, Billy, Vegeta, Riccardo Pacio e Iori: spero di portarvi con me per tutta la vita.

Un ringraziamento fondamentale va a te, Carlottina. Solo io e te sappiamo quanto mi sei stata vicina e quanta forza mi hai dato in questi anni. Non ce l’avrei fatta senza il tuo sostegno costante: grazie per tutto.

I must thank my supervisor, Luca Dell'Amico, for believing in me when I struggled to do so myself, and for the constant support and guidance he has provided over the years. Thanks to him, I have been able to grow significantly, both as a scientist and as a person.

I am also deeply grateful to the entire Dell'Amico group: we have been an extraordinary team, almost a family, and without you these years would have been far more difficult. I will always carry you in my heart. A special thanks goes to Riccardo, Vasco and Josè, with whom I had the honour of working closely—you are outstanding chemists and I have learned so much from you. I also warmly thank Jorge, Cristian, Daniele, Gorka, Sara, Giulio, Katy, Chun, Loris, Chandu, Raphael, Gabriel, Luis (el mentiroso), Stefano, Elia, Alessia, Andrea, Serafino, and Michael, Tommaso e Pietro.

I would also like to remember all the people with whom I had the pleasure of sharing parts of this journey: Marina, Thomas (without your screen the writing of this thesis would have been much harder), Giorgio, Leonardo, Giuseppe, Paolo, Francesco, Ilaria, Jintao, Yunshuo, Robin, Gianpaolo, Simone G., Giulia, Valentina, Elena Fredda, Elena Tacchi, Jie, Emanuele, Catia, Greta, Martina, la Betta, Piero, Fatima, Emanuele, and of course Stefano, the one we all turned to.

My sincere thanks go to Professor Mark Lautens for giving me the opportunity to spend time in his group in Toronto—months that proved extremely formative for me. I am equally grateful to the entire Lautens group, especially Xavier Abel-Snape and Clara Jans.

Finally, I have left Gianluca and Giorgia for last: with you I have shared this journey side by side from the very beginning. And although we started out as the Harry Potter trio, we soon became four with the arrival of Simone Baldone, who quickly became an essential part of us. I could not have asked for better companions—your conversations, advice, and friendship have helped me more than I can ever express.

List of symbols and abbreviations

A list of abbreviations used throughout the thesis is reported here in alphabetical order.

4CzIPN: 2,4,5,6-Tetrakis(9H-carbazol-9-yl) isophthalonitrile
5TCzBN: 2,3,4,5,6-pentakis(3,6-di-tert-butyl-9H-carbazol-9-yl)benzonitrile
ABB: 1-Azabicyclo[1.1.0]butane
Ac_2O: Acetic anhydride
AcOH: Acetic acid
AMPA: α-Amino-3-hydroxy-5-methyl-4-isoxazolepropionic acid
ATR: Attenuated Total Reflectance
ATRA: Atom Transfer Radical Addition
BCB: Bicyclo[1.1.0]butane
BCH: Bicyclo[2.1.1]hexane
Bn: Benzyl group
Boc: tert-Butoxycarbonyl
Bpin: Pinacol boronic ester
BCP: Bicyclo[1.1.1]pentane
Bpy: 2,2′-Bipyridyl
Bz: benzoyl group
Cat: Catalyst
CCDC: Cambridge Crystallographic Data Centre
CDMT: 2-Chloro-4,6-dimethoxy-1,3,5-triazine
CMD: Concerted Metalation–Deprotonation
Cy: Cyclohexyl group
d: Doublet
DART: Direct Analysis in Real Time
dba: Dibenzylideneacetone
DCM: Dichloromethane
DFT: Density Functional Theory
DMAP: 4-(Dimethylamino)pyridine
DME: Dimethoxyethane
DMF: Dimethylformamide
DMSO: Dimethyl sulfoxide
dr: Diastereomeric ratio
E: Energy or potential
E^+: Electrophile
$E_{0,0}$: Zero–zero transition energy
ee: Enantiomeric excess
EI: Electron ionization
EnT: Energy Transfer
Equiv: Equivalents
ε: Molar extinction coefficient

EPR: Electron Paramagnetic Resonance
EtOH: Ethanol
EtOAc: Ethyl acetate
FC: Franck–Condon
FRET: Förster Resonance Energy Transfer
GC: Glassy carbon (electrode)
GC–MS: Gas Chromatography–Mass Spectrometry
GS: Ground State
h: Hours
HAT: Hydrogen Atom Transfer
HOMO: Highest Occupied Molecular Orbital
HPLC: High-Performance Liquid Chromatography
HRMS: High-Resolution Mass Spectrometry
HSOMO: Highest Singly Occupied Molecular Orbital
I: Intensity
IC: Internal Conversion
IEFPCM: Integral Equation Formalism Polarizable Continuum Model
IPA: Isopropanol
***i*Pr:** Isopropyl group
IR: Infrared spectroscopy
$Ir(ppy)_3$: Tris(2-phenylpyridine)iridium(III) (ppy = 2-phenylpyridine)
ISC: Intersystem Crossing
JEOL: Japanese Electron Optics Laboratory
LC: Liquid Chromatography
LDA: Lithium diisopropylamide
LED: Light Emitting Diode
LFP: Laser Flash Photolysis
LSOMO: Lowest Singly Occupied Molecular Orbital
LUMO: Lowest Unoccupied Molecular Orbital
m: Multiplet
Me: Methyl
MeCN: Acetonitrile
MEK: Mitogen-activated protein kinase kinase (also known as MAP2K)
MECP: Minimum Energy Crossing Point
MeCzTrz: 9,9',9"-(5-(4,6-Diphenyl-1,3,5-triazin-2-yl)benzene-1,2,3-triyl)tris(3,6-dimethyl-9H-carbazole)
MeOH: Methanol
Mes: Mesityl
Mes-Acr$^+$Ph: 3,6-di-tert-butyl-9-mesityl-10-phenylacridin-10-ium
MI: Migratory Insertion
MP: Melting Point
$Ni(dtbbpy)Br_2$: Nickel(II) bromide–4,4′-di-tert-butyl-2,2′-bipyridine complex
NBE: Norbornene
NBD: Norbornadiene
NBS: N-Bromosuccinimide
NMM: N-Methylmorpholine

NMR: Nuclear Magnetic Resonance
NOE: Nuclear Overhauser Effect
NTO: Natural Transition Orbital
NTC: Naphthochromenone
Nu: Nucleophile
OA: Oxidative Addition
OLED: Organic Light-Emitting Diode
OrgPCs: Organic Photocatalysts
OND: Oxanorbornadiene
OPiv: Pivalate group
ORTEP: Oak Ridge Thermal Ellipsoid Plot (molecular thermal ellipsoid diagram)
OTs: Tosylate group
oxa-BCH: Oxa-bicyclo[2.1.1]hexane
PBN: α-Phenyl tert-butylnitrone (spin trap)
PC: Photocatalyst
PC*: Excited-state Photocatalyst
PCM: Polarizable Continuum Model
[Pd(cinnamyl)Cl]$_2$: Palladium(π-cinnamyl) chloride dimer
[Pd(allyl)Cl]$_2$: Palladium(η^3-allyl) chloride dimer
Pd(dba)$_2$: Bis(dibenzylideneacetone)palladium(0)
Pd(TFA)$_2$: Palladium(II) trifluoroacetate
PET: Photoinduced Electron Transfer
Ph: Phenyl
PhCF$_3$: Trifluorotoluene
PHT: 10-Phenylphenothiazine
PMP: para-Methoxyphenyl
ppm: parts per million
Ppy: 2-Phenylpyridine
PS: photosensitizer
q: Quartet
QY: Luminescence quantum yield
R: Generic substituent
rDA: retro-Diels–Alder
RE: Reductive Elimination
Rh$_2$(esp)$_2$: Bis[rhodium(α,α,α′,α′-tetramethyl-1,3-benzenedipropionic acid)]
RISC: Reverse Intersystem Crossing
RSR: radical strain-release
Ru(bpy)$_3^{2+}$: Tris(2,2′-bipyridine)ruthenium(II) (bpy = 2,2′-bipyridine)
rt: Room temperature
RT: Residence time
S$_0$: Ground Singlet State
S$_1$: First Excited Singlet State
Sn: Higher Excited Singlet State
SCE: Saturated Calomel Electrode
SCF$_3$: Trifluoromethylthio group
SFC: Supercritical Fluid Chromatography

SM: Starting material
SOMO: Singly Occupied Molecular Orbital
T_1: First Excited Triplet State
t: Time (in kinetics) or triplet (context-dependent)
T: Temperature
TADF: Thermally Activated Delayed Fluorescence
$TBABF_4$: Tetrabutylammonium tetrafluoroborate
TBAF: Tetrabutylammonium fluoride
TBADT: Tetra-n-butylammonium decatungstate
$TBAPF_6$: Tetrabutylammonium hexafluorophosphate
TBCzTrz:9,9',9''-(5-(4,6-Diphenyl-1,3,5-triazin-2-yl)benzene-1,2,3-triyl)tris(3,6-di-*tert*-butyl-9*H*-carbazole)
TBTA: Tris(benzyltriazolylmethyl)amine
TFA: Trifluoroacetic acid
TCP: [1.1.1]Propellane
TCSPC: Time-Correlated Single-Photon Counting
TD-DFT: Time-Dependent Density Functional Theory
Tf: Trifluoromethanesulfonyl
TLC: Thin-Layer Chromatography
TM: Transition Metal
TMS: Tetramethylsilane
Tn: Higher Triplet State
TOF: Time-of-Flight (mass spectrometry)
Tol: tolyl
Ts: tosyl group (or tolylsulfonyl group)
TS: Transition State
TTEnT: Triplet–Triplet Energy Transfer
TXO: Thioxanthen-9-one
UPC2: UltraPerformance Convergence Chromatography
UV: Ultraviolet
UV–Vis: Ultraviolet–visible (spectroscopy)
VR: Vibrational Relaxation
XRD: X-ray Diffraction
λ: Wavelength
τ: Lifetime
Φ: Reaction quantum yield
ΔG: Gibbs free energy change
ΔG‡: Gibbs free energy of activation
ΔST: Singlet–triplet energy gap

Table of contents

Chapter I – Background Concepts

1. Introduction 3
1.1. General Introduction to Photochemistry....3
1.1.1. Direct Photochemistry: Fundamentals and Applications....5
1.1.2. Photosensitisation via energy transfer (EnT) 7
1.2. Strain release chemistry 9
1.2.1. Strain-Release Photocatalysis 11
1.2.2. Thermal strain release 14
1.3. Reactions with Transition Metals....17
1.3.1. Palladium chemistry 18
1.3.2. C–H Activation....22
1.4. Aim of the thesis 26
1.5. References 27

Chapter II – Triplet state reactivity of iminium ions in organocatalytic asymmetric [2 + 2] photocycloadditions

2.1. Introduction 35
2.1.1. Principles of Asymmetric Organocatalysis with Emphasis on Iminium Ions....35
2.1.2. Excited-State Iminium-Ion Catalysis: Singlet Reactivity and the Challenge of Triplets....37
2.1.3. Photochemical Dearomatization as a Simple Strategy for the Generation of Complex Molecules……42
2.2. Aim of the project....45
2.3. Results and discussion....46
2.3.1. Optimization studies....46
2.3.2. Mechanistic investigations2.3.2 Mechanistic studies 47
2.3.3. Computational investigations....52
2.3.4. Generality of the reaction....53
2.4. Conclusions....56
2.5. Experimental part....57
2.6. References....121

Chapter III – Radical strain-release photocatalysis for the synthesis of azetidines

3.1. Introduction....127
3.1.1. The Principle of Bioisosteric Replacement in Drug Design....127
3.1.2. The Role of Azetidines in Modern Bioisosterism....129
3.1.3. Approaches to the synthesis of azetidines: opportunities and limitations....131
3.2. Aim of the project....135
3.3.1. Reaction design and optimization....136
3.3.2. Mechanistic investigations....139
3.3.3. Generality of the reaction....141
3.3.4. Conclusions....145
3.4. Experimental part....146
3.5. References....199

Chapter IV – Synthesis of Spiroindenes via Palladium-Catalysis Using Oxabicycles as Acetylene Surrogates

4.1. Introduction....205
4.1.1. Biological Relevance and Synthetic Challenges of Spiroindenes....205
4.1.2. Strained Bicyclic Scaffolds as Acetylene Equivalents....207
4.1.3. Remote Asymmetric Induction via Chiral Oxabicycles....211
4.2. Aim of the project....216
4.3. Results and discussion....217
4.3.1. Optimization studies....217
4.3.2. Proposed mechanism....223
4.3.3. Scope of the reaction....224
4.4. Conclusion....226
4.5. Experimental part....227
4.6. References....254

Chapter I

General Overview on the Introduction

1.1 Photochemistry

- Direct Photochemistry
- Energy Transfer

1.2 Strain Release Chemistry

aza[1.1.0]BB

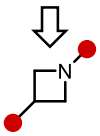

- Strain-Release Photocatalysis
- Thermal strain release

1.3 Transition Metals Catalysis

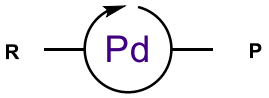

- Palladium Chemistry
- C-H Activation

1. Introduction

1.1. General Introduction to Photochemistry

The use of light as a source of energy and transformation in chemistry has long captured the imagination of scientists. One of the earliest and most visionary voices in this field was Giacomo Ciamician, who, in his 1912 address *"The Photochemistry of the Future"*, anticipated the use of sunlight as a sustainable alternative to fossil fuels and as a fundamental tool for chemical synthesis. He envisioned a future where light-driven processes would replace traditional industrial chemistry, exploiting the inexhaustible energy of the sun to power chemical reactions with unprecedented elegance and efficiency.[1]

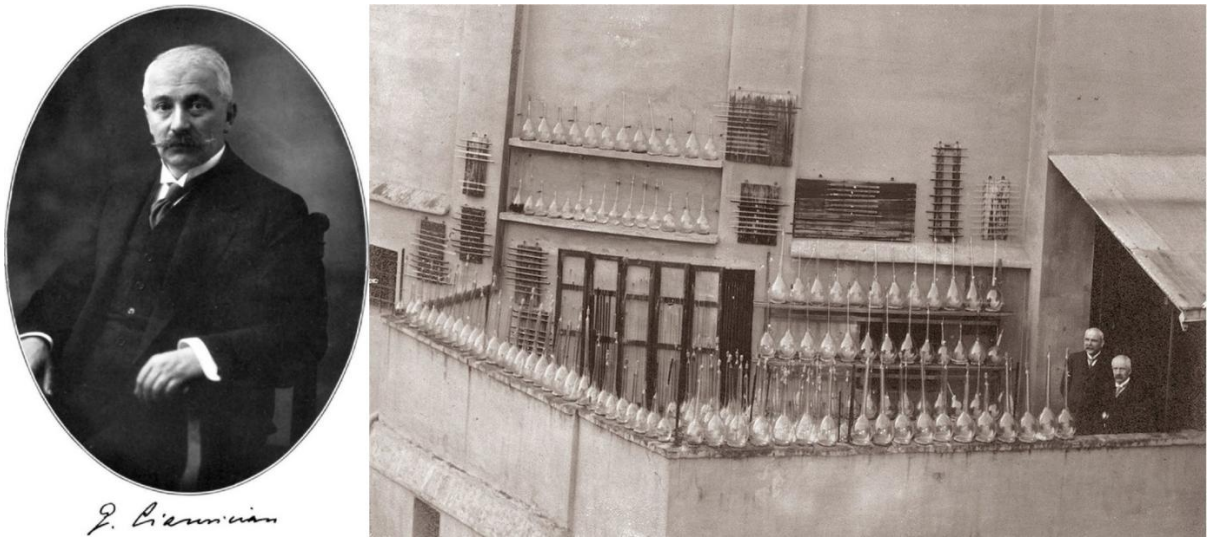

Figure 1. Giacomo Ciamician (1857–1922), pioneer of photochemistry, and a photograph circa 1910 of his solar laboratory terrace in Bologna.

Over a century later, photochemistry has indeed emerged as one of the most dynamic and versatile branches of modern synthetic chemistry. By harnessing photons to access reactive excited states, photochemical methods offer unique reactivities and selectivities that are often unattainable through classical thermal pathways. Crucially, these transformations can proceed under mild conditions and often with excellent functional group tolerance, making photochemistry not only conceptually attractive but also practically relevant in the context of green and sustainable synthesis.[2] A key distinction within this domain lies between direct photochemistry and photocatalysis. In direct photochemistry, the substrate itself absorbs light and enters an excited electronic state, which subsequently undergoes chemical transformation. This approach is typically limited to chromophoric molecules that possess accessible singlet or triplet states capable of undergoing productive rearrangements or bond cleavages. While powerful, direct photochemistry can be less predictable and is often sensitive to structural and electronic factors. In contrast, photocatalysis relies on the use of a separate light-absorbing species—a photocatalyst (PC)—which, upon excitation, transfers energy or electrons to the substrate, thereby activating it for further reaction. This distinction not only expands the range of compatible substrates but also offers additional control over the reaction mechanism, redox properties, and selectivity profiles.[3] Modern photocatalysis encompasses three main mechanistic paradigms: single electron transfer

(SET), energy transfer (EnT), and hydrogen atom transfer (HAT). In photoredox catalysis (SET), a photocatalyst is excited by visible light and engages in redox events with organic substrates, acting either as an excited-state oxidant or reductant. This enables the formation of radical or radical-ion intermediates that are typically inaccessible by conventional methods.[2,3] These mechanisms are typically categorized into *oxidative* or *reductive quenching cycles*, depending on whether the catalyst donates or accepts an electron in its excited state. Transition metal complexes such as $Ru(bpy)_3^{2+}$ or $Ir(ppy)_3$ have long been the prototypical catalysts in this domain, owing to their long-lived triplet excited states and tunable redox potentials.[4,5]

In energy transfer (EnT) processes, the photocatalyst transfers its excitation energy to a substrate without a net electron exchange. EnT is particularly attractive for initiating reactions from electronically excited substrates that are otherwise challenging to access thermally. A third, increasingly recognized mechanism is hydrogen atom transfer (HAT), in which the excited photocatalyst abstracts a hydrogen atom from a donor molecule, typically resulting in the generation of a radical intermediate.[6] This pathway is especially relevant in the activation of strong, non-polar C–H bonds and is often employed in conjunction with SET processes to access dual catalytic manifolds. Over the past decade, a noticeable shift in focus has occurred from traditional metal-based photoredox catalysts to organic photocatalysts (OrgPCs). This transition has been driven by the desire for metal-free, sustainable systems with high tunability, structural diversity, and reduced environmental impact. Organic photocatalysts, including dyes such as eosin Y, the cyanoarene core, and acridinium salts, have proven effective in mediating both SET and EnT processes, often with performances comparable to or exceeding their transition metal counterparts (Figure 2).[7]

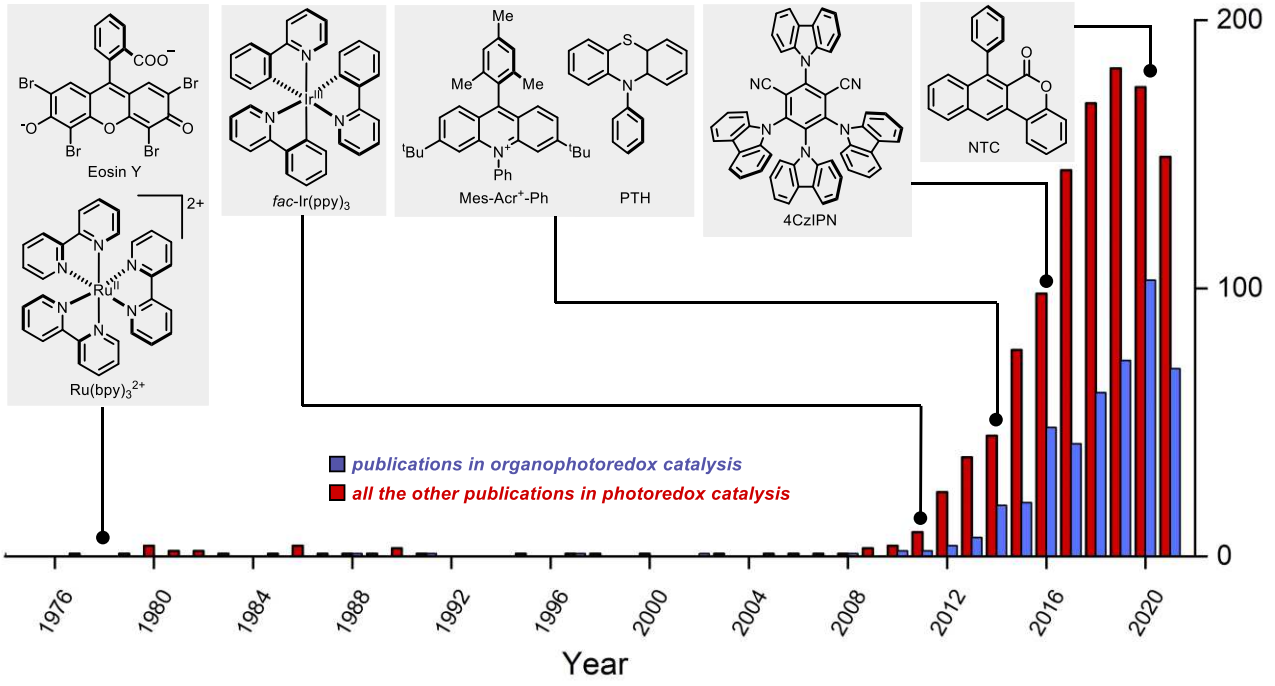

Figure 2. Annual publications in synthetic photoredox catalysis. Blue bars represent organophotoredox reports, red bars other contributions. Structures of selected photocatalysts are linked to their first synthetic application.

Moreover, recent research has revealed that structural modifications to OrgPCs—such as the introduction of electron-donating or -withdrawing groups, steric modulation, or non-covalent substrate preassembly—can profoundly influence their excited-state properties, aggregation behavior, and mechanistic preferences.[2] In summary, photochemistry has evolved from a conceptual curiosity into a mature and highly strategic field of synthetic chemistry. The continuing refinement of mechanistic understanding and catalyst design, particularly

in the realm of organophotocatalysis, promises to drive innovation in molecular construction and reactivity far into the future.

1.1.1. Direct Photochemistry: Fundamentals and Applications

Photochemistry relies on the interaction between light and matter to enable chemical transformations. At its foundation lie two historical principles: the Grotthuss–Draper law, which states that light must be absorbed by a chemical substance for a photochemical reaction to occur, and the Stark–Einstein law, which establishes that each absorbed photon activates a single molecule, highlighting the quantized nature of photochemical excitation.[8] These principles set the stage for understanding how a photon, by interacting with a molecule, initiates a cascade of photophysical and photochemical events that can be harnessed in synthetic chemistry.

When a molecule absorbs a photon of sufficient energy, it is promoted from its electronic ground state (**S_0**) to an excited singlet state (**S_1** or higher, **Sn**). The energy of this transition is governed by the Planck-Einstein relation (Equation 1), indicating that shorter wavelengths correspond to higher photon energies.[9]

$$E = h\nu = \mathrm{h}\frac{c}{\lambda} \qquad \textbf{Equation 1}$$

Due to the Franck–Condon principle, this excitation typically places the molecule in an excited vibrational level of the electronic excited state. Rapid vibrational relaxation (VR) then dissipates excess vibrational energy, bringing the molecule to the lowest vibrational level of S_1.[10]

From this excited singlet state, the molecule can follow several fates. It may return to the ground state via fluorescence, emitting a photon, or undergo internal conversion (IC), where the energy is dissipated as heat. Alternatively, the molecule may undergo intersystem crossing (ISC) to a triplet excited state (**T_1**), which, due to the spin-forbidden nature of phosphorescence, is typically longer-lived and more reactive under mild conditions.[11] These unimolecular pathways define the fundamental behavior of an excited molecule and are elegantly summarized in the Jablonski diagram, a conceptual representation introduced in 1933 to visualize excited state processes.[12]

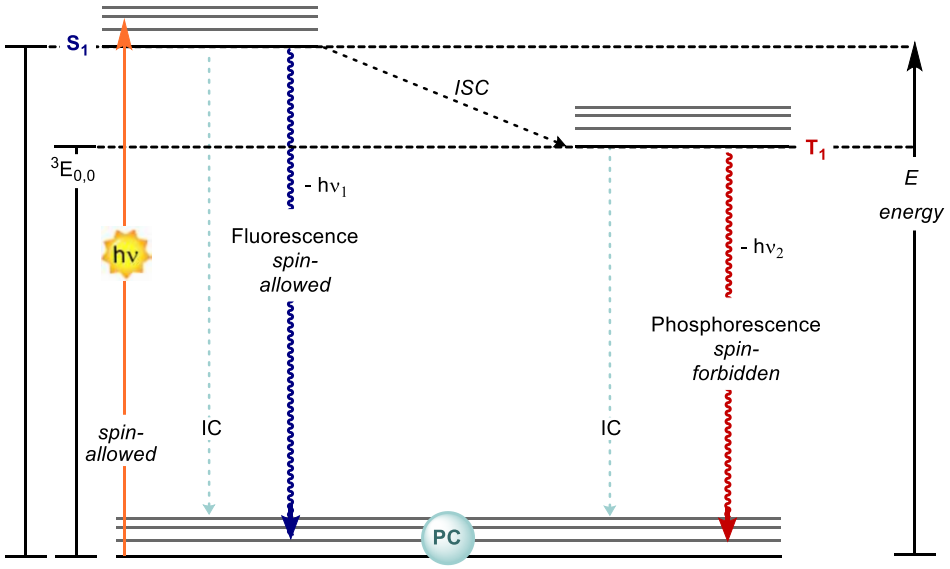

Figure 3. A simplified Jablonski diagram depicting the photophysical processes between the ground (S_0), first excited singlet (S_1), and first excited triplet (T_1) states of a molecule. The grey lines depict the vibrational levels of each Sn or Tn state.

The reactivity of molecules in direct photochemistry stems from the unique chemical properties acquired upon photoexcitation. This approach is inherently substrate-dependent: only compounds bearing suitable chromophores—functional groups capable of absorbing light at specific wavelengths—can engage in such processes. Once excited, the chromophore behaves as a distinct chemical species, often with reactivity inaccessible from the ground state. In this context, the excited state serves as the true reactive intermediate, opening pathways beyond the reach of conventional thermal activation.

Historically, many important transformations have exploited direct excitation strategies. Among the most prominent are [2+2] cycloadditions of enones and alkenes, which proceed through triplet diradical intermediates formed after intersystem crossing of the excited enone (Scheme 1). In a typical mechanism, excitation of the unsaturated substrate **1** generates the singlet excited state S_1, which rapidly undergoes ISC to the longer-lived triplet state T_1. From here, radical addition produces a triplet diradical intermediate **3** that, after spin inversion, closes to the cyclobutane product **4**.[13]

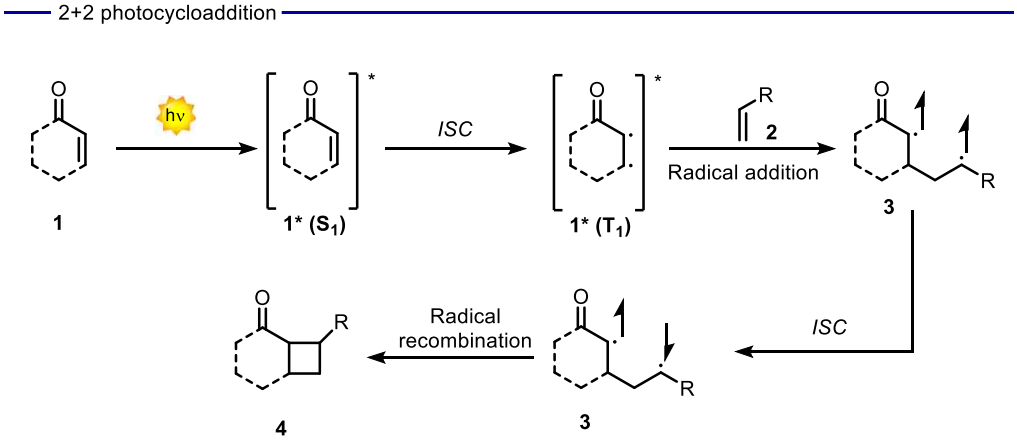

Scheme 1. General mechanism of enone-alkene [2+2] photocycloaddition.

These reactions provide rapid access to strained four-membered rings and have been widely applied in the synthesis of complex molecules.[8] Other notable classes include photoisomerizations of alkenes, cyclizations, and photoinduced electron transfer (PET) processes, wherein light absorption generates radical ions capable of undergoing redox-based bond disconnections or rearrangements.[14,15]

Despite its rich potential, direct photochemistry is inherently limited by optical constraints. Most organic molecules lack significant absorption in the visible spectrum and require ultraviolet (UV) light for excitation, typically wavelengths below 300 nm. This introduces several practical challenges. First, safety is a concern, as UV radiation—especially in the UVB and UVC regions—can damage biological tissue and requires specialized shielding and protocols. Second, equipment limitations arise because standard laboratory glassware, such as borosilicate, absorbs UV below 300 nm, making quartz-based vessels necessary. Third, selectivity becomes an issue since UV light has high energy, increasing the risk of non-selective activation, product decomposition, and uncontrolled background reactivity.[16,17]

These limitations become particularly problematic when working with complex molecular mixtures or sensitive functional groups. The fact that optical absorption and chemical reactivity are inseparably linked in direct photochemistry restricts its generality and often necessitates substrate-specific tuning of the excitation wavelength.[8]

In recent years, many of the inherent limitations of direct photochemistry have been addressed using photocatalysis, as outlined in Section 1.1. By employing an external photocatalyst—often a transition metal complex or an organic chromophore—light absorption can be decoupled from the substrate's optical properties. Selective excitation of the photocatalyst, typically in the visible range, allows the activation of the substrate

via the three main mechanistic pathways already discussed: energy transfer (EnT), single-electron transfer (SET), and hydrogen atom transfer (HAT). This approach has greatly expanded the scope of light-driven transformations, enabling higher selectivity, broader substrate compatibility, and more sustainable reaction conditions.[18] In summary, while direct photochemistry provided the foundational reactions and mechanistic understanding of light-induced organic transformations, its dependency on UV light and substrate-specific absorption has limited its scope. The development of photocatalysis has retained the benefits of photochemical activation while greatly expanding functional group tolerance, selectivity, and practical accessibility.

1.1.2. Photosensitisation via energy transfer (EnT)

Energy transfer (EnT) is a photophysical process in which the electronic excitation of one molecular entity—the donor—is transferred to another molecule—the acceptor—without direct photon absorption by the latter. In the context of visible-light photocatalysis, the photocatalyst (PC) acts as the donor, transferring energy to the substrate (acceptor), which is thereby promoted to an excited state.[10] This process allows activation of substrates that are poorly absorbing at the wavelength of the irradiation source, thus circumventing one of the key limitations of direct photochemistry.[19] Two main mechanisms govern EnT: Förster resonance energy transfer (FRET), which operates through long-range dipole–dipole interactions and requires spectral overlap between the donor's emission and the acceptor's absorption spectra; and Dexter energy transfer, which involves short-range electron exchange and is the predominant pathway in solution-phase photochemistry.[20] In the context of organic photocatalysis, Dexter transfer is by far the most common mechanism .[21] It requires close-range interaction between the excited photocatalyst (PC*) and the substrate, enabling orbital overlap necessary for the two-electron exchange. Due to the short lifetime of the singlet excited state (S_1), EnT in photocatalysis almost always originates from the longer-lived triplet state (T_1), whose microsecond-scale lifetime allows sufficient time for bimolecular encounters (Scheme 2a).[19]

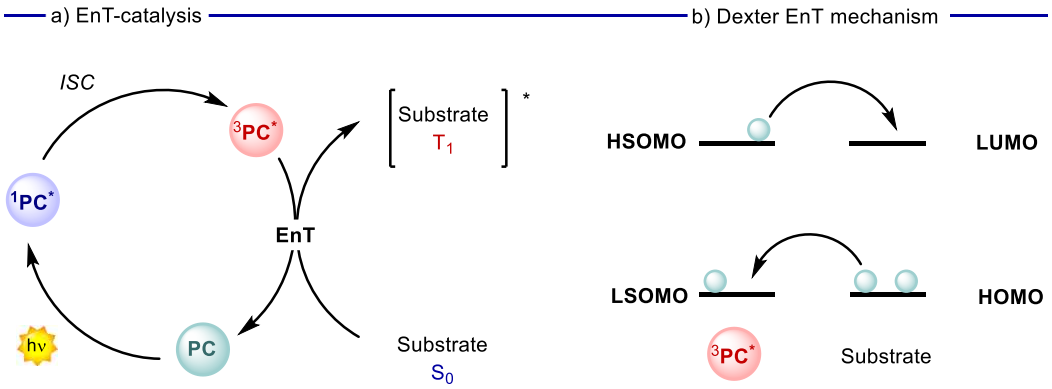

Scheme 2. Schematic representation of: (a) a photocatalytic mechanism based on EnT; (b) the Dexter energy

The Dexter process is initiated when PC* and the substrate diffuse together to form an encounter complex in which their molecular orbitals overlap. This orbital overlap enables a simultaneous two-electron exchange: an electron from the highest singly occupied molecular orbital (HSOMO) of the triplet PC is transferred to the lowest unoccupied molecular orbital (LUMO) of the substrate, while an electron from the highest occupied molecular orbital (HOMO) of the substrate moves to the lowest singly occupied molecular orbital (LSOMO) of the PC (Scheme 2b).[22] At the end of the process, the photocatalyst returns to its ground state, while the substrate is promoted to its triplet excited state. In photocatalysis, triplet–triplet energy transfer (TTEnT) is the dominant pathway. For the process to be thermodynamically favorable, the triplet energy of the photocatalyst

($^3E_{0,0}$[PC]) must be higher than that of the substrate ($^3E_{0,0}$[Sub]); the driving force is typically expressed as $\Delta E = {}^3E_{0,0}[Sub] - {}^3E_{0,0}[PC]$, with negative values indicating diffusion-limited processes.[21]

From a synthetic perspective, EnT can be considered a form of indirect excitation or photosensitization, as the net result is the generation of an electronically excited substrate via energy transfer rather than direct absorption.[20] This approach provides several advantages:

1. Milder irradiation conditions – by using visible light instead of high-energy UV, photodegradation and undesired side reactions are minimised;
2. Broader substrate scope – molecules with low extinction coefficients or requiring short-wavelength excitation can be activated indirectly;
3. Enhanced selectivity – only the photocatalyst is directly excited, allowing selective activation of one component in complex mixtures.

Among the most established applications of EnT is olefin isomerization, where triplet–triplet energy transfer (TTEnT) enables the selective population of the alkene triplet state, allowing for controlled *E/Z* interconversion under mild conditions (Scheme 3a) .[23] Another classical transformation is cycloaddition, in which triplet excitation of the substrate promotes specific bond-forming events that are inaccessible under thermal conditions (Scheme 3b).[24]

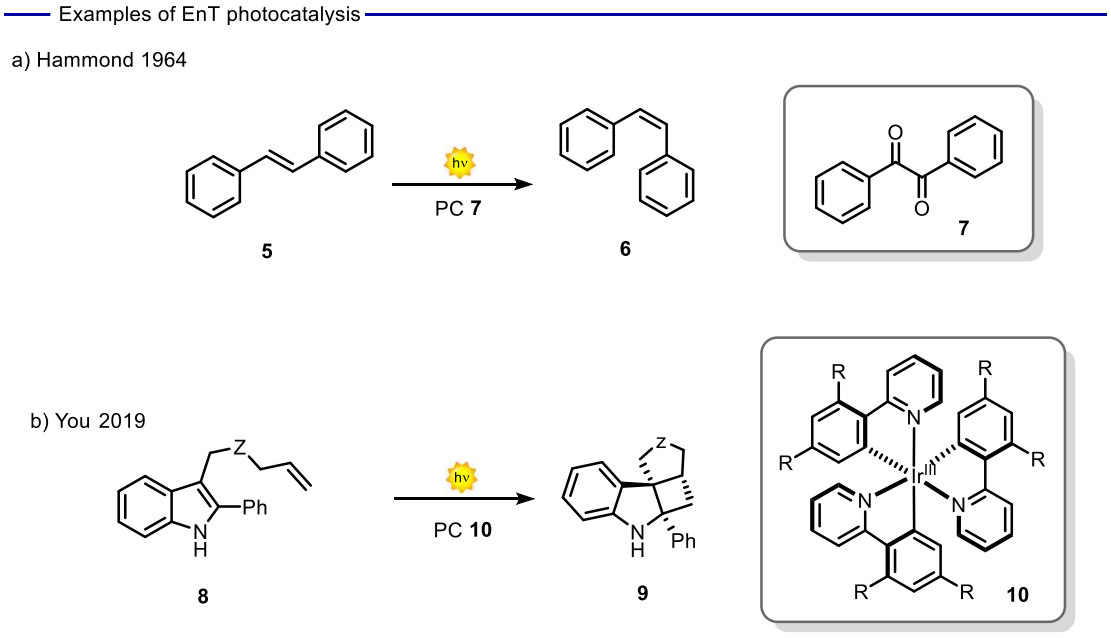

*Scheme 3. Examples of EnT photocatalysis with organic [Pitro,23] (**7**) and metal-based [Pietro,24] (**10**) photosensitisers.*

Notably, the use of photocatalysts with high triplet energies—whether transition-metal complexes or carefully designed organic sensitizers—has expanded the range of accessible substrates. Modern developments have introduced purely organic triplet sensitizers with triplet energies exceeding 60 kcal·mol^{-1}, allowing activation of challenging substrates while avoiding the cost and sustainability concerns of precious metals.[25]

In summary, EnT photocatalysis represents a versatile and selective activation mode that overcomes many intrinsic limitations of direct photochemistry. By exploiting the long-lived triplet state of a photocatalyst and the Dexter energy transfer mechanism, it enables controlled access to reactive triplet states in substrates that are otherwise difficult to excite directly. This strategy continues to inspire new synthetic applications, particularly in contexts where mild, visible-light-driven activation is crucial for functional group compatibility and reaction selectivity.

1.2. Strain release chemistry

In 1885, Adolf von Baeyer introduced the concept of "ring-strain," proposing that cyclic organic compounds whose bond angles deviate from the ideal tetrahedral angle of 109.5° are inherently destabilized, leading to significant reactivity and a tendency toward ring-opening transformations.[26] This departure from optimal geometry elevates the internal energy of small ring systems, such as cyclopropanes and cyclobutanes, rendering them more reactive than their open-chain analogues.[27] Subsequent theoretical and experimental work refined this foundational idea by identifying additional contributors to molecular strain: bond length distortions, torsional or Pitzer strain, non-bonded (transannular) interactions, and energy effects due to rehybridization. Collectively, these factors account for distinct destabilizations that vary with ring size and composition.[28]

The quantification of strain energy is typically achieved by comparing the experimentally determined heat of formation (ΔH_f) of a molecule with the value expected for a hypothetical strain-free analogue of identical composition. The difference between these two values provides a direct measure of the intrinsic strain energy of the system, offering a unified scale for comparing structurally diverse scaffolds. From a thermodynamic perspective, reactions of strained molecules are generally driven by the release of this excess enthalpy, leading to products with lower overall energy (negative ΔH). However, strain alone does not guarantee reactivity: the free energy profile of the transformation (ΔG) and the height of the activation barrier ($\Delta G^{\ddagger}$) are decisive. As highlighted by the Hammond postulate, strained molecules tend to display early transition states, where partial relief of strain lowers the barrier and enhances reactivity. Conversely, in cases where the transition state retains much of the original strain, even a strongly favorable thermodynamic driving force ($\Delta G \ll 0$) may not translate into a correspondingly low activation energy, and the reaction can remain sluggish.[29]

In modern organic chemistry, highly strained small bicyclic and tricyclic structures—such as bicyclo[1.1.1]pentanes (BCPs), bicyclo[1.1.0]butanes (BCBs), 1-azabicyclo[1.1.0]butanes (ABBs), and bicyclo[2.1.0]pentanes (housanes)—have gained prominence as bioisosteres in medicinal chemistry. Incorporation of these rigid, saturated motifs promotes increased three-dimensionality, metabolic stability, aqueous solubility, and reduced off-target binding, while preserving useful exit vectors typical of unsaturated systems. These features enhance both clinical success rates and patent diversification via exploration of synthetic chemical space.[30]

The exceptional reactivity of these systems is directly linked to their high ring strain energies (Scheme 4), which range from 98–113 kcal·mol^{-1} for [1.1.1]propellane (**11**), to ~66 kcal·mol^{-1} for bicyclo[1.1.0]butane (**12**) and ABB (**13**), and ~55 kcal·mol^{-1} for housane (**14**).[28] Upon bond cleavage, a significant fraction of this stored energy is released, thereby lowering the barrier to transformation and providing a powerful thermodynamic driving force.

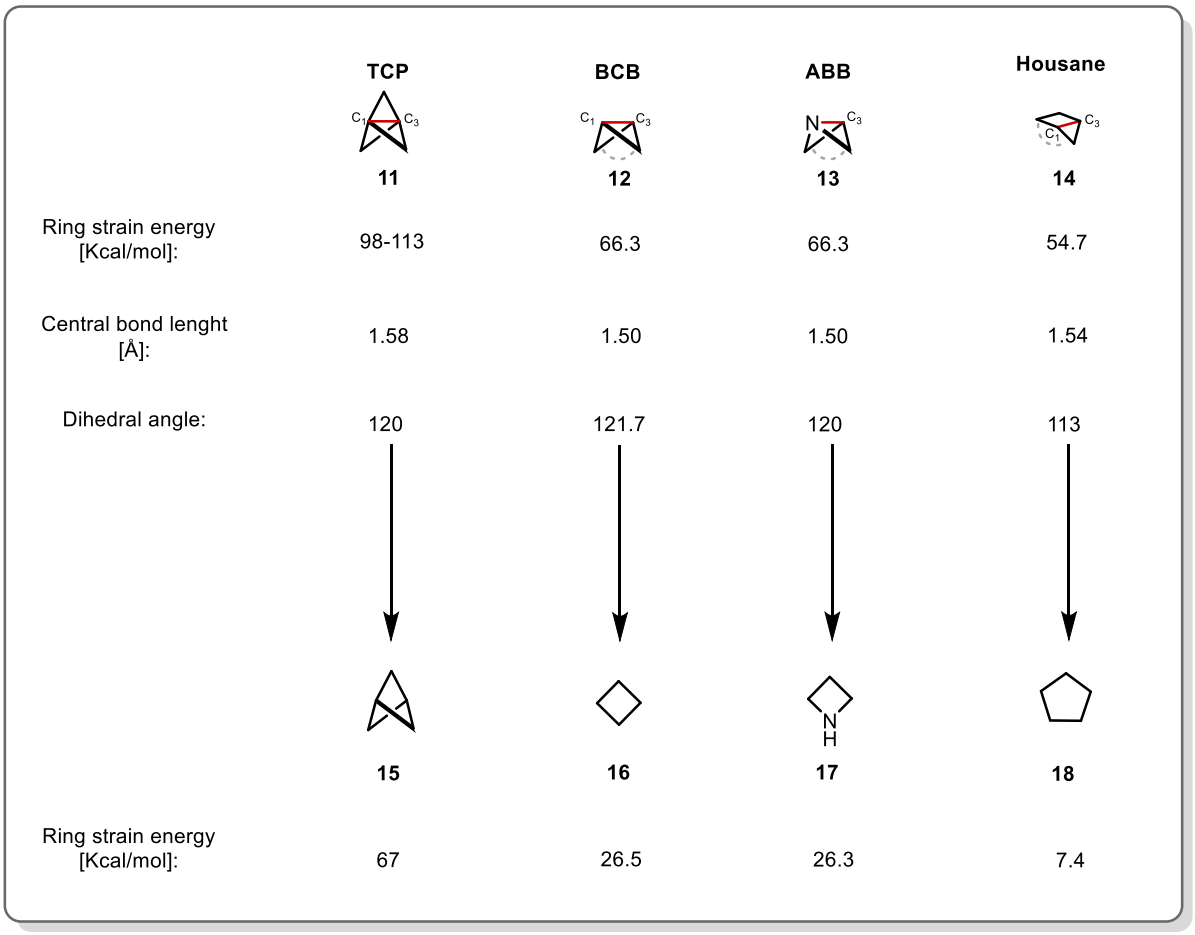

Scheme 4 Characterization and reactivity of strain-release compounds.

A particularly distinctive feature of these motifs lies in their central bridging bonds. In the case of [1.1.1]propellane (**11**), the character of the C1–C3 bond has been the subject of long-standing debate, with early studies unable to clearly distinguish between an ionic or covalent description. Eventually, it was classified as a charge-shift bond, with electron density delocalized in a manner intermediate between classical covalent and ionic interactions. Cleavage of this unusual bond releases a substantial fraction of the stored strain energy, thereby enabling the broad and often "omniphilic" reactivity that makes such systems uniquely versatile. [31,32]

To summarize, strain-release chemistry leverages the stored energy in small, rigid ring systems to drive transformations that are otherwise kinetically or thermodynamically challenging. These structures act as "spring-loaded" entities—release of strain offers a powerful thermodynamic push to facilitate bond cleavage and new bond formation. Importantly, such strained cyclic cores are not limited to a single reaction paradigm. They can engage in polar (thermal) processes, such as nucleophilic or electrophilic ring-opening, as well as radical-mediated processes, such as photochemical transformations. The dual applicability in both thermal and photoinduced contexts sets the stage for a versatile repertoire of synthetic methodologies, which will be explored in the subsequent sections addressing radical-mediated strain release and thermal strain release strategies.

1.2.1. Strain-Release Photocatalysis

The advent of visible-light photocatalysis has revolutionized modern organic synthesis by enabling radical processes under mild conditions, with broad functional group tolerance and high chemoselectivity. When combined with strained small-ring systems, photocatalysis provides an effective strategy. The strain energy stored in these systems couples with the controlled generation of radical intermediates to promote bond disconnections that are otherwise difficult to achieve. This synergy has given rise to the field of strain-release photocatalysis, in which light-induced cleavage of strained bonds enables the synthesis of structurally complex molecules.

At the conceptual level, the appeal of this strategy lies in the confluence of two complementary factors. First, strained systems such as bicyclo[1.1.1]pentane (BCP) and bicyclo[1.1.0]butane (BCB), along with their analogues, possess large reservoirs of internal energy that can be unlocked through selective bond cleavage. Second, photocatalysis provides precisely the activation mode required to generate reactive radical species, either via single-electron transfer (SET) or energy-transfer pathways, without recourse to harsh reagents or conditions. As a result, photoredox strain-release transformations have become an important strategy for the selective functionalization of otherwise inert systems, with applications ranging from methodology development to medicinal chemistry.[28,29] Historically, one of the earliest demonstrations of photoredox strain-release reactivity was reported by Bunker in 2011 (Scheme 5a), who described the visible-light mediated opening of [1.1.1]propellane under photoredox catalysis.[33]

This study showed that the central C1–C3 bond of propellane can undergo homolytic cleavage upon photoactivation, generating radical intermediates that can be trapped to give functionalized bicyclo[1.1.1]pentanes. The significance of this work extended beyond methodology: it demonstrated that the unique “spring-loaded” character of TCP could be exploited under photocatalytic conditions, thus introducing the broader concept of strain-release photoredox chemistry.

Building on this foundation, Molander and co-workers reported the efficient preparation of alkyl- and (hetero)aryl-substituted BCP derivatives under photoredox conditions (Scheme 5b),[34] as well as complementary approaches for the synthesis of BCP–alkyl amines, further broadening the portfolio of accessible scaffolds (Scheme 5c).[35]

In addition, Dell’Amico and co-workers in 2023 reported a visible-light-mediated atom transfer radical addition (ATRA) of difluoroalkyl halides to TCP (Scheme 5b).[36] By exploiting photocatalyst-mediated SET processes, they achieved selective cleavage of the strained C–C bond, enabling the efficient incorporation of difluoroalkyl groups into the bicyclo[1.1.1]pentane motif. This transformation quickly became a benchmark in the field, illustrating how the merger of photocatalysis and strain release could give rise to highly useful building blocks for medicinal chemistry.

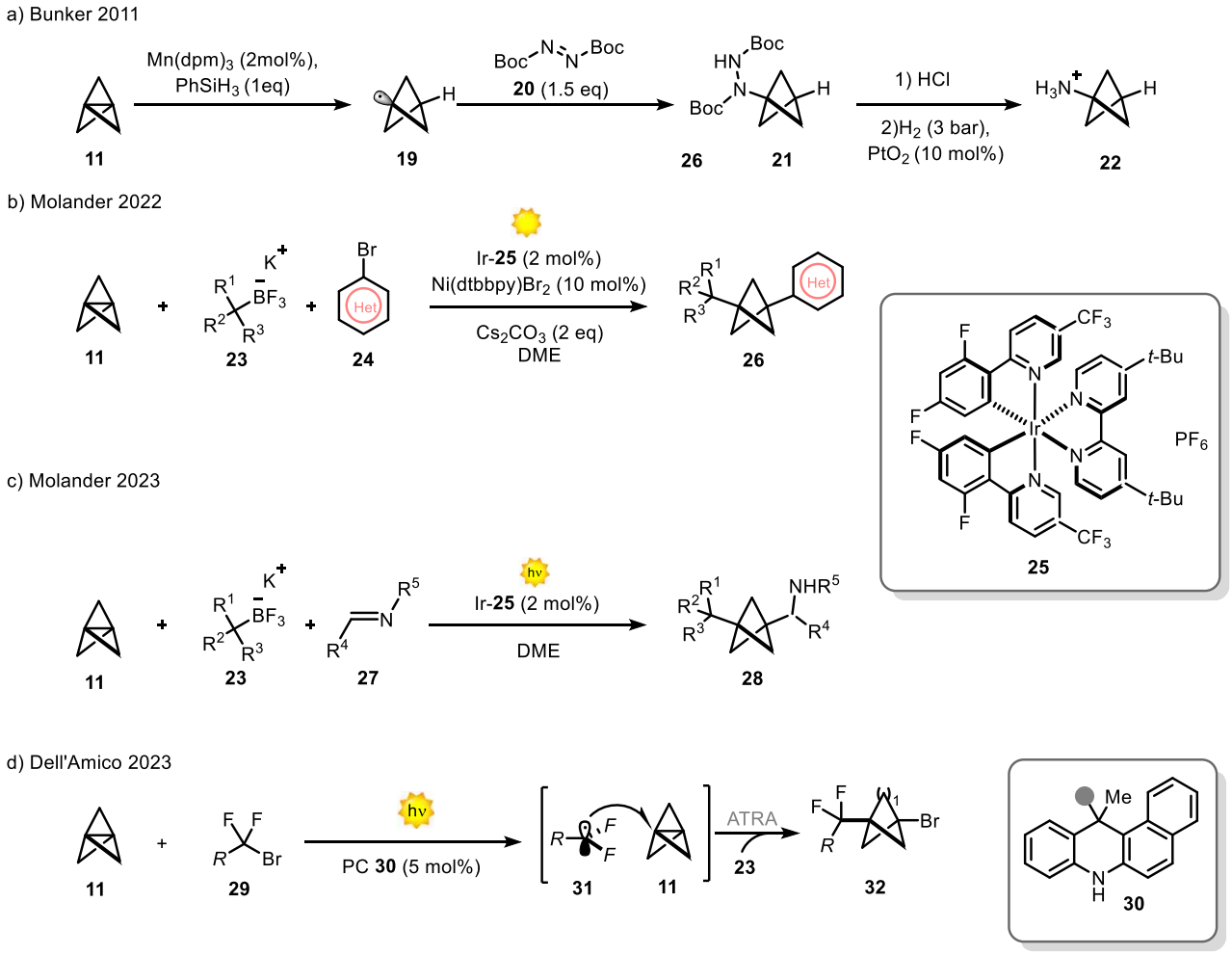

Scheme 5. Historical and modern developments in photocatalytic strain-release functionalizations of [1.1.1]propellane.

The case of bicyclo[1.1.0]butane (BCB) provides a complementary perspective. With a strain energy of ca. 66 kcal·mol^{-1}, BCB represents one of the most strained bicyclic systems known. Photocatalysis offers a pathway to harness this energy through cleavage of the central C1–C3 bridging bond, producing radical intermediates with broad reactivity. In contrast to propellane chemistry, which has been widely explored, photocatalytic transformations of BCBs are comparatively less developed but are now rapidly gaining attention.

For instance, Aggarwal and co-workers showed that BCB–boronate complexes behave as alkene analogues, undergoing radical additions at the strained bridging bond under visible-light irradiation to furnish functionalized products with high diastereoselectivity (Scheme 6a).[37]

In a complementary vein, Ernouf and co-workers reported a photoredox-mediated decarbonylative alkylation of BCB derivatives (Scheme 6).[38] Together, these studies illustrate how strain-release photocatalysis can unlock the rich reactivity of BCB structures and broaden their synthetic utility.

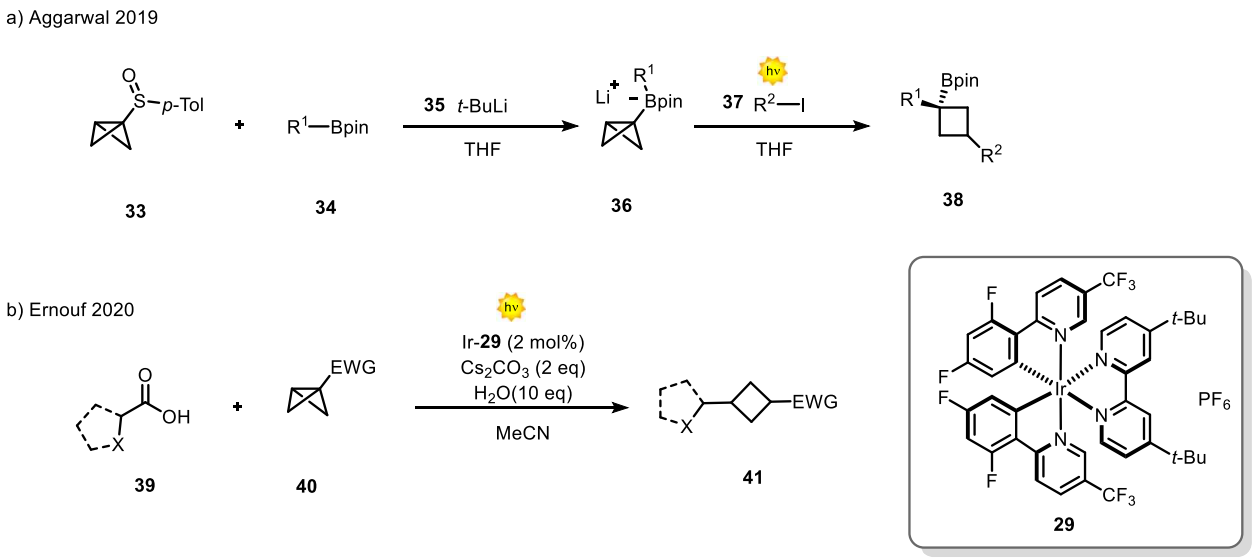

Scheme 6. Selected examples of photocatalytic strain-release functionalizations of bicyclo[1.1.0]butane (BCB).

Closely related to BCB are the 1-azabicyclo[1.1.0]butanes (ABB), which share similar strain characteristics and structural features, with the incorporation of nitrogen having a profound influence on their electronic properties. In particular, the presence of a bridging N atom alters the acidity and electronic polarization of the structure, suggesting that ABBs could be equally well-suited for strain-release photocatalysis. However, despite these parallels, no photocatalytic strain-release examples have yet been reported for ABBs. This absence highlights a significant gap in the current methodology and identifies ABBs as a fertile ground for future research exploration. Their reactivity under photocatalytic conditions, while still to be demonstrated, promises to open new directions in strain-release chemistry—an aspect that will be directly relevant to the experimental work described in chapter III. Beyond these archetypal structures, strain-release photocatalysis has also enabled access to more intricate architectures such as bicyclo[2.1.1]hexanes (BCHs) and oxa-BCHs. In particular, Glorius[39] and Brown[40] independently developed strategies for formal [2π + 2σ] cycloadditions of BCBs with unsaturated partners, exploiting triplet–triplet energy transfer (Scheme 7).

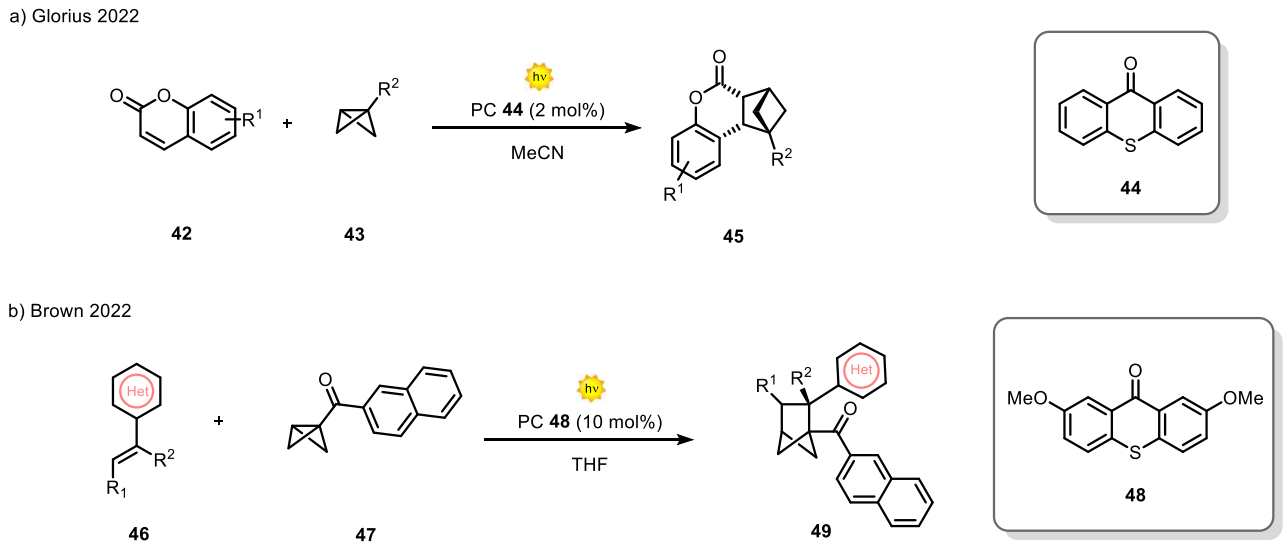

Scheme 7. Selected examples of photocatalytic [2π + 2σ] cycloadditions of BCBs with unsaturated partners.

These studies are conceptually significant, as they demonstrate how energy-transfer photocatalysis can activate highly strained BCB scaffolds. The resulting reactivity can be merged with heteroaryl or alkene partners, expanding the synthetic space accessible through strain-release chemistry. In both cases, the release of ring strain lowers the effective activation barrier, making bond cleavage not only thermodynamically favorable but also kinetically accessible under mild visible-light irradiation. Taken together, these advances show how the combination of photocatalysis with the intrinsic reactivity of strained small-ring systems has established a robust and versatile methodology. The historical development—from Bunker's pioneering 2011 photoredox opening of [1.1.1]propellane to Dell'Amico's difluoroalkylation ATRA of [1.1.1]propellanes—shows the growing power and flexibility of this approach. Beyond methodology, the implications are profound: photocatalytic strain release enables access to functionalized, three-dimensional scaffolds of direct relevance to discovery-oriented synthesis. As the field continues to mature, the incorporation of new strained systems—including ABBs, which remain largely unexplored under photocatalytic conditions—promises to further expand the scope and impact of strain-release photocatalysis.

1.2.2. Thermal strain release

Whereas visible-light photocatalysis enables access to high-energy open-shell manifolds under exceptionally mild conditions, it is important to recognize that strain release can also be triggered exclusively by heating, without recourse to photons, transition metals, or external reagents. In such cases, the stored enthalpy of the strained structure is sufficient—once the appropriate activation barrier is surmounted—to drive unimolecular bond scission or pericyclic rearrangements that relieve angular and torsional distortion. As emphasized in recent overviews, the reactivity of strained systems reflects a balance of thermodynamic and kinetic factors. Ring strain provides the driving force, while the accessibility of the transition states determines whether a purely thermal pathway can proceed at practical temperatures.[41] Accordingly, thermal strain release represents a complementary activation mode, one that relies solely on heating to access the stored energy of strained frameworks. From a mechanistic perspective, thermally induced transformations of strained rings usually follow two main courses. The first involves unimolecular fragmentations or bond reorganizations, which may

proceed through diradicaloid or asynchronous pathways. The second includes pericyclic processes such as retro-Diels–Alder (rDA) reactions, where product formation is facilitated by the relief of geometric strain. Because no external reagents are involved in the rate-limiting step, these reactions offer a direct view of the intrinsic stability of strained structures and of the energy profile that governs their rearrangements.[42] In practice, they also offer strategic opportunities in synthesis. A molecule can be equipped with a spring-loaded unit and later triggered by simple heating, providing modular access to ring-opened or reorganized scaffolds, in some cases resembling a protecting-group strategy. A paradigmatic case is the thermal rearrangement of [1.1.1]propellane. In a definitive gas-phase study, Szeimies, Walsh, and co-workers established that neat heating of [1.1.1]propellane leads unimolecularly to 1,2-dimethylenecyclopropane (**50**) (with equilibration to ethenylidenecyclopropane (**51**)), without evidence for chain-radical pathways under carefully controlled conditions (Scheme 8).[43]

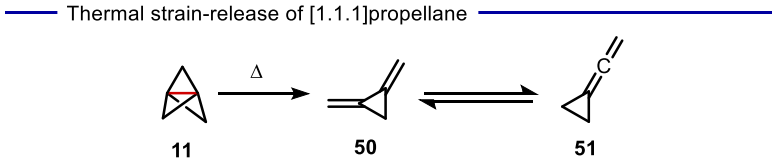

*Scheme 8. Thermal rearrangement of [1.1.1]propellane (**11**) to 1,2-dimethylenecyclopropane (**50**) and ethenylidenecyclopropane (**51**) as reported by Szeimies.*

Kinetic analysis furnished an activation barrier of ~39–40 kcal·mol^{-1}, consistent with a strongly asynchronous bond reorganization that liberates a substantial fraction of the intrinsic strain. Notably, trace by-products such as methylenecyclobutene or acyclic polyenes were shown to arise from heterogeneous surface processes, rather than the intrinsic thermal pathway, underscoring the genuinely heat-only character of the rearrangement. The outcome highlights a broader theme in propellane chemistry, namely that thermal strain release often directs the system toward multiply substituted alkenes.[42] This principle extends beyond propellanes to other strained frameworks, where diradicaloid or pericyclic pathways can similarly harness strain energy under heat-only regimes. In particular, concerted retro-Diels–Alder (rDA) pathways and Alder–ene rearrangements become feasible through the enthalpic dividend of strain release, enabling ring-expanded or ring-opened motifs without the need for extrinsic activators. A representative case is the work of Wipf and co-workers, who showed that allyl amine–substituted bicyclo[1.1.0]butanes undergo intramolecular Alder–ene reactions upon heating, delivering [4.3] spirocyclic pyrrolidines with high stereoselectivity (Scheme 9).[44]

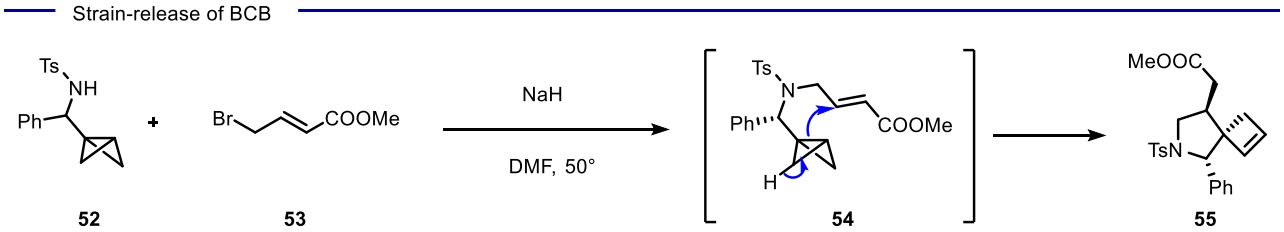

*Scheme 9. Wipf's example of thermal strain-release reactivity: bicyclo[1.1.0]butane **54** rearranges upon heating to give cyclopentene **55**.*

This reactivity proved general across several substitution patterns, including propargyl alcohol and α,β-unsaturated aldehyde derivatives, underscoring how thermal strain release can drive ene-type rearrangements toward complex spirocyclic frameworks.[45] These examples show that the strain of small bicyclic systems can be relieved by pericyclic reactions, affording reorganized products without the need for external reagents. Among strained molecules, oxabicyclic systems are notable because their oxygen bridge and rigid topology

favor retro-Diels–Alder fragmentations. These reactions extrude a small, stable co-product (most often furan) upon heating, and proceed through purely thermal activation. Foundational studies by Verlaak and Marita demonstrated that oxabicyclic intermediates can act as spring-loaded scaffolds: once assembled, they undergo clean retro-Diels–Alder fragmentation upon heating, extruding furan and delivering ring-opened products in the absence of metals or external reagents.[46,47] Several representative cases highlight the utility of this principle. In one example thermal retro-Diels–Alder fragmentation of adduct **56**, derived from N-substituted maleimides, furnished the corresponding unsaturated imides, including N-acetoxymaleimide (Scheme 10a), upon heating at 150–300 °C.

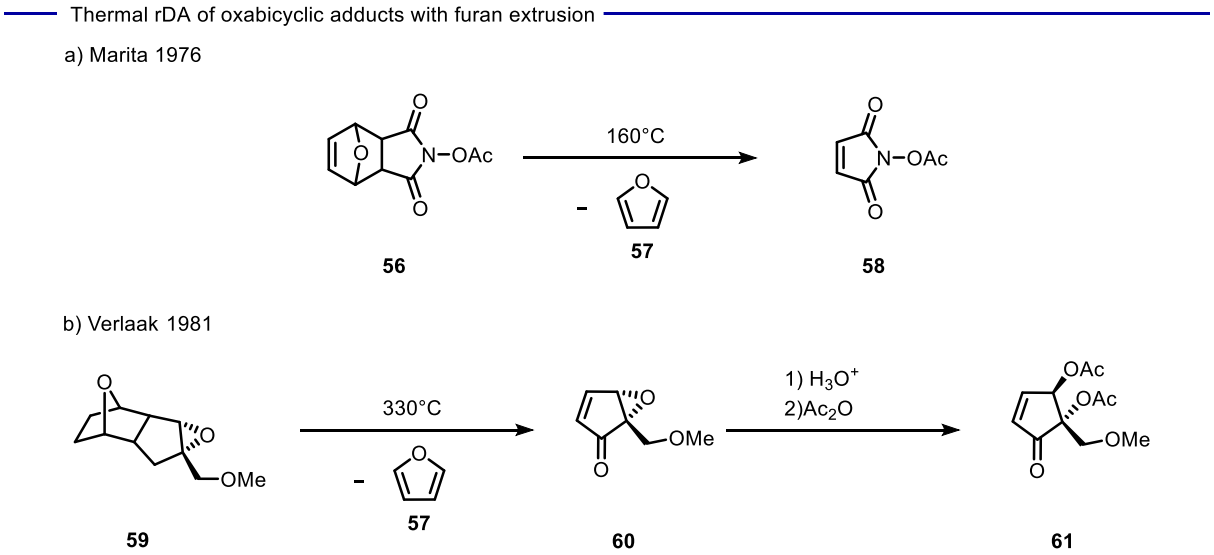

Scheme 10. Selected examples of thermal retro-Diels–Alder fragmentation of oxabicyclic adducts with furan extrusion.

Similarly, furan-derived oxabicyclic adducts were employed to access cyclopentadienone epoxides: under pyrolytic conditions (≈330 °C), the retro-Diels–Alder fragmentation of adduct **59** furnished epoxide **60** in nearly quantitative yield, which could then be elaborated into epipentenomycin derivatives such as **61** (scheme 10b).[48]

Taken together, these heat-only case studies—ranging from propellane thermolysis to oxabicyclic retro-Diels–Alder—demonstrate that thermal strain release is a robust, conceptually distinct activation mode. Its strengths are the limited need for reagents, the clear mechanistic pathways (unimolecular or pericyclic), and the broad functional-group tolerance that results from the absence of external reactants in the rate-limiting step. At the same time, practical limitations merit consideration. First, temperature windows can be relatively high for some scaffolds, reflecting the need to surmount sizeable activation barriers despite favorable thermodynamics; careful control of phase, pressure, and reactor surfaces may be required to avoid heterogeneous side pathways.[43,46]

Second, chemo- and regioselectivity are encoded primarily by intrinsic conformational and electronic bias, leaving less room for the fine-tuning that catalysts afford. Nevertheless, when strategically embedded within synthetic sequences, heat-only ring openings and rearrangements serve as reliable strategies for the temporary "masking" of reactive units that can later be unveiled through controlled heating. In this way, thermal strain release not only provides access to otherwise challenging molecular architectures but also introduces a level of strategic flexibility that can be harnessed in complex molecule construction.[42,47]

1.3. Reactions with Transition Metals

Transition-metal catalysis represents one of the most transformative developments in modern synthetic chemistry. The unique ability of d-block elements to shuttle between multiple oxidation states, adopt variable coordination geometries, and stabilize otherwise fleeting organometallic intermediates has enabled the discovery of highly efficient bond constructions across academic and industrial settings. Industrial processes such as olefin polymerization, hydroformylation, hydrogenation, and metathesis exemplify how transition-metal catalysis has reshaped chemical manufacturing. In parallel, the widespread adoption of cross-coupling reactions has revolutionized molecular construction in both natural product synthesis and pharmaceutical discovery. The scientific impact of these advances is reflected in Nobel Prizes recognizing olefin metathesis (2005) and palladium-catalyzed cross-couplings (2010).[49,50]

At a conceptual level, the field is defined by the capacity of transition metals to couple thermodynamic driving forces with kinetic control, thereby achieving transformations with high chemo-, regio-, and stereoselectivity.[51] In parallel, recent years have witnessed a strong shift toward earth-abundant first-row metals, motivated by considerations of cost, toxicity, and sustainability. Iron, cobalt, nickel, copper, and manganese are now widely studied in catalytic contexts once dominated by late transition metals, with breakthroughs spanning hydrogenations, dehydrogenations, C–H activations, and electrocatalytic transformations.[52]

The fundamental basis of transition-metal reactivity lies in several key features. Their redox flexibility allows facile movement between oxidation states, enabling the activation of strong covalent bonds and the turnover of catalytic cycles. Their ability to adopt diverse coordination geometries stabilizes reactive intermediates while accommodating the demands of incoming substrates. These properties converge in a set of canonical elementary steps that underpin virtually all catalytic manifolds. Oxidative addition (OA) incorporates an electrophile—typically a halide or pseudohalide—into the coordination sphere of the metal, raising its oxidation state and setting the stage for subsequent bond-forming events. Reductive elimination (RE) is the microscopic reverse, forging a new σ-bond between two ligands and regenerating the lower-valent active species; it is this step that ultimately delivers the target C–C or C–heteroatom linkage. Migratory insertion (MI) channels unsaturated fragments such as alkenes, alkynes, or carbonyls into metal–ligand bonds, generating new organometallic intermediates in ways that often define the regio- and stereochemical course of the reaction. β-Hydride elimination (β-HE), often coupled to migratory insertion, allows the re-formation of double bonds . Together, these steps form a mechanistic “toolkit” that explains the versatility and predictability of organometallic catalysis, while also offering synthetic chemists a modular logic for designing transformations.[53,54] A further dimension of control arises from the ligands that surround the metal center: by tuning their steric and electronic properties, ligands modulate the rates, selectivities, and even the accessible pathways of catalytic cycles. This modularity of ligand design has been central to expanding the scope of transition-metal catalysis, allowing chemists to adapt a common mechanistic framework to highly diverse substrates and reaction environments.[55]

1.3.1. Palladium chemistry

Among the many transition metals that have reshaped modern organic synthesis, palladium occupies a uniquely prominent role. Few elements have had such a transformative effect on how chemists think about bond construction, to the point that "palladium catalysis" has become almost synonymous with modern cross-coupling. The recognition of this achievement with the 2010 Nobel Prize in Chemistry, awarded to Heck, Negishi, and Suzuki, underscored both the practical utility and the conceptual depth of this field.[50]

The historical growth of palladium catalysis is well illustrated by bibliometric analyses that trace the extraordinary rise in publications from the 1970s onward (Figure 4).[56] What had been an esoteric curiosity confined to a handful of groups rapidly expanded into a central pillar of organic methodology within two decades. This surge reflects not only the accumulation of individual reactions—Heck,[57] Suzuki–Miyaura,[58] Stille,[59] Sonogashira,[60] Buchwald–Hartwig C–N coupling[61,62]—but also the clarification of a shared mechanistic framework that rendered Pd catalysis clear, predictable, and modular. The impact extended far beyond academic curiosity: cross-coupling methods quickly diffused into pharmaceutical discovery, materials science, and fine chemicals manufacturing, making palladium one of the most industrially exploited catalysts of the late 20th century.[50,51,63]

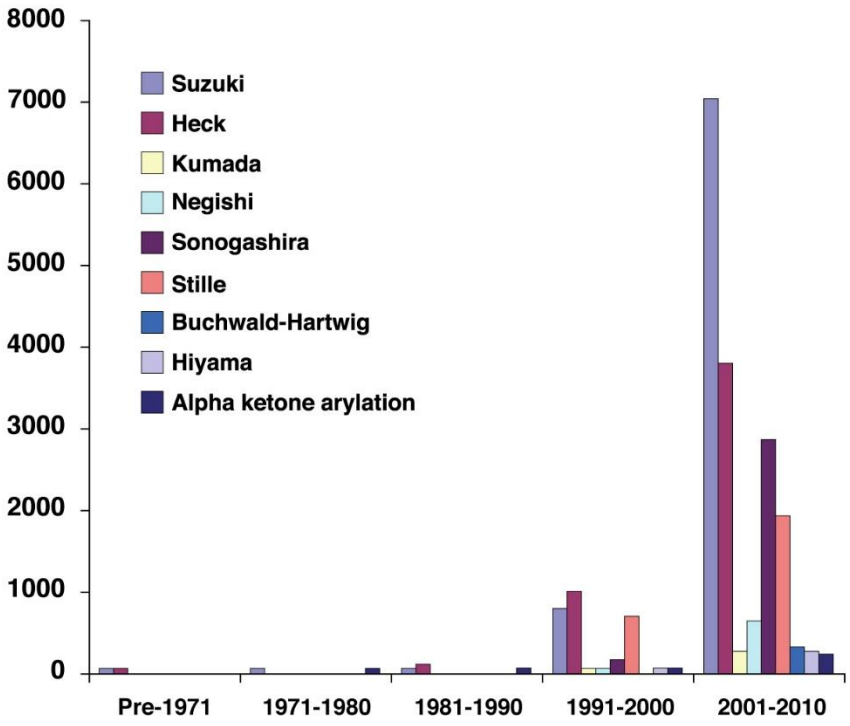

Figure 4. Increase in scientific publications and patents related to named metal-catalyzed cross-coupling reactions.

As summarized in Scheme 11, the palladium cross-coupling manifold presents a unifying design in which the shared entry event is oxidative addition of an aryl (or vinyl) halide/pseudohalide to a catalytically active Pd(0) complex. From this common gateway, the cycle bifurcates into two archetypal pathways.

In the Mizoroki–Heck branch, the Pd(II) species coordinates an alkene and undergoes syn migratory insertion into the Pd–C bond. The regioselectivity of this step depends on the substitution pattern of the alkene, the ligand environment, and the reaction conditions employed. The resulting alkyl–Pd intermediate then undergoes β-hydride elimination to release the substituted alkene, followed by base-assisted removal of HX from the Pd–H–X complex, which restores Pd(0) to close the cycle.[64]

In contrast, in Suzuki–Miyaura and Negishi couplings—together with the Corriu–Kumada, Stille, and Hiyama variants—the oxidative addition adduct engages in transmetalation with the organometallic nucleophile (B, Zn, Mg, Sn, Si). This delivers a bis-organopalladium(II) intermediate that undergoes reductive elimination to forge the new C–C bond, again regenerating Pd(0).[58]

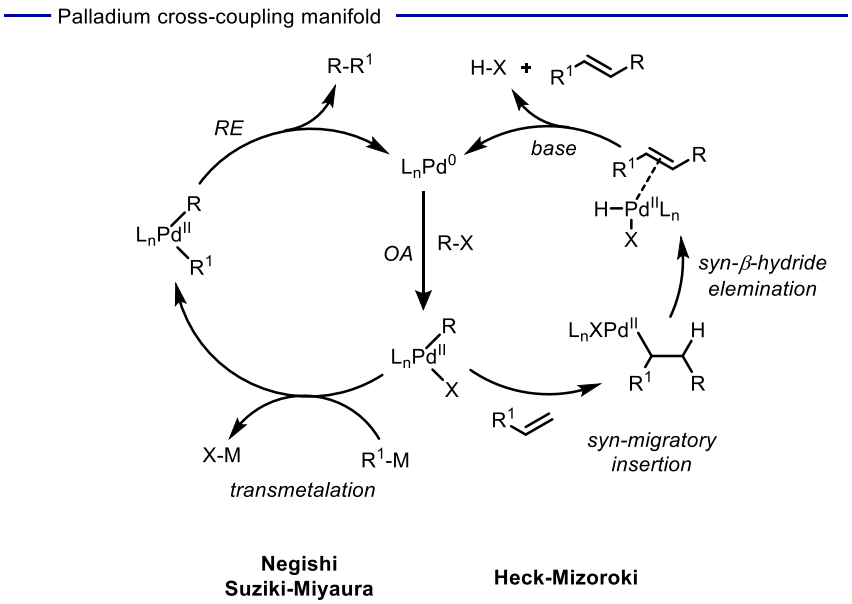

Scheme 11. General mechanistic pathways of palladium catalysis: Heck–Mizoroki vs. Negishi/Suzuki–Miyaura.

Conceptually, oxidative addition defines the entry point of the cycle. From there, the catalyst can proceed through alkene insertion and β-hydride elimination, as in Heck-type processes, or through transmetalation and reductive elimination, as in classical cross-couplings with preformed organometallic partners. Taken together, these elementary events— oxidative addition, migratory insertion, β-hydride elimination, transmetalation, and reductive elimination—constitute the "mechanistic language" of palladium chemistry. Their modularity means that seemingly disparate transformations can be rationalized as different permutations of the same fundamental processes. This insight is one of the main reasons why palladium catalysis became so rapidly accessible and adaptable to synthetic chemists worldwide: it offered not just a collection of named reactions, but a coherent conceptual toolkit.

The emergence of palladium in organic chemistry can be traced back to the mid-20th century, when the element—first discovered by William Hyde Wollaston in 1803[65]—moved from an academic curiosity in coordination chemistry to a genuine catalyst for bond construction. A decisive turning point came in 1959 with the discovery of the Wacker process, in which ethylene (**62**) is oxidized to acetaldehyde (**63**) using a $PdCl_2$–$CuCl_2$ catalytic system under industrially scalable conditions (Scheme 12).[66]

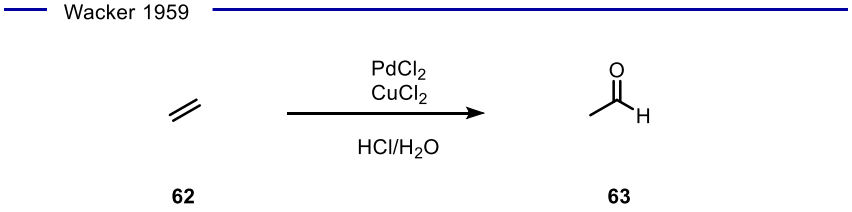

Scheme 12. The Wacker Process.

This transformation demonstrated for the first time that palladium could operate catalytically in homogeneous solution and set the stage for its broader use in organic synthesis. The Wacker oxidation remains not only a cornerstone of industrial chemistry but also a conceptual prototype for subsequent Pd-catalyzed oxidations.

Building on this precedent, researchers in the 1960s began to recognize that palladium's facility for oxidative addition and reductive elimination could be harnessed in C–C bond-forming reactions. Mizoroki (Scheme 13b) and independently Heck (Scheme 13a-c) showed that aryl halides could be coupled with alkenes under Pd catalysis to form substituted olefins.[57] This Mizoroki–Heck reaction soon emerged as a general strategy for functionalizing alkenes, establishing one of the earliest pillars of the cross-coupling canon.

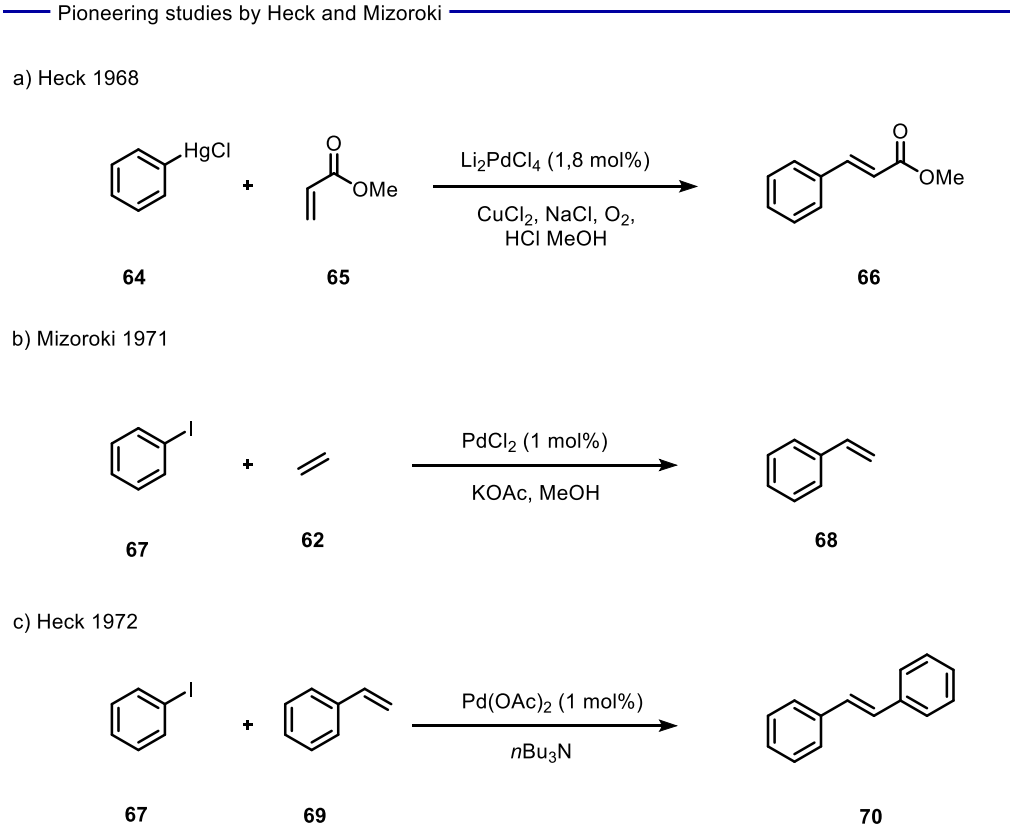

Scheme 13. The first palladium(II)-catalyzed coupling reactions.

The 1970s and early 1980s saw the explosion of cross-coupling methodologies in which palladium mediated the union of electrophilic halides/triflates with nucleophilic organometallic partners. Seminal breakthroughs included the Sonogashira coupling for terminal alkynes (Scheme 14a),[60] the Negishi coupling with organozinc reagents (Scheme 14 b),[67] the Suzuki–Miyaura coupling with organoboron compounds(Scheme 14c),[58] and the Stille coupling with organostannanes (Scheme 14d).[59] Collectively, these reactions established palladium as the unrivaled workhorse of synthetic organic chemistry, offering chemists a modular toolkit for forging bonds with unprecedented generality and predictability. By the 1990s, the reach of palladium catalysis expanded further with the development of C–N bond formation, most famously through the Buchwald–Hartwig amination (Scheme 14e).[61,62] These advances broadened the palette of accessible transformations, anchoring Pd not only in C–C but also in C–heteroatom bond construction. Thus, beginning with the industrial Wacker oxidation and continuing through decades of discovery in C–C and C–N coupling, palladium catalysis evolved from isolated case studies into a cohesive discipline. This historical trajectory underpins the modern perception of palladium as both a practical catalyst and a conceptual benchmark for organometallic chemistry. Beyond these now-classical cross-coupling paradigms, palladium catalysis has continued to evolve in directions that extend far beyond the reliance on prefunctionalized partners.

Among the most far-reaching of these advances is the direct activation of C–H bonds, which bypasses the need for halides or organometallic reagents altogether. Because of its conceptual and practical impact, C–H activation will be treated in detail in the following section.

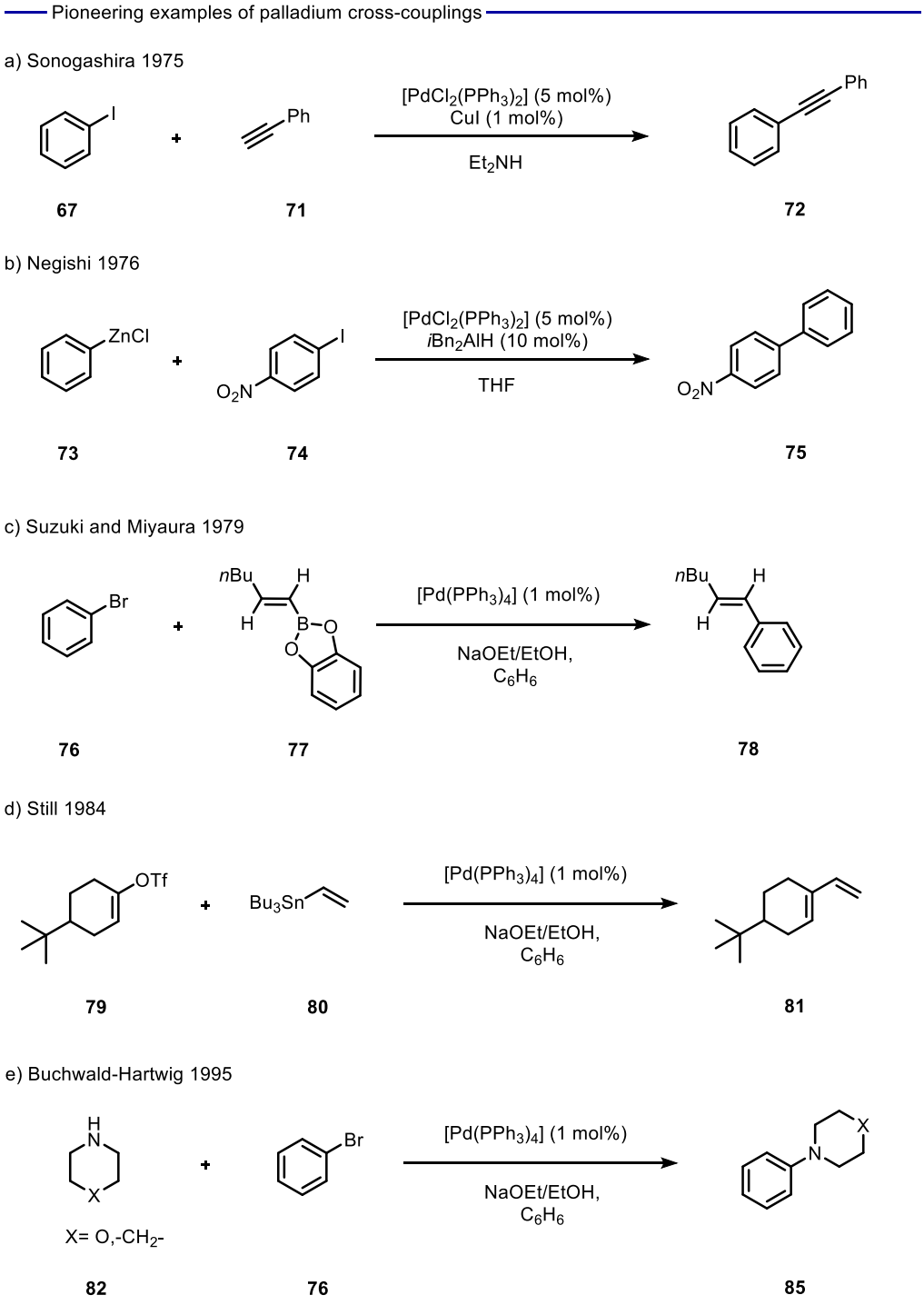

Scheme 14. Selected pioneering examples of palladium-catalyzed cross-coupling reactions, including Sonogashira, Negishi, Suzuki–Miyaura, Stille, and Buchwald–Hartwig couplings.

1.3.2. C–H Activation

The development of C–H activation as a synthetic strategy has redefined the scope of transition-metal catalysis. Its conceptual appeal emerges most clearly when contrasted with classical cross-coupling chemistry, which has dominated organic synthesis for decades. As illustrated in Scheme 15, cross-coupling requires two prefunctionalized partners: an electrophilic component, typically an aryl or vinyl halide/pseudohalide, and a nucleophilic organometallic reagent such as those based on boron, tin, silicon, or zinc.[54]

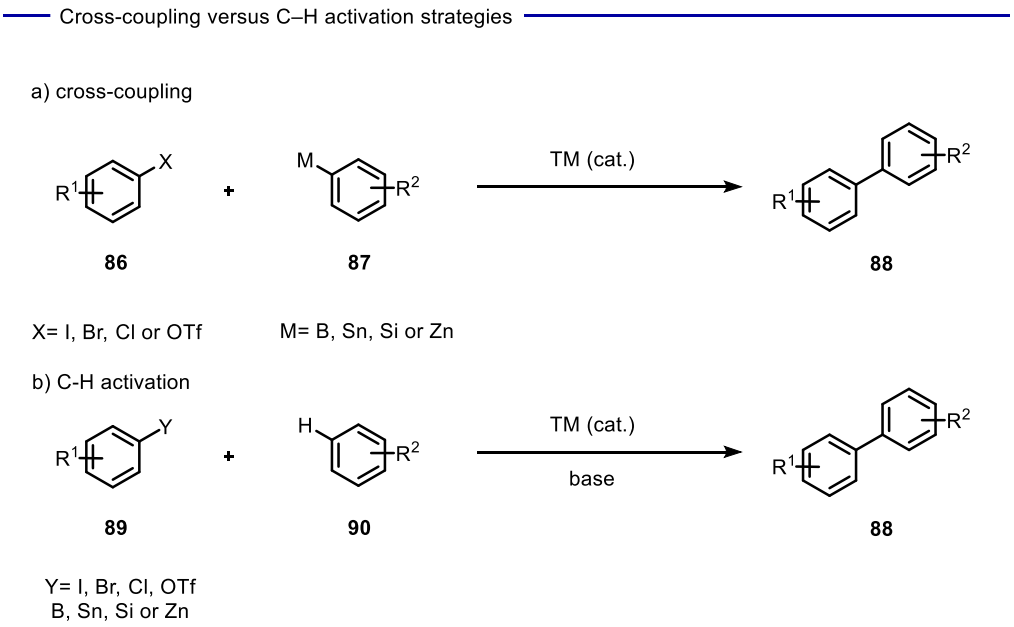

Scheme 15. Conceptual comparison between traditional cross-coupling (a) and C–H activation (b)

This prefunctionalization ensures high reactivity but comes at the cost of additional synthetic steps and waste generation. By contrast, C–H activation (or direct arylation) bypasses the need for dual prefunctionalization. Instead, it couples a prefunctionalized partner with a simple, unactivated arene, relying on the metal catalyst to cleave a specific C–H bond and incorporate it directly into the new C–C framework.[54] In practice, this makes the transformation more step- and atom-economical, allowing chemists to convert abundant hydrocarbons or heteroarenes into functionalized products directly. This shift also enables late-stage functionalization, a compelling feature for the diversification of complex natural products, pharmaceuticals, and conjugated organic materials. [68,69] Despite these clear advantages, C–H activation is not without challenges. The foremost limitation is regioselectivity: most arenes contain several inequivalent C–H bonds, many of which can interact with the transition-metal catalyst at similar rates. Achieving site selectivity, therefore, requires either intrinsic electronic/steric control or external elements such as directing groups.[70] Moreover, the act of cleaving a strong C–H bond and embedding it within a productive catalytic cycle demands careful orchestration of redox events, ligand environments, and reaction conditions. In this context, the use of bases is often crucial, as they facilitate C–H cleavage by assisting in proton abstraction, thereby lowering the energetic barrier for metalation and stabilizing key intermediates. Taken together, this conceptual contrast with cross-coupling highlights why C–H activation has emerged as both a complementary and, in some cases, superior strategy. It offers a new blueprint for molecular construction—one that transforms the ubiquitous yet inert C–H bond into a functional handle for catalysis.

In palladium-catalyzed C–H activation, several mechanistic pathways have been proposed to account for the formation of the key metal–carbon bond (Scheme 16). One possibility is oxidative addition, in which the C–H

bond undergoes formal insertion into the metal center, producing a high-valent intermediate that subsequently evolves to the cyclometalated species. An alternative is the electrophilic aromatic substitution (SEAr) pathway, where metalation proceeds stepwise: initial coordination of the metal generates a Wheland-type intermediate, followed by deprotonation by an external base to restore aromaticity and yield the palladacycle. Finally, the concerted metalation–deprotonation (CMD) pathway has become the most widely accepted model for Pd(II) catalysis. In this case, C–H cleavage and Pd–C bond formation occur in a single concerted step, assisted by a basic ligand such as acetate or carbonate. The CMD mechanism elegantly rationalizes the ubiquitous role of carboxylate additives and highlights how subtle geometric and electronic factors determine the feasibility of C–H bond activation.[71,72] Although CMD, SEAr, and oxidative addition represent the dominant paradigms, other possibilities, such as one-electron or two-electron oxidation events, have also been proposed, underscoring the mechanistic diversity of C–H activation.

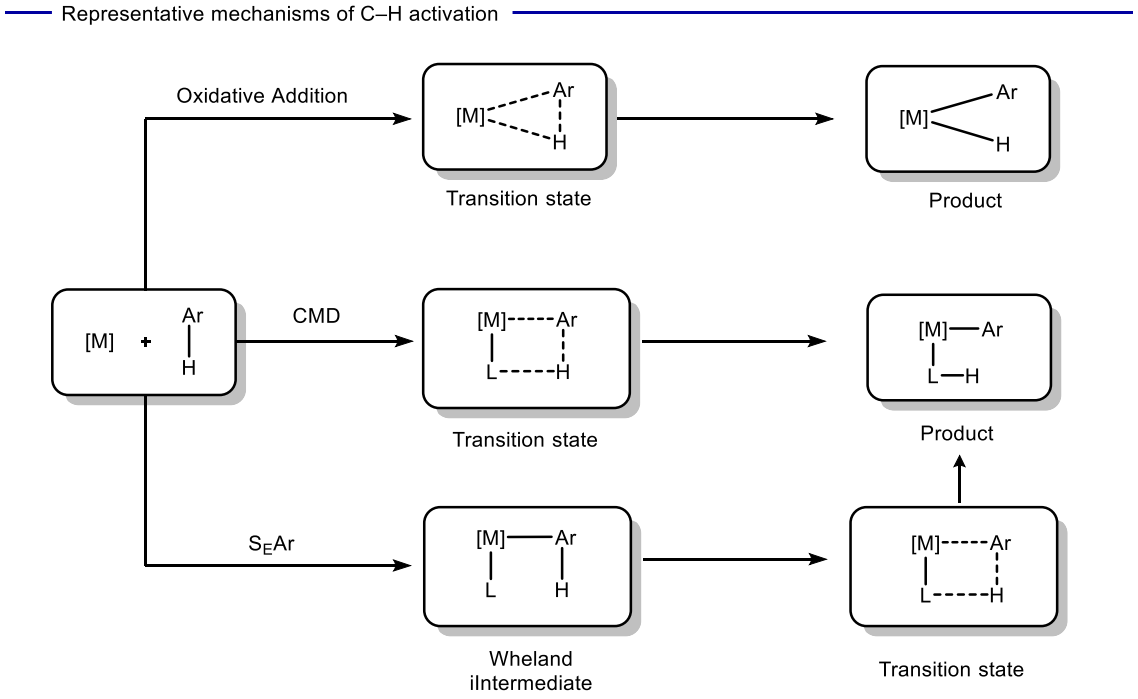

Scheme 16. General mechanistic pathways proposed for metal-mediated C–H bond cleavage.

With this framework in place, the field's evolution can be traced through a series of seminal case studies that demonstrated how palladium could translate these mechanistic principles into practical bond constructions.

One of the first demonstrations of ligand-directed C–H functionalization was reported using $Pd(OAc)_2$ together with $PhI(OAc)_2$ as the oxidant, which enabled the ortho-acetoxylation of arenes bearing coordinating nitrogen groups (Scheme 17).

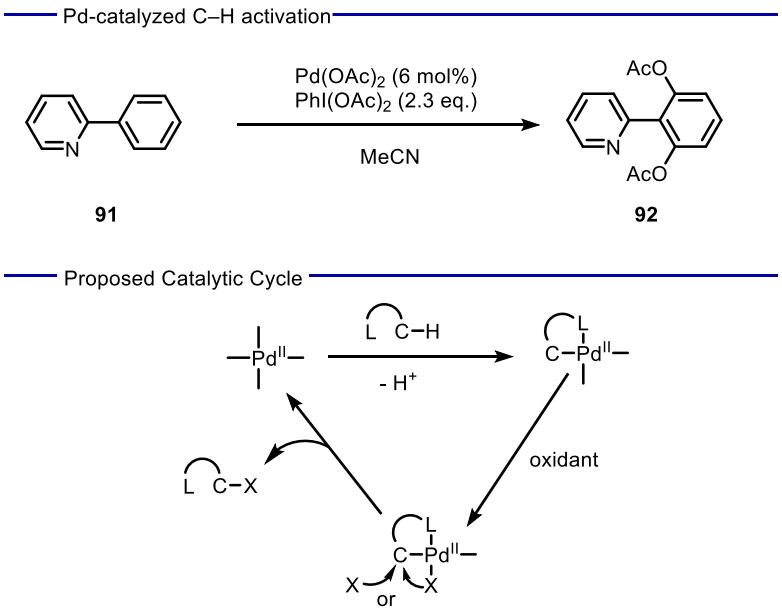

Scheme 17. Pd(II)-catalyzed ortho-acetoxylation of arenes with $PhI(OAc)_2$ and proposed catalytic cycle.

In this transformation, the directing group coordinates the Pd(II) center, allowing activation of the proximal C–H bond, after which the external oxidant delivers the acetate fragment to form the functionalized product.[73] This study provided a clear early example of how cyclopalladated intermediates could be intercepted by an oxidizing electrophile to achieve C–H oxygenation under relatively simple catalytic conditions. A different direction was established with the intramolecular activation of C(sp^3)–H bonds. In 1994, Dyker reported that palladium could mediate intramolecular C(sp^3)–H activation to assemble polycyclic scaffolds (Scheme 18).

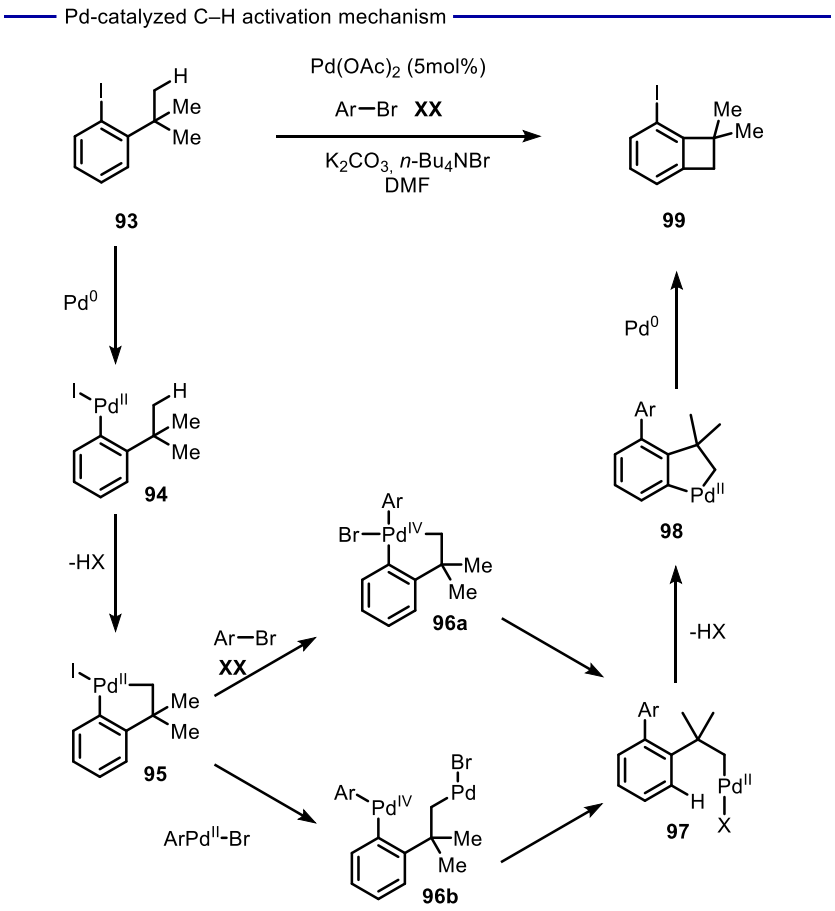

Scheme 18. Proposed catalytic cycle for the Pd-catalyzed intramolecular C(sp³)–H activation of 2-iodo-tert-butylbenzene leading to the formation of 1,2-dihydrocyclobutabenzene derivatives.

The process begins with oxidative addition of an aryl iodide to Pd(0), generating an aryl–Pd(II) complex (**94**). This species then undergoes intramolecular activation of a nearby C(sp³)–H bond, forming a five-membered palladacycle (**95**). From this key intermediate, two mechanistic routes have been considered. In the first, intermolecular coupling with an aryl bromide produces a Pd(II)/Pd(IV) (**96a**) sequence in which reductive elimination delivers the new C(sp²)–C(sp²) bond (**97**). In the second, supported by computational analysis, aryl transfer between the initial palladacycle and a [aryl–Pd(II)–Br] species generates a dinuclear Pd(II) complex (**96b**) that can then converge on the same product (**97**). In either case, a subsequent C(sp²)–H activation event and final reductive elimination complete the sequence, affording a 1,2-dihydrocyclobutabenzene derivative (**99**).[74]

1.4. Aim of the thesis

The introduction outlines the general principles of direct photochemistry and photocatalysis, the state of the art of strain-release chemistry, and a concise overview of palladium catalysis, as these represent the main themes developed throughout my PhD research. The body of the thesis is structured into three research chapters, each comprising a specific introduction, results and discussion, an experimental section, and conclusions.

Chapter II is devoted to a project in direct photochemistry, where iminium ions embedded within extended π-systems were designed to overcome intrinsic photophysical limitations and engage in [2+2] cycloadditions with high stereocontrol.

Chapter III focuses on the merger of photocatalysis with strain-release reactivity, leading to the synthesis of structurally complex and highly functionalised azetidines.

Finally, Chapter IV presents the work carried out during my visit to Professor Lautens' group at the University of Toronto. This project describes the development of a palladium-catalyzed approach to the enantioselective synthesis of spiroindenes, employing chiral oxabicycles both as acetylene substitutes and as structural motifs capable of transferring stereochemical information to the newly formed products.

Together, these three research directions reflect complementary strategies to expand the scope of modern catalysis and to address long-standing challenges in the selective construction of complex molecular frameworks

1.5. References

(1) Ciamician, G. The Photochemistry of Future. *Science* **1912**, *36* (926), 385–394.

(2) Mandigma, M. J. P.; Kaur, J.; Barham, J. P. Organophotocatalytic Mechanisms: Simplicity or Naïvety Diverting Reactive Pathways by Modifications of Catalyst Structure, Redox States and Substrate Preassemblies. *ChemCatChem* **2023**, *15* (11). https://doi.org/10.1002/cctc.202201542.

(3) Prier, C. K.; Rankic, D. A.; MacMillan, D. W. C. Visible Light Photoredox Catalysis with Transition Metal Complexes: Applications in Organic Synthesis. *Chem. Rev.* **2013**, *113* (7), 5322–5363. https://doi.org/10.1021/cr300503r.

(4) Balzani, A. J. V.; Barigelletti, F.; Campagna, S.; Belser, P.; Zelewsky, A. Von. Ru(II) Polypyridine Complexs: Photophysics, Photochemistry, Electrochemistry, and Chemiluminescence. *Coord. Chem. Rev.* **1998**, *57*, 85–277. https://doi.org/10.1053/euhj.1997.0770.

(5) Shaw, M. H.; Twilton, J.; MacMillan, D. W. C. Photoredox Catalysis in Organic Chemistry. *J. Org. Chem.* **2016**, *81* (16), 6898–6926. https://doi.org/10.1021/acs.joc.6b01449.

(6) Mayer, J. M. Understanding Hydrogen Atom Transfer : From Bond Strengths to Marcus Theory. **2011**.

(7) Bortolato, T.; Cuadros, S.; Simionato, G.; Dell'Amico, L. The Advent and Development of Organophotoredox Catalysis. *Chem. Commun.* **2022**, *58* (9), 1263–1283. https://doi.org/10.1039/d1cc05850a.

(8) Sumida, Y.; Ohmiya, H. Direct Excitation Strategy for Radical Generation in Organic Synthesis. *Chem. Soc. Rev.* **2021**, *50* (11), 6320–6332. https://doi.org/10.1039/d1cs00262g.

(9) Nau, W. Modern Molecular Photochemistry of Organic Molecules. by N. J. Turro, V. Ramamurthy, J. C. Scaiano. *ChemPhysChem* **2011**, *12* (13), 2496–2497. https://doi.org/10.1002/cphc.201000976.

(10) Braslavsky, S. E. Glossary of Terms Used in Photochemistry 3rd Edition: (IUPAC Recommendations 2006). *Pure Appl. Chem.* **2007**, *79* (3), 293–465. https://doi.org/10.1351/pac200779030293.

(11) Kaur, N. Photochemical Reactions as Key Steps in Five-Membered N-Heterocycle Synthesis. *Synth. Commun.* **2018**, *48* (11), 1259–1284. https://doi.org/10.1080/00397911.2018.1443218.

(12) Lakowicz, J. R. *Principles of Fluorescence Spectroscopy*.

(13) Leung, M. -k.; Luh, T.-Y. *[2+2] Cycloaddition*; 2007.

(14) Albrecht, E.; Averdung, J.; Bischof, E. W.; Heidbreder, A.; Kirschberg, T.; Müller, F.; Mattay, J. Photoinduced Electron Transfer (PET) in Organic Synthesis. [3 + 2]-Type Cycloaddition, Cyclization and CC Bond Cleavage Reactions. *J. Photochem. Photobiol. A Chem.* **1994**, *82* (1–3), 219–232. https://doi.org/10.1016/1010-6030(94)02015-9.

(15) Dunning, H. N. Review of Olefin Isomerization. *Ind. Eng. Chem.* **1953**, *45* (3), 551–564. https://doi.org/10.1021/ie50519a029.

(16) Moore, J. H. An Investigation of the Low Energy Singlet-Triplet and Singlet-Singlet Transitions in Ethylene Derivatives by Ion Impact. *J. Phys. Chem.* **1972**, *76* (8), 1130–1133. https://doi.org/10.1021/j100652a007.

(17) Sauers, I.; Grezzo, L. A.; Staley, S. W.; Moore, J. H. Low-Energy Singlet-Triplet and Singlet-Singlet Transitions in Cycloalkenes. *J. Am. Chem. Soc.* **1976**, *98* (14), 4218–4222. https://doi.org/10.1021/ja00430a036.

(18) Zimmerman, H. E. Five Decades of Mechanistic and Exploratory Organic Photochemistry. *Pure Appl. Chem.* **2006**, *78* (12), 2193–2203. https://doi.org/10.1351/pac200678122193.

(19) Strieth-Kalthoff, F.; Glorius, F. Triplet Energy Transfer Photocatalysis: Unlocking the Next Level. *Chem* **2020**, *6* (8), 1888–1903. https://doi.org/10.1016/j.chempr.2020.07.010.

(20) Neveselý, T.; Wienhold, M.; Molloy, J. J.; Gilmour, R. Advances in the E → Z Isomerization of Alkenes Using Small Molecule Photocatalysts. *Chem. Rev.* **2022**, *122* (2), 2650–2694. https://doi.org/10.1021/acs.chemrev.1c00324.

(21) Dutta, S.; Erchinger, J. E.; Strieth-Kalthoff, F.; Kleinmans, R.; Glorius, F. Energy Transfer

Photocatalysis: Exciting Modes of Reactivity. *Chem. Soc. Rev.* **2024**, *53* (3), 1068–1089. https://doi.org/10.1039/d3cs00190c.

(22) Dexter, D. L. A Theory of Sensitized Luminescence in Solids. *J. Chem. Phys.* **1953**, *21* (5), 836–850. https://doi.org/10.1063/1.1699044.

(23) Hammond, G. S.; Saltiel, J.; Lamola, A. A.; Turro, N. J.; Bradshaw, J. S.; Cowan, D. O.; Counsell, R. C.; Vogt, V.; Dalton, C. Mechanisms of Photochemical Reactions in Solution. XXII.1 Photochemical Cis-Trans Isomerization. *J. Am. Chem. Soc.* **1964**, *86* (16), 3197–3217. https://doi.org/10.1021/ja01070a002.

(24) Zhu, M.; Zheng, C.; Zhang, X.; You, S. L. Synthesis of Cyclobutane-Fused Angular Tetracyclic Spiroindolines via Visible-Light-Promoted Intramolecular Dearomatization of Indole Derivatives. *J. Am. Chem. Soc.* **2019**, *141* (6), 2636–2644. https://doi.org/10.1021/jacs.8b12965.

(25) Paulisch, T. O.; Mai, L. A.; Strieth-Kalthoff, F.; James, M. J.; Henkel, C.; Guldi, D. M.; Glorius, F. Dynamic Kinetic Sensitization of β-Dicarbonyl Compounds—Access to Medium-Sized Rings by De Mayo-Type Ring Expansion. *Angew. Chem. Int. Ed.* **2022**, *61* (5). https://doi.org/10.1002/anie.202112695.

(26) Baeyer, A. Ueber Polyacetylenverbindungen. *Berichte der Dtsch. Chem. Gesellschaft* **1885**, *18* (2), 2269–2281. https://doi.org/10.1002/cber.18850180296.

(27) Wiberg, K. B. The Concept of Strain in Organic Chemistry. *Angew. Chemie Int. Ed. English* **1986**, *25* (4), 312–322. https://doi.org/10.1002/anie.198603121.

(28) Turkowska, J.; Durka, J.; Gryko, D. Strain Release - an Old Tool for New Transformations. *Chem. Commun.* **2020**, *56* (43), 5718–5734. https://doi.org/10.1039/d0cc01771j.

(29) Bellotti, P.; Glorius, F. Strain-Release Photocatalysis. *J. Am. Chem. Soc.* **2023**, *145* (38), 20716–20732. https://doi.org/10.1021/jacs.3c08206.

(30) Subbaiah, M. A. M.; Meanwell, N. A. Bioisosteres of the Phenyl Ring: Recent Strategic Applications in Lead Optimization and Drug Design. *J. Med. Chem.* **2021**, *64* (19), 14046–14128. https://doi.org/10.1021/acs.jmedchem.1c01215.

(31) Galasso, V. Theoretical Study of the 1J(13C13C) Indirect Nuclear Spin-Spin Coupling Constant of the Bridgehead Bond in [1.1.1]Propellane and Related Systems. *Chem. Phys. Lett.* **1994**, *230* (4–5), 387–390. https://doi.org/10.1016/0009-2614(94)01174-5.

(32) Wu, W.; Gu, J.; Song, J.; Shaik, S.; Hiberty, P. C. The Inverted Bond in [1.1.1]Propellane Is a Charge-Shift Bond. *Angew. Chem. Int. Ed.* **2009**, *121* (8), 1435–1438. https://doi.org/10.1002/ange.200804965.

(33) Bunker, K. D.; Sach, N. W.; Huang, Q.; Richardson, P. F. Scalable Synthesis of 1-Bicyclo[1.1.1]Pentylamine via a Hydrohydrazination Reaction. *Org. Lett.* **2011**, *13* (17), 4746–4748. https://doi.org/10.1021/ol201883z.

(34) Huang, W.; Keess, S.; Molander, G. A. Dicarbofunctionalization of [1.1.1]Propellane Enabled by Nickel/Photoredox Dual Catalysis: One-Step Multicomponent Strategy for the Synthesis of BCP-Aryl Derivatives. *J. Am. Chem. Soc.* **2022**, *144* (28), 12961–12969. https://doi.org/10.1021/jacs.2c05304.

(35) Huang, W.; Zheng, Y.; Keess, S.; Molander, G. A. A General and Modular Approach to BCP Alkylamines via Multicomponent Difunctionalization of [1.1.1]Propellane. *J. Am. Chem. Soc.* **2023**, *145* (9), 5363–5369. https://doi.org/10.1021/jacs.2c13298.

(36) Cuadros, S.; Goti, G.; Barison, G.; Raulli, A.; Bortolato, T.; Pelosi, G.; Costa, P.; Dell'Amico, L. A General Organophotoredox Strategy to Difluoroalkyl Bicycloalkane (CF2-BCA) Hybrid Bioisosteres. *Angew. Chem. Int. Ed.* **2023**, *135* (31). https://doi.org/10.1002/ange.202303585.

(37) Silvi, M.; Aggarwal, V. K. Radical Addition to Strained σ-Bonds Enables the Stereocontrolled Synthesis of Cyclobutyl Boronic Esters. *J. Am. Chem. Soc.* **2019**, *141* (24), 9511–9515. https://doi.org/10.1021/jacs.9b03653.

(38) Ernouf, G.; Chirkin, E.; Rhyman, L.; Ramasami, P.; Cintrat, J. Photochemical Strain-Release-Driven Cyclobutylation of C(Sp 3)-Centered Radicals. *Angew. Chem. Int. Ed.* **2020**, *132* (7), 2640–2644. https://doi.org/10.1002/ange.201908951.

(39) Kleinmans, R.; Pinkert, T.; Dutta, S.; Paulisch, T. O.; Keum, H.; Daniliuc, C. G.; Glorius, F. Intermolecular [2π+2σ]-Photocycloaddition Enabled by Triplet Energy Transfer. *Nature* **2022**, *605* (7910), 477–482. https://doi.org/10.1038/s41586-022-04636-x.

(40) Guo, R.; Chang, Y. C.; Herter, L.; Salome, C.; Braley, S. E.; Fessard, T. C.; Brown, M. K. Strain-

Release [2π + 2σ] Cycloadditions for the Synthesis of Bicyclo[2.1.1]Hexanes Initiated by Energy Transfer. *J. Am. Chem. Soc.* **2022**, *144* (18), 7988–7994. https://doi.org/10.1021/JACS.2C02976.

(41) Golfmann, M.; Walker, J. C. L. Bicyclobutanes as Unusual Building Blocks for Complexity Generation in Organic Synthesis. *Commun. Chem.* **2023**, *6* (1), 1–13. https://doi.org/10.1038/s42004-022-00811-3.

(42) Dilmaç, A. M.; Spuling, E.; de Meijere, A.; Bräse, S. Propellanes—From a Chemical Curiosity to "Explosive" Materials and Natural Products. *Angew. Chem. Int. Ed.* **2017**, *56* (21), 5684–5718. https://doi.org/10.1002/anie.201603951.

(43) Jarosch, O.; Walsh, R.; Szeimies, G. Kinetics and Mechanism of the Thermal Rearrangement of [1.1.1]Propellane. *J. Am. Chem. Soc.* **2000**, *122* (35), 8490–8494. https://doi.org/10.1021/ja994043v.

(44) Ueda, M.; Walczak, M. A. A.; Wipf, P. Formal Alder-Ene Reaction of a Bicyclo[1.1.0]Butane in the Synthesis of the Tricyclic Quaternary Ammonium Core of Daphniglaucins. *Tetrahedron Lett.* **2008**, *49* (41), 5986–5989. https://doi.org/10.1016/j.tetlet.2008.07.179.

(45) Kerner, M. J.; Wipf, P. Semipinacol-Type Rearrangements of [3-(Arylsulfonyl)Bicyclo[1.1.0]Butan-1-Yl]Alkanols. *Org. Lett.* **2021**, *23* (9), 3615–3619. https://doi.org/10.1021/acs.orglett.1c01004.

(46) Sweger, R. W.; Czarnik, A. W. Retrograde Diels–Alder Reactions. *Compr. Org. Synth.* **1991**, 551–592. https://doi.org/10.1016/b978-0-08-052349-1.00132-3.

(47) Chiu, P.; Lautens, M. Using Ring-Opening Reactions of Oxabicyclic Compounds as a Strategy in Organic Synthesis. **1997**, *190*, 1–85. https://doi.org/10.1007/bfb0119245.

(48) Klunder, A. J. H.; Bos, W.; Verlaak, J. M. M.; Zwanenburg, B. A Facile Synthesis of Functionalized Cyclopentadienone Epoxides by Flash Thermolytic Cycloreversion of Tricyclopecenones. *Tetrahedron Lett.* **1981**, *22* (45), 4553–4556. https://doi.org/10.1016/S0040-4039(01)93039-4.

(49) Grubbs, R. H. Olefin Metathesis. *Tetrahedron* **2004**, *60* (34), 7117–7140. https://doi.org/10.1016/j.tet.2004.05.124.

(50) Johansson Seechurn, C. C. C.; Kitching, M. O.; Colacot, T. J.; Snieckus, V. Palladium-Catalyzed Cross-Coupling: A Historical Contextual Perspective to the 2010 Nobel Prize. *Angew. Chem. Int. Ed.* **2012**, *51* (21), 5062–5085. https://doi.org/10.1002/anie.201107017.

(51) Ciogli, A.; Iazzetti, A. Advances in Transition Metal Catalysis—Preface to the Special Issue. *Catalysts* **2024**, *14* (7), 10–12. https://doi.org/10.3390/catal14070438.

(52) Beller, M. Introduction: First Row Metals and Catalysis. *Chem. Rev.* **2019**, *119* (4), 2089. https://doi.org/10.1021/acs.chemrev.9b00076.

(53) Crabtree, R. H. (ed). *The Organometallic Chemistry of the Transition Metals*; Crabtree, R. H., Ed.; Wiley, 2014.

(54) Hartwig, J. *Organotransition Metal Chemistry*; 2010.

(55) Engle, K. M.; Yu, J. Q. Developing Ligands for Palladium(II)-Catalyzed C-H Functionalization: Intimate Dialogue between Ligand and Substrate. *J. Org. Chem.* **2013**, *78* (18), 8927–8955. https://doi.org/10.1021/jo400159y.

(56) Colacot, T. J.; Matthey, J. The 2010 Nobel Prize in Chemistry: Palladium-Catalysed Cross-Coupling the Importance of Carbon-Carbon Coupling for Real World Applications. *Platin. Met. Rev.* **2011**, *55* (2), 84–90. https://doi.org/10.1595/147106711X558301.

(57) Dieck, A.; Heck, R. F. Organophosphinepalladium Complexes as Catalysts for Vinylic Hydrogen Substitution Reactions. *J. Am. Chem. Soc.* **1974**, *96* (4), 1133–1136. https://doi.org/10.1021/ja00811a029.

(58) Miyaura, N. A. S.; Chem, S. Stereoselective Synthesis of Arylated (E)-Alkenes by the Reaction of Alk-1 -Enylboranes with Aryl Halides in the Presence of Palladium Catalyst. *J. C. S. Chem. Comm.* **1979**, No. 866, 866–867. https://doi.org/10.1039/C39790000866.

(59) William J. Scott, G. T. Crisp, and J. K. S. Palladium-Catalyzed Coupling of Vinyl Triflates with Organostannanes. A Short Synthesis of Pleraplysillin-1. *J. Am. Chem. Soc.* **1984**, No. 106, 4630–4632.

(60) Kenkichi Sonogashira, Yasuo Tohda, and N. H. A Convenient Synthesis of Acetylenes: Catalytic Substitutions of Acetylenic Hydrogen with Bromoalkenes, Iodoarenes, and Bromopyridines. *Tetrahedron* **1975**, No. 50, 4467–4470. https://doi.org/10.1055/s-0042-108582.

(61) Wolfe, J. P.; Singer, R. A.; Yang, B. H.; Buchwald, S. L. Highly Active Palladium Catalysts for Suzuki

Coupling Reactions. *J. Am. Chem. Soc.* **1999**, *121* (41), 9550–9561. https://doi.org/10.1021/ja992130h.

(62) Shelby, Q.; Kataoka, N.; Mann, G.; Hartwig, J. Unusual in Situ Ligand Modification to Generate a Catalyst for Room Temperature Aromatic C-O Bond Formation [8]. *J. Am. Chem. Soc.* **2000**, *122* (43), 10718–10719. https://doi.org/10.1021/ja002543e.

(63) Smith, A. B.; Beauchamp, T. J.; Lamarche, M. J.; Kaufman, M. D.; Qiu, Y.; Arimoto, H.; Jones, D. R.; Kobayashi, K. Evolution of a Gram-Scale Synthesis of (+)-Discodermolide. *J. Am. Chem. Soc.* **2000**, *122* (36), 8654–8664. https://doi.org/10.1021/ja0015287.

(64) Mizoroki, T.; Reaction, H.; Oestreich, M. The Mizoroki – Heck. *John Wiley Sons* **2009**, 37.

(65) Kronberg, B. I.; Coatsworth, L. L.; Usselman, M. C. The Artifact as Historical Document Part 2: The Palladium and Rhodium of W. H. Wollaston. *Ambix* **1981**, *28* (1), 20–35. https://doi.org/10.1179/amb.1981.28.1.20.

(66) Smidt, J.; Haftner, W.; Jira, R.; Sedlmeier, J.; Sieber, R.; Rüttinger, R.; Kojer, H. Katalytische Umsetzungen von Olefinen an an Platinmetall-Verbindungen. *Angew. Chemie* **1959**, *71* (5), 176–182. https://doi.org/10.1002/ange.19590710503.

(67) Negishi, E.; King, A. O.; Okukado, N. Derivatives with Aryl Halides. *J. Org. Chem.* **1977**, *42* (10), 1821–1823.

(68) Lyons, T. W.; Sanford, M. S.; Formation, I. C. N. B. Palladium-Catalyzed Ligand-Directed C - H Functionalization Reactions. **2010**, 1147–1169.

(69) He, J.; Wasa, M.; Chan, K. S. L.; Shao, Q.; Yu, J. Q. Palladium-Catalyzed Transformations of Alkyl C-H Bonds. *Chem. Rev.* **2017**, *117* (13), 8754–8786. https://doi.org/10.1021/acs.chemrev.6b00622.

(70) Dupont, J.; Consorti, C. S.; Spencer, J. The Potential of Palladacycles: More than Just Precatalysts. *Chem. Rev.* **2005**, *105* (6), 2527–2571. https://doi.org/10.1021/cr030681r.

(71) Balcells, D.; Clot, E.; Eisenstein, O. C-H Bond Activation in Transition Metal Species from a Computational Perspective. *Chem. Rev.* **2010**, *110* (2), 749–823. https://doi.org/10.1021/cr900315k.

(72) Musaev, D. G.; Figg, T. M.; Kaledin, A. L. Versatile Reactivity of Pd-Catalysts: Mechanistic Features of the Mono-N-Protected Amino Acid Ligand and Cesium-Halide Base in Pd-Catalyzed C-H Bond Functionalization. *Chem. Soc. Rev.* **2014**, *43* (14), 5009–5031. https://doi.org/10.1039/c3cs60447k.

(73) Dick, A. R.; Hull, K. L.; Sanford, M. S. A Highly Selective Catalytic Method for the Oxidative Functionalization of C-H Bonds. *J. Am. Chem. Soc.* **2004**, *126* (8), 2300–2301. https://doi.org/10.1021/ja031543m.

(74) Peters, S.; Bielefeldt, T.; Meldal Bock H Paulsen, M. K. Reuktionen Und Synlhesen Im Orgunisch-Chemisehen Prukrikum, Thieme. *Angen. Chem. Int. Ed. Engl* **1982**, *108*, 19.

Chapter II

Triplet state reactivity of iminium ions in organocatalytic asymmetric [2 + 2] photocycloadditions

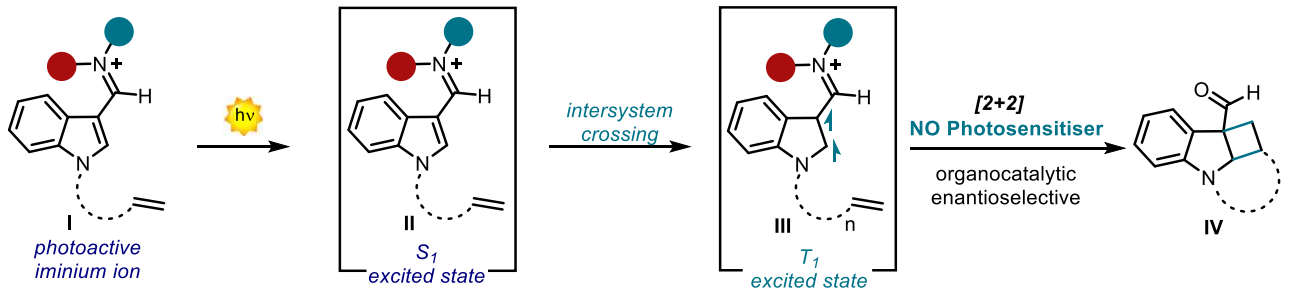

Contributions to the project:

This project was carried out in collaboration with Dr. Vasco Corti and PhD student Gianluca Simionato, who were responsible for the optimization of the process. My personal contribution involved the preparation of most of the starting materials, the isolation of the majority of scope entries, and part of the mechanistic synthetic experiments. The project also benefited from collaborations with several Italian universities: Professor Mirco Natali (University of Ferrara) conducted all spectroscopic investigations, Dr. Stefano A. Serapian (Univerisy of Pavia) performed the computational studies, and Professor Giorgio Pelosi (University of Parma) was responsible for X-ray crystallographic analyses.

Published in *Nature Chemistry*.
DOI: https://doi.org/10.1038/s41557-025-01960-3

Figures, schemes, tables and references in this Chapter are numbered independently.

2.1. Introduction

2.1.1. Principles of Asymmetric Organocatalysis with Emphasis on Iminium Ions

Asymmetric organocatalysis has rapidly evolved from a niche concept into a central discipline of modern synthetic chemistry. Over the past two decades, it has been recognized as the "third pillar" of catalysis, complementing the long-established fields of enzymatic and transition-metal catalysis. Organocatalysis is valued for its operational simplicity, the use of readily available small organic molecules, and its capacity to address synthetic challenges that once required complex metal systems. A decisive turning point occurred in the early 2000s, when the field experienced a dramatic surge of activity—the so-called "gold rush of asymmetric aminocatalysis"—that established organocatalysis as a mainstream strategy for asymmetric synthesis. This growth was fueled both by conceptual innovation and by the discovery of broadly applicable catalytic motifs, which enabled access to stereochemically complex molecules under mild and environmentally benign conditions.[1–4]

At a conceptual level, organocatalysis can be divided into two major activation strategies: covalent and non-covalent catalysis.[5–7] In the context of this thesis, attention will focus on covalent modes of activation, as they are most directly pertinent to the transformations under study. These approaches leverage the ability of small organic catalysts to form covalent bonds with substrates reversibly, thereby generating transient intermediates that can access new reactive pathways. As summarized in Scheme 1, covalent activation, within the field of aminocatalysis, encompasses several distinct but interrelated modes:[7]

- Catalysis via enamine intermediates operates through the condensation of a primary or secondary amine catalyst **2** with a carbonyl compound **1** to form intermediate **3** (Scheme 1a). The resulting HOMO-raised enamine engages electrophiles, enabling α-functionalization of carbonyl compounds with excellent stereocontrol **4**. This strategy has been pivotal in the development of asymmetric aldol and Michael reactions.[8] In addition, transient enamine intermediates can also display absorption in the visible region, allowing access to photochemical pathways that are not available to the ground-state carbonyl precursor.
- Catalysis via iminium-ion intermediates follows the opposite polarity: condensation of a primary or secondary amine catalyst **2** with an *α,β*-unsaturated carbonyl compound **5** yields an iminium-ion **6**, which lowers the LUMO of the activated substrate and enhances its electrophilicity (Scheme 1b). This allows efficient conjugate additions **7** and cycloadditions. Importantly, the transient iminium species can absorb visible light, thereby opening pathways to photochemical reactivity that are otherwise inaccessible to the ground-state enone (a point that will be elaborated on in the following section).[9]
- SOMO activation involves, for example, single-electron oxidation of enamines **3** to generate radical cation intermediates **8** (Scheme 1c) . This activation mode provides access to α-alkylation **9** and other transformations that are challenging with conventional two-electron reactivity.[10]

In all these strategies, the catalyst transiently modifies the substrate, turning it into a more reactive species that can transform before the catalyst is restored to complete the cycle. This principle has greatly expanded the range of reactions available in organic synthesis, introducing modes of reactivity that complement those accessible with metals and enzymes.

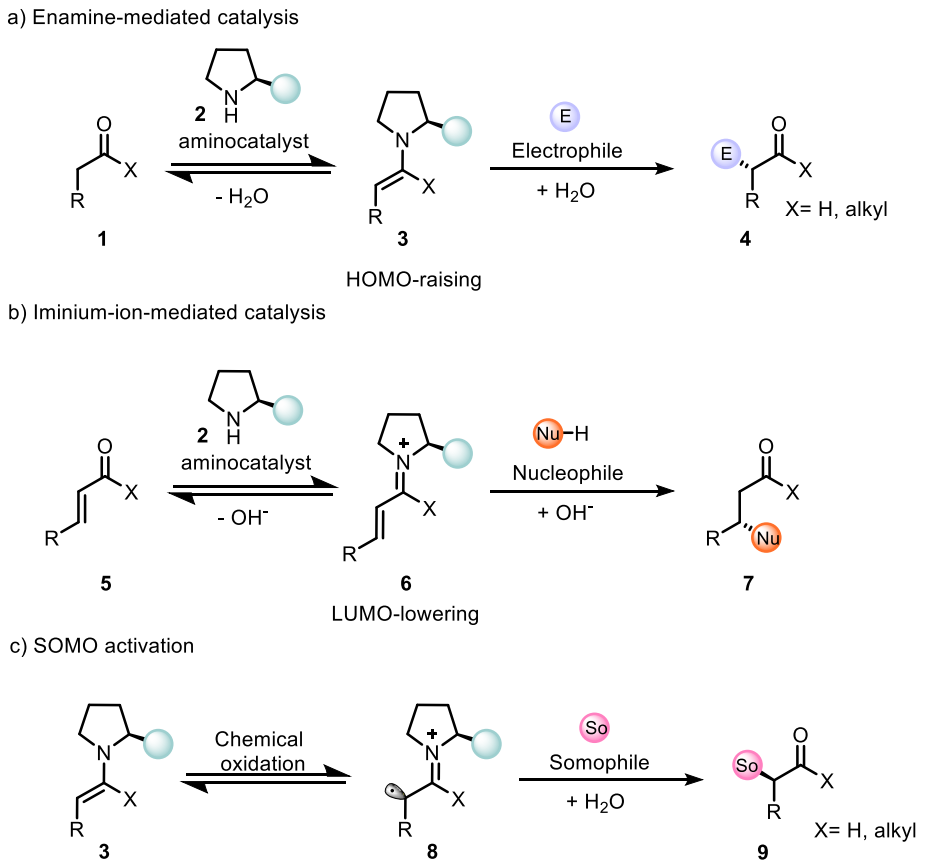

Scheme 1. Covalent activation modes in organocatalysis: a) enamine-mediated, b) iminium-ion catalysis, c) SOMO catalysis.

In the following discussion, representative examples will be drawn primarily from iminium catalysis because it is the most directly relevant to the aims of the present chapter. Among the different covalent activation modes, iminium-ion mediated transformations have proven particularly important. By transiently converting an enal into its activated iminium form, these catalysts lower the energy of the π orbital and render the conjugated system far more susceptible to nucleophilic attack.[11] A landmark demonstration of this principle was provided by MacMillan and co-workers with the development of the imidazolidinone catalyst **12**, which promoted the asymmetric Diels–Alder reaction between enals and simple dienes with excellent levels of yield and enantioselectivity.[1] This pioneering study established the concept of "iminium catalysis" and opened the way to a broad family of enantioselective transformations of activated carbonyl compounds. The versatility of this activation strategy was further illustrated in subsequent applications of the same catalyst (Scheme 2). For example, the [3+2] cycloaddition of nitrones with enals, also mediated by **12**, proceeds via the same LUMO-lowering effect of the iminium-ion and delivers highly enantioenriched heterocycles.[12] Similarly, the Friedel–Crafts alkylation of electron-rich heteroarenes such as pyrroles with α,β-unsaturated aldehydes could be accomplished in the presence of imidazolidinone **12**, highlighting the broad mechanistic generality of this platform.[13] Taken together, these studies (Scheme 2) illustrate how a single conceptual strategy—iminium catalysis—enabled the application of a single activation principle across a wide spectrum of bond-forming processes, consolidating organocatalysis as a cornerstone of modern synthetic methodology.

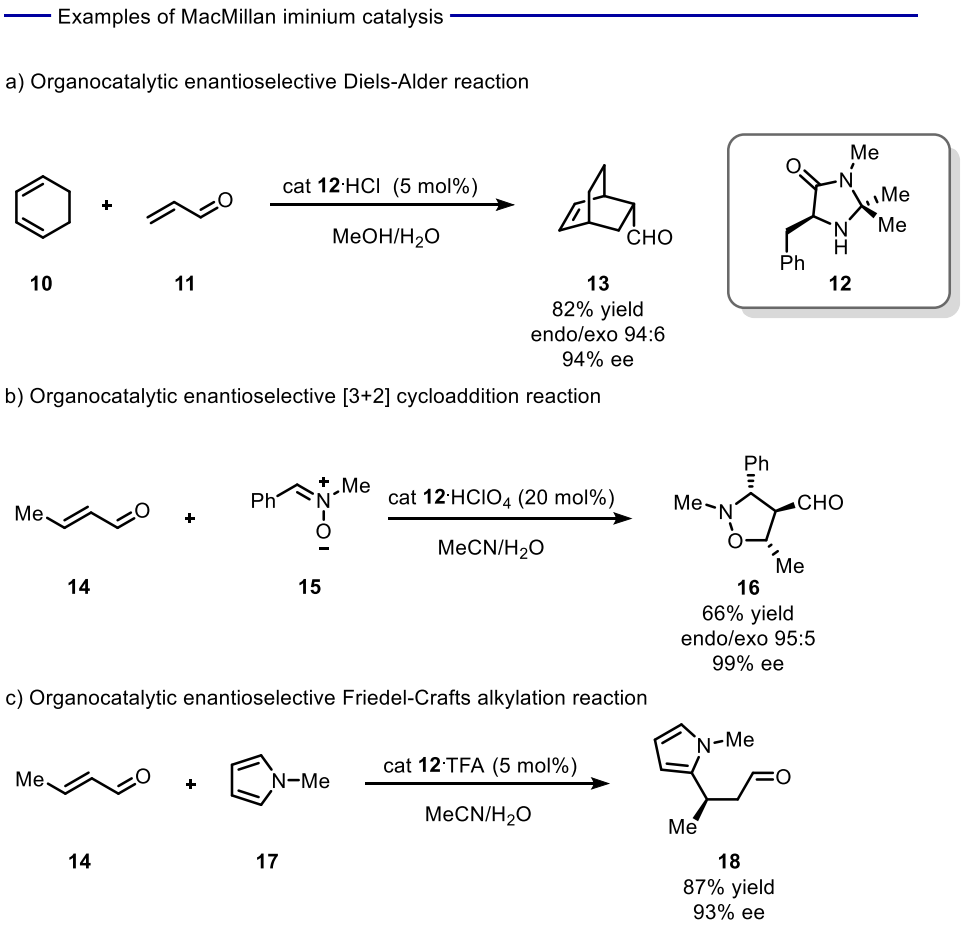

Scheme 2. Representative examples of iminium-ion catalysis promoted by imidazolidinone 12: a) enantioselective Diels–Alder reaction, b) [3+2] cycloaddition, and c) Friedel–Crafts alkylation of pyrroles.

2.1.2. Excited-State Iminium-Ion Catalysis: Singlet Reactivity and the Challenge of Triplets

The chemistry of electronically excited iminium ions has opened new avenues of reactivity, distinct from those observed in the ground state. Early pioneering work by Mariano established the conceptual foundation that photoexcited iminium ions could serve as highly reactive intermediates, capable of engaging in radical processes or photochemical cycloadditions with levels of efficiency and stereocontrol that were unprecedented at the time.[14,15] These studies demonstrated that iminium catalysis, long appreciated in the ground-state manifold for polar transformations, could be extended into photochemistry, unlocking new avenues where excited-state intermediates enable bond construction.

A decisive advance came with the demonstration that photoexcited iminium-ions can control radical reactivity with high enantioselectivity. Melchiorre and colleagues have demonstrated that chiral iminium-ions can be used for the enantioselective interception of α-amino radicals generated photochemically (Scheme 3).[16] In this process, the chiral amine condenses with the carbonyl substrate to form the iminium-ion **24**. Upon irradiation, the photocatalyst initiates a hydrogen atom transfer (HAT) from the radical precursor **20**, generating radical **25**. This radical is then trapped by the iminium-ion with high stereocontrol, affording the radical cation **26**. Owing to the spatial proximity of the electron-rich carbazole, an intramolecular reduction occurs, giving the carbazoliumyl radical cation **27**. A rapid tautomerization converts this intermediate into the imine **28**, which is

sufficiently long-lived and oxidizing to be reduced by the photocatalyst. This step closes the photoredox cycle and regenerates the iminium-ion **29**, which upon hydrolysis delivers the final product **23** while restoring the catalyst.

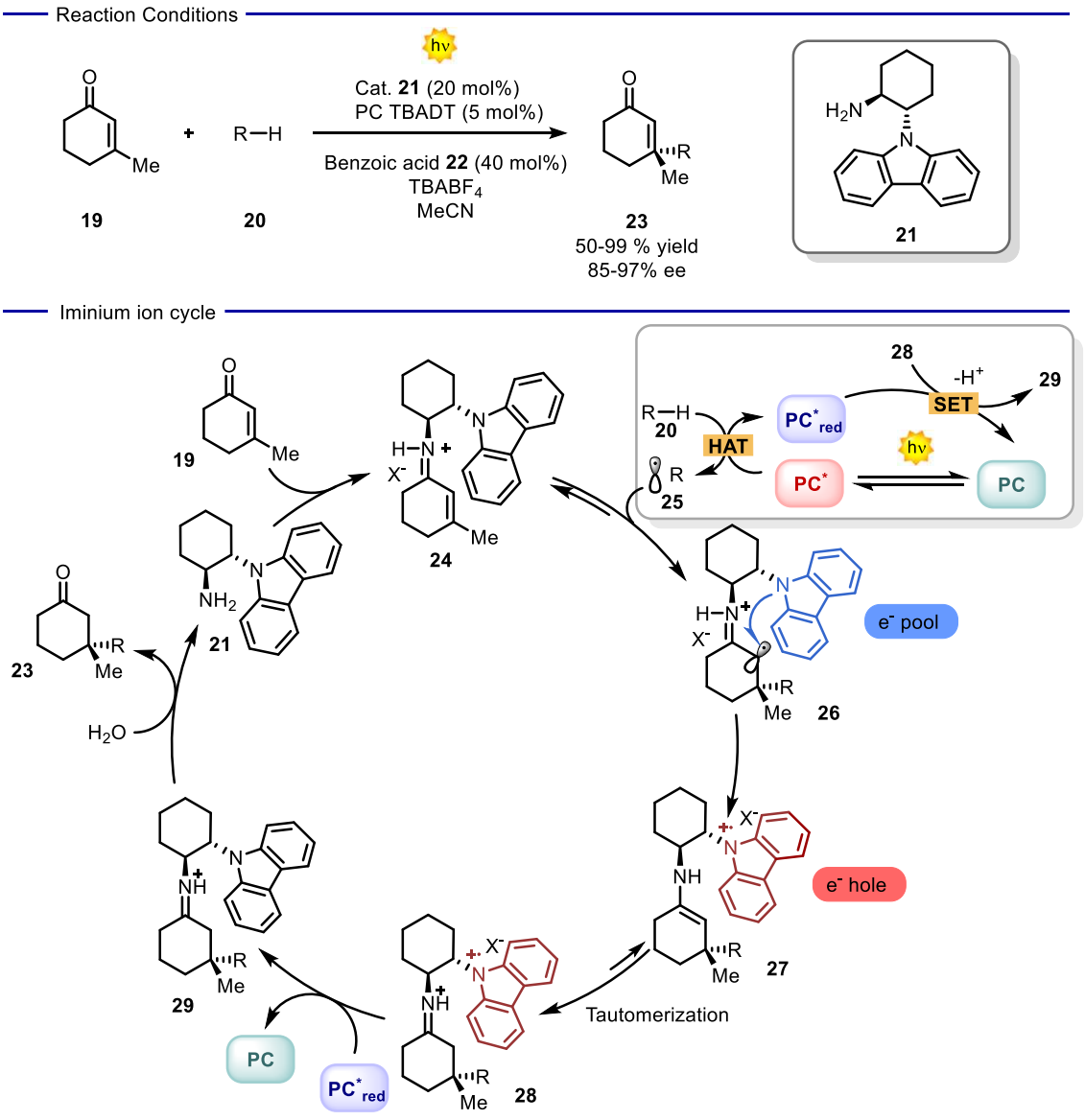

Scheme 3. Reaction conditions and proposed photocatalytic iminium-ion cycle.

This landmark study established that even inherently unselective radical processes could be channeled into highly enantioenriched products through excited-state iminium catalysis, a breakthrough that broadened the conceptual scope of asymmetric organocatalysis.[5]

In addition to radical capture, excited-state iminium-ions can act as powerful photooxidants. Melchiorre and co-workers elegantly demonstrated this principle in the β-alkylation of enals (Scheme 4).[17] Here, the chiral amine catalyst condenses with the enal **29** to form the iminium-ion **33**, which acts as the key photoactive species. Upon visible-light irradiation, **33** is promoted to its excited state (**33***), a strong oxidant capable of engaging in a single-electron transfer (SET) with the alkyl silanes **30**. This event generates the radical cation **30**$^{\bullet+}$, which after desilylation furnishes the nucleophilic benzyl radical **35**. Then, this radical couples with the β-position of the iminium-ion **34**, yielding intermediate **36** with high enantioselectivity induced by the chiral

environment of the catalyst. Finally, hydrolysis of **36** regenerates the catalyst and releases the β-alkylated aldehyde product **32**.

This dual role—as both a photogenerated oxidant and a stereocontrolling template—illustrates the versatility of iminium-ions, highlighting their ability to merge polar and radical reactivity within a single catalytic platform.[17]

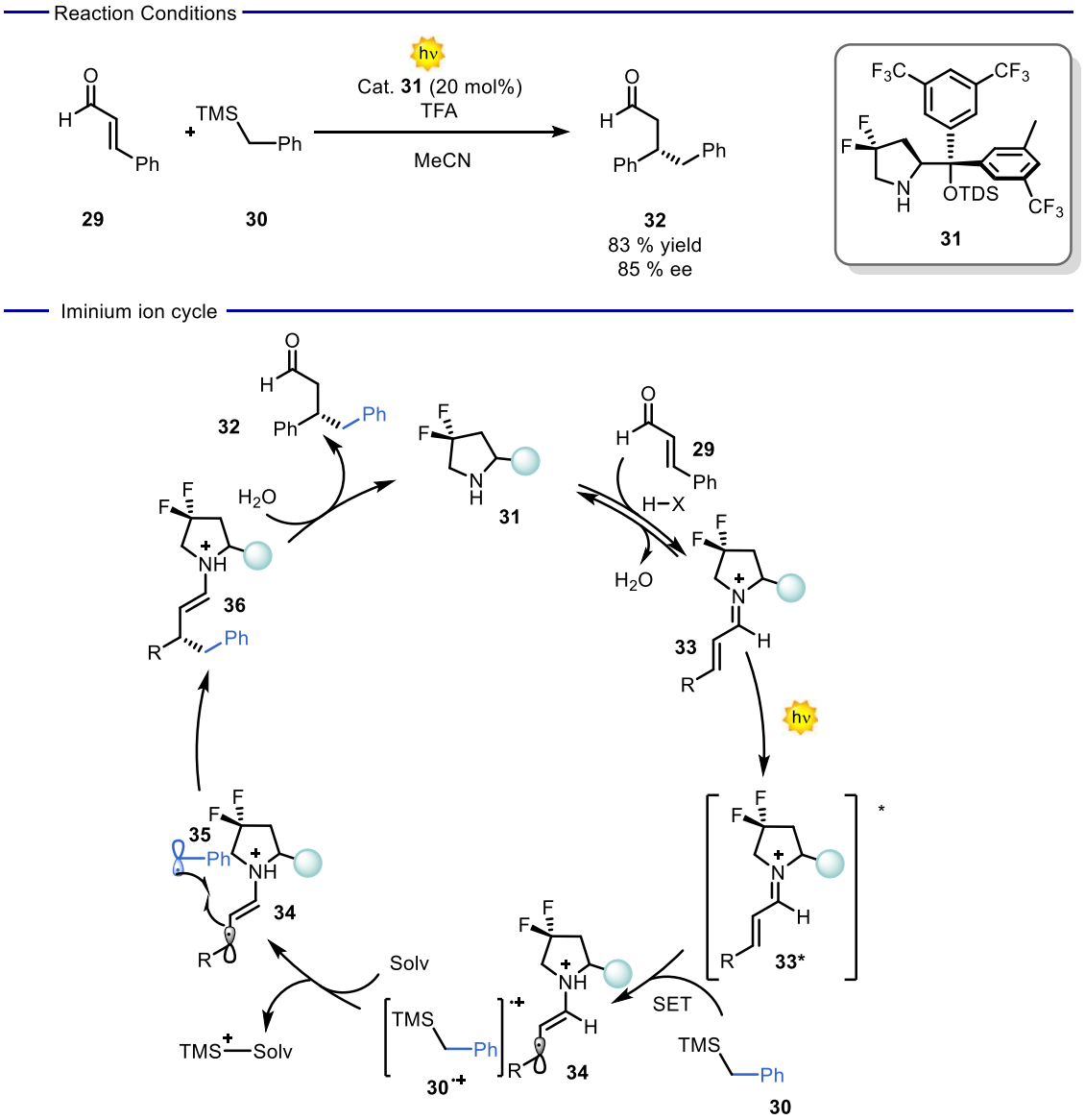

Scheme 4.Enantioselective β-alkylation of enals enabled by visible-light excitation of iminium ions, which act as both chiral templates and photooxidants.

Alemán and co-workers later introduced an important development, reporting an enantioselective [2+2] photocycloaddition driven by the visible-light excitation of iminium ions (Scheme 5).[18] The strategy relied on the activation of enals through reversible iminium formation with a chiral amine catalyst. Upon condensation, the enone substrate and the diamine catalyst generate an iminium-ion intermediate **41**. After the excitation, the iminium species engages the alkene partner in a [2+2] cycloaddition, leading to the formation of a 1,4-biradical intermediate **42**. This species rapidly evolves into the cyclobutyl iminium-ion **43**, which, upon hydrolysis, furnishes the enantioenriched cyclobutane product **40** while regenerating the catalyst.

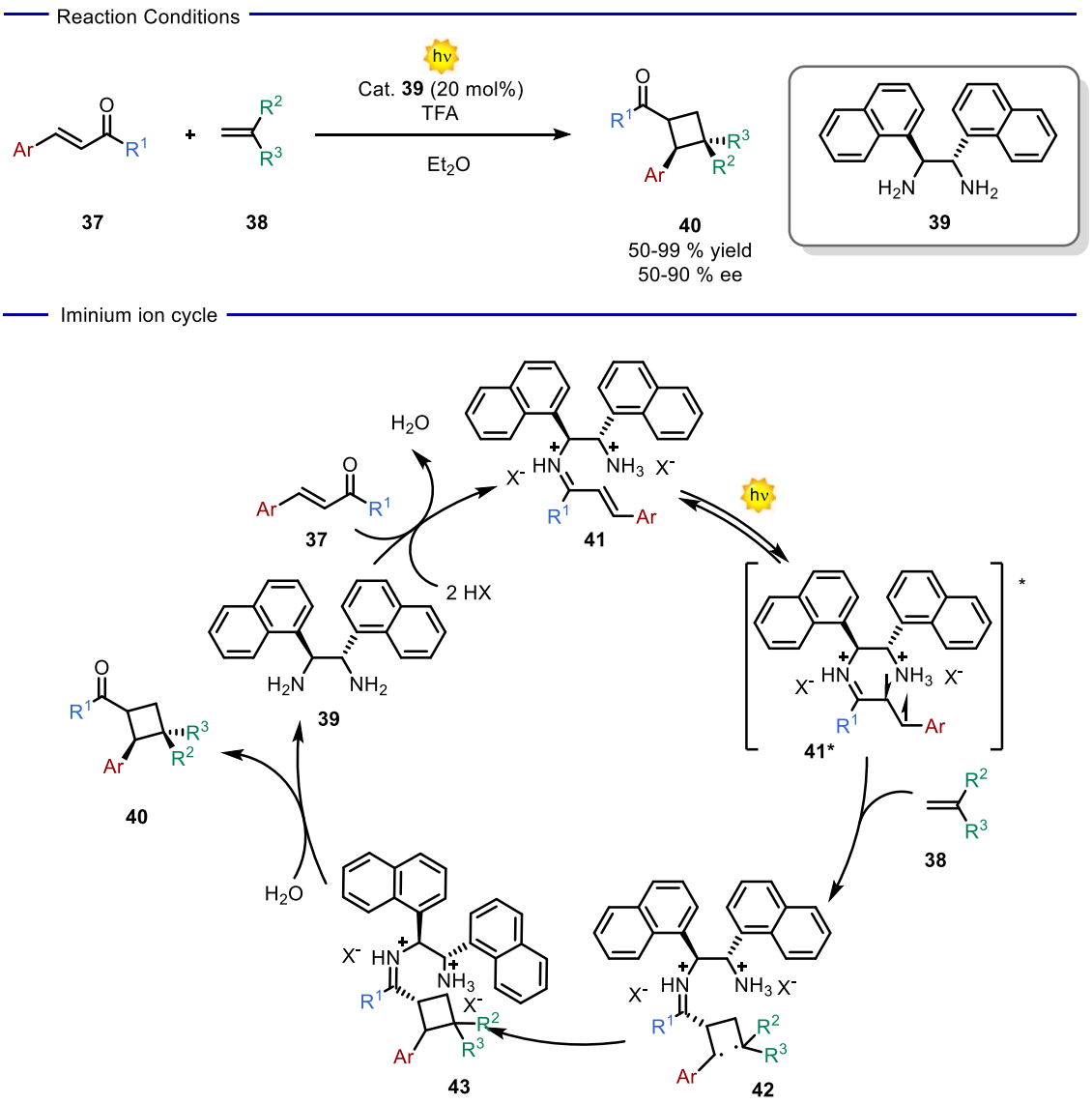

Scheme 5.Organocatalytic enantioselective [2+2] photocycloaddition of enals with alkenes via excited-state iminium catalysis.

This mechanism is consistent with the singlet-state reactivity observed in earlier stoichiometric studies by Mariano,[14] where [2+2] photocycloadditions of preformed iminium salts were reported. Interestingly, Alemán and co-workers also showed that when an external triplet sensitizer such as $Ru(bpy)_3Cl_2$ was added, the transformation could proceed via a triplet energy-transfer pathway.[18] This change in the nature of the reactive excited state had a marked influence on the stereochemical outcome, yielding a different diastereoisomeric ratio compared to the direct singlet pathway. Such observations clearly illustrate how the outcome of iminium-ion photocycloadditions is dictated by the electronic manifold—singlet versus triplet—through which the reaction proceeds.

While the chemistry of singlet excited states of iminium-ions has been widely exploited, their triplet reactivity has remained largely elusive. Indeed, all known examples require the intervention of an external photosensitizer. A seminal breakthrough came from Bach and co-workers, who provided the first direct evidence that chiral iminium-ions can participate in [2+2] photocycloadditions via a triplet pathway when coupled to visible-light-absorbing transition-metal complexes (Scheme 6).[19]

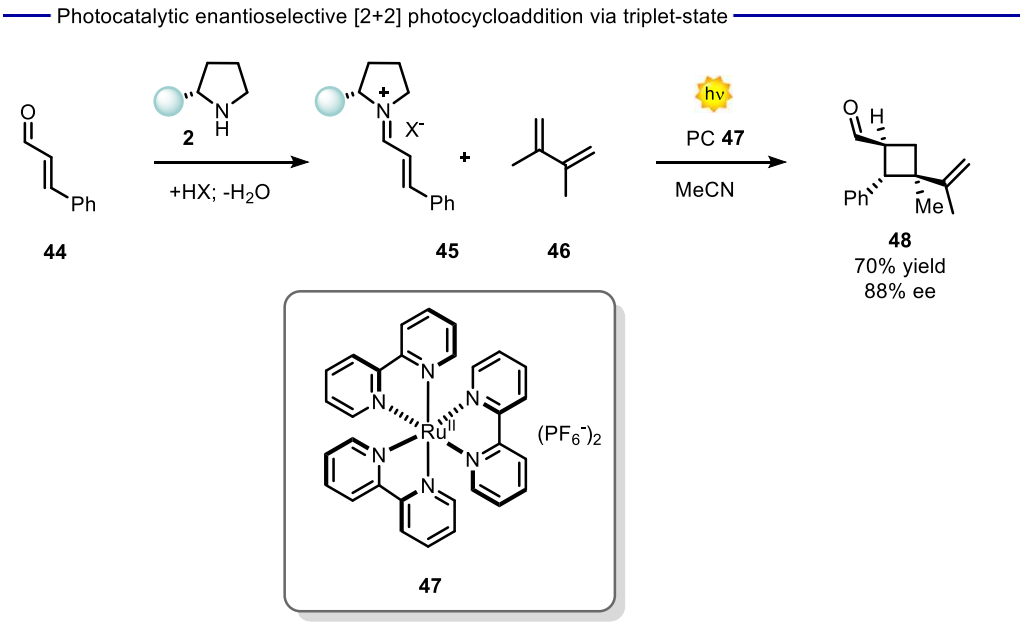

Scheme 6. Photocatalytic enantioselective [2+2] photocycloaddition proceeding via triplet-state iminium catalysis enabled by photosensitization

A key mechanistic insight is the comparison between enones and iminium-ions (Scheme 7): whereas enones undergo intersystem crossing (ISC) efficiently due to their n→π* transitions, iminium-ions are dominated by π→π* excitations, which disfavor ISC and thus hinder access to triplet states.[20] By employing triplet energy transfer from an iridium photosensitizer, Bach circumvented this intrinsic limitation and demonstrated that iminium-ions could indeed access a triplet manifold, enabling enantioselective [2+2] photocycloadditions. These results were later reinforced by complementary photophysical investigations and expanded catalytic applications.[21]

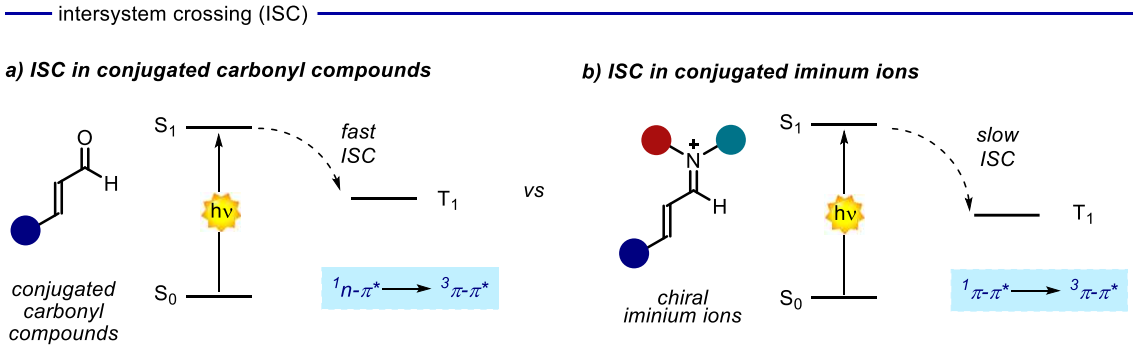

Scheme 7. Comparison of intersystem crossing (ISC) efficiency: conjugated carbonyl compounds undergo rapid ISC due to n→π transitions, whereas conjugated iminium ions, dominated by π→π* transitions, show much slower ISC.*

As a result, direct excitation into reactive triplet states remains unfeasible, and only sensitization strategies have succeeded in unlocking this reactivity. This contrast highlights both the maturity of singlet-state iminium photochemistry—already a robust platform for asymmetric radical and cycloaddition processes—and the untapped potential of the triplet manifold, which remains a frontier accessible only through triplet-triplet energy transfer.

2.1.3. Photochemical Dearomatization as a Simple Strategy for the Generation of Complex Molecules

Dearomatization has emerged as a powerful synthetic strategy for converting flat, aromatic scaffolds into structurally complex, three-dimensional molecules. Aromatic compounds are among the most abundant and stable building blocks in organic chemistry, and traditionally, their transformations have focused on functionalization reactions that retain aromaticity. In contrast, the inherent stability of aromatic systems makes their disruption through dearomatization particularly challenging (Figure 1).

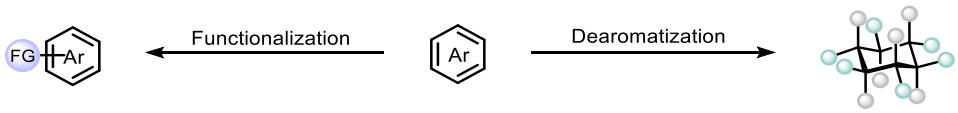

Figure 1. Comparison between aromatic functionalization, which retains aromaticity, and dearomatization, which disrupts aromatic stabilization to afford complex three-dimensional structures.

The process of breaking aromaticity requires surmounting substantial kinetic barriers while providing products that are often thermodynamically less stable than their precursors. As a result, dearomatization reactions are frequently associated with high activation energies, an endergonic character, and, in some cases, thermal reversibility of the products to the aromatic starting materials (Figure 2).[22]

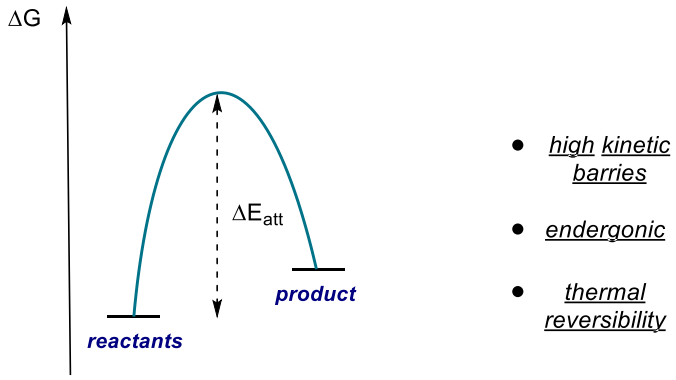

Figure 2. Energy profile of dearomatization reactions, typically characterized by high activation barriers, endergonicity, and possible thermal reversibility.

Despite these intrinsic limitations, the synthetic appeal of dearomatization lies in its ability to rapidly increase molecular complexity, accessing scaffolds of high value in natural products, pharmaceuticals, and functional materials.[23] To address the intrinsic kinetic and thermodynamic challenges of breaking aromaticity, visible-light photocatalysis has emerged as a particularly powerful tool. By promoting substrates into excited states, photocatalysis enables access to otherwise inaccessible reactivity patterns, destabilizing the aromatic core and channeling it into productive transformations. Within this context, both photooxidative single-electron pathways and triplet energy-transfer mechanisms can be engaged, providing distinct strategies for converting flat aromatic scaffolds into complex, three-dimensional structures under mild conditions.[24]

Within this broad field, heteroaromatic compounds have attracted sustained attention, both for their prevalence in bioactive molecules and for the unique opportunities offered by the heteroatom in modulating reactivity. Indoles, in particular, stand out as a privileged motif. Their aromatic stabilization renders them robust building blocks, but at the same time, controlled dearomatization of indoles unlocks fused, and polycyclic scaffolds that

are otherwise difficult to access. Such motifs are prevalent in natural products and drug candidates, where three-dimensionality is increasingly associated with improved biological properties.[25,26] From a reactivity standpoint, the electron-rich nature of indoles, combined with their well-defined positions of activation (C2, C3), makes them versatile yet challenging substrates for selective dearomatization.[23] Recent years have witnessed the development of a variety of visible-light-driven dearomatization reactions of indoles, which elegantly showcase the power of excited-state chemistry in overcoming the intrinsic barriers of these transformations. A representative set of examples is shown in Scheme 8, where visible-light photocatalysis was applied to the dearomative [2+2] cycloaddition of indoles bearing alkenyl side chains. The groups of You,[27] Fu,[28] and Dhar[29] independently demonstrated that such substrates undergo efficient transformation in the presence of iridium photocatalysts, affording indoline-fused cyclobutane with high selectivity. This transformation takes advantage of the ability of indoles to participate in photochemical processes mediated by energy transfer, triggering controlled dearomative cycloadditions that deliver structurally complex fused polycyclic scaffolds. Mechanistically, excitation of the indole substrate enables an intramolecular cycloaddition with a pendant olefin, giving access to strained yet synthetically valuable fused polycyclic scaffolds. Importantly, these photocycloadditions convert aromatic indoles into cyclobutane-fused indoline derivatives, often with good levels of diastereocontrol, although the outcome remains substrate-dependent.

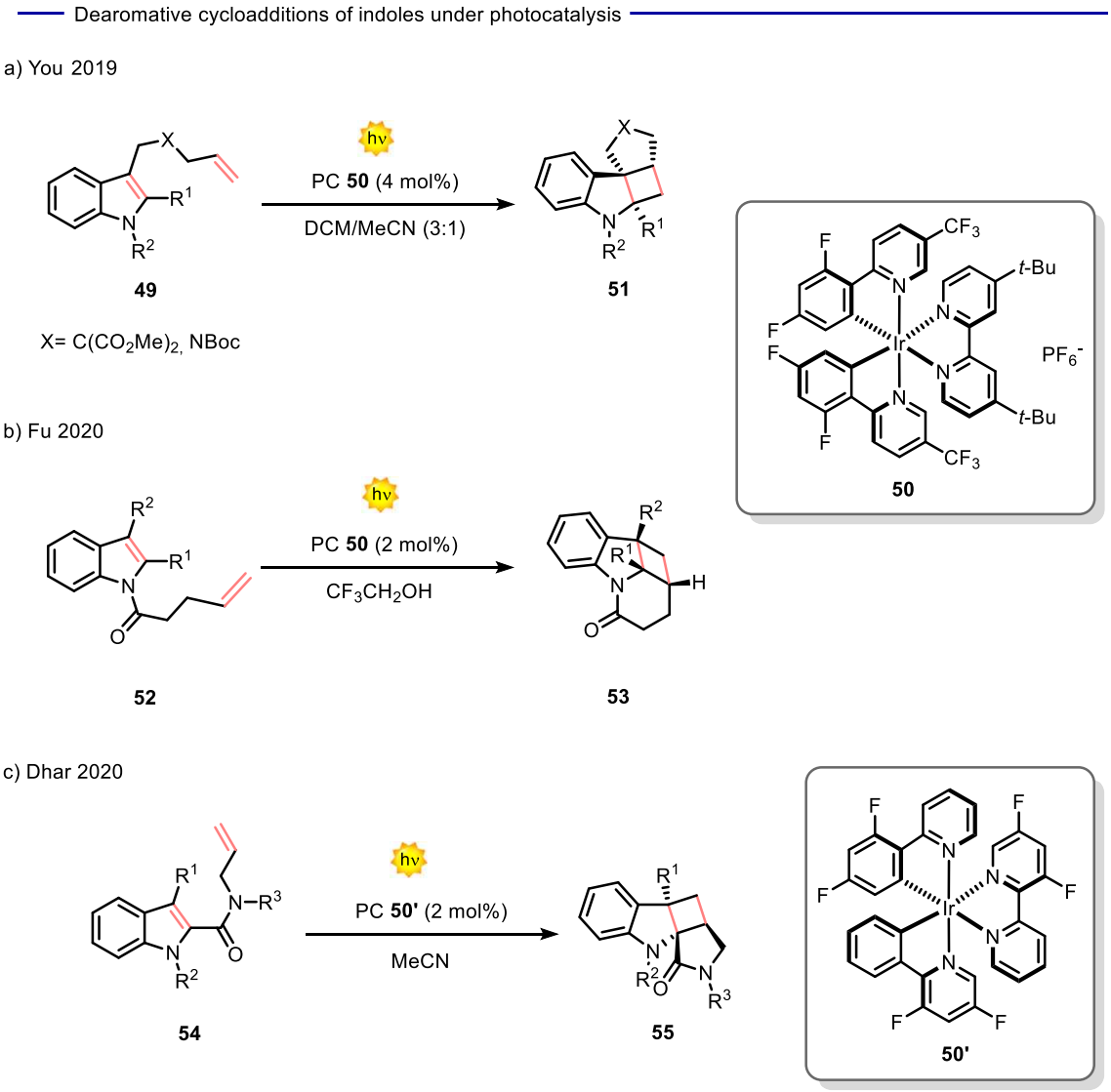

Scheme 8. Visible-light photocatalytic dearomatization of indoles leading to fused indoline scaffolds through [2+2] cycloadditions and related transformations.

The example above highlights a key aspect of modern dearomatization: instead of treating the loss of aromaticity only as a thermodynamic drawback, it can be used as a tool to build complex molecular architectures. In the case of indoles, success depends on three main factors: efficient activation of the aromatic ring, careful control of regioselectivity —and stereoselectivity when chiral catalysts are used—, and stabilization of the dearomatized products to prevent re-aromatization. Advances in photocatalysis have provided elegant solutions to these challenges, enabling not only intramolecular but also intermolecular dearomatizations, the latter offering broader functional diversity but remaining comparatively underdeveloped.[23] Overall, these advances show the dual importance of dearomatization. On one side, it is a real challenge, since chemists must overcome the natural stability of aromatic systems. On the other, it offers a powerful strategy for molecular design, turning simple aromatic building blocks into complex and biologically relevant structures. Among heteroaromatics, indoles clearly illustrate both the challenges and the opportunities of this approach, and their visible-light-driven dearomatization is a striking example of how modern catalysis can expand the limits of reactivity and selectivity.

2.2. Aim of the project

In this project, the iminium ion was embedded within a π-extended framework to promote efficient ISC from the S_1 to a reactive triplet state without external sensitization. The indole motif was selected as the most promising scaffold for this approach. Indoles have already demonstrated their potential in dearomative [2+2] photocycloadditions,[24] and their ability to undergo intersystem crossing has also been documented.[30] Embedding the reactive iminium functionality into an extended and rigid π-aromatic structure provides a rational design to mitigate the photophysical shortcomings of classical iminium systems, potentially facilitating population of the triplet state upon visible-light excitation. The strategic value of this approach lies in its capacity to address a long-standing challenge: the catalytic enantioselective construction of cyclobutane-containing scaffolds.[31–33] By combining indole dearomatization with photoactive iminium-ion catalysis, this strategy enables access to polycyclic cyclobutane-containing products with high levels of enantiocontrol, thereby expanding both the reactivity and the synthetic utility of organocatalysis.

In this chapter an organocatalytic asymmetric [2+2] dearomative photocycloaddition is described, proceeding through the triplet state of a photoactive iminium ion. Upon light absorption, the iminium intermediate undergoes intersystem crossing to a reactive triplet species, which then engages in stereoselective bond formation with a pendant alkene. This transformation generates a diverse family of chiral fused polycyclic scaffolds under mild conditions, without the need for external sensitization. Mechanistic studies, including transient spectroscopy and TD-DFT calculations, confirm the involvement of the T_1 manifold as the key reactive intermediate. In summary, the aim of this project is to challenge the established paradigm that iminium catalysis is restricted to singlet-state reactivity. By designing π-extended photoactive iminium-ions based on indole motifs, direct triplet reactivity was unlocked and harnessed for enantioselective dearomative [2+2] photocycloadditions (Scheme 9). This work provides not only a synthetic solution to the preparation of enantioenriched cyclobutanes, but also a conceptual advance in the photochemistry of organocatalytic intermediates, expanding the frontiers of excited-state iminium catalysis.

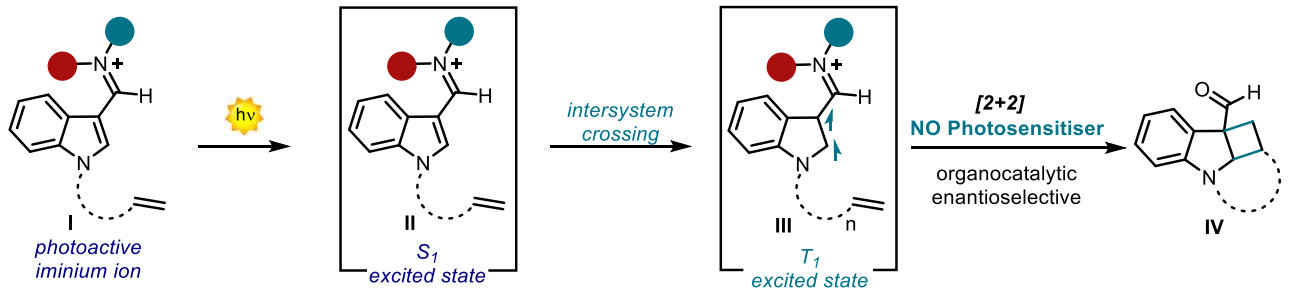

Scheme 9. Leveraging the triplet excited state reactivity of iminium-ions I for the development of organocatalytic enantioselective [2 + 2] dearomative photocycloadditions.

2.3. Results and discussion

2.3.1. Optimization studies

At the beginning of the investigation, the intramolecular enantioselective [2+2] photocycloaddition of 1-(pent-4-enoyl)-1H-indole-3-carbaldehyde **56** was selected as the model transformation (Table 1). The reaction was carried out in the presence of trifluoroacetic acid (TFA) and the Jørgensen–Hayashi catalyst **57a** (20 mol%), under visible-light irradiation with a Kessil lamp (427 nm). However, no detectable product was obtained after 24 hours (Table 1, entry 1). This lack of reactivity can be rationalized by considering the significant steric hindrance of catalyst **57a**, together with the relatively low electrophilicity of aldehyde **56**, which likely hampers the initial condensation step.

Attention was then directed toward primary amine-based catalysts, which gave more promising results (Table 1, entries 2–4). In particular, chiral diamine **57d** proved to be the most effective, affording the desired cycloadduct **58** in 62% yield and 91% ee under the standard conditions (entry 4). The beneficial role of this catalyst can be ascribed to its reduced steric encumbrance and enhanced ability to promote the formation of the reactive iminium intermediate.

Optimization of the reaction medium further highlighted $CHCl_3$ as the solvent of choice (Table 3 in the section 2.5.3). Moreover, increasing the amount of TFA additive from 1.0 to 2.5 equivalents markedly improved both the efficiency of the process, raising the yield to 97% while simultaneously reducing the reaction time from 24 to 6 hours (Table 1, entry 5; Table 4 in the section 2.5.3).

Finally, a set of control experiments was performed to probe the nature of the transformation (Table 1, entries 6–8). The reaction was completely suppressed in the absence of light or of the organocatalyst, confirming that both are essential for product formation. Moreover, when the reaction was conducted under air, the yield dropped significantly, suggesting the involvement of radical intermediates in the process.

Table 1. ***Selected results from the reaction conditions****: **a)** Substrate **56** (0.1 mmol) was treated with the corresponding organocatalyst (20 mol%, 0.02 mmol) and trifluoroacetic acid (TFA, equiv. as indicated) in $CHCl_3$ (0.4 mL) under inert atmosphere. **b)** Reaction yields were quantified by ^1H NMR analysis of the crude mixture using dibromomethane as internal standard. **c)** The ee values were measured by chiral stationary phase ultra-performance convergence chromatography (UPC²) after derivatization of the [2+2] cycloadduct with (carbethoxymethylene)triphenylphosphorane **57**. **d)** 1, 1,2-dichloroethane was used in place of $CHCl_3$.*

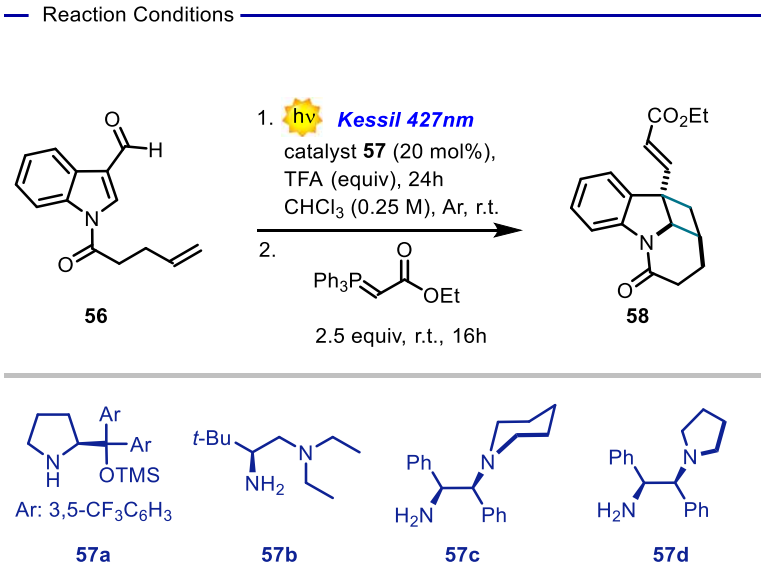

Entry[a]	Catalyst	TFA (equiv)	Yield (%)[b]	ee (%)[c]
1[d]	**57a**	1.0	<5	not determined
2[d]	**57b**	1.0	64	63
3[d]	**57c**	1.0	67	89
4[d]	**57d**	1.0	62	91
5	**57d**	**2.5**	**97**	**92**
6	no catalyst	2.5	<5	not determined
7	**57d**, no light	2.5	<5	not determined
8	**57d**, air	2.5	44	not determined

2.3.2. Mechanistic investigations

To gain deeper insight into the mechanism of this transformation, the photophysical behavior of the reactive iminium ion was next examined. When aldehyde **56** and organocatalyst **57d** were combined in the presence of TFA, the UV–vis spectrum revealed the appearance of a new absorption band in the visible region, consistent with the formation of the photoactive iminium-ion **59** (Fig. 3a).[17]

Having established its light-absorbing ability, a key mechanistic question was addressed: which excited state of 59 is responsible for driving the enantioselective [2+2] cycloaddition? To clarify this point, the analogue

iminium ion **60** was prepared, lacking the terminal olefin and thus unable to undergo the photocycloaddition. This compound served as a mechanistic probe to compare its photophysical properties with those of the reactive intermediate **59**. Steady-state luminescence measurements upon excitation at 360 nm were performed. Both **59** and **60** displayed intense fluorescence centered at 445 nm, corresponding to emission from the singlet excited state (S_1). Moreover, the fluorescence quantum yields and lifetimes, measured by time-correlated single-photon counting (TCSPC), were nearly identical for the two species ($\Phi \approx 0.14–0.15$; $\tau \approx 2$ ns; Fig. 3a, Figures 9–12 in the section 2.5.9). These data strongly indicate that the singlet state does not account for the observed reactivity. Laser flash photolysis (LFP) experiments were carried out to probe the triplet excited states of both iminium-ions. Upon 355 nm laser excitation, both **59** and **60** exhibited transient absorption spectra characterized by ground-state bleaching below 400 nm, a distinct band at 410 nm, and a broad absorption extending into the red region of the spectrum (Fig. 3b). These features are consistent with population of the triplet ($\mathbf{T_1}$) state. For the unreactive analogue **60**, the transient absorption signal at 700 nm decayed back to baseline within ~100 µs, with an estimated lifetime of $\tau \approx 12$ µs under N_2 atmosphere. The sensitivity of this decay to oxygen further supports its assignment as a triplet state. Crucially, the behaviour of **59** was markedly different. In this case, the 700 nm transient signal decayed much more rapidly (Fig. 3b, right), consistent with quenching of the triplet by the pendant olefin moiety. By contrast, in the control iminium-ion **60**, where the olefin is absent, the triplet state persists for a significantly longer lifetime, underscoring the key role of the alkene in triggering the photocycloaddition pathway. This observation provides compelling experimental evidence that the triplet state of the iminium-ion is indeed the key reactive species that initiates the [2+2] photocycloaddition, ultimately leading to the formation of the desired cycloadduct.

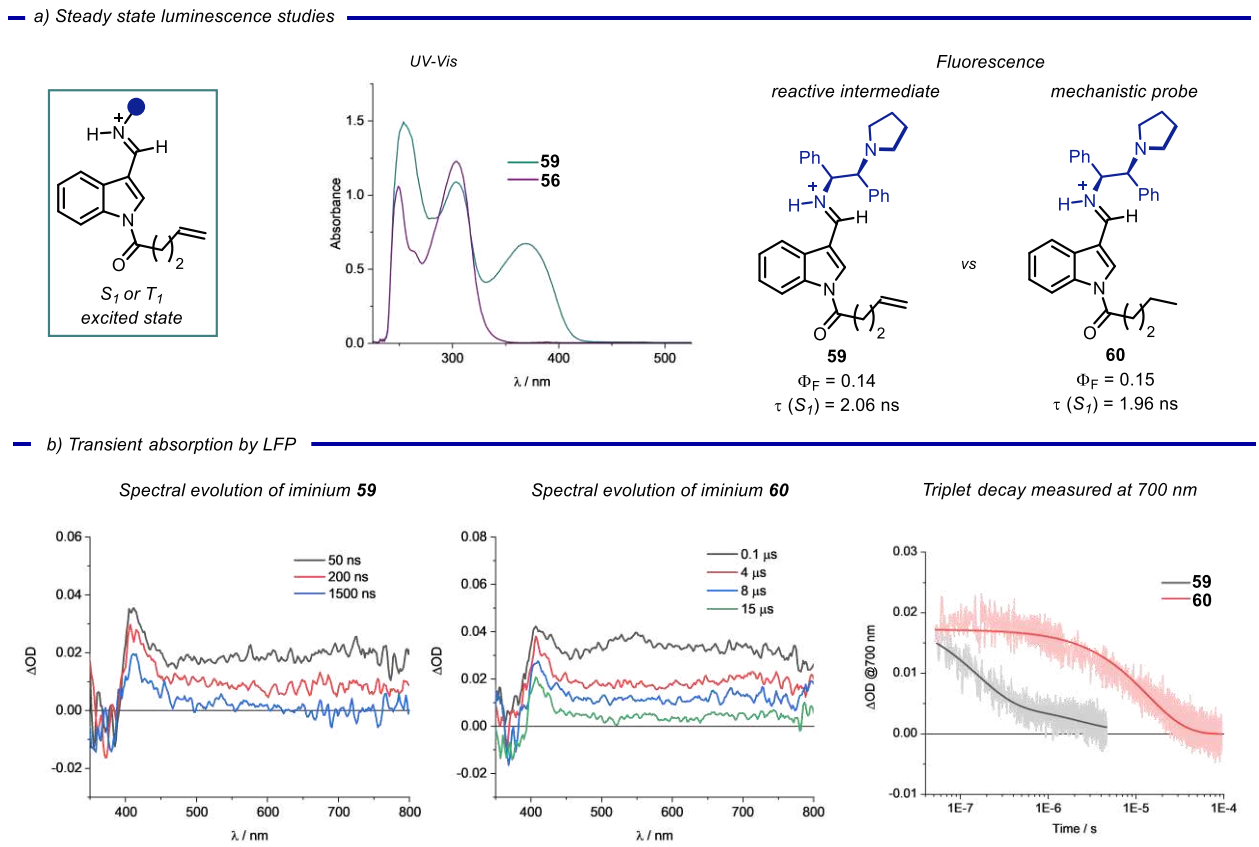

*Figure 3. Mechanistic investigations: **a**) Steady-state luminescence studies: UV–vis absorption spectra confirming the formation of iminium **59** and its absorption in the visible region, together with fluorescence measurements compared to compound **60**. **b**) Left and middle: transient absorption spectra of **59** and **60** recorded by laser flash photolysis. Right: kinetic decay profiles of the triplet excited state of **59** versus **60**. ΔOD = change in optical density.*

In order to consolidate our conclusion that the transformation involves a triplet manifold, further mechanistic studies were conducted under the optimized conditions (Scheme 10a). To this end, substrate **56** was modified by introducing a terminal methyl substituent, allowing us to separate and evaluate both stereoisomers, **61-(E)** and **61-(Z)**, as mechanistic probes. This approach was motivated by the well-established distinction between singlet- and triplet-mediated [2+2] photocycloadditions.[18] Reactions proceeding from the singlet excited state (S_1) typically follow a concerted, stereospecific pathway, in which the stereochemistry of the starting alkene is preserved in the cycloadduct. In contrast, triplet-state reactivity (T_1) generally involves a stepwise mechanism, where the intermediacy of a 1,4-diradical allows for bond rotation or conformational equilibration prior to C–C bond formation. In such cases, stereoconvergent outcomes—where E and Z isomers of the starting material converge to the same major product—are often observed. Experimental data were fully consistent with the latter scenario. When **61-(E)** was subjected to the optimized photocycloaddition conditions, the desired cycloadduct was obtained in 50% yield after 2 hours, with a 6.5:1 diastereomeric ratio (d.r.) in favor of a single major isomer. Strikingly, the reaction of **61-(Z)** furnished the *same* major diastereoisomer, albeit with a significantly reduced 1.5:1 d.r., confirming that both stereoisomers converge toward a common intermediate pathway. Importantly, the diastereomeric ratio remained unchanged even at lower conversions, excluding the possibility of post-reaction isomerization of the cycloadducts.[15] Together, these findings strongly support a stepwise triplet-state mechanism, rather than a stereospecific singlet pathway.

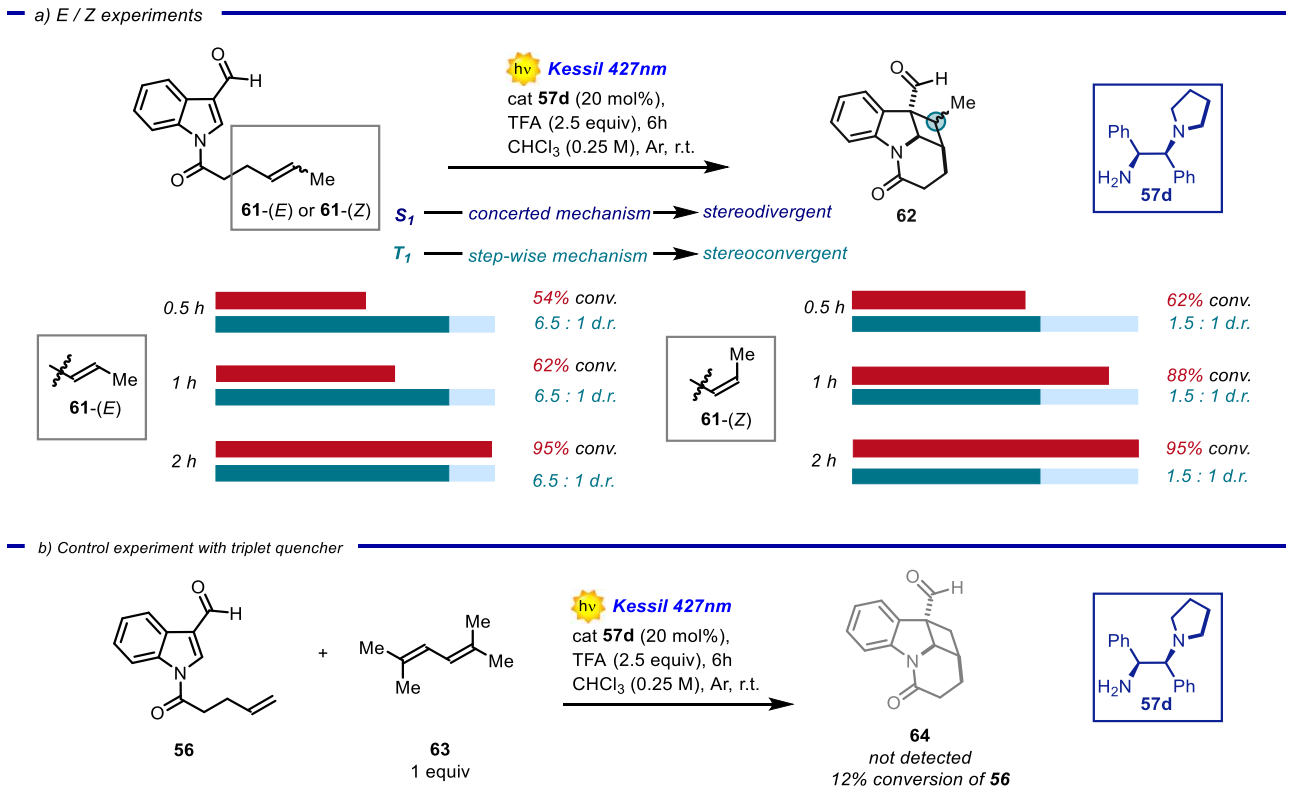

Scheme 10. ***Mechanistic studies****.* ***a****) Evaluation of the stereochemical outcome of the enantioselective [2+2] photocycloaddition starting from the two diastereoisomers* ***61****-(E) and* ***61****-(Z). A stereospecific process would indicate a singlet-state pathway, whereas the observed stereoconvergent outcome supports the involvement of a triplet intermediate.* ***b****) Control experiment using a triplet quencher.*

TTo further corroborate the role of the triplet state, additional control experiments were carried out. Performing the reaction in the presence of one equivalent of 2,5-dimethylhexa-2,4-diene (**63**), a well-known triplet quencher, completely suppressed product formation, and starting material **56** was quantitatively recovered (Scheme 10b). This observation provides strong evidence that the productive photocycloaddition proceeds through a triplet-excited iminium-ion.

Finally, the effect of external triplet sensitizers on the reactivity was evaluated. If the mechanism indeed involves a T_1 manifold, then energy transfer from a suitable iridium photocatalyst should accelerate the process. Consistent with this hypothesis, the addition of iridium complexes markedly increased the reaction rate, leading to full conversion of substrate **56** within just 1 hour (Scheme 11). However, the stereochemical outcome strongly depended on the nature of the sensitizer. With Ir-**65**, the rate acceleration was accompanied by a pronounced drop in enantiomeric excess, attributable to non-selective background excitation of both aldehyde **56** and iminium intermediate **59**. In contrast, Ir-**66** preserved higher optical purity while still promoting a substantial rate enhancement. This difference suggests that Ir-**66** displays greater selectivity for the iminium ion intermediate over the aldehyde, thereby ensuring that the reaction proceeds predominantly within the chiral organocatalytic environment. Taken all together, these mechanistic studies provide compelling evidence that the reaction operates through the triplet excited state of the iminium-ion intermediate.

a)

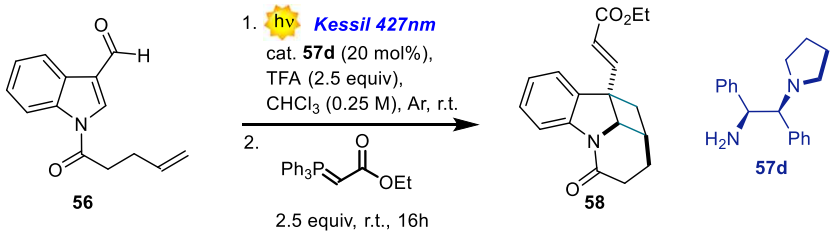

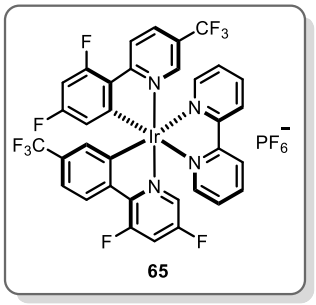

time = 1h	Entry	[Ir{dFCF$_3$ppy}$_2$(bpy)]PF$_6$ **Ir-65**	conversion (%)	yield (%)	ee (%)
	1	-	64	45	91
	2	2.5 mol%	> 95	90	40
time = 2h	Entry	[Ir{dFCF$_3$ppy}$_2$(bpy)]PF$_6$ **Ir-65**	conversion (%)	yield (%)	ee (%)
	3	-	80	62	91
	4	2.5 mol%	> 95	88	40
time = 4h	Entry	[Ir{dFCF$_3$ppy}$_2$(bpy)]PF$_6$ **Ir-65**	conversion (%)	yield (%)	ee (%)
	5	-	> 95	94	91
	6	2.5 mol%	> 95	86	40

b)

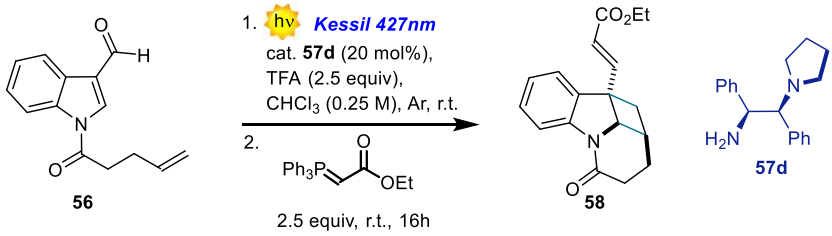

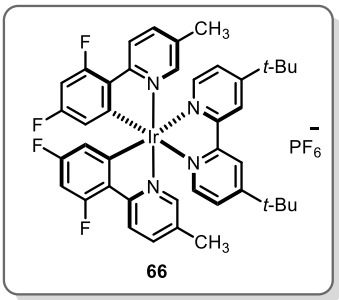

time = 1h	Entry	[Ir(dF(Me)ppy)$_2$(dtbbpy)]PF$_6$ **Ir-66**	conversion (%)	yield (%)	ee (%)
	1	-	60	43	91
	2	2.5 mol%	> 95	84	69
time = 2h	Entry	[Ir(dF(Me)ppy)$_2$(dtbbpy)]PF$_6$ **Ir-66**	conversion (%)	yield (%)	ee (%)
	3	-	83	63	91
	4	2.5 mol%	> 95	89	69

Scheme 11.Rate-acceleration experiments with Ir-based triplet sensitizers. Conversion and yields were determined by ^{1}H NMR of the crude mixture using CH_2Br_2 as internal standard.

2.3.3. Computational investigations

To complement the experimental evidence and provide further insights into the nature of the intermediates and excited states involved, this part of the study was carried out through a series of DFT and TD-DFT investigations (Figure 4). The calculations revealed that photoexcitation of **59** (S_0) generates the relaxed singlet excited intermediate **59** (S_1). In this state, the iminium moiety deviates from planarity, distorting out of the indole core plane towards the Re face of the reactive C=C bond (+75.2°; Figure 21 in the section 2.5.11). However, this relaxed S_1 intermediate was found to be unproductive for the observed reactivity (Figure 22 in the section 2.5.11), thus supporting the conclusion that the transformation must proceed through a triplet state.

By following the potential energy surfaces of the other excited states as the iminium distorts towards the *Re* face of the C=C bond, it was observed that the S_1 surface approaches the T_1 surface within 1.66 kcal mol^{-1} but does not cross it (Figure 4a, Figure 23 in the section). Instead, a minimum energy crossing point (**$MECP_1$**) was identified between the S_1 and T_2 states (located at +37.4° in the case examined in Figure 4b). These findings indicate that the observed triplet reactivity most likely involves the T_2 state, with direct $S_1 \rightarrow T_1$ intersystem crossing being improbable.

From here, two possible pathways emerge: while a fraction of photoexcited **59** (S_1) may directly access T_2 through **$MECP_1$**, it is more likely that most molecules relax first to the stabilized S_1 minimum and then climb back to **$MECP_1$**. Relaxation along the T_2 surface from **$MECP_1$** reveals that, as the iminium moiety begins to return towards planarity from +37.4°, the T_1 state becomes accessible at a second minimum energy crossing point (**$MECP_2$**). The T_1 state then relaxes to a first-order transition state (TS1), which corresponds to the formation of the first C–C bond. The resulting intermediate (Int-A) undergoes an essentially barrierless crossing to the open-shell singlet (Int-B). Finally, a second transition state (TS2) leads to radical–radical recombination, affording the observed cycloadduct.

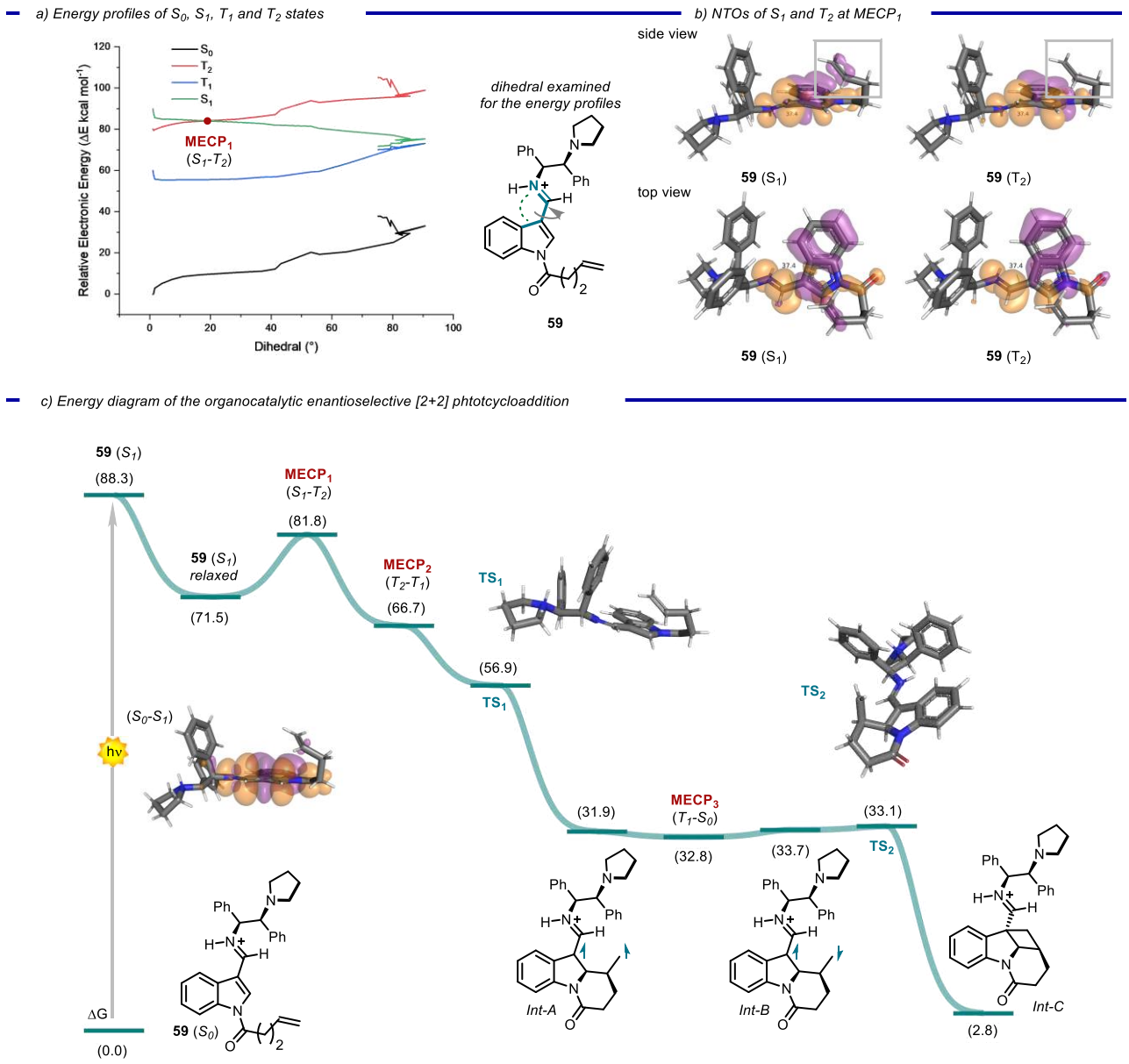

Figure 4. ***DFT and TD-DFT studies:*** ***a****) Energy profile of 4 (S_1) relaxation after excitation from 4 (S_0), showing iminium distortion towards the Re face; S_0, T_1, and T_2 surfaces included for comparison.* ***b****) NTOs representations of S_1 and T_2 states at MECP1 (S_1–T_2), shown as electron–hole pairs.* ***c****) Free energy profile (ΔG) of the proposed enantioselective [2+2] photocycloaddition, limited to the pathway affording the observed enantiomer.*

2.3.4. Generality of the reaction

After establishing the optimal conditions, the generality of the [2+2] photocycloaddition was investigated. At this stage, the Wittig reaction was performed after the cycloaddition to remove the aldehyde functionality and thereby facilitate product purification. The reaction proved to be remarkably tolerant to structural variation on the indole core. A broad range of substituents—predominantly electron-withdrawing groups at different positions of the aromatic system—were well accommodated, delivering the corresponding spirocyclic products in consistently good yields (44–84%) and with excellent levels of enantioselectivity (72–92% Scheme 12, products **69**–**84**). In contrast, when an electron-donating group was introduced, no reaction occurred. To determine the stereochemical outcome of the transformation, a single crystal of product **73** was subjected to

X-ray diffraction analysis, which allowed us to assign both its absolute and relative configuration. The stereochemical configurations of all other derivatives were then assigned by analogy. The effect of modifying the tethered olefin was also investigated. Variants bearing different substituents on the double bond underwent the cycloaddition efficiently, furnishing products **85** and **86** in high yield and with excellent stereoselectivity (40%, 80% yield and 94%, 84% ee, respectively). Particularly striking was the formation of derivative **87**, which features four contiguous stereogenic centers, including two quaternary carbon atoms. This highly congested cyclobutane framework was obtained in 84% yield, 75% ee, and with a 9:1 diastereomeric ratio, underscoring the ability of this methodology to construct architecturally complex scaffolds in a single step.

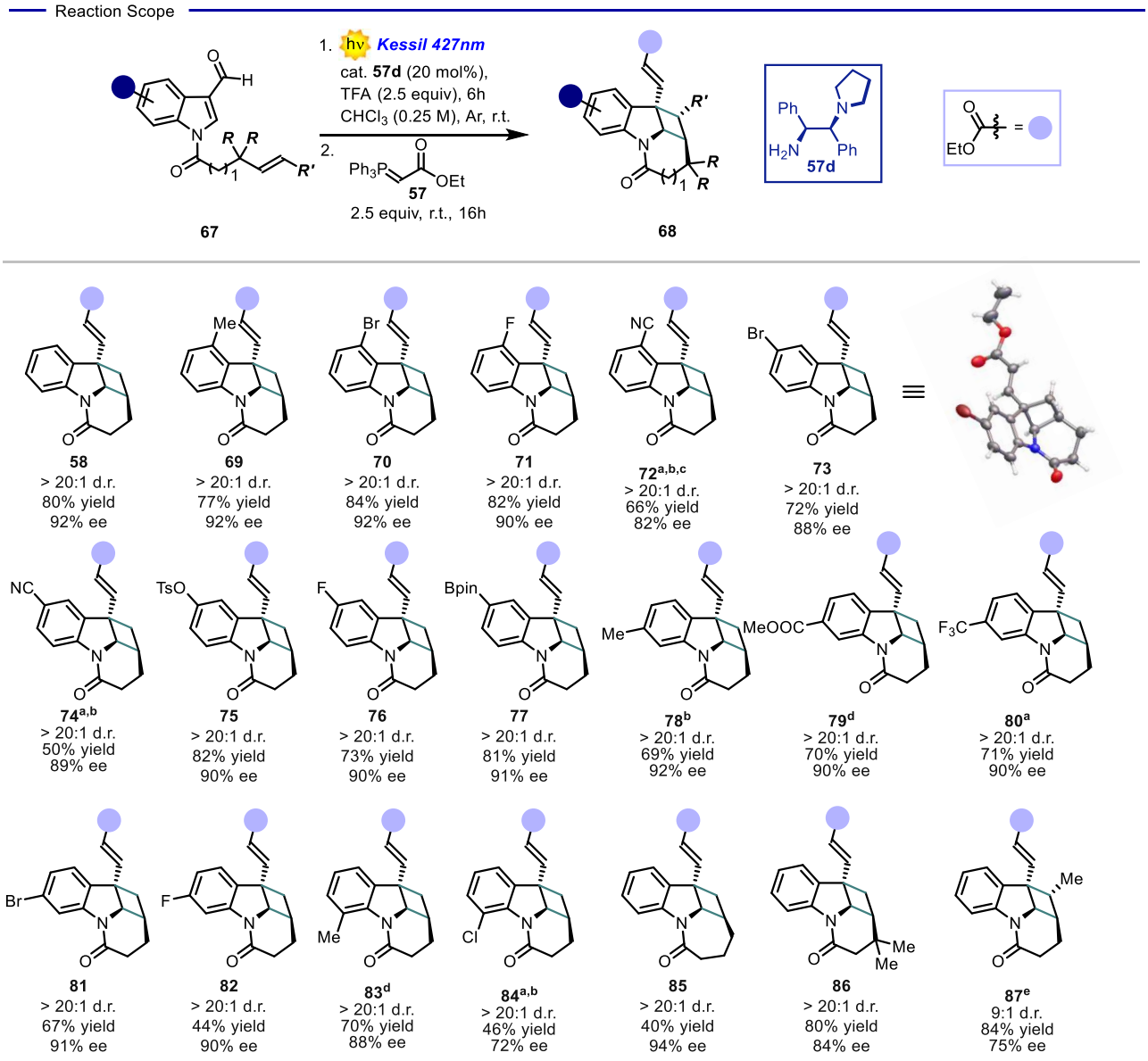

Scheme 12. Generality of the developed method. ***a****) Kessil lamp at 400nm.* ***b****)18h of reaction time.* ***c****)Solvent mixture: $CHCl_3$/PhCl (1:1).* ***d****)12h of reaction time.* ***e****) 0 °C and 3h of reaction time.*

Encouraged by these results, attention was turned to the intermolecular variant of the process. Indole **88** reacted smoothly with a wide array of alkenes under the very same optimized conditions, furnishing the desired enantioenriched cyclobutanes with generally good efficiency (Scheme 13). With simple 1-hexene **91** as the reaction partner, products **95** and **95′** were isolated in 51% combined yield with a 2.5:1 diastereomeric ratio, both adducts maintaining good enantioselectivity (74–77%). Methylene cyclohexane **92** proved to be an even

more efficient partner, giving the corresponding cycloadduct **96** in 70% yield and 94% ee as a single diastereoisomer. Interestingly, electron-deficient alkenes such as methyl acrylate **93** were also competent, albeit less reactive: product **97** was obtained in 30% yield but with excellent stereocontrol (88% ee, single diastereomer). More complex reaction partners could also be employed. When (*R*)-(–)-carvone **94** was used, the reaction produced a mixture of diastereoisomers **98** and **98′** in 45% combined yield and a 1.5:1 dr. Importantly, both diastereoisomers could be isolated, providing access to intricate polycyclic scaffolds featuring four contiguous stereogenic centers, including two adjacent all-carbon quaternary stereocenters—structural motifs of considerable synthetic value.

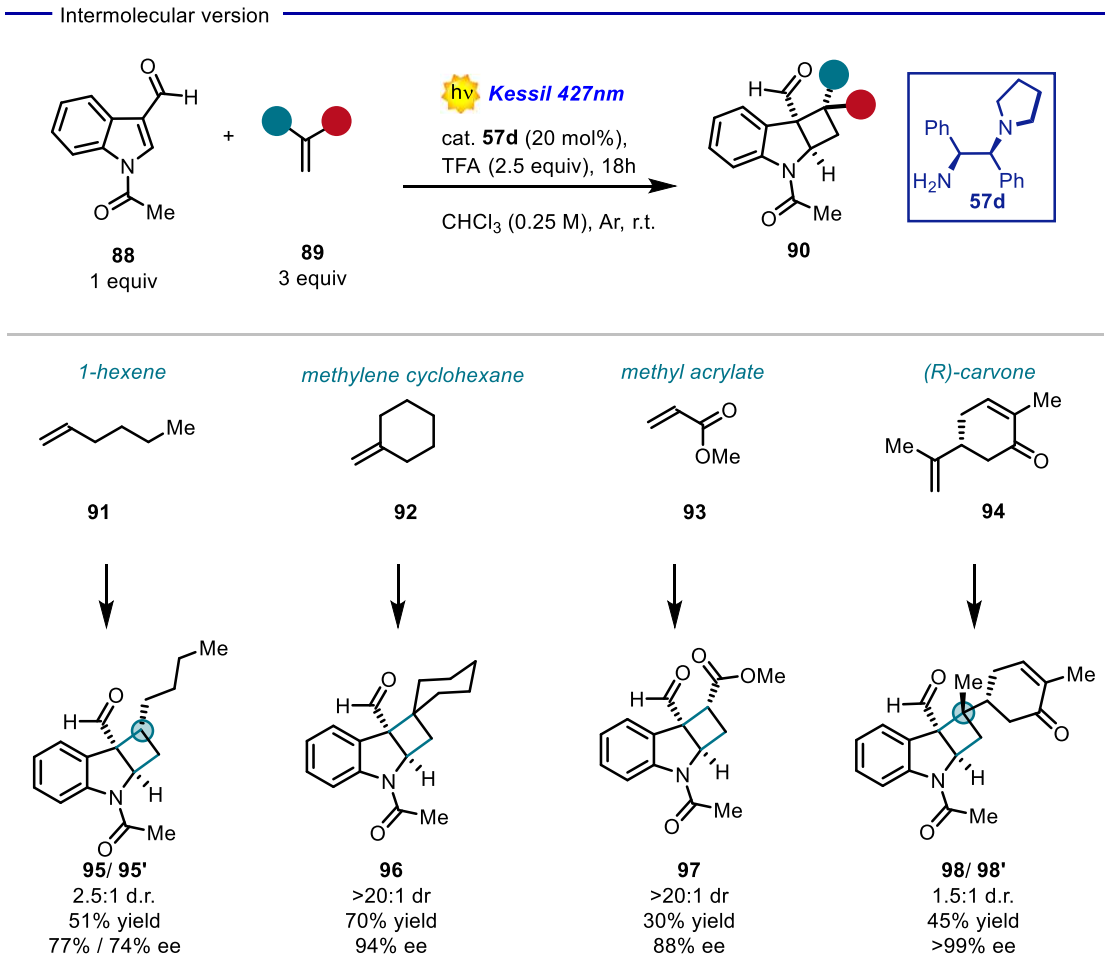

Scheme 13. Intermolecular enantioselective [2+2] photocycloaddition with good yields and high stereocontrol.

Finally, to highlight the synthetic utility of the products, a series of late-stage functionalizations was carried out starting from cycloadduct **64** (Scheme 14). The aldehyde functionality could be transformed into either a carboxylic acid (product **99**, 68% yield, 92% ee) or a terminal alkyne (**100**, 55% yield, 92% ee), both highly versatile handles for downstream derivatization and bioconjugation strategies. Alternatively, a reductive protocol allowed the simultaneous reduction of both the amide and aldehyde groups, delivering compound **101** in 64% yield and 91% ee. These manipulations not only underscore the robustness of the method but also demonstrate how the complex polycyclic scaffolds accessible through this photocycloaddition can serve as versatile building blocks for further elaboration.

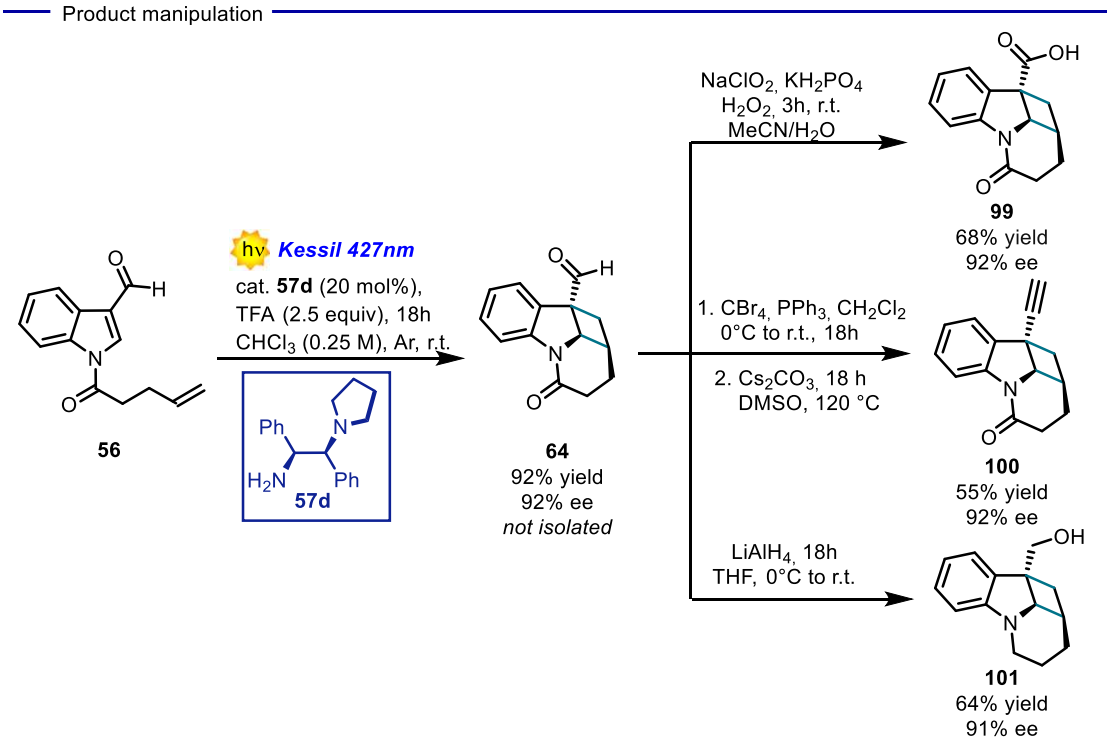

Scheme 14. Product manipulations demonstrating the synthetic versatility of the cycloadduct scaffold.

2.4. Conclusions

In conclusion, this work demonstrates how structural modification of iminium-ions can unlock reactivity modes that were previously considered inaccessible. By embedding the iminium functionality within an extended π-system, direct access to the triplet excited state was enabled, which proved to be the key intermediate for an enantioselective organocatalytic [2+2] photocycloaddition.

Mechanistic investigations provided compelling support for this reactivity. UV-vis absorption and transient spectroscopy clearly indicated the participation of the triplet state in the catalytic cycle, while computational studies confirmed a viable pathway involving intersystem crossing ($S_1 \rightarrow T_2$) followed by relaxation to the reactive T_1 manifold. This dual experimental–theoretical approach firmly establishes the role of the triplet state as the productive excited intermediate.

Beyond mechanistic insights, the method also proved to be highly general. A wide range of indole derivatives and olefinic partners were successfully transformed into fused polycyclic products, typically in high yield and with excellent levels of enantioselectivity. Importantly, the strategy was not limited to intramolecular reactions but could also be extended to intermolecular variants, tolerating complex and structurally diverse alkenes, including naturally occurring substrates such as (*R*)-(–)-carvone. Finally, synthetic manipulations of the cycloadducts showcased the versatility of the products, which can serve as valuable intermediates for further functionalization.

Altogether, these findings establish a new platform in asymmetric photochemistry, showing that carefully engineered iminium ions can function not only as chiral activators but also as intrinsically photoactive species.This approach expands the frontiers of organocatalytic excited-state chemistry, opening the way to new classes of enantioselective transformations driven by triplet reactivity.

2.5. Experimental part

2.5.1. General information

Reagents, solvents and experimental conditions

All required fine chemicals were purchased from Acros (Fisher), Aldrich (Merck), Alfa Aesar (Fisher), Fluorochem, TCI, BLDpharm and used without further purification unless otherwise stated. Organic solvents were purchased from Sigma–Aldrich and dried with 4 Å molecular sieves. $CHCl_3$ was neutralized by passing it through a column of basic alumina and then dried with 4 Å molecular sieves. Organocatalyst **57d**[34] and the related derivatives, as well as 4CzIPN[35] were prepared according to reported literature procedures.

The photocatalyzed reactions were set-up under an argon atmosphere in flame-dried screw-cap 4 mL glass vials and sealed with parafilm®. Photochemical reactions at controlled temperatures were carried out glass reactors equipped with a cooling jacket and a huber minichiller 300.

Thin-layer chromatography (TLC) analysis was performed on pre-coated Merck TLC plates (silica gel 60 GF254, 0.25 mm). Visualization of the developed chromatography was performed by checking UV absorbance (254 nm) as well as with aqueous ceric ammonium molybdate and potassium permanganate solutions.

Chromatographic purification of products was accomplished using flash chromatography on silica gel (SiO2, 0.04-0.063 mm, 60 Å) purchased from Machery-Nagel, with the indicated solvent system according to the standard techniques or using a Biotage Isolera automated flash chromatography system with cartridges packed with silica (SiO2, 0.04-0.063 mm, 60 Å).

Organic solutions were concentrated under reduced pressure on a Heidolph rotary evaporator.

The Kessil lamps PR160L (50W) were purchased from Kessil webpage and used as light sources at 400 and 427 nm. The light emission spectra of Kessil lamps can be found at the same website: www.kessil.com/science/PR160L.php.

Analytical techniques

NMR spectra were recorded on Bruker 400 Avance III HD equipped with a BBI-z grad probe head 5mm and Bruker 500 Avance III equipped with a BBI-ATM-z grad probe head 5mm. The chemical shifts (δ) for ^{1}H and ^{13}C are given in ppm relative to residual signals of the solvents ($CHCl_3$ @ 7.26 ppm for ^{1}H NMR, and @ 77.16 ppm for ^{13}C NMR; $CFCl_3$ @ 0.0 ppm for ^{19}F NMR spectra). Coupling constants are given in Hz. The following abbreviations are used to indicate the multiplicity: s, singlet; d, doublet; dd, double doublet; t, triplet; q, quartet; m, multiplet; br, broad signal. NMR yields were calculated by using trimethoxy benzene or dibromomethane as internal standard.

Enantiomeric excess (ee) values were determined with Waters Acquity UPC2-MS (Ultraperformance Convergence Chromatography) analysis, employing a chiral stationary phase column from Daicel Chiralpak with the model and the mobile phase specified in the individual experiment, by comparing the samples with the appropriate racemic mixtures. The peaks of the enantiomers were verified by identical UV-Vis spectra for the integrated peaks.

Optical rotations were determined with a Jasco P-1010 Polarimeter at 589 nm at the specified temperature. Data are reported as follows: $[\alpha]_D^{temp}$, concentration (c; g/100 mL), and solvents.

Steady-state absorption spectroscopy

UV-vis absorption spectroscopy studies were performed at room temperature on a Varian Cary 50 UV-Vis double beam spectrophotometer; 1 cm and 300 µm path length Hellma Analytics quartz cuvettes have been used.

Steady-state fluorescence spectroscopy

Emission spectra were taken on an Edinburgh Instrument spectrofluorometer equipped with a 900 W Xe arc lamp as an excitation source, a photomultiplier tube, and an InGaAs detector for the visible and the NIR detection, respectively. Fluorescence quantum yields were estimated with the relative method using quinine disulphate as a standard (Φ = 0.54 in 0.1 M H_2SO_4).

Time-correlated single-photon counting (TCSPC)

Fluorescence lifetimes were measured using a TCSPC apparatus (PicoQuant Picoharp 300) equipped with subnanosecond LED sources at 380 nm (500−700 ps pulse width) powered by a PicoQuant PDL 800-B variable (2.5−40 MHz) pulsed power supply. The decays were analyzed by means of PicoQuant FluoFit Global Fluorescence Decay Analysis Software.

Nanosecond laser flash photolysis

Laser flash photolysis measurements were conducted using a custom laser spectrometer comprised of a Continuum Surelite II Nd:YAG laser (FWHM = 8 ns) with a frequency tripled option (355 nm, 18 mJ/pulse) and an Applied Photophysics xenon light source. Laser excitation was provided at 90° with respect to the white light probe beam. Light transmitted by the sample was focused onto the entrance slit of a 300 mm focal length Acton SpectraPro 2300i triple grating, double exit monochromator equipped with a photomultiplier detector (Hamamatsu R3896) and a Princeton Instruments PIMAX II gated intensified CCD camera. PMT signals (kinetic traces) were processed using a Teledyne LeCroy 604Zi (400 MHz, 20 GS/s) digital oscilloscope.

High-Resolution Mass Spectra (HRMS)

were obtained using Waters GCT gas chromatograph coupled with a time-of-flight mass spectrometer (GC/MS-TOF) with electron ionization (EI).

Computational details

All unrestricted Density Functional Theory (DFT) and Time-Dependent-DFT (TD-DFT)[36,37] calculations were carried out using the *Gaussian16* suite (*Rev. C02*), at the ωB97XD level[38] of DFT, and with a 6-31+G** basis set. Open-shell S_0 (OSS_0), closed-shell S_0, and T_1 geometries were modelled with unrestricted DFT (using the guess=(Mix,Always) option). Optimization of T_1 downstream of the T_2-T_1 crossing point was also explored with TD-DFT. The complete pathway leading to the observed enantiomer was explored, and key points in the pathway toward the unobserved enantiomer, formed when the olefin attacks the indole from the Re face of the C=C bond, were also examined. All calculations featured in this work, along with exact inputs and resulting geometries, are accessible from a dedicated repository on the *ioChem-BD* platform.

Calculations were carried out in implicit $CHCl_3$, as modelled by the C-PCM implicit solvation modelBefore the main investigation, a systematic conformational exploration of intermediate **59** and smaller models was carried out under slightly different conditions. On this basis, the substrate conformer selected to initiate the in silico investigation was identified. Details of this exploration are reported in the "Computational Studies" section, and the corresponding calculations are provided electronically.[39,40]

Optimization of structures along the reaction path to minima or 1st-order transition states (TSs) was carried out using standard *Gaussian16* algorithms, with no tightening of convergence conditions. Similarly, standard convergence criteria were retained in the solution of SCF equations, with the quadratic convergence algorithm[24] required in a minority of cases. For TD-DFT calculations, we intentionally considered a high number of transitions (nstates=30).

Minima and TSs were discriminated *via* frequency calculations, expecting no negative vibrations in the former case, and one in the latter. TSs themselves were located with either the Opt=TS option (after a relaxed PES scan), or the STQN method.[41] All encountered TSs leading to the observed enantiomer were subjected to IRC calculations[42] for a few steps on either side of the TS, whence their re-optimization to the expected adjacent minima was duly verified.

Minimum Energy Crossing Points (MECPs;) were located using the *easyMECP* code, which exploits *Gaussian16* and is a redevelopment of the original *Fortran* implementation by Harvey *et al.*. Initial MECP

geometries for **MECP$_1$** with the iminium distorted towards the *Re* face of the indole C=C and for **MECP$_2$** were extracted from the optimization of **59** (S_1) and **MECP$_1$**, respectively. The initial geometry for **MECP$_3$** was directly derived from *Int-A* and those for **MECP$_1$** but with the iminium distorting towards the *Si* face of the indole C=C were obtained *via* a 180°-rotation of the iminium-photocatalyst moiety.

Orbital and electron density illustrations were drawn using dedicated *Gaussian16* utilities cubegen and cubman. Different isosurfaces were chosen to represent orbitals in individual cases, for the sake of easier discussion and better representability: chosen values are clearly reported in each figure. When illustrating changes in electronic distribution in TD-DFT calculations, the more intuitive Natural Transition Orbital (NTO) representation[43] was employed, for example by taking differences of individual squared NTOs. Cases where this approach was used are indicated in the text. Orbital figures were prepared using PyMO.[44]

2.5.2. Experimental setup for light irradiation

Figure 5 shows the general setup of a batch reaction performed at room temperature (left) or at controlled temperature (center) under Kessil LED PR160L light irradiation (400 nm, 427 nm, 467 nm). For the reaction at room temperature the reaction vessel is placed at a fixed distance (about 5 cm) from the light source and stirred vigorously. A maximum of three reaction vessels were irradiated at the same time placing them following the lines of homogeneous irradiance provided by the producer. To maintain a stable reaction temperature one fan was placed above the irradiated vials.

For the reactions at controlled temperature: the glass reactor (detailed in Figure 5c*, internal diameter = 1 cm, external diameter = 2cm*) containing the reaction mixture was placed at 1 cm from the light source and stirred vigorously. The temperature was controlled with a chiller connected to the glass reactor, using a mixture of H_2O/i-PrOH 7:3 as the circulating refrigerant liquid.

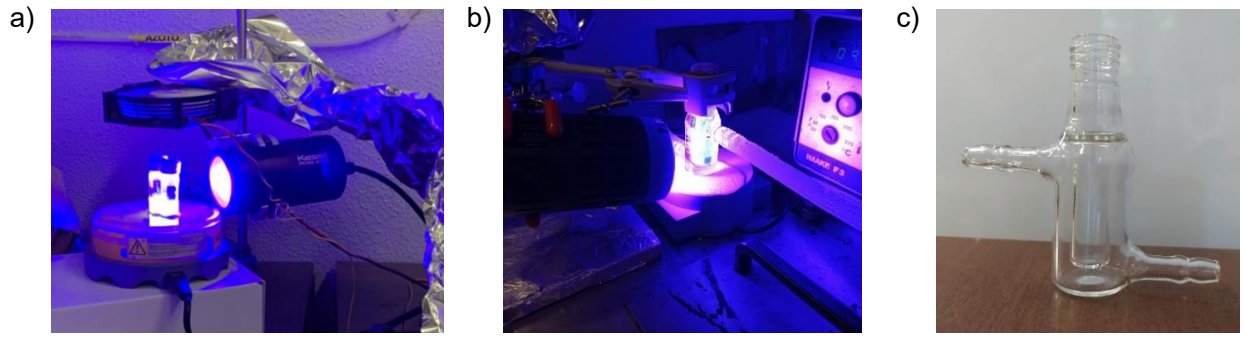

Figure 5. Panel a: Reaction set up. Panel b: reaction set up at low temperature. Panel c: glass vial provided with a cooling jacket.

2.5.3. Reaction optimization

Table 2.Screening of various organocatalysts. a) Substrate 1 (0.1 mmol), organocatalyst (20 mol%, 0.02 mmol), TFA (1 equiv), 1,2-dichloroethane (0.4 mL), inert atmosphere. b) Reaction yields were measured by 1H NMR analysis of the crude reaction mixtures using dibromomethane as internal standard. c) The ee values were determined by chiral stationary phase ultra-performance convergence chromatography (UPC2) after derivatization of the [2 + 2] adduct with (carbethoxymethylene)triphenylphosphorane.

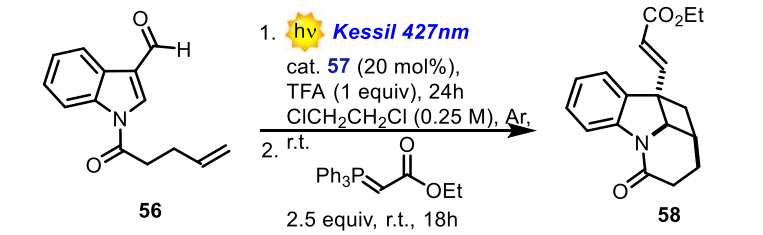

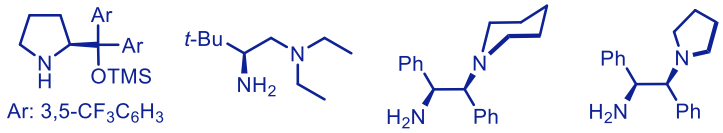

57a **57b** **57c** **2d**

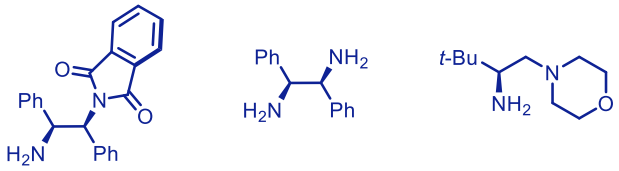

2e **2f** **2g**

Entry[a]	*cat.*	*yield (%)*[b]	*ee (%)*[c]
1	**57a**	< 5	n.d.
2	**57b**	64	63
3	**57c**	67	89
4	**57d**	62	91
5	**57e**	41	30
6	**57f**	26	32
7	**57g**	50	70

*Table 3.Screening of various solvents. a) Substrate **56** (0.1 mmol), organocatalyst **57d** (20 mol%, 0.02 mmol), TFA (1 equiv), solvent (0.4 mL), inert atmosphere. b) Reaction yields were measured by ^1H NMR analysis of the crude reaction mixtures using dibromomethane as internal standard. c) The ee values were determined by chiral stationary phase ultra-performance convergence chromatography (UPC^2) after derivatization of the [2 + 2] adduct with (carbethoxymethylene)triphenylphosphorane.*

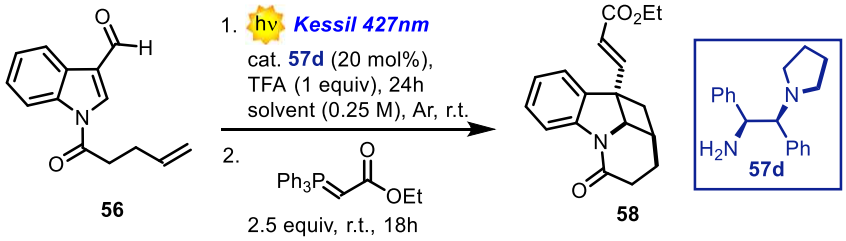

Entry[a]	solvent	yield (%)[b]	ee (%)[c]
1	$ClCH_2CH_2Cl$	62	91
2	AcOEt	< 5%	n.d.
3	MeCN	< 5%	n.d.
4	THF	< 5%	n.d.
5	CH_2Cl_2	62	92
6	$CHCl_3$	67	92
7	PhMe	35	87
	PhCl		

*Table 4.Screening of various acids, catalyst loadings or reaction temperatures. a) Substrate **56** (0.1 mmol), organocatalyst **57d** (20 mol%, 0.02 mmol), TFA (1 equiv), $CHCl_3$ (0.4 mL), inert atmosphere. b) Reaction yields were measured by ^1H NMR analysis of the crude reaction mixtures using dibromomethane as internal standard. c) The ee values were determined by chiral stationary phase ultra-performance convergence chromatography (UPC^2) after derivatization of the [2 + 2] adduct with (carbethoxymethylene)triphenylphosphorane. d) Reaction carried out in presence of 10 mol% of organocatalyst **57d**. e) Reaction carried out at 0 °C.*

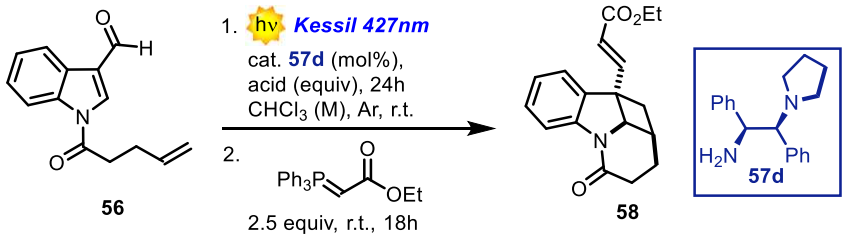

Entry[a]	acid (equiv)	yield (%)[b]	ee (%)[c]
1	TFA (1)	67	92
2	MsOH (1)	30	92
3	$(PhO)_2POOH$ (1)	39	88
4	TFA (0.5)	27	n.d.
5	TFA (2)	96	92
6	TFA (2.5)	97	92
7	TFA (3)	88	92
8[d]	TFA (2.5)	67	92
9[e]	TFA (2.5)	65	95

2.5.4. Synthesis and characterisation of starting materials

Vilsmeier-Haack formylation reaction.

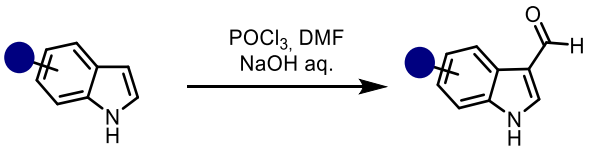

The Vilsmeier-Haack formylation procedure was carried out following a reported literature procedure.[45]

General Procedure A

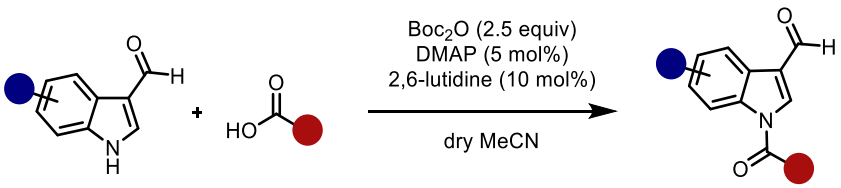

The synthesis follows the reported literature procedure.[46] A 50 mL round bottom flask equipped with a magnetic stirring bar, was charged with the corresponding substituted 1H-indole-3-carbaldehyde (2.5 equiv.),

the corresponding carboxylic acid (1 equiv.), 2,6-lutidine (0.1 equiv.) and DMAP (0.05 equiv.) in dry MeCN (1mL/mmol of 1H-indole-3-carbaldehyde) under Ar atmosphere. Then Boc_2O was added and the reaction mixture was warmed to 30 °C by water bath and stirred overnight. The resulting mixture was concentrated under reduced pressure and the crude was purified by silica gel column chromatography.

General Procedure B

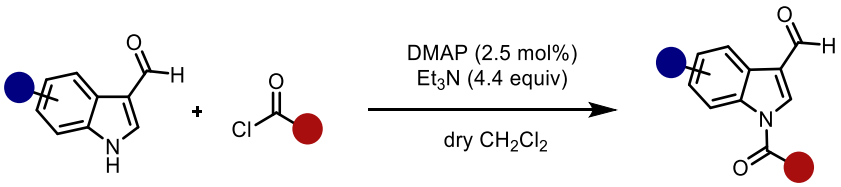

A 50 mL round bottom flask, equipped with a magnetic stirring bar, was charged with the corresponding carboxylic acid (2.5 equiv.) and $SOCl_2$ (3.25 equiv.) under Ar atmosphere. Then the mixture was heated to 50 °C and stirred for 2 hours. The resulting mixture was dissolved in dry CH_2Cl_2 (2mL/mmol of carboxylic acid) and added to a 100 mL round bottom flask charged with the corresponding 1*H*-indole-3-carbaldehyde derivative (1 equiv.), DMAP (0.025 equiv.) and Et_3N (4.4 equiv.) in dry CH_2Cl_2 (3mL/mmol of 1*H*-indole-3-carbaldehyde) under Ar atmosphere. The addition of the acyl chloride was performed at 0 °C using a syringe pump with a 0.5 mL/min addition rate. After 3 hours the reaction was quenched with a saturated aqueous solution of Na_2CO_3. The layers are separated and the aqueous phase is extracted with CH_2Cl_2. The combined organic layers are washed with brine, dried over $MgSO_4$ and concentrated under reduced pressure. The crude mixture was purified by silica gel column chromatography.
Note: In some cases, the excess of carboxylic acid contaminated the desired product. However, this impurity could be easily removed by dissolving the desired product in AcOEt and washing it with a saturated solution of Na_2CO_3. The collected organic phase was dried over $MgSO_4$ and concentrated under reduced pressure to afford the pure desired compound.

1-(Pent-4-enoyl)-1*H*-indole-3-carbaldehyde 56.

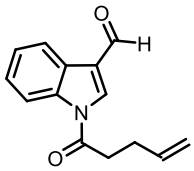

56

Synthesized following the general procedure A starting from 1*H*-indole-3-carbaldehyde (1.09 g, 7.5 mmol, 2.5 equiv.), 4-pentenoic acid (306 µL, 3 mmol, 1 equiv.), DMAP (18.3 mg, 0.15 mmol, 0.05 equiv), 2,6-lutidine (35 µL, 0.3 mmol, 0.1 equiv.) and Boc_2O (1.7 mL, 7.5 mmol, 2.5 equiv.) in 7.5 mL of dry MeCN. Purification by column chromatography (petroleum ether/AcOEt 9:1) yielded **56** (511 mg, 75%) as a white solid.

^{1}H NMR (400 MHz, Chloroform-*d*) δ 10.12 (s, 1H), 8.42 (dd, *J* = 7.3, 1.4 Hz, 1H), 8.27 (dd, *J* = 7.3, 1.7 Hz, 1H), 8.10 (s, 1H), 7.53 – 7.37 (m, 2H), 5.94 (ddt, *J* = 16.9, 10.2, 6.5 Hz, 1H), 5.22 – 5.14 (m, 1H), 5.14 – 5.09 (m, 1H), 3.10 (t, *J* = 7.4 Hz, 2H), 2.68 – 2.58 (m, 2H).
^{13}C NMR (101 MHz, Chloroform-*d*) δ 185.7, 170.8, 136.6, 135.9, 134.6, 127.0, 126.1, 125.5, 122.8, 122.0, 116.7, 116.6, 35.3, 28.3.
HRMS (ESI+): m/z calcd. for $[C_{14}H_{13}NO_2]^+$: 242.1176; found: 242.1173.

5-Bromo-1-(pent-4-enoyl)-1*H*-indole-3-carbaldehyde SM1.

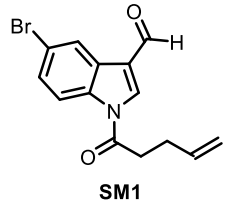

SM1

Synthesized following the general procedure B starting from 5-bromo-1*H*-indole-3-carbaldehyde (672 mg, 3 mmol, 1 equiv.), 4-pentenoic acid (765 µL, 7.5 mmol, 2.5 equiv.), $SOCl_2$ (711 µL 9.75 mmol, 3.25 equiv.), Et_3N (1.8 mL, 13.2 mmol, 4.4 equiv.) and DMAP (9.2 mg, 0.075 mmol, 0.025 equiv.) in 24 mL of dry CH_2Cl_2. Purification by column chromatography (petroleum ether/AcOEt 9:1 to 8:2) yielded **SM1** (578 mg, 63 %) as a light pink solid.

^{1}H NMR (400 MHz, Chloroform-*d*) δ 10.06 (s, 1H), 8.40 (d, *J* = 2.0 Hz, 1H), 8.28 (d, *J* = 8.8 Hz, 1H), 8.08 (s, 1H), 7.52 (dd, *J* = 8.9, 2.0 Hz, 1H), 5.93 (ddt, *J* = 16.9, 10.2, 6.5 Hz, 1H), 5.21 – 5.14 (m, 1H), 5.14 – 5.08 (m, 1H), 3.09 (t, *J* = 7.3 Hz, 2H), 2.72 – 2.51 (m, 2H).

^{13}C NMR (101 MHz, Chloroform-*d*) δ 185.2, 170.6, 135.8, 135.8, 135.2, 135.0, 129.9, 127.6, 124.8, 121.8, 119.1, 118.0, 116.9, 116.8, 35.1, 28.2.

HRMS (ESI+): m/z calcd. for $[C_{14}H_{12}BrNO_2]^+$: 306.0124; found: 306.0145.

5-Fluoro-1-(pent-4-enoyl)-1H-indole-3-carbaldehyde SM2.

SM2

Synthesized following the general procedure A starting from 5-fluoro-1*H*-indole-3-carbaldehyde (1.22 g, 7.5 mmol, 2.5 equiv.), 4-pentenoic acid (306 µL, 3 mmol, 1 equiv.), DMAP (18.3 mg, 0.15 mmol, 0.05 equiv.), 2,6-lutidine (35 µL, 0.3 mmol, 0.1 equiv.) and Boc_2O (1.7 mL, 7.5 mmol, 2.5 equiv.) in 7.5 mL of dry MeCN. Purification by column chromatography (petroleum ether/AcOEt 9:1 to 7:3) yielded **SM2** (489 mg, 61%) as an off-white solid.

^{1}H NMR (400 MHz, Chloroform-*d*) δ 10.09 (s, 1H), 8.40 (dd, *J* = 9.1, 4.5 Hz, 1H), 8.14 (s, 1H), 7.94 (dd, *J* = 8.7, 2.6 Hz, 1H), 7.16 (ddd, *J* = 9.4, 8.9, 2.6 Hz, 1H), 5.93 (ddt, *J* = 16.9, 10.1, 6.6 Hz, 1H), 5.22 – 5.14 (m, 1H), 5.14 – 5.08 (m, 1H), 3.10 (t, *J* = 7.6 Hz, 2H), 2.69 – 2.58 (m, 2H).

^{13}C NMR (101 MHz, Chloroform-*d*) δ 185.3, 170.6, 160.7 (d, *J* = 243.0 Hz), 135.8, 135.4, 132.9, 127.2 (d, *J* = 10.9 Hz), 122.37 (d, *J* = 4.1 Hz), 117.85 (d, *J* = 9.2 Hz), 116.8, 114.9 (d, *J* = 24.9 Hz), 108.0 (d, *J* = 25.0 Hz), 35.0, 28.3.

^{19}F NMR (377 MHz, Chloroform-*d*) δ -116.31.

HRMS (ESI+): m/z calcd. for $[C_{14}H_{12}FNO_2]^+$: 246.0925; found: 246.0956.

3-Formyl-1-(pent-4-enoyl)-1H-indole-5-carbonitrile SM3.

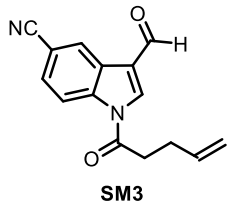

SM3

Synthesized following the general procedure A starting from 5-cyano-1*H*-indole-3-carbaldehyde (1.27 g, 7.5 mmol, 2.5 equiv.), 4-pentenoic acid (306 µL, 3 mmol, 1 equiv.), DMAP (18.3 mg, 0.15 mmol, 0.05 equiv), 2,6-lutidine (35 µL, 0.3 mmol, 0.1 equiv.) and Boc_2O (1.7 mL, 7.5 mmol, 2.5 equiv.) in 7.5 mL of dry MeCN. Purification by column chromatography (petroleum ether/AcOEt 9:1 to 6:4) yielded **SM3** (295 mg, 39%) as an off-white solid.

^{1}H NMR (400 MHz, Chloroform-*d*) δ 10.14 (s, 1H), 8.65 – 8.62 (m, 1H), 8.56 (d, *J* = 8.7 Hz, 1H), 8.24 (s, 1H), 7.69 (dd, *J* = 8.7, 1.6 Hz, 1H), 5.93 (ddt, *J* = 16.9, 10.2, 6.5 Hz, 1H), 5.24 – 5.15 (m, 1H), 5.15 – 5.10 (m, 1H), 3.14 (t, *J* = 7.3 Hz, 2H), 2.69 – 2.59 (m, 2H).

^{13}C NMR (101 MHz, Chloroform-*d*) δ 185.1, 185.0, 184.9, 170.7, 138.2, 136.0, 135.6, 135.5, 130.2, 127.1, 126.9, 126.2, 122.1, 119.0, 117.7, 117.6, 117.1, 109.3, 35.3, 28.1.

HRMS (ESI+): m/z calcd. for $[C_{15}H_{12}N_2O_2]^+$: 253.0972; found: 253.0976.

3-Formyl-1-(pent-4-enoyl)-1*H*-indol-5-yl 4-methylbenzenesulfonate SM4.

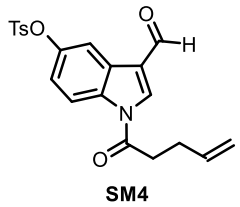

SM4

Synthesized following the general procedure B starting from 3-formyl-1H-indol-5-yl 4-methylbenzenesulfonate (946 mg, 3 mmol, 1 equiv.), 4-pentenoic acid (765 µL, 7.5 mmol, 2.5 equiv.), $SOCl_2$ (711 µL 9.75 mmol, 3.25 equiv.), Et_3N (1.8 mL, 13.2 mmol, 4.4 equiv.) and DMAP (9.2 mg, 0.075 mmol, 0.025 equiv.) in 24 mL of dry CH_2Cl_2. Purification by column chromatography (petroleum ether/CH_2Cl_2 80:20 to 70:30) yielded **SM4** (918 mg, 77 %) as a white solid.

^{1}H NMR (400 MHz, Chloroform-*d*) δ 10.01 (s, 1H), 8.35 (d, J = 9.1 Hz, 1H), 8.15 (s, 1H), 7.87 (d, J = 2.5 Hz, 1H), 7.78 – 7.67 (m, 2H), 7.32 (d, J = 8.0 Hz, 2H), 7.07 (dd, J = 9.1, 2.4 Hz, 1H), 6.05 – 5.85 (m, 1H), 5.26 – 5.06 (m, 2H), 3.10 (t, J = 7.3 Hz, 2H), 2.62 (q, J = 7.1 Hz, 2H), 2.46 (s, 3H).

^{13}C NMR (101 MHz, Chloroform-*d*) δ 185.0, 170.6, 147.0, 145.6, 135.7, 135.4, 134.7, 132.3, 129.8, 128.5, 126.7, 122.1, 121.2, 117.4, 116.7, 115.6, 34.9, 28.1, 21.7.

HRMS (ESI+): m/z calcd. for $[C_{21}H_{20}NO_5S]^+$: 398.1057; found 398.1089.

1-(Pent-4-enoyl)-5-(4,4,5,5-tetramethyl-1,3,2-dioxaborolan-2-yl)-1*H*-indole-3-carbaldehyde SM5.

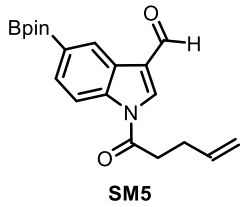

SM5

Synthesized following the general procedure B starting from 5-(4,4,5,5-tetramethyl-1,3,2-dioxaborolan-2-yl)-1H-indole-3-carbaldehyde (813 mg, 3 mmol, 1 equiv.), 4-pentenoic acid (765 µL, 7.5 mmol, 2.5 equiv.), $SOCl_2$ (711 µL 9.75 mmol, 3.25 equiv.), Et_3N (1.8 mL, 13.2 mmol, 4.4 equiv.) and DMAP (9.2 mg, 0.075 mmol, 0.025 equiv.) in 24 mL of dry CH_2Cl_2. Purification by column chromatography (petroleum ether/CH_2Cl_2 80:20 to 70:30) yielded **SM5** (397 mg, 37 %) as a white solid.

^{1}H NMR (400 MHz, Chloroform-*d*) δ 10.16 (s, 1H), 8.73 (s, 1H), 8.41 (d, J = 8.4 Hz, 1H), 8.12 (s, 1H), 7.90 (dd, J = 8.4, 1.3 Hz, 1H), 6.07 – 5.79 (m, 1H), 5.32 – 5.02 (m, 2H), 3.12 (t, J = 7.4 Hz, 2H), 2.64 (q, J = 7.1 Hz, 2H), 1.39 (s, 12H).

^{13}C NMR (101 MHz, Chloroform-*d*) 185.4, 170.8, 138.3, 135.8, 134.2, 133.1, 128.7, 125.6, 122.8, 116.6, 115.7, 84.0, 35.2, 28.1, 24.9.

HRMS (ESI+): m/z calcd. for $[C_{20}H_{25}BNO_4]^+$: 354.1821 found 354.1898.

1-(Pent-4-enoyl)-6-(trifluoromethyl)-1H-indole-3-carbaldehyde SM6.

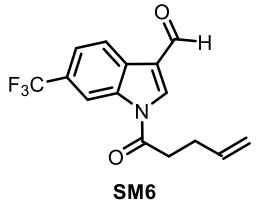

SM6

Synthesized following the general procedure B starting from 5-(trifluoromethyl)-1*H*-indole-3-carbaldehyde (639 mg, 3 mmol, 1 equiv.), 4-pentenoic acid (765 µL, 7.5 mmol, 2.5 equiv.), $SOCl_2$ (711 µL 9.75 mmol, 3.25 equiv.), Et_3N (1.8 mL, 13.2 mmol, 4.4 equiv.) and DMAP (9.2 mg, 0.075 mmol, 0.025 equiv.) in 24 mL of dry CH_2Cl_2. Purification by column chromatography (petroleum ether/CH_2Cl_2 1:1 to 1:2) yielded **SM6** (522 mg, 59 %) as a yellowish solid.

^{1}H NMR (400 MHz, Chloroform-*d*) δ 10.07 (s, 1H), 8.70 (s, 1H), 8.28 (d, *J* = 8.3 Hz, 1H), 8.19 (s, 1H), 7.58 (dd, *J* = 8.3, 1.6 Hz, 1H), 5.93 (ddt, *J* = 16.9, 10.2, 6.5 Hz, 1H), 5.21 – 5.14 (m, 1H), 5.14 – 5.08 (m, 1H), 3.11 (t, *J* = 7.3 Hz, 2H), 2.69 – 2.58 (m, 2H).

^{13}C NMR (101 MHz, Chloroform-*d*) δ 185.2, 170.7, 136.1, 135.7, 128.8 (q, *J* = 32.3 Hz), 128.5, 124.4 (q, *J* = 273.3 Hz), 122.4, 122.2 (q, *J* = 3.6 Hz), 122.1, 116.8, 114.1 (q, *J* = 4.4 Hz), 35.0, 28.0.

^{19}F NMR (377 MHz, Chloroform-*d*) δ -61.32.

HRMS (ESI+): m/z calcd. for $[C_{15}H_{12}F_3NO_2]^+$: 296.0893; found: 296.0930.

6-Methyl-1-(pent-4-enoyl)-1*H*-indole-3-carbaldehyde SM7.

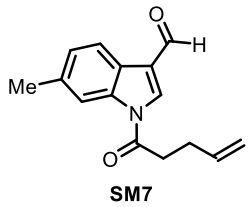

SM7

Synthesized following the general procedure A starting from 6-methyl-1*H*-indole-3-carbaldehyde (1.19 g, 7.5 mmol, 2.5 equiv.), 4-pentenoic acid (306 µL, 3 mmol, 1 equiv.), DMAP (18.3 mg, 0.15 mmol, 0.05 equiv.), 2,6-lutidine (35 µL, 0.3 mmol, 0.1 equiv.) and Boc_2O (1.7 mL, 7.5 mmol, 2.5 equiv.) in 7.5 mL of dry MeCN. Purification by column chromatography (petroleum ether/AcOEt 9:1 to 8:2) yielded **SM7** (391 mg, 54%) as an off-white solid.

^{1}H NMR (400 MHz, Chloroform-*d*) δ 10.08 (s, 1H), 8.25 (s, 1H), 8.12 (d, *J* = 8.0 Hz, 1H), 8.02 (s, 1H), 7.23 (dd, *J* = 8.0, 1.4 Hz, 1H), 5.94 (ddt, *J* = 16.9, 10.2, 6.5 Hz, 1H), 5.23 – 5.14 (m, 1H), 5.14 – 5.06 (m, 1H), 3.08 (t, *J* = 7.3 Hz, 2H), 2.67 – 2.58 (m, 2H), 2.50 (s, 3H).

^{13}C NMR (101 MHz, Chloroform-*d*) δ 185.7, 170.9, 137.3, 137.0, 136.0, 134.1, 126.9, 123.7, 122.9, 121.5, 116.74, 116.67, 35.2, 28.3, 22.2.

HRMS (ESI+): m/z calcd. for $[C_{15}H_{15}NO_2]^+$: 242.1176; found: 242.1170.

6-Bromo-1-(pent-4-enoyl)-1*H*-indole-3-carbaldehyde SM8.

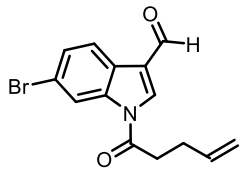

SM8

Synthesized following the general procedure B starting from 6-bromo-1*H*-indole-3-carbaldehyde (672 mg, 3 mmol, 1 equiv.), 4-pentenoic acid (765 µL, 7.5 mmol, 2.5 equiv.), $SOCl_2$ (711 µL 9.75 mmol, 3.25 equiv.), Et_3N (1.8 mL, 13.2 mmol, 4.4 equiv.) and DMAP (9.2 mg, 0.075 mmol, 0.025 equiv.) in 24 mL of dry CH_2Cl_2. Purification by column chromatography (petroleum ether/AcOEt 9:1 to 8:2) yielded **SM8** (587 mg, 64 %) as a dark orange solid.

^{1}H NMR (400 MHz, Chloroform-*d*) δ 10.07 (s, 1H), 8.62 (d, *J* = 1.7 Hz, 1H), 8.10 (d, *J* = 8.4 Hz, 1H), 8.05 (s, 1H), 7.50 (dd, *J* = 8.4, 1.8 Hz, 1H), 5.92 (ddt, *J* = 16.9, 10.2, 6.5 Hz, 1H), 5.21 – 5.14 (m, 1H), 5.14 – 5.09 (m, 1H), 3.08 (t, *J* = 7.3 Hz, 2H), 2.67 – 2.58 (m, 2H).

^{13}C NMR (101 MHz, Chloroform-*d*) δ 185.3, 170.6, 137.0, 135.8, 134.5, 128.8, 124.8, 123.1, 122.4, 120.8, 119.8, 116.9, 35.1, 28.2.

HRMS (ESI+): m/z calcd. for $[C_{14}H_{12}BrNO_2]^+$: 306.0124; found: 306.0145.

Methyl 3-formyl-1-(pent-4-enoyl)-1*H*-indole-6-carboxylate SM9.

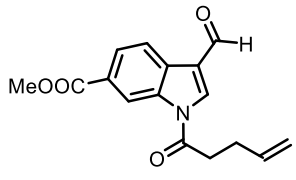

SM9

Synthesized following the general procedure B starting from methyl 3-formyl-1*H*-indole-5-carboxylate (609 mg, 3 mmol, 1 equiv.), 4-pentenoic acid (765 µL, 7.5 mmol, 2.5 equiv.), $SOCl_2$ (711 µL 9.75 mmol, 3.25 equiv.), Et_3N (1.8 mL, 13.2 mmol, 4.4 equiv.) and DMAP (9.2 mg, 0.075 mmol, 0.025 equiv.) in 24 mL of dry CH_2Cl_2. Purification by column chromatography (petroleum ether/AcOEt 9:1 to 6:4) yielded **SM9** (256 mg, 33 %) as a white solid.

^{1}H NMR (400 MHz, Chloroform-*d*) δ 10.13 (s, 1H), 9.08 (d, *J* = 1.5 Hz, 1H), 8.30 (d, *J* = 8.4 Hz, 1H), 8.25 (s, 1H), 8.09 (dd, *J* = 8.3, 1.4 Hz, 1H), 5.94 (ddt, *J* = 16.8, 10.2, 6.5 Hz, 1H), 5.22 – 5.14 (m, 1H), 5.14 – 5.08 (m, 1H), 3.96 (s, 3H), 3.14 (t, *J* = 7.3 Hz, 2H), 2.70 – 2.60 (m, 2H).

^{13}C NMR (101 MHz, Chloroform-*d*) δ 185.3, 170.6, 167.1, 136.4, 136.0, 135.8, 129.7, 128.7, 126.7, 122.3, 121.8, 118.3, 116.9, 52.5, 35.3, 28.2.

HRMS (ESI+): m/z calcd. for $[C_{16}H_{16}NO_4]^+$:286.1074; found: 286.1068.

6-Fluoro-1-(pent-4-enoyl)-1*H*-indole-3-carbaldehyde SM10.

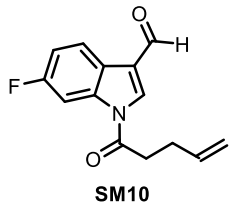

SM10

Synthesized following the general procedure B starting from 6-fluoro-1*H*-indole-3-carbaldehyde (489 mg, 3 mmol, 1 equiv.), 4-pentenoic acid (765 µL, 7.5 mmol, 2.5 equiv.), $SOCl_2$ (711 µL 9.75 mmol, 3.25 equiv.), Et_3N (1.8 mL, 13.2 mmol, 4.4 equiv.) and DMAP (9.2 mg, 0.075 mmol, 0.025 equiv.) in 24 mL of dry CH_2Cl_2. Purification by column chromatography (petroleum ether/AcOEt 9:1 to 8:2) yielded **SM10** (368 mg, 50 %) as a light yellow solid.

^{1}H NMR (400 MHz, Chloroform-*d*) δ 10.08 (s, 1H), 8.26 – 8.14 (m, 2H), 8.09 (s, 1H), 7.19 – 7.11 (m, 1H), 5.93 (ddt, *J* = 16.9, 10.2, 6.5 Hz, 1H), 5.21 – 5.14 (m, 1H), 5.14 – 5.09 (m, 1H), 3.09 (t, *J* = 7.3 Hz, 2H), 2.67 – 2.58 (m, 2H).

^{13}C NMR (101 MHz, Chloroform-*d*) δ 185.4, 170.7, 162.1 (d, *J* = 243.9 Hz), 136.8 (d, *J* = 13.0 Hz), 134.6 (d, *J* = 3.2 Hz), 123.0 (d, *J* = 9.8 Hz), 122.6, 122.30 (d, *J* = 1.7 Hz), 116.8, 113.9 (d, *J* = 24.0 Hz), 104.2 (d, *J* = 28.9 Hz), 35.1, 28.2.

^{19}F NMR (377 MHz, Chloroform-*d*) δ -113.16.

HRMS (ESI+): m/z calcd. for $[C_{14}H_{12}FNO_2]^+$: 246.0925; found: 246.0956.

4-Methyl-1-(pent-4-enoyl)-1*H*-indole-3-carbaldehyde SM11.

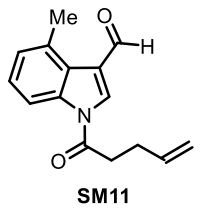

SM11

Synthesized following the general procedure B starting from 4-methyl-1*H*-indole-3-carbaldehyde (477 mg, 3 mmol, 1 equiv.), 4-pentenoic acid (765 µL, 7.5 mmol, 2.5 equiv.), $SOCl_2$ (711 µL 9.75 mmol, 3.25 equiv.), Et_3N (1.8 mL, 13.2 mmol, 4.4 equiv.) and DMAP (9.2 mg, 0.075 mmol, 0.025 equiv.) in 24 mL of dry CH_2Cl_2. Purification by column chromatography (petroleum ether/AcOEt 9:1 to 8:2) yielded **SM11** (485 mg, 67 %) as a light brown solid.

^{1}H NMR (400 MHz, Chloroform-*d*) δ 10.25 (s, 1H), 8.34 (d, *J* = 8.4 Hz, 1H), 8.16 (s, 1H), 7.32 (dd, *J* = 8.4, 7.4 Hz, 1H), 7.18 (d, *J* = 7.4 Hz, 1H), 5.93 (ddt, *J* = 16.9, 10.3, 6.5 Hz, 1H), 5.20 – 5.13 (m, 1H), 5.13 – 5.07 (m, 1H), 3.09 (t, *J* = 7.4 Hz, 2H), 2.79 (s, 3H), 2.66 – 2.57 (m, 2H).

^{13}C NMR (101 MHz, Chloroform-*d*) δ 185.9, 171.0, 137.2, 136.0, 133.5, 132.0, 127.1, 126.5, 125.6, 124.4, 116.6, 114.4, 35.2, 28.3, 22.6.

HRMS (ESI+): m/z calcd. for $[C_{15}H_{15}NO_2]^+$: 242.1176; found: 242.1170.

3-Formyl-1-(pent-4-enoyl)-1*H*-indole-4-carbonitrile SM12.

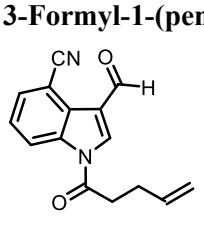

SM12

Synthesized following the general procedure B starting from 4-cyano-1*H*-indole-3-carbaldehyde (510 mg, 3 mmol, 1 equiv.), 4-pentenoic acid (765 µL, 7.5 mmol, 2.5 equiv.), $SOCl_2$ (711 µL 9.75 mmol, 3.25 equiv.), Et_3N (1.8 mL, 13.2 mmol, 4.4 equiv.) and DMAP (9.2 mg, 0.075 mmol, 0.025 equiv.) in 24 mL of dry CH_2Cl_2. Purification by column chromatography (petroleum ether/CH_2Cl_2 2:1 to 1:2) yielded **SM12** (560 mg, 74 %) as an off-white solid.

^{1}H NMR (400 MHz, Chloroform-*d*) δ 10.67 (s, 1H), 8.80 (dd, *J* = 8.6, 1.5 Hz, 1H), 8.38 (s, 1H), 7.75 (dd, *J* = 7.7, 1.5 Hz, 1H), 7.57 – 7.48 (m, 1H), 5.91 (ddt, *J* = 16.8, 9.6, 6.5 Hz, 1H), 5.20 – 5.14 (m, 1H), 5.14 – 5.08 (m, 1H), 3.14 (t, *J* = 7.1 Hz, 2H), 2.66 – 2.57 (m, 2H).

^{13}C NMR (101 MHz, Chloroform-*d*) δ 184.9, 171.0, 136.7, 135.4, 132.1, 130.8, 127.3, 126.2, 121.9, 121.0, 118.6, 116.9, 103.3, 35.1, 28.0.

HRMS (ESI+): m/z calcd. for $[C_{15}H_{12}N_2O_2]^+$: 253.0972; found: 253.0975.

4-Fluoro-1-(pent-4-enoyl)-1*H*-indole-3-carbaldehyde SM13.

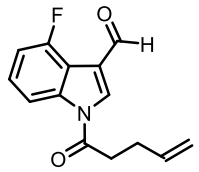

SM13

Synthesized following the general procedure B starting from 4-fluoro-1*H*-indole-3-carbaldehyde (489 mg, 3 mmol, 1 equiv.), 4-pentenoic acid (765 µL, 7.5 mmol, 2.5 equiv.), $SOCl_2$ (711 µL 9.75 mmol, 3.25 equiv.), Et_3N (1.8 mL, 13.2 mmol, 4.4 equiv.) and DMAP (9.2 mg, 0.075 mmol, 0.025 equiv.) in 24 mL of dry CH_2Cl_2. Purification by column chromatography (petroleum ether/CH_2Cl_2 1:1 to 1:2) yielded **SM13** (441 mg, 60 %) as a white solid.

^{1}H NMR (400 MHz, Chloroform-*d*) δ 10.35 (s, 1H), 8.30 (d, *J* = 8.4 Hz, 1H), 8.19 (s, 1H), 7.43 – 7.34 (m, 1H), 7.12 (dd, *J* = 10.1, 8.1 Hz, 1H), 5.92 (ddt, *J* = 16.9, 10.2, 6.5 Hz, 1H), 5.22 – 5.13 (m, 1H), 5.13 – 5.06 (m, 1H), 3.10 (t, *J* = 7.3 Hz, 2H), 2.69 – 2.54 (m, 2H).

^{13}C NMR (101 MHz, Chloroform-*d*) δ 186.3 (d, *J* = 4.1 Hz), 171.2, 156.3 (d, *J* = 249.6 Hz), 138.3 (d, *J* = 9.9 Hz), 135.8, 129.4, 127.3 (d, *J* = 7.3 Hz), 121.0 (d, *J* = 5.5 Hz), 116.8, 115.7 (d, *J* = 21.6 Hz), 113.3 (d, *J* = 4.0 Hz), 111.01 (d, *J* = 18.9 Hz), 35.2, 28.2.

^{19}F NMR (377 MHz, Chloroform-*d*) δ -115.20.

HRMS (ESI+): m/z calcd. for $[C_{14}H_{12}FNO_2]^+$: 246.0925; found: 246.0956.

4-Bromo-1-(pent-4-enoyl)-1*H*-indole-3-carbaldehyde SM14.

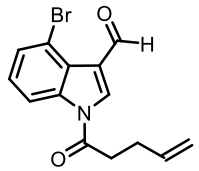

SM14

Synthesized following the general procedure B starting from 4-bromo-1*H*-indole-3-carbaldehyde (672 mg, 3 mmol, 1 equiv.), 4-pentenoic acid (765 µL, 7.5 mmol, 2.5 equiv.), $SOCl_2$ (711 µL 9.75 mmol, 3.25 equiv.), Et_3N (1.8 mL, 13.2 mmol, 4.4 equiv.) and DMAP (9.2 mg, 0.075 mmol, 0.025 equiv.) in 24 mL of dry CH_2Cl_2. Purification by column chromatography (petroleum ether/CH_2Cl_2 1:1 to 1:2) yielded **SM14** (569 mg, 62 %) as an off-white solid.

^{1}H NMR (400 MHz, Chloroform-*d*) δ 10.98 (s, 1H), 8.56 – 8.50 (m, 1H), 8.29 (s, 1H), 7.62 – 7.55 (m, 1H), 7.32 – 7.23 (m, 1H), 5.91 (ddt, *J* = 16.9, 10.2, 6.5 Hz, 1H), 5.22 – 5.13 (m, 1H), 5.12 – 5.07 (m, 1H), 3.10 (t, *J* = 7.4 Hz, 2H), 2.70 – 2.54 (m, 2H).

^{13}C NMR (101 MHz, Chloroform-*d*) δ 187.1, 171.2, 137.8, 135.7, 130.3, 129.4, 127.0, 126.9, 122.4, 116.8, 116.3, 113.5, 35.2, 28.2.

HRMS (ESI+): m/z calcd. for $[C_{14}H_{12}BrNO_2]^+$: 306.0124; found: 306.0145.

7-Methyl-1-(pent-4-enoyl)-1*H*-indole-3-carbaldehyde SM15.

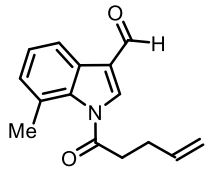

SM15

Synthesized following the general procedure B starting from 7-methyl-1*H*-indole-3-carbaldehyde (477 mg, 3 mmol, 1 equiv.), 4-pentenoic acid (765 µL, 7.5 mmol, 2.5 equiv.), $SOCl_2$ (711 µL 9.75 mmol, 3.25 equiv.), Et_3N (1.8 mL, 13.2 mmol, 4.4 equiv.) and DMAP (9.2 mg, 0.075 mmol, 0.025 equiv.) in 24 mL of dry CH_2Cl_2. Purification by column chromatography (petroleum ether/AcOEt 9:1 to 7:3) yielded **SM15** (521 mg, 72 %) as a light yellow solid.

^{1}H NMR (400 MHz, Chloroform-*d*) δ 10.10 (s, 1H), 8.15 (d, *J* = 7.8 Hz, 1H), 8.06 (s, 1H), 7.36 – 7.31 (m, 1H), 7.24 (d, *J* = 7.5 Hz, 1H), 5.93 (ddt, *J* = 16.8, 10.2, 6.5 Hz, 1H), 5.22 – 5.15 (m, 1H), 5.14 – 5.06 (m, 1H), 3.13 (t, *J* = 7.3 Hz, 2H), 2.74 – 2.59 (m, 2H), 2.51 (s, 3H).

^{13}C NMR (101 MHz, Chloroform-*d*) δ 185.5, 170.3, 136.10, 136.05, 135.8, 129.9, 127.5, 126.5, 125.8, 122.5, 119.5, 116.9, 36.0, 29.1, 22.5.

HRMS (ESI+): m/z calcd. for $[C_{15}H_{15}NO_2]^+$: 242.1176; found: 242.1170.

7-Chloro-1-(pent-4-enoyl)-1*H*-indole-3-carbaldehyde SM16.

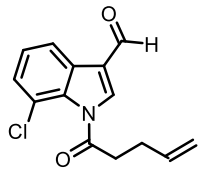

SM16

Synthesized following the general procedure B starting from 7-chloro-1*H*-indole-3-carbaldehyde (539 mg, 3 mmol, 1 equiv.), 4-pentenoic acid (765 µL, 7.5 mmol, 2.5 equiv.), $SOCl_2$ (711 µL 9.75 mmol, 3.25 equiv.), Et_3N (1.8 mL, 13.2 mmol, 4.4 equiv.) and DMAP (9.2 mg, 0.075 mmol, 0.025 equiv.) in 24 mL of dry CH_2Cl_2. Purification by column chromatography (petroleum ether/AcOEt 9:1 to 8:2) yielded **SM16** (149 mg, 19 %) as a yellowish solid.

^{1}H NMR (400 MHz, Chloroform-*d*) δ 10.10 (s, 1H), 8.26 (dd, *J* = 7.8, 1.2 Hz, 1H), 8.08 (d, *J* = 1.6 Hz, 1H), 7.45 (dd, *J* = 7.8, 1.2 Hz, 1H), 7.36 (dd, *J* = 8.6, 7.1 Hz, 1H), 5.89 (ddt, *J* = 16.8, 10.2, 6.6 Hz, 1H), 5.20 – 5.12 (m, 1H), 5.12 – 5.04 (m, 1H), 3.13 (d, *J* = 7.1 Hz, 2H), 2.77 – 2.56 (m, 2H).

^{13}C NMR (101 MHz, Chloroform-*d*) δ 185.2, 170.5, 136.9, 135.5, 133.4, 129.7, 128.3, 126.4, 121.7, 121.0, 120.8, 117.0, 37.2, 29.2.

HRMS (ESI+): m/z calcd. for $[C_{14}H_{12}ClNO_2]^+$: 262.0629; found: 262.0627.

1-(Hex-5-enoyl)-1*H*-indole-3-carbaldehyde SM17.

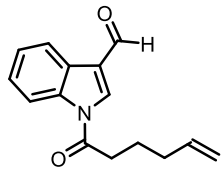

SM17

Synthesized following the general procedure A starting from 1*H*-indole-3-carbaldehyde (1.09 g, 7.5 mmol, 2.5 equiv.), 5-hexenoic acid (356 µL, 3 mmol, 1 equiv.), DMAP (18.3 mg, 0.15 mmol, 0.05 equiv), 2,6-lutidine (35 µL, 0.3 mmol, 0.1 equiv.) and Boc_2O (1.7 mL, 7.5 mmol, 2.5 equiv.) in 7.5 mL of dry MeCN. Purification by column chromatography (petroleum ether/AcOEt 9:1 to 8:2) yielded **SM17** (304 mg, 42%) as a light brown solid.

^{1}H NMR (400 MHz, Chloroform-*d*) δ 10.12 (s, 1H), 8.44 – 8.39 (m, 1H), 8.31 – 8.23 (m, 1H), 8.10 (s, 1H), 7.51 – 7.36 (m, 2H), 5.84 (ddt, *J* = 16.9, 10.1, 6.7 Hz, 1H), 5.14 – 5.04 (m, 2H), 3.00 (t, *J* = 7.3 Hz, 2H), 2.30 – 2.20 (m, 2H), 1.99 (p, *J* = 7.3 Hz, 2H).

^{13}C NMR (101 MHz, Chloroform-*d*) δ 185.7, 171.5, 137.3, 136.6, 134.7, 127.0, 126.1, 125.5, 122.7, 122.0, 116.6, 116.3, 34.9, 32.9, 23.4.

HRMS (ESI+): m/z calcd. for $[C_{15}H_{15}NO_2]^+$: 242.1176; found: 242.1170.

(*E*)-1-(hex-4-enoyl)-1*H*-indole-3-carbaldehyde 61-(E).

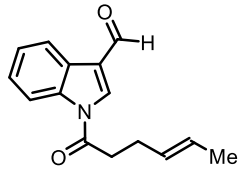

61-(E)

Synthesised following the general procedure B starting from 1*H*-indole-3-carbaldehyde (435 mg, 3 mmol, 1 equiv.), (*E*)-hex-4-enoic acid (856 mg, 7.5 mmol, 2.5 equiv.), $SOCl_2$ (711 µL 9.75 mmol, 3.25 equiv.), Et_3N (1.8 mL, 13.2 mmol, 4.4 equiv.) and DMAP (9.2 mg, 0.075 mmol, 0.025 equiv.) in 24 mL of dry CH_2Cl_2. Purification by column chromatography (petroleum ether/AcOEt 9:1 to 7:3) yielded **61-(E)** (608 mg, 84%) as a white solid.

^{1}H NMR (400 MHz, Chloroform-*d*) δ 10.12 (s, 1H), 8.46 – 8.39 (m, 1H), 8.27 (dd, *J* = 8.1, 1.5 Hz, 1H), 8.11 (s, 1H), 7.49 – 7.36 (m, 2H), 5.57 (qt, *J* = 15.0, 7.5 Hz, 2H), 3.06 (t, *J* = 7.3 Hz, 2H), 2.63 – 2.51 (m, 2H), 1.72 – 1.65 (m, 3H).

^{13}C NMR (101 MHz, Chloroform-*d*) δ 185.7, 171.1, 136.6, 134.7, 128.4, 127.5, 127.0, 126.1, 125.5, 122.8, 122.0, 116.6, 36.1, 27.4, 18.0.

HRMS (ESI+): m/z calcd. for $[C_{15}H_{15}NO_2]^+$: 242.1176; found:242.1170.

(*E*)-hex-4-enoic acid was synthesized following a reported literature procedure. [cit17sup]

(*Z*)-1-(hex-4-enoyl)-1*H*-indole-3-carbaldehyde 61-(Z).

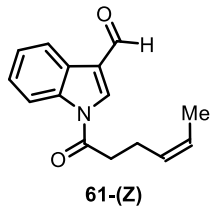

61-(Z)

Synthesized following the general procedure B starting from 1*H*-indole-3-carbaldehyde (435 mg, 3 mmol, 1 equiv.), (*Z*)-hex-4-enoic acid (856 mg, 7.5 mmol, 2.5 equiv.), $SOCl_2$ (711 µL, 9.75 mmol, 3.25 equiv.), Et_3N (1.8 mL, 13.2 mmol, 4.4 equiv.) and DMAP (9.2 mg, 0.075 mmol, 0.025 equiv.) in 24 mL of dry CH_2Cl_2. Purification by column chromatography (petroleum ether/AcOEt 9:1 to 7:3) yielded **61-(Z)** (246mg, 34%) as a yellow oil.

^{1}H NMR (400 MHz, Chloroform-*d*) δ 10.11 (s, 1H), 8.49 – 8.39 (m, 1H), 8.27 (dd, *J* = 7.4, 1.7 Hz, 1H), 8.11 (s, 1H), 7.52 – 7.32 (m, 2H), 5.64 – 5.54 (m, 1H), 5.52 – 5.43 (m, 1H), 3.05 (t, *J* = 7.4 Hz, 2H), 2.70 – 2.56 (m, 2H), 1.68 (dd, *J* = 6.8, 1.8 Hz, 3H).

^{13}C NMR (101 MHz, Chloroform-*d*) δ 185.7, 171.1, 136.6, 134.7, 127.5, 127.0, 126.6, 126.1, 125.5, 122.7, 122.0, 116.6, 35.8, 21.9, 13.0.

HRMS (ESI+): m/z calcd. for $[C_{15}H_{15}NO_2]^+$: 242.1176; found: 242.1173.

(*Z*)-hex-4-enoic acid was synthesized following a reported literature procedure. [cit18sup]

1-(3,3-Dimethylpent-4-enoyl)-1*H*-indole-3-carbaldehyde SM18.

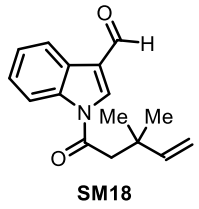

SM18

Synthesized following the general procedure B starting from 1*H*-indole-3-carbaldehyde (435 mg, 3 mmol, 1 equiv.), 3,3-dimethylpent-4-enoic acid (961 mg, 7.5 mmol, 2.5 equiv.), $SOCl_2$ (711 µL, 9.75 mmol, 3.25 equiv.), Et_3N (1.8 mL, 13.2 mmol, 4.4 equiv.) and DMAP (9.2 mg, 0.075 mmol, 0.025 equiv.) in 24 mL of dry CH_2Cl_2. Purification by column chromatography (petroleum ether/CH_2Cl_2 2:1 to 1:3) yielded **SM18** (597 mg, 78%) as an off-white solid.

^{1}H NMR (400 MHz, Chloroform-*d*) δ 10.12 (s, 1H), 8.52 – 8.41 (m, 1H), 8.32 – 8.19 (m, 1H), 8.09 (s, 1H), 7.50 – 7.37 (m, 2H), 6.00 (dd, *J* = 17.4, 10.7 Hz, 1H), 5.07 (dd, *J* = 17.4, 1.2 Hz, 1H), 5.02 (dd, *J* = 10.7, 1.2 Hz, 1H), 2.98 (s, 2H), 1.30 (s, 6H).

^{13}C NMR (101 MHz, Chloroform-*d*) δ 185.7, 169.8, 146.0, 136.7, 135.3, 126.9, 126.2, 125.5, 122.5, 121.9, 116.9, 112.2, 47.2, 37.1, 27.3.

HRMS (ESI+): m/z calcd. for $[C_{16}H_{17}NO_2]^+$:256.1332; found: 256.1348.

3,3-dimethylpent-4-enoic acid was synthesized following a reported literature procedure.[47]

1-Pentanoyl-1*H*-indole-3-carbaldehyde SM19.

SM19

Synthesized following the general procedure B starting from 1*H*-indole-3-carbaldehyde (435 mg, 3 mmol, 1 equiv.), valeric acid (815 µL, 7.5 mmol, 2.5 equiv.), $SOCl_2$ (711 µL, 9.75 mmol, 3.25 equiv.), Et_3N (1.8 mL, 13.2 mmol, 4.4 equiv.) and DMAP (9.2 mg, 0.075 mmol, 0.025 equiv.) in 24 mL of dry CH_2Cl_2. Purification by column chromatography (petroleum ether/AcOEt 9:1 to 8:2) yielded **SM19** (323 mg, 47 %) as a white solid.

^{1}H NMR (400 MHz, Chloroform-*d*) δ 10.12 (s, 1H), 8.47 – 8.40 (m, 1H), 8.31 – 8.23 (m, 1H), 8.11 (s, 1H), 7.50 – 7.35 (m, 2H), 2.99 (t, *J* = 7.4 Hz, 2H), 1.86 (p, *J* = 7.5 Hz, 2H), 1.56 – 1.43 (m, 2H), 1.01 (t, *J* = 7.4 Hz, 3H).

^{13}C NMR (101 MHz, Chloroform-*d*) δ 185.7, 171.7, 136.6, 134.7, 126.9, 126.1, 125.4, 122.7, 122.0, 116.6, 35.7, 26.6, 22.4, 13.9.

HRMS (ESI+): m/z calcd. for $[C_{14}H_{15}NO_2]^+$: 230.1176; found: 230.1175.

1-Acetyl-1*H*-indole-3-carbaldehyde 88.

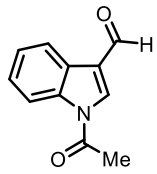

88

Synthesised according to a reported literature procedure[i] starting from 1*H*-indole-3-carbaldehyde (435 mg, 3 mmol, 1 equiv.), acetic anhydride (500 µL, 5 mmol, 1.7 equiv.), Et_3N (1.0 mL, 7.5 mmol, 2.5 equiv.) and DMAP (37 mg, 0.3 mmol, 0.1 equiv.) in 18 mL of dry CH_2Cl_2. Purification by column chromatography (petroleum ether/AcOEt 9:1 to 8:2) yielded **88** (454 mg, 81 %) as a white solid.

^{1}H NMR (400 MHz, Chloroform-*d*) δ 10.14 (s, 1H), 8.40 (d, J = 8.2 Hz, 1H), 8.28 (d, J = 7.6 Hz, 1H), 8.08 (s, 1H), 7.48-7.39 (m, 2H), 2.75 (s, 3H).

2.5.5. Organocatalytic enantioselective dearomative [2 + 2] cycloaddition

General Procedure C for the preparation of enantioenriched cycloadducts.

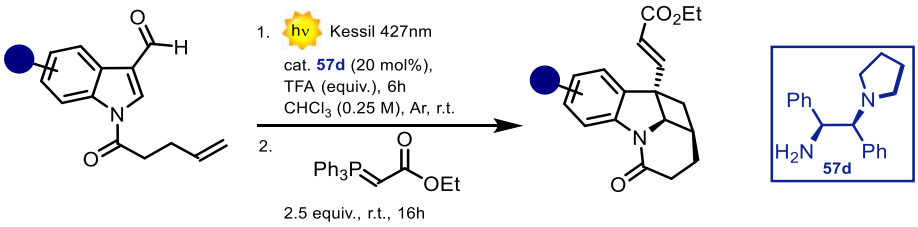

A 4 mL screw-cap vial equipped with a magnetic stirring bar, was charged with the indole substrate (1 equiv.), organocatalyst **57d** (20 mol%) and filled with Argon. Then, $CHCl_3$ (0.25 M) was added after being dried with 4 Å molecular sieves and degassed by sparging Argon for ten minutes. TFA was added (2.5 equiv.) and the vial was sealed. The mixture was irradiated until full consumption of the starting material with a Kessil lamp set at 50% of its maximum output power, unless otherwise stated. Then, the solvent was evaporated and the crude product was subjected to ^{1}H-NMR analysis to determine the NMR yield and the d.r. value. Afterwards, the crude of the reaction was dissolved in CH_2Cl_2 (0.25 M) and ethyl(triphenylphosphoranylidene)acetate (2.5 equiv.) was added. After stirring for 16 hours, the crude mixture was directly purified by column chromatography on silica gel. The products were obtained as an inseparable mixture of *E* and *Z* isomers deriving from the Wittig derivatization. The enantiomeric excess was determined by UPC^2 analysis on chiral stationary phase.

General Procedure D for the preparation of racemic samples.

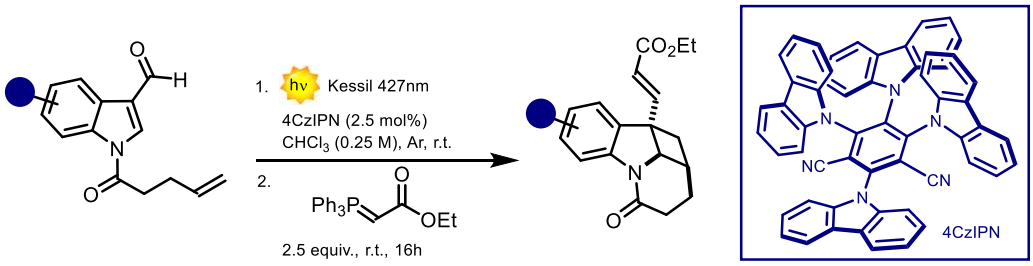

A 4 mL screw-cap vial equipped with a magnetic stirring bar, was charged with the indole substrate (1 equiv.), 4CzIPN (2.5 mol%) and filled with Argon. Then, $CHCl_3$ (0.25 M) was added after being degassed by sparging Argon for ten minutes and the vial was sealed. The mixture was irradiated until full consumption of the starting material with a Kessil lamp set at 50% of its maximum output power, unless otherwise stated. Then, the solvent was evaporated and the crude product was subjected to ^{1}H-NMR analysis to determine the d.r. value. Afterwards, the crude of the reaction was dissolved in CH_2Cl_2 (0.25 M) and ethyl(triphenylphosphoranylidene)acetate (2.5 equiv.) was added. After stirring for 16 hours, the crude mixture was directly purified by column chromatography on silica gel. The crude mixture was directly purified by column chromatography on silica gel eluting with pure CH_2Cl_2 first to remove all the 4CzIPN and then with a mixture of petroleum ether/AcOEt 7:3, affording the desired products.

General Procedure E

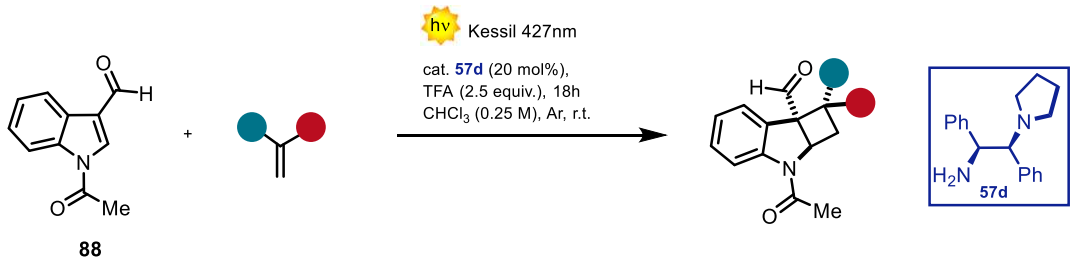

A 4 mL screw-cap vial equipped with a magnetic stirring bar, was charged with the indole substrate (1 equiv.), organocatalyst **57d** (20 mol%), the appropriate olefine (3 equiv.) and filled with Argon. Then, $CHCl_3$ (0.25 M) was added after being dried with 4 Å molecular sieves and degassed by sparging Argon for ten minutes. TFA was added (2.5 equiv.) and the vial was sealed. The mixture was irradiated for 18 h with a Kessil lamp set at 50% of its maximum output power, unless otherwise stated. Then, the solvent was evaporated and the crude product was subjected to ^{1}H-NMR analysis to determine the NMR yield and the d.r. value. The crude mixture was directly purified by column chromatography on silica gel affording the desired products. The enantiomeric excess was determined by UPC^2 analysis on chiral stationary phase.

General Procedure F

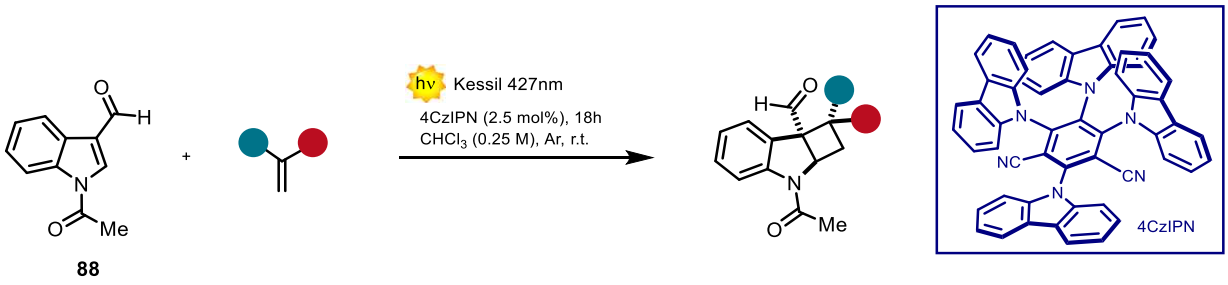

A 4 mL screw-cap vial equipped with a magnetic stirring bar, was charged with the indole substrate (1 equiv.), 4CzIPN (2.5 mol%), the appropriate olefine (3 equiv.) and filled with Argon. Then, $CHCl_3$ (0.25 M) was added after being degassed by sparging Argon for ten minutes and the vial was sealed. The mixture was irradiated for 18 h with a Kessil lamp set at 50% of its maximum output power, unless otherwise stated. Then, the solvent was evaporated and the crude product was subjected to ^{1}H-NMR analysis to determine the d.r. value. Afterwards, the crude mixture was directly purified by column chromatography on silica gel eluting with pure CH_2Cl_2 first to remove all the 4CzIPN and then with a mixture of petroleum ether/AcOEt 7:3, affording the desired products.

2.5.6. Characterisation of cycloadducts

Ethyl (*E*)-3-((1a*R*,1a$_1$*R*,9b*S*)-4-oxo-1a,2,3,4-tetrahydro-1*H*-benzo[*b*]cyclobuta[*hi*]indolizin-9b(1a$_1$*H*)-yl)acrylate 58.

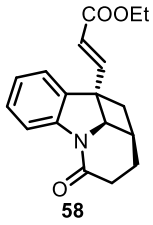

58

Following the General Procedure C applying 1-(pent-4-enoyl)-1*H*-indole-3-carbaldehyde **56** (22.7 mg, 0.1 mmol, 1 equiv.), (1*S*,2*S*)-1,2-diphenyl-2-(pyrrolidin-1-yl)ethan-1-amine **57d** (5.3 mg, 0.02 mmol, 20 mol%) and TFA (19 µL, 0.25 mmol, 2.5 equiv.) in 400 µL of $CHCl_3$, full conversion of **56** was observed after 6 h under 427 nm irradiation (>20:1 d.r.). The final product was obtained after reaction with ethyl(triphenylphosphoranylidene)acetate (87 mg, 0.25 mmol, 2.5 equiv.). Two reactions were conducted in parallel under identical conditions and then combined. The reported yield is calculated based on a total of 0.2 mmol. Purification by column chromatography (hexane/AcOEt 9:1 to 7:3) yielded **58** as a mixture of E and Z isomers (47.6 mg, 80 % yield, 92% e.e., E:Z = 95:5).

^{1}H NMR (400 MHz, Chloroform-*d*) δ 7.91 (d, *J* = 7.8 Hz, 1H), 7.28 – 7.19 (m, 2H), 7.07 – 6.95 (m, 2H), 6.14 :12.4, 8.9, 3.4 Hz, 1H), 2.53 – 2.43 (m, 1H), 2.35 – 2.14 (m, 3H), 1.67 – 1.51 (m, 1H), 1.32 (t, *J* = 7.1 Hz, 3H).

^{13}C NMR (101 MHz, Chloroform-*d*) δ 171.2, 166.3, 146.7, 145.3, 136.2, 128.4, 124.4, 122.9, 122.7, 117.7, 77.2, 67.4, 60.8, 50.1, 41.0, 34.9, 28.4, 26.1, 14.4.

HRMS (ESI+): m/z calcd. for $[C_{18}H_{19}NO_3]^+$: 298.1438; found: 298.1503.

UPC^2: IBN-3, CO_2/*i*-PrOH, isocratic [90:10], automatic back-pressure regulator (ABPR) = 2500 psi, 40 °C, 3 mL/min; t_{major} = 3.73 min; t_{minor} = 3.24 min.

$[\alpha]_D^{35}$= +97.4 (c=0.63, $CHCl_3$) for 92% e.e.

Ethyl (*E*)-3-((1a*R*,1a$_1$*R*,9b*S*)-9-methyl-4-oxo-1a,2,3,4-tetrahydro-1*H*-benzo[*b*]cyclobuta[*hi*]indolizin-9b(1a$_1$*H*)-yl)acrylate 69.

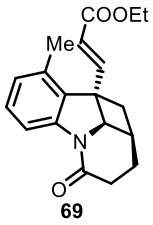

69

Following the General Procedure C applying 1-(pent-4-enoyl)-4-methyl-1*H*-indole-3-carbaldehyde **SM11** (24.1 mg, 0.1 mmol, 1 equiv.), (1*S*,2*S*)-1,2-diphenyl-2-(pyrrolidin-1-yl)ethan-1-amine **57d** (5.3 mg, 0.02 mmol, 20 mol%) and TFA (19 µL, 0.25 mmol, 2.5 equiv.) in 400 µL of $CHCl_3$, full conversion of **SM11** was observed after 6 h under 427 nm irradiation (>20:1 d.r.). The final product was obtained after reaction with ethyl(triphenylphosphoranylidene)acetate (87 mg, 0.25 mmol, 2.5 equiv.). Two reactions were conducted under identical conditions and then combined. The reported yield is calculated based on a total of 0.2 mmol. Purification by column chromatography (hexane/AcOEt 9:1 to 6:4) yielded **69** as a mixture of E and Z isomers (47.9 mg, 77 % yield, 92% e.e., E:Z = 99:1).

^{1}H NMR (500 MHz, Chloroform-*d*) δ 7.75 (d, *J* = 8.0 Hz, 1H), 7.29 (d, *J* = 15.9 Hz, 1H), 7.13 (t, *J* = 7.8 Hz, 1H), 6.80 (d, *J* = 7.7 Hz, 1H), 6.15 (d, *J* = 15.9 Hz, 1H), 4.35 (dd, *J* = 6.0, 3.7 Hz, 1H), 4.24 (q, *J* = 7.1 Hz, 2H), 3.10 – 2.93 (m, 2H), 2.45 (ddd, *J* = 14.2, 3.5, 2.4 Hz, 1H), 2.32 – 2.24 (m, 1H), 2.22 – 2.11 (m, 2H), 2.10 (s, 3H), 1.60 – 1.50 (m, 1H), 1.31 (t, *J* = 7.1 Hz, 3H).

^{13}C NMR (126 MHz, Chloroform-*d*) δ 171.2, 166.3, 148.5, 145.4, 134.7, 133.9, 128.4, 126.6, 122.1, 115.2, 67.2, 60.8, 49.9, 38.4, 34.9, 28.0, 26.2, 19.3, 14.4.

HRMS (ESI+): m/z calcd. for $[C_{19}H_{21}NO_3]^+$: 312.1594; found: 312.1657.

UPC^2: IG-3, CO_2/MeOH, isocratic [80:20], automatic back-pressure regulator (ABPR) = 2500 psi, 40 °C, 3 mL/min; t_{major} = 2.14 min; t_{minor} = 2.46 min.

$[\alpha]_D^{30}$= +180.0 (c=0.77, $CHCl_3$) for 92% e.e.

Ethyl (*E*)-3-((1a*R*,1a$_1$*R*,9b*S*)-9-bromo-4-oxo-1a,2,3,4-tetrahydro-1*H*-benzo[*b*]cyclobuta[*hi*]indolizin-9b(1a$_1$*H*)-yl)acrylate 70.

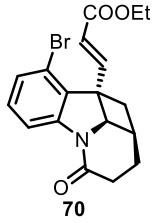

70

Following the General Procedure C applying 1-(pent-4-enoyl)-4-bromo-1*H*-indole-3-carbaldehyde **SM14** (30.6 mg, 0.1 mmol, 1 equiv.), (1*S*,2*S*)-1,2-diphenyl-2-(pyrrolidin-1-yl)ethan-1-amine **57d** (5.3 mg, 0.02 mmol, 20 mol%) and TFA (19 μL, 0.25 mmol, 2.5 equiv.) in 400 μL of $CHCl_3$, full conversion of **SM14** was observed after 6 h under 427 nm irradiation (>20:1 d.r.). The final product was obtained after reaction with ethyl(triphenylphosphoranylidene)acetate (87 mg, 0.25 mmol, 2.5 equiv.). Two reactions were conducted under identical conditions and then combined. The reported yield is calculated based on a total of 0.2 mmol. Purification by column chromatography (hexane/AcOEt 9:1 to 7:3) yielded **70** as a mixture of E and Z isomers (63.2 mg, 84 % yield, 92% e.e., E:Z = 85:15).

^{1}H NMR (400 MHz, Chloroform-*d*) δ 7.86 (d, *J* = 7.6 Hz, 1H), 7.38 (d, *J* = 15.9 Hz, 1H), 7.18 – 7.06 (m, 2H), 6.15 (d, *J* = 15.9 Hz, 1H), 4.39 (dd, *J* = 6.1, 3.7 Hz, 1H), 4.24 (q, *J* = 7.1 Hz, 2H), 3.13 – 2.95 (m, 2H), 2.47 (dt, *J* = 14.3, 3.1 Hz, 1H), 2.35 – 2.25 (m, 1H), 2.25 – 2.15 (m, 2H), 1.62 – 1.49 (m, 1H), 1.31 (t, *J* = 7.1 Hz, 3H).

^{13}C NMR (101 MHz, Chloroform-*d*) δ 171.3, 166.3, 147.4, 146.8, 136.3, 130.0, 128.4, 122.5, 117.9, 116.4, 67.0, 60.8, 50.9, 38.9, 34.9, 28.1, 26.1, 14.4.

HRMS (ESI+): m/z calcd. for $[C_{18}H_{18}BrNO_3]^+$:376.0543; found: 376.0613.

UPC^2: IC-3, CO_2/MeOH, isocratic [80:20], automatic back-pressure regulator (ABPR) = 2500 psi, 40 °C, 3 mL/min; t_{major} = 3.24 min; t_{minor} = 3.56 min.

$[\alpha]_D^{30}$= not measured because product **70** was isolated as a 85:15 mixture of E:Z isomers.

Ethyl (*E*)-3-((1a*R*,1a$_1$*R*,9b*S*)-9-fluoro-4-oxo-1a,2,3,4-tetrahydro-1*H*-benzo[*b*]cyclobuta[*hi*]indolizin-9b(1a$_1$*H*)-yl)acrylate 71.

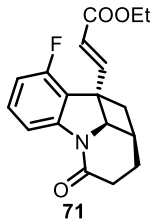

71

Following the General Procedure C applying 1-(pent-4-enoyl)-4-fluoro-1*H*-indole-3-carbaldehyde **SM13** (24.5 mg, 0.1 mmol, 1 equiv.), (1*S*,2*S*)-1,2-diphenyl-2-(pyrrolidin-1-yl)ethan-1-amine **57d** (5.3 mg, 0.02 mmol, 20 mol%) and TFA (19 μL, 0.25 mmol, 2.5 equiv.) in 400 μL of $CHCl_3$, full conversion of **SM13** was observed after 6 h under 427 nm irradiation (>20:1 d.r.). The final product was obtained after reaction with ethyl(triphenylphosphoranylidene)acetate (87 mg, 0.25 mmol, 2.5 equiv.). Two reactions were conducted under identical conditions and then combined. The reported yield is calculated based on a total of 0.2 mmol. Purification by column chromatography (hexane/AcOEt 9:1 to 7:3) yielded **71** as a mixture of E and Z isomers (51.7 mg, 82 % yield, 90% e.e., E:Z = 82:18).

^{1}H NMR (400 MHz, Chloroform-*d*) δ 7.70 (d, *J* = 8.0 Hz, 1H), 7.36 (d, *J* = 15.8 Hz, 1H), 7.24 – 7.16 (m, 1H), 6.72 (t, *J* = 8.8 Hz, 1H), 6.11 (d, *J* = 15.9 Hz, 1H), 4.51 (dd, *J* = 6.2, 3.4 Hz, 1H), 4.24 (q, *J* = 7.2 Hz, 2H), 3.12 – 3.01 (m, 1H), 2.94 (ddd, *J* = 12.6, 9.1, 3.5 Hz, 1H), 2.57 – 2.43 (m, 1H), 2.35 – 2.14 (m, 3H), 1.65 – 1.50 (m, 1H), 1.37 – 1.28 (m, 3H).

^{13}C NMR (101 MHz, Chloroform-*d*) δ 171.2, 166.3, 158.2 (d, *J* = 247.7 Hz), 147.4 (d, *J* = 7.7 Hz), 145.9 (d, *J* = 1.7 Hz), 130.4 (d, *J* = 8.1 Hz), 122.24 (d, *J* = 18.7 Hz), 122.19, 113.6 (d, *J* = 3.3 Hz), 112.1 (d, *J* = 20.4 Hz), 67.4, 60.8, 48.7 (d, *J* = 1.9 Hz), 40.9, 34.9, 28.3, 26.0, 14.4.

^{19}F NMR (377 MHz, Chloroform-*d*) δ -118.27.

HRMS (ESI+): m/z calcd. for $[C_{18}H_{18}FNO_3]^+$: 316.1343; found: 316.1431.

UPC^2: IC-3, CO_2/EtOH, isocratic [80:20], automatic back-pressure regulator (ABPR) = 2500 psi, 40 °C, 3 mL/min; t_{major} = 2.09 min; t_{minor} = 2.25 min.

$[\alpha]_D^{30}$= not measured because product **71** was isolated as a 85:15 mixture of E:Z isomers.

Ethyl (*E*)-3-((1a*R*,1a$_1$*R*,9b*S*)-9-cyano-4-oxo-1a,2,3,4-tetrahydro-1*H*-benzo[*b*]cyclobuta[*hi*]indolizin-9b(1a$_1$*H*)-yl)acrylate 72.

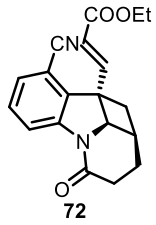

72

Following the General Procedure C applying 3-formyl-1-(pent-4-enoyl)-1*H*-indole-4-carbonitrile **SM12** (25.2 mg, 0.1 mmol, 1 equiv.), (1*S*,2*S*)-1,2-diphenyl-2-(pyrrolidin-1-yl)ethan-1-amine **57d** (5.3 mg, 0.02 mmol, 20 mol%) and TFA (19 µL, 0.25 mmol, 2.5 equiv.) in 400 µL of a 1:1 mixture of $CHCl_3$ and chlorobenzene, full conversion of **SM12** was observed after 18 h under 400 nm irradiation (>20:1 d.r.). The final product was obtained after reaction with ethyl(triphenylphosphoranylidene)acetate (87 mg, 0.25 mmol, 2.5 equiv.). Two reactions were conducted under identical conditions and then combined. The reported yield is calculated based on a total of 0.2 mmol. Purification by column chromatography (hexane/AcOEt 9:1 to 6:4) yielded **72** as a mixture of E and Z isomers (42.6 mg, 66 % yield, 82% e.e., E:Z = 95:5).

^{1}H NMR (400 MHz, Chloroform-*d*) δ 8.13 (dd, *J* = 7.9, 1.2 Hz, 1H), 7.37 – 7.27 (m, 3H), 6.23 (d, *J* = 15.8 Hz, 1H), 4.52 (dd, *J* = 6.1, 3.6 Hz, 1H), 4.26 (q, *J* = 7.1 Hz, 2H), 3.18 – 3.01 (m, 2H), 2.58 – 2.46 (m, 1H), 2.40 – 2.28 (m, 1H), 2.28 – 2.15 (m, 2H), 1.65 – 1.52 (m, 1H), 1.32 (t, *J* = 7.1 Hz, 3H).

^{13}C NMR (101 MHz, Chloroform-*d*) δ 171.3, 165.8, 146.5, 143.8, 139.5, 129.4, 128.2, 124.7, 121.6, 116.2, 107.8, 67.6, 61.0, 49.9, 40.0, 34.8, 28.4, 25.9, 14.3.

HRMS (ESI+): m/z calcd. for $[C_{19}H_{19}N_2O_3]^+$: 323.1390; found: 323.1438.

UPC^2: IC-3, CO_2/EtOH, isocratic [80:20], automatic back-pressure regulator (ABPR) = 2500 psi, 40 °C, 3 mL/min; t_{major} = 2.96 min; t_{minor} = 3.55 min.

$[\alpha]_D^{35}$= +111.4 (c=0.65, $CHCl_3$) for 82% e.e.

Ethyl (*E*)-3-((1a*R*,1a$_1$*R*,9b*S*)-8-bromo-4-oxo-1a,2,3,4-tetrahydro-1*H*-benzo[*b*]cyclobuta[*hi*]indolizin-9b(1a$_1$*H*)-yl)acrylate 73.

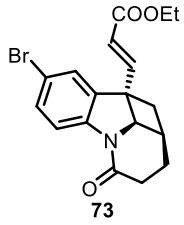

73

Following the General Procedure C applying 5-bromo-1-(pent-4-enoyl)-1*H*-indole-3-carbaldehyde **SM1** (30.6 mg, 0.1 mmol, 1 equiv.), (1*S*,2*S*)-1,2-diphenyl-2-(pyrrolidin-1-yl)ethan-1-amine **57d** (5.3 mg, 0.02 mmol, 20 mol%) and TFA (19 µL, 0.25 mmol, 2.5 equiv.) in 400 µL of $CHCl_3$, full conversion of **SM1** was observed after 6 h under 427 nm irradiation (>20:1 d.r.). The final product was obtained after reaction with ethyl(triphenylphosphoranylidene)acetate (87 mg, 0.25 mmol, 2.5 equiv.). Two reactions were conducted under identical conditions and then combined. The reported yield is calculated based on a total of 0.2 mmol. Purification by column chromatography (hexane/AcOEt 9:1 to 6:4) yielded **73** as a mixture of E and Z isomers (54.2 mg, 72 % yield, 88% e.e., E:Z = 95:5).

^{1}H NMR (400 MHz, Chloroform-*d*) δ 7.78 (d, *J* = 8.4 Hz, 1H), 7.34 (dd, *J* = 8.4, 2.0 Hz, 1H), 7.19 (d, *J* = 15.8 Hz, 1H), 7.07 (d, *J* = 2.0 Hz, 1H), 6.13 (d, *J* = 15.9 Hz, 1H), 4.51 (dd, *J* = 6.1, 3.5 Hz, 1H), 4.25 (q, *J* = 7.1 Hz, 2H), 3.10 – 2.97 (m, 1H), 2.87 (ddd, *J* = 12.5, 9.0, 3.5 Hz, 1H), 2.53 – 2.44 (m, 1H), 2.35 – 2.13 (m, 3H), 1.64 – 1.51 (m, 1H), 1.33 (t, *J* = 7.2 Hz, 3H).

^{13}C NMR (101 MHz, Chloroform-*d*) δ 171.1, 166.1, 145.6, 144.4, 138.5, 131.2, 126.2, 123.3, 119.0, 116.9, 67.7, 61.0, 49.9, 41.1, 34.8, 28.6, 26.1, 14.4.

HRMS (ESI+): m/z calcd. for $[C_{18}H_{18}BrNO_3]^+$: 376.0543; found: 376.0533.

UPC^2: IC-3, CO_2/MeOH, isocratic [80:20], automatic back-pressure regulator (ABPR) = 2500 psi, 40 °C, 3 mL/min; t_{major} = 3.27 min; t_{minor} = 3.82 min.

$[\alpha]_D^{35}$= +95.0 (c=0.55, $CHCl_3$) for 88% e.e.

Ethyl (*E*)-3-((1a*R*,1a$_1$*R*,9b*S*)-8-cyano-4-oxo-1a,2,3,4-tetrahydro-1*H*-benzo[*b*]cyclobuta[*hi*]indolizin-9b(1a$_1$*H*)-yl)acrylate 74.

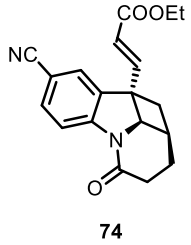

74

Following the General Procedure C applying 3-formyl-1-(pent-4-enoyl)-1*H*-indole-5-carbonitrile **SM3** (25.2 mg, 0.1 mmol, 1 equiv.), (1*S*,2*S*)-1,2-diphenyl-2-(pyrrolidin-1-yl)ethan-1-amine **57d** (5.3 mg, 0.02 mmol, 20 mol%) and TFA (19 µL, 0.25 mmol, 2.5 equiv.) in 400 µL of $CHCl_3$, full conversion of **SM3** was observed after 18 h under 400 nm irradiation (>20:1 d.r.). The final product was obtained after reaction with ethyl(triphenylphosphoranylidene)acetate (87 mg, 0.25 mmol, 2.5 equiv.). Two reactions were conducted under identical conditions and then combined. The reported yield is calculated based on a total of 0.2 mmol. Purification by column chromatography (hexane/AcOEt 9:1 to 6:4) yielded **74** as a mixture of E and Z isomers (32.2 mg, 50 % yield, 89% e.e., E:Z = 95:5).

^{1}H NMR (400 MHz, Chloroform-*d*) δ 7.99 (d, *J* = 8.2 Hz, 1H), 7.56 (dd, *J* = 8.3, 1.6 Hz, 1H), 7.25 – 7.15 (m, 2H), 6.16 (d, *J* = 15.8 Hz, 1H), 4.57 (dd, *J* = 6.1, 3.5 Hz, 1H), 4.27 (q, *J* = 7.2 Hz, 2H), 3.17 – 3.03 (m, 1H), 2.92 (ddd, *J* = 12.4, 9.0, 3.4 Hz, 1H), 2.59 – 2.49 (m, 1H), 2.39 – 2.17 (m, 3H), 1.68 – 1.56 (m, 1H), 1.34 (t, *J* = 7.1 Hz, 3H).

^{13}C NMR (101 MHz, Chloroform-*d*) δ 171.4, 165.9, 148.9, 144.8, 137.6, 133.7, 126.7, 123.9, 119.0, 117.8, 107.6, 67.7, 61.1, 49.8, 41.2, 34.9, 28.8, 25.9, 14.4.

HRMS (ESI+): m/z calcd. for $[C_{19}H1_8N_2O_3]^+$: 323.1390; found: 323.1438.

UPC^2: IG-3, CO_2/EtOH, isocratic [80:20], automatic back-pressure regulator (ABPR) = 2500 psi, 40 °C, 3 mL/min; t_{major} = 2.31 min; t_{minor} = 2.64 min.

$[\boldsymbol{\alpha}]_{\boldsymbol{D}}^{\mathbf{30}}$= +136.4 (c=0.60, $CHCl_3$) for 89% e.e.

Ethyl (*E*)-3-((1a*R*,1a$_1$*R*,9b*S*)-4-oxo-8-(tosyloxy)-1a,2,3,4-tetrahydro-1*H*-benzo[*b*]cyclobuta[*hi*]indolizin-9b(1a$_1$*H*)-yl)acrylate 75.

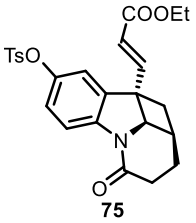

75

Following the General Procedure C applying 3-formyl-1-(pent-4-enoyl)-1H-indol-5-yl 4-methylbenzenesulfonate **SM4** (39.7 mg, 0.1 mmol, 1 equiv.), (1*S*,2*S*)-1,2-diphenyl-2-(pyrrolidin-1-yl)ethan-1-amine **57d** (5.3 mg, 0.02 mmol, 20 mol%) and TFA (19 µL, 0.25 mmol, 2.5 equiv.) in 400 µL of $CHCl_3$, full conversion of **SM4** was observed after 18 h under 427 nm irradiation (>20:1 d.r.). The final product was obtained after reaction with ethyl(triphenylphosphoranylidene)acetate (87 mg, 0.25 mmol, 2.5 equiv.). Two reactions were conducted under identical conditions and then combined. The reported yield is calculated based on a total of 0.2 mmol. Purification by column chromatography (hexane/AcOEt 8:2 to 1:1) yielded **75** as a mixture of E and Z isomers (76 mg, 82 % yield, 90% e.e., E:Z = 95:5).

^{1}H NMR (400 MHz, Chloroform-*d*) δ 7.76 (d, J = 8.6 Hz, 1H), 7.68 (d, J = 8.1 Hz, 2H), 7.31 (d, J = 8.1 Hz, 2H), 7.13 (d, J = 15.9 Hz, 1H), 6.72 (dd, J = 8.6, 2.4 Hz, 1H), 6.66 (d, J = 2.4 Hz, 1H), 6.08 (d, J = 15.9 Hz, 1H), 4.51 (dd, J = 6.1, 3.4 Hz, 1H), 4.26 (q, J = 7.1 Hz, 2H), 3.10 – 2.98 (m, 1H), 2.90 – 2.78 (m, 1H), 2.45 (s, 4H), 2.36 – 2.22 (m, 1H), 2.22 – 2.12 (m, 2H), 1.65 – 1.51 (m, 1H), 1.34 (t, J = 7.1 Hz, 3H).

^{13}C NMR (101 MHz, Chloroform-*d*) δ 171.0, 165.9, 145.9, 145.5, 145.3, 143.9, 137.8, 132.1, 129.8, 128.5, 123.2, 121.9, 117.8, 117.7, 67.8, 60.8, 49.6, 41.0, 34.6, 28.4, 25.9, 21.7, 14.3.

HRMS (ESI+): m/z calcd. for $[C_{25}H_{26}NO_6S]^+$: 468.1475; found: 468.1533.

UPC^2: IG-3, CO_2/MeOH, isocratic [70:30], automatic back-pressure regulator (ABPR) = 2500 psi, 40 °C, 3 mL/min; t_{major} = 2.80 min; t_{minor} = 3.06 min.

$[\boldsymbol{\alpha}]_{\boldsymbol{D}}^{\mathbf{22}}$= +29.5 (c=0.80, $CHCl_3$) for 90% e.e.

Ethyl (*E*)-3-((1a*R*,1a$_1$*R*,9b*S*)-8-fluoro-4-oxo-1a,2,3,4-tetrahydro-1*H*-benzo[*b*]cyclobuta[*hi*]indolizin-9b(1a$_1$*H*)-yl)acrylate 76.

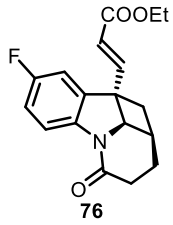

76

Following the General Procedure C applying 5-fluoro-1-(pent-4-enoyl)-1*H*-indole-3-carbaldehyde **SM2** (24.5 mg, 0.1 mmol, 1 equiv.), (1*S*,2*S*)-1,2-diphenyl-2-(pyrrolidin-1-yl)ethan-1-amine **57d** (5.3 mg, 0.02 mmol, 20 mol%) and TFA (19 µL, 0.25 mmol, 2.5 equiv.) in 400 µL of $CHCl_3$, full conversion of **SM2** was observed after 6 h under 427 nm irradiation (>20:1 d.r.). The final product was obtained after reaction with ethyl(triphenylphosphoranylidene)acetate (87 mg, 0.25 mmol, 2.5 equiv.). Two reactions were conducted under identical conditions and then combined. The reported yield is calculated based on a total of 0.2 mmol. Purification by column chromatography (hexane/AcOEt 9:1 to 6:4) yielded **76** as a mixture of E and Z isomers (46.1 mg, 73 % yield, 90% e.e., E:Z = 95:5).

^{1}H NMR (400 MHz, Chloroform-*d*) δ 7.84 (dd, *J* = 8.7, 4.7 Hz, 1H), 7.20 (d, *J* = 15.8 Hz, 1H), 6.95 – 6.87 (m, 1H), 6.68 (dd, *J* = 8.0, 2.6 Hz, 1H), 6.14 (d, *J* = 15.9 Hz, 1H), 4.52 (dd, *J* = 6.1, 3.5 Hz, 1H), 4.25 (q, *J* = 7.1 Hz, 2H), 3.12 – 2.97 (m, 1H), 2.87 (ddd, *J* = 12.5, 9.0, 3.5 Hz, 1H), 2.53 – 2.43 (m, 1H), 2.34 – 2.12 (m, 3H), 1.65 – 1.52 (m, 1H), 1.32 (t, *J* = 7.1 Hz, 3H).

^{13}C NMR (101 MHz, Chloroform-*d*) δ 170.9, 166.1, 159.8 (d, *J* = 243.4 Hz), 145.8, 141.3 (d, *J* = 2.2 Hz), 138.2 (d, *J* = 7.8 Hz), 123.1, 118.4 (d, *J* = 8.3 Hz), 114.4 (d, *J* = 23.0 Hz), 110.6 (d, *J* = 24.6 Hz), 67.9, 60.9, 49.9 (d, *J* = 1.8 Hz), 41.0, 34.6, 28.4, 26.1, 14.3.

^{19}F NMR (377 MHz, Chloroform-*d*) δ -117.91.

HRMS (ESI+): m/z calcd. for $[C_{18}H_{18}FNO_3]^+$: 316.1343; found: 316.1431.

UPC^2: IC-3, CO_2/MeOH, isocratic [80:20], automatic back-pressure regulator (ABPR) = 2500 psi, 40 °C, 3 mL/min; t_{major} = 2.17 min; t_{minor} = 2.32 min.

$[\alpha]_D^{30}$= +105.2 (c=0.59, $CHCl_3$) for 90% e.e.

Ethyl (*E*)-3-((1a*R*,1a$_1$*R*,9b*S*)-4-oxo-8-(4,4,5,5-tetramethyl-1,3,2-dioxaborolan-2-yl)-1a,2,3,4-tetrahydro-1*H*-benzo[*b*]cyclobuta[*hi*]indolizin-9b(1a$_1$*H*)-yl)acrylate 77.

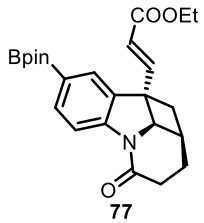

77

Following the General Procedure C applying 1-(pent-4-enoyl)-5-(4,4,5,5-tetramethyl-1,3,2-dioxaborolan-2-yl)-1H-indole-3-carbaldehyde **SM5** (35.3 mg, 0.1 mmol, 1 equiv.), (1*S*,2*S*)-1,2-diphenyl-2-(pyrrolidin-1-yl)ethan-1-amine **57d** (5.3 mg, 0.02 mmol, 20 mol%) and TFA (19 µL, 0.25 mmol, 2.5 equiv.) in 400 µL of $CHCl_3$, full conversion of **SM5** was observed after 6 h under 427 nm irradiation (>20:1 d.r.). The final product was obtained after reaction with ethyl(triphenylphosphoranylidene)acetate (87 mg, 0.25 mmol, 2.5 equiv.). Two reactions were conducted under identical conditions and then combined. The reported yield is calculated based on a total of 0.2 mmol. Purification by column chromatography (hexane/AcOEt 8:2 to 1:1) yielded **77** as a mixture of E and Z isomers (68 mg, 81 % yield, 91% e.e., E:Z = 95:5).

^{1}H NMR (400 MHz, Chloroform-*d*) δ 7.91 (d, *J* = 7.9 Hz, 1H), 7.73 (d, *J* = 7.9 Hz, 1H), 7.40 (s, 1H), 7.27 (d, *J* = 15.8 Hz, 1H), 6.15 (d, *J* = 15.8 Hz, 1H), 4.51 (dd, *J* = 6.1, 3.4 Hz, 1H), 4.26 (q, *J* = 7.2 Hz, 2H), 3.09 – 2.96 (m, 1H), 2.90 – 2.82 (m, 1H), 2.53 – 2.44 (m, 1H), 2.34 – 2.12 (m, 3H), 1.62 – 1.51 (m, 1H), 1.34 – 1.32 (m, 14H).

^{13}C NMR (101 MHz, Chloroform-*d*) δ 171.2, 166.3, 147.7, 146.5, 135.8, 135.7, 128.9, 122.7, 116.8, 83.9, 67.2, 60.8, 49.9, 41.0, 35.0, 28.5, 26.0, 24.95, 24.89, 14.4.

HRMS (ESI+): m/z calcd. for $[C_{24}H_{31}BNO_5]^+$: 424.2290; found: 424.2326.

UPC^2: IC-3, CO_2/MeOH, isocratic [80:20], automatic back-pressure regulator (ABPR) = 2500 psi, 40 °C, 3 mL/min; t_{major} = 2.27 min; t_{minor} = 2.70 min.

$[\alpha]_D^{22}$= +97.2 (c=0.76, $CHCl_3$) for 91% e.e.

Ethyl (*E*)-3-((1a*R*,1a$_1$*R*,9b*S*)-7-methyl-4-oxo-1a,2,3,4-tetrahydro-1*H*-benzo[*b*]cyclobuta[*hi*]indolizin-9b(1a$_1$*H*)-yl)acrylate 78.

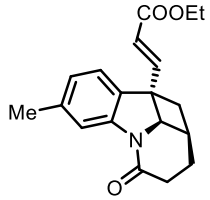

78

Following the General Procedure C applying 6-methyl-1-(pent-4-enoyl)-1*H*-indole-3-carbaldehyde **SM7** (24.1 mg, 0.1 mmol, 1 equiv.), (1*S*,2*S*)-1,2-diphenyl-2-(pyrrolidin-1-yl)ethan-1-amine **57d** (5.3 mg, 0.02 mmol, 20 mol%) and TFA (19 µL, 0.25 mmol, 2.5 equiv.) in 400 µL of $CHCl_3$, full conversion of **SM7** was observed after 18 h under 427 nm irradiation (>20:1 d.r.). The final product was obtained after reaction with ethyl(triphenylphosphoranylidene)acetate (87 mg, 0.25 mmol, 2.5 equiv.). Two reactions were conducted under identical conditions and then combined. The reported yield is calculated based on a total of 0.2 mmol. Purification by column chromatography (hexane/AcOEt 9:1 to 7:3) yielded **78** as a mixture of E and Z isomers (43.0 mg, 69 % yield, 92% e.e., E:Z = 95:5).

^{1}H NMR (400 MHz, Chloroform-*d*) δ 7.76 (s, 1H), 7.23 (d, *J* = 15.9 Hz, 1H), 6.84 (d, *J* = 2.0 Hz, 2H), 6.13 (d, *J* = 15.8 Hz, 1H), 4.48 (dd, *J* = 6.2, 3.5 Hz, 1H), 4.24 (q, *J* = 7.1 Hz, 2H), 3.08 – 2.95 (m, 1H), 2.85 (ddd, *J* = 12.4, 9.0, 3.5 Hz, 1H), 2.52 – 2.42 (m, 1H), 2.36 (s, 3H), 2.32 – 2.12 (m, 3H), 1.64 – 1.51 (m, 1H), 1.32 (t, *J* = 7.1 Hz, 3H).

^{13}C NMR (101 MHz, Chloroform-*d*) δ 171.2, 166.4, 147.0, 145.4, 138.6, 133.5, 125.0, 122.6, 122.5, 118.5, 67.7, 60.8, 49.8, 41.1, 34.9, 28.4, 26.2, 21.7, 14.4.

HRMS (ESI+): m/z calcd. for $[C_{19}H_{21}NO_3]^+$: 312.1594; found: 312.1657.

UPC^2: IC-3, CO_2/MeOH, isocratic [80:20], automatic back-pressure regulator (ABPR) = 2500 psi, 40 °C, 3 mL/min; t_{major} = 2.48 min; t_{minor} = 2.87 min.

$[\alpha]_D^{30}$= +82.1 (c=0.66, $CHCl_3$) for 92% e.e.

Methyl (1a*R*,1a$_1$*R*,9b*S*)-9b-((*E*)-3-ethoxy-3-oxoprop-1-en-1-yl)-4-oxo-1a,1a1,2,3,4,9b-hexahydro-1*H*-benzo[*b*]cyclobuta[*hi*]indolizine-7-carboxylate 79.

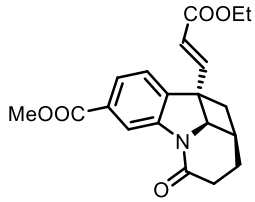

79

Following the General Procedure C applying methyl methyl 3-formyl-1-(pent-4-enoyl)-1*H*-indole-6-carboxylate **SM9** (28.5 mg, 0.1 mmol, 1 equiv.), (1*S*,2*S*)-1,2-diphenyl-2-(pyrrolidin-1-yl)ethan-1-amine **57d** (5.3 mg, 0.02 mmol, 20 mol%) and TFA (19 µL, 0.25 mmol, 2.5 equiv.) in 400 µL of $CHCl_3$, full conversion of **SM9** was observed after 12 h under 427 nm irradiation (>20:1 d.r.). The final product was obtained after reaction with ethyl(triphenylphosphoranylidene)acetate (87 mg, 0.25 mmol, 2.5 equiv.). Two reactions were conducted under identical conditions and then combined. The reported yield is calculated based on a total of 0.2 mmol. Purification by column chromatography (hexane/AcOEt 9:1 to 7:3) yielded **79** as a mixture of E and Z isomers (49.8 mg, 70 % yield, 90% e.e., E:Z = 95:5).

^{1}H NMR (400 MHz, Chloroform-*d*) δ 8.47 (d, *J* = 1.7 Hz, 1H), 7.74 (dd, *J* = 7.8, 1.5 Hz, 1H), 7.22 (d, *J* = 15.8 Hz, 1H), 7.02 (d, *J* = 7.8 Hz, 1H), 6.14 (d, *J* = 15.8 Hz, 1H), 4.54 (dd, *J* = 6.1, 3.4 Hz, 1H), 4.24 (q, *J* = 7.1 Hz, 2H), 3.89 (s, 3H), 3.14 – 3.00 (m, 1H), 2.88 (ddd, *J* = 12.4, 9.0, 3.4 Hz, 1H), 2.56 – 2.43 (m, 1H), 2.35 – 2.13 (m, 3H), 1.67 – 1.51 (m, 1H), 1.31 (t, *J* = 7.2 Hz, 3H).

^{13}C NMR (101 MHz, Chloroform-*d*) δ 171.1, 166.7, 166.1, 145.7, 145.5, 141.3, 130.5, 126.5, 123.2, 122.7, 118.1, 67.5, 60.9, 52.3, 50.0, 41.2, 34.7, 28.6, 26.0, 14.3.

HRMS (ESI+): m/z calcd. for $[C_{20}H_{21}NO_5]^+$: 356.1492; found: 356.1588.

UPC^2: IC-3, CO_2/MeOH, gradient [90:10 to 60:40 in 5 min , then 60:40 for 6 min], automatic back-pressure regulator (ABPR) = 2500 psi, 40 °C, 3 mL/min; t_{major} = 6.26 min; t_{minor} = 8.27 min.

$[\alpha]_D^{30}$= +55.2 (c=0.70, $CHCl_3$) for 90% e.e.

Ethyl (*E*)-3-((1a*R*,1a$_1$*R*,9b*S*)-7-(trifluoromethyl)-4-oxo-1a,2,3,4-tetrahydro-1*H*-benzo[*b*]cyclobuta[*hi*]indolizin-9b(1a$_1$*H*)-yl)acrylate 80.

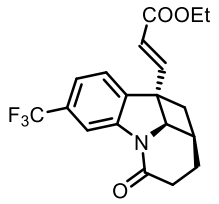

80

Following the General Procedure C applying 1-(pent-4-enoyl)-6-(trifluoromethyl)-1*H*-indole-3-carbaldehyde **SM6** (29.5 mg, 0.1 mmol, 1 equiv.), (1*S*,2*S*)-1,2-diphenyl-2-(pyrrolidin-1-yl)ethan-1-amine **57d** (5.3 mg, 0.02 mmol, 20 mol%) and TFA (19 µL, 0.25 mmol, 2.5 equiv.) in 400 µL of $CHCl_3$, full conversion of **SM6** was observed after 6 h under 400 nm irradiation (>20:1 d.r.). The final product was obtained after reaction with ethyl(triphenylphosphoranylidene)acetate (87 mg, 0.25 mmol, 2.5 equiv.). Two reactions were conducted under identical conditions and then combined. The reported yield is calculated based on a total of 0.2 mmol. Purification by column chromatography (hexane/AcOEt 9:1 to 7:3) yielded **80** as a mixture of E and Z isomers (51.9 mg, 71 % yield, 90% e.e., E:Z = 95:5).

^{1}H NMR (400 MHz, Chloroform-*d*) δ 8.15 (d, *J* = 1.8 Hz, 1H), 7.34 – 7.26 (m, 1H), 7.23 (d, *J* = 15.8 Hz, 1H), 7.06 (d, *J* = 7.8 Hz, 1H), 6.15 (d, *J* = 15.8 Hz, 1H), 4.55 (dd, *J* = 6.0, 3.4 Hz, 1H), 4.24 (q, *J* = 7.1 Hz, 2H), 3.13 – 3.01 (m, 1H), 2.89 (ddd, *J* = 12.5, 9.0, 3.4 Hz, 1H), 2.53 – 2.44 (m, 1H), 2.38 – 2.16 (m, 3H), 1.67 – 1.51 (m, 1H), 1.31 (t, *J* = 7.1 Hz, 3H).

^{13}C NMR (101 MHz, Chloroform-*d*) δ 171.2, 166.0, 145.7, 145.5, 140.1 (q, *J* = 1.5 Hz), 130.8 (q, *J* = 32.4 Hz), 124.1 (q, *J* = 272.5 Hz), 123.4, 123.1, 121.6 (q, *J* = 4.0 Hz), 114.44 (q, *J* = 3.9 Hz), 67.6, 61.0, 49.9, 41.1, 34.7, 28.7, 26.0, 14.3.

^{19}F NMR (377 MHz, Chloroform-*d*) δ -62.22.

HRMS (ESI+): m/z calcd. for $[C_{19}H_{18}F_3NO_3]^+$: 366.1312; found: 366.1402.

UPC^2: IG-3, CO_2/EtOH, isocratic [80:20], automatic back-pressure regulator (ABPR) = 2500 psi, 40 °C, 3 mL/min; t_{major} = 1.05 min; t_{minor} = 1.22 min.

$[\alpha]_D^{35}$= +97.1 (c=0.69, $CHCl_3$) for 90% e.e.

Ethyl (*E*)-3-((1a*R*,1a$_1$*R*,9b*S*)-7-bromo-4-oxo-1a,2,3,4-tetrahydro-1*H*-benzo[*b*]cyclobuta[*hi*]indolizin-9b(1a$_1$*H*)-yl)acrylate 81.

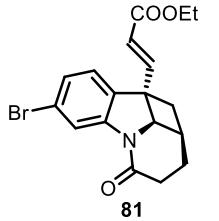

81

Following the General Procedure C applying 6-bromo-1-(pent-4-enoyl)-1*H*-indole-3-carbaldehyde **SM8** (30.6 mg, 0.1 mmol, 1 equiv.), (1*S*,2*S*)-1,2-diphenyl-2-(pyrrolidin-1-yl)ethan-1-amine **57d** (5.3 mg, 0.02 mmol, 20 mol%) and TFA (19 µL, 0.25 mmol, 2.5 equiv.) in 400 µL of $CHCl_3$, full conversion of **SM8** was observed after 6 h under 427 nm irradiation (>20:1 d.r.). The final product was obtained after reaction with ethyl(triphenylphosphoranylidene)acetate (87 mg, 0.25 mmol, 2.5 equiv.). Two reactions were conducted under identical conditions and then combined. The reported yield is calculated based on a total of 0.2 mmol. Purification by column chromatography (hexane/AcOEt 9:1 to 7:3) yielded **81** as a mixture of E and Z isomers (50.4 mg, 67 % yield, 91% e.e., E:Z = 95:5).

^{1}H NMR (400 MHz, Chloroform-*d*) δ 8.08 (d, *J* = 1.8 Hz, 1H), 7.20 (d, *J* = 15.9 Hz, 1H), 7.15 (dd, *J* = 8.0, 1.8 Hz, 1H), 6.82 (d, *J* = 7.9 Hz, 1H), 6.12 (d, *J* = 15.8 Hz, 1H), 4.51 (dd, *J* = 6.1, 3.4 Hz, 1H), 4.24 (q, *J* = 7.1 Hz, 2H), 3.13 – 2.96 (m, 1H), 2.86 (ddd, *J* = 12.4, 9.0, 3.4 Hz, 1H), 2.55 – 2.44 (m, 1H), 2.36 – 2.09 (m, 3H), 1.65 – 1.51 (m, 1H), 1.32 (t, *J* = 7.1 Hz, 3H).

^{13}C NMR (101 MHz, Chloroform-*d*) δ 171.2, 166.1, 146.5, 145.9, 135.4, 127.3, 124.0, 123.1, 122.0, 120.8, 67.8, 60.9, 49.7, 41.1, 34.8, 28.5, 26.1, 14.4.

HRMS (ESI+): m/z calcd. for $[C_{18}H_{18}BrNO_3]^+$: 376.0543; found: 376.0613.

UPC^2: IC-3, CO_2/MeOH, isocratic [80:20], automatic back-pressure regulator (ABPR) = 2500 psi, 40 °C, 3 mL/min; t_{major} = 3.63 min; t_{minor} = 4.54 min.

$[\alpha]_D^{30}$= +60.5 (c=0.66, $CHCl_3$) for 91% e.e.

Ethyl (*E*)-3-((1a*R*,1a$_1$*R*,9b*S*)-7-fluoro-4-oxo-1a,2,3,4-tetrahydro-1*H*-benzo[*b*]cyclobuta[*hi*]indolizin-9b(1a$_1$*H*)-yl)acrylate 82.

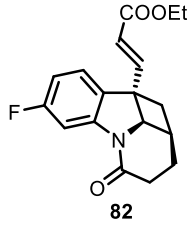

82

Following the General Procedure C applying 6-fluoro-1-(pent-4-enoyl)-1*H*-indole-3-carbaldehyde **SM10** (24.5 mg, 0.1 mmol, 1 equiv.), (1*S*,2*S*)-1,2-diphenyl-2-(pyrrolidin-1-yl)ethan-1-amine **57d** (5.3 mg, 0.02 mmol, 20 mol%) and TFA (19 µL, 0.25 mmol, 2.5 equiv.) in 400 µL of $CHCl_3$, full conversion of **SM10** was observed after 24 h under 427 nm irradiation (>20:1 d.r.). The final product was obtained after reaction with ethyl(triphenylphosphoranylidene)acetate (87 mg, 0.25 mmol, 2.5 equiv.). Two reactions were conducted under identical conditions and then combined. The reported yield is calculated based on a total of 0.2 mmol. Purification by column chromatography (hexane/AcOEt 9:1 to 7:3) yielded **82** as a mixture of E and Z isomers (27.7 mg, 44 % yield, 90% e.e., E:Z = 95:5).

^{1}H NMR (400 MHz, Chloroform-*d*) δ 7.64 (dd, *J* = 9.6, 2.5 Hz, 1H), 7.21 (d, *J* = 15.8 Hz, 1H), 6.88 (dd, *J* = 8.3, 5.4 Hz, 1H), 6.76 – 6.64 (m, 1H), 6.13 (d, *J* = 15.8 Hz, 1H), 4.54 (dd, *J* = 6.1, 3.4 Hz, 1H), 4.24 (q, *J* = 7.1 Hz, 2H), 3.11 – 2.95 (m, 1H), 2.87 (ddd, *J* = 12.5, 9.0, 3.5 Hz, 1H), 2.54 – 2.43 (m, 1H), 2.36 – 2.10 (m, 3H), 1.64 – 1.51 (m, 1H), 1.32 (t, *J* = 7.1 Hz, 3H).

^{13}C NMR (101 MHz, Chloroform-*d*) δ 171.2, 166.2, 162.8 (d, *J* = 244.9 Hz), 146.6 (d, *J* = 12.5 Hz), 146.3, 131.81 (d, *J* = 2.6 Hz), 123.4 (d, *J* = 10.1 Hz), 122.9, 110.7 (d, *J* = 22.9 Hz), 106.11 (d, *J* = 28.1 Hz), 68.2, 60.9, 49.5, 41.2, 34.8, 28.4, 26.1, 14.4.

^{19}F NMR (377 MHz, Chloroform-*d*) δ -112.97.

HRMS (ESI+): m/z calcd. for $[C_{18}H_{18}FNO_3]^+$: 316.1343; found: 316.1431.

UPC^2: IC-3, CO_2/EtOH, isocratic [80:20], automatic back-pressure regulator (ABPR) = 2500 psi, 40 °C, 3 mL/min; t_{major} = 2.07 min; t_{minor} = 2.38 min.

$[\alpha]_D^{35}$= +100.5 (c=0.68, $CHCl_3$) for 90% e.e.

Ethyl (*E*)-3-((1a*R*,1a$_1$*R*,9b*S*)-6-methyl-4-oxo-1a,2,3,4-tetrahydro-1*H*-benzo[*b*]cyclobuta[*hi*]indolizin-9b(1a$_1$*H*)-yl)acrylate 83.

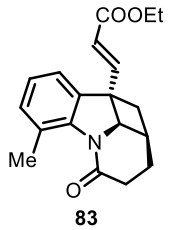

83

Following the General Procedure C applying 7-methyl-1-(pent-4-enoyl)-1*H*-indole-3-carbaldehyde **SM15** (24.1 mg, 0.1 mmol, 1 equiv.), (1*S*,2*S*)-1,2-diphenyl-2-(pyrrolidin-1-yl)ethan-1-amine **57d** (5.3 mg, 0.02 mmol, 20 mol%) and TFA (19 µL, 0.25 mmol, 2.5 equiv.) in 400 µL of $CHCl_3$, full conversion of **SM15** was observed after 6 h under 427 nm irradiation (>20:1 d.r.). The final product was obtained after reaction with ethyl(triphenylphosphoranylidene)acetate (87 mg, 0.25 mmol, 2.5 equiv.). Two reactions were conducted under identical conditions and then combined. The reported yield is calculated based on a total of 0.2 mmol. Purification by column chromatography (hexane/AcOEt 9:1 to 6:4) yielded **83** as a mixture of E and Z isomers (48.6 mg, 78 % yield, 88% e.e., E:Z = 95:5).

^{1}H NMR (400 MHz, Chloroform-*d*) δ 7.14 (d, *J* = 15.8 Hz, 1H), 7.09 – 6.96 (m, 2H), 6.78 (dd, *J* = 7.3, 1.4 Hz, 1H), 6.11 (d, *J* = 15.8 Hz, 1H), 4.57 (dd, *J* = 5.9, 3.7 Hz, 1H), 4.23 (q, *J* = 7.1 Hz, 2H), 3.08 – 2.95 (m, 1H), 2.82 (ddd, *J* = 12.4, 8.9, 3.7 Hz, 1H), 2.51 – 2.43 (m, 1H), 2.41 (s, 3H), 2.38 – 2.25 (m, 2H), 2.21 (dd, *J* = 12.1, 9.9 Hz, 1H), 1.75 – 1.59 (m, 1H), 1.30 (t, *J* = 7.1 Hz, 3H).

^{13}C NMR (101 MHz, Chloroform-*d*) δ 171.4, 166.3, 147.2, 144.4, 137.7, 130.9, 129.7, 125.7, 122.5, 120.2, 70.5, 60.8, 51.1, 39.1, 34.6, 28.3, 26.4, 21.0, 14.3.

HRMS (ESI+): m/z calcd. for $[C_{19}H_{21}NO_3]^+$: 312.1594; found: 312.1657.

UPC^2: IG-3, CO_2/MeOH, isocratic [80:20], automatic back-pressure regulator (ABPR) = 2500 psi, 40 °C, 3 mL/min; t_{major} = 1.64 min; t_{minor} = 1.86 min.

$[\alpha]_D^{30}$= +185.9 (c=0.69, $CHCl_3$) for 88% e.e.

Ethyl (*E*)-3-((1a*R*,1a$_1$*R*,9b*S*)-6-chloro-4-oxo-1a,2,3,4-tetrahydro-1*H*-benzo[*b*]cyclobuta[*hi*]indolizin-9b(1a$_1$*H*)-yl)acrylate 84.

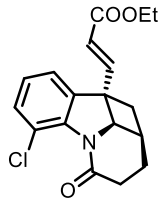

84

Following the General Procedure C applying 7-chloro-1-(pent-4-enoyl)-1*H*-indole-3-carbaldehyde **SM16** (26.1 mg, 0.1 mmol, 1 equiv.), (1S,2S)-1,2-diphenyl-2-(pyrrolidin-1-yl)ethan-1-amine **57d** (5.3 mg, 0.02 mmol, 20 mol%) and TFA (19 µL, 0.25 mmol, 2.5 equiv.) in 400 µL of $CHCl_3$, almost full conversion of **SM16** was observed after 18 h under 400 nm irradiation (>20:1 d.r.). The final product was obtained after reaction with ethyl(triphenylphosphoranylidene)acetate (87 mg, 0.25 mmol, 2.5 equiv.). Two reactions were conducted under identical conditions and then combined. The reported yield is calculated based on a total of 0.2 mmol. Purification by column chromatography (hexane/AcOEt 9:1 to 7:3) yielded **84** as a mixture of E and Z isomers (30.52 mg, 46 % yield, 72% e.e., E:Z = 95:5).

^{1}H NMR (400 MHz, Chloroform-*d*) δ 7.26 (dd, *J* = 8.1, 1.2 Hz, 1H), 7.12 (d, *J* = 15.8 Hz, 1H), 7.03 (t, *J* = 7.8 Hz, 1H), 6.87 (dd, *J* = 7.3, 1.3 Hz, 1H), 6.13 (d, *J* = 15.9 Hz, 1H), 4.66 (dd, *J* = 5.7, 3.7 Hz, 1H), 4.24 (q, *J* = 7.1 Hz, 2H), 3.11 – 2.95 (m, 1H), 2.84 (ddd, *J* = 12.4, 8.9, 3.7 Hz, 1H), 2.58 – 2.47 (m, 1H), 2.44 – 2.30 (m, 2H), 2.25 (dd, *J* = 12.2, 10.1 Hz, 1H), 1.79 – 1.65 (m, 1H), 1.32 (t, *J* = 7.1 Hz, 3H).

^{13}C NMR (101 MHz, Chloroform-*d*) δ 171.0, 166.1, 146.2, 143.3, 140.5, 130.2, 126.8, 125.4, 123.2, 121.3, 71.6, 61.0, 51.6, 39.1, 34.3, 28.3, 26.5, 14.4.

HRMS (ESI+): m/z calcd. for $[C_{18}H_{18}ClNO_3]^+$: 332.1048; found: 332.1106.

UPC^2: IG-3, CO_2/MeOH, isocratic [80:20], automatic back-pressure regulator (ABPR) = 2500 psi, 40 °C, 3 mL/min; t_{major} = 2.22 min; t_{minor} = 2.38 min.

$[\alpha]_D^{30}$= +14.1 (c=0.58, $CHCl_3$) for 72% e.e.

Ethyl (*E*)-3-((1a*R*,1a$_1$*R*,9b*S*)-5-oxo-1a,1a1,2,3,4,5-hexahydro-5a-azabenzo[*a*]cyclobuta[*cd*]azulen-9b(1*H*)-yl)acrylate 85.

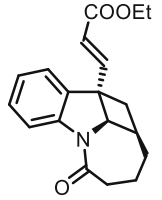

85

Following the General Procedure C applying 1-(hex-5-enoyl)-1*H*-indole-3-carbaldehyde **SM17** (24.1 mg, 0.1 mmol, 1 equiv.), (1*S*,2*S*)-1,2-diphenyl-2-(pyrrolidin-1-yl)ethan-1-amine **57d** (5.3 mg, 0.02 mmol, 20 mol%) and TFA (19 µL, 0.25 mmol, 2.5 equiv.) in 400 µL of $CHCl_3$, full conversion of **SM17** was observed after 18 h under 427 nm irradiation (>20:1 d.r.). The final product was obtained after reaction with ethyl(triphenylphosphoranylidene)acetate (87 mg, 0.25 mmol, 2.5 equiv.). Two reactions were conducted under identical conditions and then combined. The reported yield is calculated based on a total of 0.2 mmol. Purification by column chromatography (hexane/AcOEt 9:1 to 6:4) yielded **85** as a mixture of E and Z isomers (24.9 mg, 40 % yield, 94% e.e., E:Z = 95:5).

^{1}H NMR (400 MHz, Chloroform-*d*) δ 8.18 (d, *J* = 8.0 Hz, 1H), 7.25 – 7.16 (m, 2H), 7.07 – 6.95 (m, 2H), 6.03 (d, *J* = 15.8 Hz, 1H), 4.68 (dd, *J* = 6.8, 2.2 Hz, 1H), 4.22 (q, *J* = 7.1 Hz, 2H), 2.85 – 2.76 (m, 1H), 2.76 – 2.65 (m, 1H), 2.51 – 2.41 (m, 2H), 2.02 (dd, *J* = 12.0, 7.0 Hz, 1H), 1.99 – 1.87 (m, 1H), 1.85 – 1.75 (m, 1H), 1.70 – 1.56 (m, 1H), 1.52 (ddd, *J* = 13.5, 11.8, 5.0 Hz, 1H), 1.30 (t, *J* = 7.1 Hz, 3H).

^{13}C NMR (101 MHz, Chloroform-*d*) δ 170.9, 166.5, 148.4, 144.2, 136.5, 128.7, 124.2, 123.3, 121.4, 117.2, 66.8, 60.8, 49.1, 39.7, 35.4, 32.3, 27.7, 21.7, 14.4.

HRMS (ESI+): m/z calcd. for $[C_{19}H_{21}NO_3]^+$: 312.1594; found: 312.1657.

UPC^2: IG-3, CO_2/EtOH, isocratic [80:20], automatic back-pressure regulator (ABPR) = 2500 psi, 40 °C, 3 mL/min; t_{major} = 2.68 min; t_{minor} = 3.36 min.

$[\alpha]_D^{30}$= +104.2 (c=0.65, $CHCl_3$) for 94% e.e.

Ethyl (*E*)-3-((1a*S*,1a$_1$*R*,9b*S*)-2,2-dimethyl-4-oxo-1a,2,3,4-tetrahydro-1*H*-benzo[b]cyclobuta[*hi*]indolizin-9b(1a1*H*)-yl)acrylate 86.

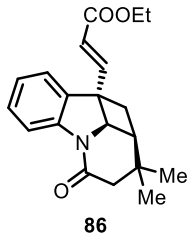

86

Following the General Procedure C applying 1-(3,3-dimethylpent-4-enoyl)-1*H*-indole-3-carbaldehyde **SM18** (25.5 mg, 0.1 mmol, 1 equiv.), (1*S*,2*S*)-1,2-diphenyl-2-(pyrrolidin-1-yl)ethan-1-amine **57d** (5.3 mg, 0.02 mmol, 20 mol%) and TFA (19 µL, 0.25 mmol, 2.5 equiv.) in 400 µL of $CHCl_3$, full conversion of **SM18** was observed after 6 h under 427 nm irradiation (>20:1 d.r.). The final product was obtained after reaction with ethyl(triphenylphosphoranylidene)acetate (87 mg, 0.25 mmol, 2.5 equiv.). Two reactions were conducted under identical conditions and then combined. The reported yield is calculated based on a total of 0.2 mmol. Purification by column chromatography (hexane/AcOEt 9:1 to 7:3) yielded **86** as a mixture of E and Z isomers (52.0 mg, 80 % yield, 84% e.e., E:Z = 95:5).

^{1}H NMR (400 MHz, Chloroform-*d*) δ 7.88 (d, *J* = 7.9 Hz, 1H), 7.29 – 7.17 (m, 2H), 7.08 – 6.90 (m, 2H), 6.15 (d, *J* = 15.8 Hz, 1H), 4.52 (dd, *J* = 6.0, 3.4 Hz, 1H), 4.24 (q, *J* = 7.1 Hz, 2H), 2.77 – 2.68 (m, 1H), 2.63 (ddd, *J* = 12.7, 9.3, 3.4 Hz, 1H), 2.34 (dd, *J* = 12.2, 9.6 Hz, 1H), 2.26 – 2.16 (m, 2H), 1.31 (t, *J* = 7.1 Hz, 3H), 1.13 (s, 3H), 0.90 (s, 3H).

^{13}C NMR (101 MHz, Chloroform-*d*) δ 170.2, 166.3, 146.7, 144.9, 136.7, 128.3, 124.4, 122.9, 122.8, 117.8, 67.7, 60.8, 49.5, 49.0, 39.3, 35.4, 33.1, 32.2, 26.1, 14.4.

HRMS (ESI+): m/z calcd. for $[C_{20}H_{23}NO_3]^+$: 326.1751; found: 326.1856.

UPC^2: IG-3, CO_2/IPA, isocratic [80:20], automatic back-pressure regulator (ABPR) = 2500 psi, 40 °C, 3 mL/min; t_{major} = 2.11 min; t_{minor} = 2.72 min.

$[\alpha]_D^{35}$= +84.9 (c=0.62, $CHCl_3$) for 84% e.e.

Ethyl (*E*)-3-((1*R*,1a*R*,1a$_1$*R*,9b*R*)-1-methyl-4-oxo-1a,2,3,4-tetrahydro-1H-benzo[*b*]cyclobuta[*hi*]indolizin-9b(1a1*H*)-yl)acrylate 87.

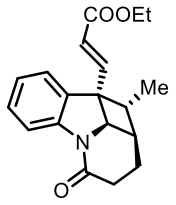

87

Following the General Procedure C applying (*E*)-1-(hex-4-enoyl)-1*H*-indole-3-carbaldehyde **61-(E)** (25.5 mg, 0.1 mmol, 1 equiv.), (1*S*,2*S*)-1,2-diphenyl-2-(pyrrolidin-1-yl)ethan-1-amine **57d** (5.3 mg, 0.02 mmol, 20 mol%) and TFA (19 µL, 0.25 mmol, 2.5 equiv.) in 400 µL of $CHCl_3$, full conversion of **61-(E)** was observed after 3 h under 427 nm irradiation at 0 °C (9:1 d.r.). The final product was obtained after reaction with ethyl(triphenylphosphoranylidene)acetate (87 mg, 0.25 mmol, 2.5 equiv.). Two reactions were conducted under identical conditions and then combined. The reported yield is calculated based on a total of 0.2 mmol. Purification by column chromatography (hexane/AcOEt 9:1 to 7:3) yielded **87** as a mixture of E and Z isomers (52.0 mg, 84 % yield, 75% e.e., E:Z = 95:5).

^{1}H NMR (400 MHz, Chloroform-*d*) δ 7.90 (d, *J* = 7.9 Hz, 1H), 7.38 (d, *J* = 15.9 Hz, 1H), 7.25 – 7.17 (m, 1H), 7.14 – 7.07 (m, 1H), 7.07 – 6.99 (m, 1H), 6.03 (d, *J* = 16.1 Hz, 1H), 4.56 (d, *J* = 5.4 Hz, 1H), 4.23 (q, *J* = 7.1 Hz, 2H), 2.61 – 2.43 (m, 3H), 2.34 – 2.18 (m, 2H), 1.61 – 1.47 (m, 1H), 1.30 (t, *J* = 7.2 Hz, 3H), 1.11 (d, *J* = 6.5 Hz, 3H).

^{13}C NMR (101 MHz, Chloroform-*d*) δ 171.0, 166.2, 144.8, 143.8, 136.5, 128.0, 124.3, 122.8, 122.1, 118.0, 64.1, 60.8, 53.1, 51.6, 37.0, 34.8, 24.7, 15.6, 14.3.

HRMS (ESI+): m/z calcd. for $[C_{19}H_{21}NO_3]^+$: 312.1594; found: 312.1657

UPC^2: IC-3, CO_2/EtOH, isocratic [80:20], automatic back-pressure regulator (ABPR) = 2500 psi, 40 °C, 3 mL/min; t_{major} = 2.51 min; t_{minor} = 2.82 min.

$[\alpha]_D^{35}$= not measured because product **87** was isolated in a 9:1 d.r.

(1*R*,2a*R*,7b*S*)-3-acetyl-1-butyl-1,2,2a,3-tetrahydro-7b*H*-cyclobuta[*b*]indole-7b-carbaldehyde 95.

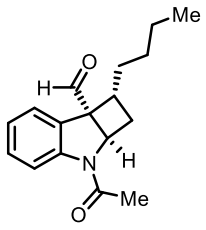

95

Following the General Procedure E applying 1-acetyl-1*H*-indole-3-carbaldehyde **88** (18.7 mg, 0.1 mmol, 1 equiv.), (1*S*,2*S*)-1,2-diphenyl-2-(pyrrolidin-1-yl)ethan-1-amine **57d** (5.3 mg, 0.02 mmol, 20 mol%), 1-hexene (38 µL, 0.3 mmol,. 3 equiv.) and TFA (19 µL, 0.25 mmol, 2.5 equiv.) in 400 µL of $CHCl_3$, 90% conversion of **88** and a 2.5:1 d.r. of the desired product were observed after 18 h under 427 nm irradiation. Purification by column chromatography (hexane/AcOEt 8:2 to 6:4) yielded the title compound **95** (10.5 mg, 38 % yield, 77% e.e.).

^{1}H NMR (400 MHz, Chloroform-*d*) δ 9.86 (s, 1H), 8.29 (d, *J* = 8.2 Hz, 1H), 7.38 (d, *J* = 7.5 Hz, 1H), 7.35 – 7.30 (m, 1H), 7.17 – 7.10 (m, 1H), 5.09 (dd, *J* = 7.6, 4.9 Hz, 1H), 2.81 – 2.71 (m, 1H), 2.40 – 2.32 (m, 1H), 2.28 – 2.21 (m, 1H), 2.19 (s, 3H), 1.81 – 1.68 (m, 1H), 1.48 – 1.37 (m, 1H), 1.36 – 1.20 (m, 3H), 1.20 – 1.10 (m, 1H), 0.89 (t, *J* = 7.1 Hz, 3H).

^{13}C NMR (101 MHz, Chloroform-*d*) δ 197.8, 168.6, 144.1, 131.2, 129.6, 124.5, 123.6, 118.3, 62.8, 55.9, 46.9, 33.1, 32.2, 29.8, 24.1, 22.6, 14.1.

HRMS (ESI+): m/z calcd. for $[C_{17}H_{22}NO_2]^+$: 272.1645; found: 272.1653.

UPC^2: IG-3, CO_2/MeOH, isocratic [80:20], automatic back-pressure regulator (ABPR) = 2500 psi, 40 °C, 3 mL/min; t_{major} = 2.35 min; t_{minor} = 2.81 min.

$[\alpha]_D^{19}$= +100.4 (c=0.25, $CHCl_3$) for 77% e.e.

(1*S*,2a*R*,7b*S*)-3-acetyl-1-butyl-1,2,2a,3-tetrahydro-7b*H*-cyclobuta[*b*]indole-7b-carbaldehyde 95'.

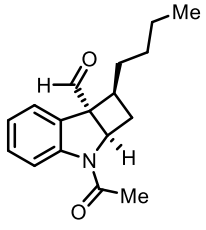

95'

Following the General Procedure E applying 1-acetyl-1*H*-indole-3-carbaldehyde **88** (18.7 mg, 0.1 mmol, 1 equiv.), (1*S*,2*S*)-1,2-diphenyl-2-(pyrrolidin-1-yl)ethan-1-amine **57d** (5.3 mg, 0.02 mmol, 20 mol%), 1-hexene (38 µL, 0.3 mmol,. 3 equiv.) and TFA (19 µL, 0.25 mmol, 2.5 equiv.) in 400 µL of $CHCl_3$, 90% conversion of **88** and a 2.5:1 d.r. of the desired product were observed after 18 h under 427 nm irradiation. As the minor diastereomer co-elutes with unreacted **88**, a second purification by column chromatography was carried out first using CH_2Cl_2 as eluent until the unreacted **88** elutes from the column then the eluent was switched to hexane/AcOEt 9:1 to 6:4. The second purification yielded the title compound **95'** (3.3 mg, 13 % yield, 73% e.e.).

^{1}H NMR (400 MHz, Chloroform-*d*) δ 9.72 (s, 1H), 8.33 (d, *J* = 8.2 Hz, 1H), 7.39 – 7.32 (m, 1H), 7.23 – 7.18 (m, 1H), 7.16 – 7.09 (m, 1H), 4.93 – 4.80 (m, 1H), 2.94 – 2.82 (m, 1H), 2.75 – 2.64 (m, 1H), 2.18 (s, 3H), 1.85 – 1.69 (m, 1H), 1.48 – 1.37 (m, 1H), 1.32 – 1.11 (m, 5H), 0.85 (t, *J* = 7.0 Hz, 3H).

^{13}C NMR (101 MHz, Chloroform-*d*) δ 198.0, 168.0, 145.6, 130.0, 126.7, 126.4, 124.2, 118.6, 64.8, 56.8, 38.7, 33.0, 31.7, 29.4, 24.1, 22.6, 14.1.

HRMS (ESI+): m/z calcd. for $[C_{17}H_{22}NO_2]^+$: 272.1645; found: 272.1653.

UPC^2: IG-3, CO_2/IPA, isocratic [80:20], automatic back-pressure regulator (ABPR) = 2500 psi, 40 °C, 3 mL/min; t_{major} = 1.97 min; t_{minor} = 1.83 min.

$[\alpha]_D^{22}$= -23.9 (c=0.15, $CHCl_3$) for 73% e.e.

(2a*R*,7b*S*)-3-acetyl-2a,3-dihydrospiro[cyclobuta[*b*]indole-1,1'-cyclohexane]-7b(2*H*)-carbaldehyde 96.

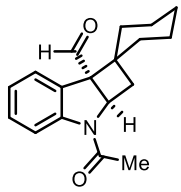

96

Following the General Procedure E applying 1-acetyl-1*H*-indole-3-carbaldehyde **88** (18.7 mg, 0.1 mmol, 1 equiv.), (1*S*,2*S*)-1,2-diphenyl-2-(pyrrolidin-1-yl)ethan-1-amine **57d** (5.3 mg, 0.02 mmol, 20 mol%), methylenecyclohexane (36 µL, 0.3 mmol,. 3 equiv.) and TFA (19 µL, 0.25 mmol, 2.5 equiv.) in 400 µL of $CHCl_3$, full conversion of **88** was observed after 18 h under 427 nm irradiation. Purification by column chromatography (hexane/AcOEt 8:2 to 7:3) yielded the title compound **96** (20.0 mg, 70 % yield, 94% e.e.).

^{1}H NMR (400 MHz, Chloroform-*d*) δ 9.81 (s, 1H), 8.35 – 8.25 (m, 1H), 7.39 – 7.31 (m, 2H), 7.17 – 7.11 (m, 1H), 5.09 (dd, *J* = 7.6, 5.8 Hz, 1H), 2.43 (dd, *J* = 12.5, 7.6 Hz, 1H), 2.22 (s, 3H), 1.85 (dd, *J* = 12.5, 5.8 Hz, 1H), 1.76 – 1.68 (m, 1H), 1.64 – 1.51 (m, 4H), 1.47 – 1.32 (m, 3H), 1.28 – 1.15 (m, 2H).

^{13}C NMR (101 MHz, Chloroform-*d*) δ 197.3, 168.4, 144.7, 129.7, 127.1, 125.9, 123.9, 118.5, 67.5, 53.6, 47.6, 38.7, 35.7, 35.0, 25.5, 24.1, 22.7, 22.6.

HRMS (ESI+): m/z calcd. for $[C_{18}H_{22}NO_2]^+$: 284.1645; found: 284.1646.

UPC²: IC-3, CO_2/MeOH, isocratic [80:20], automatic back-pressure regulator (ABPR) = 2500 psi, 40 °C, 3 mL/min; t_{major} = 2.84 min; t_{minor} = 3.05 min.

$[\boldsymbol{\alpha}]_{\boldsymbol{D}}^{\mathbf{19}}$= -73.2 (c=0.58, $CHCl_3$) for 94% e.e.

Methyl (1*R*,2a*R*,7b*S*)-3-acetyl-7b-formyl-2,2a,3,7b-tetrahydro-1*H*-cyclobuta[*b*]indole-1-carboxylate 97.

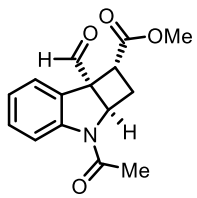

97

Following the General Procedure E applying 1-acetyl-1*H*-indole-3-carbaldehyde **88** (18.7 mg, 0.1 mmol, 1 equiv.), (1*S*,2*S*)-1,2-diphenyl-2-(pyrrolidin-1-yl)ethan-1-amine **57d** (5.3 mg, 0.02 mmol, 20 mol%), methyl acrylate (27 µL, 0.3 mmol,. 3 equiv.) and TFA (19 µL, 0.25 mmol, 2.5 equiv.) in 400 µL of $CHCl_3$, 91% conversion of **88** was observed after 18 h under 427 nm irradiation. Purification by column chromatography (hexane/AcOEt 8:2 to 6:4) yielded the title compound **97** (10.0 mg, 30 % yield, 88% e.e.).

^{1}H NMR (400 MHz, Chloroform-*d*) δ 9.68 (s, 1H), 8.30 (d, J = 8.2 Hz, 1H), 7.42 – 7.31 (m, 2H), 7.21 – 7.11 (m, 1H), 5.26 – 5.21 (m, 1H), 3.78 (s, 3H), 3.50 (dd, J = 9.6, 4.6 Hz, 1H), 2.93 – 2.82 (m, 1H), 2.49 – 2.39 (m, 1H), 2.23 (s, 3H).

^{13}C NMR (101 MHz, Chloroform-*d*) δ 194.8, 172.8, 168.2, 144.4, 130.6, 128.7, 124.9, 124.8, 118.6, 62.1, 57.8, 52.7, 46.8, 30.0, 24.1.

HRMS (ESI+): m/z calcd. for $[C_{15}H_{16}NO_4]^+$: 274.1074; found: 274.1110

UPC²: IC-3, CO_2/IPA, gradient [95:5 to 60:40 in 5 min, then 60:40 for 2 min], automatic back-pressure regulator (ABPR) = 2500 psi, 40 °C, 3 mL/min; t_{major} = 2.64 min; t_{minor} = 3.50 min.

$[\boldsymbol{\alpha}]_{\boldsymbol{D}}^{\mathbf{22}}$= -13.8 (c=0.30, $CHCl_3$) for 88% e.e.

(1*S*,2a*R*,7b*S*)-3-acetyl-1-methyl-1-((*R*)-4-methyl-5-oxocyclohex-3-en-1-yl)-1,2,2a,3-tetrahydro-7b*H*-cyclobuta[*b*]indole-7b-carbaldehyde 98.

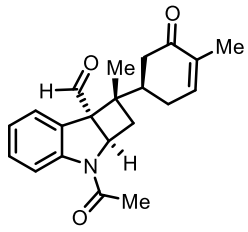

98

Following the General Procedure E applying 1-acetyl-1*H*-indole-3-carbaldehyde **88** (18.7 mg, 0.1 mmol, 1 equiv.), (1*S*,2*S*)-1,2-diphenyl-2-(pyrrolidin-1-yl)ethan-1-amine **57d** (5.3 mg, 0.02 mmol, 20 mol%), (*R*)-(-)-carvone (46 µL, 0.3 mmol,. 3 equiv.) and TFA (19 µL, 0.25 mmol, 2.5 equiv.) in 400 µL of $CHCl_3$, 94% conversion of **88** and a 1.7:1 d.r. of the desired product were observed after 18 h under 427 nm irradiation. Purification by column chromatography (hexane/AcOEt 8:2 to 1:1) yielded the title compound **98** (11.0 mg, 33 % yield).

^{1}H NMR (400 MHz, Chloroform-*d*) δ 9.92 (s, 1H), 8.31 (d, *J* = 8.2 Hz, 1H), 7.44 – 7.31 (m, 1H), 7.29 – 7.25 (m, 1H), 7.21 – 7.12 (m, 1H), 6.77 (d, *J* = 6.3 Hz, 1H), 4.99 (dd, *J* = 7.9, 4.8 Hz, 1H), 2.58 (dd, *J* = 13.0, 7.9 Hz, 1H), 2.52 – 2.40 (m, 1H), 2.36 – 2.21 (m, 3H), 2.17 (s, 3H), 2.13 – 2.01 (m, 1H), 1.87 (dd, *J* = 13.0, 4.8 Hz, 1H), 1.78 (s, 3H), 0.93 (s, 3H).

^{13}C NMR (101 MHz, Chloroform-*d*) δ 198.2, 197.0, 168.6, 145.3, 144.1, 136.0, 130.0, 127.1, 125.4, 124.3, 118.4, 67.1, 53.5, 50.7, 42.1, 40.5, 38.5, 27.0, 24.1, 20.3, 15.7.

HRMS (ESI+): m/z calcd. for $[C_{21}H_{24}NO_3]^+$: 338.1751; found: 338.1731.

$[\alpha]_D^{22}$= -140.0 (c=0.30, $CHCl_3$).

(1*R*,2a*R*,7b*S*)-3-acetyl-1-methyl-1-((*R*)-4-methyl-5-oxocyclohex-3-en-1-yl)-1,2,2a,3-tetrahydro-7b*H*-cyclobuta[*b*]indole-7b-carbaldehyde 98'.

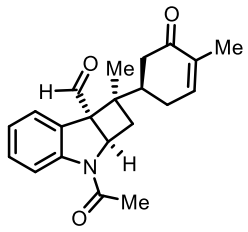

98'

Following the General Procedure E applying 1-acetyl-1*H*-indole-3-carbaldehyde **88** (18.7 mg, 0.1 mmol, 1 equiv.), (1*S*,2*S*)-1,2-diphenyl-2-(pyrrolidin-1-yl)ethan-1-amine **57d** (5.3 mg, 0.02 mmol, 20 mol%), (*R*)-(-)-carvone (46 µL, 0.3 mmol,. 3 equiv.) and TFA (19 µL, 0.25 mmol, 2.5 equiv.) in 400 µL of $CHCl_3$, 94% conversion of **88** and a 1.7:1 d.r. of the desired product were observed after 18 h under 427 nm irradiation. Purification by column chromatography (hexane/AcOEt 8:2 to 1:1) yielded the title compound **98'** (4.0 mg, 12 % yield).

^{1}H NMR (400 MHz, Chloroform-*d*) δ 9.70 (s, 1H), 8.33 (d, J = 8.1 Hz, 1H), 7.40 – 7.32 (m, 1H), 7.28 – 7.25 (m, 1H), 7.16 – 7.09 (m, 1H), 6.79 (d, J = 5.5 Hz, 1H), 5.13 – 5.08 (m, 1H), 2.54 – 2.44 (m, 1H), 2.37 – 2.27 (m, 1H), 2.26 – 2.14 (m, 5H), 2.11 – 2.01 (m, 2H), 1.91 (dd, J = 12.1, 6.8 Hz, 1H), 1.74 (s, 3H), 1.21 (s, 3H).

^{13}C NMR (101 MHz, Chloroform-*d*) δ 199.0, 196.4, 168.1, 145.1, 143.8, 136.2, 130.5, 126.0, 125.9, 124.4, 119.1, 68.7, 54.3, 48.3, 40.9, 39.1, 38.3, 28.7, 24.2, 19.6, 15.8.

HRMS (ESI+): m/z calcd. for $[C_{21}H_{24}NO_3]^+$: 338.1751; found: 338.1731.

$[\alpha]_D^{22}$= -51.2 (c=0.10, $CHCl_3$).

2.5.7. Synthetic transformations: Synthesis and Characterization

(1a*R*,1a$_1$*R*,9b*S*)-4-oxo-1a,2,3,4-tetrahydro-1*H*-benzo[*b*]cyclobuta[*hi*]indolizine-9b(1a$_1$*H*)-carboxylic acid 99.

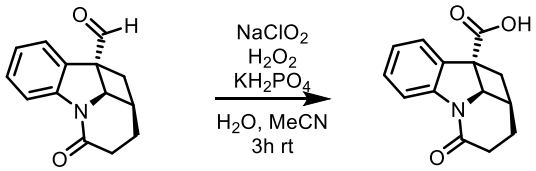

64 **99**

Cycloadduct **64** was obtained following General Procedure C starting from indole **56** (45.4 mg. 0.2 mmol, 1 equiv.). The yield of the reaction was measured by ^{1}H NMR analysis of the crude reaction mixture using dibromomethane as internal standard. This value was used for the stoichiometric calculations and the yield determination of the following reaction. After evaporation of the solvent the crude is dissolved in EtOAc and washed with a 2M solution of HCl. The organic phase was washed with brine, dried over $MgSO_4$ and concentrated under reduced pressure. The crude was used for the next step without further purification.

A 8 mL screw-cap vial equipped with a magnetic stirring bar, was charged with the cycloadduct **64** (36.4 mg, 0.16 mmol, 1 equiv.), KH_2PO_4 (24.5 mg, 0.18 mmol, 1.1 equiv.) and dissolved with 420 µL of MeCN and 100 µL of H_2O. Then 20 µL of a 30% aqueous solution of H_2O_2 were added. In another vessel, $NaClO_2$ (16.3 mg, 0.18 mmol, 1.1 equiv.) is dissolved in 100 µL of H_2O and added dropwise to the reaction. The mixture is left stirring 3h at room temperature. The reaction was then quenched with a saturated aqueous solution of $NaHSO_3$, and diluted with AcOEt. The organic phase was separated and washed 3 times with a saturated aqueous solution of Na_2CO_3. The aqueous fractions were collected, acidified to pH 1 with concentrated HCl and extracted with CH_2Cl_2. The organic layer was separated, dried over $MgSO_4$. Removal of the solvent yielded **99** (26 mg, 68% yield, 92% e.e.) as a yellow solid.

^{1}H NMR (400 MHz, Chloroform-d) δ 7.96 (d, J = 8.0 Hz, 1H), 7.41 (d, J = 7.5 Hz, 1H), 7.33 – 7.29 (m, 1H), 7.09 (t, J = 7.5 Hz, 1H), 4.88 (dd, J = 6.2, 3.4 Hz, 1H), 3.35 – 3.22 (m, 1H), 3.22 – 3.11 (m, 1H), 2.59 – 2.47 (m, 1H), 2.41 – 2.18 (m, 3H), 1.73 – 1.51 (m, 1H).

^{13}C NMR (101 MHz, Chloroform-*d*) δ δ 175.7, 171.3, 145.3, 132.4, 128.6, 124.4, 123.5, 117.6, 64.9, 51.9, 41.6, 34.8, 29.2, 26.2.

HRMS (ESI+): m/z calcd. for $[C_{14}H_{14}NO_3]^+$: 244.0968; found: 244.0988

UPC^2: IC-3, CO_2/MeOH, isocratic [80:20], automatic back-pressure regulator (ABPR) = 2500 psi, 40 °C, 3 mL/min; t_{major} = 1.48 min; t_{minor} = 2.25 min

$[\alpha]_D^{22}$= +96.0 (c=0.50, MeOH) for 92% e.e.

(1a*R*,1a1*R*,9b*S*)-9b-(2,2-dibromovinyl)-1,1a,1a1,2,3,9b-hexahydro-4*H*-benzo[*b*]cyclobuta[*hi*]indolizin-4-one 100'.

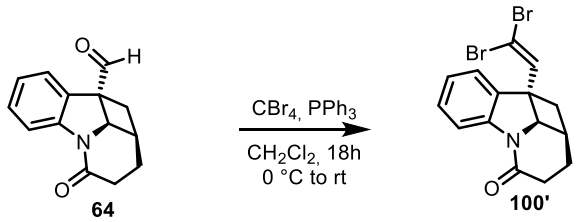

Cycloadduct **64** was obtained following General Procedure C starting from indole **56** (45.4 mg. 0.2 mmol, 1 equiv.). The yield of the reaction was measured by ^{1}H NMR analysis of the crude reaction mixture using dibromomethane as internal standard. This value was used for the stoichiometric calculations and the yield determination of the following reaction. After evaporation of the solvent the crude is dissolved in EtOAc and washed with a 2M solution of HCl. The organic phase was washed with brine, dried over $MgSO_4$ and concentrated under reduced pressure. The crude was used for the next step without further purification.
A 8 mL screw-cap vial equipped with a magnetic stirring bar, was charged with the CBr_4 (200 mg, 0.6 mmol, 3 equiv.) and dissolved with 800 µL of anhydrous CH_2Cl_2 under Argon atmosphere. In a separated vessel, PPh_3 (315 mg, 1.2 mmol, 6 equiv.) was dissolved with 1.2 mL of anhydrous CH_2Cl_2 under Argon atmosphere and added dropwise at 0°C to the CBr_4 solution. After 5 min of stirring at 0°C, a solution of cycloadduct **64** (43.1 mg, 0.19 mmol, 1 equiv.) in 800 µL of anhydrous CH_2Cl_2 was added to the reaction mixture. Then it is let reaching room temperature and stirred overnight. The reaction was then diluted with a saturated aqueous solution of NH_4Cl and extracted with AcOEt. The organic phase was washed with brine, dried over $MgSO_4$ and concentrated under reduced pressure. Purification by column chromatography (hexane/AcOEt 7:3) yielded **100'** (57 mg, 80% yield, 92% e.e.) as a yellow solid.
^{1}H NMR (400 MHz, Chloroform-d) δ 7.9 (d, J = 7.91 Hz, 1H), 7.3 – 7.2 (m, 1H), 7.2 – 7.1 (m, 1H), 7.1 – 7.0 (m, 2H), 4.7 (dd, J = 5.81, 3.86 Hz, 1H), 3.1 – 3.0 (m, 2H), 2.6 – 2.4 (m, 1H), 2.4 – 2.1 (m, 3H), 1.6 – 1.5 (m, 1H).
^{13}C NMR (101 MHz, Chloroform-*d*) δ 171.0, 145.3, 139.0, 135.5, 128.0, 124.3, 122.9, 117.4, 93.4, 67.1, 51.0, 43.2, 34.8, 29.1, 26.1.
HRMS (ESI+): m/z calcd. for $[C_{15}H_{14}Br_2NO]^+$: 381.9437; found: 381.9474.
UPC^2: IC-3, CO_2/MeOH, isocratic [80:20], automatic back-pressure regulator (ABPR) = 2500 psi, 40 °C, 3 mL/min; t_{major} = 3.32 min; t_{minor} = 3.58 min.

(1a*R*,1a1*R*,9b*S*)-9b-ethynyl-1,1a,1a1,2,3,9b-hexahydro-4*H*-benzo[*b*]cyclobuta[*hi*]indolizin-4-one 100.

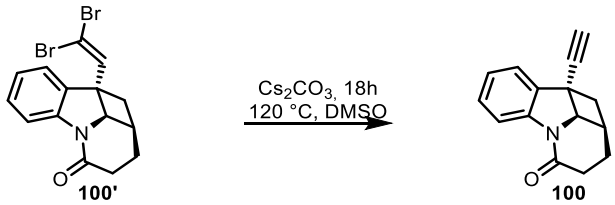

A 8 mL screw-cap vial equipped with a magnetic stirring bar, was charged with dibromide **100'** (57 mg, 0.15 mmol, 1 equiv.) and dissolved with 2.8 mL of DMSO. Cs_2CO_3 (150 mg, 0.45 mmol, 3 equiv.) was added and the reaction was stirred overnight at 120°C. Then it was diluted with CH_2Cl_2 and washed with 5 times with water. The organic phase was washed with brine, dried over $MgSO_4$ and concentrated under reduced pressure. Purification by column chromatography (hexane/AcOEt 7:3) yielded **100** (23 mg, 69% yield, 92% e.e.) as a yellow solid. The overall yield of the two steps is 55%.

^{1}H NMR (400 MHz, Chloroform-d) δ 7.89 (d, J = 7.9 Hz, 1H), 7.28 – 7.22 (m, 2H), 7.09 (td, J = 7.5, 1.1 Hz, 1H), 4.65 (dd, J = 6.0, 3.5 Hz, 1H), 3.34 (dtd, J = 15.3, 9.4, 5.7 Hz, 1H), 2.96 (ddd, J = 12.2, 9.0, 3.4 Hz, 1H), 2.54 – 2.46 (m, 2H), 2.37 – 2.18 (m, 3H), 1.58 (tdd, J = 12.6, 5.2, 3.3 Hz, 1H).

^{13}C NMR (101 MHz, Chloroform-*d*) δ 170.8, 144.5, 135.4, 128.3, 124.5, 122.7, 117.5, 83.8, 72.4, 68.1, 44.7, 41.0, 34.6, 28.9, 26.0.

HRMS (ESI+): m/z calcd. for $[C_{15}H_{14}NO]^+$: 224.1070; found: 224.1074.

UPC²: IC-3, CO_2/MeOH, isocratic [80:20], automatic back-pressure regulator (ABPR) = 2500 psi, 40 °C, 3 mL/min; t_{major} = 1.54 min; t_{minor} = 1.66 min.

$[\boldsymbol{\alpha}]_{\boldsymbol{D}}^{\mathbf{22}}$= +22.6 (c=0.20, $CHCl_3$) for 92% e.e.

((1a*R*,1a$_1$*R*,9b*S*)-1a,2,3,4-tetrahydro-1*H*-benzo[*b*]cyclobuta[*hi*]indolizin-9b(1a$_1$*H*)-yl)methanol 101.

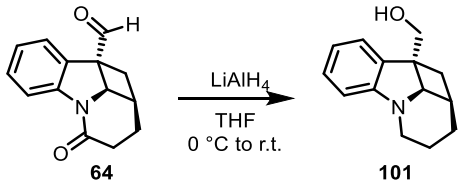

Cycloadduct **64** was obtained following General Procedure C starting from indole **57** (45.4 mg. 0.2 mmol, 1 equiv.). The yield of the reaction was measured by ^{1}H NMR analysis of the crude reaction mixture using dibromomethane as internal standard. This value was used for the stoichiometric calculations and the yield determination of the following reaction. After evaporation of the solvent the crude is dissolved in EtOAc and washed with a 2M solution of HCl. The organic phase was washed with brine, dried over $MgSO_4$ and concentrated under reduced pressure. The crude was used for the next step without further purification.

A 8 mL screw-cap vial equipped with a magnetic stirring bar, was charged with the cycloadduct **64** (40.9 mg, 0.18 mmol, 1 equiv.) and dissolved with 1.5 mL of anhydrous THF under Argon atmosphere. Then $LiAlH_4$ (38 mg, 1 mmol, 5.5 equiv.) was added portion wise at 0 °C. The mixture was let stirring overnight at room temperature. The reaction was then quenched with H_2O, diluted with AcOEt and filtrated through a celite pad. The organic phase was washed with brine, dried over $MgSO_4$ and concentrated under reduced pressure. Purification by column chromatography (CH_2Cl_2/MeOH 98:2) yielded **101** (25 mg, 64% yield, 91% e.e.) as a yellow oil.

^{1}H NMR (400 MHz, Chloroform-*d*) δ 7.12 – 7.05 (m, 1H), 6.91 (d, *J* = 7.2 Hz, 1H), 6.64 (t, *J* = 7.3 Hz, 1H), 6.56 (d, *J* = 7.9 Hz, 1H), 4.14 (dd, *J* = 6.5, 2.5 Hz, 1H), 4.04 (d, *J* = 11.3 Hz, 1H), 3.96 (d, *J* = 11.3 Hz, 1H), 3.65 – 3.55 (m, 1H), 3.04 – 2.91 (m, 1H), 2.79 – 2.62 (m, 1H), 2.25 (ddd, *J* = 12.5, 10.1, 2.6 Hz, 1H), 1.98 (dd, *J* = 12.2, 8.7 Hz, 1H), 1.81 – 1.59 (m, 2H), 1.56 – 1.48 (m, 1H), 1.46 – 1.39 (m, 1H).

^{13}C NMR (101 MHz, Chloroform-*d*) δ 155.3, 136.5, 128.4, 121.3, 118.2, 109.8, 64.5, 60.1, 50.7, 45.7, 36.0, 29.4, 25.2, 19.8.

HRMS (ESI+): m/z calcd. for $[C_{14}H_{18}NO]^+$: 216.1383; found: 216.1387.

UPC^2: IG-3, CO_2/MeOH, isocratic [80:20], automatic back-pressure regulator (ABPR) = 2500 psi, 40 °C, 3 mL/min; t_{major} = 2.26 min; t_{minor} = 2.02 min.

$[\alpha]_D^{22}$= +37.0 (c=0.10, $CHCl_3$) for 91% e.e.

2.5.8. X-Ray Crystallographic data

X-ray crystallographic data for compound 73:

Compound	**73**
Empirical formula	C18 H18 Br N O3
Formula weight	376.24
Temperature/K	200.0
Diffractometer/detector	Bruker D8 Venture / PhotonII area detector
Radiation	CuKα (λ = 1.54184)
Crystal system	Orthorhombic
Space group	$P2_12_12_1$
a/Å	5.10490(10)
b/Å	8.37430(10)
c/Å	38.8682(7)
α/°	90
β/°	90
γ/°	90
Volume/Å^3	1661.61(5)
Z	4
ρ_{calc}/g·cm^{-3}	1.504
μ/mm^{-1}	3.494
F(000)	768
Θ range for data	4.55-72.28
	-6<h<6
Index ranges	-10<k<10
	-47<l<47
Reflections collected	32627
Unique reflections	3191
Parameters	209
Goodness-of-fit on F^2	1.056
Final R indexes [I>=2σ (I)]	R=0.038, wR2=0.099
Flack Parameter	-0.026(9)
CCDC Number	**2392077**

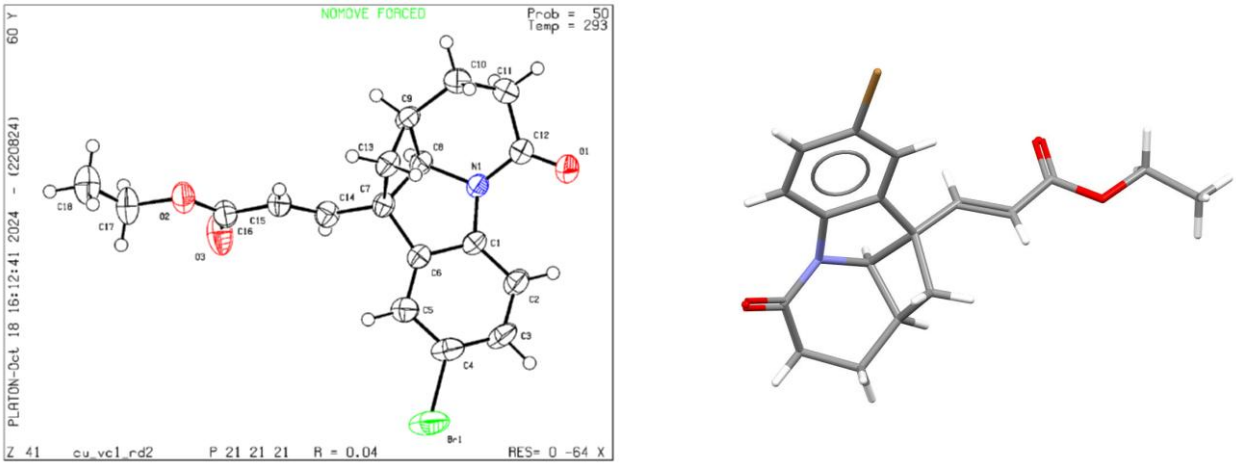

*Figure 6. ORTEP representation of compound **73**.*

2.5.9. Steady-state absorption spectroscopy

The UV-vis spectra were recorded $CHCl_3$ as solvent.

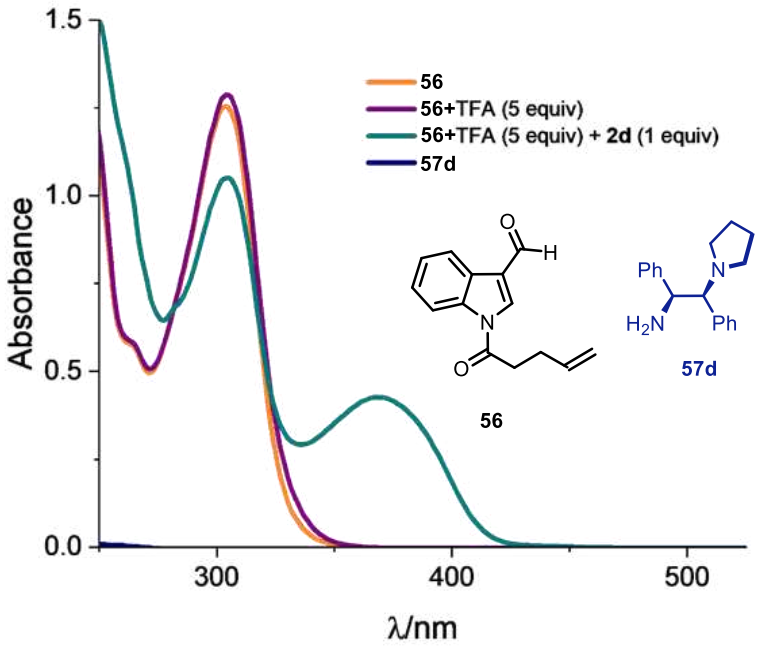

*Figure 7. Absorption profiles of the reaction components: **56** (1 mM), **57d** (1 mM).*

2.5.10. Photophysical characterization of iminium **59** and **60**.

Figure 8 and Figure 10 display the fluorescence of iminium **59** and **60**, respectively, measured in CLF solution upon excitation at 360 nm. A quantum yield of $\varphi_F = 0.14$ and $\varphi_F = 0.15$ can be estimated for **59** and **60**, respectively, using quinine disulfate as a standard. A lifetime of $\tau = 2.06$ ns and $\tau = 1.96$ ns can be estimated for **59** and **60**, respectively, by TCSPC upon excitation at 380 nm (see Figure 9 and Figure 11).

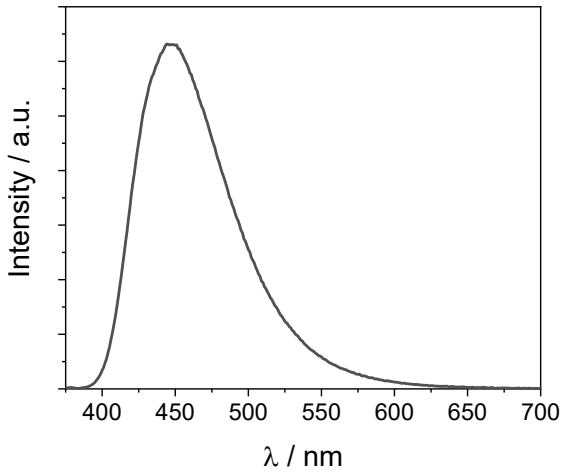

*Figure 8. Luminescence spectrum of iminium **59** in CLF upon excitation at 360 nm.*

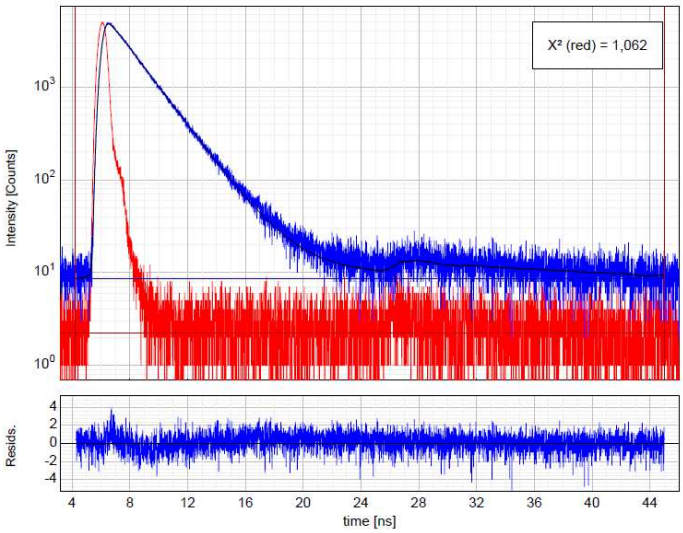

*Figure 9. Fluorescence decay of **59** in CLF measured by TCSPC (excitation at 380 nm, analysis at 450 nm): a lifetime of 2.06 ns is estimated upon deconvolution and single-exponential fitting (top panel shows the experimental trace associated with the decay in blue, the instrument response function in red and the fitting in black. The bottom panel shows the residuals associated with the fitting).*

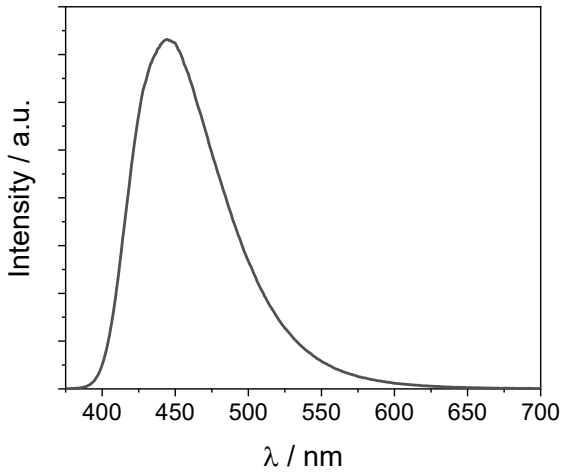

*Figure 10. Luminescence spectrum of iminium **60** in CLF upon excitation at 360 nm.*

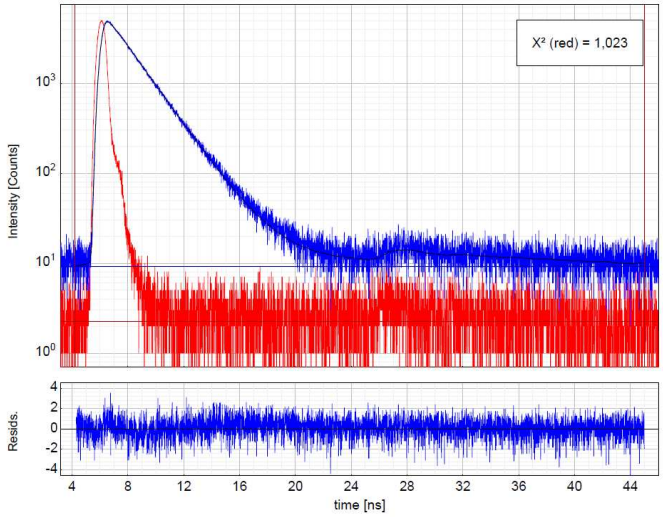

Figure 11. Fluorescence decay of 5 in CLF measured by TCSPC (excitation at 380 nm, analysis at 450 nm): a lifetime of 1.96 ns is estimated upon deconvolution and single-exponential fitting (top panel shows the experimental trace associated with the decay in blue, the instrument response function in red and the fitting in black. The bottom panel shows the residuals associated with the fitting).

The similar behaviour observed in both **59** and **60** confirms that the singlet excited state (S_1) is not involved in the photoreaction. Laser flash photolysis (LFP) studies were then performed to follow the fate of the triplet excited state expected to be populated upon intersystem crossing from the singlet.Figure 12 and Figure 13 compare the spectral evolution obtained by LFP of **59** and **5**, respectively, upon excitation at 355 nm. For both compounds the prompt spectra detected immediately after the laser pulse are similar and show the ground-state bleaching below 400 nm, a sharp absorption centred at 410 nm, and a broad absorption in the red portion of the visible. In this regard, the absorption spectrum of the triplet T_1 (Figure 29) simulated by TD-DFT shows the presence of a broad absorption above 500 nm as a characteristic spectral fingerprint. Thus, the transient absorption band above 500 nm in both **59** and **60** can be reasonably assigned to the triplet T_1 of the iminium-ion.

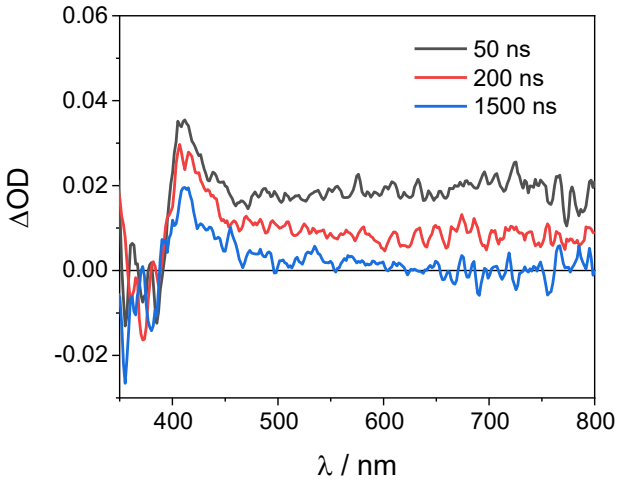

*Figure 12. Transient absorption spectra (gate width = 50 ns) of **59** in CLF obtained by LFP (excitation at 355 nm).*

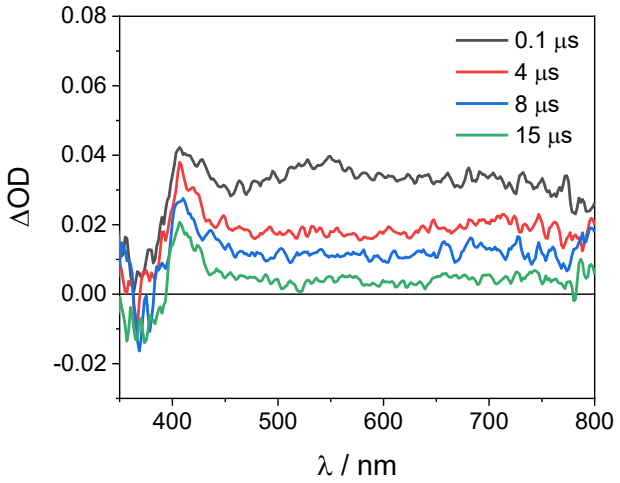

*Figure 13. Transient absorption spectra (gate width = 50 ns) of **60** (bottom) in CLF obtained by LFP (excitation at 355 nm).*

To further substantiate the attribution made, in the case of the model iminium **60** the decay of the absorption at 700 nm was studied both under air-equilibrated conditions and under N_2. The kinetic traces are reported in Figure 14 and show that the lifetime of the transient-associated species becomes longer upon removal of dioxygen. This behaviour is characteristic of triplet excited states, thus confirming the assignment made. A lifetime of τ = 12 μs can be estimated for the T_1 in **60** from a single-exponential fitting of the kinetic trace under oxygen-free conditions (Figure 16).

The fate of the triplet excited state in iminium ions 59 and 60 was next investigated by monitoring the kinetic traces at 700 nm. As it can be seen from Figure 15 and Figure 16, the decay of the transient absorption at 700 nm is considerably faster in **59** than in **60**. This is consistent with reactivity of the triplet T_1 with the olefin fragment.

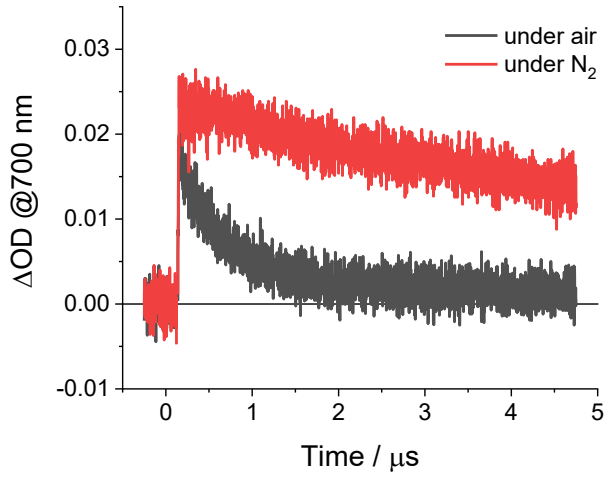

*Figure 14. Kinetic traces at 700 nm obtained by LFP (excitation at 355 nm) of **60** in CLF under air-equilibrated conditions and under N_2.*

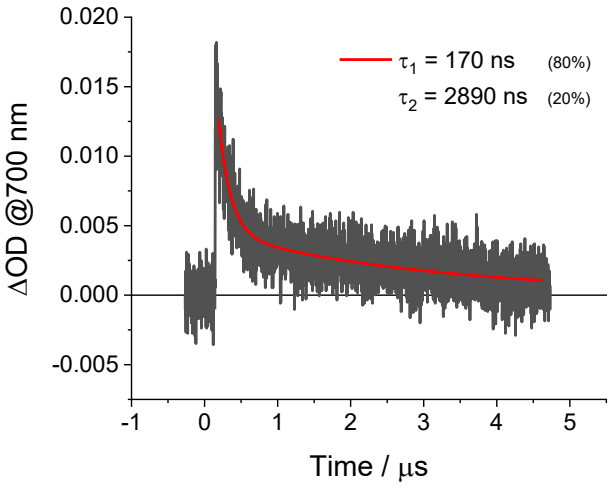

*Figure 15. Kinetic traces at 700 nm obtained by LFP (excitation at 355 nm) of **59** in CLF under N_2 with related fitting.*

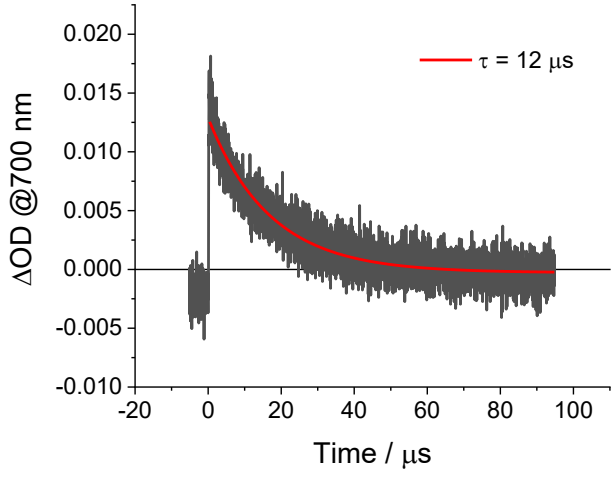

*Figure 16. Kinetic traces at 700 nm obtained by LFP (excitation at 355 nm) of **60** in CLF under N_2 with related fitting.*

Interestingly, the decay of the transient absorption at 700 nm in the case of the iminium-ion **59** is well described using a bi-exponential function (Figure 15). The first component (time-constant of τ_1 = 170 ns) can be presumably assigned to the reaction between the T_1 state and the olefin leading to the formation of the reaction intermediate *Int-A* (see Figure 4c). For this latter, TD-DFT indeed predicts an absorption band in the red portion of the visible spectrum but featuring lower absorption coefficients than the triplet T_1 (Figure 30). The subsequent event (time-constant of τ_2 = 2890 ns) can be reasonably attributed to the eventual formation of the cycloadduct from the reaction intermediate (*Int-A*).

2.5.11. Computational studies

The following subsections begin with an account of the conformational exploration of the photocatalyst, followed by a detailed overview of the mechanism and a discussion of likely sources of enantioselectivity based on evidence collected from the calculations. All calculations are provided electronically.

Conformational exploration of the photocatalyst: Introduction. To ensure that mechanistic calculations on the substrate were run on its global minimum, or at least on a conformer close to it, a series of systematic conformational explorations was performed using the substrate itself, as well as **Models 1** and **2** shown in Figure 17. Torsions around bonds marked A, B, C, and D (Figure 17, left), together with rotations of the phenyl rings, were considered.

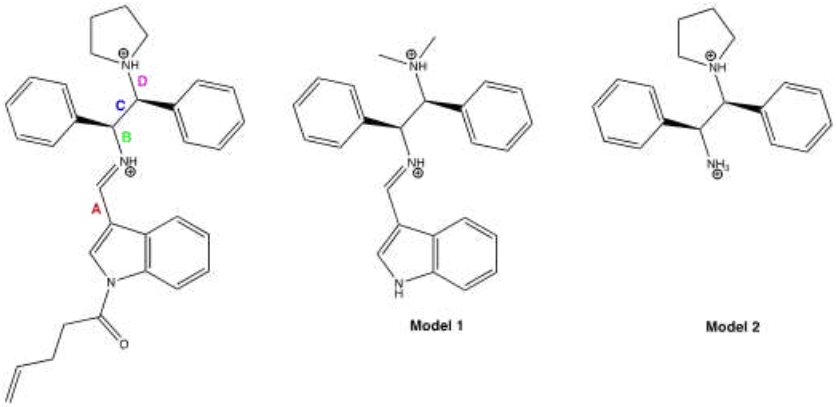

*Figure 17. **59** (left) with four of its rotatable bonds explicitly marked, and reduced **Models 1** and **2** used in its conformational exploration.*

2D Potential Energy Scan of Torsions B and C on Model 1. To begin with, a full relaxed two-dimensional potential energy surface scan of torsions **B** and **C** (360° × 360°) was performed using **Model 1** (Figure 17).This systematic scan was carried out at the same level of theory discussed in the main text, but in the gas phase. Results shown in**Errore. L'origine riferimento non è stata trovata.** suggest an overall minimum at **B** = + 90.3°, as measured from the iminium C to its closest phenyl C, and **C** = +72.0°, as measured from one phenyl C to the other.

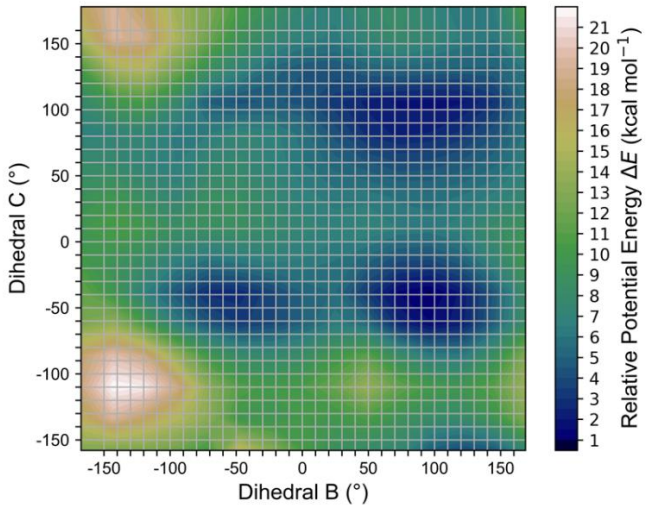

Figure 18. Relaxed 2D potential energy surface scan about the complete torsions of dihedrals B and C in Model 1 (Figure 17).

Potential Energy Scans of Torsion D on Model 1. Since bond **D** was observed to rotate spontaneously during the 2D scan shown in Figure 18, a full (360°) scan of its torsion was performed at the three different minima in Figure 18 to clarify which rotamer was the most stable energetically. The scans confirmed that the overall minimum for this torsion features the proton on the pyrrolidine N and the methine H *trans* to each other (*cf.* electronically provided calculations).

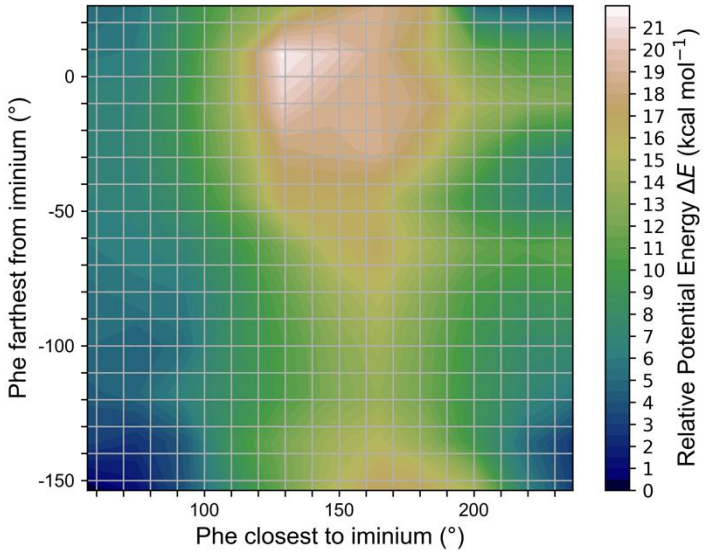

*Figure 19. Relaxed 2D potential energy surface scan about the 180°-torsions of the two phenyl dihedrals in **Model 1** (Figure 17).*

2D Potential Energy Scan of Phenyl Torsions on Model 1. Having established the lowest-energy combination of torsions **B**, **C**, and **D**, the preferred orientation of the phenyl rings was next explored. To this end, another relaxed 2D scan was performed on **Model 1**, in which each phenyl was allowed to rotate 180°. The results are shown in Figure 19, and the overall minimum of this scan was used to define the final phenyl conformation adopted in the calculations.**Further Tests on Torsion C and Trial of the PCM Solvation Model using Model 2.** Introducing PCM as a first candidate implicit solvation model, further tests were carried out by optimizing **Model 2** (Figure 17) at various geometries, differing in their starting value of dihedral **C**. Results are shown in Table 5, whereby it is once again confirmed that the torsion shows a lowest-energy minimum in the region of +67.7°C (compared to +72.0°C in the gas phase).

*Table 5. Optimization of **Model 2** at different values of torsion C (Figure 17).*

Min.	Relative electronic energy kcal mol^{-1}	Relative free energy kcal mol^{-1}	Value of C (°)
1	5.70	5.84	171.3
2	5.29	5.27	–25.0
3	4.31	5.23	138.9
4	5.01	6.76	154.4
5	0.00	0.00	67.7
6	6.03	6.25	–48.3

Tests on Dihedral A using the Full Substrate and the PCM Solvation Model. Due to iminium-indole conjugation, dihedral **A** can only either orient NH^+ *trans* to the bulk of the indole ring, or *cis* (*i.e.*, as represented in Figure 17).

Table 6. Optimization of 15 randomly selected representative isomers of the full substrate.

Min.	Relative electronic energy kcal mol^{-1}	Relative free energy kcal mol^{-1}	A as:	Value of B (°)	Value of C (°)
CIS_+145.5_+168.6	5.39	7.73	CIS	145.5	168.6
TRANS_+30.5_+148.0	7.40	9.54	TRANS	30.5	148
CIS_+150.2_+146.0	4.78	7.62	CIS	150.2	146
CIS_+153.1_+145.7	4.83	8.21	CIS	153.1	145.7
TRANS_+24.9_+142.4	7.30	8.99	TRANS	24.9	142.4
TRANS_+28.4_+142.3	7.33	7.99	TRANS	28.4	142.3
TRANS_+105.4_+75.3	2.79	4.54	TRANS	105.4	75.3
TRANS_+85.6_+74.2	3.35	10.31	TRANS	85.6	74.2
CIS_+90.3_+72.6	0.00	0.00	CIS	90.3	72.6
CIS_-147.7_-29.6	11.30	12.30	CIS	–147.7	–29.6
CIS_-87.4_-36.8	5.46	9.10	CIS	–87.4	–36.8
CIS_+121.4_-37.6	5.32	7.34	CIS	121.4	–37.6
TRANS_+27.8_-46.6	11.91	13.04	TRANS	27.8	–46.6
TRANS_+92.7_-47.3	7.14	11.87	TRANS	92.7	–47.3
CIS_+103.4_-53.3	3.88	3.88	CIS	103.4	–53.3

To assess which of the two orientations of **A** was preferred, the full substrate (with the olefin positioned for Si-face attack) was systematically optimized using 15 randomly chosen initial combinations of **B** and **C**: seven of these geometries had **A** in the trans configuration and the remaining eight in the cis configuration.. Results in Table 5 suggest that *cis* configurations are generally favored over their conformationally closest *trans* counterpart. Again, the combination of torsion **C** at +67.7°C and torsion **B** at +90.3° are confirmed to constitute the most energetically favorable conformation (minimum labeled CIS_+90.3_+72.6).

In fact, other combinations of **B** and **C** were explored in this phase, and when it became clear that the PCM solvation model led to several convergence issues, it was replaced by the C-PCM method referenced earlier.

Olefin Conformation and Configuration of Iminium C=N bond. Remaining degrees of freedom were not explored systematically, since:

- a *cis* configuration of the substituents on the iminium C=N bond is sterically impossible; and
- formation of the first C–C bond between the olefin and the indole is only sterically possible with the amide carbonyl pointing *cis* to the indole ring, as represented in Figure 17.
-

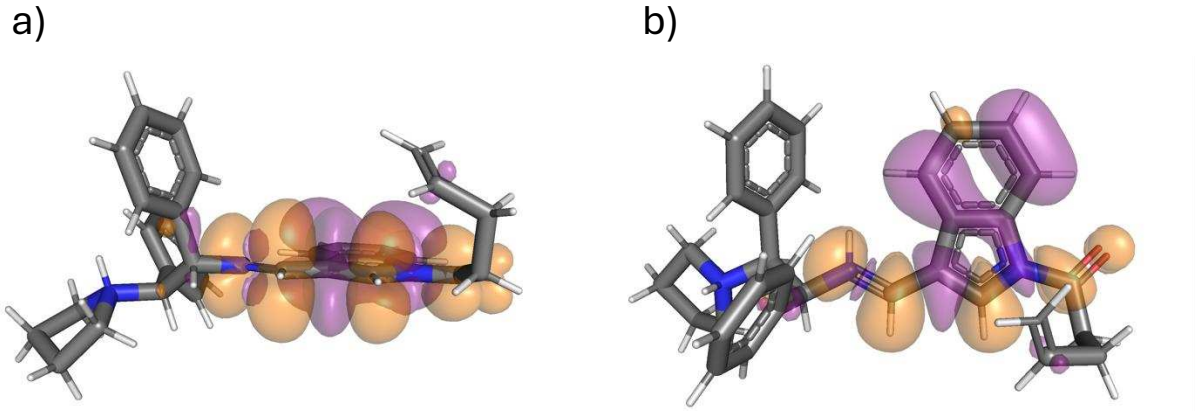

*Figure 20. Representation of the **59** (S0) to **59** (S1) excitation as the difference between its highest occupied and lowest unoccupied natural transition orbitals (NTOs), squared. a): side view; b): view from above the Si face, with the indole ring parallel to the plane of the page. Orange areas show whereto the electron is excited; purple areas denote the hole left behind. Atom colors: grey, C; blue, N; red, O; white, H. Isosurface: 0.0004.*

The proposed mechanism: T_1 is mainly accessible from S_1 *via* T_2. DFT and TD-DFT calculations show that the mainly HOMO-LUMO photoexcitation of the reactant **59** (S_0) to S_1 (Figure 20; with the inner olefin ready to attack the *Si*-face of the indole C=C) leads to relaxed intermediates **59** (S_{1+}) or **59** (S_{1-}), in which the iminium moiety has distorted, respectively, by about +75.2° or –77.0° towards the *Re* or *Si* face of the indole ring (Figure 21 panels a and b). **59** (S_{1+}) is simply referred to as **59** (S_1) in the main text, as we believe (*vide infra*) that the reaction is likelier to proceed from this intermediate. Absence of direct reactivity in **59** (S_{1+}), despite electron density being slightly depleted in the inner olefin carbon (Figure 20; only visible at isosurface 0.0004), is confirmed through a relaxed TD-DFT potential energy surface scan forcing the formation of the first C–C bond in the final 4-membered ring: this clearly shows there is no energetic minimum (Figure 22; the scan had to be interrupted once the ground state function began to be contaminated).

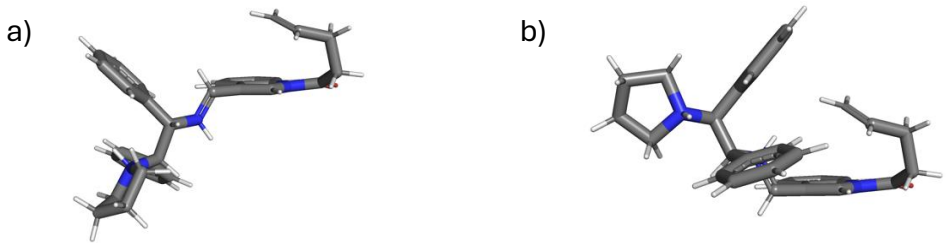

*Figure 21. a), Structure of **59** (S1+). b), Structure of **59** (S1-). Atom colors in a) and b) are the same as in Figure 18.*

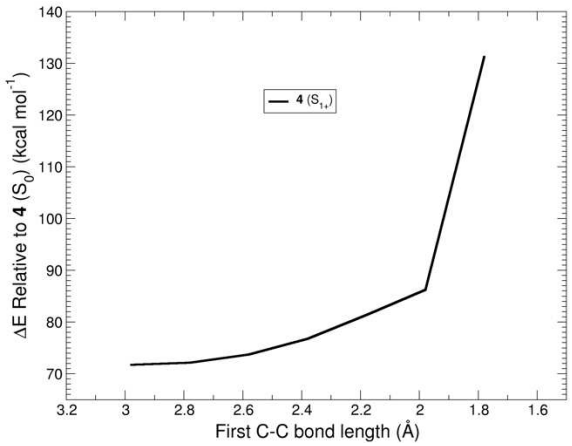

*Figure 22. TD-DFT relaxed potential energy surface scans for C-C bond formation in **59** (S1+), shown until emergence of spin contamination of in the perturbed S0 wavefunction.*

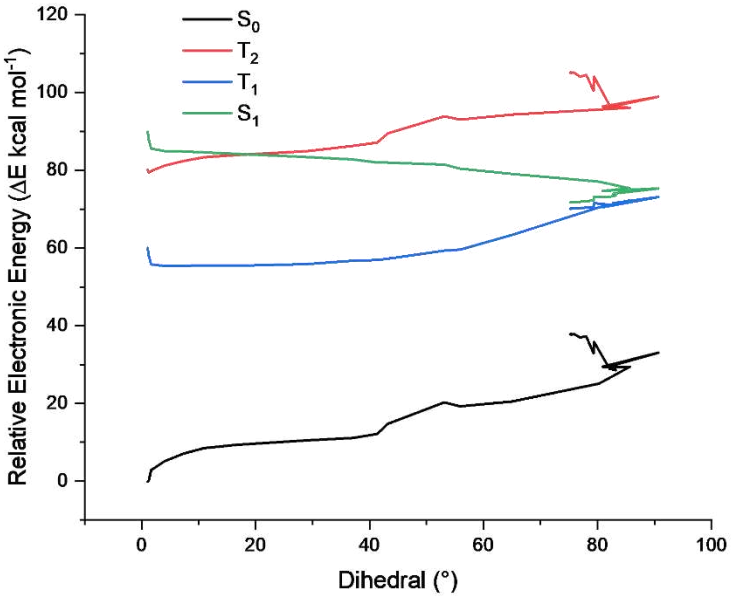

*Figure 23. Relative electronic energy profile for the unconstrained TD-DFT minimization of **59** (S1+) upon photoexcitation of **59** (S0), viewed with out-of-plane iminium distortion towards the Re face as the reaction coordinate (in °): surfaces for S0, T1, and T2 are also shown for comparison; all other low-lying excited states are omitted. The plot is the same as the one in Figure 4a.*

While the singlet state of **59** alone cannot be responsible for reactivity (as is indeed confirmed by our own spectroscopic studies which detect a triplet), calculations also clearly show that direct S_1–T_1 crossing is unattainable during iminium distortion—see for example Figure 23 and Figure 4a showing all states during relaxation from photoexcited **4** (S_1) to relaxed **4** (S_{1+})—on top of being spin- and symmetry-forbidden (S_1 and T_1 transitions are characterized by exactly the same orbitals). While there still remains a possibility of a S_1–T_1 intersystem crossing given the +1.66 kcal mol^{-1} gap, we therefore believe that in order to reach T_1, S_1 has easier access by transiting through a third electronic state; our calculations suggest that this is in all likelihood T_2, which (*cf.* again Figure 24) is encountered roughly halfway along the distortion paths from **4** (S_1) to relaxed **4** (S_{1+}) (and—we find—to relaxed **4** (S_{1-})). Similar types of S_1–T_2–T_1 decay are indeed reported in the literature.[48]

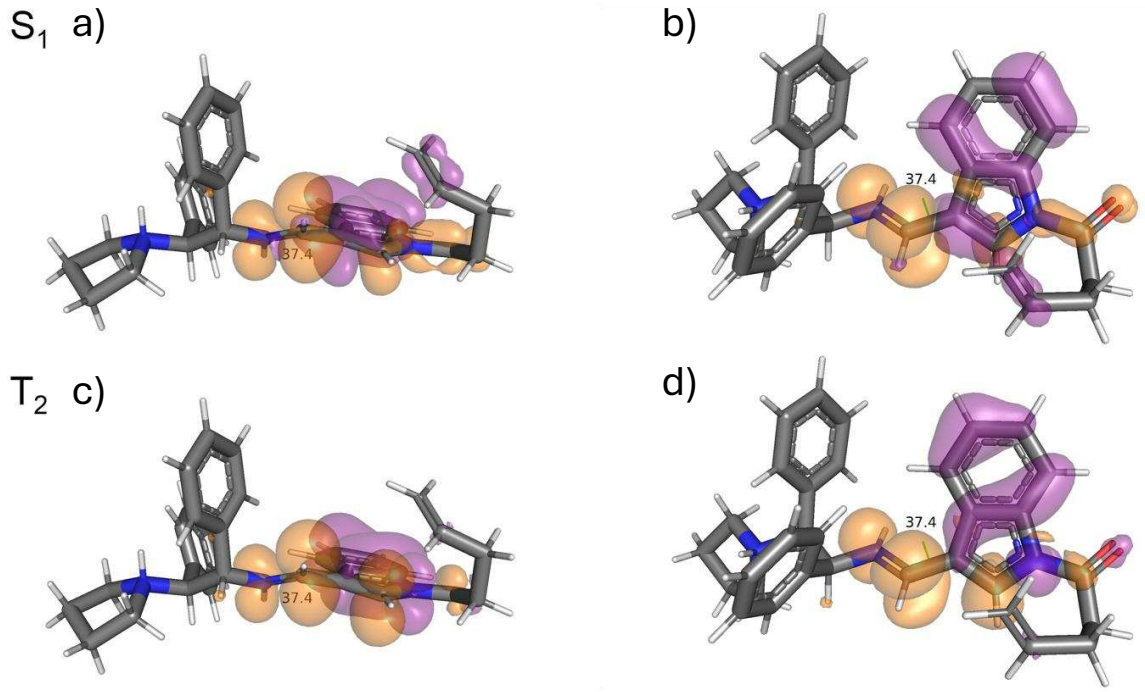

*Figure 24. Representations of (top) the S_1 and (bottom) the T_2 excited states at **MECP$_{1+}$**, as electron-hole pairs (difference between squared NTOs). a), c): side view; b), d) right: view from above the Si face, with the indole ring parallel to the plane of the page. The iminium distortion dihedral is labeled and marked in green (units: degrees). Atom and orbital color codes are identical to Figure 18. Isosurface: 0.001. The Figure is also reported in Figure 4b.*

We were indeed able to locate[49] the two S_1–T_2 MECPs encountered by **59** (S_1) on the way to **59** (S_{1+}) and **59** (S_{1-}): we term these, respectively, **MECP$_{1+}$** (simply referred to as **MECP$_1$** in the main text) and **MECP$_{1-}$**, and show the former in Figure 24 and Figure 4b, wherein it is clear that the iminium is distorted at +37.4° towards the *Re* face (–42.3° in the *Si*-face-distorted **MECP$_{1-}$**).

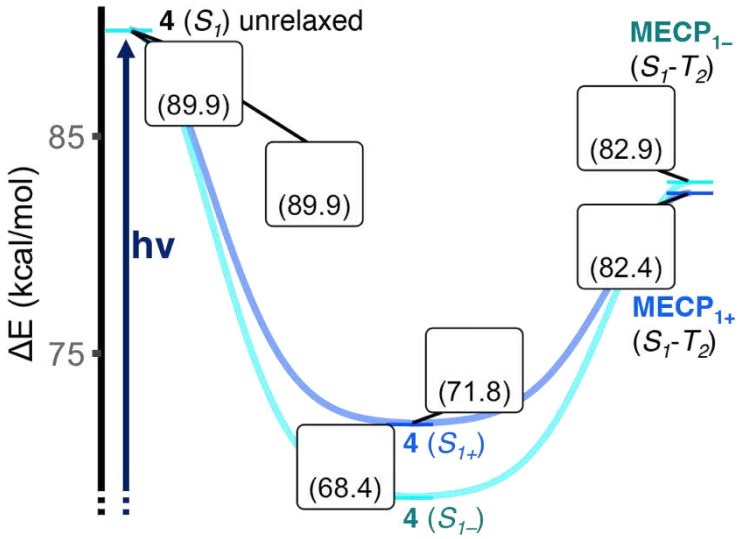

*Figure 25. Relative electronic energy profile (ΔE) of the reaction in the segments **59** (S_0) - **59** (S_{1+}) - **MECP$_{1+}$** (blue) and **59** (S_0) - **59** (S_{1-}) - **MECP$_{1-}$** (cyan), accessible immediately after photoexcitation of **59** (S_0) to **59** (S_1) and its subsequent relaxation. All energies are relative to **59** (S_0) (ΔE = 0.0), which is omitted from the scale for clarity.*

Incidentally, while TD-DFT does not allow for precise quantification of spin-orbit coupling effects, it is safe to assume that due to the spin-prohibited nature of S_1–T_2 transition only a fraction of all photoexcited **59** (S_1) molecules will directly cross to T_2 as soon as they reach **MECP$_{1+}$** or **MECP$_{1-}$**. On the other hand, it is likelier that most photoexcited **59** (S_1) molecules have the time to reach relaxed **59** (S_{1+}) or **59** (S_{1-}) (Figure 21) first, before either fluorescing to restore **4** (S_0), or reclimbing up to **MECP$_{1+}$** or **MECP$_{1-}$**. In this respect, if we focus on the relative electronic energy profile (ΔE) for the **4** (S_0) - **4** (S_{1+}) - **MECP$_{1+}$** and **4** (S_0) - **4** (S_{1-}) - **MECP$_{1-}$** segments of the reaction (blue and cyan, respectively in Figure 25), we note that while **MECP$_{1+}$** and **MECP$_{1-}$** are roughly similar in electronic energy, **59** (S_{1+}) is less stable than **59** (S_{1-}), and has a more modest barrier to overcome to reach its corresponding **MECP$_{1+}$** (+10.6 *vs.* +14.5 kcal mol^{-1}): once compared to profiles for *Re*-face attack (see Figure 28), we speculate that this might be one of the sources of the observed enantioselectivity. Given the two different barriers, going forth from **MECP$_{1+}$** we have only chosen to explore the '+' route (iminium distorted to *Re* face of the reactive double bond of the indole moiety), and this is why we have dropped the + subscript from subsequent points and in the main text.

Natural Transition Orbital (NTO) representations[Errore. Il segnalibro non è definito.] of states S_1 and T_2 at crossing point **MECP$_{1+}$** in Figure 24a and 24b, respectively, show that while the excited electron localizes at almost identical spots, *i.e.*, indole C2 and iminium N and C atoms, the hole left by the transition (*i.e.*, its 'source') differs significantly in shape and extent, spanning differently shaped areas of the indole and of the olefin. However, precise quantification of the spin-orbit coupling effects behind this event would require higher-level calculations.

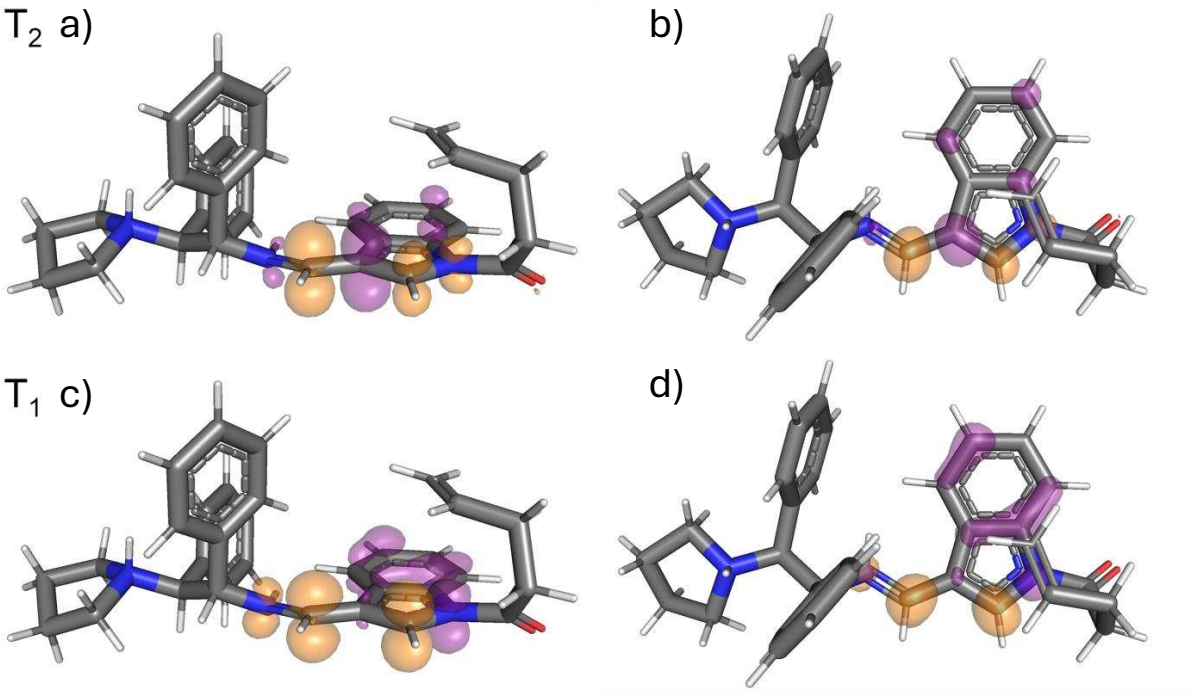

*Figure 26. Representations of (top) the T_2 and (bottom) the T_1 excited states at **MECP$_2$**, again represented as electron-hole pairs (difference between NTOs, squared). a), c): side view; b), d): view from above the Si face, with the indole ring parallel to the plane of the page. Color codes are identical to Figure 24. Isosurface 0.004*

In any case, once **MECP$_{1+}$** has crossed to T_2, further unconstrained TD-DFT reveals that, unlike S_1, T_2 readily encounters a crossing point with T_1 once the iminium moiety has almost fully re-planarized: This second MECP is labeled **MECP$_2$** and is illustrated in Figure 26. Squared NTO analysis of **MECP$_2$** (contracted to a higher isosurface for better visualization) show that the excited electron mainly delocalizes across the iminium carbon and indole C_2.

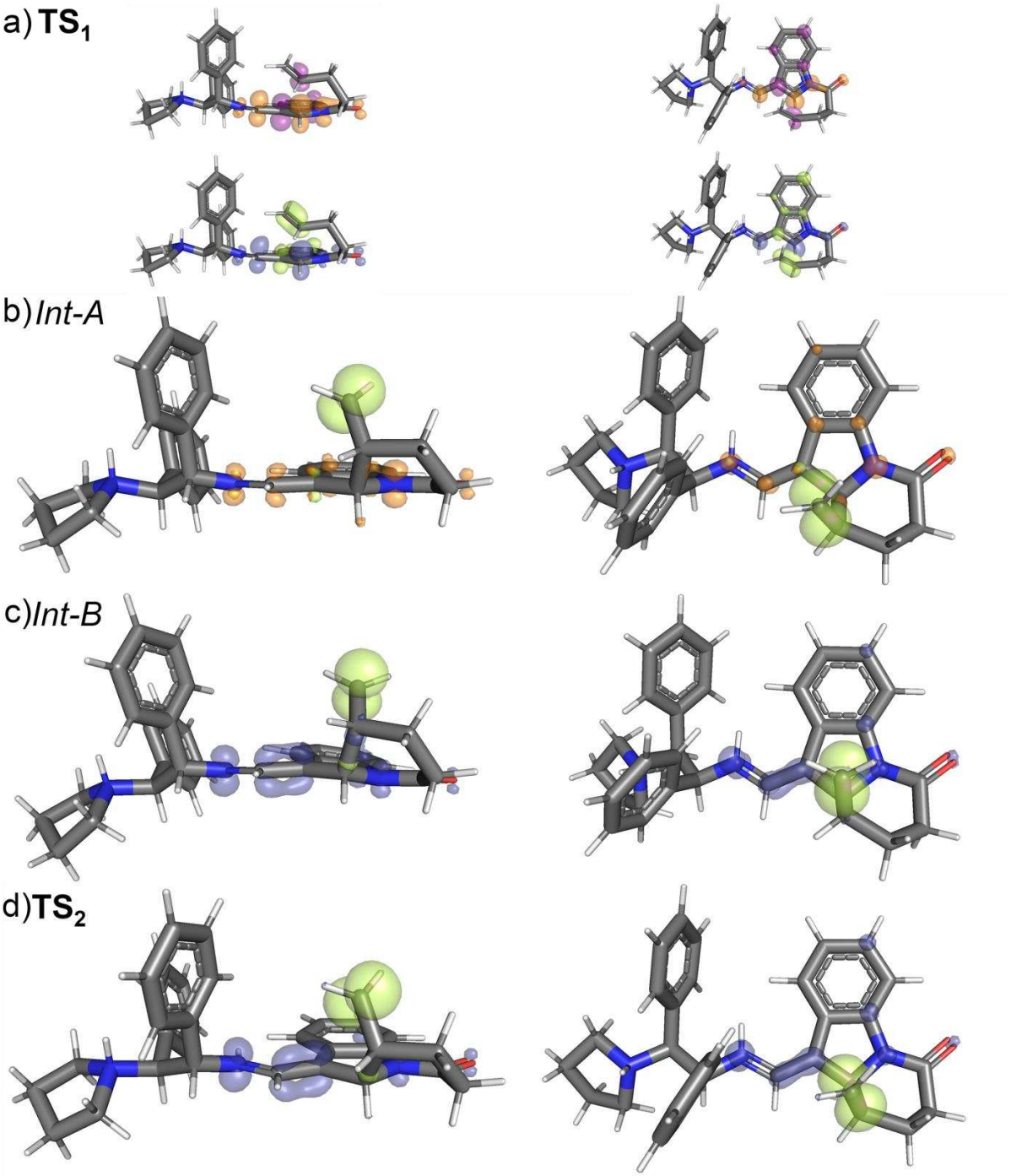

Figure 27. Final stages of cycloaddition. (a) ***TS₁****. Top: {[α-SOMO]2 – [β-SUMO]2} (orange >0; purple <0); bottom: {[α-SOMO₋₁]2 – [β-SUMO₊₁]²} (green: > 0; dark blue < 0). (b) Int-A (orange: [α-SOMO]²; green: [α-SOMO₋₁]²). (c) Int-B, β – α spin difference (green: maximum α; dark blue: maximum β); (d)* ***TS₂****, β – α spin difference (green: maximum α; dark blue: maximum β). Chosen isosurfaces: 0.004 in (a); 0.008 in (b); 0.01 in (c) and (d). In all panels: left: side view; right: view from above the Si face, with the indole ring parallel to the plane of the page. Atom color codes are identical to Figure 24.*

Anatomy of the [2+2] cycloaddition. As shown in the main text (Figure 4c), access to T_1 finally paves the way for the formation of the first C–C bond. While olefin involvement in **MECP₂** excitations is negligible (Figure 26), a last bout of TD-DFT optimization on T_1 shows that **MECP₂** relaxes towards the TS for the first C–C bond formation (**TS₁**), with a T_1 minimum **59** (T_1) also theoretically accessible (*cf.* electronically provided calculations). Analysis of the two spin-α unpaired electrons in **TS₁** and their holes (Figure 27a; top and bottom) clearly shows one unpaired spin-α electron located on the indole C2 ready to occupy a hole on the inner olefin

carbon, and, conversely, another unpaired spin-α electron in the π system of the olefin ready to occupy a hole located on the indole C_2.

In the ensuing T_1 intermediate *Int-A* with the first C–C bond fully formed (Figure 27b), one can clearly recognize one unpaired electron on the external (former) olefin carbon, and another delocalized not just on the indole C_3 but also across both iminium atoms. Spin inversion of one of these *via* **MECP$_3$** yields the open-shell S_0 counterpart *Int-B* (Figure 27c), in which the $–CH_2^{\bullet}$ tail rotates in an attempt to maximally antiparallelize the now opposite-spin electrons (spin contamination: $S^2 = 0.1263$). This step is predicted to be virtually barrierless (ΔE = + 0.06 kcal mol^{-1};Figure 28b and ΔG = – 0.90 kcal mol^{-1}; Figure 28a and main text Figure 4c).

Formation of the second and final C–C bond that completes the 4-membered ring transits through a second **TS$_2$** (Figure 27d). It was observed that the negative mode characterizing **TS$_2$** is not a C···C compression, but rather a rotation of $–CH_2•$ that orients its spin-α electron within equidistance of indole C3 and the iminium C, over which the unpaired spin-β electron is partly delocalized. Since this electron is not confined to C3, the $–CH_2•$ tail could be expected to attack the iminium C to form a five-membered ring as readily as it could attack indole C3 to form the main cycloadduct product **Int-C**. Our calculations fully support this picture: proceeding downhill from **TS$_2$**, it was found that, concomitantly with S_0 shell closure, there is a bifurcation on the potential energy surface. One branch of the bifurcation leads to product **Int-C**, the other to a side product *SP* that features a 5-membered ring. Proper elucidation of this bifurcation (in essence, making sure that **TS$_2$** could directly optimize to both *SP* and **Int-C**) required repeatedly optimizing a geometry issued from the customary IRC calculation on (open-shell singlet) **TS$_2$** (see *Computational Details* in *General Information*) with increasingly frequent Hessian evaluation and increasingly narrow optimization steps.

It should be noted that the side product is itself theoretically convertible to **Int-C** through a closed-shell **TS$_3$**, but this pathway requires overcoming a free energy barrier of +19.7 kcal mol^{-1}. Calculations to characterize *SP* and **TS$_3$** are provided electronically.

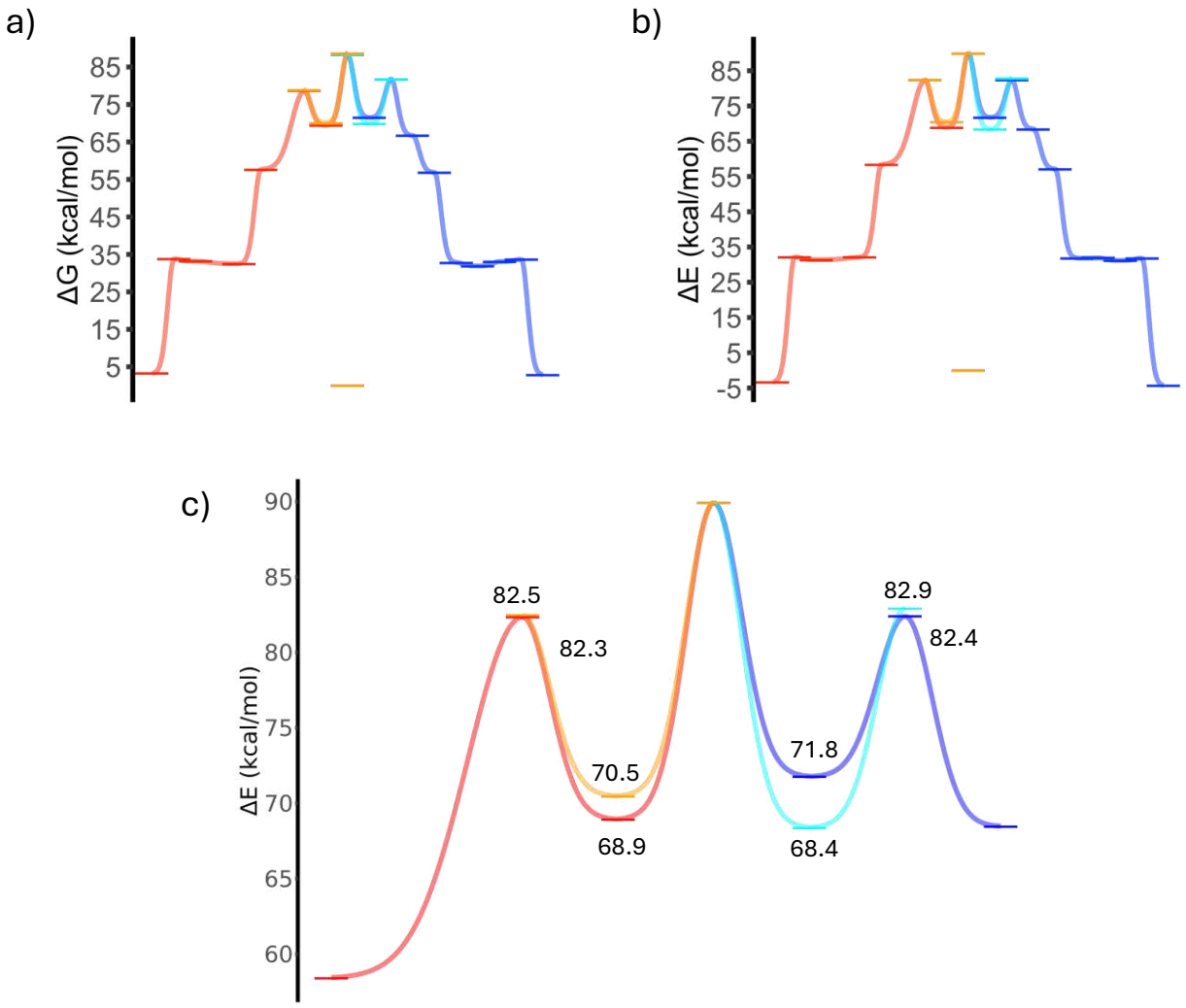

Figure 28. ***a*** *Replot of the relative free energy profile (ΔG) of the proposed reaction path for the [2+2] cycloaddition, as shown in the main text (Figure 4c) for Si-face olefin attack (blue line), but this time with calculated energies for Re-face olefin attack also added and displayed in red. We also add free energy profiles for the Si-**59** (S_{1-}) – Si-**MECP**$_{1-}$ segment (cyan) and that for the Re-**59** (S_{1-}) – Re-**MECP**$_{1-}$ (orange; see text for label details).* ***b*** *Exactly as in* ***a****, but with relative electronic energies (ΔE); the segment shown in Figure 25 is in fact a portion of this plot. All energies are relative to* ***59*** *(S_0). Note that some points are missing from the Re-face attack pathways, as they were not determined.* ***c****. Zoom of the energy profiles plotted in panel b) to better show the energy differences between the pathways leading to the enantiomers of the desired product.*

Possible source of enantioselectivity. While not central to the aims of our investigation, we wondered if a further series of TD-DFT calculations—this time retracing key stages of a hypothetical *Re* face attack (*i.e.*, towards the enantiomer that is experimentally unobserved)—could help us get closer to explaining the causes of the evident enantioselectivity that is observed experimentally. In Figure 28a, we juxtapose the free energy profile for the *Re* attack pathway next to the one previously shown in Figure 4c (and show the corresponding electronic energy profile in Figure 28b and its zoomed plot better showing the profile up to **MECP**$_1$). While both profiles show that energies beyond **MECP**$_1$ are generally slightly higher for the (disfavored) *Re*-face olefin attack than for the (favored) *Si*-face attack, the relatively small gap between the two is not really consistent with the elevated enantiopurity encountered experimentally.

Rather, we speculate that such a clear enantiopreference for *Si*-face attack could arise from the four different electronic energy barriers (Δ*E*;Figure 28b) that each of the four *post*-excitation intermediates *Si*-**59** (S_{1+}), *Si*-**59** (S_{1-}), *Re*-**59** (S_{1+}), and *Re*-**59** (S_{1-}) has to overcome to reach its corresponding S_1–T_2 crossing point (*i.e.*, *Si*-**MECP**$_{1+}$, *Si*-**MECP**$_{1-}$, *Re*-**MECP**$_{1+}$ or *Re*-**MECP**$_{1-}$). (Prefixes *Re-* / *Si-* indicate the indole C=C face undergoing olefin attack, while—as mentioned earlier—+ / – denote iminium distortion towards the *Re* or *Si*

face, respectively). Combined with the spin-prohibited nature of the S_1–T_2 transition itself, these four different **59** (S_1) – **MECP$_1$** barriers (*vide infra*)—which are a direct consequence of the asymmetry of the photocatalytic moiety—are the highest in the reaction profile; this is likely to make the S_1 to T_2 transition the rate-determining step for the entire reaction, and even relatively small energy differences at this step could have large effects on the stereochemistry of the final product.

That said, if one assumes similarly sized spin-orbit coupling effects governing the S_1–T_2 crossing in all four scenarios (*Re- vs. Si-* attack × *Re- vs. Si-* iminium distortion), and that a majority of photoexcited molecules won't have the opportunity to cross directly to T_2 but will first relax to **59** (S_1) before returning to **MECP$_1$**, it is encouraging to note that the lowest potential energy barrier to overcome is precisely one of the two that paves the way for the observed product **Int-C**—*i.e.*, the *Si*-**59** (S_{1+}) to *Si*-**MECP$_{1+}$** barrier at ΔE = +10.6 kcal mol^{-1}. For comparison, the most favorable barrier on the path to the unobserved enantiomer of **Int-C** is the one from *Re*-**59** (S_{1+}) to *Re*-**MECP$_{1+}$**, at +12.0 kcal mol^{-1}.

Further consolidation of this hypothesis requires quantification of S_1–T_2 spin-orbit coupling effects at *Si*-**MECP$_{1+}$**, *Si*-**MECP$_{1-}$**, *Re*-**MECP$_{1+}$**, and *Re*-**MECP$_{1-}$** in order to calculate overall transition rates. Quantification of spin-orbit coupling effects in *Gaussian16* is not directly possible at the TD-DFT level, either requiring a switch of software; or adoption of a computationally demanding and tedious CASSCF approach; or reliance on an *ad hoc Python* wrapper.[cit22sup] For these reasons, and in light of our clear confirmation of T_1 accessibility, we opted not to explore this issue further.

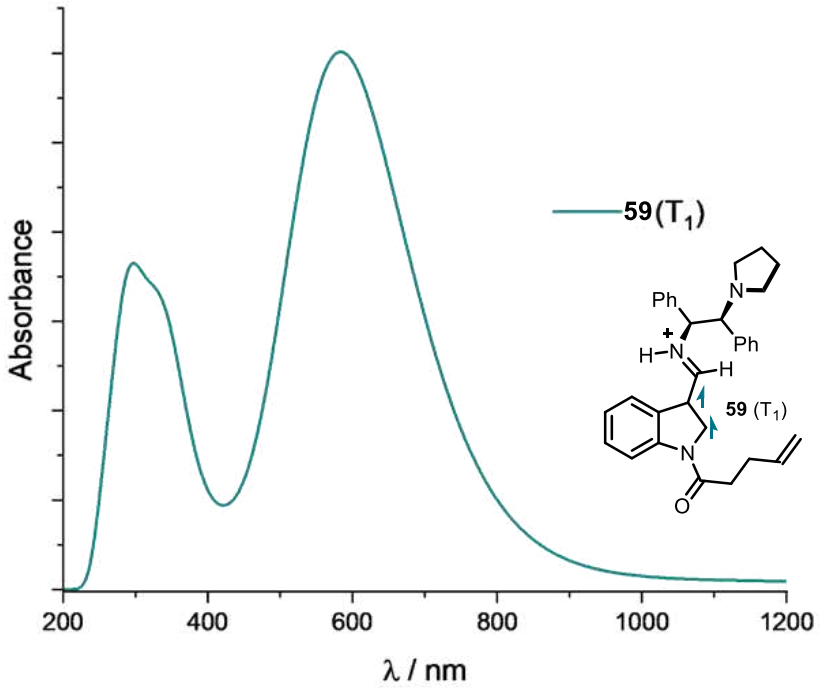

*Figure 29. Simulated spectrum of **59** (T1), directly issuing from the TD-DFT calculation on the optimised geometry.*

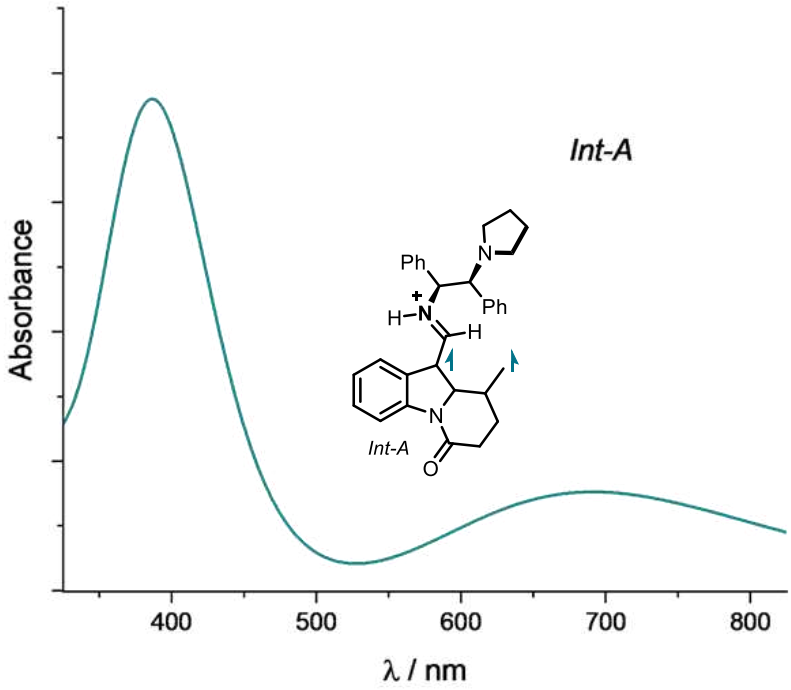

Figure 30. Simulated spectrum of Int-A, directly issuing from the TD-DFT calculation on the optimised geometry.

2.5.12. Determination of the relative configuration through selective NOESY experiments

***NOE-NMR spectra of* 87**

The stereocenters below marked with asterisks (*) were assigned by $^{1}H—^{1}H$ NOESY correlations:

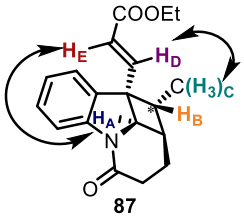

87

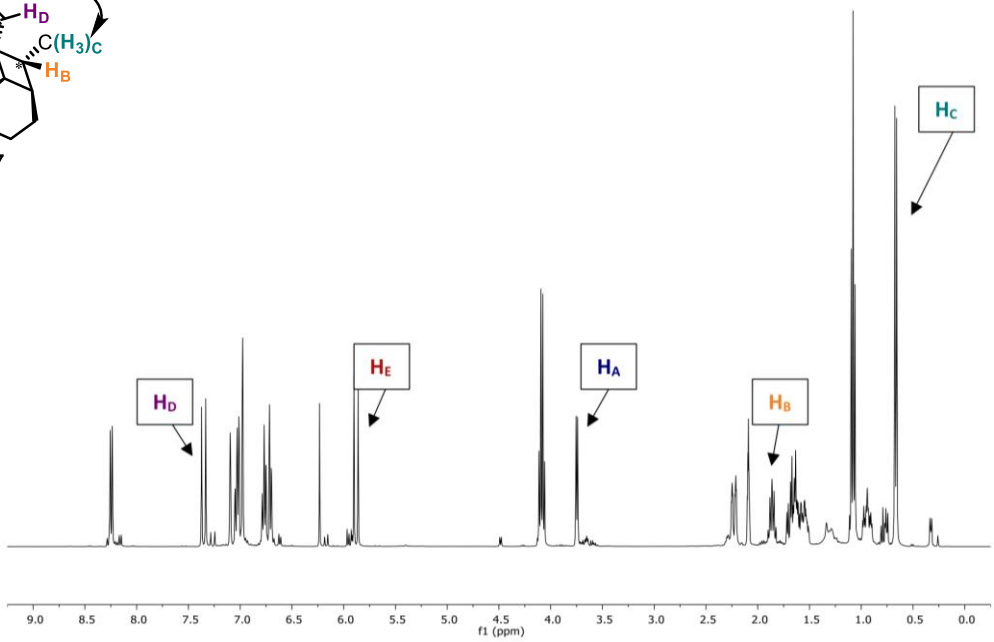

Figure 31. NMR spectrum (400 MHz in Toluene-d8) of ***87****.*

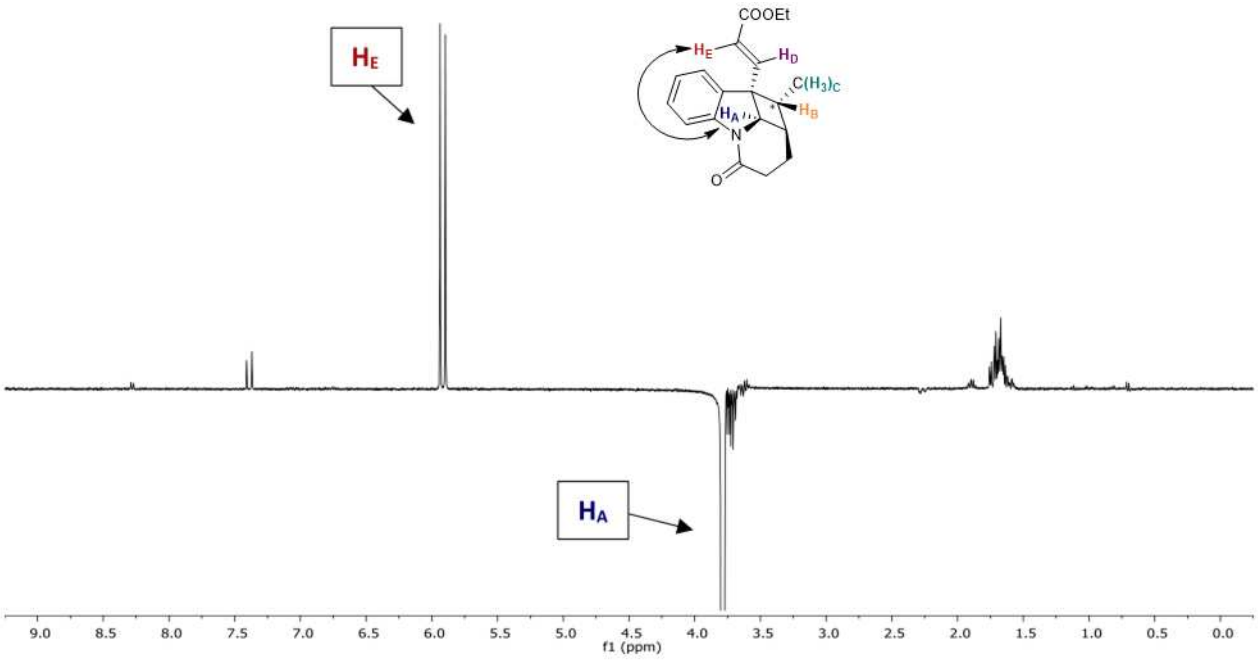

Figure 32. NOE spectrum (400 MHz in Toluene d8) on saturation of H_A*.*

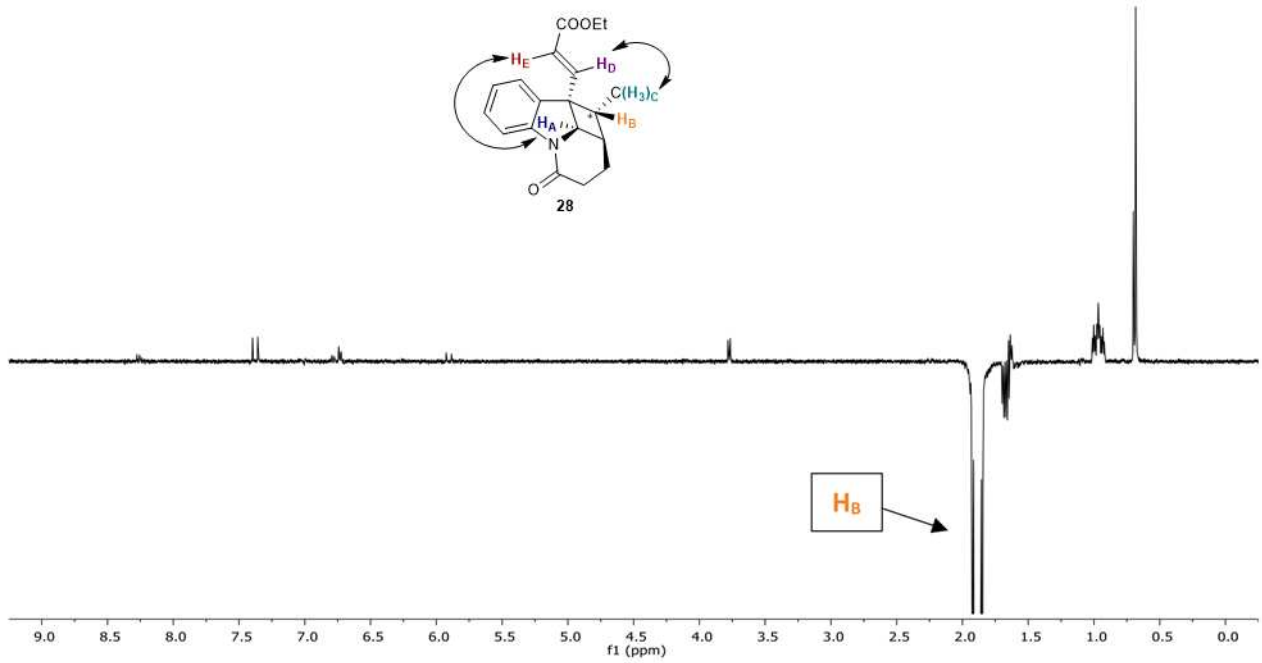

Figure 33. NOE spectrum (400 MHz in Toluene d8) on saturation of H_B.

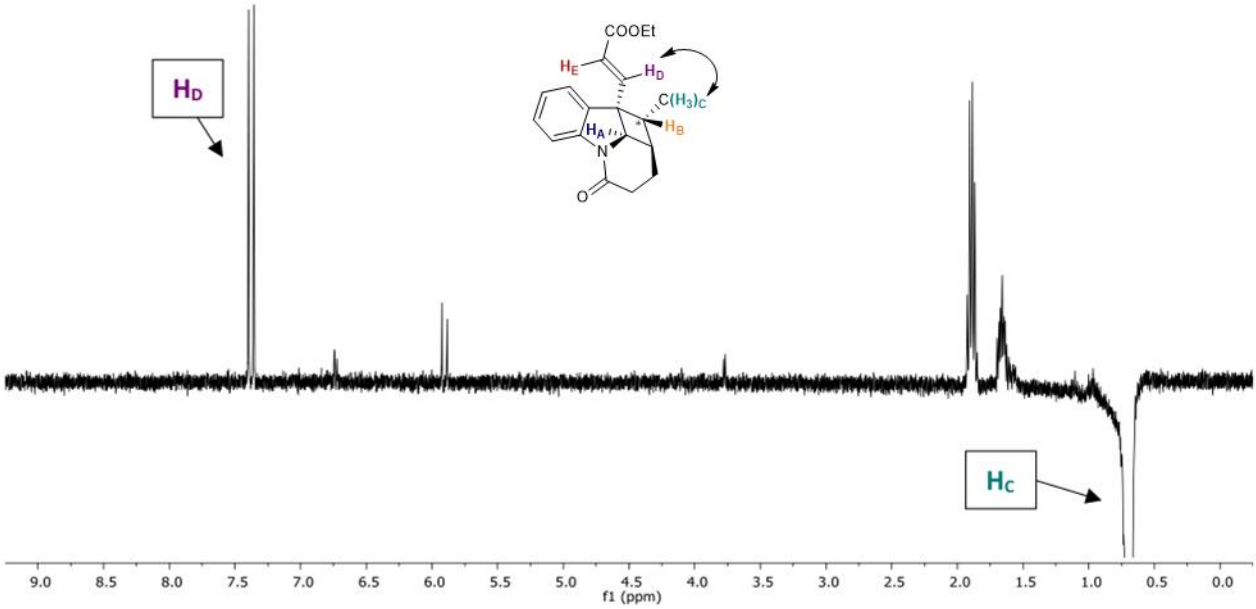

Figure 34. NOE spectrum (400 MHz in Toluene d8) on saturation of H_C.

***NOE-NMR spectra of* 97**

The stereocenters below marked with asterisks (*) were assigned by $^{1}H—^{1}H$ NOESY correlations:

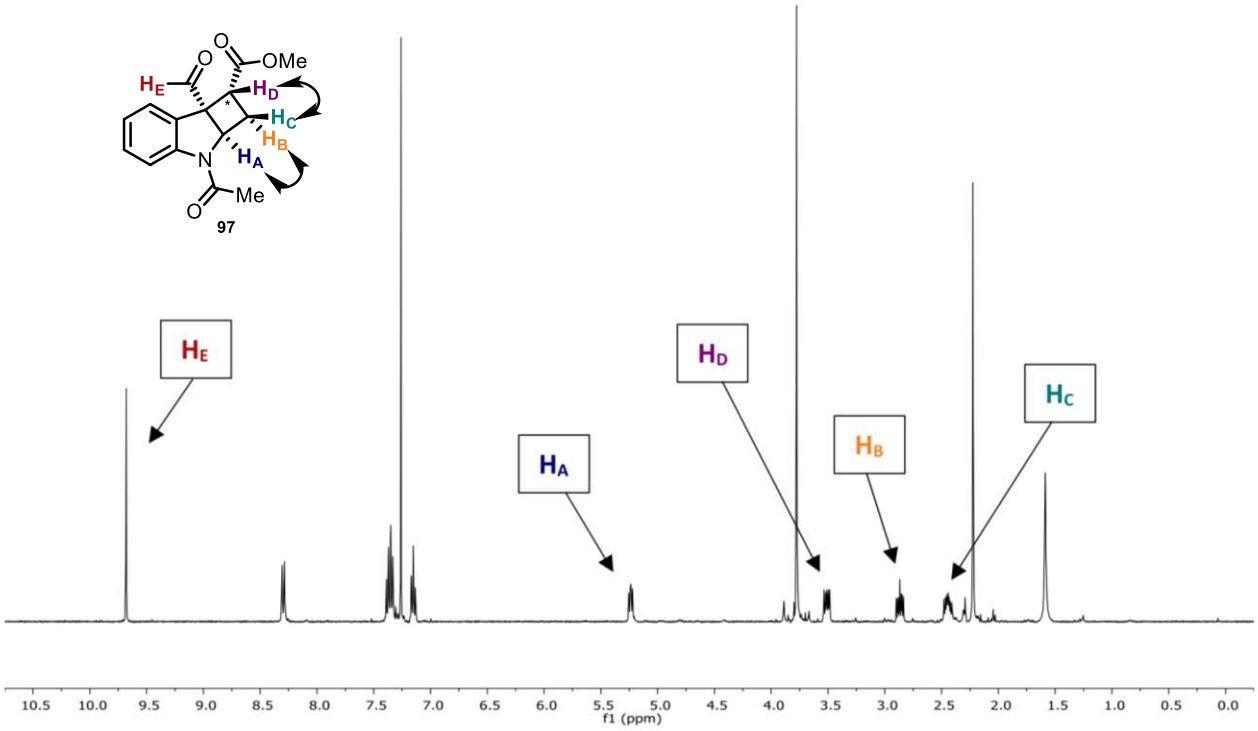

Figure 35. NMR spectrum (400 MHz in $CDCl_3$) of ***97****.*

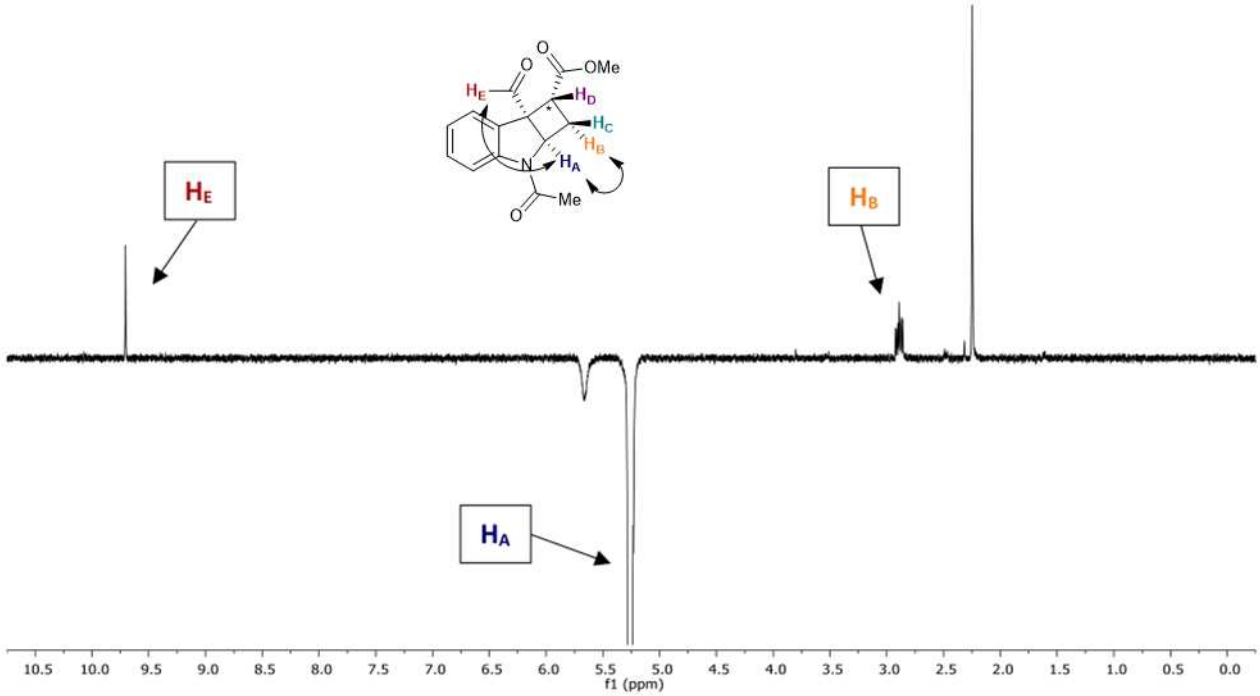

Figure 36. NOE spectrum (400 MHz in $CDCl_3$) on saturation of H_A.

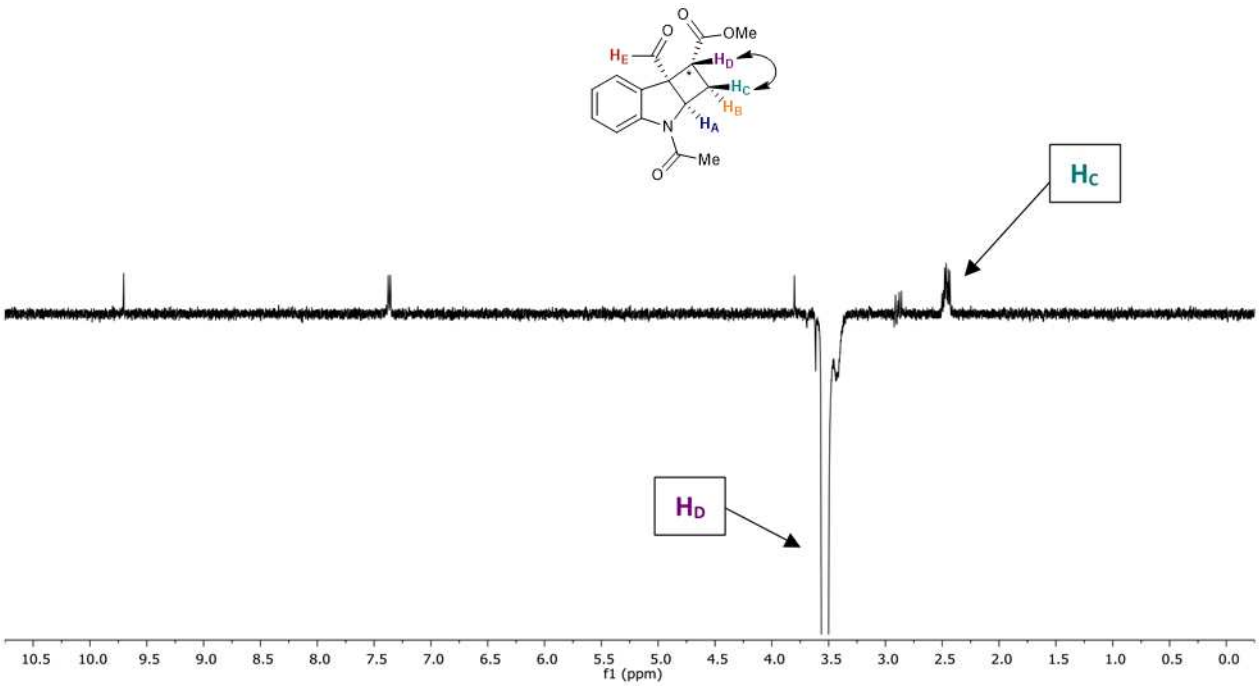

Figure 37. NOE spectrum (400 MHz in $CDCl_3$) on saturation of H_D.

NOE-NMR spectra of 95.

The stereocenters below marked with asterisks (*) were assigned by $^{1}H—^{1}H$ NOESY correlations:

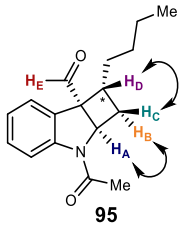

95

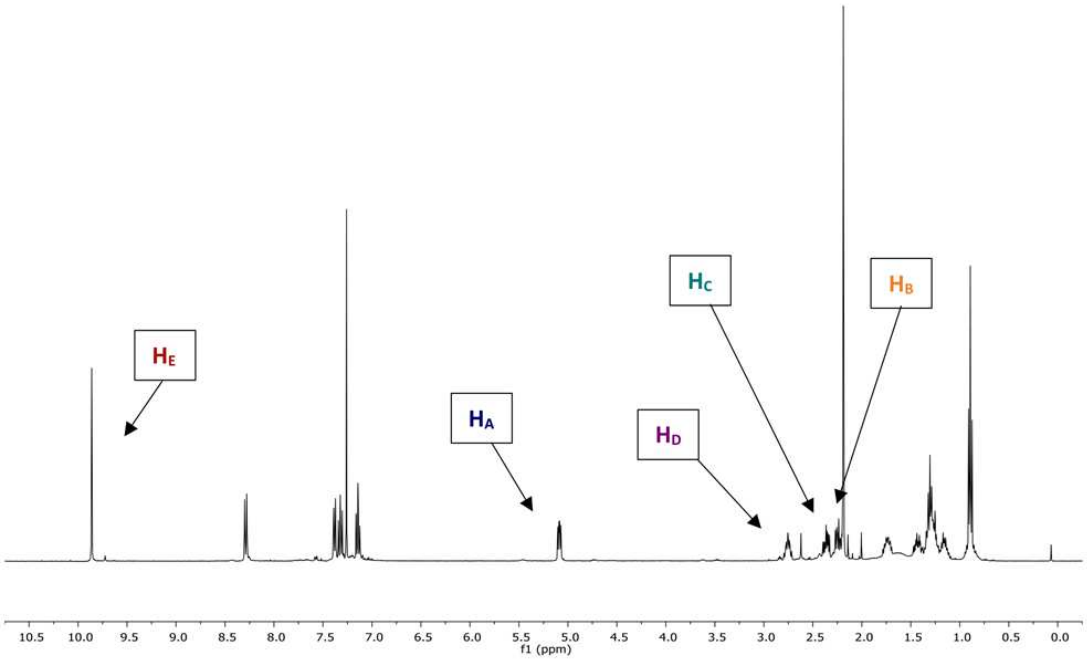

*Figure 38. NMR spectrum (400 MHz in $CDCl_3$) of **95**.*

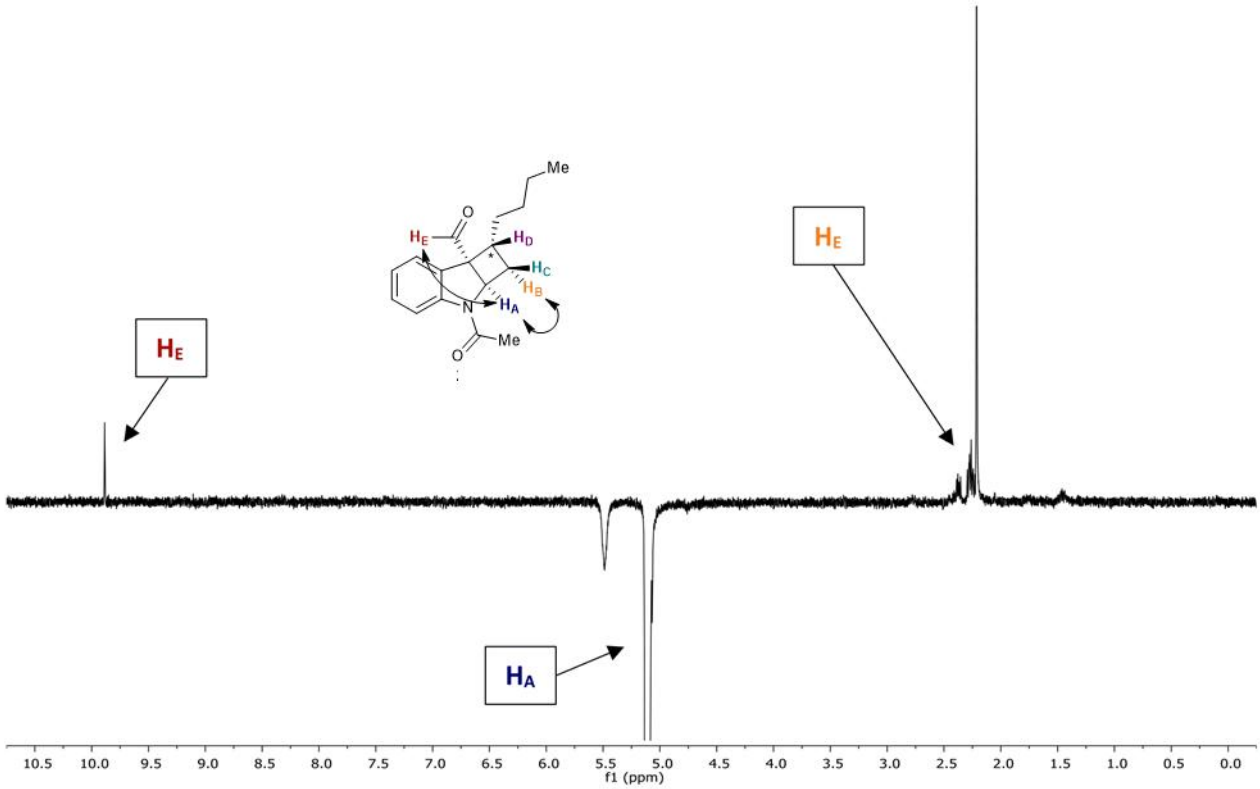

Figure 39. NOE spectrum (400 MHz in $CDCl_3$) on saturation of H_A.

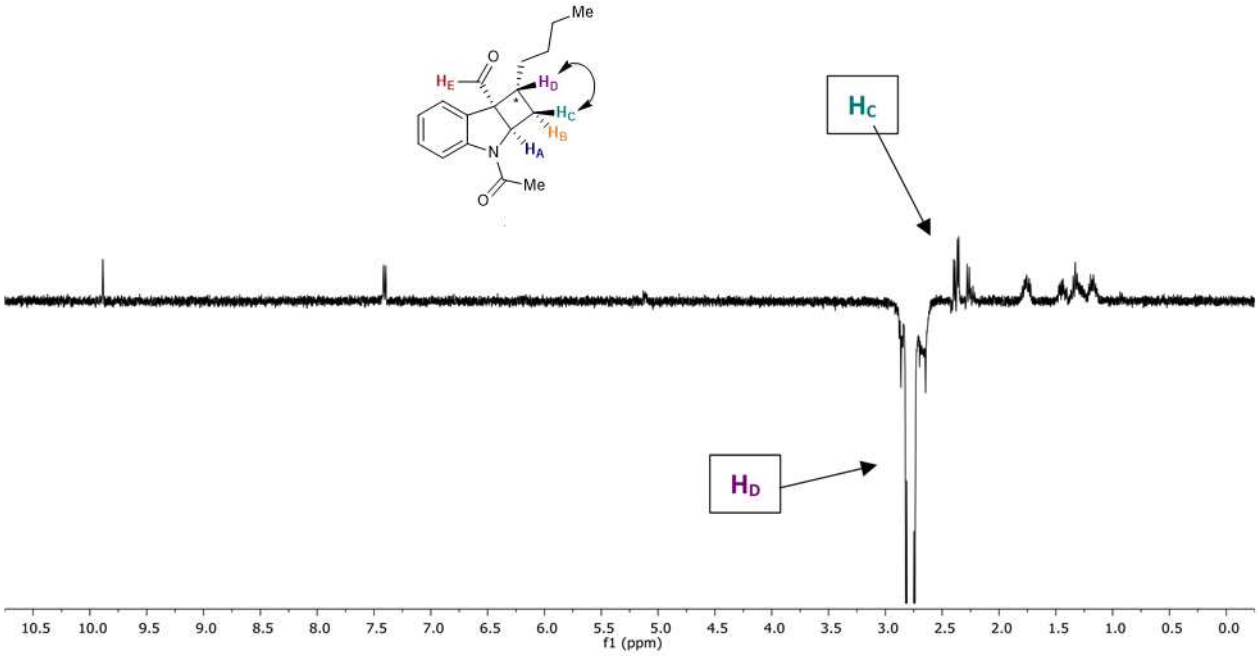

Figure 40. NOE spectrum (400 MHz in $CDCl_3$) on saturation of H_D.

NOE-NMR spectra of 95'.

The stereocenter below marked with asterisk (*) was assigned by $^{1}H—^{1}H$ NOESY correlations:

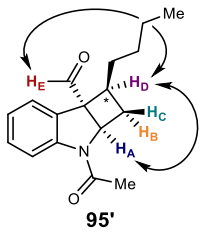

95'

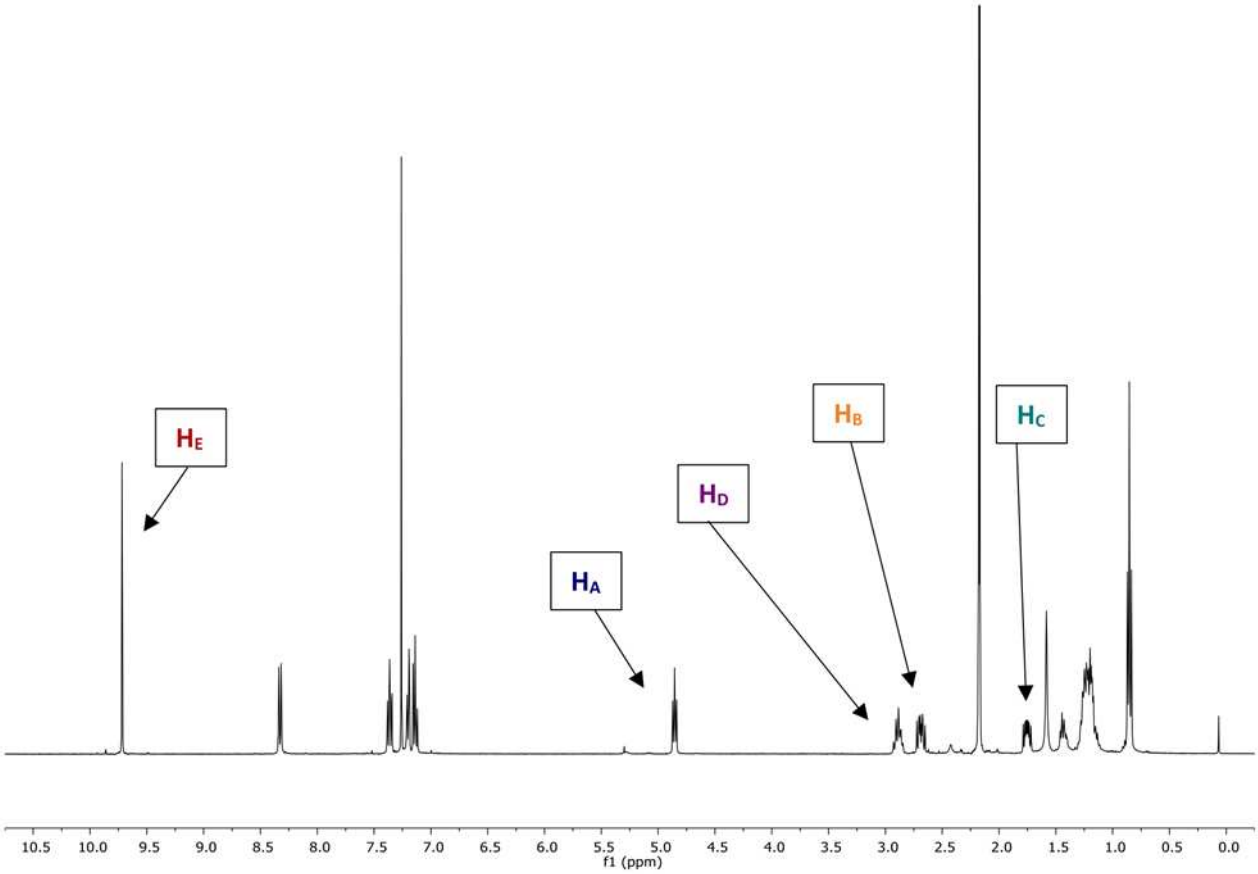

*Figure 41. NMR spectra (400 MHz in $CDCl_3$) of **95'**.*

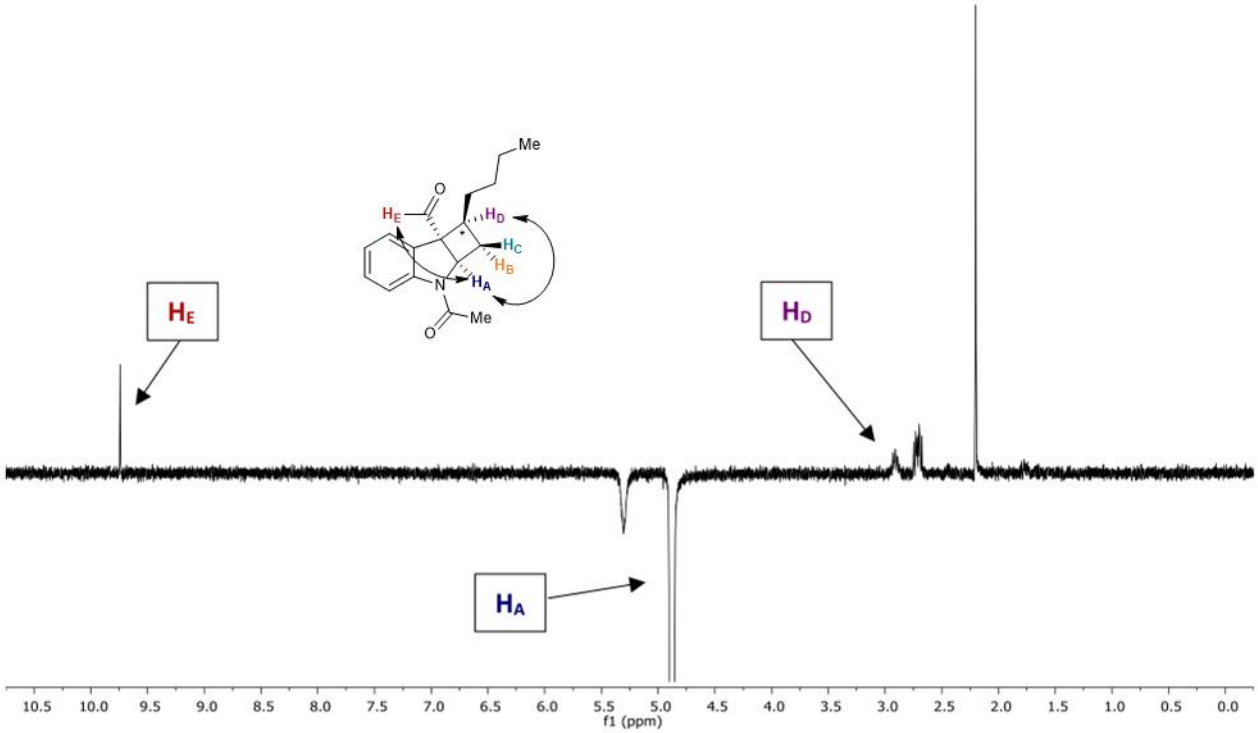

Figure 42. NOE spectrum (400 MHz in $CDCl_3$) on saturation of H_A.

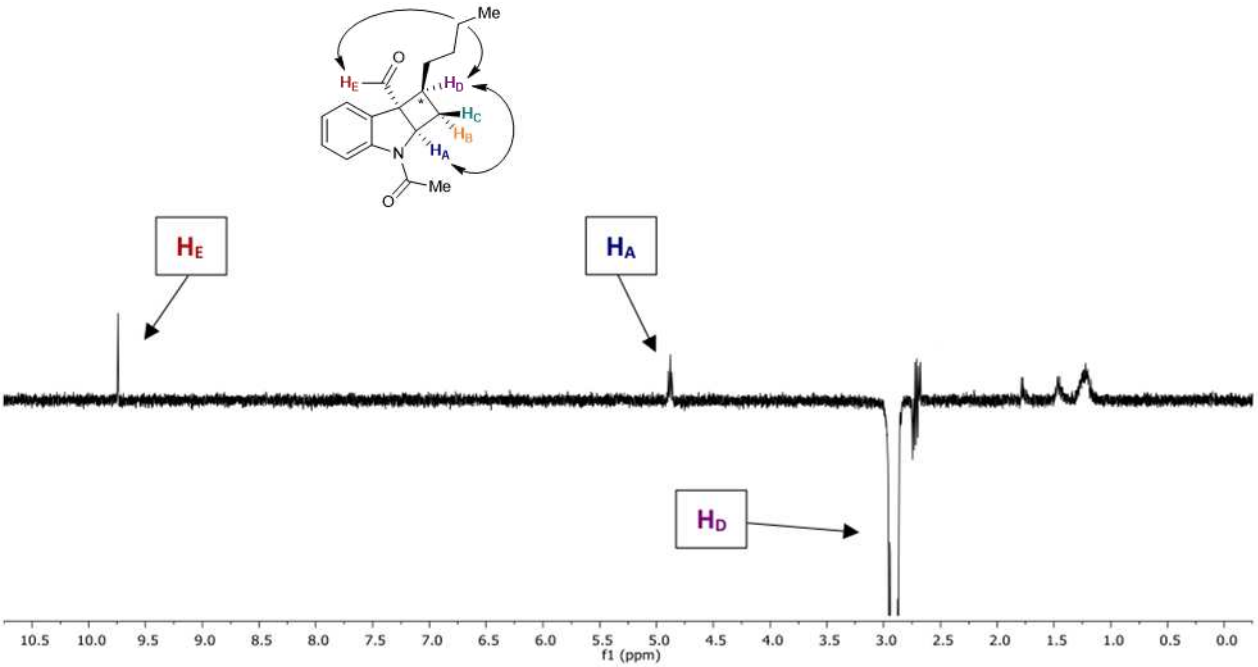

Figure 43. NOE spectrum (400 MHz in $CDCl_3$) on saturation of H_D.

***NOE-NMR spectra of* 98**.

H_A = 4.99 ppm	H_B = 2.58 ppm
H_C = 1.87 ppm	H_D = 0.93 ppm
H_E = 9.92 ppm	

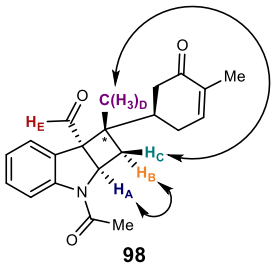

98

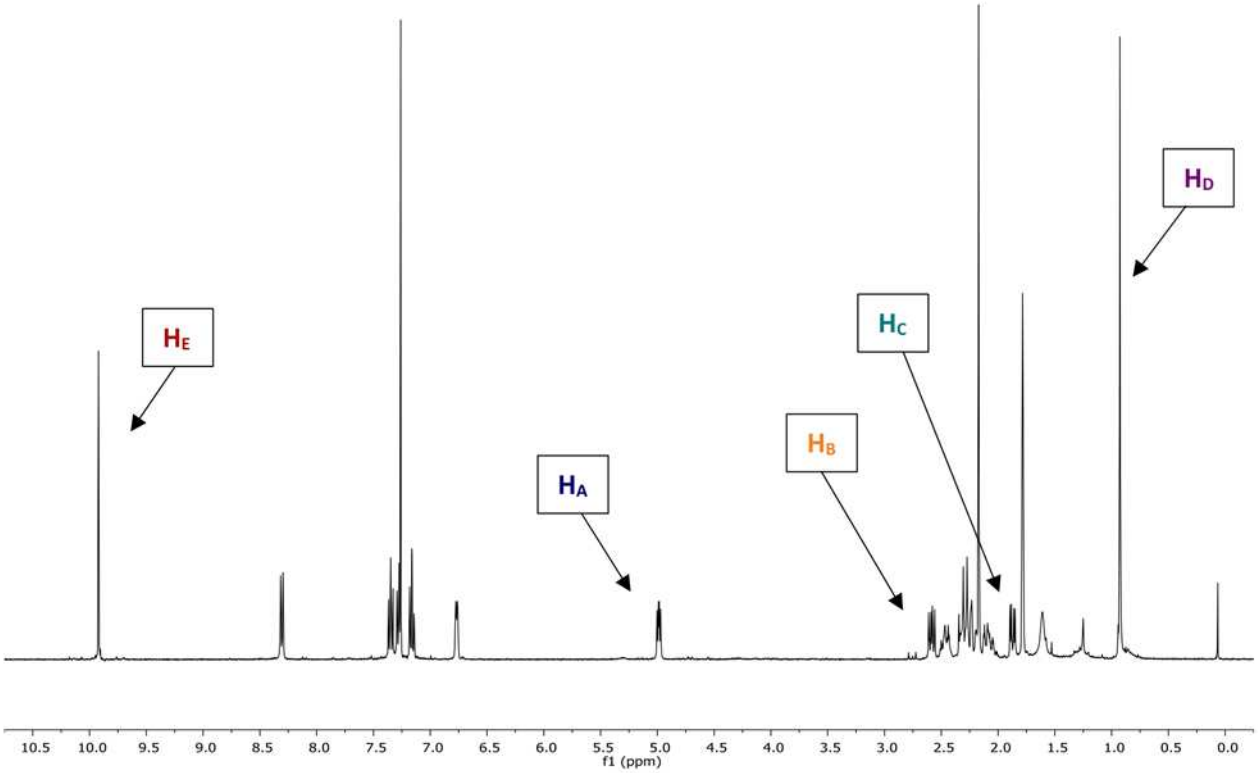

Figure 44. NMR spectrum (400 MHz in $CDCl_3$) of ***98***.

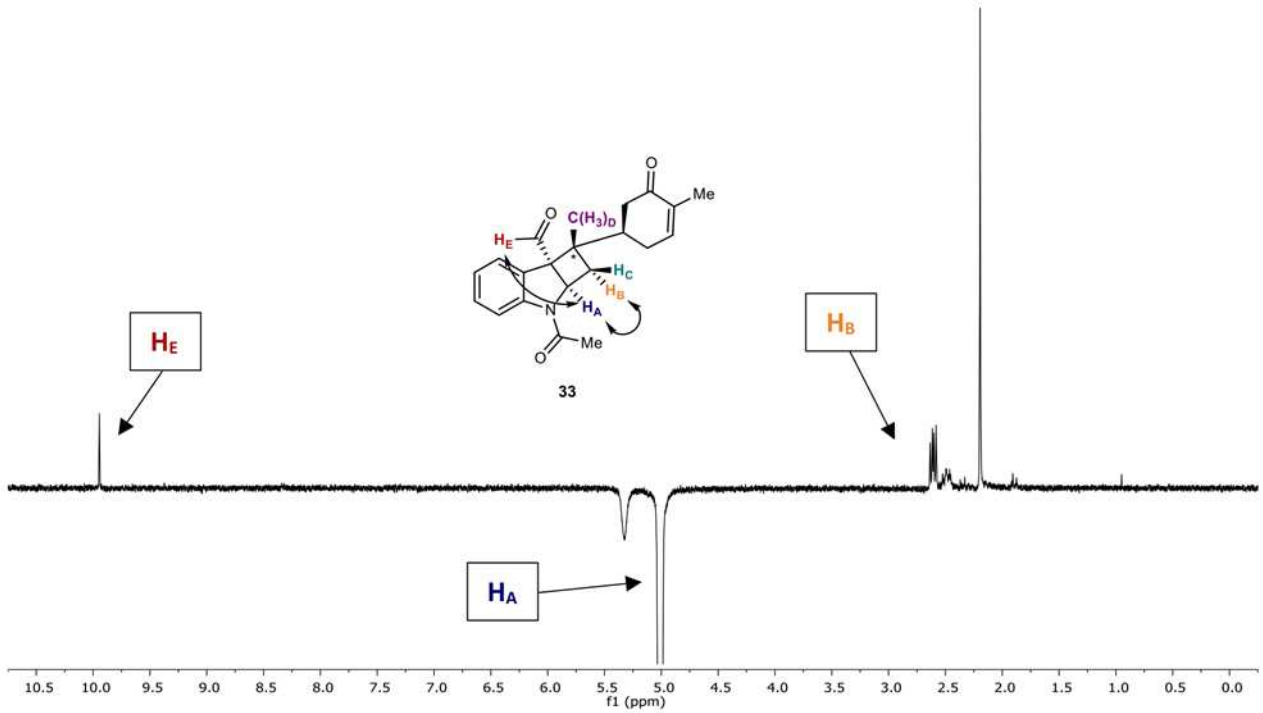

Figure 45. NOE spectrum (400 MHz in $CDCl_3$) on saturation of H_A.

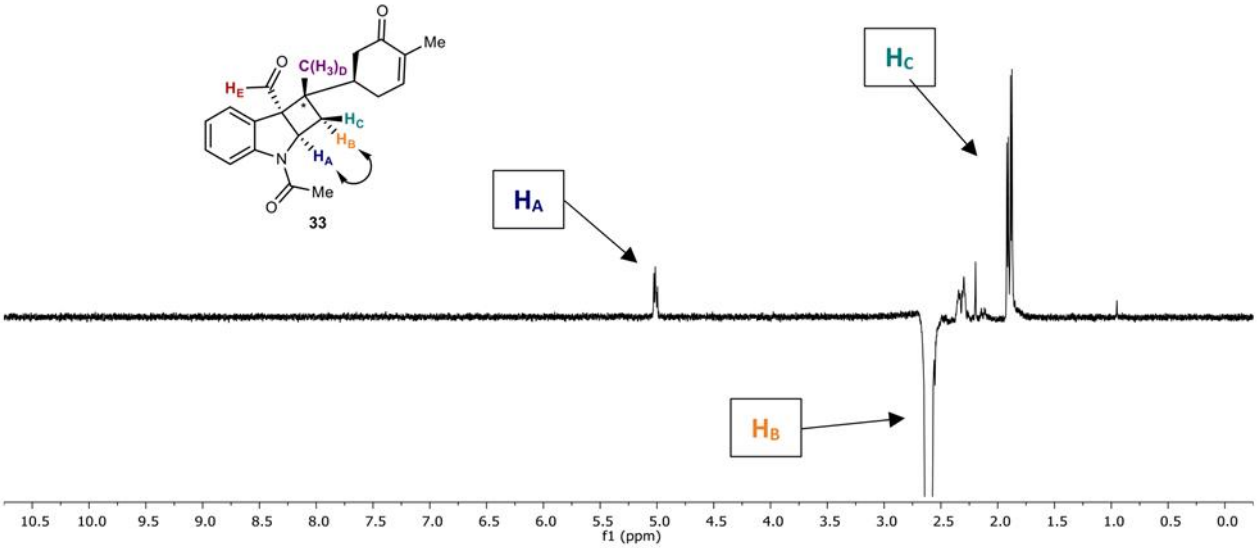

Figure 46. NOE spectrum (400 MHz in $CDCl_3$) on saturation of H_B.

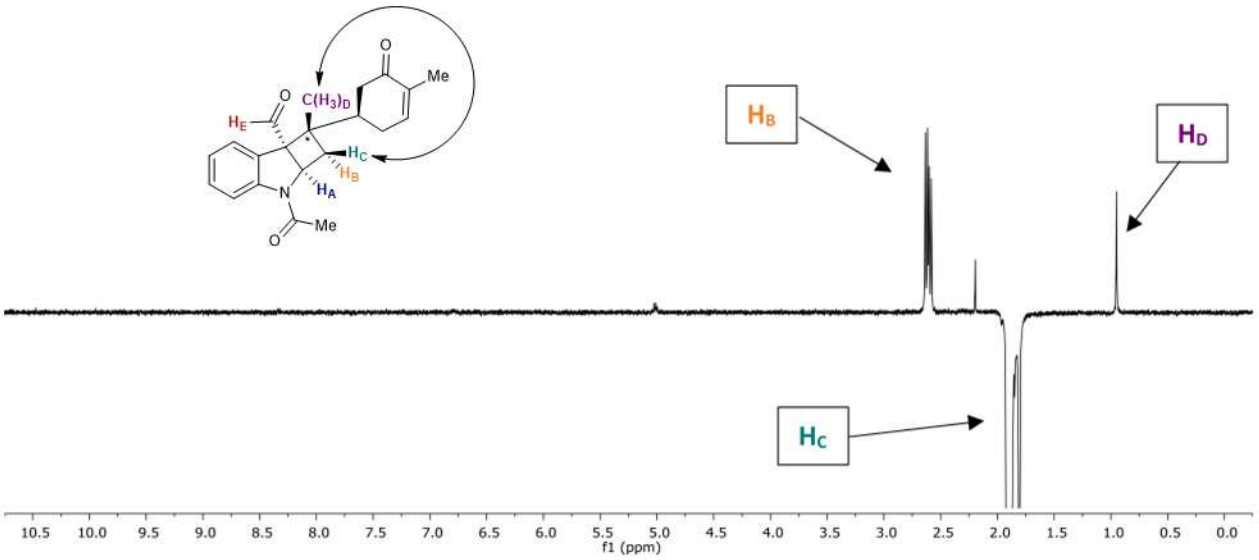

Figure 47. NOE spectrum (400 MHz in $CDCl_3$) on saturation of H_C.

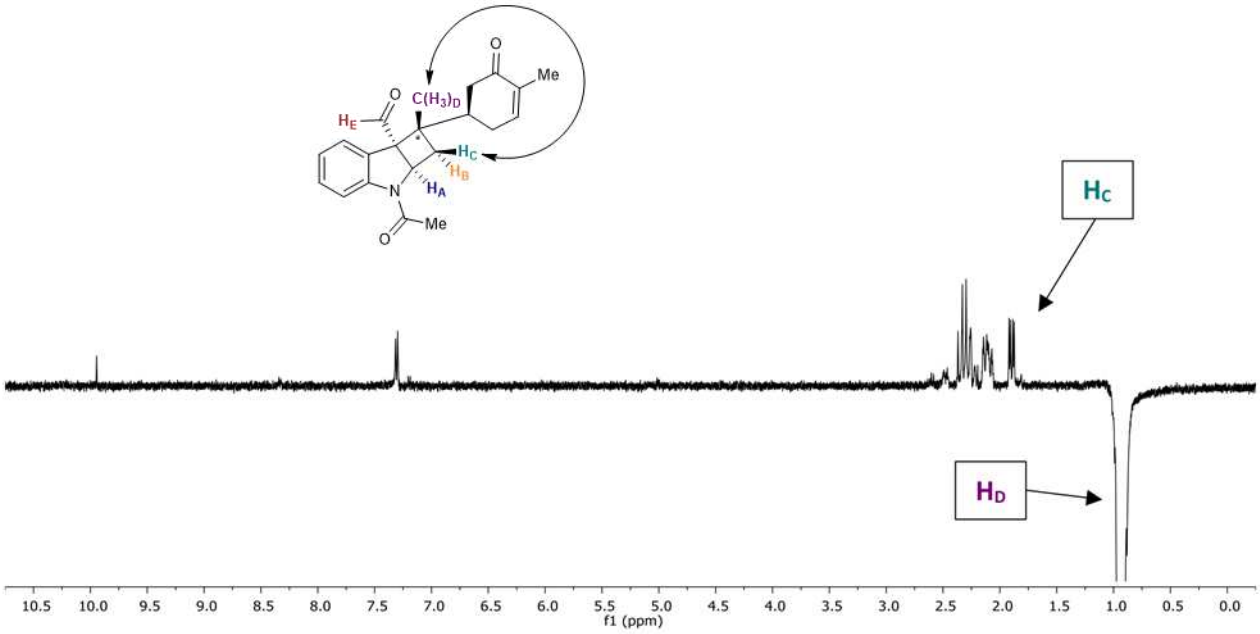

Figure 48. NOE spectrum (400 MHz in $CDCl_3$) on saturation of H_D.

2.6. References

(1) Ahrendt, K. A.; Borths, C. J.; Macmillan, D. W. C.; January, R. V. New Strategies for Organic Catalysis: The First Highly Enantioselective Organocatalytic Diels-Alder Reaction. **2000**, *122* (17), 4243–4244. https://doi.org/10.1021/ja000092s.

(2) List, B.; Lerner, R. A.; Iii, C. F. B.; Torrey, N.; Road, P.; Jolla, L.; December, R. V. Proline-Catalyzed Direct Asymmetric Aldol Reactions. **2000**, *122* (10), 2395–2396. https://doi.org/10.1021/ja994280y.

(3) List, B.; Yang, J. W. The Organic Approach to Asymmetric Catalysis. *Science* **2006**, *313* (5793), 1584–1586. https://doi.org/10.1126/science.1131945.

(4) Melchiorre, P.; Marigo, M.; Carlone, A.; Bartoli, G. Asymmetric Aminocatalysis - Gold Rush in Organic Chemistry. *Angew. Chem. Int. Ed.* **2008**, *47* (33), 6138–6171. https://doi.org/10.1002/anie.200705523.

(5) Xiang, S. H.; Tan, B. Advances in Asymmetric Organocatalysis over the Last 10 Years. *Nat. Commun.* **2020**, *11* (1). https://doi.org/10.1038/s41467-020-17580-z.

(6) Macmillan, D. W. C. The Advent and Development of Organocatalysis. **2008**, *455* (September). https://doi.org/10.1038/nature07367.

(7) Silvi, M.; Melchiorre, P. Enhancing the Potential of Enantioselective Organocatalysis with Light. *Nature* **2018**, *554* (7690), 41–49. https://doi.org/10.1038/nature25175.

(8) Mukherjee, S.; Yang, J. W.; Hoffmann, S.; List, B. Asymmetric Enamine Catalysis. *Chem. Rev.* **2007**, *107* (12), 5471–5569. https://doi.org/10.1021/cr0684016.

(9) Lelais, G.; MacMillan, D. W. C. Modern Strategies in Organic Catalysis: The Advent and Development of Iminium Activation. *Aldrichimica Acta* **2006**, *39* (3), 79–87.

(10) Teresa D. Beeson, Anthony Mastracchio, J.-B. H.; Kate Ashton, D. W. C. M. Enantioselective Organocatalysis Using SOMO Activation. *Science* **2007**, *316* (5824), 582–585. https://doi.org/10.1126/science.1142696.

(11) Jung, M. E.; Vaccaro, W. D.; Buszek, K. R. Asymmetric Diels-Alder Reactions of Chiral Alkoxy Iminium Salts. *Tetrahedron Lett.* **1989**, *30* (15), 1893–1896. https://doi.org/10.1016/S0040-4039(00)99606-0.

(12) Jen, W. S.; Wiener, J. J. M.; MacMillan, D. W. C. New Strategies for Organic Catalysis: The First Enantioselective Organocatalytic 1,3-Dipolar Cycloaddition [20]. *J. Am. Chem. Soc.* **2000**, *122* (40), 9874–9875. https://doi.org/10.1021/ja005517p.

(13) Para, N. A.; MacMillan, D. W. C. New Strategies in Organic Catalysis: The First Enantioselective Organocatalytic Friedel-Crafts Alkylation [18]. *J. Am. Chem. Soc.* **2001**, *123* (18), 4370–4371. https://doi.org/10.1021/ja015717g.

(14) Mariano, P. S. Electron-Transfer Mechanisms in Photochemical Transformations of Iminium Salts. *Acc. Chem. Res.* **1983**, *16* (4), 130–137. https://doi.org/10.1021/ar00088a003.

(15) Xiaolu, C.; Virginia, C.; Chuanfeng, C.; Kim Hyun Jin; Mariano Patrick S. A Potentially General Method to Control Relative Stereochemistry in Enone-Olefin 2+2-Photocycloaddition Reactions by Using Eniminium Salt Surrogates. *Tetrahedron Lett.* **2000**, *41* (49), 9445–9449. https://doi.org/10.1016/S0040-4039(00)01581-1.

(16) Murphy, J. J.; Bastida, D.; Paria, S.; Fagnoni, M.; Melchiorre, P. Asymmetric Catalytic Formation of Quaternary Carbons by Iminium Ion Trapping of Radicals. *Nature* **2016**, *532* (7598), 218–222. https://doi.org/10.1038/nature17438.

(17) Silvi, M.; Verrier, C.; Rey, Y. P.; Buzzetti, L.; Melchiorre, P. Visible-Light Excitation of Iminium Ions Enables the Enantioselective Catalytic β-Alkylation of Enals. *Nat. Chem.* **2017**, *9* (9), 868–873. https://doi.org/10.1038/nchem.2748.

(18) Rigotti, T.; Mas-Ballesté, R.; Alemán, J. Enantioselective Aminocatalytic [2 + 2] Cycloaddition through Visible Light Excitation. *ACS Catal.* **2020**, *10* (9), 5335–5346. https://doi.org/10.1021/acscatal.0c01413.

(19) Hörmann, F. M.; Chung, T. S.; Rodriguez, E.; Jakob, M.; Bach, T. Evidence for Triplet Sensitization in the Visible-Light-Induced [2+2] Photocycloaddition of Eniminium Ions. *Angew. Chem. Int. Ed.* **2018**, *57* (3), 827–831. https://doi.org/10.1002/anie.201710441.

(20) El-Sayed, M. A. The Triplet State: Its Radiative and Nonradiative Properties. *Acc. Chem. Res.* **1968**, *1* (1), 8–16. https://doi.org/10.1021/ar50001a002.

(21) Hörmann, F. M.; Kerzig, C.; Chung, T. S.; Bauer, A.; Wenger, O. S.; Bach, T. Triplet Energy Transfer from Ruthenium Complexes to Chiral Eniminium Ions: Enantioselective Synthesis of Cyclobutanecarbaldehydes by [2+2] Photocycloaddition. *Angew. Chem. Int. Ed.* **2020**, *132* (24), 9746–9755. https://doi.org/10.1002/ange.202001634.

(22) Cheng, Y. Z.; Feng, Z.; Zhang, X.; You, S. L. Visible-Light Induced Dearomatization Reactions. *Chem. Soc. Rev.* **2022**, *51* (6), 2145–2170. https://doi.org/10.1039/c9cs00311h.

(23) Zhu, M.; Zhang, X.; Zheng, C.; You, S. L. Energy-Transfer-Enabled Dearomative Cycloaddition Reactions of Indoles/Pyrroles via Excited-State Aromatics. *Acc. Chem. Res.* **2022**, *55* (17), 2510–2525. https://doi.org/10.1021/acs.accounts.2c00412.

(24) Ji, P.; Duan, K.; Li, M.; Wang, Z.; Meng, X.; Zhang, Y.; Wang, W. Photochemical Dearomative Skeletal Modifications of Heteroaromatics. *Chem. Soc. Rev.* **2024**, *53* (12), 6600–6624. https://doi.org/10.1039/d4cs00137k.

(25) Roche, S. P.; Porco, J. A. Dearomatization Strategies in the Synthesis of Complex Natural Products. *Angew. Chem. Int. Ed.* **2011**, *50* (18), 4068–4093. https://doi.org/10.1002/anie.201006017.

(26) Zheng, C.; You, S. L. Catalytic Asymmetric Dearomatization (CADA) Reaction-Enabled Total Synthesis of Indole-Based Natural Products. *Nat. Prod. Rep.* **2019**, *36* (11), 1589–1605. https://doi.org/10.1039/c8np00098k.

(27) Zhu, M.; Zheng, C.; Zhang, X.; You, S. L. Synthesis of Cyclobutane-Fused Angular Tetracyclic Spiroindolines via Visible-Light-Promoted Intramolecular Dearomatization of Indole Derivatives. *J. Am. Chem. Soc.* **2019**, *141* (6), 2636–2644. https://doi.org/10.1021/jacs.8b12965.

(28) Zhang, Z.; Yi, D.; Zhang, M.; Wei, J.; Lu, J.; Yang, L.; Wang, J.; Hao, N.; Pan, X.; Zhang, S.; Wei, S.; Fu, Q. Photocatalytic Intramolecular [2 + 2] Cycloaddition of Indole Derivatives via Energy Transfer: A Method for Late-Stage Skeletal Transformation. *ACS Catal.* **2020**, *10* (17), 10149–10156. https://doi.org/10.1021/acscatal.0c01841.

(29) Oderinde, M. S.; Mao, E.; Ramirez, A.; Pawluczyk, J.; Jorge, C.; Cornelius, L. A. M.; Kempson, J.; Vetrichelvan, M.; Pitchai, M.; Gupta, A.; Gupta, A. K.; Meanwell, N. A.; Mathur, A.; Dhar, T. G. M. Synthesis of Cyclobutane-Fused Tetracyclic Scaffolds via Visible-Light Photocatalysis for Building Molecular Complexity. *J. Am. Chem. Soc.* **2020**, *142* (6), 3094–3103. https://doi.org/10.1021/jacs.9b12129.

(30) Julian, D. R.; Foster, R. Photoaddition of Olefins to Indoles: Synthesis of Tetrahydro-1H-Cyclobut[b] Indoles. *J. Chem. Soc. Chem. Commun.* **1973**, No. 9, 311–312. https://doi.org/10.1039/C39730000311.

(31) Inanaga, K.; Takasu, K.; Ihara, M. Rapid Assembly of Polycyclic Substances by a Multicomponent Cascade (4 + 2)-(2 + 2) Cycloadditions: Total Synthesis of the Proposed Structure of Paesslerin A. *J. Am. Chem. Soc.* **2004**, *126* (5), 1352–1353. https://doi.org/10.1021/ja039808k.

(32) Chung, H. M.; Chen, Y. H.; Lin, M. R.; Su, J. H.; Wang, W. H.; Sung, P. J. Rumphellaone A, a Novel Caryophyllane-Related Derivative from the Gorgonian Coral Rumphella Antipathies. *Tetrahedron Lett.* **2010**, *51* (46), 6025–6027. https://doi.org/10.1016/j.tetlet.2010.09.032.

(33) Shen, J.; Chowdhury, S.; Agarwal, N.; Karsh, L. I.; Oudard, S.; Gartrell, B. A.; Feyerabend, S.; Saad, F.; Pieczonka, C. M.; Chi, K. N.; Brookman-May, S. D.; Rooney, B.; Bhaumik, A.; McCarthy, S. A.; Bevans, K. B.; Mundle, S. D.; Small, E. J.; Smith, M. R.; Graff, J. N. Apalutamide Efficacy, Safety and Wellbeing in Older Patients with Advanced Prostate Cancer from Phase 3 Randomised Clinical Studies TITAN and SPARTAN. *Br. J. Cancer* **2024**, *130* (1), 73–81. https://doi.org/10.1038/s41416-023-02492-8.

(34) Yue, H.; Huang, H.; Bian, G.; Zong, H.; Li, F.; Song, L. Enantioselectivity Switch Controlled by N,N′-Di- or N,N,N′,N′-Tetra-Substituted Chiral Thiophosphorodiamide Ligands, Structural Relatives of Thioureas, in Catalytic Additions of Diethylzinc to Aldehydes. *Tetrahedron Asymmetry* **2014**, *25* (2), 170–180. https://doi.org/10.1016/j.tetasy.2013.12.014.

(35) Speckmeier, E.; Fischer, T. G.; Zeitler, K. A Toolbox Approach to Construct Broadly Applicable Metal-Free Catalysts for Photoredox Chemistry: Deliberate Tuning of Redox Potentials and Importance of Halogens in Donor-Acceptor Cyanoarenes. *J. Am. Chem. Soc.* **2018**, *140* (45), 15353–15365. https://doi.org/10.1021/jacs.8b08933.

(36) Bauernschmitt, R.; Ahlrichs, R. Treatment of Electronic Excitations within the Adiabatic Approximation of Time Dependent Density Functional Theory. *Chem. Phys. Lett.* **1996**, *256* (4–5), 454–464. https://doi.org/10.1016/0009-2614(96)00440-X.

(37) Scalmani, G.; Frisch, M. J.; Mennucci, B.; Tomasi, J.; Cammi, R.; Barone, V. Geometries and Properties of Excited States in the Gas Phase and in Solution: Theory and Application of a Time-Dependent Density Functional Theory Polarizable Continuum Model. *J. Chem. Phys.* **2006**, *124* (9). https://doi.org/10.1063/1.2173258.

(38) Chai, J. Da; Head-Gordon, M. Long-Range Corrected Hybrid Density Functionals with Damped Atom-Atom Dispersion Corrections. *Phys. Chem. Chem. Phys.* **2008**, *10* (44), 6615–6620. https://doi.org/10.1039/b810189b.

(39) Álvarez-Moreno, M.; De Graaf, C.; López, N.; Maseras, F.; Poblet, J. M.; Bo, C. Managing the Computational Chemistry Big Data Problem: The IoChem-BD Platform. *J. Chem. Inf. Model.* **2015**, *55* (1), 95–103. https://doi.org/10.1021/ci500593j.

(40) Cossi, M.; Rega, N.; Scalmani, G.; Barone, V. Energies, Structures, and Electronic Properties of Molecules in Solution with the C-PCM Solvation Model. *J. Comput. Chem.* **2003**, *24* (6), 669–681. https://doi.org/10.1002/jcc.10189.

(41) Fukui, K. The Path of Chemical Reactions — The IRC Approach. *Acc. Chem. Res.* **1968**, *46* (4), 5. https://doi.org/10.1021/cen-v046n004.p005.

(42) Harvey, J. N.; Aschi, M.; Schwarz, H.; Koch, W. The Singlet and Triplet States of Phenyl Cation. A Hybrid Approach for Locating Minimum Energy Crossing Points between Non-Interacting Potential Energy Surfaces. *Theor. Chem. Acc.* **1998**, *99* (2), 95–99. https://doi.org/10.1007/s002140050309.

(43) Chen, W.; Xia, Y.; Lin, L.; Yuan, X.; Guo, S.; Liu, X.; Feng, X. Asymmetric Synthesis of Furo[3,4-b]Indoles by Catalytic [3+2] Cycloaddition of Indoles with Epoxides. *Chem. - A Eur. J.* **2015**, *21* (43), 15104–15107. https://doi.org/10.1002/chem.201502448.

(44) Umehara, A.; Ueda, H.; Tokuyama, H. Condensation of Carboxylic Acids with Non-Nucleophilic N-Heterocycles and Anilides Using Boc2O. *J. Org. Chem.* **2016**, *81* (22), 11444–11453. https://doi.org/10.1021/acs.joc.6b02097.

(45) Palomo, E.; Sharma, A. K.; Wang, Z.; Jiang, L.; Maseras, F.; Suero, M. G. Generating Fischer-Type Rh-Carbenes with Rh-Carbynoids. *J. Am. Chem. Soc.* **2023**, *145* (9), 4975–4981. https://doi.org/10.1021/jacs.3c00012.

(46) Brimioulle, R.; Bauer, A.; Bach, T. Enantioselective Lewis Acid Catalysis in Intramolecular [2 + 2] Photocycloaddition Reactions: A Mechanistic Comparison between Representative Coumarin and Enone Substrates. *J. Am. Chem. Soc.* **2015**, *137* (15), 5170–5176. https://doi.org/10.1021/jacs.5b01740.

(47) Onodera, K.; Takashima, R.; Suzuki, Y. Selective Synthesis of Acylated Cross-Benzoins from Acylals and Aldehydes via N-Heterocyclic Carbene Catalysis. *Org. Lett.* **2021**, *23* (11), 4197–4202. https://doi.org/10.1021/acs.orglett.1c01134.

(48) Aizawa, N.; Harabuchi, Y.; Maeda, S.; Pu, Y. J. Kinetic Prediction of Reverse Intersystem Crossing in Organic Donor–Acceptor Molecules. *Nat. Commun.* **2020**, *11* (1), 1–6. https://doi.org/10.1038/s41467-020-17777-2.

(49) Martin, R. L. Natural Transition Orbitals. *J. Chem. Phys.* **2003**, *118* (11), 4775–4777. https://doi.org/10.1063/1.1558471.

Chapter III

Radical strain-release photocatalysis for the synthesis of azetidines

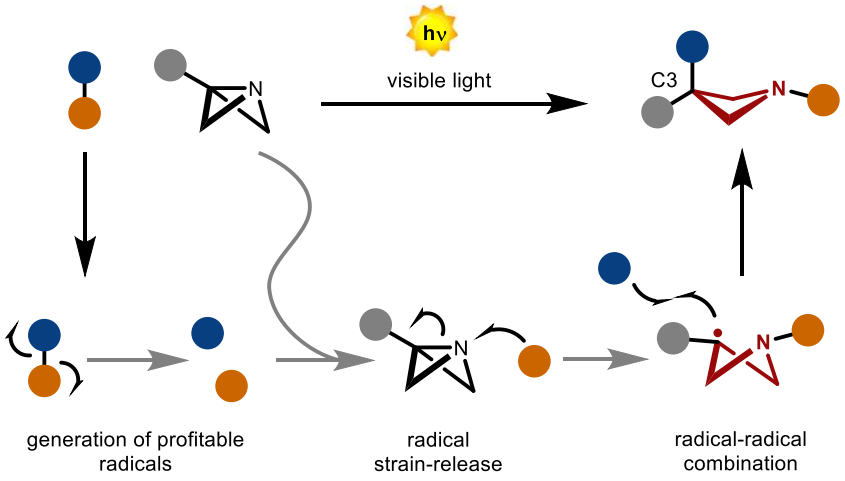

Contributions to the project:

This project was carried out in collaboration with Dr. Ricardo I. Rodríguez, Dr. Vasco Corti, and PhD student Stefano Visentini. My personal contribution involved the preparation of most of the starting materials, the isolation of the majority of scope entries, and the development of the three-component reaction. The project also benefited from collaborations with different Italian universities: Professor Mirco Natali (University of Ferrara) conducted all spectroscopic investigations, and Professor Giorgio Pelosi (University of Parma) was responsible for X-ray crystallographic analyses. At the University of Padua, Professor Marco Bortolus carried out EPR analyses, while Dr. Paolo Costa performed the computational calculations.

Rodríguez, R.I., Corti, V., Rizzo, L., Visentini S., Bortolus M., Amati A., Natali M., Pelosi G., Costa P. & Dell'Amico L.

Radical strain-release photocatalysis for the synthesis of azetidines. *Nat Catal* **7**, 1223–1231 (2024). https://doi.org/10.1038/s41929-024-01206-4

Figures, schemes, tables and references in this Chapter are numbered independently.

3.1. Introduction

3.1.1. The Principle of Bioisosteric Replacement in Drug Design

The concept of bioisosterism represents one of the most fundamental strategies in medicinal chemistry, providing a rational approach to molecular modification with the aim of improving pharmacological and physicochemical properties of drug candidates. The origins of this idea can be traced back to the early twentieth century, when Langmuir first introduced the notion of "isosteres" to describe atoms or groups of atoms with similar electronic configurations.[1] Subsequent refinements by Grimm, Erlenmeyer, and later Friedman and Burger extended this purely structural principle into the biological context, leading to the definition of "bioisosteres" as substituents or groups that, while not necessarily identical in size or composition, can elicit broadly similar biological activity when introduced into a lead compound.[2] This evolution from a purely chemical to a biologically oriented definition highlights the intrinsic flexibility of the concept, which today encompasses both simple, classical replacements and more sophisticated, non-classical modifications that address complex pharmacological demands.[3]

Classical bioisosteres are generally classified into monovalent, divalent, trivalent, and ring equivalents.[2] Typical examples include the replacement of hydrogen with fluorine,[4] hydroxyl with amino groups,[5] or benzene with pyridine.[6] These modifications exploit similarities in valency and electronic distribution, enabling relatively predictable changes in molecular recognition and binding. Non-classical bioisosteres, by contrast, are defined less by strict electronic equivalence and more by functional mimicry, often arising from empirical observations. Examples include heteroaromatic replacements for phenyl rings, tetrazoles as surrogates for carboxylic acids, or sulfonamides as bioisosteres of hydroxyl groups. Over time, such modifications have become indispensable tools in the medicinal chemist's arsenal, guiding the design of more effective, selective, and safer drugs.[2,5,6]

While the early applications of bioisosterism were primarily directed toward improving binding affinity and potency, it soon became evident that this principle could also be harnessed to address liabilities associated with drug metabolism. Many functional groups, although beneficial for activity, are prone to undesirable biotransformations leading to reactive or toxic metabolites. The strategic replacement of such groups with bioisosteres provides a powerful approach to mitigate these risks, thereby improving the overall safety profile of drug candidates. For instance, the substitution of metabolically unstable carboxylic acids with tetrazoles can prevent the formation of reactive acyl glucuronides, while heteroaromatic surrogates for phenolic groups can reduce susceptibility to rapid conjugation. In this way, bioisosteric replacement extends beyond receptor recognition to encompass metabolism-related liabilities.[7]

A further conceptual expansion of bioisosterism has been introduced with the recognition of the importance of molecular geometry and saturation in drug design. Lovering and co-workers, in their seminal analysis "Escape from Flatland", demonstrated that compounds with a higher fraction of sp^3-hybridized carbons (Fsp^3) and greater stereochemical complexity are more likely to progress successfully through clinical development.[8] This correlation was further refined in a subsequent study, which showed that increased saturation reduces promiscuity and improves selectivity by minimizing excessive planarity and aromatic character.[9] The strategic replacement of flat aromatic systems with more saturated, three-dimensional scaffolds therefore represents a modern form of bioisosterism, in which local substitutions are accompanied by global topological modifications to improve solubility, selectivity, and pharmacokinetic behavior (Figure 1).

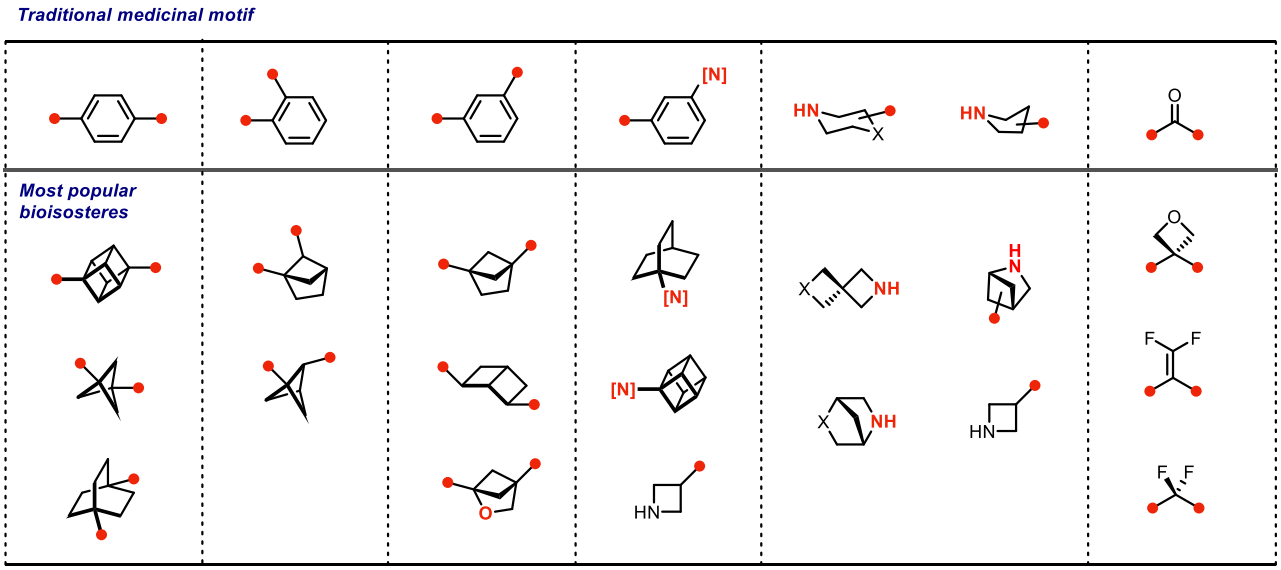

Figure 1. Representative examples of traditional medicinal motifs (top) and their most common bioisosteric replacements (bottom).

In recent years, the strategic incorporation of fluorine atoms and fluorinated motifs as bioisosteres has gained great attention. Owing to its small size and high electronegativity, fluorine can mimic hydrogen while profoundly altering properties such as acidity, lipophilicity, and metabolic stability.[4] The substitution of a C–H bond with C–F, or the introduction of trifluoromethyl and difluoromethyl groups, represents a versatile means of modulating drug-like properties while maintaining overall steric compatibility.[10] Beyond simple atom-for-atom replacements, fluorine can also act as a higher-order bioisostere, influencing conformational preferences and mimicking more complex functional groups such as carbonyls or nitriles. Although fluorine-based bioisosteres have become some of the most frequently employed modifications in contemporary medicinal chemistry, their discussion here will remain brief, as the subsequent focus will shift toward saturated nitrogen heterocycles as emerging bioisosteric motifs.

In recent years, the replacement of planar aromatic rings with three-dimensional, saturated scaffolds has become a central theme in medicinal chemistry. Data-driven analyses such as the BioSTAR workflow have demonstrated that benzene bioisosteres—including bicyclo[2.1.1]hexane, bicyclo[1.1.1]pentane, cubane, and related scaffolds—can improve solubility, metabolic stability, and overall developability while maintaining bioactivity.[11] This strategy directly responds to the long-recognized limitations of flat, sp^2-rich scaffolds, and aligns with the "Escape from Flatland" paradigm, where increasing Fsp^3 and stereochemical richness correlates with reduced promiscuity and improved pharmacokinetic properties. Alongside these carbocyclic alternatives, small aliphatic rings such as oxetanes, and azetidines have also been increasingly employed as bioisosteres, offering compact, rigid structureswith well-defined exit vectors.[8,12] These scaffolds not only increase three-dimensionality but can also modulate lipophilicity (LogD) and pKa, contributing to enhanced solubility and reduced metabolic liabilities compared to their aromatic counterparts.

Within this landscape, azetidines stand out as particularly attractive motifs. Their small ring size, intrinsic strain, and three-dimensional geometry allow them to act as bioisosteres for a range of commonly used nitrogen heterocycles such as pyrrolidines, piperidines, and even pyridines (Figure 1). Although their incorporation in marketed drugs remains limited, growing synthetic accessibility and the expanding interest in saturated, sp^3-rich scaffolds have highlighted their potential as privileged building blocks in drug discovery.[13,14] A more detailed discussion of azetidines, including their physicochemical advantages and emerging synthetic strategies, will be presented in the following sections.

3.1.2. The Role of Azetidines in Modern Bioisosterism

Four-membered nitrogen heterocycles hold a distinctive position in medicinal chemistry. Azetidines combine compact size, pronounced ring strain, and a high degree of saturation into a scaffold that is simultaneously polar, rigid, and three-dimensional, with exit vectors arranged to sample conformational space more efficiently than larger, flatter congeners. In comparative analyses of small rings, azetidines exhibit median puckering angles comparable to those of cyclobutane but maintain basic pKa values (≈ 11.3 at 25 °C in water) close to those of pyrrolidine and piperidine, while being markedly more strained (≈ 25 kcal mol^{-1} vs ~0 kcal mol^{-1} for piperidine). These features tend to orient molecules toward higher Fsp^3, reduced planarity, and tighter shape complementarity at binding sites, with frequent downstream benefits for solubility, lipophilicity, metabolic stability and pharmacokinetics.[15,16,17] Representative examples of pharmaceuticals and natural products incorporating the azetidine ring are shown in Scheme 1, highlighting its presence in both clinically approved drugs and bioactive natural scaffolds.

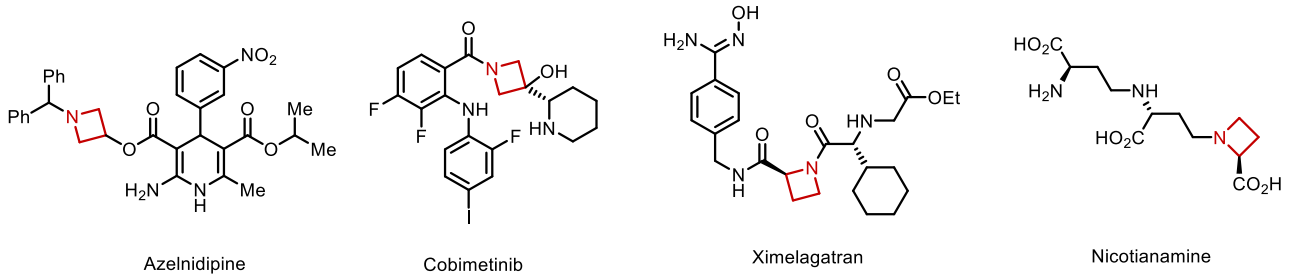

Scheme 1. Pharmaceuticals and natural products with azetidine ring.

From a design perspective, azetidines are attractive bioisosteres of common N-heterocycles. Replacement of piperidine or pyrrolidine by an azetidine core can decrease lipophilicity and adjust basicity without sacrificing the vector geometry needed for key H-bond or ionic contacts; in matched molecular pairs, medicinal campaigns have leveraged 1,3-disubstituted azetidines as viable surrogates of 1,4-disubstituted piperidines, often reducing promiscuity and improving developability.[18] Stretched azetidines, such as 3-((hetero)cyclobutyl)azetidines, have been designed to mimic the shape of piperidine, piperazine, and morpholine. Crystallographic analyses show that these analogues preserve the spatial orientation of substituents, while offering slightly larger radii and adjustable flexibility, thereby widening the possibilities for lead optimization.[19]

The relevance of azetidines in drug discovery is well exemplified by selected case studies in which this small heterocycle proved to be more than a cosmetic replacement, but rather a decisive element for potency and selectivity. In the development of MEK inhibitors that led to XL518 (cobimetinib), the introduction of an azetidin-3-ol motif provided a rigid and compact core that improved target interactions and enhanced biochemical activity. Compared to the more flexible morpholine analogue (**2**, PD-0325901) or the methylene-extended variant (**3**), the azetidine ring enforces a geometry that positions both the hydroxyl and the secondary amine in an orientation ideally suited to engage Asp190 and Asn195 within the MEK1 catalytic loop (Figure 2).[20] This conformational constraint translates into higher biochemical potency and improved cellular activity, highlighting how the azetidine fragment can function as a privileged linker rather than a simple isosteric substitution.

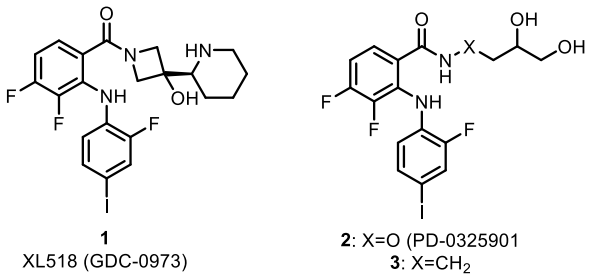

*Figure 2. MEK inhibitors: comparison of cobimetinib (**1**) with morpholine (**2**) and methylene (**3**) analogues, highlighting the advantage of the azetidine scaffold.*

A different example comes from the field of antimalarial agents. A bicyclic azetidine scaffold was identified as a potent inhibitor of phenylalanyl-tRNA synthetase in *Plasmodium*, showing activity across multiple stages of the parasite life cycle. The lead compound, BRD3914, displayed nanomolar efficacy and curative in vivo profiles, supported by a streamlined synthetic route that exploited direct C–H arylation of the azetidine ring. This case illustrates how the rigid geometry and well-defined exit vectors of azetidines can enable productive interactions in confined binding pockets (Figure 3).[13]

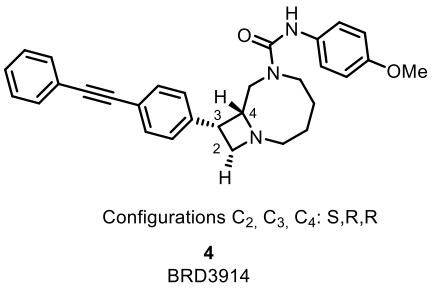

*Figure 3. Structure of BRD391(**4**), a bicyclic azetidine antimalarial acting as a potent inhibitor of phenylalanyl-tRNA synthetase.*

Other studies have explored azetidines as surrogates for piperidines, piperazines, and morpholines. In the case of an MCHr1 antagonist, the introduction of the four-membered ring (Figure 4) lowered lipophilicity and improved metabolic stability, while retaining the necessary basicity to maintain the ionic interaction with the target.[21] This substitution also increased the overall three-dimensionality of the scaffold, in line with the "Escape from Flatland" design principles.

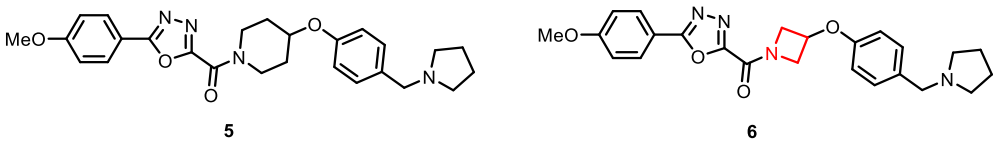

*Figure 4. Example of piperidine (**5**) to azetidine (**6**) replacement in an MCHr1 antagonist, showing improved lipophilicity and metabolic stability.*

Despite these promising applications, the clinical adoption of azetidines remains limited. Recent analyses indicate that only about nine approved drugs contain an azetidine ring, in stark contrast to the dominance of piperidines and pyridines in approved drugs.[18,22] This discrepancy is largely attributed to the historical synthetic challenges associated with azetidines, which restricted systematic exploration in medicinal chemistry. The next section will therefore focus on the classical methods available for the synthesis of azetidines, highlighting how advances in strain-release strategies are now helping to overcome these limitations.[14]

3.1.3. Approaches to the synthesis of azetidines: opportunities and limitations

The discrepancy between the recognized potential of azetidines as valuable bioisosteres and their limited occurrence in approved drugs is largely attributable to the challenges associated with their synthesis and commercialization. Over the decades, several strategies have been devised to construct strained four-membered nitrogen heterocycles, ranging from classical disconnections rooted in lactam chemistry to modern photochemical and strain-release approaches. While these methods have significantly expanded the available toolbox, each of them suffers from intrinsic limitations in scope, selectivity, or practicality, which have historically discouraged systematic exploration in medicinal chemistry. This section provides an overview of the principal synthetic avenues to azetidines, highlighting representative examples that illustrate both the progress made and the unresolved challenges. Early methods to access azetidines typically relied on β-lactams (2-azetidinones) as precursors. A wealth of strategies has been developed to build β-lactams, most prominently the Staudinger[23] [2+2] ketene–imine cycloaddition and the Kinugasa reaction[24] (nitrone–alkyne cycloaddition). Among these, the Kinugasa cycloaddition is particularly illustrative, as it proceeds under copper catalysis between nitrones and terminal alkynes to afford β-lactams in good yields and with considerable functional-group tolerance (Scheme 2).[25]

Once formed, β-lactams can be chemoselectively reduced to the parent azetidines. For example, Mykhailiuk demonstrated the AlH_3-mediated reduction of β-lactams obtained by thermal [2+2] cycloaddition, furnishing 2-substituted azetidines in useful yields (Scheme 2).[26]

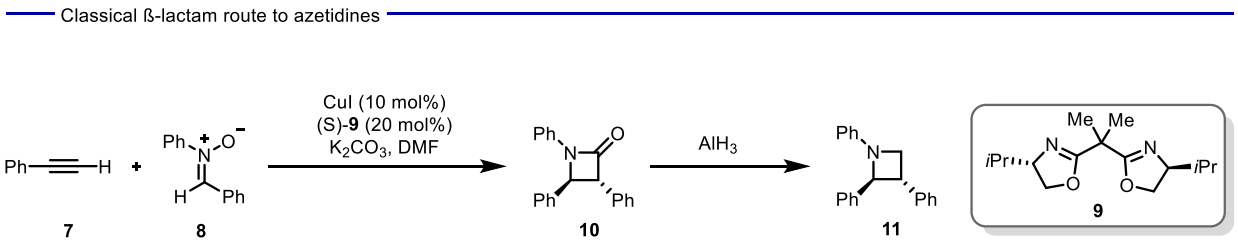

Scheme 2. Kinugasa cycloaddition affording β-lactams, followed by reductive transformation to azetidines.

This simple two-step sequence—formation of a β-lactam followed by carbonyl reduction—epitomizes the classical logic of azetidine synthesis. However, its generality is limited: the need for tailored ketenes or nitrones, the poor tolerance of reactive functionalities, and the frequent lack of stereocontrol significantly restrict its application. Moreover, reductive conditions often lead to competing ring-opening or over-reduction, further diminishing the utility of this pathway.

Alternative classical routes include intramolecular S_N2 displacements and related ring closures. In this context, Du Bois and co-workers reported an elegant sequence combining Rh-catalyzed C–H amination with intramolecular cyclization, which provided direct access to azetidines from simple alkyl precursors (Scheme 3a).[27] Complementarily, Mucsi and co-workers achieved the regio- and diastereoselective cyclization of oxiranylmethyl benzylamines (**15**), where deprotonation under strongly basic conditions triggers intramolecular nucleophilic attack to yield 2-aryl-3-hydroxymethyl azetidines (**17**) with predictable stereochemical outcome (Scheme 3b).[28]

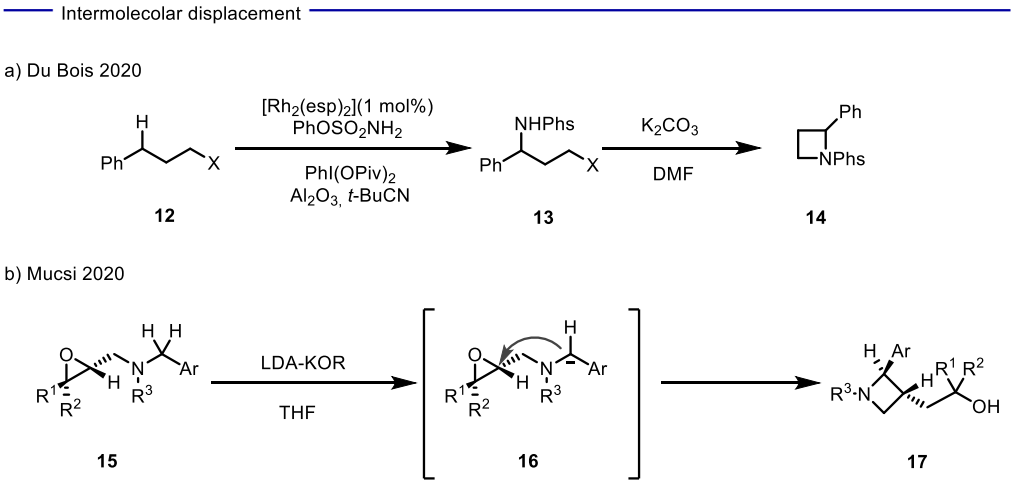

*Scheme 3. Intramolecular displacement strategies for azetidine synthesis:(a) Rh-catalyzed C–H amination/cyclization;(b) base-induced epoxide opening to 2-aryl-3-hydroxymethyl azetidines **17**.*

While both approaches underscore the synthetic versatility of intramolecular displacement strategies, they share common drawbacks, including the need for activated precursors, strong bases, or carefully optimized conditions, which limit their broader applicability.

Building on these limitations, researchers have increasingly turned to photochemical methodologies to access azetidines in a more direct and versatile manner. Among these, the [2+2] photocycloaddition of alkenes and imines—commonly termed the aza-Paternò–Büchi (aza-PB) reaction—offers a conceptually straightforward entry to azetidines. Historically, however, its potential remained largely untapped due to the intrinsic photophysical limitations of imines and the poor regio- and stereo-control of the process. Direct excitation of imines often leads to rapid deactivation or side reactions, while triplet energy transfer to aryl imines typically produces complex mixtures or simple isomerization. As a result, classical examples of aza-PB suffered from low selectivity and limited scope.[29]

A major breakthrough was achieved by Schindler and co-workers, who demonstrated that 2-isoxazoline-3-carboxylates can effectively participate in triplet energy transfer (EnT) from visible-light photocatalysts. Upon sensitization, these imine surrogates undergo [2+2] cycloaddition with alkenes to yield protected azetidines under mild conditions (Scheme 4). The use of 2-isoxazolines was rationally designed, since free imines were shown to be unsuitable for triplet sensitization, typically undergoing only E–Z isomerization under EnT conditions.[30] Embedding the imine within the five-membered isoxazoline scaffold lowers the triplet energy into the range accessible by common photocatalysts and stabilizes the substrate sufficiently to engage in productive cycloaddition.[31]

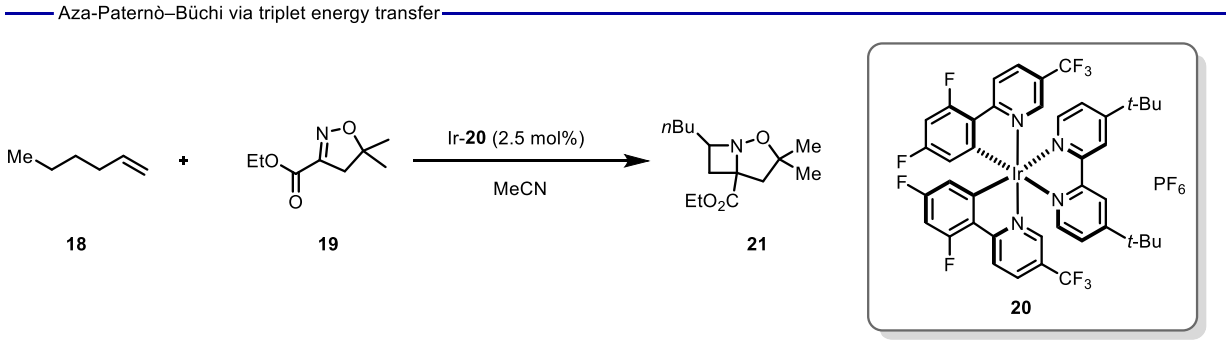

*Scheme 4. Visible-light EnT enables the [2+2] cycloaddition of 2-isoxazoline-3-carboxylates (**15**) with alkenes to give protected azetidines (**17**).*

Despite these advances, limitations remain significant. Even with optimized substrates, the regioselectivity of the cycloaddition is difficult to predict, and diastereoselectivity is often modest. Moreover, extension to acyclic imines or more complex scaffolds remains challenging, and the stereochemical outcome is frequently substrate-dependent. Thus, while visible-light aza-PB reactions represent a conceptual and practical leap forward, they do not fully overcome the selectivity issues that have historically plagued this transformation.

Among the most powerful modern approaches to azetidines are those that exploit the extreme strain of 1-azabicyclo[1.1.0]butane (ABB) as a reactive precursor. A particularly elegant example was reported by Aggarwal and co-workers, who demonstrated that ABB lithium, generated in situ from the corresponding ammonium salt, can be intercepted by boronic esters. Upon protonation, a 1,2-metalate rearrangement takes place, releasing the ring strain and furnishing azetidinyl boronic esters with complete stereospecificity (Scheme 5a).[32]

This strategy is highly modular and compatible with a wide range of alkyl, aryl, and alkenyl boronic esters, thereby providing a general platform for the preparation of diversely substituted azetidines. The method also offers the significant advantage of preserving stereochemical information from the starting materials, making it particularly appealing for applications in asymmetric synthesis. At the same time, the approach relies on the availability of ABB precursors, which are themselves challenging to prepare, and requires careful control of the acidic activation step, which can limit functional-group tolerance and lead to variable yields.

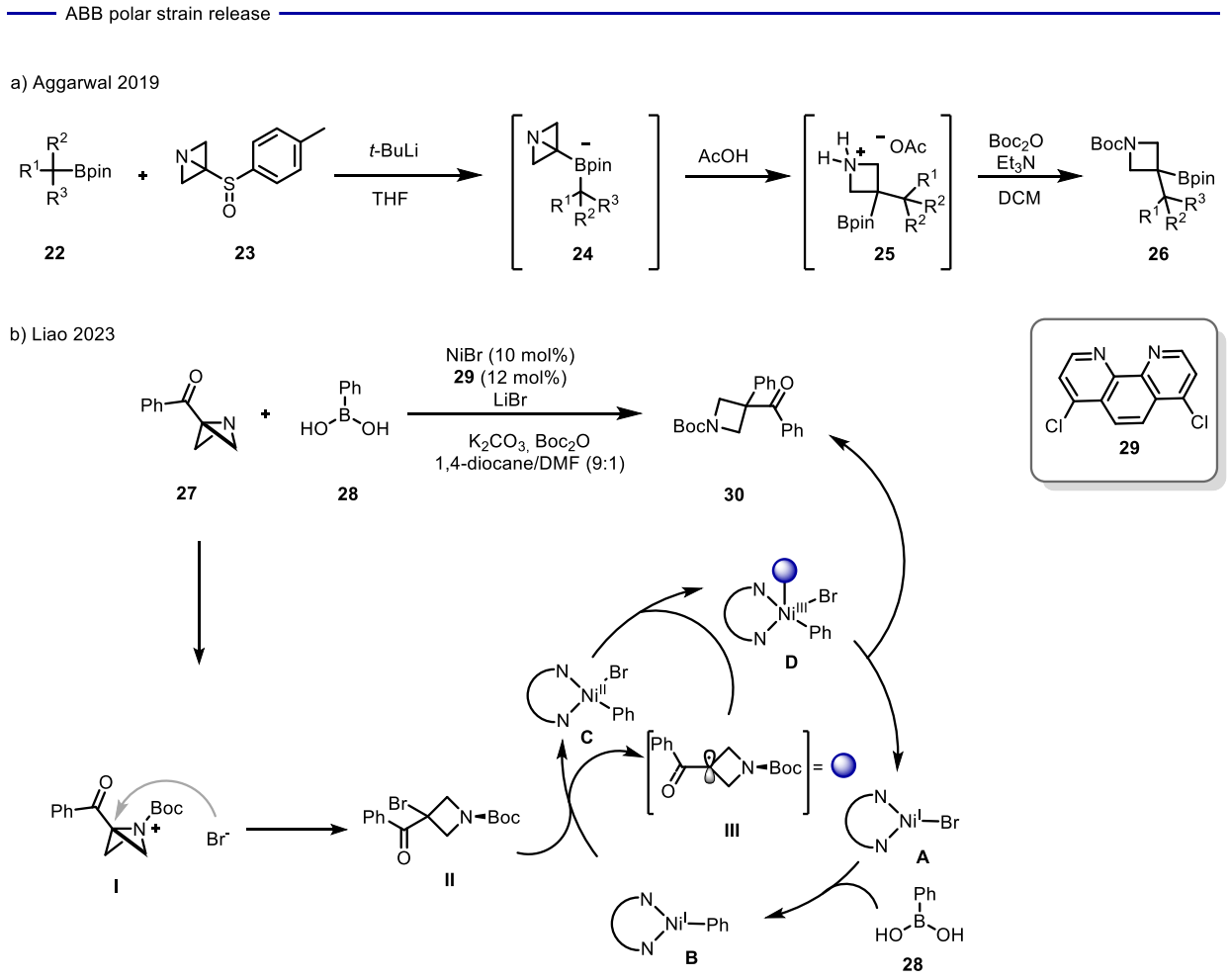

Scheme 5. Polar strain-release of ABBs: (a) stereospecific boronate rearrangement; (b) Ni/Br relay cross-coupling to C3-substituted azetidines.

Further diversification of ABB chemistry has been achieved by Luisi and co-workers, who adapted its generation and functionalization to continuous-flow technology. This contribution provides a more practical and sustainable platform for the generation and diversification of strained intermediates. The approach underscores the potential for scalability and safer handling of highly reactive species, although the requirement for specialized flow setups may still limit its broader adoption.[33]

More recently, Liao and coworkers merged strain-release with nickel catalysis in a polar–radical relay mechanism (Scheme 5b).[34] In this system, benzoyl-protected ABBs are activated by bromide in the presence of $NiBr_2$·diglyme, generating an azetidinyl radical intermediate that undergoes Suzuki-type cross-coupling with aryl or alkenyl boronic acids. The catalytic cycle proposed by the authors is as follows: catalytic bromide—originating from $NiBr_2$ or added LiBr—promotes the strain-release opening of the Boc-activated azetidinium species **I**, generated from substrate **27**, furnishing the redox-active intermediate **II** via a polar pathway. Concurrently, the active Ni(I)–Br complex **A** is generated in situ through comproportionation of Ni(0) and Ni(II) species derived from the $NiBr_2$ precatalyst.. Transmetalation of arylboronic acid **28** with complex **A** affords the corresponding aryl–Ni(I) intermediate **B**, which enters the catalytic cycle. Single-electron reduction of **II** by aryl–Ni(I) species **B** produces the azetidinyl radical **III**, along with formation of the Ni(II)–Br complex **C**. Radical recombination between **III** and **C** delivers the high-valent Ni(III) intermediate **D**. Subsequent reductive elimination from **D** then furnishes the desired C3-arylated azetidine **30**, while simultaneously regenerating the catalytically active Ni(I)–Br complex **A**, thus closing the catalytic cycle.

This sequence efficiently installs quaternary substituents at the C3 position of the azetidine ring. The method exhibits broad substrate scope, high functional-group tolerance, and scalability up to gram quantities, and it has been successfully applied to the modification of complex bioactive molecules, including derivatives of clofibrate, indometacin, and estrone. Particularly notable is the demonstration that azetidines can serve as viable bioisosteres of piperidines in pharmacologically relevant scaffolds, such as VAChT inhibitors[35] and MC-1R agonists.[34]

These features establish the approach as one of the most versatile and medicinally relevant ABB-based strategies to date, though the reliance on nickel catalysis and protected ABB precursors may still pose challenges for industrial translation. The synthetic landscape for azetidines has expanded dramatically in recent years, yet no single method has emerged as a universally applicable solution. Classical approaches remain conceptually simple but lack generality and display poor tolerance toward sensitive functional groups. Photochemical aza-PB reactions provide conceptual elegance and visible-light compatibility, but their outcome is often undermined by unpredictable regio- and stereo-chemical control. ABB strain-release chemistry currently offers the highest degree of modularity and stereospecificity, enabling efficient access to substituted azetidines, but it relies on unstable precursors and requires carefully controlled conditions that limit broader adoption. So far, ABB transformations have only been achieved through polar strain-release pathways, while their potential for radical reactivity has not yet been demonstrated. As emphasized in recent surveys,[36] the most pressing challenges lie in developing more predictable regio- and stereo-control in [2+2] photocycloadditions, in broadening the substrate generality of ABB-based methods while simplifying precursor access, and in establishing scalable protocols that reconcile strain release with functional-group tolerance for industrial application. In summary, while the methodological repertoire for constructing azetidines is now richer than ever, selectivity, practicality, and precursor accessibility remain limiting factors. These constraints have so far hindered the systematic exploration of azetidines in drug discovery, underscoring the need for alternative strategies that address both synthetic efficiency and stereo-control.

3.2. Aim of the project

The growing interest in four-membered heterocycles in medicinal chemistry has revealed a striking gap in synthetic methodology. While carbocyclic scaffolds have been widely explored, azetidines remain underrepresented, with only a limited set of approaches available to access them. The use of azabicyclo[1.1.0]butanes (ABBs) as strain-release precursors has proven extremely powerful in polar chemistry,[32,33] yet an equivalent radical-based strategy has not been established, despite its potential to generate densely substituted products through complementary reactivity.[36] Building on this premise, the concept of radical strain-release (RSR) from ABBs becomes particularly compelling. Unlike their polar counterparts, no general method has been reported that couples visible-light radical generation with ABB activation. Establishing such an approach would not only provide direct access to functionalized azetidines, but also demonstrate how radical strain-release (RSR) can expand the synthetic scope of strained nitrogen heterocycles.

The aim of this project was therefore to design and implement a photocatalytic strategy that merges the reactivity of ABBs with the radical manifold unlocked by visible light. Our conceptual design required the simultaneous generation of two complementary radical intermediates, which could then be intercepted by the strained system of an ABB through a polarity-matched strain-release process. This strategy was envisioned to enable the opening of the bicyclic system and the installation of two new substituents in a single step, as outlined in Figure 5.

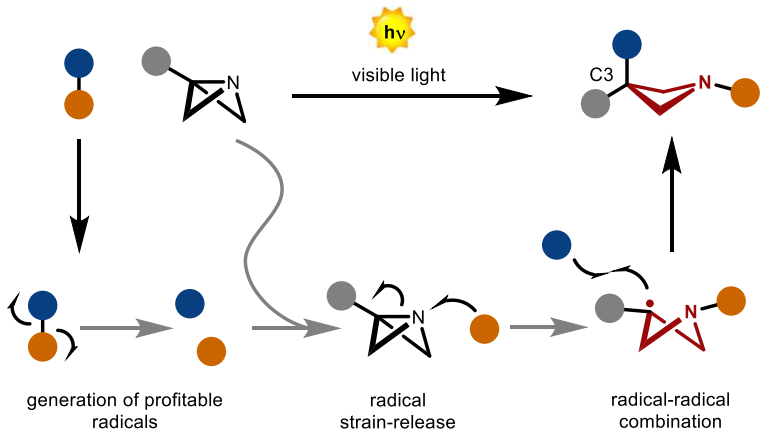

Figure 5. Conceptual design of the photocatalytic radical strain-release strategy.

For the radical precursor, we selected N-sulfonyl imines, a class of compounds known to undergo homolytic N–S bond cleavage upon photoexcitation or energy transfer, thereby furnishing both sulfonyl and iminyl radicals under mild conditions.[37,38] This photochemical lability has made them valuable partners in diverse radical transformations, particularly in visible-light catalysis. Beyond their reactive behavior, sulfonamide-derived motifs represent an important structural class in medicinal chemistry, widely represented in bioactive molecules and approved drugs owing to their metabolic stability and capacity to engage in hydrogen-bonding interactions.[39] Ultimately, this project sought to demonstrate that radical photocatalysis could overcome long-standing limitations in azetidine synthesis. By establishing a general and scalable protocol that provides access to densely functionalized azetidines, we aimed not only to enrich the synthetic repertoire of strained heterocycles, but also to highlight new opportunities for their integration into medicinal chemistry programs.

3.3. Results and discussion

3.3.1. Reaction design and optimization

A central requirement for functionalizing ABB **31** was the generation of two complementary radical species in situ, capable of installing substituents at nitrogen and at the C3 position of the strained bicyclic scaffold. Because these two sites possess markedly different electronic characters, the choice of the radical precursor and the excitation strategy was critical. Direct photoredox activation represented some putativesetbacks, as a one-electron oxidation of ABB could not be excluded and would likely lead to unproductive decomposition pathways.[40] To circumvent this risk, we turned to triplet energy transfer (EnT), selecting N-sulfonyl imine **32** as the radical progenitor. As a first choice of photocatalyst, 5TCzBN 33 was employed, owing to its high triplet energy (2.6 eV), broad solubility in common solvents, and strong absorption in the visible range, which prevents direct excitation of the imine. Upon sensitization, this class of substrates was expected to undergo efficient N–S bond homolysis, delivering both sulfonyl and iminyl radicals under mild conditions. A solvent screen identified trifluorotoluene ($PhCF_3$) as the optimal medium (Table 1), affording the highest yield of azetidine **34** (30%). Comparable results were obtained with ethyl acetate (entry 1) and toluene (entry 9), while the other tested solvents gave lower efficiencies. Based on these data, $PhCF_3$ was selected for subsequent optimization.

It is also mandatory to employ rigorously anhydrous solvents, since control experiments revealed that hydrolysis of sulfonylketimine **32** markedly reduces the yield, highlighting the sensitivity of the process to trace moisture.

*Table 1. Solvent screening for the model reaction between ABB **31** and N-sulfonyl imine **32**.*

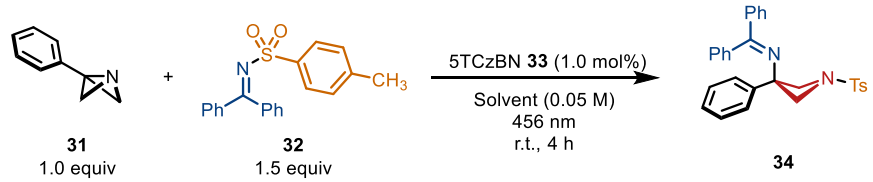

31 1.0 equiv | **32** 1.5 equiv | **34**

Entry	Solvent	Yield (%)	Entry	Solvent	Yield (%)
1	AcOEt	28	6	Dimethylcarbonate	22
2	MeCN	24	7	Acetone	11
3	DMSO	0	8	$PhCF_3$	30
4	1,2 Dichloroethane	21	9	Toluene	28
5	DCM	15	10	THF	0

Yields were determined by analysis of the ^{1}H NMR spectrum using 1.0 equiv. of trichloroethene as internal standard.

We next evaluated the stoichiometry between ABB **31** and sulfonyl imine **32**, which proved to be a decisive parameter (Table 2). Using ABB in excess (entry 3), significantly improved the yield compared to conditions with excess imine (entry 2). Reaction time had only a minor effect, since the consumption of **32** was essentially complete within the first 8 hours. By contrast, temperature exerted a more pronounced influence: raising the reaction temperature to 40 °C increased the yield of **34** to 44% (entry 9). Beyond this point, however, further heating proved detrimental, with efficiency dropping again at 50 °C (entry 10). Taken together, these results

established ABB excess and a reaction temperature of 40 °C as the optimal conditions, affording higher yields while maintaining straightforward purification. With these parameters in hand, we next turned to the evaluation of the photocatalyst.

*Table 2. Optimization of stoichiometry, time, and temperature for the model reaction between ABB **31** and sulfonyl imine **32**.*

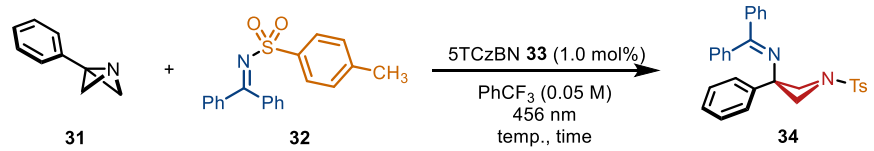

31 + 32 → 34

Entry	Ratio of 31/32	Temperature (°C)	Time (h)	Yield (%)
1	1/1.5	26	4	30
2	1/2	26	4	24
3	2/1	26	4	36
4	3/1	26	4	28
5	2/1	26	8	41
6	2/1	26	12	41
7	2/1	26	22	40
8	2/1	32	22	42
9	2/1	40	22	44
10	2/1	50	22	22

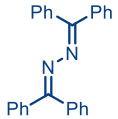

35

Yields were determined by analysis of the ^{1}H NMR spectrum using 1.0 equiv. of trichloroethene as internal standard.

During this optimisation phase, we observed that the only detectable by-product of the model reaction was the imine dimer **35**, formed through recombination of two transiently generated iminyl radicals. The issue became even more evident when the choice of photosensitizer was examined. In fact, when thioxanthen-9-one (TXO, **38**) was employed, full conversion of imine **32** was achieved, yet the desired azetidine **34** was obtained in only about 10% yield, with the majority of the mass balance accounted for by the dimeric by-product **35** (Scheme 6 and Table 3). These results suggest that the concentration of the iminyl radical in the reaction mixture is critical. We therefore reasoned that moderating the rate of iminyl radical formation could direct the reactivity towards productive interception by ABB, ultimately favoring the formation of the target azetidine **34**.[41–43]

To gain finer control over the concentration of iminyl radicals in solution, we next evaluated different classes of photosensitizers at a reduced loading of 0.25 mol%. Two main photophysical requirements guided this selection: a sufficiently high triplet excited-state energy (T_1 $E_{0,0}$) above 2.55 eV, ensuring the capacity for effective energy transfer to the imine, and a small singlet–triplet energy gap (ΔST).[44] The ΔST parameter, defined as the energy difference between the first singlet (S_1) and triplet (T_1) excited states, plays a decisive role in intersystem dynamics. A small ΔST facilitates rapid $S_1 \rightarrow T_1$ intersystem crossing (ISC) and the reverse $T_1 \rightarrow S_1$ interconversion (RISC), enabling efficient population exchange between spin states. In the context of our system, this mechanism effectively downregulates the steady-state population of the photocatalyst's T_1 state, thus moderating the rate of imine sensitization and suppressing the uncontrolled build-up of iminyl radicals that would otherwise lead to recombination into dimer **35**.

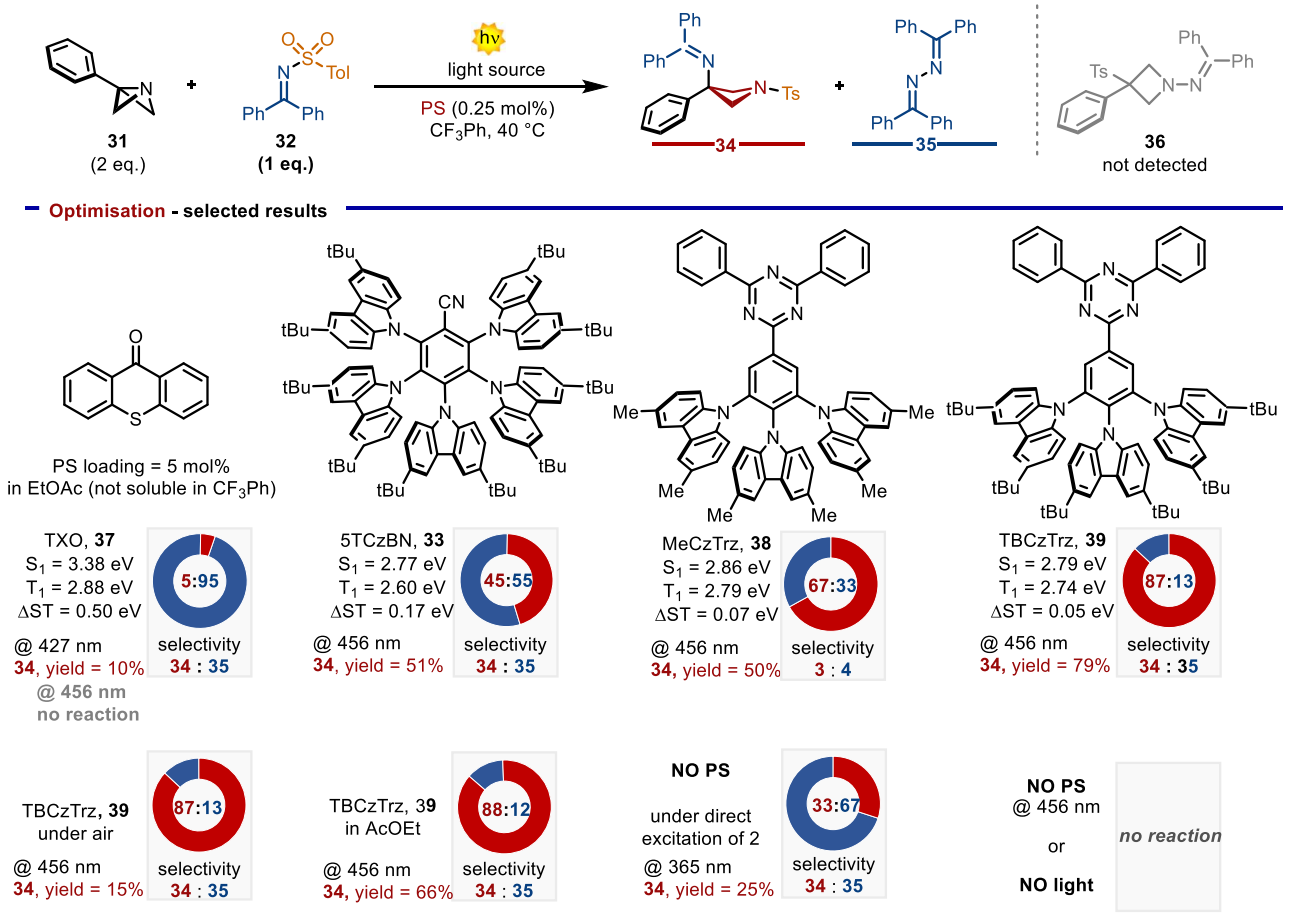

*Scheme 6. Evaluation of photosensitizers in the model reaction. Photocatalysts with smaller ΔST values provided improved selectivity and higher yields of azetidine **34** over the dimeric by-product **35**.*

This hypothesis was supported by the consistent trend observed between ΔST values and product selectivity (Scheme 6 and Table 3). Photocatalysts with lower ΔST values delivered higher selectivity for the desired azetidine **34** with respect to the dimeric by-product **35**. Additional parameters, including photocatalyst loading, λ_{max} (absorption maximum), the absorption tail, and solubility in the chosen solvent, were also found to modulate efficiency (Figure 8). For instance, when the loading was maintained at 0.25 mol%, catalysts combining a small ΔST with sufficient solubility in $PhCF_3$ consistently afforded superior selectivity. Among all tested systems, the photosensitizer **39** emerged as the optimal choice, characterized by the lowest ΔST value (0.05 eV) and a T_1 $E_{0,0}$ of 2.74 eV (calculated: 2.83 eV). Its design was inspired by recent progress in the development of thermally activated delayed fluorescence (TADF) emitters and their application in photocatalysis.[45,46] The photophysical behavior of **39** was rigorously characterized, covering prompt and delayed lifetimes, ISC/RISC rate constants (See in the Experimental part the Equations 3 and 4; Table 4), triplet energy, HOMO–LUMO separation, and spin-density distribution in the T_1 state (Figure 38). The molecular structure was unambiguously confirmed by single-crystal X-ray diffraction (Figure 49). Notably, under all conditions explored, we never detected the formation of the alternative regioisomer (**36**) in which the sulfonyl substituent is attached at the C3 position. This consistent outcome highlights the intrinsic regioselectivity of the process, demonstrating that the polarity-matched radical addition pathway overwhelmingly favors N–C3 bond formation over competing modes of reactivity. The absence of any detectable amounts of the reversed isomer, even under extended irradiation or varied photocatalytic conditions, underscores the robustness of this selectivity and distinguishes the present strategy from many previously reported radical processes where regioisomeric mixtures are a common limitation.

3.3.2. Mechanistic investigations

Here, we first lay out our mechanistic proposal (Scheme 7a). Under visible-light excitation, the photosensitizer **39** transfers triplet energy to the sulfonyl imine **32**, generating a reactive triplet that undergoes homolytic N–S cleavage to furnish a tosyl radical **40** and a complementary iminyl radical **41**. The tosyl radical engages ABB **31** via polarity-matched, strain-release addition to form the corresponding azetidinyl radical **42**, which is then trapped by the iminyl partner to deliver the N–C3 difunctionalised azetidine **34**.

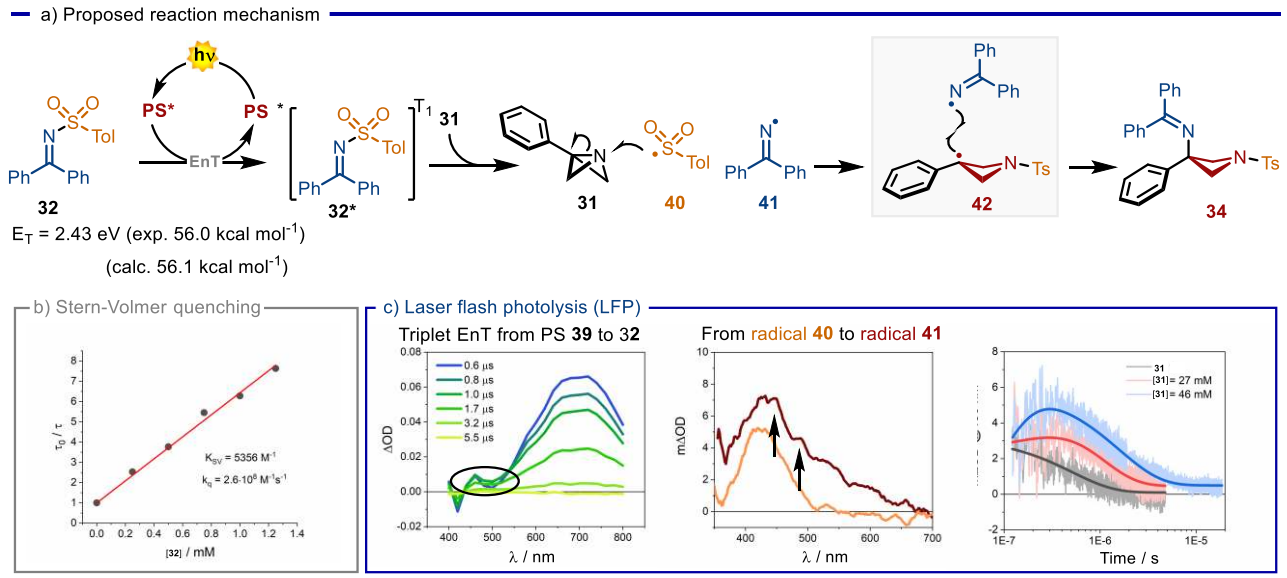

Scheme 7. a) Proposed mechanism. b) Stern–Volmer analysis. c) Laser flash photolysis (LFP) experiments

To test this proposal, we first interrogated the energy-transfer step. Time-correlated single-photon counting established that the singlet excited state of the photosensitizer is unreactive toward either imine **32** or ABB **31**, effectively ruling out a productive singlet pathway. In contrast, laser-flash photolysis showed that the triplet state of the photosensitizer is efficiently quenched by imine **32** ($k = 2.6 \times 10^8$ M^{-1} s^{-1}), whereas quenching by ABB **31** is two orders of magnitude slower ($k = 3.7 \times 10^6$ M^{-1} s^{-1}) (Figure 7b and Figures 28–30). These data establish the sulfonyl imine, rather than the ABB, as the primary acceptor of triplet energy, in agreement with the design of the process. Transient absorption measurements further corroborated this pathway. Upon excitation of photocatalyst **39** in the presence of imine **32**, a weak absorption band appeared in the 420–520 nm region (Scheme 7c, left panel), consistent with the rapid formation of radical intermediates **40** and **41** through N–S bond homolysis. The absorption signal in the 420–520 nm region was short-lived, decaying more rapidly than it developed, which prevented its clear assignment. To probe this step more directly, LFP experiments were conducted under direct excitation of imine **32**, both in the presence and absence of ABB **31**. To probe these steps more directly, LFP experiments were carried out under direct excitation of imine **32**, with and without ABB **31**. Under these conditions, a prompt absorption centered at 410 nm appeared (time delay ≈ 50 ns), which is characteristic of the tosyl radical **40** (Scheme 7c, middle panel).[47,48] In the absence of additional reagents, this signal returned to baseline within a few microseconds due to radical recombination (Scheme 7c, right panel). In the presence of ABB **31**, a second species subsequently developed, with an absorption maximum at 435 nm and a pronounced long-wavelength tail; this band is consistent with formation of the azetidinyl radical intermediate **42** (Scheme 7c, middle panel; time delay ≈ 750 ns). At 450 nm (Scheme 7c, right panel), the absorption intensity increased proportionally with the concentration of ABB **31**, consistent with a bimolecular process in which the tosyl radical **40** adds to the strained bicyclic scaffold.

The ensuing decay on the microsecond timescale is consistent with capture by the iminyl partner and formation of azetidine **34** (Figures 34–36).

To further substantiate our mechanistic hypothesis and to obtain direct evidence for the nature of the radical intermediates, we carried out electron paramagnetic resonance (EPR) experiments in the presence of the spin-trapping agent α-phenyl-*tert*-butylnitrone (PBN, **43**) and photocatalyst **39**. When sulfonyl imine **32** was irradiated in the absence of ABB **31**, the resulting spectrum (Scheme 8a, blue trace) revealed the presence of mixed radical species, with parameters consistent with an approximately equal population of nitrogen- and sulfur-centered radicals. These species were assigned to the sulfonyl (**40**) and iminyl (**41**) radicals generated by N–S bond cleavage. In striking contrast, when the reaction was performed under standard conditions in the presence of ABB **31**, a completely different and much more intense spectrum was obtained (Scheme 8a, red trace). Analysis indicated that the major trapped species (≈70%) corresponded to the carbon-centered radical **42**, which we proposed as the key intermediate formed upon tosyl radical addition to the bicyclic scaffold. Control experiments showed no radical signal when PBN was irradiated in the absence of both ABB **31** and imine **32**, confirming that these substrates are the exclusive sources of radicals under the reaction conditions.

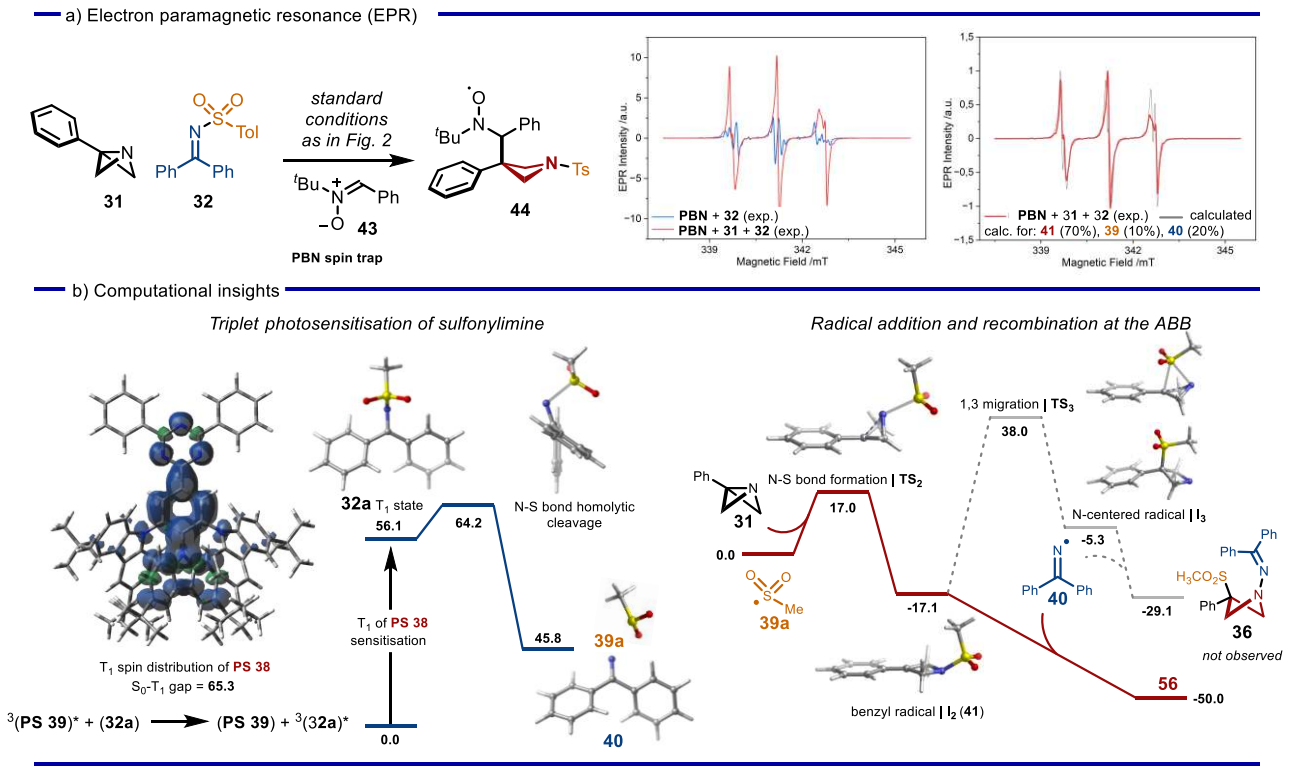

Scheme 8. a) EPR experiments. b) Computational studies.

To complement the spectroscopic data and rationalize the observed outcome, we conducted density functional theory (DFT) calculations at the (U)M06-2X/def2-TZVP level, including a solvent model (IEFPCM, toluene) for the reaction profile. For computational efficiency, a mesyl-substituted sulfonyl imine (**32a**) was used in place of the bulkier tosyl analogue (Scheme 8b). The S_0 and T_1 states of **32a** and photocatalyst **39** were computed, and the energy-transfer step was analysed according to ^{3}(PS)* + **32a** → PS + ^{3}(**32a**)*. A free-energy change of ΔG = –9.2 kcal mol^{-1} was obtained (computed without solvent model), underscoring the exergonic nature of EnT (Scheme 8b, left). Spin-density analysis of the relaxed triplet state of **39**, together with time-resolved quenching data, suggests that EnT initiates via a collision complex involving the triazine moiety of **39** and the sulfonyl imine **32a** (Figures 38-39). Subsequent steps were then evaluated. N–S bond homolysis of the excited imine to give the sulfonyl radical **40** and the complementary iminyl radical **41** is exergonic (ΔG =

–10.3 kcal mol^{-1}) and proceeds over a modest barrier ($\Delta G^{\ddagger}$ = 8.1 kcal mol^{-1}). Addition of the sulfonyl radical **40** to C3 of ABB **31**, followed by radical–radical combination with the iminyl partner, furnishes the observed azetidine product **56** (Scheme 8b, right). The alternative regioisomer—never observed experimentally—was computed to lie 21.9 kcal mol^{-1} higher in energy than the product, indicating kinetic rather than purely thermodynamic exclusion. Consistently, the productive pathway via the azetidinyl radical intermediate shows a barrier of 17.0 kcal mol^{-1} (TS_2), whereas the competing route toward the unobserved isomer requires surmounting a prohibitive barrier of 55.1 kcal mol^{-1} (between intermediates I2 and I3, nitrogen-centred radical).

Together, the EPR trapping experiments and the DFT calculations converge to support the proposed mechanistic model. They confirm the participation of iminyl- and sulfonyl-derived radicals, validate the formation of the carbon-centered radical **42**, and explain both the efficiency and the regioselectivity of the radical strain-release process.

3.3.3. Generality of the reaction

With the mechanistic foundations in place, we next turned to exploring the generality of this photocatalytic strain-release protocol (Scheme 9). A broad range of N-sulfonyl imines were competent partners, encompassing both ketimine and aldimine derivatives. Substrates bearing electron-donating as well as electron-withdrawing substituents were efficiently transformed, affording azetidines **45**–**70** in yields of up to 79%. Likewise, systematic variation at the sulfonyl group was well tolerated, delivering the corresponding products **50**–**57** in moderate to excellent yields (47–80%).

Attention was then directed to the ABB partner. Structural diversification at this strained precursor proved equally viable: aryl- and carbonyl-substituted ABBs furnished products **59**–**62** in yields reaching 84%. Moreover, 2-substituted ABBs provided access to azetidines **63**–**66** with good efficiency and useful levels of diastereocontrol (2.3:1 d.r.). Crystalline samples of both diastereomers **65** and **66** were obtained, and their relative configurations were unambiguously established by single-crystal X-ray diffraction (Figure 65-66).

Importantly, mild conditions and broad functional-group tolerance make this strategy particularly attractive for late-stage functionalization. As a demonstration, we showcased its application to biologically relevant scaffolds from both sides of the reaction manifold. On one hand, the celecoxib-derived sulfonyl imine **67** reacted smoothly to furnish the corresponding azetidine **68** in 71% yield. On the other hand, the ABB derived from naproxen **69** underwent efficient conversion to product **70** in 66% yield, notably preserving the optical purity of the parent chiral scaffold. These examples highlight the unique strength of this methodology: bioactive motifs can be installed directly from either reaction partner, enabling rapid access to densely functionalized azetidines decorated with pharmacologically relevant substituents.

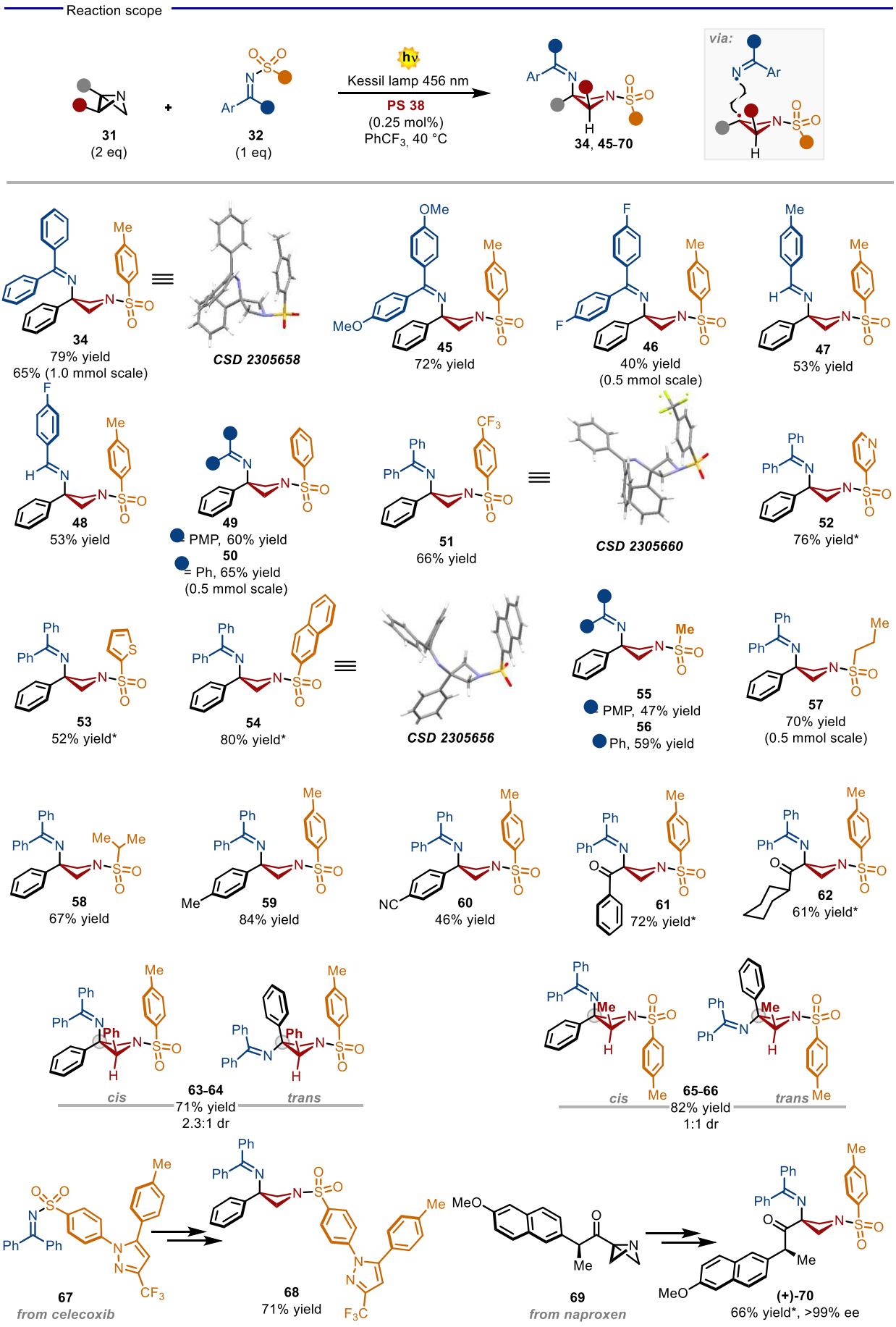

Scheme 9. Substrate scope of the radical strain-release photocatalytic protocol. [a]Reaction performed in ethyl acetate. PMP=p-OMePh.

Building on the broad generality of the two-component protocol, we next asked whether the key C_3-radical intermediate could be intercepted by alternative SOMO-philes to further expand the reactivity landscape (Scheme 10a). In this context, we designed a three-component variant combining ABBs, aldimines, and suitable radical acceptors. Aldimines, known to be less efficient than ketimines as precursors of iminyl radicals,[49] were deliberately chosen to favor the interception of the C_3 radical. In the presence of supersilane **74**, this strategy furnished azetidines bearing an additional substituent in excellent yields, reaching up to 90%. Importantly, this manifold allows direct access to families of densely functionalized azetidines without the need for further optimization, underscoring the flexibility of the method. Motivated by the pharmaceutical relevance of the SCF_3 group,[10,50] we next employed a phthalimide–SCF_3 **75** reagent as SOMO-phile. The transformation proceeded efficiently, affording thiotrifluoromethylated azetidines in up to 71% yield, including derivatives of celecoxib. These results highlight the capacity of the radical strain-release platform to unlock new reactivity channels and to rapidly diversify the azetidine scaffold.

Finally, we explored the synthetic versatility of the obtained azetidines through a series of post-functionalization studies designed to reveal their embedded amino functionalities (Scheme 10b). For instance, the benzylated intermediate **83** was obtained either by reduction of **47** or by reductive amination of **34**, both routes delivering excellent yields of up to 95% without the need for column chromatography. Hydrolysis of compounds **34**, **56** and **59** furnished the corresponding hydrochloride salts **84–86**, which could be directly neutralized to provide free amino sulfonyl azetidine **87** in quantitative yield. This intermediate proved to be a valuable synthetic linchpin, enabling access to tertiary amines such as the pyrrolidine-containing derivative **88**, a scaffold of established biological relevance.

In addition, selective tosyl group cleavage of **87** furnished the orthogonally substituted 3-aminoazetidine **89**, which could be further elaborated into structural variants of kinase modulators **90**. Finally, oxidative cleavage of the phenyl substituent in **87** under RuO_4-mediated conditions gave rise to the spiroazetidine amino acid **91** in 52% yield, providing an unexpected yet synthetically attractive scaffold.[51,52]

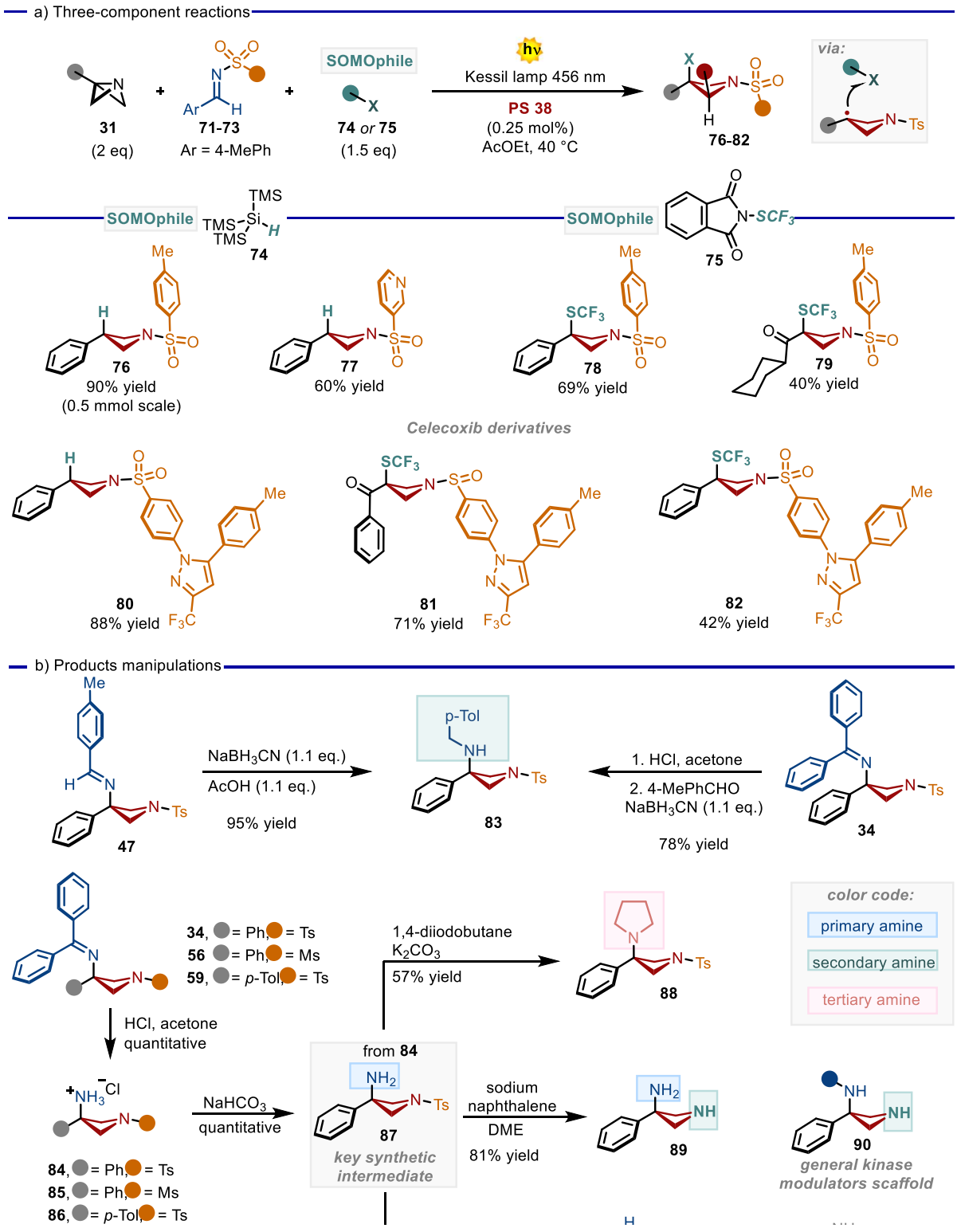

Scheme 10. Utility of the developed method for diversification of azetidine scaffolds. a) Three-component variants with different SOMOphiles. b) Unmasking and post-functionalization of amino azetidines.

3.3.4. Conclusions

In summary, this work has established a photocatalytic radical strain-release strategy that unlocks the reactivity of azabicyclo[1.1.0]butanes (ABBs) under mild and selective conditions. Central to the success of the method is the design of an organic photosensitizer with a minimal singlet–triplet energy gap, which enables finely tuned activation of sulfonyl imines and precise control over the concentration of reactive intermediates. This feature proved essential to prevent undesired recombination pathways and to channel the reactivity toward productive azetidine formation. Importantly, the transformation consistently proceeded with complete regiocontrol, as no trace of the alternative regioisomer was ever detected, highlighting the intrinsic bias of the system toward N–C_3 bond formation. The developed protocol demonstrates that ABBs can be efficiently engaged in free-radical chemistry, providing access to a broad family of densely functionalized azetidines in consistently good yields. Mechanistic investigations confirmed the key role of a transient carbon-centred radical, generated by selective ring opening, which operates as a versatile intermediate capable of forging new σ-bonds with nitrogen, sulfur, and hydrogen atoms. This finding not only rationalizes the observed outcome but also highlights the intrinsic potential of ABBs as radical acceptors. Furthermore, the extension of the method to three-component processes established its robustness and generality, showing that a wide range of SOMOphiles can intercept the key radical intermediate. This strategic expansion effectively unlocks new synthetic pathways for the preparation of densely and diversely functionalized azetidines, further broadening their chemical space and enhancing their potential applications in medicinal chemistry. Crucially, this work addresses a long-standing gap in the field: while ABBs had previously only been exploited through polar strain-release pathways, here their radical reactivity is demonstrated for the first time, opening an entirely new dimension of their synthetic utility. Looking forward, the ability to exploit ABBs in radical strain-release reactivity is expected to inspire new methodologies, further enriching the synthetic repertoire available for the construction of azetidines and related small-ring heterocycles.

3.4. Experimental part

3.4.1. General information

Reagents, solvents and experimental conditions

All required fine chemicals were purchased from Acros (Fisher), Aldrich (Merck), Alfa Aesar (Fisher), Fluorochem, TCI, BLDpharm and used without further purification unless otherwise stated. THF was purified by distillation over sodium-ketyl benzophenone under argon atmosphere. Dichloromethane, toluene, nhexane, and N,N,N',N'-tetramethylethylenediamine were purified by distillation over CaH_2 under argon. Trifluorotoluene and ethyl acetate were freshly distilled over phosphorus pentoxide prior to its use for the photocatalyzed reactions. All other dry solvents were purchased from Acros in AcroSeal® bottles or Aldrich (Merck) Sure/SealTM and were directly stored under 3 or 4 Å molecular sieves. The photocatalyzed reactions were set-up under an argon atmosphere in oven-dried Schlenk tubes and degassed with 3 freeze-pump-thaw cycles, see general procedures J and K for more details. Thioxanthone was purchased and used as received. All other organic photocatalysts were prepared according to reported literature procedures.

Analytical techniques

NMR spectra were recorded on Bruker 400 Avance III HD equipped with a BBI-z grad probe head 5mm and Bruker 500 Avance III equipped with a BBI-ATM-z grad probe head 5mm (^{1}H: 400 MHz, ^{13}C: 100.5 MHz, ^{19}F: 376 MHz). The chemical shifts (δ) for ^{1}H and ^{13}C are given in ppm relative to residual signals of the solvents ($CHCl_3$ @ 7.26 ppm for ^{1}H NMR, and @ 77.16 ppm for ^{13}C NMR; $CFCl_3$ @ 0.0 ppm for ^{19}F NMR spectra). Coupling constants are given in Hz. The following abbreviations are used to indicate the multiplicity: s, singlet; d, doublet; t, triplet; q, quartet; m, multiplet; br, broad signal. NMR yields were calculated by using trichloroethylene as internal standard unless otherwise noted. All the cyclic voltammograms were recorded with a scan rate of 0.1 V/s and were carried out in acetonitrile (CH_3CN, 0.1 M) tetrabutylammonium hexafluorophosphate ($TBAPF_6$) at room temperature, on a BASi EC Epsilon potentiostat-galvanostat in a glass cell. A typical three-electrode cell was employed, which was composed of a glassy carbon (GC) working electrode (3 mm diameter), a platinum wire as counter electrode and a saturated aqueous calomel electrode (SCE) as reference electrode. Oxygen was removed by purging the solvent with high-purity Nitrogen (N_2), introduced from a line into the cell by means of a glass pipe. The potential of ferrocenium/ferrocene (Fc^+/Fc) couple was used as an internal reference system to calibrate the potentiostat. All the results are subsequently converted in V vs SCE, in agreement with the value reported in literature [$E_{1/2}(Fc^+/Fc)$ = +0.38 V vs SCE]. Thin-layer chromatography (TLC) analysis was performed on pre-coated Merck TLC plates (silica gel 60 GF254, 0.25 mm). Visualization of the developed chromatography was performed by checking UV absorbance (254 nm) as well as with cerium molybdate or 2,4-dinitrophenyl hydrazine stain solutions. Organic solutions were concentrated under reduced pressure on a Heidolph rotary evaporator.

High-Resolution Mass Spectra (HRMS): were obtained using Waters GCT gas chromatograph coupled with a time-of-flight mass spectrometer (GC/MS-TOF) with electron ionization (EI). Routine MS for calculating the ration of 3:4 was conducted in a Waters Acquity UPC^2 using CO_2/MeOH as mobile phase. **Computational details**. TD-DFT calculations involving 30 states were performed at the same level of theory to compute the electronic excitation energies and the corresponding oscillator strengths of the optimized structures. All the calculations were carried out using Gaussian 16 software package, Revision C.01. All geometry optimizations were performed using M06-2X functional, including the integral equation formalism of the polarizable continuum model (IEFPCM) to model solvation effects, except for the computed ΔG of the energy transfer process, which was performed in gas phase. The def2TZVP basis set was employed. Frequencies were calculated in order to ensure that the structures are actual relative minima of energy. The energy values for all computed structures discussed in this text, including the energy transfer (EnT) process from the excited

photosensitizer to the ground-state sulfonylimine, are expressed in terms of Gibbs free energy. These values encompass thermal corrections computed at standard conditions of 298.15 Kelvin and 1 atmosphere pressure. **Steady-state absorption spectroscopy**: the studies have been performed at room temperature on a Varian Cary 5000 UV-Vis double beam spectrophotometer; 300 µm path length Hellma Analytics quartz cuvettes have been used. **Steady-state fluorescence spectra**: room-temperature luminescence measurements were recorded on a Varian Cary Eclipse Fluorescence spectrometer, while emission spectra at 77 K were measured using an Edinburgh instrument spectrofluorometer equipped with a cryostat; 10 mm path length Hellma Analytics 117.100F QS quartz cuvettes were used.

Time-correlated single-photon counting (TCSPC): Fluorescence lifetimes were measured using a TCSPC apparatus (PicoQuant Picoharp 300) equipped with subnanosecond LED sources (280, 380, 460, and 600 nm and 500−700 ps pulse width) powered by a PicoQuant PDL 800-B variable (2.5−40 MHz) pulsed power supply. The decays were analyzed by means of PicoQuant FluoFit Global Fluorescence Decay Analysis Software. **Nanosecond laser flash photolysis**: Laser Flash photolysis measurements were performed with a custom laser spectrometer that consists of a Continuum Surelite II Nd:YAG laser (FWHM 6−8 ns) with a frequencytripled (355 nm, 16 mJ) option, and an Applied Photophysics xenon light source including a mod. 720p resolution 150 W lamp housing, a mod. 620p power-controlled lamp supply, and a mod. 03-102 arc lamp pulser. Laser excitation was provided at 90°, with respect to the white light probe beam. Light transmitted by the sample was focused onto the entrance slit of a 300 mm focal length Acton SpectraPro 2300i triple grating, flat field, double exit monochromator equipped with a photomultiplier detector (Hamamatsu R3896), and a Princeton Instruments PIMAX II gated intensified CCD camera, using an RB Gen II intensifier, a ST133 controller and a PTG pulser. Signals from the photomultiplier (kinetic traces) were processed by means of a TeledyneLeCroy 604Zi (400 MHz, 20 GS/s) digital oscilloscope. Standard cuvettes with a 1 cm path length were employed and solutions were degassed with nitrogen before all the experiments.

Compound purification

Chromatographic purification of products was accomplished using flash chromatography on silica gel (SiO2, 0.04-0.063 mm, 60 Å) purchased from Machery-Nagel, with the indicated solvent system according to the standard techniques or using a Biotage Isolera automated flash chromatography system with cartridges packed with silica (SiO2, 0.04-0.063 mm, 60 Å).

Photoreactor setup

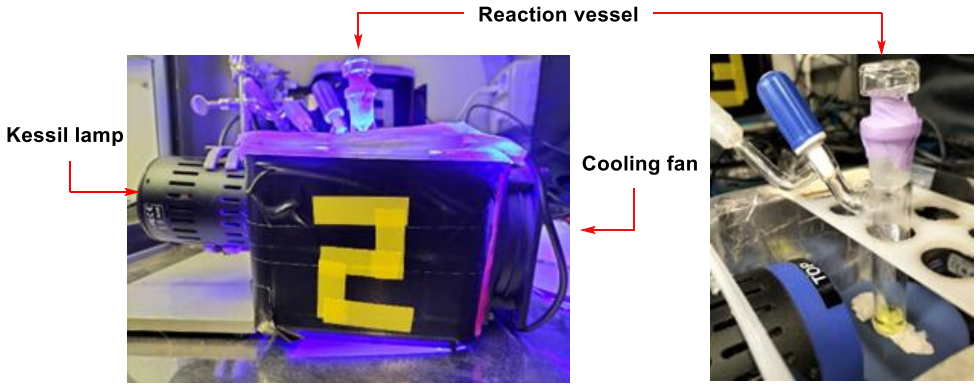

Figure 6.(Left) side view of the photoreactor setup. (Right) inside view of the photoreactor setup.

The employed photoreactor was designed by Dr. José J. Garrido and it is comprised of a Kessil lamp, an IKA stirring plate and a fan. Temperature is controlled using an infrared thermometer. A tutorial video is available at: https://www.youtube.com/watch?v=gLE8nYWPPNQ.

Light source at 456 nm: The Kessil lamp PR160L-456 (50W) was purchased from Kessil webpage: https://www.kessil.com/science/PR160L.php. The light emission spectra of Kessil lamps can be found at the same website.

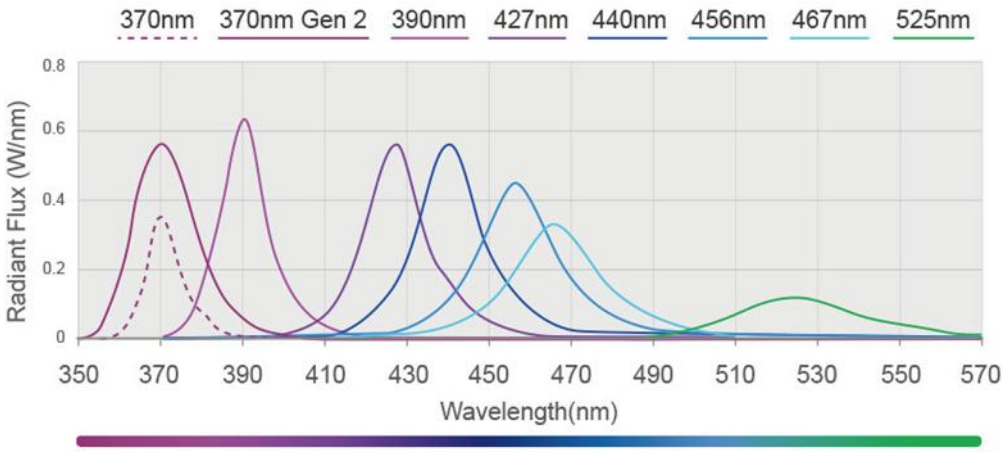

Figure 7.Emission spectra of Kessil PR160L lamps, obtained from: https://www.kessil.com/science/PR160L.php

3.4.2. Experimental Details

Several previously reported triplet photosensitizers were prepared, including PS **95**, PS **38**, and PS **39**. In the case of PS **38** and PS **39**, their synthesis was complemented by a more comprehensive photophysical characterization. This is the first time that PS **39** is reported. Scheme 11 showcases the first singlet (S_1) and first triplet (T_1) excited state of each photocatalyst in eV and the values were taken from the indicated references. In the case of **PS 9**, there were not previously described properties, therefore the reported values were obtained in our laboratory. Additionally, to have a comparison with the bibliographic data, we measured the properties of PS **38,** and the experimental values are provided as well. The model reaction is clean, having the desired product **34**, dimer **35** and in some cases benzophenone (the result of partial hydrolysis of the sulfonyl ketimine). In this regard, the challenge was to diminish the yield of **35** by enhancing the formation of **34**. Testing PS **33**, which has a slightly lower T_1 and smaller ΔST in comparison to PS **93,** had a favorable effect (Table 3, entries 1 and 2). Moreover, decreasing the photocatalyst loading conducted to a decent increase of yield (Table 3, entries 3 and 4). Afterwards, we tested PS **37**, thioxanthenone (TXO), which is known to be an excellent triplet photosensitizer. Interestingly, dimer **35** was formed as practically the only product of the reaction (entry 5). Attempting to have a fair comparison related the photosensitizer loading, PS **37** was tested at 0.25 mol% using both $PhCF_3$ and AcOEt (compare entries 5, 6, and 7). Furthermore, the loading was increased to 5.0 mol% and the reaction was irradiated at 400 nm (entry 8). Although poorly promising, these results were intriguing. It is well known that an ideal triplet sensitizer must bear a sufficiently high triplet energy (ET1) and a longlived triplet excited state, when following an exchange energy transfer (Dexter typer) scenario. To some extent, we were witnessing a very effective triplet sensitization of 3**2** by PS **37**, as full consumption of it was observed, with a ratio 3:4 completely unbalanced towards **35**, however. These observations, along with the results derived from PS **93** and PS **33**, made us think that we needed to design a scenario in which the sensitisation was still thermodynamically feasible (ET_1 of PS > ET_1 of 3**2**), in other words, mainly governed by diffusion, but which was intentionally ineffective. The latter ideally would downregulate the formation of iminyl-radical intermediates, preventing its homocoupling (product **35**). With this in mind, we decided to test molecules that are successfully used for OLED manufacturing because of their small ΔST. Its high capacity of undergoing reverse intersystem crossing (RISC) would potentially serve as a

tactic to generate less triplet excited state of the photosensitizer. PS **94** was the first one to showcase a ratio 3:4 favoring the formation of **34**, however, observing low yield (entry 9). Testing PS **95** conducted to unsuccessful results in terms of 3:4 ratio and yield.

Employed photosensitisers

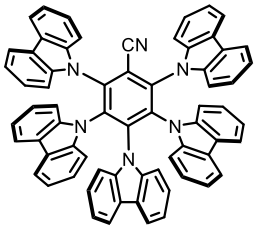

PS 93
S_1 = 2.90 eV
T_1 = 2.68 eV
ΔST = 0.22 eV

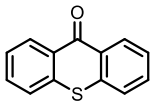

PS 37
S_1 = 3.38 eV
T_1 = 2.88 eV
ΔST = 0.5 eV

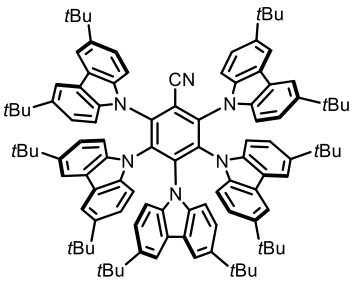

PS 33
S_1 = 2.77 eV
T_1 = 2.60 eV
ΔST = 0.17 eV

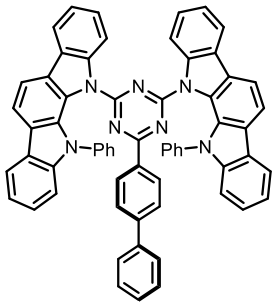

PS 94
S_1 = 2.66 eV
T_1 = 2.55 eV
ΔST = 0.11 eV

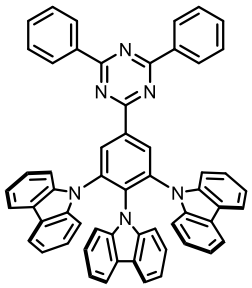

PS 95
S_1 = 2.96 eV
T_1 = 2.80 eV
ΔST = 0.16 eV

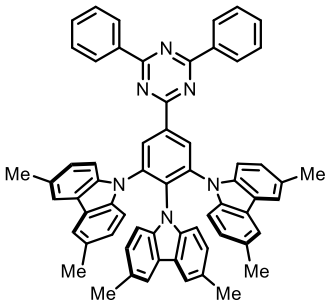

PS 38
S_1 = 2.86 / 2.81[a] eV
T_1 = 2.79 / 2.75[a] eV
ΔST = 0.07 / 0.06[a] eV

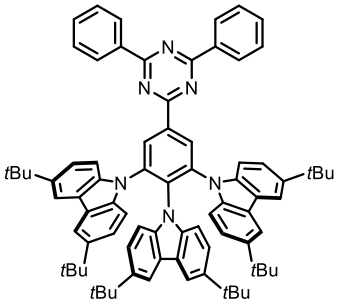

PS 39[a]
S_1 = 2.79 eV
T_1 = 2.74 eV
ΔST = 0.05 eV

PS	Acronym	Reference
PS 93	5CzBN	*Mater. Horiz.*, **2016,** *3*, 145
PS 37	TXO	*Chem. Rev.*, **2016,** *116,* 10075
PS 33	5TCzBN	*Mater. Horiz.*, **2016,** *3*, 145
PS 94	PIC-TRZ	*Asian J. Org. Chem.*, **2020,** *9*, 1
PS 95	TCzTrz	*Adv. Mater.* **2015,** *27,* 5861
PS 38	TmCzTrz	*Adv. Mater.* **2015,** *27,* 5861
PS 39	TBCzTrz	--

Scheme 11. Employed photosensitizers and their properties. a) Experimentally obtained.

The latter might be attributed to the fact that its UV-vis absorption edge is located at 414 nm and we irradiated using a 400 nm Kessil lamp, in such scenario the direct photolysis of 3**2** (Blank reaction: **31** + **32** without PS, $PhCF_3$ as solvent and irradiation at 385 leads to 11% yield of **34**) cannot be ruled out for contributing. Moving to PS **38** which UV-vis absorption edge is located at 447 nm, a notorious improvement was observed (entry 11). Replacing the CH_3- groups located at the carbazole cores, for the *t*Bu- moiety (PS **39**), conducted to a modest improvement (compare entries 11 and 12), showcasing the same 3:4 ratio. (Note: it has been reported

that the introduction of *t*Bu groups in TADF emitters, aids to diminish the ΔST,)[45]. Finally, decreasing the catalyst loading just proved deleterious for the reaction outcome (entry 13), and irradiating at a slightly higher energetic wavelength diminished the yield as well (entry 14).

Table 3. Screening of stoichiometric ratio, temperature and time.

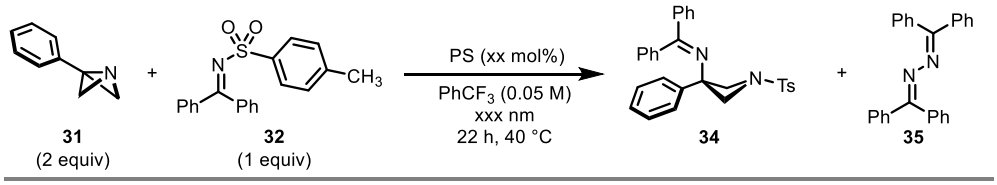

Entry	PS/mol%	Ratio 34/35[a]	Wavelenght (nm)	Yield of 34 (%)[c]
1	**PS 93** / 1.0	40:60	456	44
2	**PS 33** / 1.0	40:60	456	47
3	**PS 33** / 0.5	40:60	456	48
4	**PS 33** / 0.25	40:60	456	50
5[b]	**PS 37** / 5.0	<5:>95	427	10
6[b]	**PS 37** / 0.25	No reaction	427	0
7	**PS 37** / 0.25	No reaction	427	0
8[b]	**PS 37** / 5.0	10:90	400	16
9	**PS B** / 0.25	59:41	427	32
10	**PS C** / 0.25	40:60	400	17
11	**PS 94** / 0.25	87:13	456	72
12	**PS 39** / 0.25	87:13	456	79
13	**PS 39** / 0.1	80:20	456	42
14	**PS 39** / 0.25	80:20	427	70

Yields were determined by analysis of the ^{1}H NMR spectrum using 1.0 equiv. of trichloroethene as internal standard.
[a]Ratio of 3/4 was measured by UPC2 analysis of the crude samples. [b]$PhCF_3$ was replaced for AcOEt for solubility purposes.
[c]In all cases except fo entries 6 and 7, full consumption of 2 was observed.

Additionally, we performed a set of experiments keeping constant the molar extinction coefficient (ε) among selected PSs at 427 nm. Although in this case the PSs concentration under the reaction mixture differs, the concentration of the excited state PSs is virtually consistent. It is interesting to note that also in this case a trend is still observable, where the inferior ΔST value correlates with an increased selectivity.

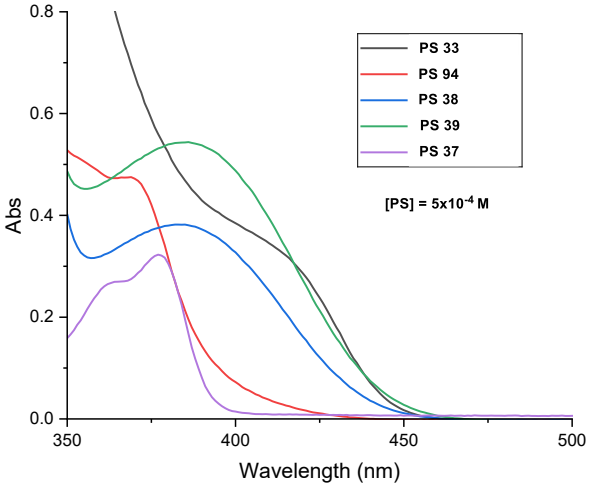

PS	ε (l)	ε (l) [yield and ratio 3:4]	ε (l) [yield and ratio 3:4]
37	151.1 (400)	6957.1 (377)	--
33	7787.9 (400)	4113.9 (427), 0.24 mol% [53% yield, 40:60 ratio]	415.4 (450) 0.24 mol% [50% yield, 40:60 ratio]
94	1438.4 (400)	--	--
38	6419.6 (400)	2030 (427) 0.48 mol% [34% yield, 50:50 ratio]	253.78 (450) 0.48 mol% [49% yield, 40:20 ratio]
39	9949.9 (400)	3899.4 (427) 0.25 mol% [63% yield, 80:20 ratio]	551.23 (450) 0.25 mol% [79% yield, 87:13]

Figure 8. Panel right: absorption spectra of photosensitizers at a constant concentration. Panel left: relationship between PS loading, molar extinction coefficient (ε), and product distribution.

To understand if this reasoning was independent of the nature of the sulfonylimine and find out if the 3:4 ratio would be extended, we prepared four different sulfonylketimines and subjected them to the optimized reaction conditions. Concluding that the ratio was not influenced but the yield was.

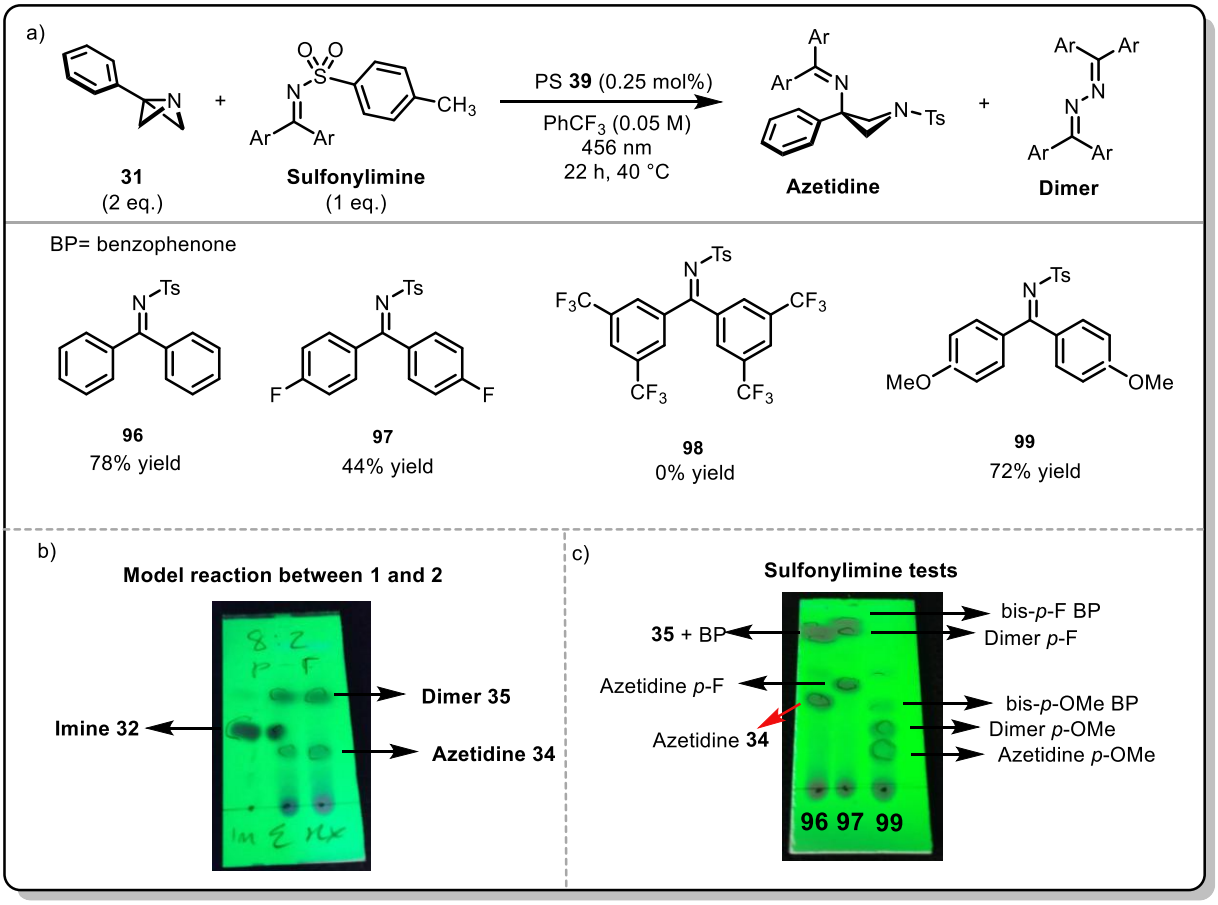

*Scheme 12. Panel a) yield of the corresponding tested sulfonylimine. Panel b) TLC of the model reaction showing the formation of dimer **35**, azetidine **34** and full consumption of imine **32**. Panel c) TLC of the reaction with different sulfonylimines (**96**, **97**, **99**) showing the formation of the corresponding dimer, azetidine and full consumption of the sulfonylimine in all the cases.*

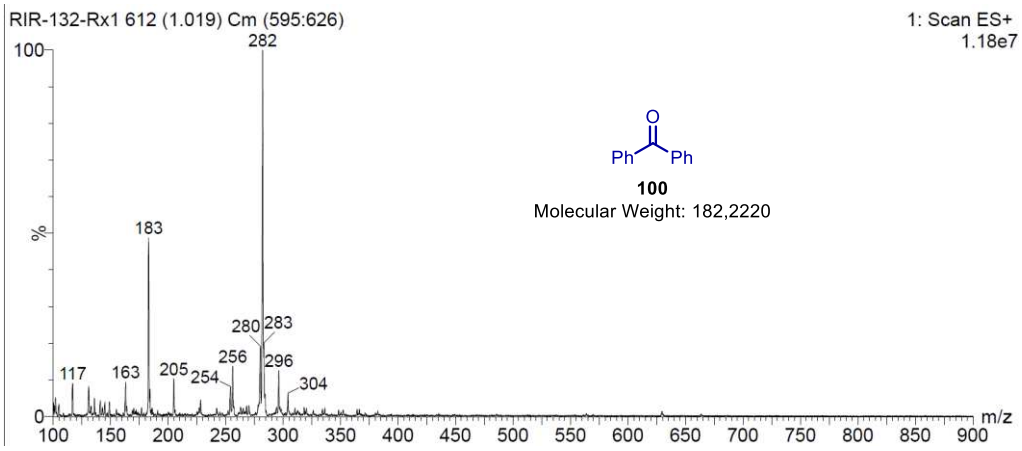

*Figure 9. ESI+ trace of benzophenone **100**.*

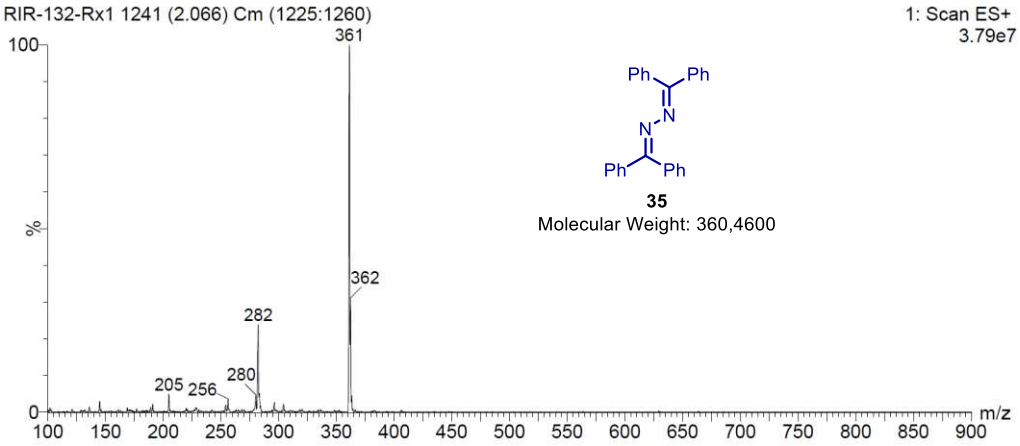

*Figure 10. ESI+ trace of dimer **35**.*

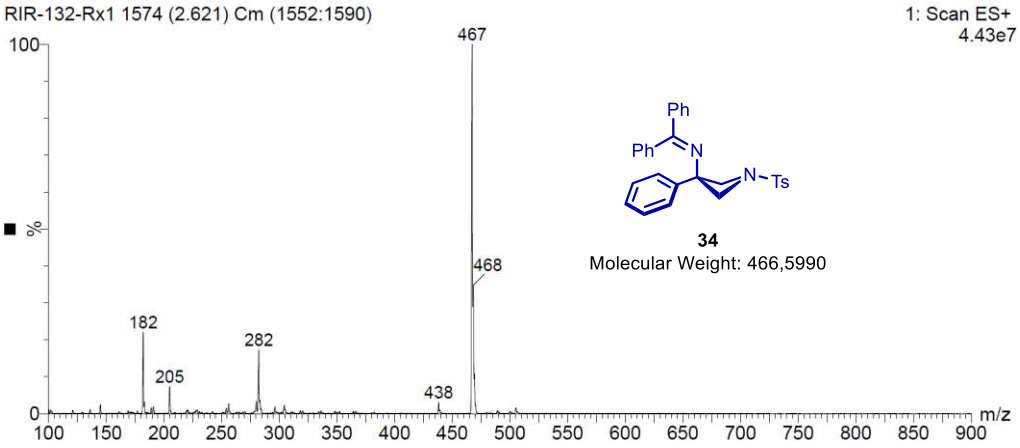

*Figure 11. ESI+ trace of azetidine **34**.*

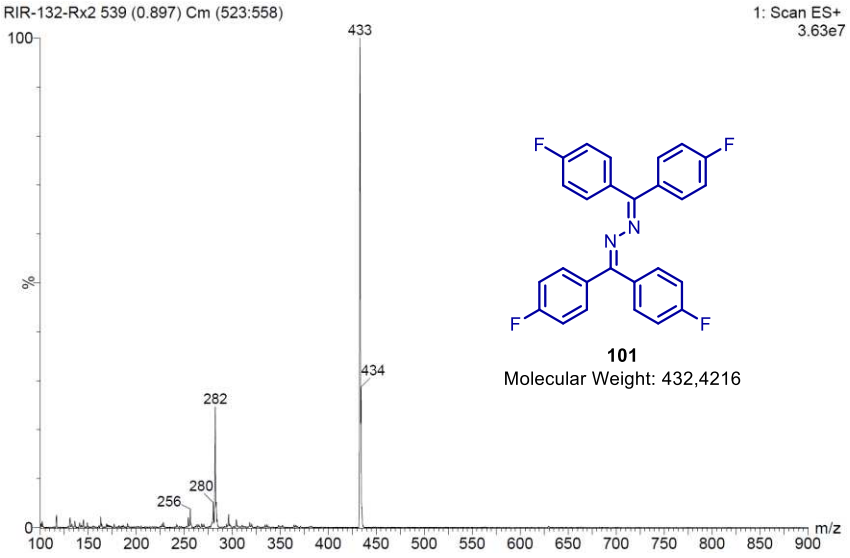

*Figure 12. ESI+ trace of dimer p-F **101**.*

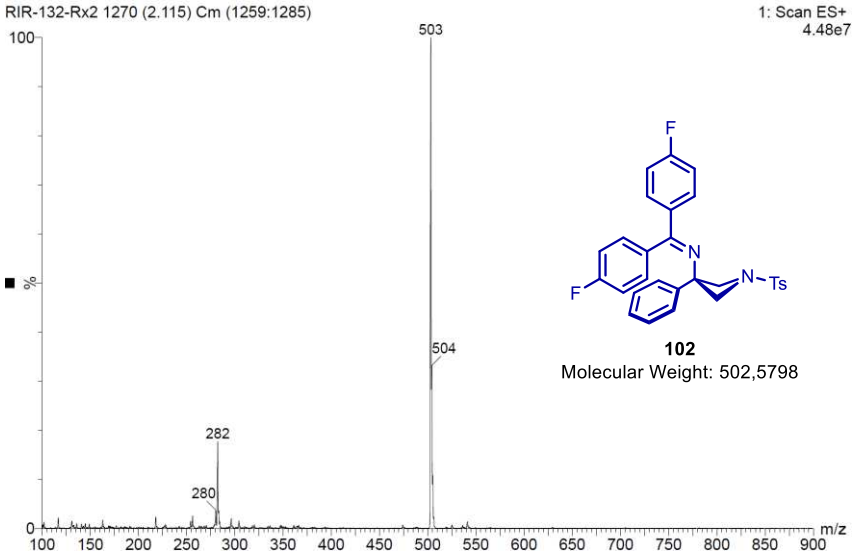

*Figure 13. ESI+ trace of azetidine p-F **102**.*

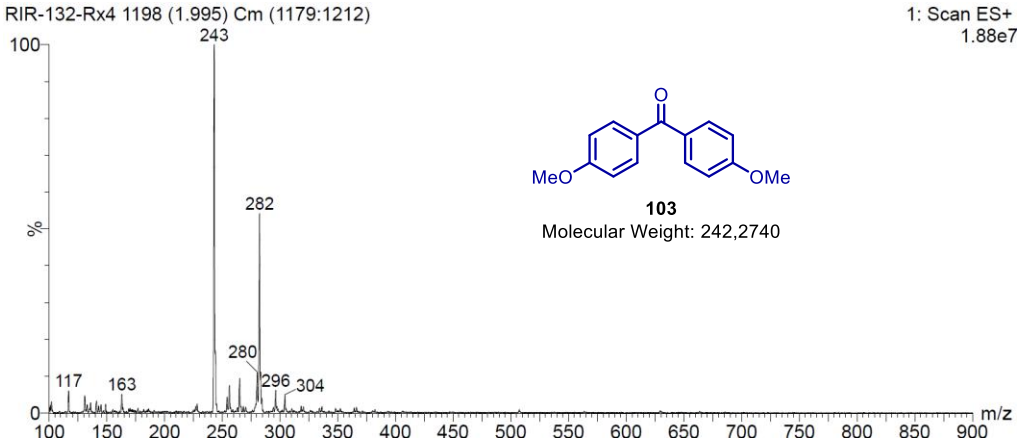

*Figure 14. ESI+ trace of bis-p-OMe BP **103**.*

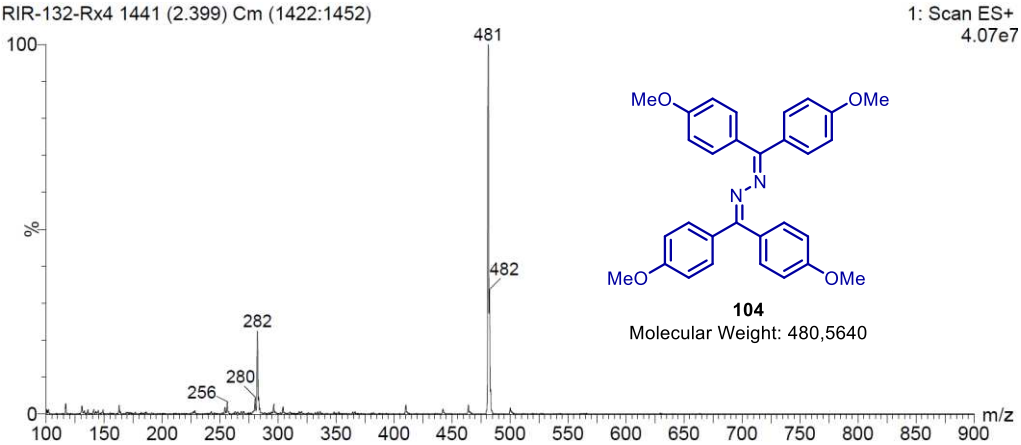

*Figure 15. ESI+ trace of p-OMe dime **104**.*

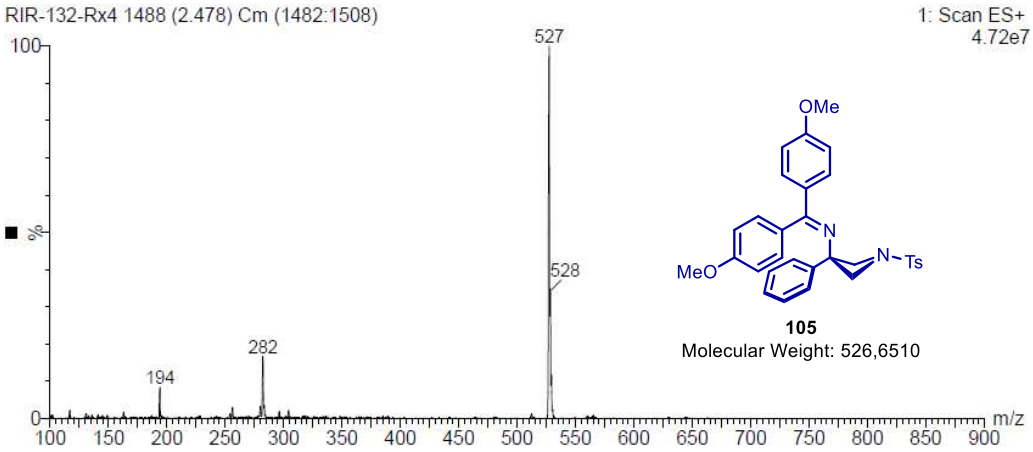

*Figure 16. ESI+ trace of azetidine p-OMe **105**.*

3.4.3. Synthesis and characterization

General Procedure A: Synthesis of 3-phenyl-1-azabicyclo[1.1.0]butane (31)

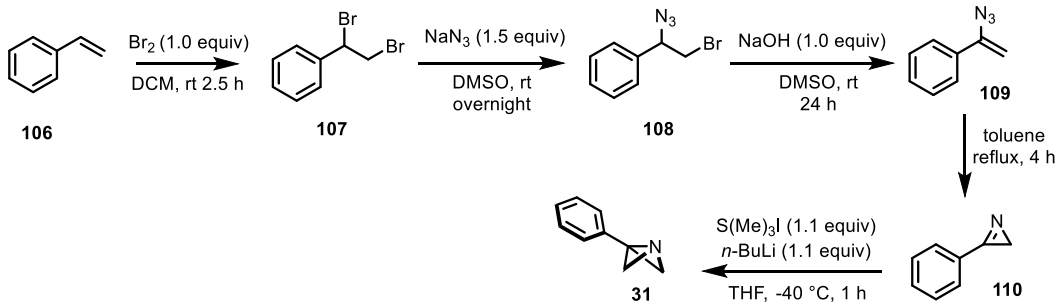

*Scheme 13. General procedure for the preparation of **ABB** 31.*

The synthesis of **31** was carried out combining two already described procedures[53,54] with some modifications. The synthetic plan is divided in Part 1 and Part 2.

Part 1. A 100 mL round bottom flask was charged with styrene **106** (20 mmol, 2.3 mL, 1.0 equiv) and dissolved in 18 mL of DCM. Bromine (20 mmol, 1.05 mL, 1.0 equiv) was added dropwise to the solution and stirred for 2.5 hours. After reaction completion, volatiles were removed under vacuum to get (1,2-dibromoethyl)benzene (**107**) as a clear orange solid (4.4 g, 93%), which was used for next step without requiring purification. (1,2-Dibromoethyl)benzene was dissolved in 28 mL of DMSO and to the resulting solution, NaN_3 (1.95 g, 30 mmol, 1.5 equiv) was added portionwise. The mixture became orange and thick with precipitated azido bromide and was stirred overnight at room temperature (**108**).

Afterwards, a solution of NaOH (0.80 g, 1.0 equiv) in 3 mL of water was added to the reaction mixture and stirred for 24 hours at room temperature. After reaction completion, a 2% aqueous solution of $NaHCO_3$ was added and extracted with dichloromethane. The extract was washed with distilled water. Dichloromethane was removed under vacuum and evaporated to yield the crude 1-azidostyrene as a yellowish oil (**109**. No purifications were required to conduct next step). The resulting product was dissolved with 40 mL of toluene and refluxed for 4 hours. After reaction completion, toluene was removed under reduced pressure, giving place to 3-phenyl-2*H*-azirine (**110**) as a brownish oil (84%, 16.8 mmol, 1.96 g). The NMR and ESI-MS spectra of all the intermediates were in accordance with the reported literature.

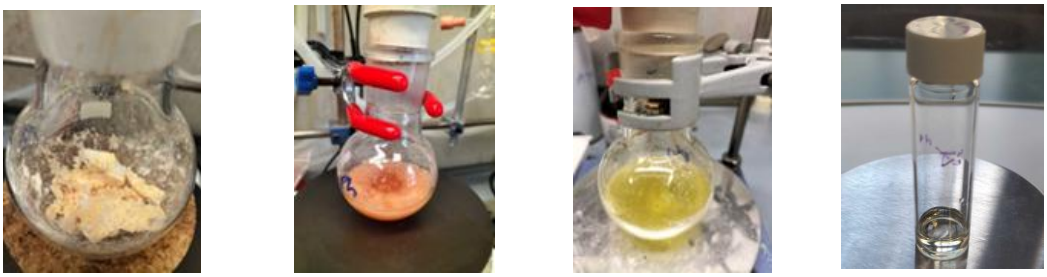

Figure 17. Identification of synthetic intermediates.

Supplementary Advice 1

To prevent residual bromine going to the vacuum pump, it is recommended to use a $Na_2S_2O_3$ (aqueous solution) trap during the distillation of DCM.

Supplementary Advice 2

We noticed that using old batches of styrene conducts to a brownish/black solid (**107**), diminishing the reaction yield. Filtering styrene through a short pad of silica does not have positive nor negative effects for this step.

Part 2. The Corey-Chaykovsky strategy. A two-neck oven dried 250 mL round bottom flask was charged with trimethylsulfonium iodide (3.6 g, 17.6 mmol, 1.1 equiv), evacuated and refilled with argon (use a needle). Freshly distilled THF 60 mL was added and cooled to -40 °C (acetonitrile/dry ice bath). To the resulting suspension, *n*-Butyl lithium (1.1 equiv, 2.3 M) was added (dropwise using an addition funnel, Figure 18, left). After addition was completed, the reaction was stirred for 30 minutes. Afterwards, a solution of 3-phenyl-2*H*-azirine (**110**, 16 mmol, 1.0 equiv,) in 5 mL of THF was slowly added (addition funnel, Figure 18, left). The resulting mixture was stirred at -40 °C for 30 minutes and quenched with cold water. The aqueous phase was extracted with DCM and the combined organic phases were dried with anhydrous sodium sulfate. Evaporation of the volatiles under reduced pressure gives place to the crude 3-phenyl-1-azabicyclo[1.1.0]butane (**31**) as a deep orange oil. The crude product is purified by distillation using classic distillation apparatus (Figure 18, middle) or a Kugelrohr apparatus (Figure 18, right), giving place to the desired product in 61% yield (1.27 g). Distillation conditions: 1.0 mbar, start at 80 °C finish at 100 °C. The pure product is a colorless liquid which can be stored at 4 °C.

^{1}H NMR (300 MHz, CDCl3) δ 7.45 – 7.30 (m, 5H), 2.80 (s, 2H), 1.55 (s, 2H). **^{13}C NMR** (75 MHz, CDCl3) δ 135.0, 128.6, 128.1, 127.6, 54.0, 31.9. **HRMS**: $[M+H]^+$ Calculated 132.0807, experimental 132.0809.

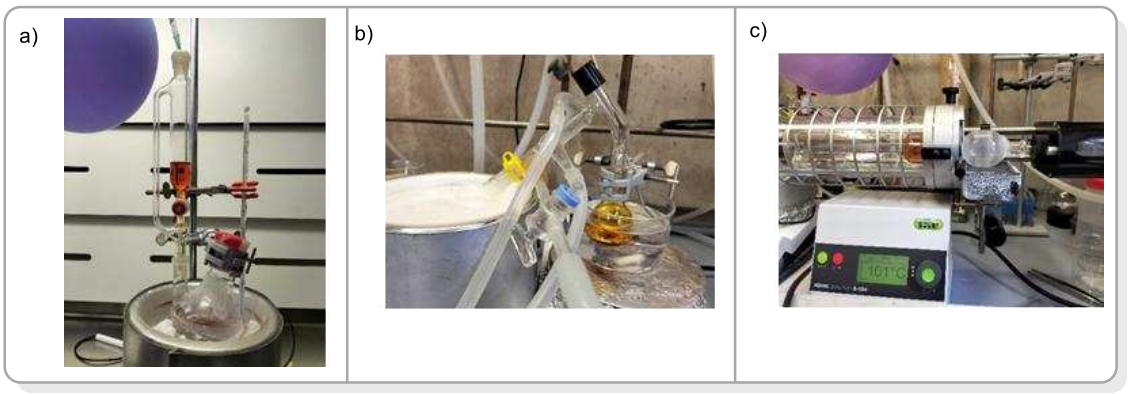

*Figure 18.Panel a: Reaction setup for the Corey-Chaykovsky strategy. Panel b: Classic distillation of **31**. Panel c: Kugelrohr distillation of ABB **31**.*

General Procedure B: Synthesis of 2-*exo*-methyl-3-phenyl-1-azabicyclobutane (SM1)

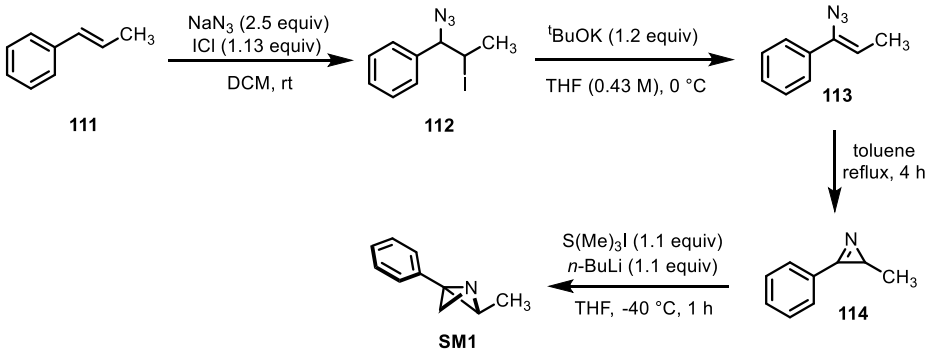

*Scheme 14. General procedure for the preparation of **SM1**.*

The synthesis of **SM1** was carried out combining two already described procedures[54] with some modifications. The synthetic plan is divided in Part 1 and Part 2.

Part 1. A suspension of NaN_3 (25 mmol, 1.6 g, 2.5 equiv,) in acetonitrile (10 mL) was carefully added to a solution of ICl (11.3 mmol, 1.83 g, 1.13 equiv,) in DCM (0.82 M, 13 mL) at -20 °C. The reaction was stirred at this temperature for 30 minutes. Then, a solution of (*E*)-prop-1-en-1- ylbenzene (**111**, 10 mmol, 1.0 equiv) in DCM (5 mL) was slowly added. The resulting mixture was stirred for additional 1 hour. The reaction was quenched with saturated aqueous $Na_2S_2O_3$ solution, and the organic materials were extracted two times with Et_2O. The combined extracts were washed with brine and dried using anhydrous sodium sulfate. After evaporation of the volatiles, the resulting crude material (**112**) was used immediately for the next step without further purification. To a solution of **112** in THF (0.43 M) was added potassium *tert*-butoxide (11.15 mmol, 1.25 g, 1,2 equiv) at 0 °C and stirred for 2 hours. After completion, the reaction mixture was filtered through a Celite plug and the solvent from the filtrate was removed under vacuum, giving place to (*Z*)-(1-azidoprop-1-en-1-yl)benzene (**113**) and was used for next step without requiring further purification. **113** was dissolved in 20 mL of toluene and was refluxed for 4 hours. After completion, evaporation of toluene conducted to 2-methyl-3-phenyl-2*H*-azirine (**114**) as a yellow oil, which was pure enough to conduct the next reaction.

Supplementary Advice 3

The use of a polycarbonate blast shield is recommended. The combination of NaN_3 and DCM might be replaced for the preparation of intermediate **112**, not tested in our lab, however .[55]

Part 2. General Procedure A, Part 2 was executed using 2-ethyl-3-phenyl-2*H*-azirine (**114**, 3.06 mmol, 402 mg, 1.0 equiv), trimethylsulfonium iodide (687 mg, 1.1 equiv), and *n*-Butyl lithium (1,1 equiv). The crude 2-*exo*-methyl-3-phenyl-1-azabicyclobutane (**SM1**) was obtained as a red oil. Kugelrohr distillation gives place to the pure product as a colorless oil in 70% yield (311 mg). Distillation conditions: 1.0 mbar, start at 80 °C finish at 100 °C. The pure product is a colorless liquid which can be stored at 4 °C.

^{1}H NMR (400 MHz, CDCl3) δ 7.43 (dd, J = 8.0, 1.7 Hz, 2H), 7.38 – 7.30 (m, 3H), 2.52 (d, J = 2.7 Hz, 1H), 1.71 (q, J = 5.8 Hz, 1H), 1.52 (dd, J = 2.7, 0.7 Hz, 1H), 1.16 (d, J = 5.8 Hz, 3H). **^{13}C NMR** (101 MHz, CDCl3) δ 133.1, 128.7, 128.3, 127.9, 62.2, 54.1, 35.1, 13.6. **HRMS**: $[M+H]^+$ Calculated 146.0963, experimental 146.0967.

General Procedure C: Synthesis of 2-exo-3-diphenyl-1-azabicyclo[1.1.0]butane (SM2)

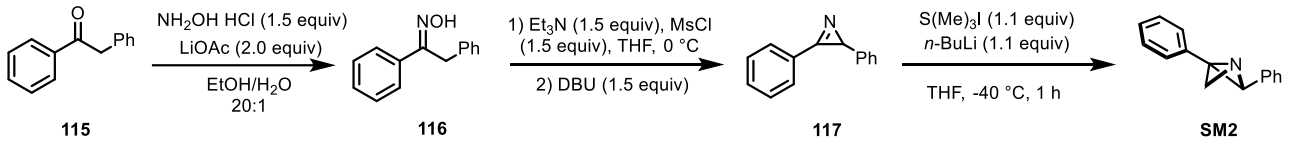

*Scheme 15. General procedure for the preparation of **SM2**.*

The synthesis of **SM2** was carried out combining two already described procedures with some modifications. The synthetic plan is divided in Part 1[53] and Part 2.

Part 1. To a solution of 1,2-diphenylethan-1-one (**115**, 10 mmol, 1.96 g, 1.0 equiv,) in a 20:1 mixture of EtOH/water (50 mL), hydroxylamine hydrochloride (15 mmol, 1.04 g, 1.5 equiv) and sodium acetate (2.0 equiv, 2.24 g) were added. The mixture was stirred under reflux for 2h. The reaction mixture was then diluted with 30% ethanol aqueous solution and allowed to cool to room temperature. When the operator detects the formation of crystals at the bottom of the vessel, filtrate the mixture. The solid was collected to afford pure 1,2-diphenylethan-1-one oxime (**116**) as a white solid (89% yield, 1.9 g). To a solution of the crude oxime (**116**, 10 mmol, 1.0 equiv) in dry THF was added triethylamine (15 mmol, 2.09 mL, 1.5 equiv,) and methanesulfonyl chloride (15 mmol, 1.16 mL, 1.5 equiv,) sequentially at 0 °C. The solution became cloudy after the addition of methanesulfonyl chloride. The resulting mixture was stirred for 30 min, and DBU (15 mmol, 2.23 mL, 1.5 equiv,) was dropwise added. After stirring for additional 30 min, the reaction mixture was passed through a pad of silica gel, washing with Et_2O. The mixture was concentrated in vacuo and the residue was purified by flash column chromatography, to give pure 2,3-diphenyl-2*H*-azirine (**117**) in 51% yield.

Part 2. General Procedure A, Part 2 was executed using 2,3-diphenyl-2*H*-azirine (**117**, 1.0 equiv, 4.36 mmol, 844 mg), trimethylsulfonium iodide (1.1 equiv, 980 mg), and *n*-Butyl lithium (1,1 equiv). The crude 2-exo-3-diphenyl-1-azabicyclo[1.1.0]butane (**SM2)** was obtained as a pale-yellow oil (62% yield, 560 mg) and was used without further purification for the photocatalyzed reaction.

^{1}H NMR (400 MHz, CDCl3) δ 7.29 – 7.21 (m, 10H), 2.72 (d, *J* = 2.7 Hz, 1H), 2.67 (s, 2H), 1.73 (d, *J* = 2.7 Hz, 1H). **^{13}C NMR** (101 MHz, CDCl3) δ 134.5, 132.2, 128.9, 128.4, 128.1, 128.0, 127.9, 127.8, 67.4, 52.1, 37.4. **HRMS**: $[M+H]^+$ Calculated 208.1121, experimental 208.1120.

General Procedure D: Synthesis of 2,3-dibromopropan-1-amine hydrobromide (SM3)

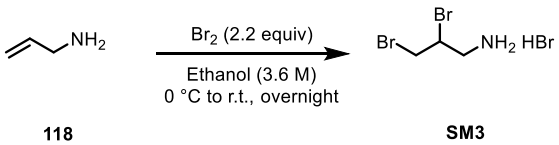

*Scheme 16. General procedure for the preparation of **SM3**.*

The following procedure has been adapted from the literature.[56] A solution of Br_2 (2.2 equiv, 99 mmol, 5 mL,) was very slowly added (dropwise) under vigorous stirring to ethanol (15 mL) in a 100 mL round bottom flask at 0 °C (Caution: exothermic, fuming). After the addition was complete, allylamine (**118**, 1.0 equiv, 45 mmol, 3.38 mL.) was added very slowly dropwise under vigorous stirring at 0 °C. The mixture was allowed to warm to room temperature and stirred at this temperature overnight. The precipitate was collected via suction filtration and washed with small portions of ice-cold Et_2O. The crude material was recrystallized from MeOH to give the hydrobromide salt **SM3** as colorless prisms (70% yield, 9.4 g after two crop collection). The spectroscopic data was identical to that reported in the literature. **^{1}H NMR** (400 MHz, CD3OD): δ 4.53 (ddd,

J= 13.7, 8.7, 3.9 Hz, 1H), 4.03 (dd, *J* = 11.0, 4.6 Hz, 1H), 3.88 (dd, *J* = 11.0, 8.7 Hz, 1H), 3.73 (dd, *J* = 14.0, 3.2 Hz,1H), 3.38 (d, *J* = 9.7 Hz, 1H).

Supplementary Advice 4

Use a big stirring bar, otherwise the thick precipitate might prevent good stirring.

General Procedure E: Preparation of Weinreb amides

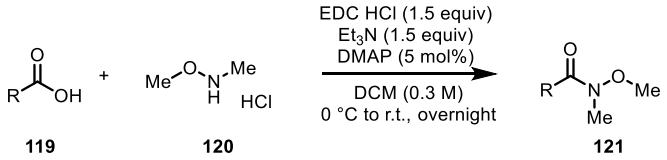

*Scheme 17. General procedure for the preparation of Weinreb amides **121**.*

The following procedure has been adapted from the literature.[34] An oven-dried flask was charged with thecorresponding carboxylic acid (**119**, 10.0 mmol, 1.0 equiv), DMAP (5.0 mol%), EDC•HCl (15.0 mmol, 1.5 equiv), and *N*,*O*-dimethylhydroxylamine hydrochloride (**120**, 12.0 mmol, 1.2 equiv). Under an argon atmosphere, dry DCM (0.3 M) was added into the flask. The reaction mixture was cooled to 0 °C and stirred for 10 minutes. Triethylamine (20.0 mmol, 2.0 equiv) was then added dropwise into the reaction vessel. Once the addition was finished, the ice bath was removed, and the mixture was stirred for 16 hours at room temperature. The reaction was quenched with a 10% solution of citric acid. After separation of the organic layer, the aqueous phase was neutralized with a saturated aqueous solution of $NaHCO_3$ and extracted with DCM. The organic layers were combined and washed with brine. The organic phase was then dried over anhydrous sodium sulfate, filtered, and concentrated under reduced pressure. The crude residue was purified by flash column chromatography to obtain the desired product.

General Procedure F: Preparation of "carbonyl ABBs"

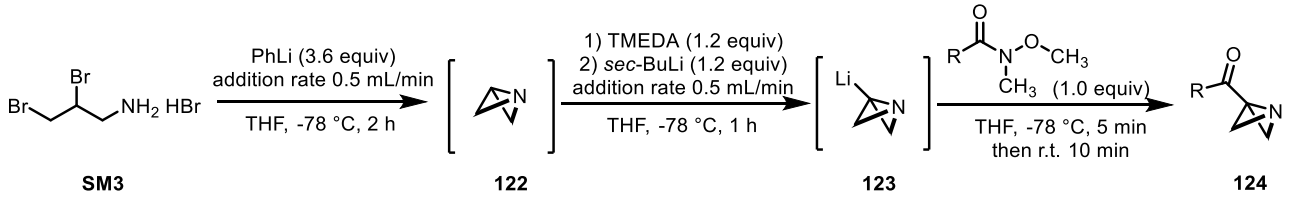

*Scheme 18. General procedure for the preparation of carbonyl ABBs **124**.*

The following procedure has been adapted from the literature.[32] Phenyl lithium (in Bu2O, 16.8 mmol, 3.6 equiv) was added dropwise (at a rate of 0.5 mL/min, syringe pump) to a suspension of salt **SM3** (1.67 g, 5.61 mmol, 1.2 equiv) in anhydrous tetrahydrofuran (20 mL) at −78 °C (dry ice/acetone). After complete addition, the resulting grey to black solution was stirred for further 2 hours at −78 °C. TMEDA (freshly distilled from CaH_2, 0.9 mL, 5.9 mmol, 1.2 equiv), followed by *sec*-butyl lithium (in hexane, 5.9 mmol, 1.2 equiv) were added dropwise (at a rate of 0.5 mL/min, syringe pump), and the resulting solution was stirred for another 1 hour at −78 °C. Then, the corresponding Weinreb amide (**121**, 4.68 mmol, 1.0 equiv) was added dropwise (at a rate of 0.5 mL/min, syringe pump) and the solution was stirred for 5 minutes before removing the cooling bath. Afterwards, the mixture was allowed to reach room temperature (approximately 10 minutes). Water (30 mL) was then added, phases were separated, and the aqueous one was extracted with ethyl acetate. The

combined organic phases were dried over anhydrous sodium sulfate, filtered, and concentrated under reduced pressure. The crude residue was purified by flash column chromatography.

Supplementary Advice 5

Do not remove Bu_2O for purification, liquid loading works perfectly.

*Figure 19. Reaction set-up for the synthesis of carbonyl ABBs **124**. Phenyl lithium addition is shown.*

General Procedure G: Preparation of sulfonyl ketimines

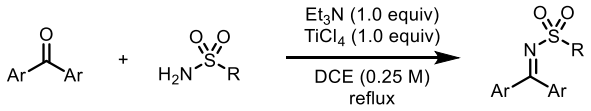

Scheme 19. General procedure for the preparation of sulfonyl ketimines.

The following procedure has been adapted from the literature.[32] To a solution of the desired ketone (5 mmol, 1.0 equiv) and a sulfonamide (5 mmol, 1.0 equiv) in dichloroethane (20 mL), Et_3N (10 mmol, 2.0 equiv) was added with stirring, followed by dropwise addition of $TiCl_4$ (2.5 mmol, 0.5 equiv). The reaction mixture was heated at reflux and monitored via TLC. After the ketone reacted completely or side-products started to appear, the mixture was allowed to cool to room temperature and filtered through Celite pad and washed with dichloromethane. The combined organic layer was washed with brine and dried with anhydrous sodium sulfate. The solvent was removed under reduced pressure and the crude was purified using flash column chromatography.

General Procedure H: Preparation of sulfonyl aldimines

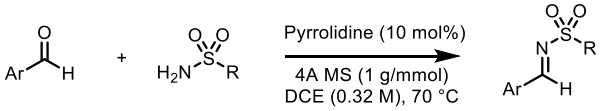

Scheme 20. General procedure for the preparation of sulfonyl aldimines.

The following procedure has been adapted from the literature. The corresponding sulfonamide (1.0 equiv, 5 mmol), 4 Å molecular sieves (previously activated at 150 °C under vacuum, 1 g/mmol) were added to a 100

mL two-neck RBF equipped with a condenser and DCE (0.32 M) was added. The corresponding aldehyde (1.0 equiv) and pyrrolidine (10 mol%) were added to the mixture and the resulting suspension was stirred at 70 °C for 48 hours. After completion, the reaction mixture was allowed to cool to room temperature, filtered through Celite pad and washed with DCM. The solvent was removed under reduced pressure and the product was purified by crystallization.

General procedure I: Synthesis of the "triazine family" photosensitizers (PS 86, PS 38 and PS 39).

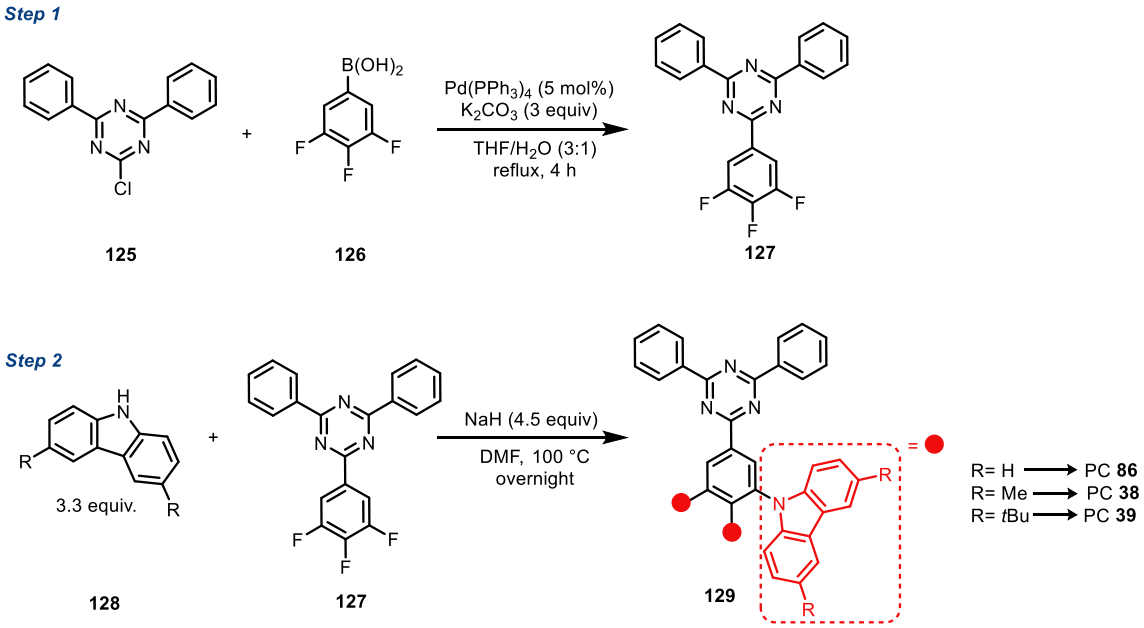

*Scheme 21. General procedure for the preparation of triazine family **129**.*

The following procedure has been adapted from the literature[57] and is divided in Step 1 and Step 2.

Step 1: 2-chloro-4,6-diphenyl-1,3,5-triazine (**125**, 5.32 g, 19.9 mmol, 1.0 equiv), (3,4,5-trifluorophenyl)boronic acid (**126,** 3.5 g, 19.9 mmol) and potassium carbonate (8.2 g, 59.90 mmol) were dissolved in tetrahydrofuran (150 ml) and distilled water (50 ml). The resulting mixture was bubbled with argon for 30 minutes, afterwards, $Pd(PPh_3)_4$ (1.15g, 5 mol%) was added. The reaction was refluxed for 10 hours under argon atmosphere and after completion, it was allowed to cool to room temperature. The mixture was filtered, the residue was washed with ethyl acetate and acetone to give 2,4-diphenyl-6-(3,4,5-trifluorophenyl)-1,3,5-triazine (**127**) as a white powder in 66% yield. The spectroscopic data is in full agreement with the reported literature.[49] **^{1}H NMR** (400 MHz, $CDCl_3$) δ 8.74 (d, J = 6.9 Hz, 4H), 8.42 (dd, J = 8.6, 6.8 Hz, 2H), 7.67 – 7.55 (m, 6H). **^{19}F NMR** (377 MHz, $CDCl_3$) δ -133.26 (dd, J = 20.3, 8.6 Hz, 2F), -154.02 (tt, J = 20.2, 6.9 Hz, 1F). MS = 364 m/z.

Step 2: A round bottom flask was charged with sodium hydride (4.95 mmol, 4.5 equiv, 60% in mineral oil) and was washed under an argon atmosphere with hexane (triplicate washing). Then, a solution of the proper carbazole derivative (**128**, 3.63 mmol, 3.3 equiv) in dry DMF (25 mL) was added to the reaction vessel at 0 °C. After 30 minutes of stirring, 2,4-diphenyl-6-(3,4,5-trifluorophenyl)-1,3,5-triazine (**127**, 1.1 mmol, 1.0 equiv) was added, and the flask was equipped with a condenser. The reaction mixture was stirred at 100 °C under an argon atmosphere overnight. After completion, the reaction was quenched with water, and the phases were separated. The aqueous phase was further extracted with diethyl ether. After washing with brine, the combined organics were dried over anhydrous sodium sulfate, and the solvent was removed under reduced

pressure. The resulting solid was washed thoroughly with cold diethyl ether, and the resulting solids were dried under vacuum, giving place to the corresponding final products, without requiring further purification. The NMR and ESI-MS spectra of triazines PS **68** and PS **38** are in full agreement with the reported literature.[49] For the undescribed triazine PS **39**, which was found to be the idoneous one for the photocatalyzed reaction under study.

Supplementary Advice 6

The operator should be aware of the hazards associated with the inherent thermal instability of NaH in DMF. In case of scaling-up step 2, NaH can be replaced by potassium *tert*-butoxide.[57]

General procedure J: Photocatalyzed difunctionalization of ABBs

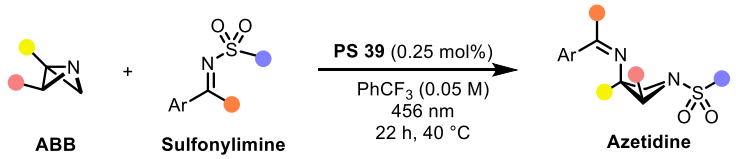

Scheme 22. General procedure for the preparation of Azetidines.

In an oven-dried 10 mL Schlenk tube containing an oven dried Teflon coated stirring bar, the corresponding ABB (0.1 mmol, 2 equiv) and sulfonylimine (0.05 mmol, 1 equiv) were dissolved using 0.6 mL of a solution of the PS **39** in $PhCF_3$ (2.1x10-4 M). The Schlenk tubes were closed with the proper greased glass stoppers. The resulting solution was subjected to three cycles of free-pump-thaw to remove the oxygen, and in the last cycle, the vessel was filled with argon. The reaction was irradiated under stirring for 22 hours using the photochemical setup shown in Figure 6. After completion, the resultant mixture was evaporated under reduced pressure and purified by flash column chromatography.

Supplementary Advice 7

Trifluorotoluene freshly distilled from phosphorus pentoxide is highly recommended.

General procedure K: Photocatalyzed difunctionalization of ABBs in a three-component protocol

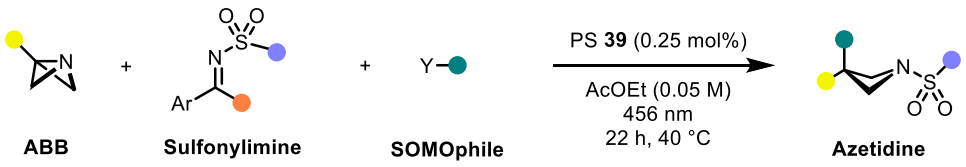

Scheme 23. General procedure for the preparation of Azetidines via three-component reaction.

In an oven-dried 10 mL Schlenk tube containing an oven dried Teflon coated stirring bar, the corresponding ABB (0.1 mmol, 2 equiv), sulfonylimine (0.05 mmol, 1 equiv) and the proper SOMOphile (0.075 mmol, 1.5 equiv) were dissolved using 0.6 mL of solution of the PS **39** in AcOEt (2.1x10-4 M). The Schlenk tubes were closed with the proper greased glass stoppers. The resulting solution was subjected to three cycles of free-pump-thaw to remove the oxygen and in the last cycle, the vessel was filled with argon. The reaction was irradiated under stirring for 22 hours using the photochemical setup shown in Figure 6. After completion, the resultant mixture was evaporated under reduced pressure and purified by flash column chromatography.

Supplementary Advice 8

Ethyl acetate freshly distilled from phosphorus pentoxide is highly recommended.

Characterization data of the employed starting materials and photosensitizers

3-(*p*-Tolyl)-1-azabicyclo[1.1.0]butane SM4

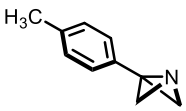

SM4

Following **General Procedure A** and starting from 1-methyl-4-vinylbenzene (10 mmol), the title compound was obtained as a clear yellowish liquid (43% yield, 62,3 mg) after Kugelrohr distillation. **^{1}H NMR** (400 MHz, $CDCl_3$) δ 7.30 (d, *J* = 7.9 Hz, 2H), 7.16 (d, *J* = 7.7 Hz, 2H), 2.77 (t, *J* = 1.2 Hz, 2H), 2.35 (s, 3H), 1.53 (t, *J* = 1.2 Hz, 2H). **^{13}C NMR** (101 MHz, $CDCl_3$) δ 137.80, 131.68, 129.23, 127.38, 53.91, 31.84, 21.24. **HRMS**: Calculated: $[M+Na]^+$ 168.0783, experimental 168.0786.

4-(1-Azabicyclo[1.1.0]butan-3-yl)benzonitrile SM5

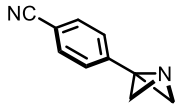

SM5

Following **General Procedure A** and starting from 4-vinylbenzonitrile (10 mmol, 624 mg), the title compound was obtained as a red solid in 40% yield. The product was used without further purification in the photochemical reaction. **^{1}H NMR** (400 MHz, $CDCl_3$) δ 7.67 (d, *J* = 8.3 Hz, 2H), 7.53 (d, *J* = 8.3 Hz, 2H), 2.87 (t, *J* = 1.1 Hz, 2H), 1.67 (t, *J* = 1.1 Hz, 2H). **^{13}C NMR** (101 MHz, $CDCl_3$) δ 141.19, 132.22, 128.27, 118.60, 111.75, 54.45, 31.24. **HRMS**: Calculated: $[M+Na]^+$ 179.0579, experimental 179.0571.

***N*-Methoxy-*N*-methylbenzamide SM6**[58]

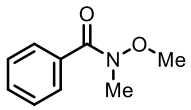

SM6

Following **General Procedure E** and starting from benzoic acid, the title compound was obtained in 58% yield. Purification: Petroleum ether/AcOEt (8:2) leads to the product as a white solid. **^{1}H NMR** (400 MHz, $CDCl_3$) δ 7.67 (d, *J* = 6.7 Hz, 2H), 7.48 – 7.36 (m, 3H),3.55 (s, 3H), 3.36 (s, 3H). **HRMS**: Calculated: $[M+Na]^+$ 188.0681, experimental 188.0687.

***N*-Methoxy-*N*-methylcyclohexanecarboxamide SM7**[59]

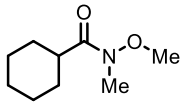

SM7

Following **General Procedure E** and starting from cyclohexanecarboxylic acid, the title compound was obtained in 82% yield. Purification: Petroleum ether/AcOEt (8:2) leads to the product as a white solid. **^{1}H NMR** (400 MHz, $CDCl_3$) δ 3.68 (s, 3H), 3.16 (s, 3H), 2.67 (s, 1H), 1.84 – 1.63 (m, 5H), 1.47 (qd, *J* = 13.1, 12.5, 3.9 Hz, 2H), 1.34 – 1.16 (m, 3H). **HRMS**: Calculated: $[M+Na]^+$ 194.1151, experimental 194.1153.

***(S)*-*N*-Methoxy-2-(6-methoxynaphthalen-2-yl)-*N*-methylpropanamide SM8**[60]

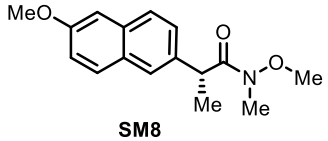

SM8

Following **General Procedure E** and starting from Naproxen, the title compound was obtained in quantitative yield as a white/yellowish solid. It was not necessary to perform further purification, the product was used for next reaction step. **^{1}H NMR** (400 MHz, $CDCl_3$) δ 7.70 (d, *J* = 8.6 Hz, 2H), 7.67 (d, *J* = 1.8 Hz, 1H), 7.42 (dd, *J* = 8.4, 1.8 Hz, 1H), 7.16 – 7.09 (m, 2H), 4.27 (bs, 1H), 3.91 (s, 3H), 3.40 (s, 3H), 3.17 (s, 3H), 1.51 (d, *J* = 7.0 Hz, 3H). **HRMS**: Calculated: $[M+H]^+$ 274.1437, experimental 274.1439.

(1-Azabicyclo[1.1.0]butan-3-yl)(phenyl)methanone SM9[34]

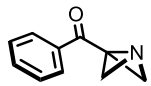

SM9

Following **General Procedure F** and starting from Weinreb amide *N*-methoxy-*N*methylbenzamide (**SM6**), the title compound was obtained in 69% yield (1.1 g, using 10 mmol of SM6). Purification: Petroleum ether/AcOEt (9:1) leads to the product as a colorless oil which can be redissolved and further evaporate using a mixture of hexane/AcOEt (1:1) to get the product as a solid. **^{1}H NMR** (400 MHz, $CDCl_3$) δ 7.97 (dt, *J* = 7.1, 1.4 Hz, 2H), 7.60 (td, *J* = 7.2, 1.4 Hz, 1H), 7.48 (t, *J* = 7.8 Hz, 2H), 3.08 – 3.01 (m, 2H), 1.75 (t, *J* = 1.3 Hz, 2H). **^{13}C NMR** (101 MHz, $CDCl_3$) δ 197.3, 136.7, 133.7, 129.0, 128.7, 56.8, 28.8. **HRMS**: Calculated: $[M+H]^+$ 160.0755, experimental 160.0758.

(1-Azabicyclo[1.1.0]butan-3-yl)(cyclohexyl)methanone SM10[34]

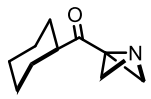

SM10

Following **General Procedure F** and starting from Weinreb amide *N*-methoxy-*N*methylcyclohexanecarboxamide (**SM7**), the title compound was obtained in 73% yield (1,2 g, using 10 mmol of SM7). Purification: Petroleum ether/AcOEt (9:1) leads to the product as a pale-yellow oil. **^{1}H NMR** (400 MHz, $CDCl_3$) δ 2.92 (s, 2H), 2.56 (tt, *J* = 11.4, 2.9 Hz, 1H), 1.88 – 1.80 (m, 4H), 1.67 –1.62 (m, 1H), 1.53 (s, 2H), 1.45 – 1.37 (m, 2H), 1.31 – 1.20 (m, 3H) ppm. **^{13}C NMR** (100 MHz, $CDCl_3$) δ 209.2, 55.0, 47.1, 29.1, 28.4, 25.7, 25.5. **HRMS**: Calculated: $[M+H]^+$ 166.1226, experimental 166.1225.

1-(1-Azabicyclo[1.1.0]butan-3-yl)-2-(6-methoxynaphthalen-2-yl)propan-1-one 69[34]

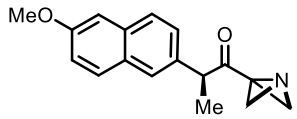

69

Following **General Procedure F** and starting from Weinreb amide *N*-methoxy-2-(6-methoxynaphthalen-2-yl)-*N*-methylpropanamide (**SM8**), the title compound wasobtained in 54% yield (1.44 g using 10 mmol of SM8). Purification: Hexane/AcOEt(9:1) leads to the product as a colorless liquid. **^{1}H NMR** (400 MHz, $CDCl_3$) δ 7.71(dd, *J* = 10.7, 8.7 Hz, 2H), 7.58 – 7.56 (m, 1H), 7.28 (d, *J* = 8.4 Hz, 1H), 7.16 (dd, *J* = 8.9, 2.5 Hz, 1H), 7.12 (d, *J* =2.5 Hz, 1H), 4.10 (q, *J* = 6.8 Hz, 1H), 3.92 (s, 3H), 2.88 (s, 2H), 1.48 (d, *J* = 6.8 Hz, 2H), 1.40 (dd, *J* = 4.7, 1.6 Hz,2H). **^{13}C NMR** (101 MHz, $CDCl_3$) δ 206.3, 157.8, 134.9, 133.6, 129.2, 129.0, 127.7, 126.6, 126.3, 119.2, 105.5,55.9, 55.5, 55.3, 49.6, 29.6, 18.2. **HRMS**: Calculated: $[M+H]^+$ 268.1332, experimental 268.1336.

***N*-(Diphenylmethylene)-4-methylbenzenesulfonamide 32**

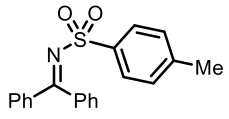

32

Following **General Procedure G** and starting from 4-methylbenzenesulfonamide and benzophenone, the title compound was obtained in 77% yield. Purification: Petroleum ether/AcOEt (95:5) leads to the product as a light yellow solid. **^{1}H NMR** (400 MHz, $CDCl_3$) δ 7.84 (dd, *J* = 8.3, 1.5 Hz, 2H), 7.57 – 7.51 (m, 6H), 7.43 (d, *J* = 7.7 Hz, 4H), 7.29 (d, *J* = 8.1 Hz, 2H), 2.44 (s, 3H). **^{13}C NMR** (101 MHz, $CDCl_3$) δ 178.9, 143.5, 138.6, 129.5, 128.3, 127.5, 21.7.

***N*-(bis(4-Methoxyphenyl)methylene)-4-methylbenzenesulfonamide SM11**

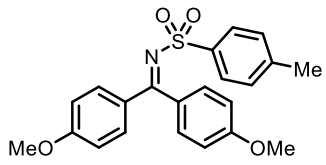

SM11

Following **General Procedure G** and starting from 4-methylbenzenesulfonamide and bis(4-methoxyphenyl)methanone, the title compound was obtained in 49% yield. Purification: Petroleum ether/AcOEt (8:2) leads to the product as a grey solid.**^{1}H NMR** (400 MHz, $CDCl_3$) δ 7.84 (d, *J* = 8.0 Hz, 2H), 7.54 (d, *J* = 8.4 Hz, 4H), 7.29 (d, *J* = 8.0 Hz, 2H), 6.91 (d, *J* = 8.4

Hz, 4H), 3.87 (s, 3H), 2.43 (d, *J* = 3.5 Hz, 3H). **^{13}C NMR** (101 MHz, $CDCl_3$) δ 165.8, 162.0,144.5, 131.0, 129.0, 127.2, 126.1, 125.9, 114.8, 55.4, 21.5.

_N_-(bis(4-fluorophenyl)methylene)-4-methylbenzenesulfonamide SM12

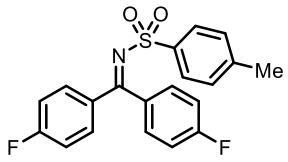

SM12

Following **General Procedure G** and starting from 4-methylbenzenesulfonamide and bis(4-fluorophenyl)methanone, the title compound was obtained in 71% yield. Purification: Petroleum ether/AcOEt (8:2) leads to the product as a white solid.**1H NMR** (400 MHz, $CDCl_3$) δ 7.83 (d, *J* = 8.0 Hz, 2H), 7.56 (bs, 4H), 7.31 (d, *J* =8.0 Hz, 2H), 7.12 (bs, 4H), 2.45 (s, 3H).

4-Methyl-_N_-(4-methylbenzylidene)benzenesulfonamide 71

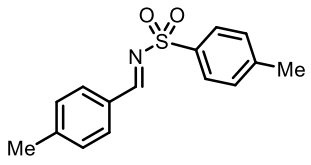

71

Following **General Procedure H** and starting from 4-methylbenzenesulfonamide and 4-methylbenzaldehyde, the title compound was obtained in 61% yield. Purification: Precipitation from Et2O at 0 °C leads to a white solid. **^{1}H NMR** (400 MHz, $CDCl_3$) δ 8.98 (d, *J* = 1.5 Hz, 2H), 7.91 – 7.86 (m, 2H), 7.81 (dd, *J* = 8.3, 1.9 Hz, 2H), 7.36 – 7.32 (m, 2H), 7.30 – 7.26 (m, 2H), 2.42 (s, 3H). **^{13}C NMR** (101 MHz, $CDCl_3$) δ 170.1, 146.5, 144.6, 135.5, 131.6, 130.1, 130.0, 129.9, 128.1, 126.6, 22.1, 21.8.

_N_-(4-Fluorobenzylidene)-4-methylbenzenesulfonamide SM13

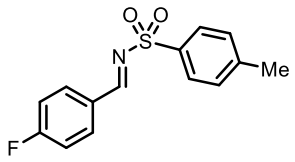

SM13

Following **General Procedure H** and starting from 4-methylbenzenesulfonamide and 4-fluorobenzaldehyde, the title compound was obtained in 69% yield. Purification: Precipitation from Et_2O at 0 °C leads to a yellow solid. **^{1}H NMR** (400 MHz, $CDCl_3$) δ 8.99 (s, 1H), 7.95 (ddd, *J* = 8.9, 5.4, 1.7 Hz, 2H), 7.88 (dd, *J* = 8.3, 1.7 Hz, 2H), 7.34 (dd, *J* = 8.4, 1.9 Hz, 2H), 7.16 (td, *J* = 8.6, 2.2 Hz, 2H), 2.43 (s, 3H). **^{13}C NMR** (101 MHz, $CDCl_3$) δ 13C NMR (101 MHz, CDCl3) δ 168.7 (d, *J* = 2.7 Hz), 166.9 (d, *J* = 258.4 Hz), 144.8, 135.2, 133.9 (d, *J* = 9.7 Hz), 130.0, 128.9 (d, *J* = 2.9 Hz), 128.2, 116.8 (d, *J* = 22.2 Hz), 21.8. **^{19}F NMR** (377 MHz, $CDCl_3$) δ -101.1 (d, *J* = 2.6 Hz).

_N_-(Diphenylmethylene)benzenesulfonamide SM14

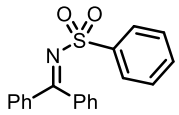

SM14

Following **General Procedure G** and starting from benzenesulfonamide and benzophenone, the title compound was obtained in 88% yield. Purification: Petroleum ether/AcOEt (8:2) leads to the product as a white solid. **^{1}H NMR** (400 MHz, $CDCl_3$) δ 7.96 (dd, *J* = 7.5, 1.8 Hz, 2H), 7.63 – 7.47 (m, 9H), 7.43 (t, *J* = 7.5 Hz, 4H). **^{13}C NMR** (101 MHz, $CDCl_3$) δ 179.3, 141.5, 133.3, 132.7, 129.4, 128.9, 128.3, 127.8, 127.4.

_N_-(Diphenylmethylene)-4-(trifluoromethyl)benzenesulfonamide SM15

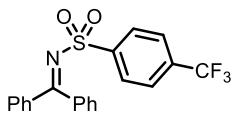

SM15

Following **General Procedure G** and starting from 4-(trifluoromethyl) benzenesulfonamide and benzophenone, the title compound was obtained in 91% yield. Purification: Petroleum ether/AcOEt (85:15) leads to the product as a white fluffy solid. **^{1}H NMR** (400 MHz, $CDCl_3$) δ 8.09 (d, *J* = 8.2 Hz, 2H), 7.77 (d, *J* = 8.2 Hz, 2H), 7.58 (t, *J* = 7.4 Hz, 6H), 7.45 (apparent t, *J* = 7.6 Hz, 4H). **^{13}C NMR** (101 MHz, $CDCl_3$) δ 180.4, 145.1, 134.3 (q, *J* = 33.0 Hz), 128.4, 127.9, 126.1 (q, *J* = 3.7 Hz), 123.5 (q, *J* = 274.4 Hz). **^{19}F NMR** (377 MHz, $CDCl_3$) δ -63.07.

***N*-(Diphenylmethylene)pyridine-3-sulfonamide SM16**

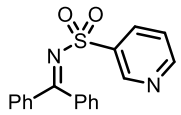

SM16

Following **General Procedure G** and starting from pyridine-3-sulfonamide and benzophenone, the title compound was obtained in 86% yield. Purification: Petroleum ether/AcOEt (85:15 to 7:30) leads to the product as a yellowish oil. **^{1}H NMR** (400 MHz, $CDCl_3$) δ 9.19 (d, *J* = 1.8 Hz, 1H), 8.80 (dd, *J* = 4.9, 1.6 Hz, 1H), 8.22 (ddd, *J* = 8.0, 2.2, 1.7 Hz, 1H), 7.81 (dd, *J* = 8.3, 1.3 Hz, 1H), 7.69 – 7.37 (m, 10H). **^{13}C NMR** (101 MHz, $CDCl_3$) δ 180.2, 153.1, 148.4, 138.1, 137.5, 134.9, 134.2, 132.3, 130.1, 128.4, 128.3, 123.7, 123.4.

***N*-(Diphenylmethylene)thiophene-2-sulfonamide SM17**

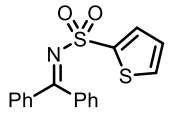

SM17

Following **General Procedure G** and starting from thiophene-2-sulfonamide and benzophenone, the title compound was obtained in 66% yield. Purification: Petroleum ether/AcOEt (75:25) leads to the product as a pale orange solid. **^{1}H NMR** (400 MHz, $CDCl_3$) δ 7.65 – 7.59 (m, 3H), 7.57 (apparent t, *J* = 7.4 Hz, 5H), 7.45 (t, *J* = 7.6 Hz, 4H), 7.08 – 6.99 (m, 1H). **^{13}C NMR** (101 MHz, $CDCl_3$) δ 179.0, 142.4, 132.4, 132.4, 128.3, 127.0.

***N*-(Diphenylmethylene)naphthalene-2-sulfonamide SM18**

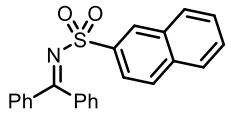

SM18

Following **General Procedure G** and starting from naphthalene-2-sulfonamide and benzophenone, the title compound was obtained in 75% yield. Purification: Petroleum ether/AcOEt (85:15 to 7:30) leads to the product as a yellowish oil. **^{1}H NMR** (400 MHz, $CDCl_3$) δ 8.44 (s, 1H), 7.98 (d, *J* = 5.7 Hz, 1H), 7.92 (dd, *J* = 8.1, 3.8 Hz, 1H), 7.81 (d, *J* = 7.6 Hz, 1H), 7.55 (ddt, *J* = 33.2, 15.3, 10.2 Hz, 9H), 7.42 (d, *J* = 7.6 Hz, 4H). **^{13}C NMR** (101 MHz, $CDCl_3$) δ 179.2, 138.3, 137.7, 135.0, 132.5, 132.2, 130.2, 129.5, 129.2, 128.9, 128.6, 128.4, 120.0, 127.4, 123.01.

***N*-(Diphenylmethylene)methanesulfonamide 32a**

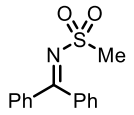

32a

Following **General Procedure G** and starting from methanesulfonamide and benzophenone, the title compound was obtained in 81% yield. Purification: Petroleum ether/AcOEt (8:2) leads to the product as a yellowish solid. **^{1}H NMR** (400 MHz, $CDCl_3$) δ 7.85 (d, *J* = 1.4 Hz, 1H), 7.60 – 7.50 (m, 5H), 7.43 (d, *J* = 7.7 Hz, 5H), 7.29 (d, *J* = 8.1 Hz, 2H), 2.44 (s, 3H). **^{13}C NMR** (101 MHz, $CDCl_3$) δ 178.9, 143.5, 138.6, 129.5, 128.3, 127.5, 21.7.

***N*-(Diphenylmethylene)propane-1-sulfonamide SM19**

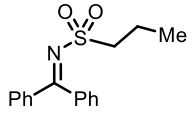

SM19

Following **General Procedure G** and starting from propane-1-sulfonamide and benzophenone, the title compound was obtained in 74% yield. Purification: Petroleum ether/AcOEt (9:1) leads to the product as a white solid. **^{1}H NMR** (400 MHz, $CDCl_3$) δ 7.56 (t, *J* = 7.3 Hz, 6H), 7.46 (d, *J* = 7.6 Hz, 4H), 3.35 – 3.22 (m, 2H), 2.02 (ddd, *J* = 10.2, 7.6, 5.4 Hz, 2H), 1.12 (t, *J* = 7.5 Hz, 3H). **^{13}C NMR** (101 MHz, $CDCl_3$) δ 179.9, 135.8, 133.5, 130.8, 128.1, 57.0, 17.4, 13.2.

***N*-(Diphenylmethylene)propane-2-sulfonamide SM20**

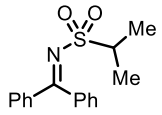

SM20

Following **General Procedure G** and starting from propane-2-sulfonamide and benzophenone, the title compound was obtained in 79% yield. Purification: Petroleum ether/AcOEt (9:1) leads to the product as a white fluffy solid. **^{1}H NMR** (400 MHz, $CDCl_3$) δ 7.67 – 7.54 (m, 10H), 3.43 (hept, *J* = 6.8 Hz, 1H), 1.52 (d, *J* = 6.8 Hz, 3H). **^{13}C NMR** (101 MHz, $CDCl_3$) δ 180.3, 133.3, 130.5, 128.0, 55.0, 16.6.

***N*-(Diphenylmethylene)-4-(5-(*p*-tolyl)-3-(trifluoromethyl)-1*H*-pyrazol-1-yl)benzenesulfonamide 67**

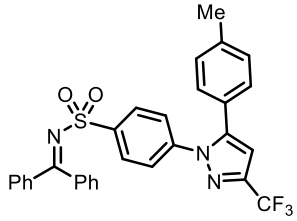

67

Following **General Procedure G** and starting from celecoxib and benzophenone, the title compound was obtained in 54% yield. Purification: Petroleum ether/AcOEt (9:1) leads to the product as a white solid. **$_{1}$H NMR** (400 MHz, $CDCl^3$) δ 7.95 (d, *J* =8.7 Hz, 2H), 7.90 (d, *J* = 8.7 Hz, 1H), 7.81 (d, *J* = 6.9 Hz, 1H), 7.63 – 7.53 (m, 4H),7.47 (dddd, *J* = 13.0, 10.8, 7.5, 4.0 Hz, 6H), 7.22 – 7.16 (m, 2H), 7.13 (d, *J* = 7.8 Hz, 2H), 6.74 (d, *J* = 3.0 Hz, 1H).**$_{13}$C NMR** (101 MHz, $CDCl^3$) δ 179.8, 145.3, 144.2, 143.9, 142.4, 141.0, 139.8, 129.8, 128.8, 128.4, 128.3, 125.8, 125.3, 122.2, 106.3, 21.3. **$_{19}$F NMR** (377 MHz, $CDCl^3$) δ -62.41.

***N*-(4-Methylbenzylidene)pyridine-3-sulfonamide 72**

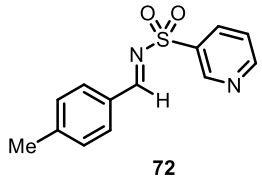

72

Following **General Procedure H** and starting from pyridine-3-sulfonamide and 4-methylbenzaldehyde, the title compound was obtained in 41% yield. Purification: Precipitation from Et_2O at 0 °C leads to a yellowish solid. **^{1}H NMR** (300 MHz, $CDCl_3$): δ 9.08 (s, 1H), 9.04 (d, *J* = 1.7 Hz, 1H), 8.80 (dd, *J* = 1.7, 4.9 Hz, 1H), 8.27 (dt, *J* = 8.0, 1.9 Hz, 1H), 7.88 (d, *J* = 8.3 Hz, 2H), 7.43 (d, *J* = 4.9, 8.0 Hz, 1H), 7.36 (d, *J* = 8.0 Hz, 2H), 2.43 (s, 3H). **^{13}C NMR** (75.5 MHz, $CDCl_3$): δ 167.5, 155.0, 152.9, 145.0, 136.8, 134.4, 129.8, 128.2, 124.1, 21.6.

***N*-(4-Methylbenzylidene)-4-(5-(*p*-tolyl)-3-(trifluoromethyl)-1*H*-pyrazol-1-yl)benzenesulfonamide 73**

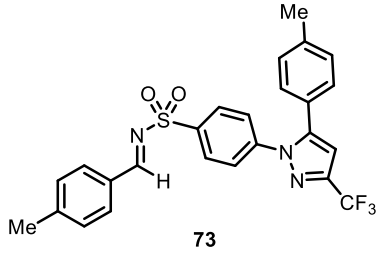

73

Following **General Procedure H** and starting from celecoxib and 4-methylbenzaldehyde, the title compound was obtained in 41% yield. Purification: Precipitation from Et_2O at 0 °C leads to a white solid. **^{1}H NMR (600 MHz, CD_2Cl_2)** δ 9.04 (s, 1H), 8.00 (d, *J* = 8.8 Hz, 2H), 7.88 (d, *J* = 8.2 Hz, 2H), 7.55 (d, *J* = 8.8 Hz, 2H), 7.38 (d, *J* = 8.5 Hz, 2H), 7.23 (d, *J* = 8.5 Hz, 2H), 7.18 (d, *J* = 8.1 Hz, 2H), 6.81 (s, 1H), 2.48 (s, 3H), 2.41 (s, 3H). **^{13}C NMR** (151 MHz, CD_2Cl_2) δ 171.1, 147.1, 145.4, 143.8 (q, *J* = 38.4 Hz), 137.9, 131.5, 130.1, 129.7, 128.9, 128.8, 125.7, 125.4, 106.3 (q, *J* = 2.0 Hz), 21.8, 21.0. **^{19}F NMR** (377 MHz, $CDCl_3$) δ -62.46.

9,9',9''-(5-(4,6-Diphenyl-1,3,5-triazin-2-yl)benzene-1,2,3-triyl)tris(9*H*-carbazole) PS 95[57]

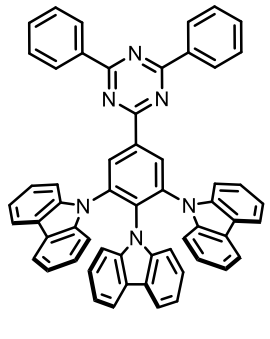

95

Following **General Procedure I** and using 9*H*-carbazole, the title compound was obtained in 48% yield as a tanned solid**. ^{1}H NMR** (400 MHz, DMSO): δ 6.68 (t, *J* = 8.2 Hz, 2H), 6.78 (t, *J* = 7.0 Hz, 2H), 7.05-7.08 (m, 8H), 7.25 (d, *J* = 8.4 Hz, 2H), 7.43-7.49 (m, 6H), 7.56 (t, *J* = 7.8 Hz, 4H), 7.65 (t, *J* = 7.8 Hz, 2H), 7.89-7.93 (m, 4H), 8.66 (d, *J* =8.8 Hz, 4H), 9.18 (s, 2H).

9,9',9''-(5-(4,6-Diphenyl-1,3,5-triazin-2-yl)benzene-1,2,3-triyl)tris(3,6-dimethyl-9*H*-carbazole) PS 38[57]

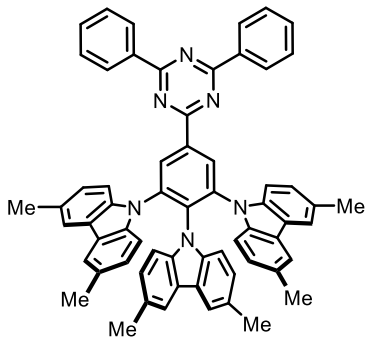

38

Following **General Procedure I** and using 3,6-dimethyl-9*H*-carbazole, the title compound was obtained in 71% (694 mg) yield as an olive green solid. **^{1}H NMR** (400 MHz, $CDCl_3$) δ 9.11 (s, 2H), 8.73 – 8.67 (m, 4H), 7.58 (d, *J* = 9.3 Hz, 6H), 7.57 – 7.47 (m, 4H), 7.16 (s, 3H), 7.13 (d, *J* = 8.3 Hz, 4H), 6.91 – 6.82 (m, 6H), 6.49 (dd, *J* = 8.6, 1.7 Hz, 2H), 2.39 (s, 12H), 2.20 (s, 6H).

9,9',9''-(5-(4,6-Diphenyl-1,3,5-triazin-2-yl)benzene-1,2,3-triyl)tris(3,6-di-*tert*-butyl-9*H*-carbazole) PS 39

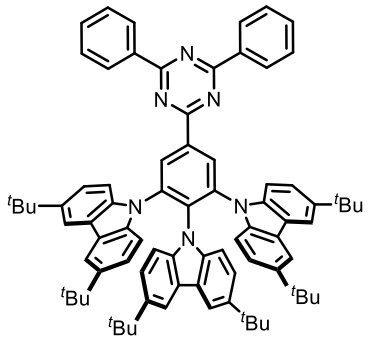

39

Following **General Procedure I** and using from 3,6-di-*tert*-butyl-9*H*-carbazole, the title compound was obtained in 84% yield (1.05 g) as a pale green solid. Suitable crystals for X-ray analysis were obtained by slow evaporation from CD_2Cl_2. **^{1}H NMR** (400 MHz, CD_2Cl_2) δ 9.21 (s, 2H), 8.80 – 8.71 (m, 4H), 7.84 (d, *J* = 1.8 Hz, 4H), 7.66 – 7.59 (m, 2H), 7.54 (dd, *J* = 8.2, 6.7 Hz, 4H), 7.36 (d, *J* = 1.9 Hz, 2H), 7.15 (d, *J* = 8.6 Hz, 4H), 7.10 (dd, *J* = 8.7, 1.9 Hz, 4H), 6.81 (d, *J* = 8.6 Hz, 2H), 6.64 (dd, *J* = 8.6, 2.0 Hz, 2H), 1.37 (s, 36H), 1.24 (s, 18H). **^{13}C NMR** (101 MHz, CD_2Cl_2) δ 172.1, 170.3, 143.0, 142.8, 138.7, 137.9, 137.4, 137.2, 135.8, 132.8, 129.7, 129.0, 128.7, 124.1, 123.7, 123.1, 122.3, 115.9, 115.3, 109.8, 109.4, 34.5, 34.2, 31.6, 31.5. **HRMS**: Calculated: $[M+H]^+$ 1141.6830, experimental: 1141.6824.

Characterization data for the sulfonyl azetdines

1,1-Diphenyl-*N*-(3-phenyl-1-tosylazetidin-3-yl)methanimine 34

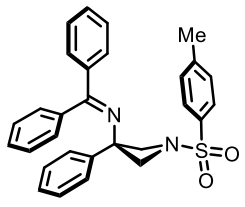

34

Following **General Procedure J**, starting from **31** and **32** using $PhCF_3$, the title compound was obtained in 79% yield (average of three reactions of 0.05 mmol). Purification: Hexane/AcOEt (9:1) or PE/AcOEt (91:9 to 85:15) leads to the product as a white solid (**Rf** of **4** = 0.6, **Rf** of **3** = 0.2). Suitable crystals for X-ray diffraction analysis were grown from slow evaporation of hexane/CHCl3. **^{1}H NMR** (400 MHz, CD_2Cl_2) δ 7.59 (d, *J* = 8.2 Hz, 2H), 7.43 – 7.33 (m, 9H), 7.33 – 7.26 (m, 5H), 7.24 (apparent t, *J* = 7.6 Hz, 2H), 6.66 (dd, *J* = 7.9, 1.5 Hz, 2H), 3.74 (d, *J* = 8.4 Hz, 2H), 3.70 (d, *J* = 8.5 Hz, 2H), 2.37 (s, 3H). **^{13}C NMR** (100 MHz, CD_2Cl_2) δ 167.6, 145.5, 144.5, 140.0, 137.0, 130.5, 130.5, 129.8, 129.5, 128.8, 128.7, 128.6, 128.3, 128.0, 127.9, 127.3, 125.2, 65.1, 60.9, 21.4. **HRMS**: Calculated: $[M+H]^+$ 467.1787, experimental: 467.1781.

1,1-bis(4-Methoxyphenyl)-*N*-(3-phenyl-1-tosylazetidin-3-yl)methanimine 45

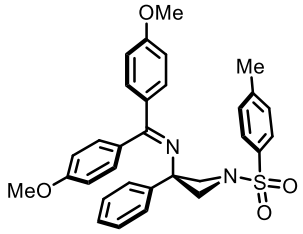

45

Following **General Procedure J**, starting from **31** and **SM11** using $PhCF_3$, the title compound was obtained in 72% yield (average of three reactions of 0.05 mmol). Purification: Hexane/AcOEt (85:15 to 70:30) leads to the product as a white solid. **^{1}H NMR** (400 MHz, $CDCl_3$) δ 7.64 (d, *J* = 8.0 Hz, 2H), 7.47 (d, *J* = 7.7 Hz, 2H), 7.38 (d, *J* = 8.5 Hz, 2H), 7.33 (dd, *J* = 8.0, 3.5 Hz, 4H), 7.28 (d, *J* = 7.3 Hz, 1H), 6.82 (d, *J* = 8.7 Hz, 2H), 6.72 (d, *J* = 8.5 Hz, 2H), 6.61 (d, *J* = 8.4 Hz, 2H), 3.83 (s, 3H), 3.80 (s, 3H), 3.77 (d, *J* = 8.4 Hz, 2H), 3.74 (d, *J* = 8.4 Hz, 2H), 2.39 (s, 3H). **^{13}C NMR** (100 MHz, $CDCl_3$) δ 166.7, 161.5, 160.3, 145.9, 144.1, 133.1, 130.9, 129.6, 129.5, 129.2, 128.7, 128.6, 127.2, 125.1, 113.5, 113.2, 65.3, 60.7, 55.4, 55.3, 21.6. **HRMS**: Calculated: $[M+H]^+$ 527.1999, experimental: 527.1996.

1,1-bis(4-Fluorophenyl)-*N*-(3-phenyl-1-tosylazetidin-3-yl)methanimine 46

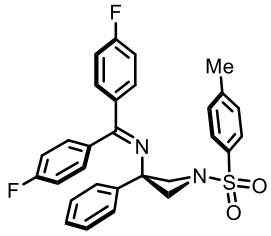

46

Following **General Procedure J**, starting from **31** and **SM12** using $PhCF_3$, the title compound was obtained in 44% yield (average of three reactions of 0.05 mmol). Applying **General Procedure J** but conducting the reaction in 0.5 mmol scale allowed the obtention of the product in 40% yield. Purification: Hexane/AcOEt (9:1) leads to the product as a whitish oil. **^{1}H NMR** (400 MHz, $CDCl_3$) δ 7.66 (d, *J* = 8.2 Hz, 2H), 7.46 (apparent d, *J* = 5.6 Hz, 1H), 7.44 (apparent d, *J* = 5.5 Hz, 1H), 7.41 – 7.36 (m, 2H), 7.34 (d, *J* = 7.7 Hz, 3H), 7.32 – 7.27 (m, 2H), 7.01 (t, *J* = 8.6 Hz, 2H), 6.93 (t, *J* = 8.6 Hz, 2H), 6.68 (apparent d, *J* = 5.4 Hz, 1H), 6.65 (apparent d, *J* = 5.4 Hz, 1H), 3.82 (d, *J* = 8.4 Hz, 2H), 3.76 (d, *J* = 8.5 Hz, 2H), 2.40 (s, 3H). **^{13}C NMR** (100 MHz, $CDCl_3$) δ 165.6, 164.4 (d, *J* = 251.9 Hz), 163.1 (d, *J* = 251.1 Hz), 145.2, 144.2, 135.9, 132.6 (d, *J* = 3.9 Hz), 131.3, 130.8 (d, *J* = 8.7 Hz), 129.9 (d, *J* = 8.2 Hz), 129.6, 128.8, 128.5, 127.4, 125.0, 115.5 (d, *J* = 48.3 Hz), 115.2 (d, *J* = 48.5 Hz), 64.8, 60.7, 21.6. **^{19}F NMR** (377 MHz, $CDCl_3$) δ -109.80, -109.87. **HRMS**: Calculated: $[M+H]^+$ 503.1599, experimental: 503.1592.

***N*-(3-Phenyl-1-tosylazetidin-3-yl)-1-(*p*-tolyl)methanimine 47**

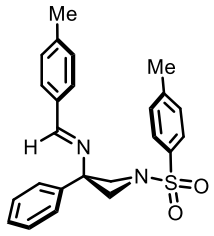

47

Following **General Procedure J**, starting from **31** and **71** using $PhCF_3$, the title compound was obtained in 53% yield (average of three reactions of 0.05 mmol). Purification: Hexane/AcOEt (9:1) leads to the product as a yellowish oil. **^{1}H NMR** (400 MHz, CD_2Cl_2) δ 7.86 (s, 1H), 7.75 (d, *J* = 8.3 Hz, 2H), 7.52 (d, *J* = 8.0 Hz, 2H), 7.38 – 7.30 (m, 3H), 7.23 – 7.17 (m, 5H), 4.27 (d, *J* = 8.4 Hz, 2H), 4.20 (d, *J* = 8.4 Hz, 2H), 2.37 (s, 3H), 2.36 (s, 3H). **^{13}C NMR** (101 MHz, CD_2Cl_2) δ 159.5, 144.5, 142.3, 133.2, 131.1, 141.8, 129.8, 129.3, 128.6, 128.4, 128.2, 127.4, 126.0, 63.1, 57.9, 21.2. **HRMS**: Calculated: $[M+H]^+$ 405.1631, experimental: 405.1640.

1-(4-Fluorophenyl)-*N*-(3-phenyl-1-tosylazetidin-3-yl)methanimine 48

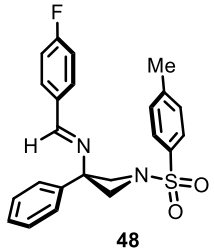

48

Following **General Procedure J**, starting from **31** and **SM13** using $PhCF_3$, the title compound was obtained in 53% yield (average of three reactions of 0.05 mmol). Purification: Hexane/AcOEt (9:1) leads to the product as a yellowish solid. **^{1}H NMR** (400 MHz, $CDCl_3$) δ 7.89 (s, 1H), 7.79 (d, *J* = 8.2 Hz, 2H), 7.69 – 7.63 (m, 2H), 7.37 – 7.29 (m, 5H), 7.23 – 7.18 (m, 2H), 7.08 (t, *J* = 8.6 Hz, 2H), 4.31 (d, *J* = 8.4 Hz, 2H), 4.24 (d, *J* = 8.4 Hz, 2H), 2.39 (s, 3H). **^{13}C NMR** (101 MHz, $CDCl_3$) δ 158.4, 144.4, 142.1, 131.8, 130.5 (d, *J* = 8.7 Hz), 129.9, 128.8, 128.6, 127.8, 127.3, 126.1, 116.0, 115.8, 63.2, 62.7, 21.7. **^{19}F NMR** (377 MHz, $CDCl_3$) δ -108.27. **HRMS**: Calculated: $[M+H]^+$ 409.1380, experimental: 409.1381.

1,1-bis(4-Methoxyphenyl)-*N*-(3-phenyl-1-(phenylsulfonyl)azetidin-3-yl)methanimine 49

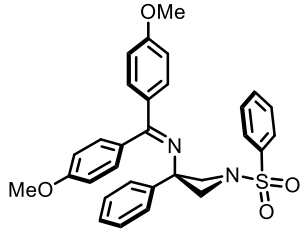

49

Following **General Procedure J**, starting from **31** and N-(bis(4-methoxyphenyl)methylene)benzenesulfonamide using $PhCF_3$, the title compound was obtained in 60% yield (average of three reactions of 0.05 mmol).

Purification: Hexane/AcOEt (8:2) leads to the product as a colorless oil. **^{1}H NMR** (400 MHz, $CDCl_3$) δ 7.76 (d, *J* = 6.8 Hz, 2H), 7.64 – 7.57 (m, 1H), 7.55 (dd, *J* = 8.2, 6.6 Hz, 2H), 7.50 – 7.45 (m, 2H), 7.38 (d, *J* = 8.8 Hz, 2H), 7.36 – 7.31 (m, 2H), 7.31 – 7.26 (m, 1H), 6.82 (d, *J* = 8.8 Hz, 2H), 6.73 (d, *J* = 8.7 Hz, 2H), 6.60 (d, *J* = 8.7 Hz, 2H), 3.83 (s, 3H), 3.81 (s, 3H), 3.79 (d, *J* = 8.3 Hz, 2H), 3.74 (d, *J* = 8.4 Hz, 2H). **^{13}C NMR** (101 MHz, $CDCl_3$) δ 166.8, 161.6, 160.4, 146.0, 134.0, 133.3, 133.2, 130.6, 129.6, 129.3, 129.1, 128.8, 128.6, 127.3, 125.2, 113.7, 113.4, 65.5, 60.8, 55.5, 55.4. **HRMS**: Calculated: $[M+H]^+$ 513.1842, experimental: 513.1847.

1,1-Diphenyl-*N*-(3-phenyl-1-(phenylsulfonyl)azetidin-3-yl)methanimine 50

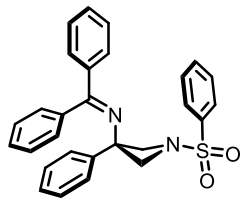

50

Following **General Procedure J**, starting from **31** and **SM14** using $PhCF_3$, the title compound was obtained in 60% yield (average of three reactions of 0.05 mmol). Applying **General Procedure J** but conducting the reaction in 0.5 mmol scale allowed the obtention of the product in 65% yield. Purification: Hexane/AcOEt (9:1) leads to the product as a colorless oil. **^{1}H NMR** (400 MHz, $CDCl_3$) δ 7.73 (d, *J* = 6.7 Hz, 2H), 7.62 – 7.57 (m, 2H), 7.46 – 7.37 (m, 6H), 7.37 – 7.21 (m, 8H), 6.66 (d, *J* = 6.8 Hz, 2H), 3.77 (d, *J* = 8.8 Hz, 2H), 3.72 (d, *J* = 8.7 Hz, 2H). **^{13}C NMR** (101 MHz, CD_2Cl_2) δ 140.5, 118.4, 112.9, 109.9, 106.5, 106.3, 103.4, 102.4, 102.1, 101.7, 101.6, 101.5, 101.2, 100.9, 100.8, 100.2, 98.1, 38.0, 33.7. **HRMS**: Calculated: $[M+H]^+$ 453.1631, experimental: 453.1633.

1,1-Diphenyl-*N*-(3-phenyl-1-((4-(trifluoromethyl)phenyl)sulfonyl)azetidin-3-yl)methanimine 20

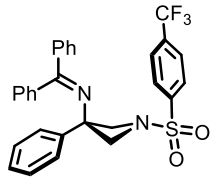

51

Following **General Procedure J**, starting from **31** and **SM15** using $PhCF_3$, the title compound was obtained in 66% yield (average of three reactions of 0.05 mmol). Purification: Hexane/AcOEt (9:1) leads to the product as a colorless oil. Suitable crystals for X-ray diffraction analysis were grown from slow evaporation of diethyl ether/CHCl3. **^{1}H NMR** (400 MHz, $CDCl_3$) δ 7.92 (d, *J* = 8.2 Hz, 2H), 7.84 (d, *J* = 8.2 Hz, 2H), 7.51 – 7.46 – 7.38 (m, 9H), 7.42 (dt, *J* = 8.1, 1.6 Hz, 1H), 7.38 – 7.30 (m, 6H), 7.26 (t, *J* = 7.6 Hz, 2H), 6.70 (d, *J* = 7.9 Hz, 2H), 3.89 (d, *J* = 8.5 Hz, 2H), 3.84 (d, *J* = 8.5 Hz, 2H). **^{13}C NMR** (100 MHz, $CDCl_3$) δ 168.18, 145.07, 138.28, 135.1, 134.7, 130.72, 129.59, 128.83, 128.80, 128.75, 128.32, 128.13, 127.82, 127.47, 126.15 (q, *J* = 3.7 Hz), 125.02, 123.3 (q, *J* = 274 Hz), 65.1, 60.8. **^{19}F NMR** (377 MHz, $CDCl_3$) δ -63.1. **HRMS**: Calculated: $[M+H]^+$ 449.1505, experimental: 449.1507.

1,1-Diphenyl-*N*-(3-phenyl-1-(pyridin-3-ylsulfonyl)azetidin-3-yl)methanimine 52

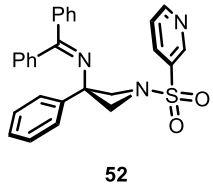

52

Following **General Procedure J**, starting from **31** and **SM16** using AcOEt, the title compound was obtained in 76% yield (average of three reactions of 0.05 mmol). Purification: exane/AcOEt (9:1) leads to the product as a yellow oil. **^{1}H NMR** (400 MHz, $CDCl_3$) δ 8.97 (d, *J* = 2.4 Hz, 1H), 8.81 (dd, *J* = 4.8, 1.7 Hz, 1H), 8.06 (dt, *J* = 7.9, 2.0 Hz, 1H), 7.54 – 7.46 (m, 3H), 7.46 – 7.39 (m, 3H), 7.39 – 7.28 (m, 6H), 7.23 (d, *J* = 7.6 Hz, 2H), 6.69 (d, *J* = 7.1 Hz, 2H), 3.83 (AB system d, *J* = 8.6 Hz, 4H). **^{13}C NMR** (101 MHz, $CDCl_3$) δ 167.9, 153.7, 153.7, 149.0, 145.1, 139.6, 136.8, 135.9, 130.6, 129.5, 129.5, 128.8, 128.8, 128.4, 128.1, 127.8, 125.0, 123.6, 65.0, 60.9. **HRMS**: Calculated: $[M+H]^+$ 454.1583, experimental: 454.1587.

1,1-Diphenyl-*N*-(3-phenyl-1-(thiophen-2-ylsulfonyl)azetidin-3-yl)methanimine 53

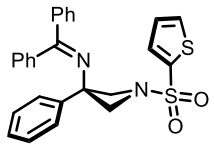

53

Following **General Procedure J**, starting from **31** and **SM17** using AcOEt, the title compound was obtained in 62% yield (average of three reactions of 0.05 mmol). Purification: Hexane/AcOEt (9:1) leads to the product as an amorphous colorless solid. **^{1}H NMR** (400 MHz, $CDCl_3$) δ 8.97 (d, *J* = 2.4 Hz, 1H), 8.81 (dd, *J* = 4.8, 1.7 Hz, 1H), 8.06 (dt, *J* = 7.9, 2.0 Hz, 1H), 7.54 – 7.46 (m, 3H), 7.46 – 7.39 (m, 3H), 7.39 – 7.28 (m, 6H), 7.23 (d, *J* = 7.6 Hz, 2H), 6.69 (d, *J* = 7.1 Hz, 2H), 3.83 (AB system d, *J* = 8.6 Hz, 4H). **^{13}C NMR** (101 MHz, $CDCl_3$) δ 167.9, 153.7, 153.7, 149.0, 145.1, 139.6, 136.8, 135.9, 130.6, 129.5, 129.5, 128.8, 128.8, 128.4, 128.1, 127.8, 125.0, 123.6, 65.0, 60.9. **HRMS**: Calculated: $[M+H]^+$ 459.1195, experimental: 459.1196.

***N*-(1-(Naphthalen-2-ylsulfonyl)-3-phenylazetidin-3-yl)-1,1-diphenylmethanimine 54**

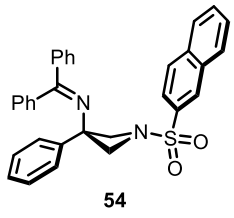

54

Following **General Procedure J**, starting from **31** and **SM18** using AcOEt, the title compound was obtained in 79% yield (average of three reactions of 0.05 mmol). Purification: Hexane/AcOEt (9:1) leads to the product as orange crystals. Suitable crystals for X-ray diffraction analysis were grown from slow evaporation of DCM. **^{1}H NMR** (400 MHz, CD_2Cl_2) δ 8.34 (d, *J* = 1.9 Hz, 1H), 8.07 (dd, *J* = 9.2, 3.3 Hz, 2H), 8.00 – 7.93 (m, 1H), 7.77 (dd, *J* = 8.6, 1.9 Hz, 1H), 7.71 (dt, *J* = 6.3, 3.4 Hz, 2H), 7.45 (dt, *J* = 6.1, 1.5 Hz, 2H), 7.43 – 7.20 (m, 11H), 6.56 (d, *J* = 6.9 Hz, 2H), 3.85 (collapsed AB system, 4H). **^{13}C NMR** (75 MHz, CD_2Cl_2) δ 167.4, 145.3, 139.8, 136.9, 135.1, 132.1, 130.7, 130.2, 130.0, 129.4, 129.2, 129.0, 128.6, 128.5, 128.2, 127.9, 127.8, 127.7, 127.2, 125.1, 65.1, 60.8. **HRMS**: Calculated: $[M+H]^+$ 503.1787, experimental: 503.1784.

1,1-bis(4-Methoxyphenyl)-*N*-(1-(methylsulfonyl)-3-phenylazetidin-3-yl)methanimine 55

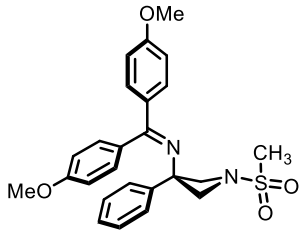

55

Following **General Procedure J**, starting from **31** and *N*-(bis(4-methoxyphenyl)methylene)methanesulfonamide using $PhCF_3$, the title compound was obtained in 47% yield (average of three reactions of 0.05 mmol).

Purification: Hexane/AcOEt (9:1) leads to the product as a colorless oil. **^{1}H NMR** (400 MHz, $CDCl_3$) δ 7.61 (d, *J* = 8.7 Hz, 2H), 7.58 – 7.51 (m, 2H), 7.37 (t, *J* = 7.5 Hz, 2H), 7.31 (d, *J* = 7.3 Hz, 1H), 6.88 (d, *J* = 8.7 Hz, 2H), 6.75 (collapsed dd, 4H), 4.11 (d, *J* = 7.9 Hz, 2H), 3.85 (s, 3H), 3.80 (s, 3H), 3.76 (d, *J* = 7.9 Hz, 2H), 2.83 (s, 3H). **^{13}C NMR** (100 MHz, $CDCl_3$) δ 167.1, 161.6, 160.2, 145.9, 132.9, 130.6, 129.6, 129.2, 28.7, 127.3, 125.1, 113.6, 113.4, 64.5, 60.3, 55.4, 55.2, 36.2. **HRMS**: Calculated: $[M+H]^+$ 451.1686, experimental: 451.1688.

***N*-(1-(Methylsulfonyl)-3-phenylazetidin-3-yl)-1,1-diphenylmethanimine 56**

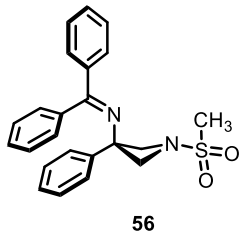

56

Following **General Procedure J**, starting from **31** and **2a** using $PhCF_3$, the title compound was obtained in 59% yield (average of three reactions of 0.05 mmol). Purification: Hexane/AcOEt (9:1) leads to the product as a colorless oil. **^{1}H NMR** (400 MHz, CD_2Cl_2) δ 7.67 (d, *J* = 8.1 Hz, 2H), 7.48 (d, *J* = 7.2 Hz, 2H), 7.44 (d, *J* = 7.4 Hz, 1H), 7.40 – 7.34 (m, 5H), 7.34 – 7.30 (m, 1H), 7.27 (t, *J* = 7.7 Hz, 2H), 6.83 (dd, *J* = 8.1, 1.4 Hz, 2H), 4.11 (d, *J* = 8.5 Hz, 2H), 3.74 (d, *J* = 8.5 Hz, 2H), 2.80 (s, 3H). **^{13}C NMR** (101 MHz, CD_2Cl_2) δ 168.4, 145.9, 140.2, 137.4, 131.0, 129.6, 129.2, 129.1, 128.6, 128.4, 128.3, 127.7, 125.6, 64.6, 60.8, 36.1. **HRMS**: Calculated: $[M+H]^+$ 391.1474, experimental: 391.1477.

1,1-Diphenyl-*N*-(3-phenyl-1-(propylsulfonyl)azetidin-3-yl)methanimine 57

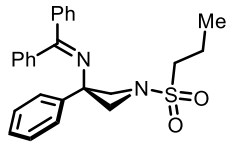

57

Following **General Procedure J**, starting from **31** and **SM19** using $PhCF_3$, the title compound was obtained in 69% yield (average of three reactions of 0.05 mmol). Applying **General Procedure J** but conducting the reaction in 0.5 mmol scale allowed the obtention of the product in 70% yield. Purification: Hexane/AcOEt (9:1) leads to the product as a colorless oil. **^{1}H NMR** (400 MHz, CD_2Cl_2) δ 7.70 (dt, *J* = 7.0, 2H), 7.55 – 7.50 (m, 2H), 7.50 – 7.45 (m, 1H), 7.40 (ddd, *J* = 9.0, 7.0, 1.9 Hz, 5H), 7.29 (t, *J* = 7.7 Hz, 2H), 7.33 – 7.26 (m, 1H), 6.87 (d, *J* = 6.9 Hz, 2H), 4.22 (d, *J* = 8.4 Hz, 2H), 3.69 (d, *J* = 8.4 Hz, 2H), 2.93 – 2.87 (m, 2H), 1.80 (sext, *J* = 7.5 Hz, 2H), 1.04 (t, *J* = 7.5 Hz, 3H). **^{13}C NMR** (100 MHz, CD_2Cl_2) δ 167.8, 145.8, 139.9, 137.1, 130.5, 129.1, 128.8, 128.6, 128.2, 128.0, 127.9, 127.2, 63.8, 60.4, 52.4, 16.9, 12.7. **HRMS**: Calculated: $[M+H]^+$ 419.1787, experimental: 419.1784.

_N_-(1-(Isopropylsulfonyl)-3-phenylazetidin-3-yl)-1,1-diphenylmethanimine 58

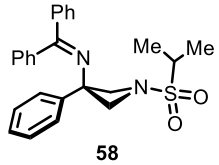

58

Following **General Procedure J**, starting from **31** and **SM20** using $PhCF_3$, the title compound was obtained in 67% yield (average of three reactions of 0.05 mmol). Purification: Hexane/AcOEt (9:1) leads to the product as a colorless oil. **^{1}H NMR** (400 MHz, $CDCl_3$) δ 7.65 (d, *J* = 7.0 Hz, 2H), 7.54 – 7.47 (m, 2H), 7.40 – 7.34 (m, 5H), 7.31 (dd, *J* = 7.0, 2.0 Hz, 2H), 7.22 (t, *J* = 7.6 Hz, 2H), 6.82 (d, *J* = 7.1 Hz, 2H), 4.31 (d, *J* = 8.4 Hz, 2H), 3.62 (d, *J* = 8.4 Hz, 2H), 3.08 (h, *J* = 7.4, 6.8 Hz, 1H), 1.31 (d, *J* = 6.9 Hz, 6H). **^{13}C NMR** (100 MHz, $CDCl_3$) δ 167.9, 146.1, 139.9, 137.1, 130.5, 129.2, 128.9, 128.7, 128.2, 128.1, 128.0, 127.2, 125.0, 64.8, 60.5, 53.5, 26.9, 16.4. **HRMS**: Calculated: $[M+H]^+$ 419.1787, experimental: 419.1788.

1,1-Diphenyl-_N_-(3-(p-tolyl)-1-tosylazetidin-3-yl)methanimine 59

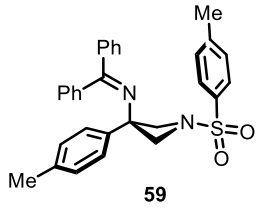

59

Following **General Procedure J**, starting from **SM4** and **32** using $PhCF_3$, the title compound was obtained in 84% yield (average of three reactions of 0.05 mmol). Purification: Hexane/AcOEt (9:1) leads to the product as a colorless oil. **^{1}H NMR** (400 MHz, CD_2Cl_2) δ 7.60 (d, *J* = 8.2 Hz, 2H), 7.44 – 7.36 (m, 5H), 7.34 – 7.27 (m, 5H), 7.25 (d, *J* = 7.6 Hz, 2H), 7.15 (d, *J* = 8.0 Hz, 2H), 6.69 (d, *J* = 6.9 Hz, 2H), 3.72 (d, *J* = 8.8 Hz, 2H), 3.69 (d, *J* = 8.6 Hz, 2H), 2.38 (s, 3H), 2.35 (s, 3H). **^{13}C NMR** (101 MHz, CD_2Cl_2) δ 167.6, 144.8, 142.9, 140.4, 137.4, 137.4, 130.9, 130.7, 130.1, 129.8, 129.7, 129.1, 129.0, 128.6, 128.3, 125.4, 65.5, 61.1, 21.7, 21.1. **HRMS**: Calculated: $[M+H]^+$ 481.1944, experimental: 481.1945.

4-(3-((Diphenylmethylene)amino)-1-tosylazetidin-3-yl)benzonitrile 60

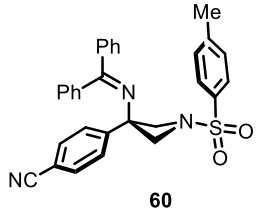

60

Following **General Procedure J**, starting from **SM5** and **32** using $PhCF^3$, the title compound was obtained in 46% yield (average of three reactions of 0.05 mmol). Purification: Hexane/AcOEt (9:1) leads to the product as a colorless oil. **^{1}H NMR** (400 MHz, $CDCl^3$) δ 7.69 – 7.60 (m, 5H), 7.51 (d, *J* = 7.0 Hz, 3H), 7.43 (t, *J* = 7.5 Hz, 2H), 7.41 – 7.33 (m, 4H), 7.29 (d, *J* = 7.8 Hz, 2H), 6.65 (d, *J* = 7.6 Hz, 2H), 3.85 (d, *J* = 8.5 Hz, 2H), 3.69 (d, *J* = 8.5 Hz, 2H), 2.41 (s, 3H). **HRMS**: Calculated: $[M+H]^+$ 492.1740, experimental: 492.1746.

(3-((Diphenylmethylene)amino)-1-tosylazetidin-3-yl)(phenyl)methanone 61

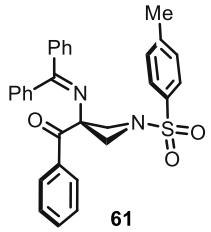

Following **General Procedure J**, starting from **SM9** and **32** using AcOEt, the title compound was obtained in 72% yield (average of three reactions of 0.05 mmol). Purification: Hexane/AcOEt (95:5 to 90:10) leads to the product as an amorphous solid. **^{1}H NMR** (400 MHz, CD_2Cl_2) δ 7.85 (d, *J* = 7.3 Hz, 2H), 7.67 (d, *J* = 8.1 Hz, 2H), 7.53 – 7.45 (m, 3H), 7.44 – 7.34 (m, 7H), 7.35 – 7.25 (m, 2H), 6.64 (d, *J* = 7.1 Hz, 2H), 4.19 (d, *J* = 8.3 Hz, 2H), 4.01 (d, *J* = 8.3 Hz, 2H), 2.40 (s, 3H). **^{13}C NMR** (101 MHz, CD_2Cl_2) δ 194.5, 170.8, 144.9, 139.4, 136.7, 133.8, 132.8, 131.9, 131.3, 130.6, 130.2, 129.9, 129.0, 128.9, 128.7, 128.6, 128.4, 127.9, 66.1, 61.4, 21.7. **HRMS**: Calculated: $[M+H]^+$ 495.1736, experimental: 495.1739.

Cyclohexyl(3-((diphenylmethylene)amino)-1-tosylazetidin-3-yl)methanone 62

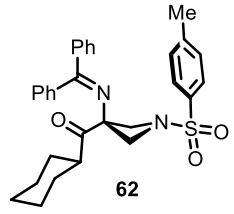

Following **General Procedure J**, starting from **SM10** and **32** using AcOEt, the title compound was obtained in 61% yield (average of three reactions of 0.05 mmol). Purification: Hexane/AcOEt (95:5 to 90:10) leads to the product as a colorless oil. **^{1}H NMR** (400 MHz, CD_2Cl_2) δ 7.57 (d, *J* = 8.0 Hz, 2H), 7.49 – 7.39 (m, 4H), 7.34 (apparent p, *J* = 7.9 Hz, 6H), 6.79 (dd, *J* = 8.0, 1.4 Hz, 2H), 3.86 (d, *J* = 8.7 Hz, 2H), 3.47 (d, *J* = 8.7 Hz, 2H), 2.82 (t, *J* = 11.5 Hz, 1H), 2.36 (s, 3H), 1.82 – 1.59 (m, 6H), 1.43 – 1.30 (m, 4H). **^{13}C NMR** (101 MHz, CD_2Cl_2) δ 208.2, 169.5, 144.9, 139.6, 136.6, 131.3, 131.1, 130.1, 130.1, 129.2, 129.0, 128.8, 128.4, 127.9, 67.4, 60.3, 47.4, 29.8, 26.0, 21.7. **HRMS**: Calculated: $[M+H]^+$ 501.2206, experimental: 501.2204.

***N*-(2,3-Diphenyl-1-tosylazetidin-3-yl)-1,1-diphenylmethanimine 63 and 64**

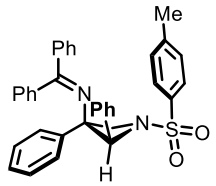

cis

63

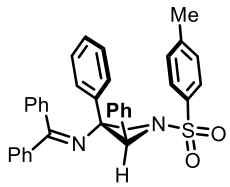

trans

64

Following **General Procedure J**, starting from **SM2** and **32** using $PhCF_3$, the title compound was obtained in 71% yield as a 2.1:1 diastereomeric mixture (average of three reactions of 0.05 mmol). Purification: Careful separation with column chromatography Hexane/Et_2O (95:5 to 90:10) allows the isolation of the major diastereomer. **64.**

Major diastereoisomer (*cis*). Yellowish oil**. ^{1}H NMR** (400 MHz, $CDCl_3$) δ 7.57 (d, *J* = 7.8 Hz, 4H), 7.46 – 7.39 (m, 1H), 7.35 (t, *J* = 7.4 Hz, 2H), 7.29 – 7.27 (m, 4H), 7.22 (t, *J* = 7.6 Hz, 2H), 7.15 – 7.05 (m, 4H), 7.06 – 6.98 (m, 5H), 6.62 (d, *J* = 7.6 Hz, 2H), 5.07 (s, 1H), 3.54 (d, *J* = 8.7 Hz, 1H), 3.47 (d, *J* = 8.7 Hz, 1H), 2.39 (s, 3H). **^{13}C NMR** (100 MHz, $CDCl_3$) δ 166.8, 144.2, 141.2, 139.5, 137.1, 135.6, 130.5, 129.5, 129.2, 128.8, 128.7, 128.1, 128.0, 128.0, 127.7, 127.3, 127.3, 127.1, 126.8, 126.8, 79.6, 68.0, 59.0, 29.7, 21.6. **HRMS**: Calculated: $[M+H]^+$ 543.2100, experimental: 543.2101.

63/64. Diastereomeric mixture. ^{1}H NMR (400 MHz, $CDCl_3$) δ 7.85 – 7.77 (m, 1H), 7.60 – 7.55 (m, 4H), 7.52 – 7.49 (m, 1H), 7.45 – 7.38 (m, 2H), 7.38 – 7.32 (m, 4H), 7.28 (d, *J* = 8.0 Hz, 3H), 7.22 (t, *J* = 7.6 Hz, 2H), 7.15 – 7.06 (m, 5H), 7.02 (td, *J* = 4.7, 4.1, 2.1 Hz, 6H), 6.76 (d, *J* = 7.0 Hz, 0.45H), 6.62 (d, *J* = 7.1 Hz, 2H), 5.20 (s, 0H), 5.07 (s, 1H), 4.11 (d, *J* = 9.7 Hz, 0.26H), 3.79 (d, *J* = 9.7 Hz, 0.24H), 3.54 (d, *J* = 8.6 Hz, 1H), 3.47 (d, *J* = 8.7 Hz, 1H), 2.44 (s, 0.67H), 2.39 (s, 3H). **^{13}C NMR** (101 MHz, $CDCl_3$) δ 167.8, 167.0, 145.8, 144.3, 141.3, 140.6, 139.7, 137.9, 137.8, 137.3, 136.7, 135.7, 132.6, 131.2, 130.6, 130.2, 129.6, 129.3, 128.9, 128.8, 128.4, 128.2, 128.2, 128.1, 127.8, 127.5, 127.5, 127.2, 127.0, 126.9, 125.4, 81.6, 79.7, 68.1, 65.3, 59.2, 21.7.

***N*-(2-Methyl-3-phenyl-1-tosylazetidin-3-yl)-1,1-diphenylmethanimine 65 and 66**

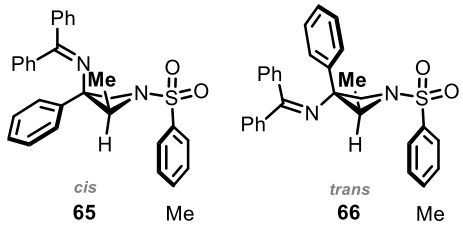

Following **General Procedure J**, starting from **SM1** and **32** using $PhCF_3$, the title compound was obtained in 82% yield as a 1:1 diastereomeric mixture (average of three reactions of 0.05 mmol). Purification: Careful separation with column hromatography Hexane/Et_2O (90:10 to 80:20) allows the separation of both diastereomers (**65** *cis* is the first one to come out from the column). Suitable crystals for X-ray diffraction analysis of both diastereomers were grown from slow evaporation of hexane/$CHCl_3$.

65 *cis*. ^{1}H NMR (400 MHz, $CDCl_3$) δ 7.68 (dd, *J* = 8.3, 1.7 Hz, 4H), 7.47 – 7.42 (m, 1H), 7.40 – 7.35 (m, 2H), 7.37 (m, 2H), 7.19 (t, *J* = 7.7 Hz, 2H), 7.16 – 7.12 (m, 1H), 7.09 (t, *J* = 7.4 Hz, 2H), 6.76 – 6.72 (m, 2H), 6.70 (d, *J* = 6.9 Hz, 2H), 4.24 (q, *J* = 6.4 Hz, 1H), 3.81 (d, *J* = 9.6 Hz, 1H), 3.72 (d, *J* = 9.6 Hz, 1H), 2.47 (s, 3H), 1.73 (d, *J* = 6.4 Hz, 3H). **^{13}C NMR** (100 MHz, $CDCl_3$) δ 168.6, 145.9, 143.7, 140.7, 137.7, 133.1, 130.4, 129.7, 128.9, 128.8, 128.4, 128.1, 128.1, 127.8, 126.6, 125.0, 75.9, 63.0, 58.8, 21.6, 16.7. **HRMS**: Calculated: $[M+H]^+$ 481.1944, experimental: 481.1941.

66 *trans*. ^{1}H NMR (400 MHz, $CDCl_3$) δ 7.63 (d, *J* = 8.3 Hz, 2H), 7.46 (d, *J* = 6.9 Hz, 2H), 7.41 – 7.37 (m, 3H), 7.37 – 7.27 (m, 8H), 7.19 (t, *J* = 7.6 Hz, 2H), 6.58 (d, *J* = 6.8 Hz, 2H), 4.05 (q, *J* = 6.4 Hz, 1H), 3.37 (d, *J* = 8.8 Hz, 1H), 3.23 (d, *J* = 8.8 Hz, 1H), 2.41 (s, 3H), 0.96 (d, *J* = 6.4 Hz, 3H). **^{13}C NMR** (100 MHz, $CDCl_3$) δ 167.1, 144.1, 141.9, 139.8, 137.2, 130.9, 130.3, 129.5, 129.2, 128.6, 128.6, 128.3, 128.1, 128.0, 127.9, 127.2, 126.7, 72.9, 65.2, 60.3, 21.6, 16.4. **HRMS**: Calculated: $[M+H]^+$ 481.1944, experimental: 481.1948.

1,1-Diphenyl-*N*-(3-phenyl-1-((4-(5-(*p*-tolyl)-3-(trifluoromethyl)-1*H*-pyrazol-1-l)phenyl)sulfonyl)azetidin-3-yl)methanimine 68

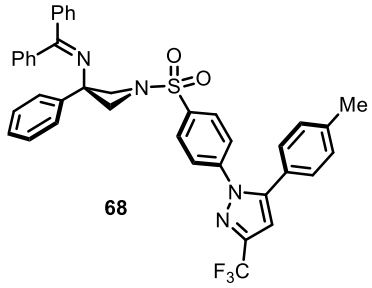

Following **General Procedure J**, starting from **31** and **67** using $PhCF_3$, the title compound was obtained in 71% yield (average of three reactions of 0.05 mmol). Purification: Hexane/AcOEt (80:20 to 70:30) leads to the product as a white solid. **^{1}H NMR** (400 MHz, $CDCl_3$) δ 7.74 (d, *J* = 8.7 Hz, 2H), 7.56 – 7.48 (m, 4H), 7.45 – 7.40 (m, 3H), 7.32 (dddd, *J* = 12.7, 7.0, 4.9, 2.6 Hz, 6H), 7.21 (t, *J* = 7.7 Hz, 2H), 7.07 (s, 4H), 6.73 (s, 1H), 6.68 (d, *J* = 6.8 Hz, 2H), 3.82 (d, *J* = 8.1 Hz, 2H), 3.75 (d, *J* = 8.7 Hz, 2H), 2.34 (s, 3H). **^{13}C NMR** (101 MHz, $CDCl_3$) δ 168.5, 145.3, 145.2, 144.3 (q, J = 38.6 Hz), 143.1, 140.0, 136.8, 133.8, 131.0 (d, J = 4.6 Hz), 129.9, 129.5, 129.0, 128.9, 128.8, 128.4, 128.3, 128.0, 127.6, 125.9, 125.3, 125.2, 121.2 (q, J = 250 Hz), 64.9, 60.9, 21.4. **^{19}F NMR** (377 MHz, $CDCl_3$) δ -62.47. **HRMS**: Calculated: $[M+H]^+$ 677.2192, experimental: 677.2192.

(*S*)-1-(3-((Diphenylmethylene)amino)-1-tosylazetidin-3-yl)-2-(6-methoxynaphthalen-2-yl)propan-1-one 70

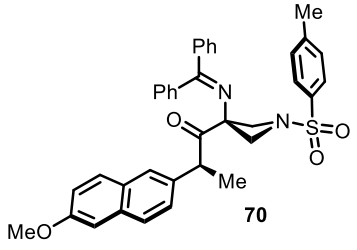

Following **General Procedure J**, starting from **69** and **32** using AcOEt, the title compound was obtained in 66% yield (average of three reactions of 0.05 mmol). Purification: Hexane/AcOEt (90:10 to 80:20) leads to the product as a white solid. **^{1}H NMR** (400 MHz, CD_2Cl_2) δ 7.58 (d, *J* = 8.5 Hz, 1H), 7.54 – 7.52 (m, 1H), 7.51 – 7.43 (m, 3H), 7.39 – 7.28 (m, 9H), 7.25 (t, *J* = 7.7 Hz, 2H), 7.07 – 7.00 (m, 2H), 6.48 (d, *J* = 6.9 z, 2H), 4.43 (q, *J* = 6.9 Hz, 1H), 3.93 (d, *J* = 8.6 Hz, 1H), 3.87 (s, 3H), 3.48 (dd, *J* = 15.8, 8.7 Hz, 2H), 3.19 (d, *J* = 8.8 Hz, 1H), 2.35 (s, 3H), 1.49 (d, *J* = 7.0 Hz, 3H). **^{13}C NMR** (151 MHz, $CDCl_3$) δ 205.94, 169.57, 158.10, 144.81, 139.62, 136.41, 135.20, 134.10, 131.19, 131.16, 130.01, 129.50, 129.30, 129.08, 128.82, 128.68, 128.35, 127.81, 127.66, 127.49, 126.67, 119.20, 105.75, 67.63, 60.43, 60.20, 55.61, 48.59, 21.65, 19.41. **$[\alpha]_D$** = -22 (*C* 0.1, $CHCl_3$). **HRMS**: Calculated: $[M+H]^+$ 603.2312, experimental: 603.2315.

3-Phenyl-1-tosylazetidine 76

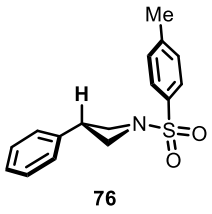

Following **General Procedure K**, starting from **31**, **71** and supersilane **74** using AcOEt, the title compound was obtained in 91% yield (average of three reactions of 0.05 mmol). Applying **General Procedure K** but conducting the reaction in 0.5 mmol scale allowed the obtention of the product in 90% yield. Purification: Hexane/AcOEt (90:10 to 80:20) leads to the product as a clear oil. **^{1}H NMR** (400 MHz, CD_2Cl_2) δ 7.76 (d, *J* = 8.2 Hz, 2H), 7.45 (d, *J* = 8.0 Hz, 2H), 7.26 – 7.17 (m, 3H), 6.93 (dd, *J* = 7.7, 1.9 Hz, 2H), 4.13 (t, *J* = 8.3 Hz, 2H), 3.74 (dd, *J* = 7.9, 7.0 Hz, 2H), 3.62 (p, *J* = 7.9 Hz, 1H), 2.50 (s, 3H). **^{13}C NMR** (101 MHz, CD_2Cl_2) δ 144.6, 141.1, 131.5, 130.3, 129.0, 128.9, 127.6, 127.2, 58.4, 33.6, 21.8. **HRMS**: Calculated: $[M+H]^+$ 288.1052, experimental: 288.1052.

3-Phenyl-1-tosylazetidine 77

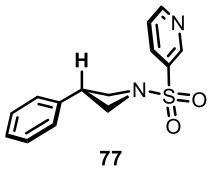

Following **General Procedure K**, starting from **31**, **72** and supersilane **74** using AcOEt, the title compound was obtained in 60% yield (average of three reactions of 0.05 mmol). Purification: Hexane/AcOEt (90:10 to 80:20) leads to the product as a clear oil. **^{1}H NMR** (400 MHz, $CDCl_3$) δ 9.16 (d, *J* = 2.3 Hz, 1H), 8.93 (dd, *J* = 4.9, 1.6 Hz, 1H), 8.21 (dt, *J* = 8.0, 2.0 Hz, 1H), 7.62 – 7.55 (m, 2H), 7.13 – 7.07 (m, 3H), 4.25 (t, *J* = 8.3 Hz, 2H), 3.93 (dd, *J* = 8.0, 6.9 Hz, 3H), 3.74 (m, 1H). **^{13}C NMR** (101 MHz, $CDCl_3$) δ 153.9, 149.2, 140.2, 136.1, 132.1, 129.1, 127.7, 126.8, 124.0, 58.6, 58.0, 33.4. **HRMS**: Calculated: $[M+Na]^+$ 297.0668, experimental: 297.0661.

3-Phenyl-1-tosyl-3-((trifluoromethyl)thio)azetidine 47

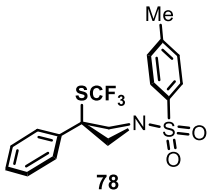

Following **General Procedure K**, starting from **31, 71** and Naphth-SCF3 **75** using AcOEt, the title compound was obtained in 69% yield (average of three reactions of 0.05 mmol). Purification: Hexane/AcOEt (97:3 to 90:10) leads to the product as a clear oil. **^{1}H NMR** (400 MHz, $CDCl_3$) δ 7.38 – 7.31 (m, 1H), 7.28 (m, below the CDCl3, 4H), 7.16 (d, *J* = 8.1 Hz, 2H), 6.91 (dd, *J* = 7.7, .6 Hz, 2H), 4.87 (d, *J* = 8.4 Hz, 2H), 4.44 (d, *J* = 8.4 Hz, 2H), 2.40 (s, 3H). **^{13}C NMR** (101 MHz, $CDCl_3$) δ 145.5, 134.6, 131.6, 130.0 129.5, 129.0, 128.8, 128.3, 66.2, 65.1, 21.8. **^{19}F NMR** (377 MHz, $CDCl_3$) δ -48.89. **HRMS**: Calculated: $[M+Na]^+$ 410.0466, experimental: 410.0468.

3-Cyclohexyl-1-tosyl-3-((trifluoromethyl)thio)azetidine 79

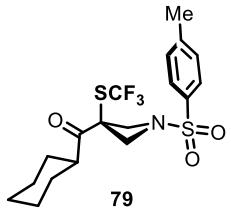

Following **General Procedure K**, starting from **SM10, 71** and Naphth-SCF3 **75** using AcOEt, the title compound was obtained in 69% yield (average of three reactions of 0.05 mmol). Purification: Hexane/AcOEt (97:3 to 90:10) leads to the product as a clear oil. **^{1}H NMR** (400 MHz, $CDCl_3$) δ 7.63 (d, *J* = 8.2 Hz, 2H), 7.35 (d, *J* = 8.2 Hz, 2H), 4.47 (d, *J* = 8.7 Hz, 2H), 4.27 (d, *J* = 8.7 Hz, 2H), 2.92 (tt, *J* = 11.5, 2.5 Hz, 1H), 2.46 (s, 3H), 1.98 – 1.67 (m, 7H), 1.43 (t, *J* = 12.2 Hz, 3H). **^{19}F NMR** (377 MHz, $CDCl_3$) δ -62.47. **HRMS**: Calculated: $[M+Na]^+$ 262.1000, experimental: 262.1001.

1-(4-((3-Phenylazetidin-1-yl)sulfonyl)phenyl)-5-(*p*-tolyl)-3-(trifluoromethyl)-1*H*-pyrazole 80

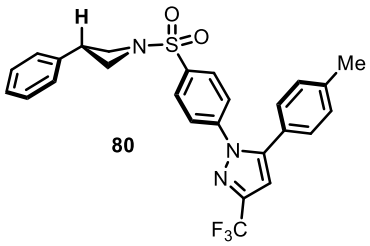

80

Following **General Procedure K**, starting from **31**, **73** and supersilane **74** using AcOEt, the title compound was obtained in 88% yield (average of three reactions of 0.05 mmol). Purification: Hexane/AcOEt (90:10 to 80:20) leads to the product as a white solid. **^{1}H NMR** (400 MHz, $CDCl_3$) δ 7.89 (d, *J* = 8.6 Hz, 2H), 7.57 (d, *J* = 8.6 Hz, 2H), 7.30 (dd, *J* = 8.2, 6.3 Hz, 3H), 7.14 (q, *J* = 8.2 Hz, 4H), 7.08 (dd, *J* = 7.0, 1.8 Hz, 2H), 6.77 (s, 1H), 4.16 (t, *J* = 8.3 Hz, 2H), 3.84 (dd, *J* = 7.9, 6.8 Hz, 2H), 3.65 (p, *J* = 7.8 Hz, 1H), 2.38 (s, 3H). **^{13}C NMR** (101 MHz, $CDCl_3$) δ 145.3, 144.5, 144.1, 143.1, 140.2, 139.9, 134.2, 129.8, 129.4, 128.9, 128.7, 127.6, 126.7, 125.7, 125.6, 121.1 (q, *J* = 269.3 Hz), 106.4 (d, *J* = 2.2 Hz), 57.9, 33.3, 21.4. **^{19}F NMR** (377 MHz, $CDCl_3$) δ -62.51. **HRMS**: Calculated: $[M+H]^+$ 498.1457, experimental: 498.1461.

Phenyl(1-((4-(5-(*p*-tolyl)-3-(trifluoromethyl)-1*H*-pyrazol-1-yl)phenyl)sulfonyl)-3-((trifluoromethyl)thio)azetidin-3-yl)methanone 81

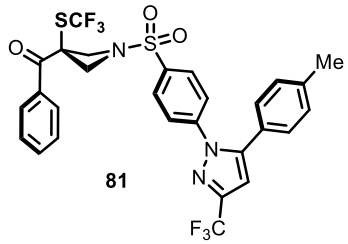

81

Following **General Procedure K**, starting from **SM9**, **73** and Naphth-SCF3 **75** using AcOEt, the title compound was obtained in 71% yield (average of three reactions of 0.05 mmol). Purification: Hexane/AcOEt (95:5 to 85:15) leads to the product as a yellowish solid. **^{1}H NMR** (400 MHz, $CDCl_3$) δ 7.85 (d, *J* = 7.5 Hz, 2H), 7.68 (d, *J* = 8.7 Hz, 2H), 7.53 – 7.44 (m, 5H), 7.19 (d, *J* = 7.9 Hz, 2H), 7.09 (d, *J* = 8.0 Hz, 2H), 6.74 (s, 1H), 4.70 (d, *J* = 9.1 Hz, 2H), 4.52 (d, *J* = 9.2 Hz, 2H), 2.39 (s, 3H). **^{13}C NMR** (101 MHz, $CDCl_3$) δ 192.1, 145.6, 144.4, 140.1, 134.7, 133.7, 133.1, 130.9, 130.5, 130.0, 128.9, 128.9, 125.8, 125.3, 106.4, 71.0, 63.6, 21.5. **^{19}F NMR** (377 MHz, $CDCl_3$) δ -48.06, -62.57. **HRMS**: Calculated: $[M+H]^+$ 626.1001, experimental: 626.1000.

1-(4-((3-Phenyl-3-((trifluoromethyl)thio)azetidin-1-yl)sulfonyl)phenyl)-5-(*p*-tolyl)-3-(trifluoromethyl)-1*H*pyrazole 82

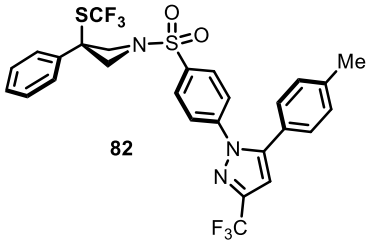

82

Following **General Procedure K**, starting from **1**, **41** and Naphth-SCF3 **43** using AcOEt, the title compound was obtained in 42% yield (average of three reactions of 0.05 mmol). Purification: Hexane/AcOEt (95:5 to 85:15) leads to the title product combined with N-H phthalimide which could not be separated by chromatographic separation. **^{1}H NMR** (400 MHz, $CDCl_3$) δ 7.34 – 7.30 (m, 1H), 7.21 – 7.10 (m, 5H), 7.08 – 7.03 (m, 1H), 6.71 (s, 1H), 4.37 (d, *J* = 8.0 Hz, 1H), 4.34 (d, *J* = 8.1 Hz, 1H), 2.38 (s, 2H). **^{13}C NMR** (101 MHz, $CDCl_3$) δ 143.9, 141.7, 138.6, 134.9 (q, *J* = 33.5 Hz), 128.9, 128.9, 128.7, 128.0, 127.5, 127.4, 126.3, 126.3, 62.5, 61.8, 58.1. **^{19}F NMR** (377 MHz, $CDCl_3$) δ -46.95, -62.43. **HRMS**: Calculated: $[M+Na]^+$ 620.0872, experimental: 620.0880.

3.4.4. Mechanistic considerations

Photophysical characterization of PS 39

The absorption, emission, and phosphorescence of PS **39** is presented below. In order to have a comparison parameter, we did the same experiments for PS **38**, which was already reported.[57]

*Figure 20. PS **38** and PS **39** under a 365 nm lamp in solid state.*

Emission intensities were recorded on a JASCO Spectrofluorometer FP-8600 equipped with a TC-815 Peltier thermostated single cell holder (water-cooled) controlled by Spectra Manager Version 2.10.01. Toluene was used for all the measurements. All the PS solutions were excited at 420 nm (PS **39**) and 415 nm (PS **38**). The energies of the S_1 excited state were calculated using the crossing point of the absorption and emission spectra (normalized). Whereas the T_1 energies were calculated from the onset wavelength of phosphorescent emission (normalized). In a typical experiment, the appropriate photosensitizer solution was degassed for 60 seconds using an argon balloon and the sample cuvette was closed with a septum.

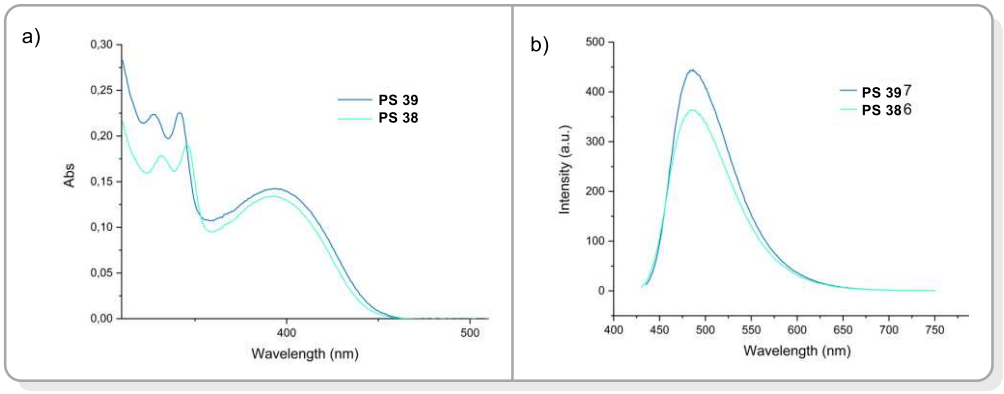

*Figure 21. Panel a) comparison of the absorption spectra between PS **38** and PS **39**. Panel b) comparison of the emission between PS **38** and PS **39***

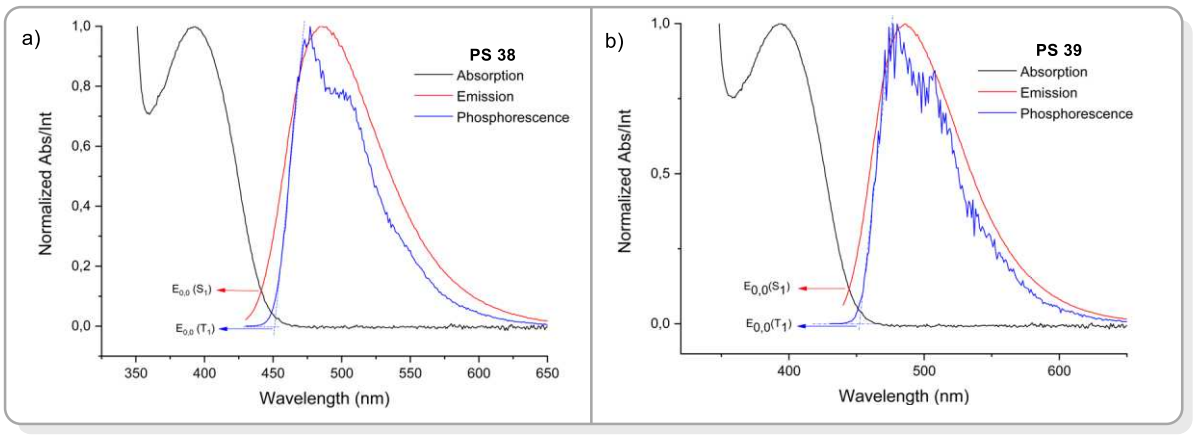

*Figure 22. Panel a) determination of the S_1 and the T_1 of PS **38**. Panel b) determination of the S_1 and the and the T_1 of PS **39***

To record the phosphorescence, the experiments were performed using a quartz tube and the sample was frozen using liquid nitrogen. The freezing process was repeated until the minor level of cracking of the solvent allowed proper spectral definition. To record the exclusive contribution of phosphorescence and discriminate the fluorescence contribution, a delay of 5ms was configured and the utilized parameters are summarized below:

Exc slit=20nm

Em slit=10 nm

Time= 0,5s

Delay=5ms

Gate time=100ms

PMT High Voltage

The emission quantum yield of PS **39** in toluene under both air-equilibrated and degassed conditions was measured using *fac*-Ir(ppy)$_3$ as a standard (Φ = 0.97 in Me-THF) leading to values of 0.61 and 0.99, respectively (Table 4). The former is assigned to the quantum yield of prompt fluorescence (Φ_{PF}), due to quenching of the triplet T1 by dioxygen, while the latter to the sum of both prompt and delayed fluorescence ($\Phi_{PF} + \Phi_{DF}$) [10].

Time-resolved luminescence measurements were then performed to extract the excited state lifetime of both the singlet S_1 and the triplet T_1. Following the luminescence decay by time-correlated single-photon counting (TCSPC) we estimated a lifetime of τ (S1) = 20.4 ns (Figure 23).

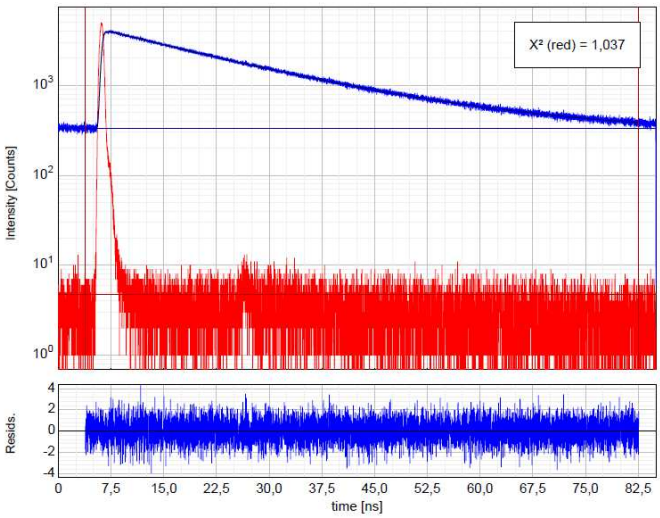

*Figure 23. Luminescence decay of PS **39** in toluene measured by TCSPC (excitation at 380 nm, analysis at 500 nm): a lifetime of 20.4 ns is estimated upon deconvolution and single-exponential fitting. Top panel shows the experimental trace associated with the luminescence decay in blue, the instrument response function (IRF) in red and the fitting in black (almost superimposed to the blue trace) obtained. The bottom panel shows the residuals associated with the fitting (i.e., the difference between the experimental trace and the fitting).*

Laser flash photolysis (excitation at 355 nm) under N_2-purged conditions was then performed to follow the delayed component of the emission. A lifetime of τ (T_1) = 20.6 µs was obtained (Figure 24).

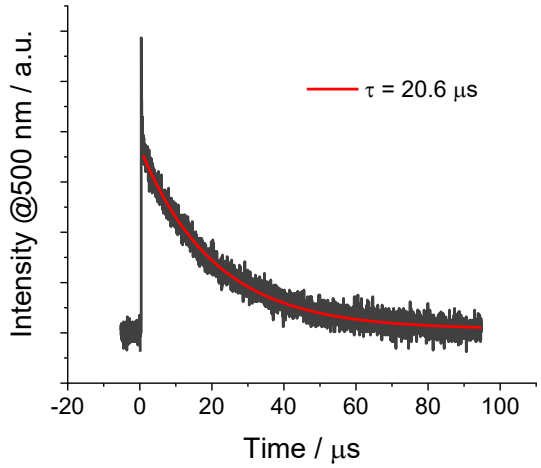

*Figure 24.Luminescence decay of PS **39** in toluene measured by laser flash photolysis (excitation at 355 nm, analysis at 500 nm): a lifetime of 20.6 μs is estimated through single-exponential fitting.*

We then employed the following equations10 to determine the relevant kinetic constants of PS **39**.

Equation 1.

$$k_{PF} = \frac{e\Phi_{PF}}{\tau_{S1}} = 3.0 \cdot 10^7\ s^{-1}$$

Equation 2.

$$k_{DF} = \frac{\Phi_{DF}}{\tau_{T1}} = 1.8 \cdot 10^4\ s^{-1}$$

Equation 3.

$$k_{ISC} = \frac{\Phi_{DF}}{\Phi_{PF}+\Phi_{DF}} \cdot k_{PF} = 1.1 \cdot 10^7\ s^{-1}$$

Equation 4.

$$k_{RISC} = \frac{\Phi_{DF}}{\Phi_{PF}} \cdot \frac{k_{PF} \cdot k_{DF}}{k_{ISC}} = 3.1 \cdot 10^4\ s^{-1}$$

Table 4. Summary report of the studied photosensitizers.

	Abs max	Abs edge	E 0,0 (S_1) exp/lit	E 0,0 (T_1) exp/lit	ΔE_{ST} exp/lit	PLQY solution	Delayed component lifetime
PS 38	390 nm	447 nm	2.81 / 2.86 (eV)	2.75 / 2.79 (eV)	0.06 / 0.07 (eV)	100% (86%)	13.3 μs
PS 39	394 nm	460 nm	2.79 (eV)	2.74 (eV)	0.05 (eV)	99% (61%)	20.6 μs

Luminescence quenching study

Quenching studies were made by monitoring the lifetime of the singlet (by TCSPC) and triplet (by laser flash photolysis) excited states as a function of the concentration of the quencher (either **31** or **32**). Toluene was used for all the measurements. In a typical experiment, the appropriate amount of quencher is added to the toluene solution of PS **39** (30 μM) in a Teflon-top 10x10 mm precision cell made of Quartz SUPRASIL®. The measurement was collected after degassing with N_2.

Quenching by sulfonyl imine 32.

The time-resolved luminescence decays measured by laser flash photolysis (excitation at 355 nm, analysis at 500 nm) of PS **39** in the presence of **32** show that the triplet T_1 is efficiently quenched by **32**. Stern-Volmer

analysis points to a dynamic quenching process and yields a bimolecular rate constant of 2.6·108 $M^{-1}s^{-1}$. On the other hand, the singlet excited state is only marginally affected by the presence of the sulfonylimine **32** (the singlet lifetime measured by TCSPC is 19.6 ns at 1.25 mM **32**, see below).

Quenching by ABB 31.

The time-resolved luminescence decays measured by laser flash photolysis (excitation at 355 nm, analysis at 500 nm) of PS **9** in the presence of **31** show that the triplet T_1 is quenched by **31**. The efficiency of the quenching process is, however, considerably lower than that recorded with the sulfonyl imine **32**. Stern-Volmer analysis points to a dynamic quenching process and yields a bimolecular rate constant of 3.7·106 $M^{-1}s^{-1}$. No detectable changes are observed when measuring the decay of the singlet excited state by TCSPC in the presence of **31** (lifetime of 20.4 ns at 18.2 mM **31**, see below).

The quenching studies thus suggest that the triplet excited state of PS **39** is the photochemically active species and that the primary photochemical step is represented by its reaction with the sulfonyl imine **32.**

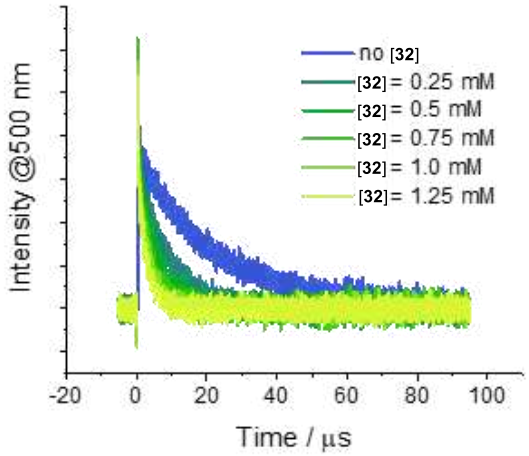

*Figure 25.Luminescence kinetic traces measured by laser flash photolysis (excitation at 355 nm) in toluene of PS **39** in the presence of variable amounts of **32.***

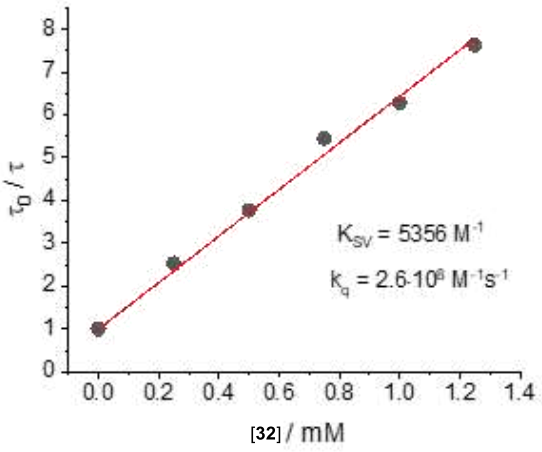

*Figure 26.Stern-Volmer plot of the quenching of the triplet T1 of PS **39** by sulfonyl imine **32**.*

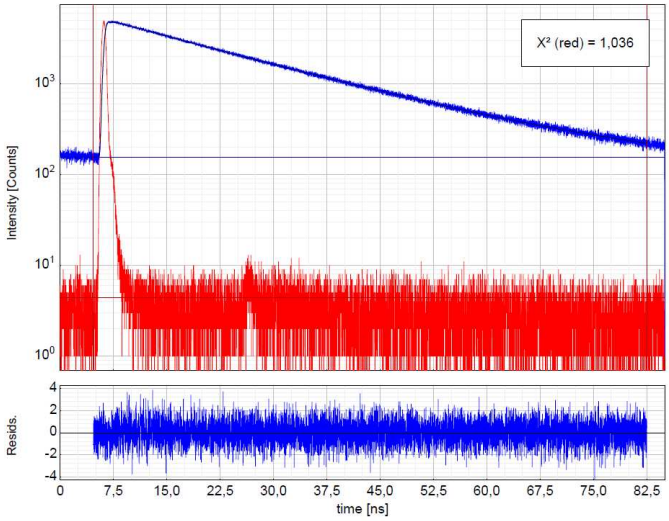

*Figure 27.Luminescence decay of PS **39** in toluene measured by TCSPC (excitation at 380 nm, analysis at 500 nm) in the presence of 1.25 mM **32**: a lifetime of 19.6 ns is estimated upon deconvolution and single-exponential fitting. Top panel shows the experimental trace associated with the luminescence decay in blue, the instrument response function (IRF) in red and the fitting in black (almost superimposed to the blue trace) obtained. The bottom panel shows the residuals associated with the fitting (i.e., the difference between the experimental trace and the fitting).*

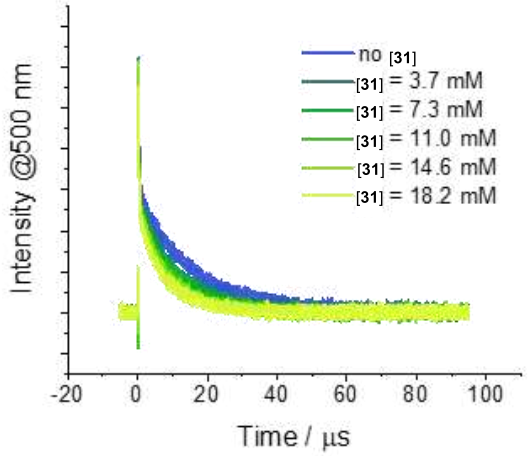

*Figure 28.Luminescence kinetic traces measured by laser flash photolysis (excitation at 355 nm) in toluene of PS **39** in the presence of variable amounts of **31**.*

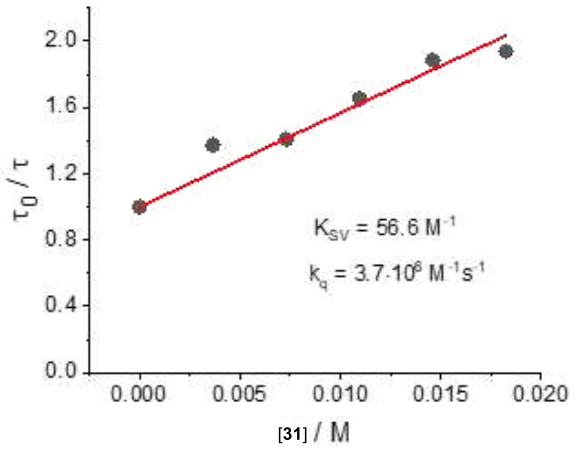

*Figure 29. Stern-Volmer plot of the quenching of the triplet T1 of PS **39** by ABB **31**.*

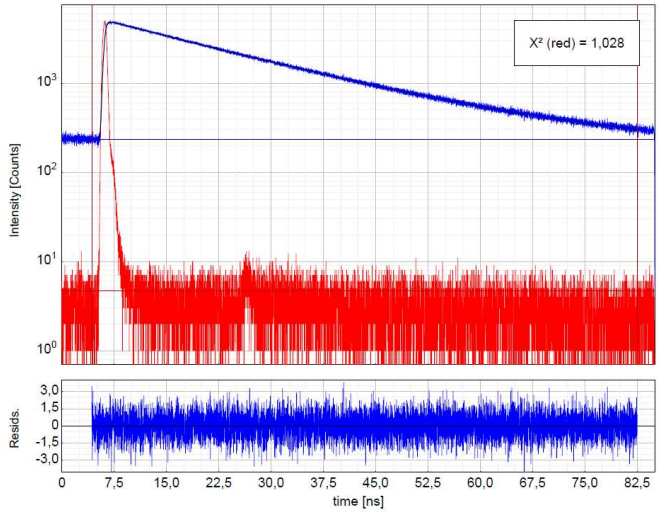

*Figure 30. Luminescence decay of PS **39** in toluene measured by TCSPC (excitation at 380 nm, analysis at 500 nm) in the presence of 18.2 mM **31**: a lifetime of 20.4 ns is estimated upon deconvolution and single-exponential fitting. Top panel shows the experimental trace associated with the luminescence decay in blue, the instrument response function (IRF) in red and the fitting in black (almost superimposed to the blue trace) obtained. The bottom panel shows the residuals associated with the fitting (i.e., the difference between the experimental trace and the fitting).*

Spin trapping experiments

Spin trapping was performed using *N-tert*-Butyl-α-phenylnitrone (PBN, **43**), from Merck (Germany). The samples were prepared adding PBN (**43**) (1.5 equiv) to the following reaction scenarios: 1) solvent alone; 2) a solution of PS **39** and **32**; 3) the full reaction mixture (**31**; **32**; PS **39**). In all the cases, the mixture under study was subjected to the optimized conditions and after reaction completion, 200 mL, were transferred to a quartz tube (3 mm i.d.). The quartz tubes were measured immediately after stopping the irradiation and after performing three freeze-pump-thaw cycles and sealing them under vacuum. The intensity of the trapped radicals was stable after the irradiation stopped.

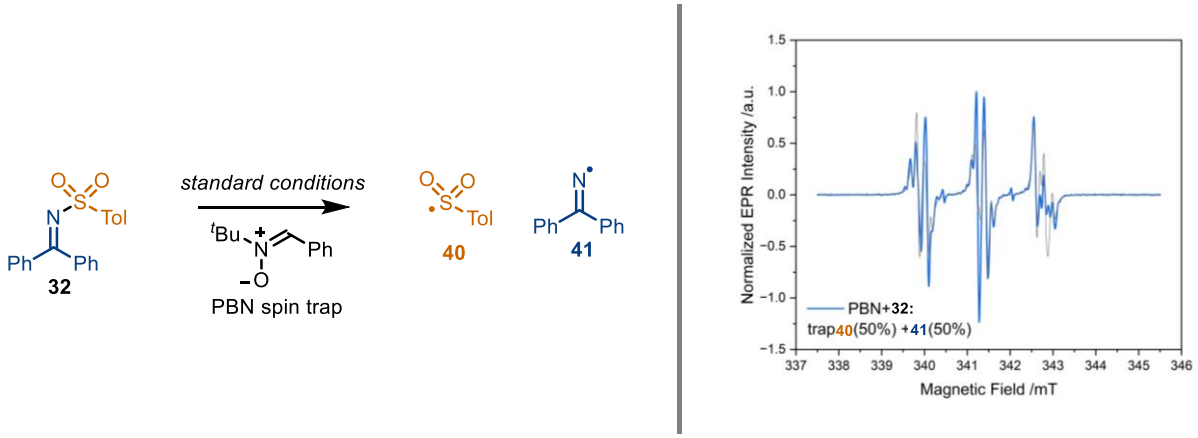

*Scheme 24. EPR detection of radical intermediates **10** and **11**.*

The continuous wave (CW) electron paramagnetic resonance (EPR) spectra of the trapped radicals were recorded on an X band Elexsys E580 spectrometer (Bruker BioSpin GmbH, Rheinstetten, Germany) using a SHQ cavity; the microwave frequency was measured by a frequency counter, HP5342A. All the EPR spectra were obtained using the following parameters: microwave power 1.5 mW (attenuation 20 dB), modulation amplitude 0.05 mT, modulation frequency 100 kHz, time constant 41 ms, conversion time 168 ms, scan width 8 mT, 1024 points, 4 scans. The magnetic field axis was calibrated measuring a diphenylpicrylhydrazyl crystal (DPPH, g = 2.0036). Spectral simulations were performed using Easyspin version 6.0.0 – dev53 using the *garlic* function and optimizing the isotropic hyperfine couplings partly through the automated fitting using a combination of Simplex and Levenberg-Marquardt algorithms (*esfit* function).[61]

Trapped Radical **10**: g = 2.0063; a_N = 1.38 mT; $a_{H\beta}$ = 0.21 mT

Trapped Radical **11**: g = 2.0061; a_N = 1.43 mT; $a_{H\beta}$ = 0.17 mT; $a_{N\beta}$ = 0.14 mT

Trapped Radical **12**: g = 2.0061; a_N = 1.48 mT; $a_{H\beta}$ = 0.13 mT

Laser flash photolysis experiments

Transient absorption studies were performed by laser flash photolysis (excitation at 355 nm) to extract mechanistic insight into the photoreaction. Toluene was used for all the measurements. Teflon-top 10x10 mm precision cell made of Quartz SUPRASIL® were employed. All the measurements were collected after degassing with N_2.

Laser flash photolysis of a toluene solution of **39** produces a transient spectrum displaying a bleaching at 420 nm and a broad absorption at longer wavelengths with two relative maxima at 460 and 700 nm (Figure 31). This spectrum decays monotonically towards the baseline with a time-constant of τ = ca 13 ms, identical to the lifetime obtained by time-resolved emission under the same experimental conditions (the smaller lifetime than previously indicated, see above, most likely stems from a non-perfect degassing procedure). This allows us to safely assign this transient absorption spectrum to the triplet excited state T_1 of **39**.

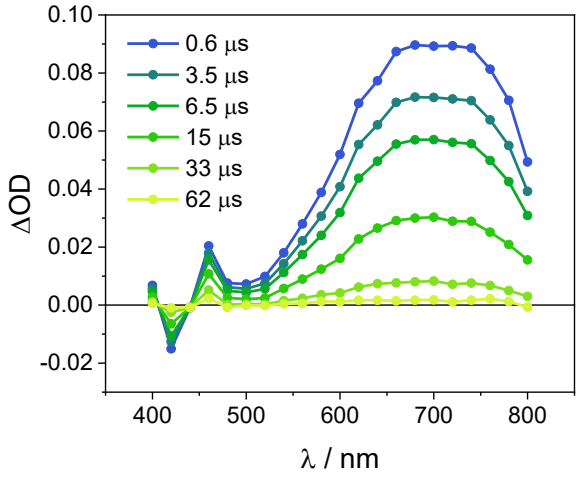

*Figure 31. Transient absorption spectra between 0.6-62 ms measured by laser flash photolysis (excitation at 355 nm) of **39** in toluene.*

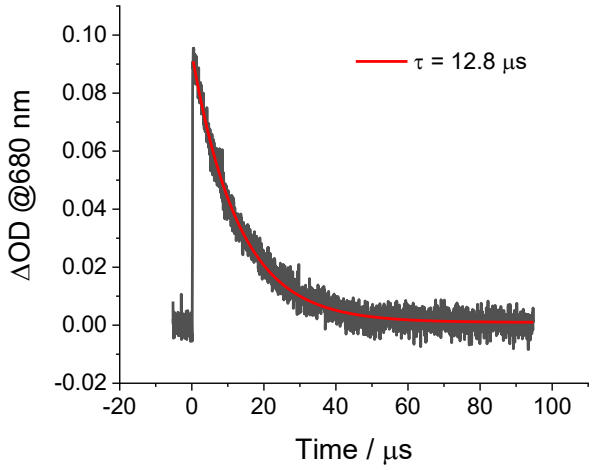

*Figure 32.Kinetic analysis at 680 nm measured by laser flash photolysis (excitation at 355 nm) of PS **39** in toluene.*

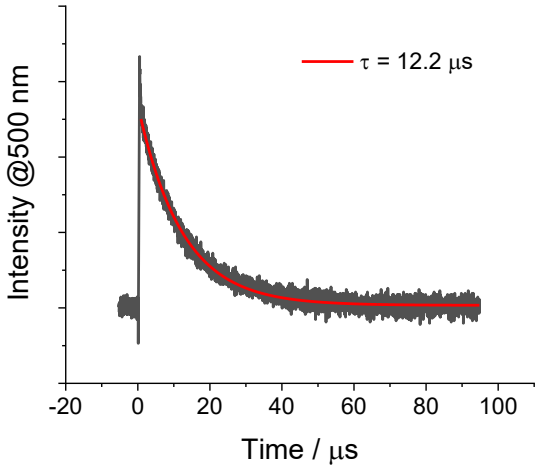

*Figure 33. Time-resolved luminescence trace at 500 nm measured by laser flash photolysis (excitation at 355 nm) of PS **39** in toluene.*

Laser flash photolysis of a toluene solution of PS **39** in the presence of 3.7 mM sulfonyl imine 3**2** (Figure 34) yields a transient spectrum similar to the one obtained in the absence of 3**2**, indicating rapid formation of the triplet state of PS **39**. Its decay is, however, faster (τ = 1.1 ms), consistent with efficient quenching of the triplet T_1 by compound **32** as observed by time-resolved emission and the corresponding Stern-Volmer analysis (see above). Interestingly, subtle (but peculiar) spectral variations can be observed at early time delays in the blue-region between 420-520 nm (see the kinetic trace at 480 nm, Figure 35). These features are not observed in the absence of the sulfonyl imine **32** and can be interpreted assuming the formation of the triplet state of compound **32** or the resulting products (**40** + **41**) upon sensitization by the T_1 of PS **39**, in which the sensitization process represents the rate determining step. Under these assumptions, for kinetic reasons the faster disappearance does not allow substantial accumulation of the resulting products which are thus only marginally detected in the early stage of the spectral evolution. In this regard, the sulfonyl radical **40** is expected to absorb in this spectral region,[47,48] which suggests that sensitization of the sulfonyl imine **32** by the triplet PS **39** most likely leads to the generation of the radical products **40** + **41**.

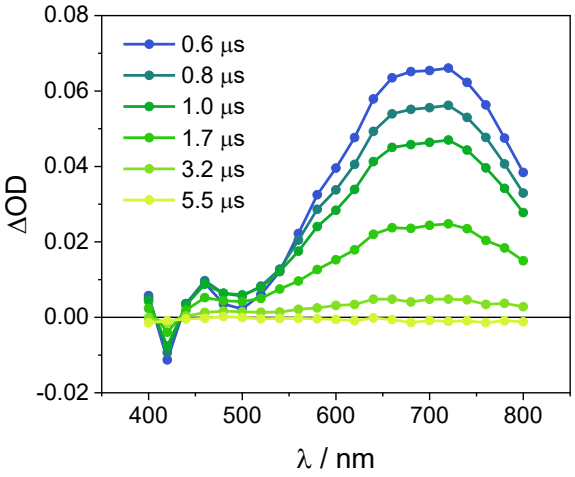

*Figure 34. Transient absorption spectra between 0.6-5.5 ms measured by laser flash photolysis (excitation at 355 nm) of PS **39** in toluene in the presence of 3.7 mM **32**.*

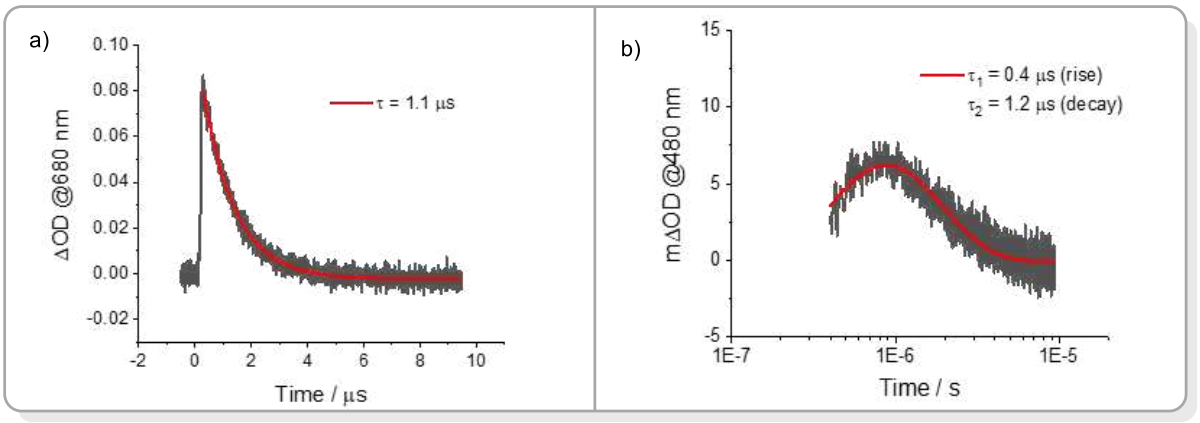

*Figure 35. Kinetic analysis at 680 nm (panel a) and 480 nm (panel b) measured by laser flash photolysis (excitation at 355 nm) of PS **9** in toluene in the presence of 3.7 mM **32**.*

The failure to accumulate for kinetic reasons the products of the sensitization process between PS **39** and **32** does not allow the possibility to follow the whole photoreaction sequence up to the formation of the azetidine **34** in a straightforward manner. Hence, we exploited direct photochemistry of **32** to attain a better insight into the reaction with ABB **31**. Flash photolysis of a solution of **32** in toluene in the presence of 46 mM **31** leads to a prompt transient spectrum (time-delay = 50 ns) with a maximum at 410 nm (black trace, Figure 36, left panel) which can be assigned to the sulfonyl radical **40** produced via photoinduced homolysis of the S-N bond.[47] This absorption occurs in a similar spectral region where subtle spectral variations were observed for the photoreaction between PS **39** and **32** (see above), possibly suggesting a similarity between the photoproducts attained via direct excitation of **32** and via triplet sensitization. This could also indicate that cleavage of the N-S bond is intrinsically fast so that triplet sensitization rapidly leads to photoproducts **40**+**41**. Subsequently, an increase of the transient absorption is observed leading to a new spectrum with a maximum at 435 nm and a tail at longer wavelengths (red trace, Figure 36, left panel). This spectrum can be assigned to the radical intermediate **42** attained by reaction of **31** with radical **40**. This attribution is supported by the dependence of the transient signal at 450 nm on the concentration of **31** (Figure 36, right panel), as expected based upon the bimolecular nature of the reaction. As a matter of fact, in the absence of substrate **31**, the transient absorption signal at 450 nm decays with a time-constant of ca 500 ns (black trace, Figure 36, right panel), while in the presence of ABB **31** the kinetic traces at 450 nm for both ABB concentrations feature a rise and decay (red and blue traces, Figure 36, right panel). Kinetic analysis of the rising component yields time-constants of ca 250 and 90 ns at 27 and 46 mM, respectively. Assuming pseudo-first order kinetic conditions, these values allow to estimate an average bimolecular rate constant of k = 2.0·108 M-1s-1 for the reaction between **40** and **31**. Finally, the spectrum associated with intermediate **42** decays to the baseline within a few ms (timeconstants of 0.8 and 1.6 ms are recorded for 27 and 46 mM concentrations of **31**, respectively, Figure 36, right panel). These changes can be mainly ascribed to recombination between **42** and the iminyl

radical **41** and concurrent formation of the desired product. As a matter of fact, the absence of detectable absorptions in the visible spectral range for both the azetidine **34** (Figure 37) and the **31**+**32** reactants is such that formation of **34** can be experimentally extracted only from the decay of the parent radical species.

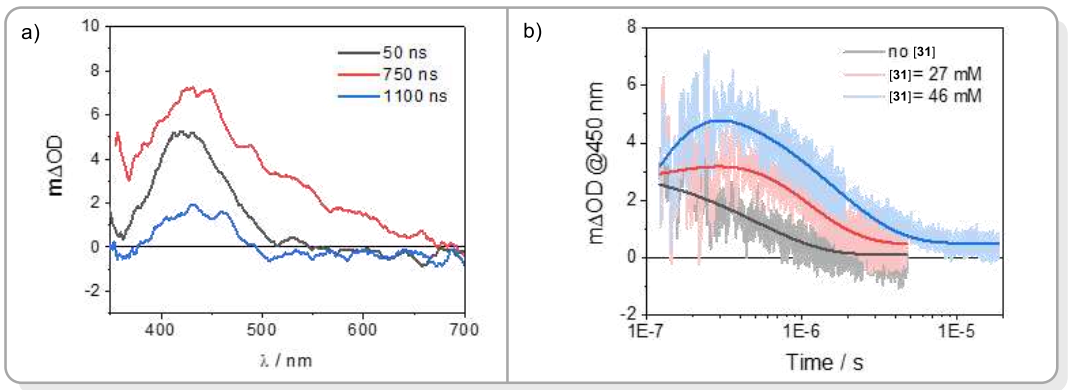

*Figure 36. a) transient absorption spectra at variable time delays obtained by laser-flash photolysis (excitation at 355 nm) of 4.5 mM **32** and 46 mM **31** in toluene. B) kinetic analysis at 450 nm in the presence of 0-46 mM **31**; fitting details: black trace, τ= 515 ns; red trace, τ_1 = 255 ns (rise), τ_2 = 830 ns (decay); blue trace, τ_1 = 89 ns (rise), τ_2 = 1600 ns (decay).*

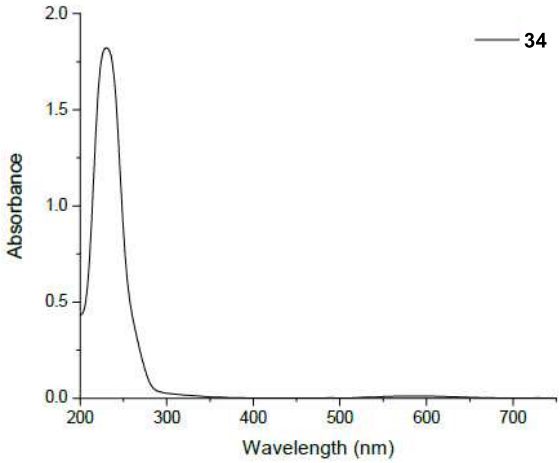

*Figure 37. Absorption spectrum of azetidine **34**.*

Computational studies

All geometry optimizations were performed using M06-2X functional, including the integral equation formalism of the polarizable continuum model (IEFPCM) to model solvation effects, except for the computed ΔG of the energy transfer process, which was performed in gas phase. The def2TZVP basis set was employed. Frequencies were calculated to ensure that the structures are actual relative minima of energy. The energy values for all computed structures discussed in this text, including the energy transfer (EnT) process from the excited photosensitizer to the ground-state sulfonylimine, are expressed in terms of Gibbs free energy. These values encompass thermal corrections computed at standard conditions of 298.15 Kelvin and 1 atmosphere pressure.

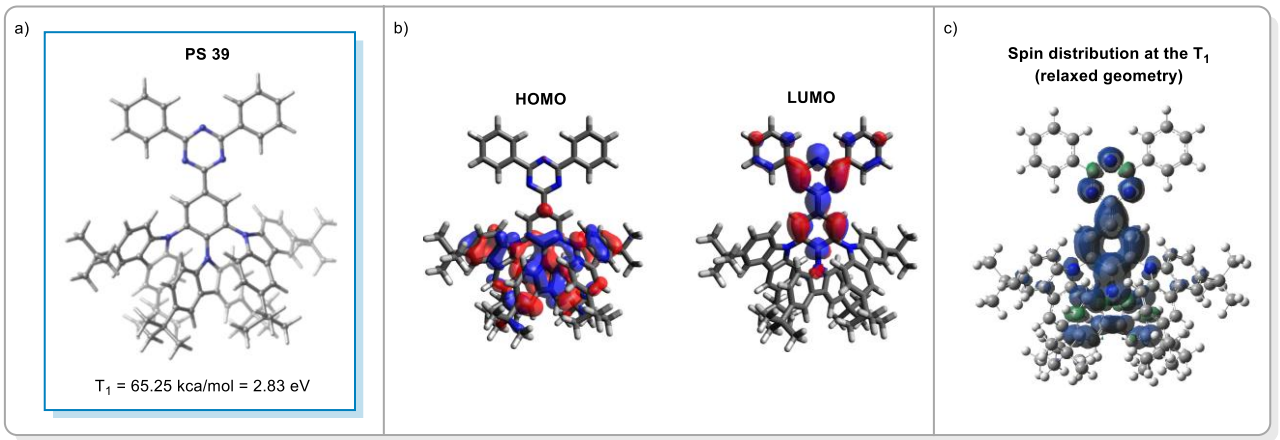

*Figure 38. a) T_1 energy of PS **39**.b) calculated HOMO and LUMO of PS **39**. c) spin distribution at the triplet excited state of PS **39**.*

Related to the collision complex between PS **39** and sulfonylimine 3**2a**: through DFT calculations at the (U)M062X/6-31G level of theory, we identified a local minimum structure that confirms that one of the phenyl rings of sulfonylimine **32a** interacts via π-π stacking with the triazine moiety of PS **39** (see figure below), consistent with our previously computed spin density map.

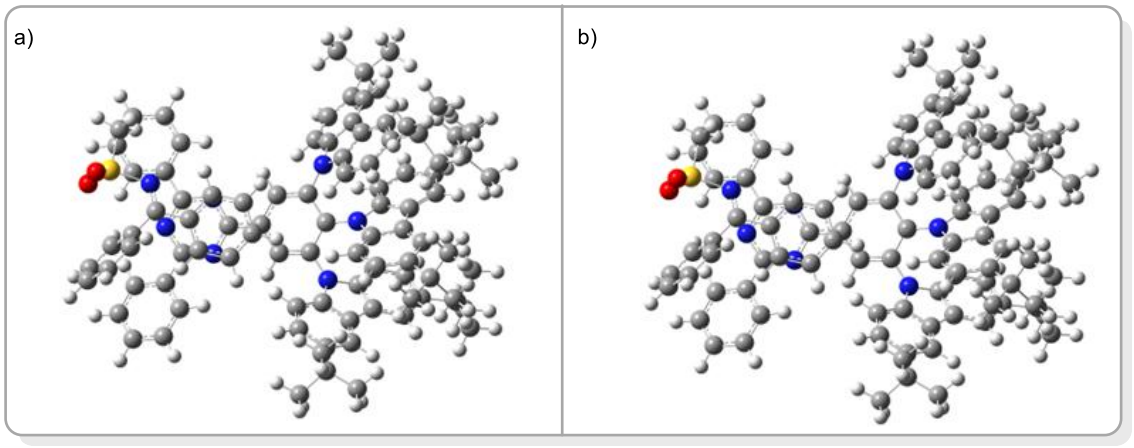

*Figure 39. a) top view of the collision complex between ^{3}(PS **39**)* and (**32a**). b) side view of the collision complex between ^{3}(PS **39**)* and (**32a**).*

3.4.5. Limitations of the reaction

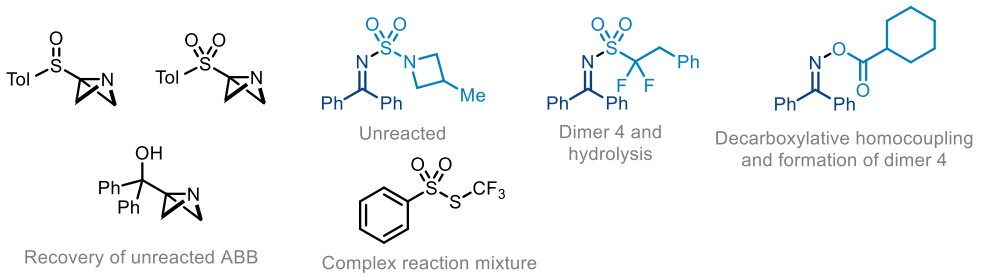

Figure 40. Unsuccessful assets under the optimized standard conditions.

During the exploration of the generality of the developed protocol, some limitations were encountered (Figure 40). Substituting C_3 at the ABB with a sulfoxide, sulfone or diphenylmethanol functionalities proved unsuccessful, recovering the unreacted material and just formation of the dimer **35**. Attempting to install a sulfamoyl radical coming from the corresponding azetidine-sulfonylimine conducted to the recovery of the unreacted starting material and partial hydrolysis of it, suggesting that either the triplet sensitization of this asset is not thermodynamically feasible or that the N-S bond of this compound is not sufficiently labile to be cleaved. Attempting to install an α-difluoro-*gem* sulfonyl backbone proved unsuccessful, observing the formation of dimer **35** and partial hydrolysis of the sulfonylimine. The result might suggest that in this particular case, extrusion of sulfur dioxide is leveraged by the formation of the stabilized *gem*-difluoro carbon centered radical which is not electronically matching with the nitrogen atom of the ABB.

To extend the last concept, when testing an iminyloxime-ester aiming to install the corresponding secondary carbon centered radical to the ABB, we detected the formation of dimer **35**, decarboxylative homocoupling and unreacted ABB.

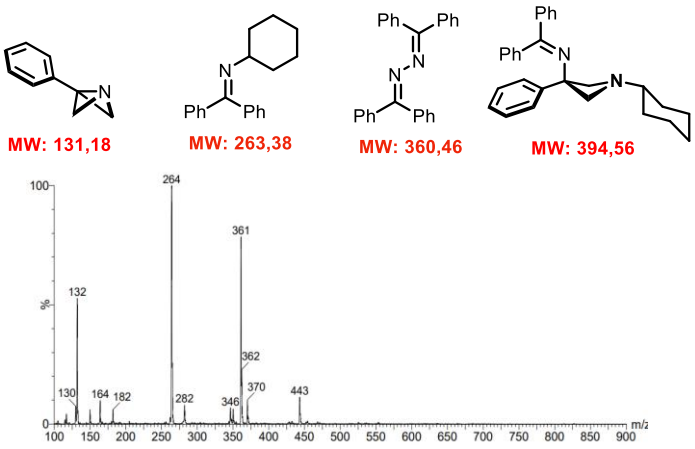

*Figure 41. ESI+ mass trace of the unsuccessful C-centred radical addition to the ABB **31**.*

Before realizing that the addition of the SCF3 moiety at the C_3 position of the ABB via the abovementioned three-component protocol was the proper strategy, we tested S-(trifluoromethyl) benzenesulfonothiolate. The plan was to triplet sensitise it and consequently generate in concomitance the SCF3- and benzenesulfonyl radical intermediates, which ideally would add to the ABB. However, this strategy proved unsuccessful, conducting to messy reaction mixtures without detecting the desired product.

3.4.6. Additional synthetic transformations

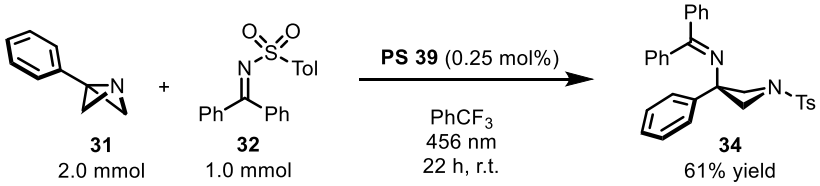

ABB **31** (2.0 mmol, 262 mg, 2.0 equiv) and sulfonylimine **32** (1.0 mmol, 336 mg, 1.0 equiv) were added to an oven-dried 50 mL Schlenk tube and were dissolved using a freshly prepared solution of PS **39** (12 mL, 0.25 mol% is the photosensitizer loading. $PhCF_3$ distilled from phosphorus pentoxide). The vessel was closed with a greased glass stoper and the reaction mixture was degassed by performing three freeze-pump-thaw cycles. The degassed solution was stirred using a Heidolph stirring plate (500 rpm) at ambient temperature under irradiation of two 456 nm Kessil lamps, for 22 hours (Figure 42). After completion, the resultant mixture was evaporated under reduced pressure and purified by flash column chromatography. Compound **34** was obtained as a white (slightly yellow) solid in 61% yield (283 mg).

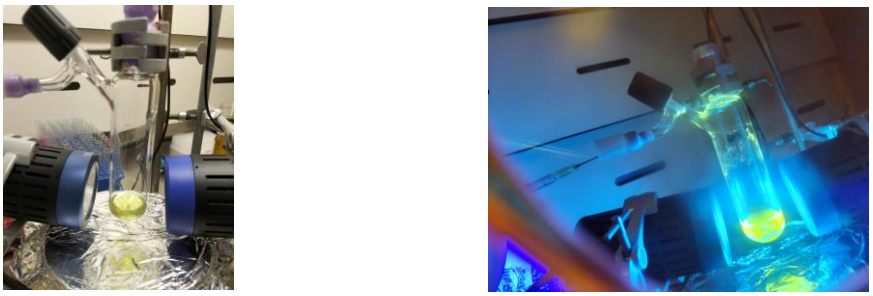

Figure 42. Photochemical arrangement for the scale-up reaction.

Synthetic manipulations of 34

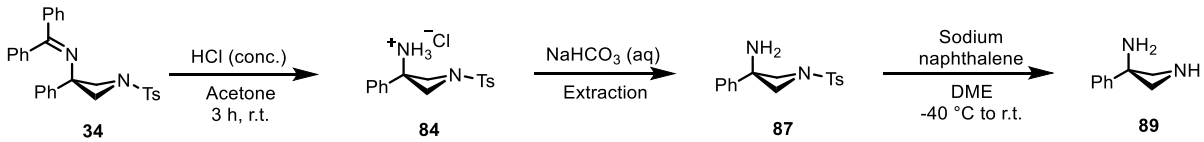

*Scheme 25. Procedure for the synthesis of **89**.*

To a solution of **34** (200 mg, 0.42 mmol) in acetone (0.09 M), concentrated hydrochloric acid (1 mL) was added dropwise. The resulting mixture was stirred for three hours at room temperature. After completion, the volatiles were removed under reduced pressure (6 mbar at 50 °C). Once dried, the resulting amorphous solid was transferred to a separatory funnel by consecutive washings of water and diethyl ether. The aqueous phase was collected and evaporated under reduced pressure (6 mbar at 50 °C), giving place to the hydrochloride salt **84** as a white solid in quantitative yield without requiring additional purifications.

^{1}H NMR (400 MHz, D_2O) δ 7.68 (d, J = 8.0 Hz, 2H), 7.46 – 7.26 (m, 5H), 7.09 (d, J = 7.4 Hz, 2H), 4.52 (d, J = 10.7 Hz, 2H), 4.33 (d, J = 10.6 Hz, 2H), 2.32 (s, 3H). **^{13}C NMR** (101 MHz, D_2O) δ 146.52, 134.9, 130.3, 129.5, 129.2, 128.2, 127.5, 125.5, 59.9, 53.3, 20.7. **84** can be washed with a 20% (v/v) aqueous solution of $NaHCO_3$ and extracted using diethyl ether. Evaporation of the volatiles gives azetidine **87** as a yellowish oil that spontaneously crystallizes.

^{1}H NMR (400 MHz, CD_2Cl_2) δ 7.74 (d, *J* = 8.2 Hz, 1H), 7.41 (d, *J* = 8.0 Hz, 1H), 7.33 – 7.21 (m, 2H), 4.07 (d, *J* = 8.3 Hz, 1H), 3.77 (d, *J* = 8.3 Hz, 1H), 2.46 (s, 1H). **^{13}C NMR** (101 MHz, CD_2Cl_2) δ 144.9, 144.1, 131.6, 130.3, 128.8 (d, *J* = 8.1 Hz), 128.7, 127.8, 125.4, 66.3, 53.8, 21.7. **HRMS**: Calculated: $[M+H]^+$ 303.1161, experimental: 303.1164.

To a solution of azetidine **87** (7.8 mg, 0.025 mmol, 1.0 equiv) in anhydrous DME (1 mL), sodium naphthalene (0.2 mL; a 0.5 M solution prepared from 516 mg of naphthalene and 71 mg of sodium in 6 mL was used) was added dropwise at -40 °C. The reaction was stirred for 2 hours at this temperature and thereafter for 30 minutes at room temperature. The reaction was quenched with water and the phases were separated. The organic phase was evaporated and dried with anhydrous sodium sulfate. The desired product **89** was spectroscopically identified as a mixture with naphthalene and was obtained in 81% yield. The spectroscopic data was in accordance with the reported one18. **^{1}H NMR** (400 MHz, CD_2Cl_2) δ 7.21 – 7.01 (m, 5H), 5.97 (s, 2H), 3.42 (s, 4H).

Figure 43. Sodium naphthalene in DME.

Preparation of hydrochloride salts 85 and 86

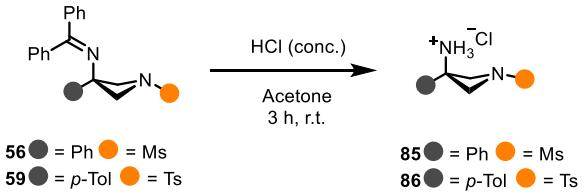

Scheme 26. General protocol for the synthesis of hydrochloride salts.

To a solution of the desired azetidine in acetone (0.09 M), concentrated hydrochloric acid (1 mL) was added dropwise. The resulting mixture was stirred for three hours at room temperature. After completion, the volatiles were removed under reduced pressure (6 mbar at 50 °C). Once dried, the resulting amorphous solid was transferred to a separatory funnel by consecutive washings of water and diethyl ether. The aqueous phase was collected and evaporated under reduced pressure (6 mbar at 50 °C), giving place to the corresponding hydrochloride salt as a white solid in quantitative yield without requiring additional purifications.

1-(Methylsulfonyl)-3-phenylazetidin-3-aminium chloride 85

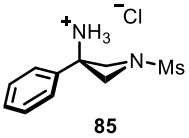

85

White solid. **^{1}H NMR** (400 MHz, D_2O) δ 7.62 – 7.44 (m, 5H), 4.62 (d, *J* = 9.1 Hz, 2H), 4.45 (d, *J* = 9.1 Hz, 2H), 3.13 (d, *J* = 1.0 Hz, 3H). **^{13}C NMR** (151 MHz, D_2O) δ 129.7, 129.4, 125.6, 59.8, 53.2, 34.6. **HRMS**: Calculated for $C_{10}H_{15}N_2O_2S^+$: 227.0854; experimental: 227.0861.

3-(*p*-Tolyl)-1-tosylazetidin-3-aminium chloride 86

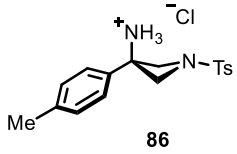

86

White solid. **^{1}H NMR** (400 MHz, D_2O) δ 7.70 (d, *J* = 8.2 Hz, 2H), 7.34 (d, *J* = 8.0 Hz, 2H), 7.18 (d, *J* = 8.0 Hz, 2H), 6.96 (d, *J* = 8.2 Hz, 2H), 4.52 (d, *J* = 10.7 Hz, 2H), 4.34 (d, *J* = 10.8 Hz, 2H), 2.36 (s, 3H), 2.32 (s, 3H). **^{13}C NMR** (101 MHz, D_2O) δ 146.6, 140.1, 131.9, 130.2, 129.7, 128.2, 127.6, 125.5, 60.0, 53.1, 20.7, 20.2. **HRMS**: Calculated for $C_{17}H_{21}N_2O_2S^+$: 317.1323; experimental: 317.1330.

Synthesis of N-(4-methylbenzyl)-3-phenyl-1-tosylazetidin-3-amine 83

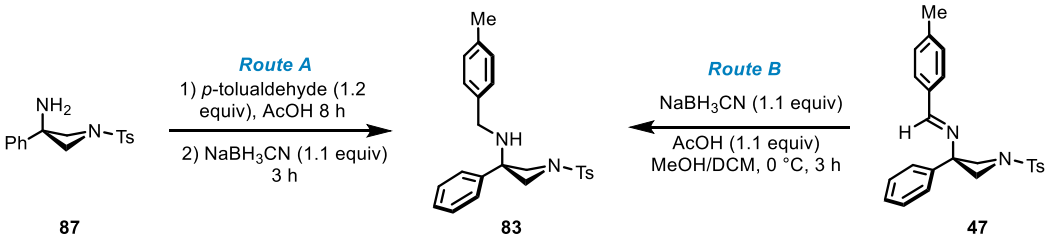

87 **83** **47**

*Scheme 27. Synthesis of amine **83**.*

The title compound was prepared employing two synthetic strategies, labeled as Route A and Route B.

Route A. To a solution of azetidine **87** (14 mg, 0.046 mmol, 1.0 equiv) in DCM/MeOH (5 mL, 1:3), *p*tolualdehyde (6 mg, 0.05 mmol, 1.1 equiv) was added in one portion, followed by some drops of acetic acid. The reaction mixture was stirred at room temperature for 8 hours. After completion, the reaction was cooled to 0 °C and $NaBH_3CN$ (3.2 mg, 0.05 mmol, 1.1 equiv) was added and left to stir for 3 hours. The reaction was quenched with water and the phases were separated. After drying and solvent removal, the crude was purified using column chromatography (Pasteur pipette) using 6:4 hexane/AcOEt as eluent. The title compound was obtained as a yellow oil in 77% yield (14 mg).

Route B. To a solution of azetidine **47** in DCM/MeOH (5 mL, 1:3), five drops (Pasteur pipette dosage) of aceti acid and $NaBH_3CN$ (3.2 mg, 0.05 mmol, 1.1 equiv) were added at 0 °C and stirred for 3 hours. After completion, water was added, and the phases were separated. The aqueous phase was extracted with DCM and was thoroughly washed with water and brine. The organic extract was dried with anhydrous sodium sulfate. Removal of the solvent under reduced pressure conducted to the title product with enough purity to avoid further purifications.

^{1}H NMR (400 MHz, CD_2Cl_2) δ 7.75 (d, *J* = 8.0 Hz, 2H), 7.43 – 7.29 (m, 7H), 7.14 – 7.10 (m, 2H), 7.05 (d, *J* = 7.8 Hz, 2H), 4.09 (d, *J* = 8.7 Hz, 2H), 3.90 (d, *J* = 8.5 Hz, 2H), 3.32 (s, 2H), 2.45 (s, 3H), 2.34 (s, 3H). **^{13}C NMR** (101 MHz, CD_2Cl_2) δ 144.8, 142.1, 137.2, 137.1, 130.2, 129.4, 128.9, 128.7, 128.3, 127.8, 126.4, 62.3, 58.1, 47.6, 21.7, 21.2. **HRMS**: Calculated: $[M+H]^+$ 407.1787, experimental: 407.1784.

Synthesis of 1-(3-phenyl-1-tosylazetidin-3-yl)pyrrolidine 88

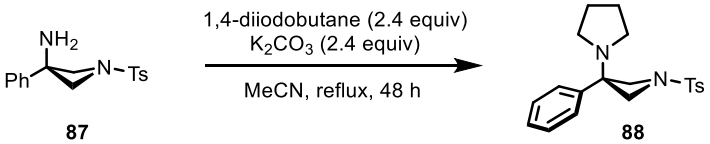

87 **88**

*Scheme 28. Synthesis of 1-(3-phenyl-1-tosylazetidin-3-yl)pyrrolidine **88***

The following procedure has been adapted from the literature.[62] A 5 mL sealed tube was charged with amino azetidine **87** (24.1 mg, 0.08 mmol. 1.0 equiv), 1,4-diiodobutane (0.19 mmol, 2.4 equiv), K_2CO_3 (0.19 mmol,

2.4 equiv) and acetonitrile (0.27 M). The reaction mixture was stirred under reflux for 48 hours and after completion, it was cooled to room temperature. After evaporation of the volatiles, the residue was diluted with DCM (3 mL) and water (3 mL). The organic layer was separated, and the aqueous phase was washed with more DCM. The combined organic layers were combined and purified by column chromatography to isolate compound **88** as a yellowish solid in 55% yield (15.6 mg).

^{1}H NMR (400 MHz, $CDCl_3$) δ 7.71 (d, *J* = 8.2 Hz, 2H), 7.32 – 7.20 (m, 5H), 7.09 (d, *J* = 8.5 Hz, 2H), 4.16 (d, *J* = 8.4 Hz, 2H), 4.02 (d, *J* = 8.4 Hz, 2H), 2.40 (s, 3H), 2.34 (bs, 4H), 1.62 (t, *J* = 3.6 Hz, 4H). **^{13}C NMR** (101 MHz, $CDCl_3$) δ 144.1, 140.4, 132.2, 129.7, 128.4, 128.2, 127.3, 126.6, 60.0, 58.3, 46.6, 23.4, 21.7. **HRMS**: Calculated: $[M+H]^+$ 357.1631, experimental: 357.1634.

Synthesis of 5-tosyl-1,5-diazaspiro[2.3]hexan-2-one 91

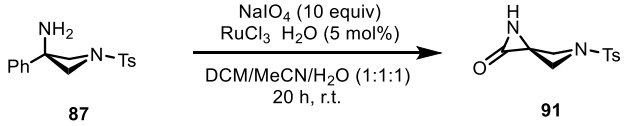

*Scheme 29.Synthesis of 5-tosyl-1,5-diazaspiro[2.3]hexan-2-one **91**.*

The following procedure has been adapted from the literature20. To a mixture of amino azetidine **87** (33 mg, 0.11 mmol, 1.0 equiv), and sodium periodate (1.10 mmol, 10.0 equiv), in DCM (1 mL)/MeCN (1.0 mL)/H_2O (1mL) was added at room temperature $RuCl3 \cdot H_2O$ (1.2 mg, 5 mol%). The reaction became brownish and was vigorously stirred for 20 hours at the same temperature. After completion, the reaction mixture was diluted with AcOEt (10 mL) and filtered over celite. Then, water (10 mL) was added, and the phases were separated. The aqueous layer was extracted with DCM and the combined organic layers were dried over anhydrous sodium sulfate, filtered and concentrated under reduced pressure. The resulting crude was purified through column chromatography (Pasteur pipette using Hex/Et2O 1:1. *Rf* = 0.3) to afford the title compound as a yellowish oil (52% yield, 14 mg). The elution of the compound was monitored using KMnO4 stain, as the compound cannot be detected by UV-vis lamp. Before column chromatography was performed, the aqueous phase was checked by 1H NMR, but any compound was detected.

^{1}H NMR (400 MHz, CD_2Cl_2) δ 7.78 (d, *J* = 7.9 Hz, 2H), 7.42 (d, *J* = 8.0 Hz, 2H), 4.60 (s, 4H), 2.46 (s, 3H). **^{13}C NMR** (101 MHz, CD_2Cl_2) δ 193.1, 145.7, 131.5, 130.6, 128.8, 73.1, 30.1, 21.8. **HRMS**: Calculated: $[M+Na]^+$ 275.0460, experimental: 275.0880.

3.4.7. X-ray Crystallographic data

*Table 5. X-ray crystallographic data for compound **34**:*

Compound	**34**
Empirical formula	C29 H26 N2 O2 S
Formula weight	343.63
Temperature/K	200.0
Diffractometer/detector	Bruker D8 Venture / PhotonII area detector
Radiation	MoKα (λ = 0.71073)
Crystal system	Monoclinic
Space group	P21/n
a/Å	10.1239(2)
b/Å	19.9371(5)
c/Å	12.2428(3)
α/°	90
β/°	97.647(1)
γ/°	90
Volume/Å^3	2449.1(1)
Z	4
ρ_{calc} /g·cm^{-3}	1.265
μ/mm^{-1}	0.161
F(000)	984
Θ range for data	1.96-26.44
	-11<h<12
Index ranges	-24<k<24
	-15<l<15
Reflections collected	76002
Unique reflections	5040
Parameters	308
Goodness-of-fit on F^2	1.034
Final R indexes [I>=2σ (I)]	R=0.044, wR2=0.1141
CCDC Number	**2305658**

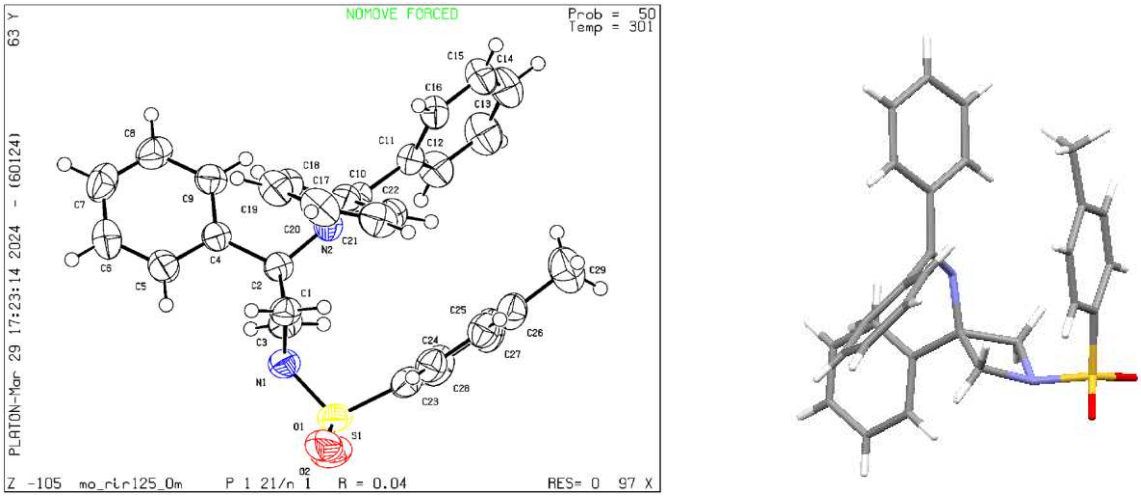

*Figure 44. ORTEP representation of compound **34**.*

*Table 6. crystallographic data for compound **51**.*

Compound	**51**
Empirical formula	C29 H23 F3 N2 O2 S
Formula weight	520.55
Diffractometer/Detector	Bruker D8 Venture / PhotonII area detector
Radiation	CuKα radiation (λ = 1.54178)
Crystal system	Monoclinic
Space group	P21/c
Z	4
a/Å	8.6875(2)
b/Å	38.9110(7)
c/Å	7.72120(10)
α/°	90
β/°	103.618(1)
γ/°	90
Volume/Å^3	2536.69(8)
ρ_{calc} /g·cm^{-3}	1.363
μ/mm^{-1}	1.583
F(000)	1080
Θ range for data	2.27-74.48
	-9<h<10
Index ranges	-47<k<48
	-9<l<9
Reflections collected	28168
Unique reflections	5183
Parameters	332
Goodness-of-fit on F^2	1.037,
Final R indexes [I>=2σ (I)]	R=0.041, wR2=0.098
CCDC Number	**2305660**

The CF3 group is disordered over two sites and was refined with bond length constraints to give a refined occupancy ratio of 0.5:0.5.

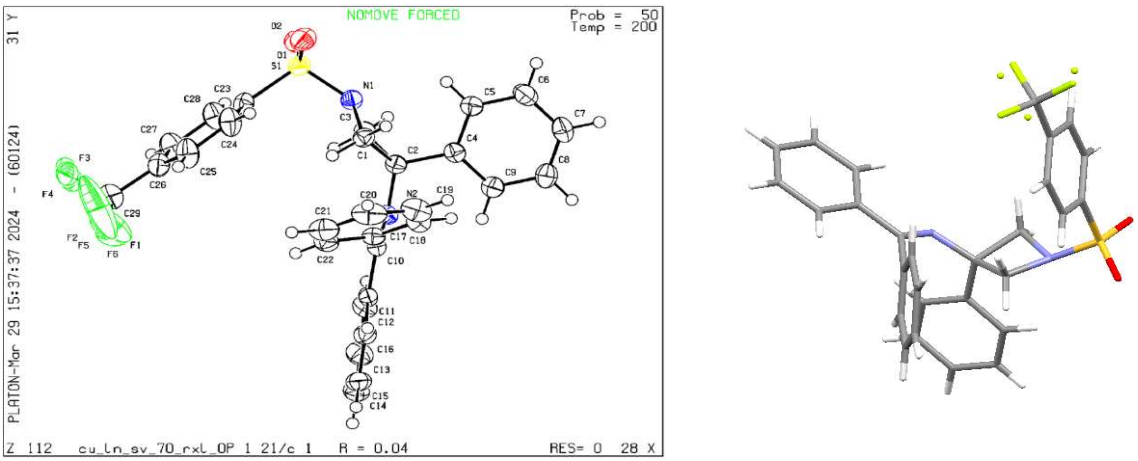

*Figure 45. ORTEP representation of compound **51**.*

*Table 7. Crystallographic data for compound **54**.*

Compound	**54**
Empirical formula	C32 H26 N2 O2 S
Formula weight	502.61
Diffractometer/detector	Bruker D8 Venture / PhotonII area detector
Radiation	CuKα radiation (λ = 1.54178)
Crystal system	Monoclinic
Space group	P21/n
Z	4
a/Å	14.925(1)
b/Å	1 0.1341(8)
c/Å	17.2603(13)
α/°	90
β/°	100.351(7)
γ/°	90
Volume/Å^3	2568.2(3)
ρ_{calc} /g·cm^{-3}	1.300
μ/mm^{-1}	1.373
F(000)	1056
Θ range for data collection/°	3.61-70.06
	-17<h<18
Index ranges	-12<k<10
	-21<l<20
Reflections collected	16937
Unique reflections	4817
Parameters	438
Goodness-of-fit on F^2	1.054
Final R indexes [I>=2σ (I)]	R=0.045, wR2=0.1099
CCDC Number	**2305656**

The CF3 group was disordered on two positions and was refined with bond length constraints to give a defined occupancy ratio of 0.5:0.5.

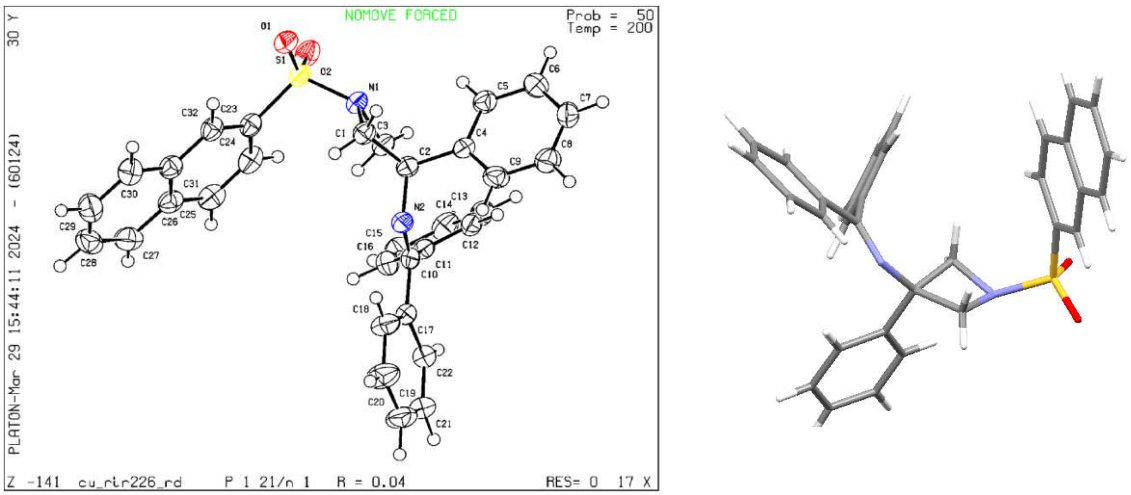

*Figure 46. ORTEP representation of compound **54**.*

*Table 8. Crystallographic data for compound **65**.*

Compound	**65**
Empirical formula	C30 H28 N2 O2 S
Formula weight	480.60
Diffractometer/detector	Bruker D8 Venture / PhotonII area detector
Radiation	CuKα radiation (λ = 1.54178)
Crystal system	Monoclinic
Space group	C2/c
Z	8
a/Å	30.8527(6)
b/Å	9.7204(2)
c/Å	19.4155(4)
α/°	90
β/°	118.600(1)
γ/°	90
Volume/Å^3	5112.2(2)
ρ_{calc} /g·cm^{-3}	1.249
μ/mm^{-1}	1.352
F(000)	2032
Θ range for data	3.26-69.98
	-37<h<37
Index ranges	-11<k<10
	-23<l<23
Reflections collected	24808
Unique reflections	4829
Parameters	417
Goodness-of-fit on F^2	1.014,
Final R indexes [I>=2σ (I)]	R=0.047, wR2=0.1103
CCDC Number	**2305659**

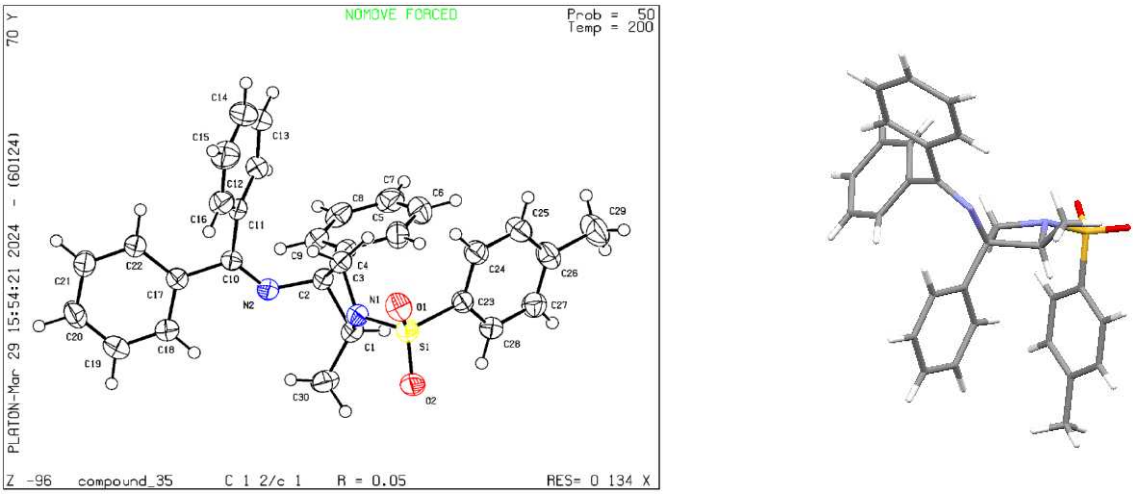

*Figure 47. ORTEP representation of compound **65**.*

*Table 9. Crystallographic data for compound **66**.*

Compound	**66**
Empirical formula	C30 H28 N2 O2 S
Formula weight	480.60
Diffractometer/detector	Bruker D8 Venture / PhotonII area detector
Radiation	CuKα radiation (λ = 1.54178)
Crystal system	Monoclinic
Space group	P21/c
Z	4
a/Å	10.1913(2)
b/Å	20.4646(4)
c/Å	16.7309(6)
α/°	90
β/°	134.624(7)
γ/°	90
Volume/Å^3	2481.3(3)
ρ_{calc} /g·cm^{-3}	1.287
μ/mm^{-1}	1.39
F(000)	1016
Θ range for data	4.29-70.04
	-12<h<12
Index ranges	-24<k<24
	-20<l<20
Reflections collected	42590
Unique reflections	4716
Parameters	428
Goodness-of-fit on F^2	1.040
Final R indexes [I>=2σ (I)]	R=0.035, wR2=0.096
CCDC Number	**2305657**

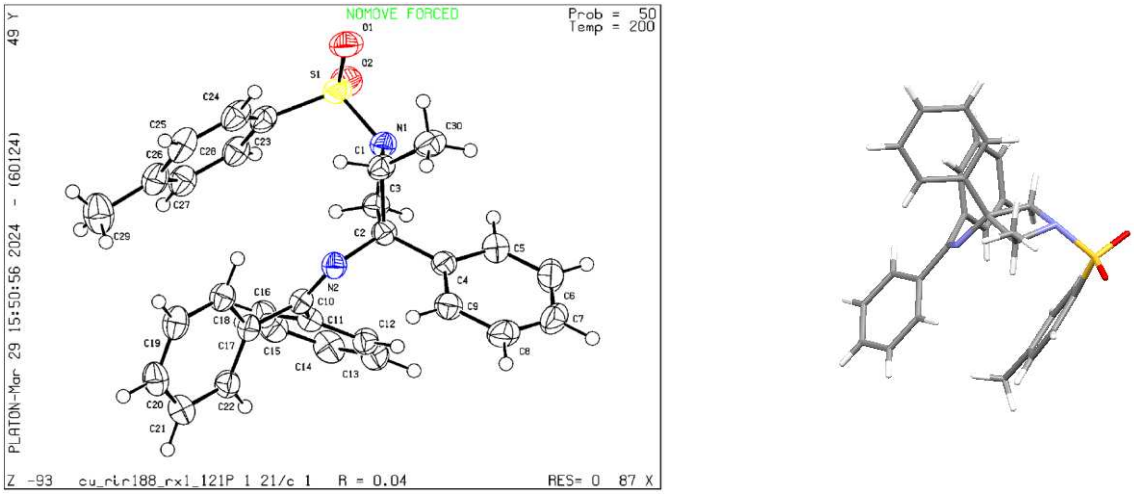

*Figure 48. ORTEP representation of compound **66**.*

Four *t*-butyl groups were disordered on two positions each and were refined with bond length constraints to give a refined occupancy ratio of 0.5:0.5. One of them also presents a splitting of the butyl group quaternary carbon. A solvent mask was calculated, and 33 electrons were found in a volume of 951A^{55} in 5 voids per unit cell. This is consistent with the presence of 0.6[H_2O] per formula unit which account for 24 electrons per unit cell.

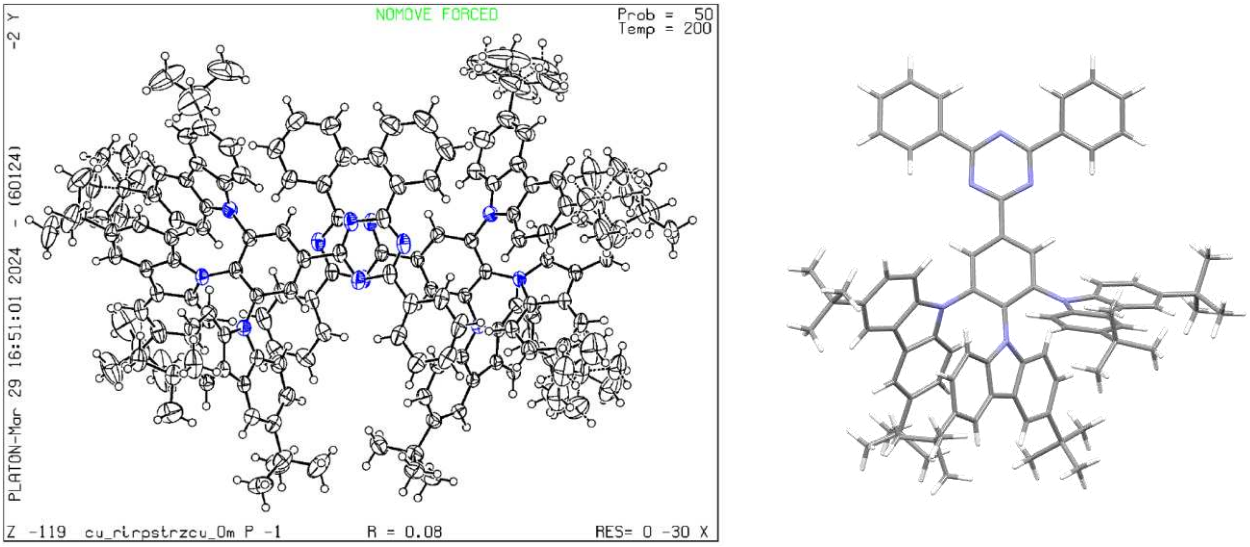

*Figure 49. ORTEP representation of compound PS **39**.*

3.5. References

(1) Langmuir, I. Isomorphism, Isosterism and Covalence. *J. Am. Chem. Soc.* **1919**, *41*, 1543–1559.

(2) Patani, G. A.; LaVoie, E. J. Bioisosterism: A Rational Approach in Drug Design. *Chem. Rev.* **1996**, *96* (8), 3147–3176. https://doi.org/10.1021/cr950066q.

(3) Jha, T. *Modeling Inhibitors of Matrix Metalloproteinases*; 2023. https://doi.org/10.1201/9781003303282.

(4) Purser, S.; Moore, P. R.; Swallow, S.; Gouverneur, V. Fluorine in Medicinal Chemistry. *Chem. Soc. Rev.* **2008**, *37* (2), 320–330. https://doi.org/10.1039/b610213c.

(5) Chauhan, A. S.; Sharma, N.; Jain, V. The Role of Bioisosterism in Modern Drug Design: Current Applications and Challenges. *Curr. Trends Pharm. Pharm. Chem.* **2025**, *7* (1), 6–9. https://doi.org/10.18231/j.ctppc.2025.002.

(6) Meanwell, N. A. Synopsis of Some Recent Tactical Application of Bioisosteres in Drug Design. *J. Med. Chem.* **2011**, *54* (8), 2529–2591. https://doi.org/10.1021/jm1013693.

(7) Shu, Y. Z.; Johnson, B. M.; Yang, T. J. Role of Biotransformation Studies in Minimizing Metabolism-Related Liabilities in Drug Discovery. *AAPS J.* **2008**, *10* (1), 178–192. https://doi.org/10.1208/s12248-008-9016-9.

(8) Lovering, F.; Bikker, J.; Humblet, C. Escape from Flatland: Increasing Saturation as an Approach to Improving Clinical Success. *J. Med. Chem.* **2009**, *52* (21), 6752–6756. https://doi.org/10.1021/jm901241e.

(9) Lovering, F. Escape from Flatland 2: Complexity and Promiscuity. *Medchemcomm* **2013**, *4* (3), 515–519. https://doi.org/10.1039/c2md20347b.

(10) Meanwell, N. A. Fluorine and Fluorinated Motifs in the Design and Application of Bioisosteres for Drug Design. *J. Med. Chem.* **2018**, *61* (14), 5822–5880. https://doi.org/10.1021/acs.jmedchem.7b01788.

(11) Hernández-Lladó, P.; Meanwell, N. A.; Russell, A. J. A Data-Driven Perspective on Bioisostere Evaluation: Mapping the Benzene Bioisostere Landscape with BioSTAR. *J. Med. Chem.* **2025**. https://doi.org/10.1021/acs.jmedchem.5c01641.

(12) Ritchie, T. J.; MacDonald, S. J. F.; Young, R. J.; Pickett, S. D. The Impact of Aromatic Ring Count on Compound Developability: Further Insights by Examining Carbo- and Hetero-Aromatic and -Aliphatic Ring Types. *Drug Discov. Today* **2011**, *16* (3–4), 164–171. https://doi.org/10.1016/j.drudis.2010.11.014.

(13) Maetani, M.; Zoller, J.; Melillo, B.; Verho, O.; Kato, N.; Pu, J.; Comer, E.; Schreiber, S. L. Synthesis of a Bicyclic Azetidine with in Vivo Antimalarial Activity Enabled by Stereospecific, Directed C(Sp3)-H Arylation. *J. Am. Chem. Soc.* **2017**, *139* (32), 11300–11306. https://doi.org/10.1021/jacs.7b06994.

(14) Andresini, M.; Degennaro, L.; Luisi, R. The Renaissance of Strained 1-Azabicyclo[1.1.0]Butanes as Useful Reagents for the Synthesis of Functionalized Azetidines. *Org. Biomol. Chem.* **2020**, *18* (30), 5798–5810. https://doi.org/10.1039/d0ob01251c.

(15) Banks, H. D. The Profound Effect of Fluorine Substitution on the Reactivity and Regioselectivity of Nucleophilic Substitution Reactions of Strained Heterocycles. A Study of Aziridine and Its Derivatives. *J. Org. Chem.* **2006**, *71* (21), 8089–8097. https://doi.org/10.1021/jo061255j.

(16) Dudev, T.; Lim, C. Ring Strain Energies from Ab Initio Calculations. *J. Am. Chem. Soc.* **1998**, *120* (18), 4450–4458. https://doi.org/10.1021/ja973895x.

(17) Searles, S.; Tamres, M.; Block, F.; Quarterman, L. A. Hydrogen Bonding and Basicity of Cyclic Imines. *J. Am. Chem. Soc.* **1956**, *78* (19), 4917–4920. https://doi.org/10.1021/ja01600a029.

(18) Bauer, M. R.; Di Fruscia, P.; Lucas, S. C. C.; Michaelides, I. N.; Nelson, J. E.; Storer, R. I.; Whitehurst, B. C. Put a Ring on It: Application of Small Aliphatic Rings in Medicinal Chemistry. *RSC Med. Chem.* **2021**, *12* (4), 448–471. https://doi.org/10.1039/d0md00370k.

(19) Feskov, I. O.; Chernykh, A. V.; Kuchkovska, Y. O.; Daniliuc, C. G.; Kondratov, I. S.; Grygorenko, O. O. 3-((Hetera)Cyclobutyl)Azetidines, "Stretched" Analogues of Piperidine, Piperazine, and Morpholine: Advanced Building Blocks for Drug Discovery. *J. Org. Chem.* **2019**, *84* (3), 1363–1371. https://doi.org/10.1021/acs.joc.8b02822.

(20) Rice, K. D.; Aay, N.; Anand, N. K.; Blazey, C. M.; Bowles, O. J.; Bussenius, J.; Costanzo, S.; Curtis, J. K.; Defina, S. C.; Dubenko, L.; Engst, S.; Joshi, A. A.; Kennedy, A. R.; Kim, A. I.; Koltun, E. S.; Lougheed, J. C.; Manalo, J. C. L.; Martini, J. F.; Nuss, J. M.; Peto, C. J.; Tsang, T. H.; Yu, P.; Johnston, S. Novel Carboxamide-Based Allosteric MEK Inhibitors: Discovery and Optimization Efforts toward XL518 (GDC-0973). *ACS Med. Chem. Lett.* **2012**, *3* (5), 416–421. https://doi.org/10.1021/ml300049d.

(21) Johansson, A.; Löfberg, C.; Antonsson, M.; Von Unge, S.; Hayes, M. A.; Judkins, R.; Ploj, K.; Benthem, L.; Lindén, D.; Brodin, P.; Wennerberg, M.; Fredenwall, M.; Li, L.; Persson, J.; Bergman, R.; Pettersen, A.; Gennemark, P.; Hogner, A. Discovery of (3-(4-(2-Oxa-6-Azaspiro[3.3]Heptan-6-Ylmethyl)Phenoxy)Azetidin-1-Yl)(5-(4-Methoxyphenyl)-1,3,4-Oxadiazol-2-Yl)Methanone (AZD1979), a Melanin Concentrating Hormone Receptor 1 (MCHr1) Antagonist with Favorable Physicochemical Properties. *J. Med. Chem.* **2016**, *59* (6), 2497–2511. https://doi.org/10.1021/acs.jmedchem.5b01654.

(22) Vitaku, E.; Smith, D. T.; Njardarson, J. T. Analysis of the Structural Diversity, Substitution Patterns, and Frequency of Nitrogen Heterocycles among U.S. FDA Approved Pharmaceuticals. *J. Med. Chem.* **2014**, *57* (24), 10257–10274. https://doi.org/10.1021/jm501100b.

(23) Stefano France, A. W.; Andrew E. Taggi, A. T. L. Advances in the Catalytic Asymmetric Synthesis of Atropisomeric Hexatomic N-Heterobiaryls. *Adv. Synth. Catal.* **2004**, *37*, 592–600. https://doi.org/10.1002/adsc.202000354.

(24) Marco-Contelles, J. β-Lactam Synthesis by the Kinugasa Reaction. *Angew. Chem. Int. Ed.* **2004**, *43* (17), 2198–2200. https://doi.org/10.1002/anie.200301730.

(25) Pitts, C. R.; Lectka, T. Chemical Synthesis of β-Lactams: Asymmetric Catalysis and Other Recent Advances. *Chem. Rev.* **2014**, *114* (16), 7930–7953. https://doi.org/10.1021/cr4005549.

(26) Kirichok, A. A.; Shton, I.; Kliachyna, M.; Pishel, I.; Mykhailiuk, P. K. 1-Substituted 2-Azaspiro[3.3]Heptanes: Overlooked Motifs for Drug Discovery. *Angew. Chem. Int. Ed.* **2017**, *129* (30), 8991–8995. https://doi.org/10.1002/ange.201703801.

(27) Betz, K. N.; Chiappini, N. D.; Du Bois, J. Intermolecular Sp3-C-H Amination for the Synthesis of Saturated Azacycles. *Org. Lett.* **2020**, *22* (5), 1687–1691. https://doi.org/10.1021/acs.orglett.9b04096.

(28) Kovács, E.; Faigl, F.; Mucsi, Z. Regio- And Diastereoselective Synthesis of 2-Arylazetidines: Quantum Chemical Explanation of Baldwin's Rules for the Ring-Formation Reactions of Oxiranes †. *J. Org. Chem.* **2020**, *85* (17), 11226–11239. https://doi.org/10.1021/acs.joc.0c01310.

(29) Franceschi, P.; Cuadros, S.; Goti, G.; Dell'Amico, L. Mechanisms and Synthetic Strategies in Visible Light-Driven [2+2]-Heterocycloadditions. *Angew. Chem. Int. Ed.* **2023**, *62* (8). https://doi.org/10.1002/anie.202217210.

(30) Becker, M. R.; Wearing, E. R.; Schindler, C. S. Synthesis of Azetidines via Visible-Light-Mediated Intermolecular [2+2] Photocycloadditions. *Nat. Chem.* **2020**, *12* (10), 898–905. https://doi.org/10.1038/s41557-020-0541-1.

(31) Rykaczewski, K. A.; Becker, M. R.; Anantpur, M. J.; Sausa, R. C.; Johnson, E. C.; Orlicki, J. A.; Bukowski, E. J.; Sabatini, J. J.; Schindler, C. S. Photochemical Strategies Enable the Synthesis of Tunable Azetidine-Based Energetic Materials. *J. Am. Chem. Soc.* **2022**, *144* (41), 19089–19096. https://doi.org/10.1021/jacs.2c08191.

(32) Fawcett, A.; Murtaza, A.; Gregson, C. H. U.; Aggarwal, V. K. Strain-Release-Driven Homologation of Boronic Esters: Application to the Modular Synthesis of Azetidines. *J. Am. Chem. Soc.* **2019**, *141* (11), 4573–4578. https://doi.org/10.1021/jacs.9b01513.

(33) Musci, P.; Colella, M.; Andresini, M.; Aramini, A.; Degennaro, L.; Luisi, R. Flow Technology Enabled Preparation of C3-Heterosubstituted 1-Azabicyclo[1.1.0]Butanes and Azetidines: Accessing Unexplored Chemical Space in Strained Heterocyclic Chemistry. *Chem. Commun.* **2022**, *58* (43), 6356–6359. https://doi.org/10.1039/d2cc01641a.

(34) Hsu, C. M.; Lin, H. B.; Hou, X. Z.; Tapales, R. V. P. P.; Shih, C. K.; Miñoza, S.; Tsai, Y. S.; Tsai, Z. N.; Chan, C. L.; Liao, H. H. Azetidines with All-Carbon Quaternary Centers: Merging Relay Catalysis with Strain Release Functionalization. *J. Am. Chem. Soc.* **2023**, *145* (34), 19049–19059. https://doi.org/10.1021/jacs.3c06710.

(35) Efange, S. M. N.; Khare, A. B.; Von Hohenberg, K.; MacH, R. H.; Parsons, S. M.; Tu, Z. Synthesis and in Vitro Biological Evaluation of Carbonyl Group-Containing Inhibitors of Vesicular

Acetylcholine Transporter. *J. Med. Chem.* **2010**, *53* (7), 2825–2835. https://doi.org/10.1021/jm9017916.

(36) Mughal, H.; Szostak, M. Recent Advances in the Synthesis and Reactivity of Azetidines: Strain-Driven Character of the Four-Membered Heterocycle. *Org. Biomol. Chem.* **2021**, *19* (15), 3274–3286. https://doi.org/10.1039/d1ob00061f.

(37) Wang, L.; Yu, Y.; Deng, L.; Du, K. Photochemical and Atom-Economical Sulfonylimination of Alkenes with Bifunctional N-Sulfonyl Ketimine. *Org. Lett.* **2023**, *25* (13), 2349–2354. https://doi.org/10.1021/acs.orglett.3c00724.

(38) Erchinger, J. E.; Hoogesteger, R.; Laskar, R.; Dutta, S.; Hümpel, C.; Rana, D.; Daniliuc, C. G.; Glorius, F. EnT-Mediated N-S Bond Homolysis of a Bifunctional Reagent Leading to Aliphatic Sulfonyl Fluorides. *J. Am. Chem. Soc.* **2023**, *145* (4), 2364–2374. https://doi.org/10.1021/jacs.2c11295.

(39) Meanwell, N. A. Improving Drug Candidates by Design: A Focus on Physicochemical Properties as a Means of Improving Compound Disposition and Safety. *Chem. Res. Toxicol.* **2011**, *24* (9), 1420–1456. https://doi.org/10.1021/tx200211v.

(40) Beatty, J. W.; Stephenson, C. R. J. Amine Functionalization via Oxidative Photoredox Catalysis: Methodology Development and Complex Molecule Synthesis. *Acc. Chem. Res.* **2015**, *48* (5), 1474–1484. https://doi.org/10.1021/acs.accounts.5b00068.

(41) Lowe, J. T.; Iv, M. D. L.; Akella, L. B.; Davoine, E.; Donckele, E. J.; Durak, L.; Duvall, J. R.; Gerard, B.; Holson, E. B.; Joliton, A.; Kesavan, S.; Lemercier, B. C.; Liu, H.; Marie, J.; Mulrooney, C. A.; Muncipinto, G.; Shea, M. W.; Panko, L. M.; Rowley, A.; Suh, B.; Thomas, M.; Wagner, F. F.; Wei, J.; Foley, M. A.; Marcaurelle, L. A. Synthesis and Pro Fi Ling of a Diverse Collection of Azetidine-Based Sca Ff Olds for the Development of CNS-Focused Lead-like Libraries. *J. Org. Chem.* **2012**, *77* (17), 7187–7211. https://doi.org/10.1021/jo300974j.

(42) Mateos, J.; Rigodanza, F.; Costa, P.; Natali, M.; Vega-Peñaloza, A.; Fresch, E.; Collini, E.; Bonchio, M.; Sartorel, A.; Dell'Amico, L. Unveiling the Impact of the Light Source and Steric Factors on [2 + 2] Heterocycloaddition Reactions. *Nat. Synth.* **2023**, *2* (1), 26–36. https://doi.org/10.1038/s44160-022-00191-5.

(43) Mateos, J.; Vega-Peñaloza, A.; Franceschi, P.; Rigodanza, F.; Andreetta, P.; Companyó, X.; Pelosi, G.; Bonchio, M.; Dell'Amico, L. A Visible-Light Paternò-Büchi Dearomatisation Process towards the Construction of Oxeto-Indolinic Polycycles. *Chem. Sci.* **2020**, *11* (25), 6532–6538. https://doi.org/10.1039/d0sc01569e.

(44) Strieth-Kalthoff, F.; James, M. J.; Teders, M.; Pitzer, L.; Glorius, F. Energy Transfer Catalysis Mediated by Visible Light: Principles, Applications, Directions. *Chem. Soc. Rev.* **2018**, *47* (19), 7190–7202. https://doi.org/10.1039/c8cs00054a.

(45) Zhang, D.; Cai, M.; Zhang, Y.; Zhang, D.; Duan, L. Sterically Shielded Blue Thermally Activated Delayed Fluorescence Emitters with Improved Efficiency and Stability. *Mater. Horizons* **2016**, *3* (2), 145–151. https://doi.org/10.1039/c5mh00258c.

(46) Bryden, M. A.; Zysman-Colman, E. Organic Thermally Activated Delayed Fluorescence (TADF) Compounds Used in Photocatalysis. *Chem. Soc. Rev.* **2021**, *50* (13), 7587–7680. https://doi.org/10.1039/d1cs00198a.

(47) Thoi, H. H.; Ito, O.; Iino, M.; Matsuda, M. Studies of Sulfonyl Radicals. 4. Flash Photolysis of Aromatic Sulfones. *J. Phys. Chem.* **1978**, *82* (3), 314–319. https://doi.org/10.1021/j100492a014.

(48) Ortica, F.; Coenjarts, C.; Scaiano, J. C.; Liu, H.; Pohlers, G.; Cameron, J. F. Mechanism of Reaction and Photoacid Generation of N-Oxysuccinimidoarylsulfonate PAGs: A Laser Flash Photolytic Study. *Chem. Mater.* **2001**, *13* (7), 2297–2304. https://doi.org/10.1021/cm000609z.

(49) Tilby, M. J.; Dewez, D. F.; Pantaine, L. R. E.; Hall, A.; Martínez-Lamenca, C.; Willis, M. C. Photocatalytic Late-Stage Functionalization of Sulfonamides via Sulfonyl Radical Intermediates. *ACS Catal.* **2022**, *12* (10), 6060–6067. https://doi.org/10.1021/acscatal.2c01442.

(50) Zhou, Y.; Wang, J.; Gu, Z.; Wang, S.; Zhu, W.; Acenã, J. L.; Soloshonok, V. A.; Izawa, K.; Liu, H. Next Generation of Fluorine-Containing Pharmaceuticals, Compounds Currently in Phase II-III Clinical Trials of Major Pharmaceutical Companies: New Structural Trends and Therapeutic Areas. *Chem. Rev.* **2016**, *116* (2), 422–518. https://doi.org/10.1021/acs.chemrev.5b00392.

(51) Nunez, M. T.; Martin, V. S. Efficient Oxidation of Phenyl Groups to Carboxylic Acids with Ruthenium

Tetraoxide. A Simple Synthesis of (R)-7-Caprolactone, the Pheromone of Trogoderma Granarium. *J. Org. Chem.* **1990**, *55* (6), 1928–1932. https://doi.org/10.1021/jo00293a044.

(52) Burkhard, J. A.; Guérot, C.; Knust, H.; Carreira, E. M. Expanding the Azaspiro[3.3]Heptane Family: Synthesis of Novel Highly Functionalized Building Blocks. *Org. Lett.* **2012**, *14* (1), 66–69. https://doi.org/10.1021/ol2028459.

(53) Hortmann, A. G.; Robertson, D. A. Synthesis and Reactions1. *J. Am. Chem. Soc.* **1972**, *1471* (9), 2758–2765.

(54) De, A.; Santra, S.; Zyryanov, G. V.; Majee, A. Self-Catalyzed Rapid Synthesis of N-Acylated/ N-Formylated α-Aminoketones and N-Hydroxymethylated Formamides from 3-Aryl-2 H-Azirines and 2-Me/Ph-3-Aryl-2 H-Azirines. *Org. Lett.* **2020**, *22* (10), 3926–3930. https://doi.org/10.1021/acs.orglett.0c01206.

(55) Rao, D. S.; Reddy, T. R.; Gurawa, A.; Kumar, M.; Kashyap, S. Photoswitchable Regiodivergent Azidation of Olefins with Sulfonium Iodate(I) Reagent. *Org. Lett.* **2019**, *21* (24), 9990–9994. https://doi.org/10.1021/acs.orglett.9b03910.

(56) Gianatassio, R.; Lopchuk, J. M.; Wang, J.; Pan, C.; Malins, L. R.; Prieto, L.; Brandt, T. A.; Collins, M. R.; Gallego, G. M.; Sach, N. W.; Spangler, J. E.; Zhu, H.; Zhu, J.; Baran, P. S. Strain-Release Amination. *Science* **2016**, *351* (6270), 241–246. https://doi.org/10.1126/science.aad6252.

(57) Lee, D. R.; Kim, M.; Jeon, S. K.; Hwang, S. H.; Lee, C. W.; Lee, J. Y. Design Strategy for 25% External Quantum Efficiency in Green and Blue Thermally Activated Delayed Fluorescent Devices. *Adv. Mater.* **2015**, *27* (39), 5861–5867. https://doi.org/10.1002/adma.201502053.

(58) Phetcharawetch, J.; Betterley, N. M.; Soorukram, D.; Pohmakotr, M.; Reutrakul, V.; Kuhakarn, C. Synthesis of Difluoromethyl Ketones from Weinreb Amides, and Tandem Addition/Cyclization of o-Alkynylaryl Weinreb Amides. *European J. Org. Chem.* **2017**, *2017* (46), 6840–6850. https://doi.org/10.1002/ejoc.201701322.

(59) Duong, H. A.; Gilligan, R. E.; Cooke, M. L.; Phipps, R. J.; Gaunt, M. J. Copper(II)-Catalyzed Meta-Selective Direct Arylation of A-Aryl Carbonyl Compounds. *Angew. Chem. Int. Ed.* **2011**, *123* (2), 483–486. https://doi.org/10.1002/ange.201004704.

(60) Colella, M.; Tota, A.; Takahashi, Y.; Higuma, R.; Ishikawa, S.; Degennaro, L.; Luisi, R.; Nagaki, A. Fluoro-Substituted Methyllithium Chemistry: External Quenching Method Using Flow Microreactors. *Angew. Chem. Int. Ed.* **2020**, *132* (27), 11016–11020. https://doi.org/10.1002/ange.202003831.

(61) Stoll, S.; Schweiger, A. EasySpin, a Comprehensive Software Package for Spectral Simulation and Analysis in EPR. *J. Magn. Reson.* **2006**, *178* (1), 42–55. https://doi.org/10.1016/j.jmr.2005.08.013.

(62) Yue, H.; Huang, H.; Bian, G.; Zong, H.; Li, F.; Song, L. Enantioselectivity Switch Controlled by N,N′-Di- or N,N,N′,N′-Tetra-Substituted Chiral Thiophosphorodiamide Ligands, Structural Relatives of Thioureas, in Catalytic Additions of Diethylzinc to Aldehydes. *Tetrahedron Asymmetry* **2014**, *25* (2), 170–180. https://doi.org/10.1016/j.tetasy.2013.12.014.

Chapter IV

Synthesis of Spiroindenes *via* Palladium-Catalysis Using Oxabicycles as Acetylene Surrogates

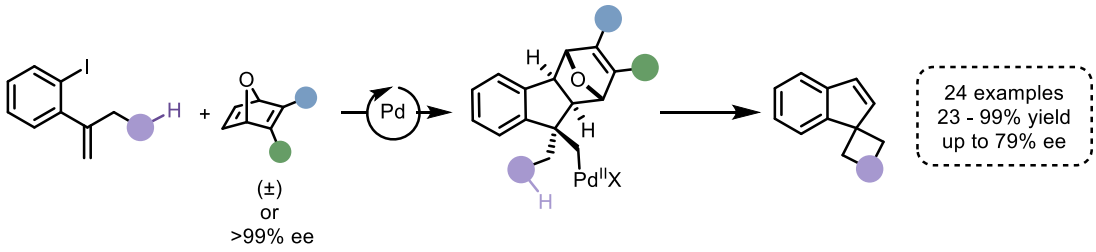

Contributions to the project:

This project was carried out during my visiting period under the supervision of Professor Mark Lautens. My personal contribution involved the optimization of the reaction and the preparation of some substrates for the scope. The remaining scope exploration was completed by Dr. Xavier Abel-Snape, PhD student Clara Jans, and PhD student Armaan Grewal.

Published in Org. Lett.
DOI: https://doi.org/10.1021/acs.orglett.5c04430

Figures, schemes, tables and references in this Chapter are numbered independently.

4.1. Introduction

4.1.1. Biological Relevance and Synthetic Challenges of Spiroindenes

Spirocyclic scaffolds have attracted sustained interest in medicinal chemistry because the spiro junction imposes a rigid, three-dimensional architecture that can profoundly modify the physicochemical and biological profiles of the parent molecules.[1,2] The breadth of biological activities associated with spiro scaffolds is exemplified in Figure 1, which presents representative azaspiro[4.4]nonanes spanning several pharmacological classes, including β-secretase inhibitors,[3] AMPA antagonists,[4] aldose-reductase inhibitors,[5,6] herbicides,[3] and anticancer agents.[7]

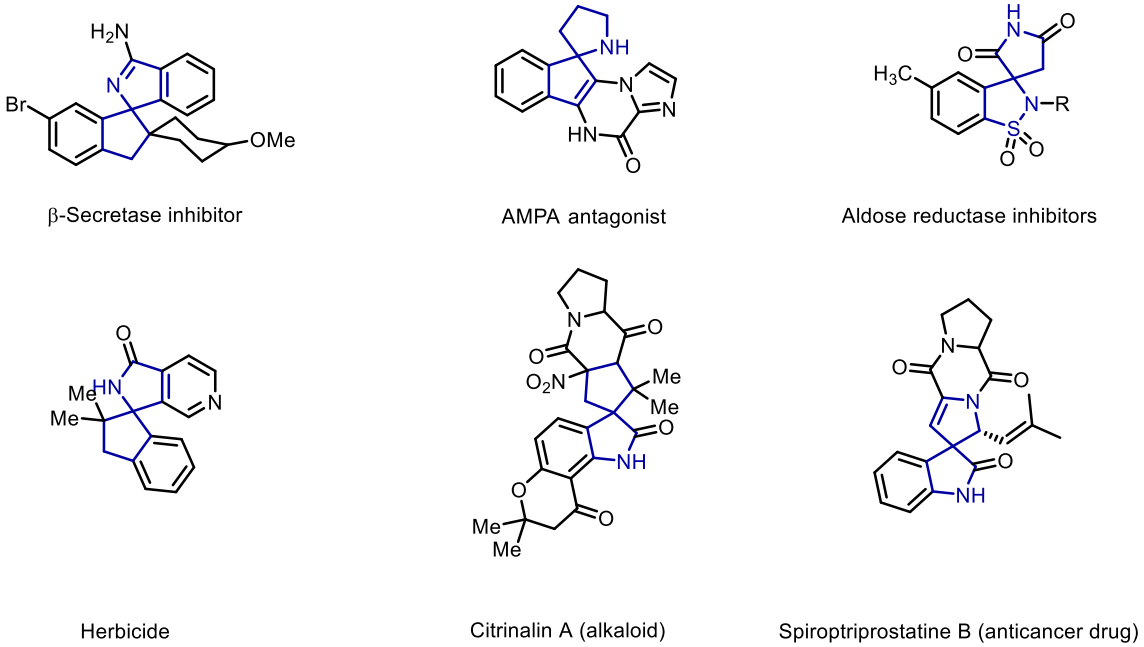

Figure 1. Representative spirocyclic scaffolds with biological activity.

Particular attention has been directed to structures derived from indene cores, whose rigid carbocyclic skeletons are recurrent in biologically active natural products and synthetic agents.[8]

A complementary line of evidence comes from recent reports that evaluate spiroindene derivatives as antioxidants.[9] In this study, Morales-García and Galano describe spiroindene-based compounds that efficiently scavenge peroxyl radicals—a type of reactive species widely recognized as a primary target for antioxidant activity[10]—and are also able to chelate Cu(II), thereby limiting redox processes known to generate highly damaging hydroxyl radicals.[11,12] These findings indicate that spiroindene motifs themselves can deliver measurable functional outcomes in chemical models of oxidative stress, without relying on indirect rationales or structural analogies. This observation complements the privileged-scaffold rationale by showing that spiroindene cores are not only architecturally appealing but can also express biologically relevant activities in well-defined assays.[9]

From a structural and natural-products perspective, indene motifs bearing chiral quaternary stereocenters are documented as key substructures in biologically active natural products and pharmaceutical agents.[13–15]

Figure 2 presents representative examples: Dalesconol A and B, reported with immunosuppressive activity comparable to Cyclosporine A;[16–18] Cyanosporaside A and B, showing significant antimicrobial activity;[19,20] and Dichroanal B, noted for anti-inflammatory and antitumor effects.[21]

Although these examples are indene-based rather than uniformly spiroindenes, they underscore the biological salience of rigid, three-dimensional indene carbocycles. In line with the same source, constructing chiral spiroindenes bearing all-carbon quaternary stereocenters remains challenging, with only a few examples reported and several cases suffering from hard conditions, low efficiency, or substrate limitations—issues attributed to ring rigidity, steric hindrance, and the difficulty of controlling spiro-quaternary stereochemistry.[22–24]

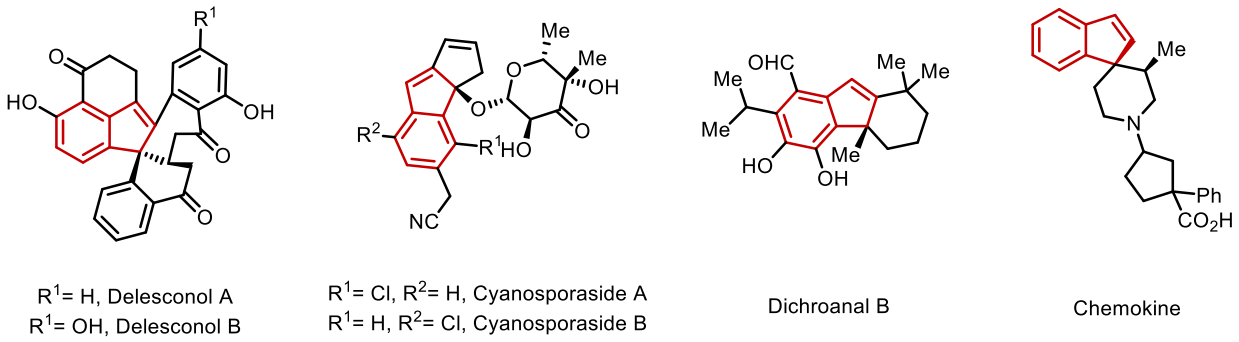

Figure 2. Examples of indene-based natural products and bioactive molecules.

As summarized by Qiu Lu et al., two broad strategies have been pursued: (i) construction of the indene ring from aromatics, including intramolecular cyclizations and intermolecular alkyne insertions (Scheme 1, left), which has delivered several elegant entries to chiral indenes bearing quaternary stereocenters via transition-metal-catalyzed domino sequences; and (ii) direct enantioselective functionalization of pre-formed indene rings (Scheme 1, right).[8]

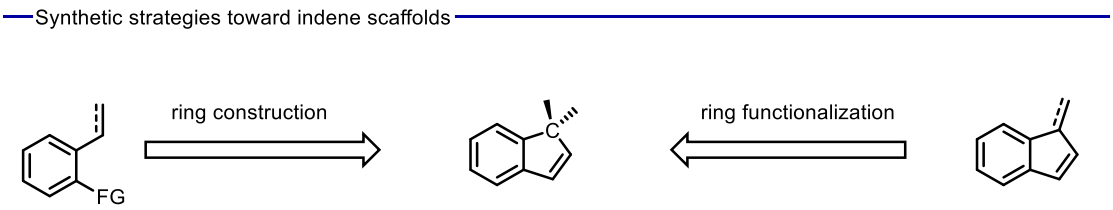

Scheme 1. General approaches to indene derivatives: construction of the carbocyclic ring (left) or direct functionalization of preformed indene scaffolds (right).

Even so, chiral spiroindenes with all-carbon quaternary stereocenters remain challenging, with only a few examples documented; some require harsh conditions, display low efficiency, or tolerate only limited substrate classes, difficulties attributed to the rigid ring and steric hindrance intrinsic to the indene skeleton, and to the difficulty of controlling spiro-quaternary stereochemistry.[25,26] Taken together, the importance of spiroindenes can be summarized in three main points. First, the introduction of a spiro junction enforces three-dimensionality and conformational restriction, features that can significantly modify physicochemical and biological properties; this is the conceptual basis for describing spirocyclic motifs as privileged scaffolds in drug discovery.[3] Second, experimental investigations on spiroindene derivatives have shown that these compounds can act as antioxidants, displaying peroxyl-radical scavenging activity and the ability to chelate Cu(II), thereby demonstrating that the spiroindene core itself can provide measurable functional outcomes.[9] Third, examples from natural products and methodological surveys emphasize both the biological relevance

of indene-based skeletons and the synthetic difficulties associated with constructing spiro-quaternary stereocenters; these challenges explain the continued interest in developing efficient and stereoselective strategies for spiroindene synthesis.[8] In this context, synthetic methods that allow spiroindenes to be obtained under mild conditions and with high stereocontrol are especially valuable, as they open access to shape-defined scaffolds whose significance is supported by medicinal-chemistry rationale as well as experimental validation in functional assays.

4.1.2. Strained Bicyclic Scaffolds as Acetylene Equivalents

Acetylene has long been considered a fundamental C_2 building block in organic synthesis, and its use under palladium catalysis has enabled a variety of bond-forming processes ranging from vinylation and carbonylation to cross-coupling reactions.[27,28] Despite this recognized synthetic value, acetylene is not well-suited for metal-catalyzed domino processes due to its reactive C–H groups that can be favoured over addition to the π-bond. Furthermore, the direct application of acetylene is limited by major safety and operational concerns. It is a highly flammable gas that, unlike most hydrocarbons, can undergo spontaneous explosive decomposition. Consequently, it is stored by being dissolved in acetone within a porous filler, yet leaks may still lead to explosive atmospheres and flashbacks can trigger cylinder rupture.[29] These hazards, combined with the difficulty of dosing a gaseous reagent in catalytic protocols requiring high precision, have historically constrained the use of acetylene and stimulated the search for safer equivalents.[30] Early strategies relied on surrogates that could release acetylene in situ (Scheme 2a). Calcium carbide, upon reaction with water, provides a practical and inexpensive source of acetylene that can be applied in vinylation of alcohols, phenols, and amines, as well as in certain cross-coupling transformations.[30] Vinyl ethers have also been exploited as liquid, easy-to-dose acetylene equivalents that avoid direct handling of the gas, extending the scope to sensitive substrates under one-pot and two-chamber methodologies.[31] These precedents illustrate the general strategy of using masked or generated forms of acetylene to enable its chemistry under more practical conditions. The concept was subsequently extended to strained bicyclic scaffolds able to undergo retro-Diels–Alder fragmentation, thereby formally releasing an acetylene moiety during the course of the reaction.[32] Norbornadiene (NBD) is a representative example of this approach (Scheme 2b).[33] In the palladium-catalyzed three-component coupling of aryl iodides **5** with *ortho*-bromoanilines **6** in the presence of NBD **7**, the strained olefin engages in a sequence comprising an oxidative addition, two successive carbopalladations and a reductive elimination. A post-catalytic retro-Diels–Alder (rDA) step then takes places, providing a *cis*-alkene within dibenzoazepines **9** – heterocycles of pharmacological interest. This study is among the many that have harnessed NBD as an acetylene surrogate in Pd catalysis, and it supported the broader concept that strained hydrocarbons can serve as carriers of reactive fragments. It should be noted that the retro-Diels–Alder step usually only takes place when the resulting alkene is conjugated, which is the main driving force of the reaction along with the increase of entropy by having one molecule fragment into two.

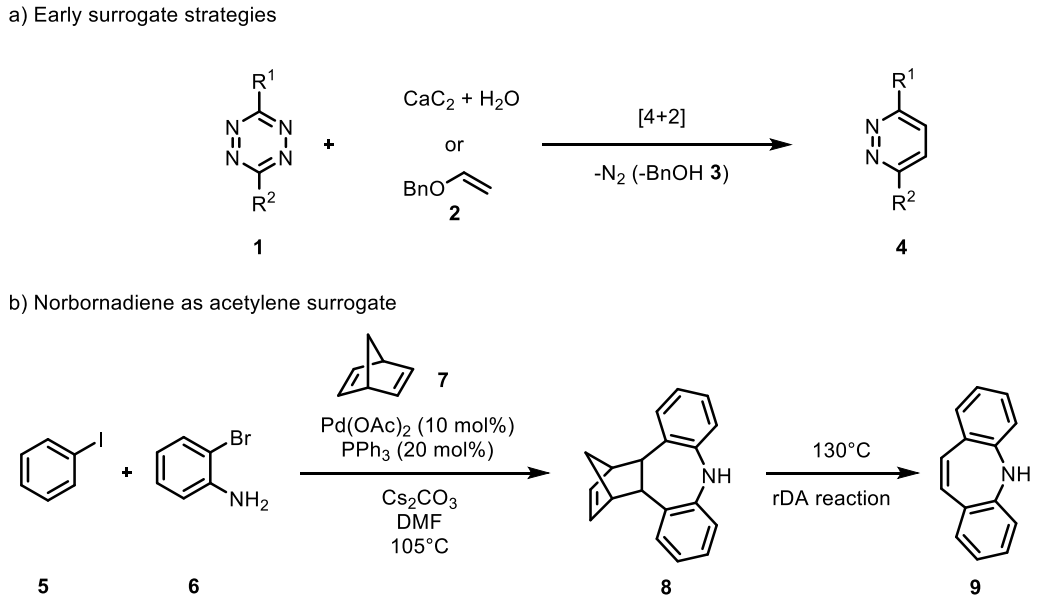

Scheme 2. Representative acetylene surrogates. a) Early surrogate strategies based on in situ acetylene generation (CaC_2/H_2O) or vinyl ethers. b) Norbornadiene as acetylene surrogate in a Pd-catalyzed annulation, with retro-Diels–Alder extrusion delivering the acetylene equivalent.

Norbornadiene and its derivatives have therefore become established as reliable acetylene surrogates in palladium catalysis, and their use has been explored in increasingly sophisticated contexts.[34–36] A notable example is the Pd-catalyzed cascade reported by Liang and co-workers, in which norbornadiene participates in the sequence leading to 1-amino phenanthrenes **12** through a retro-Diels–Alder step (Scheme 3).[37]

In this transformation, palladium(0) undergoes oxidative addition into the C–I bond of 2-iodobiphenyl **10**, followed by migratory insertion of NBD **7** into the C–Pd bond and C–H activation to generate the aryl–norbornyl–palladacycle (ANP) **14**. Subsequent oxidative addition of O-benzoylhydroxylamine **11** furnishes Pd(IV) intermediate **15**, which undergoes reductive elimination to install the C–N bond in intermediate **16**. A second C–H activation step across the biaryl scaffold generates seven-membered palladacycle **17**, which then undergoes another reductive elimination, thus closing the catalytic cycle by regenerating Pd(0) and providing adduct **18**. This direct product of the catalytic cycle then undergoes a retro-Diels-Alder step, releasing the acetylene equivalent and providing the highly conjugated phenanthrene skeleton. Control experiments provided support for this mechanism: adduct **18** was isolated at a lower temperature of 50 °C and shown to fragment to the product upon heating at 100 C, thereby validating the retro-Diels–Alder pathway.[37] These results demonstrate how NBD can be integrated into complex catalytic cascades, underscoring its role as a versatile acetylene surrogate and revealing reactivity that extends beyond straightforward annulation pathways. While norbornadiene derivatives have proven effective, the development of oxanorbornadienes (OND) has expanded the scope of acetylene surrogates by providing additional advantages. In particular, the extrusion step is facilitated by the formation of a stable aromatic furan molecule after the retro-Diels–Alder step, making the release of the acetylene equivalent more thermodynamically favorable and therefore allowing for milder conditions.[38]

OND derivatives are easily accessible by Diels–Alder chemistry and have been increasingly adopted as reliable surrogates in palladium catalysis, often providing higher efficiency and broader substrate tolerance compared to their hydrocarbon counterparts.[32,38–40]

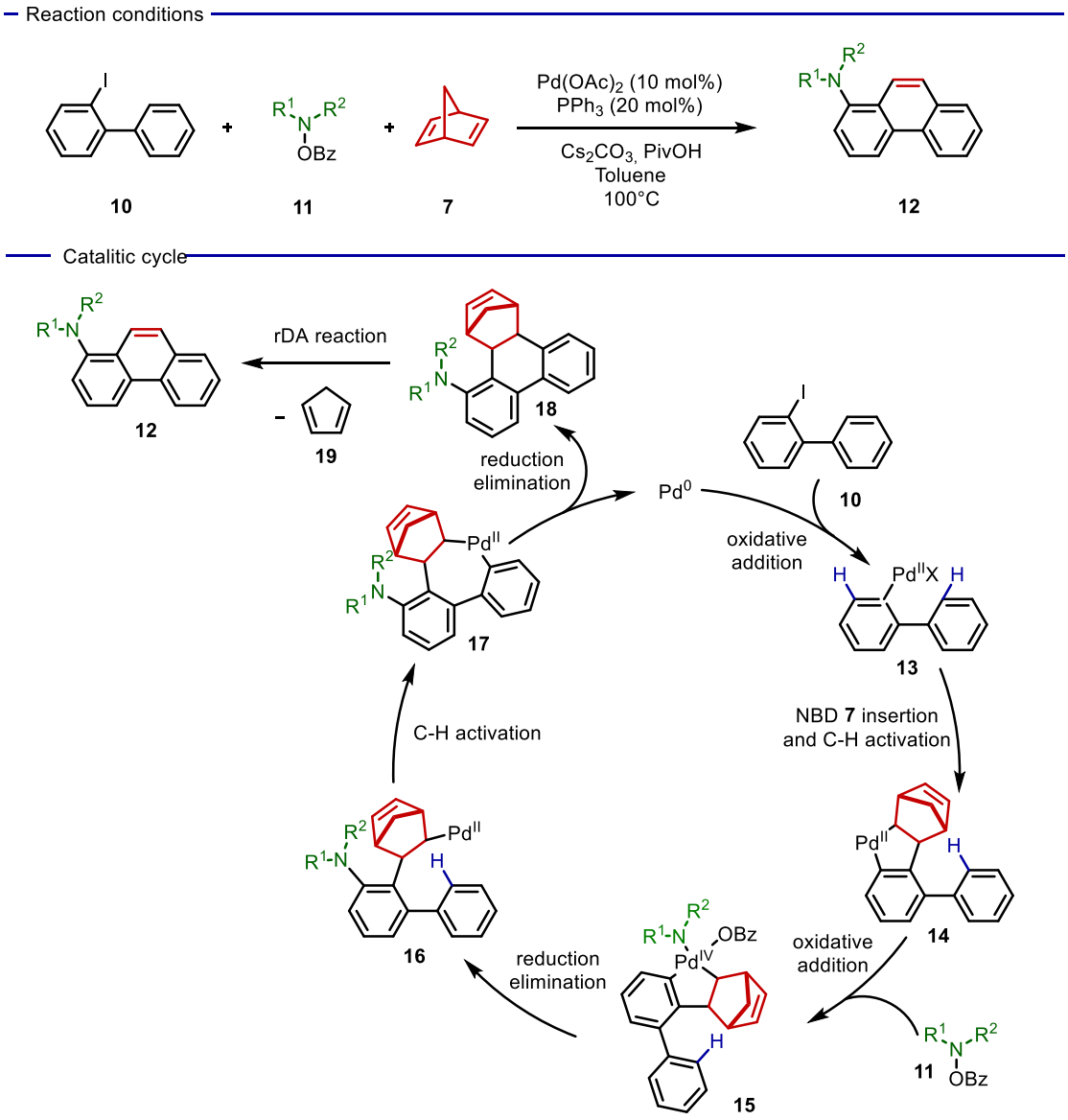

*Scheme 3.Pd-catalyzed cascade of 2-iodobiphenyls **10**, O-benzoylhydroxylamines **11**, and norbornadiene **7** affording 1-amino phenanthrenes **12** via a retro-Diels–Alder step.*

The utility of ONDs in Pd-catalyzed processes is exemplified by the work of Lautens and co-workers, who developed a three-component coupling that constructs indene scaffolds (Scheme 4).[38] In this transformation, palladium(0) undergoes oxidative addition into the aryl iodide **20**, generating the aryl-Pd(II) species **24**. Subsequent coordination and migratory insertion of oxanorbornadiene **21** provides complex **25**, which incorporates the two-carbon fragment from the strained oxabicycle. This intermediate then undergoes a second migratory insertion across the pendent styrene double bond, affording intermediate **26**. At this stage, transmetalation with the arylboronate **22** transfers the aryl group to palladium, furnishing intermediate **28**. Reductive elimination from this species delivers indane **29** and regenerates Pd(0), thereby closing the catalytic cycle. Finally, compound **29** undergoes a retro-Diels–Alder step to release the desired indene product **23** and the aromatic furan by-product **30**. This sequence exemplifies how oxabicycle **21** acts as an efficient acetylene surrogate: the strained scaffold is introduced early in the catalytic cycle and later fragmented via a retro-Diels–Alder step to release the C_2 unit only after the key bond-forming steps. The method proceeds in good yields across a variety of substrates and tolerates different termination steps, such as Suzuki, Miyaura borylation and decarboxylative Sonogashira terminations, underscoring the robustness and diversification of the approach.

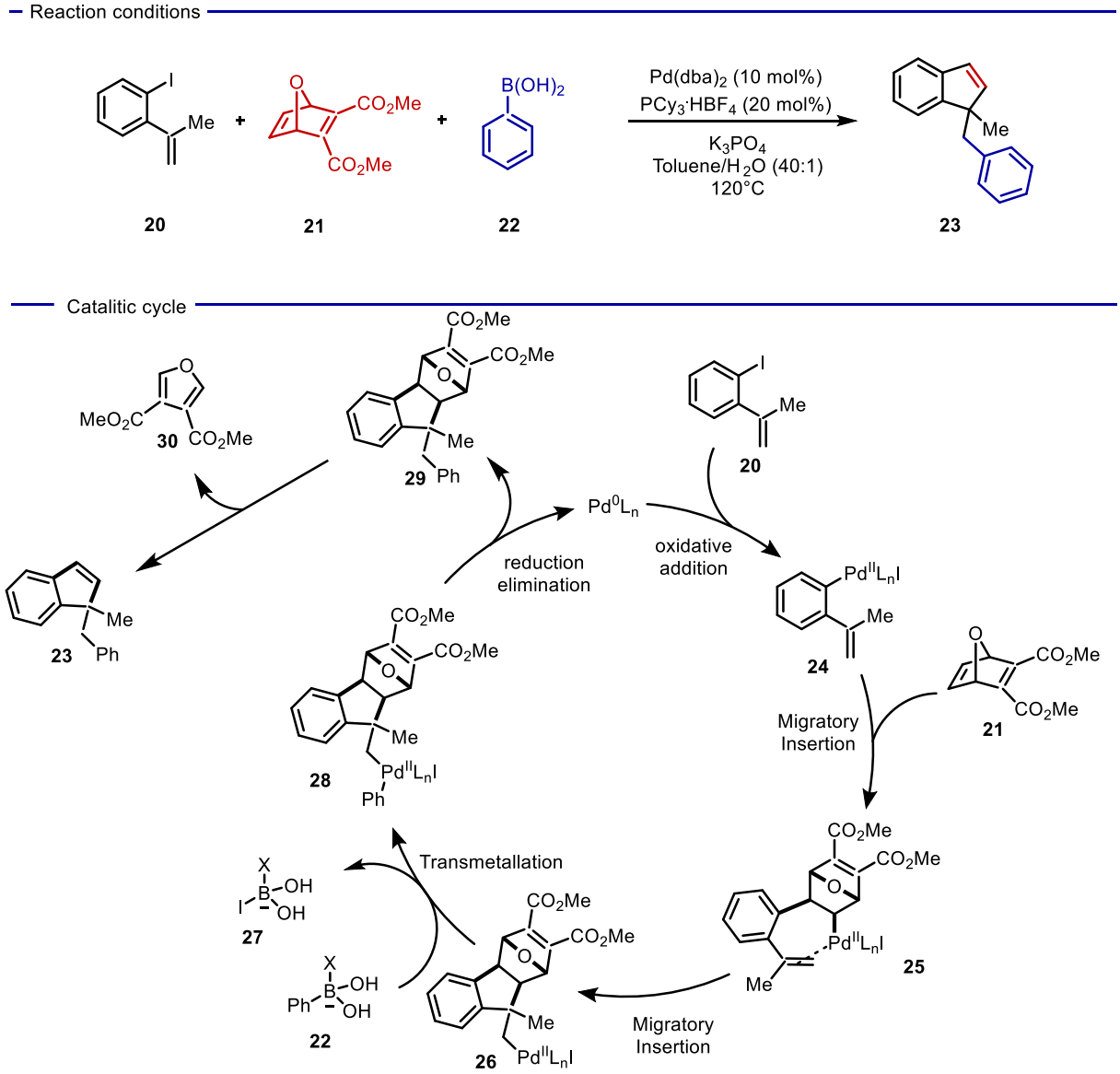

*Scheme 4. Pd-catalyzed three-component coupling of aryl iodides **20**, oxanorbornadiene **21**, and arylboronic acids **22** to give indenes **23** via retro-Diels–Alder extrusion.*

Further confirmation of the generality of oxabicycle **21** as an acetylene surrogate was provided by Zhang and co-workers, who demonstrated their application in palladium-catalyzed multicomponent assemblies of stereodefined alkenylborons.[39] In addition, Abel-Snape and co-workers reported the first example of the formal insertion of acetylene into a palladacycle, thereby establishing a strategy that enabled the synthesis of various N-heterocycles.[41] Although mechanistically distinct from an indene formation synthesis, these results support the broader conclusion that OND derivatives constitute reliable and versatile acetylene surrogates in Pd catalysis, enabling access to diverse functional products under practical conditions.

4.1.3. Remote Asymmetric Induction via Chiral Oxabicycles

The control of enantioselectivity in transition-metal catalysis has traditionally been achieved through the use of chiral ligands, which transfer asymmetry during the stereodetermining step of the catalytic cycle.[42–44] This approach has been a cornerstone of asymmetric synthesis for several decades, enabling access to highly enantioenriched molecules through ligand-controlled bond-forming events.[45,46] In this classical paradigm, the ligand bound to the metal center creates a chiral environment that differentiates between the enantiotopic faces of a prochiral substrate or transition state, thus dictating the configuration of the product.[47]

A representative example of the chiral-ligand strategy was provided by Lautens and co-workers, who developed a sequential Rh/Pd catalytic system in which the two metals play complementary roles (Scheme 5a).[48] In this transformation, rhodium, in combination with a chiral diene ligand, promotes the enantiodetermining conjugate addition of arylboronic acids to acrylamides, thereby setting the stereochemical course of the reaction. Palladium, coordinated to an achiral biarylphosphine ligand, subsequently mediates an intramolecular C–N bond-forming step via Buchwald–Hartwig amination. The introduction of chirality thus relies exclusively on the Rh-bound chiral ligand, while the Pd component serves to close the heterocyclic motif. This study exemplifies how ligand-based asymmetric catalysis can achieve high enantioselectivity in complex, dual-metal-catalyzed syntheses.

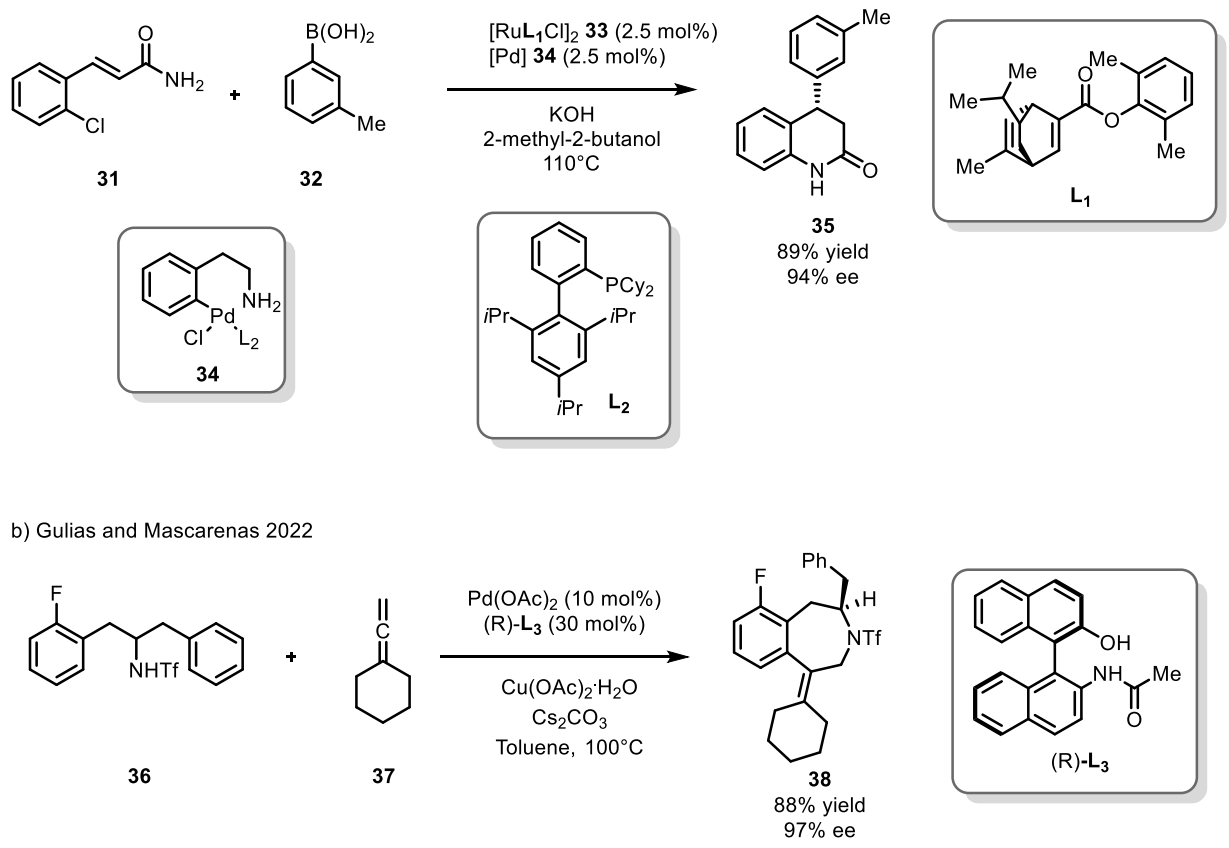

Scheme 5. Ligand-controlled enantioselective transformations: a)sequential Rh/Pd catalysis where a Rh–diene complex induces enantioselectivity and Pd catalyzes C–N bond formation. b) Pd-catalyzed enantioselective annulation using a chiral ligand.

A more recent contribution that further underscores this paradigm is the work of González and co-workers, who developed a family of binaphthyl-derived chiral ligands tailored for Pd-catalyzed enantioselective C–H activation (Scheme 5b).[49] Their results showed that subtle modifications of the ligand structure, involving both steric and electronic tuning, were decisive to reach high levels of enantio- and regioselectivity across structurally diverse substrates. This study shows how palladium catalysis can be adapted through rational ligand design, with well-designed ligands providing effective stereocontrol in more than one stereoselective step even in demanding reactions.

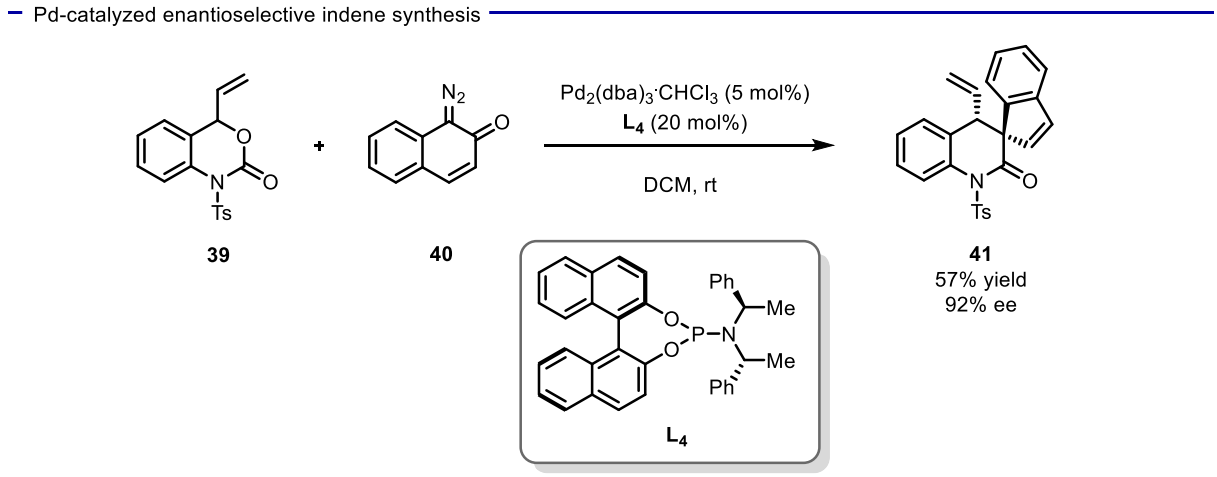

Scheme 6. Representative example of Pd-catalyzed enantioselective indene formation using a chiral phosphoramidite ligand.

The reliance on ligand design as the primary source of stereocontrol is well illustrated by the enantioselective synthesis of spiroindenes developed by Qiu Lu and co-workers (Scheme 6).[8] In this Pd-catalyzed (4+2) cyclization, classical ligand families, including those widely employed in asymmetric catalysis, proved ineffective. In contrast, a newly designed phosphoramidite ligand enabled the transformation to proceed in good yield and with excellent enantioselectivity. This study demonstrates how the creation of a tailored chiral environment at the metal center can efficiently govern the stereochemical outcome of complex annulations. At the same time, it exemplifies a recurring limitation of ligand-controlled systems: the highest levels of performance are often contingent on finely engineered ligands whose synthesis and availability may not always be straightforward.

Taken together, these studies exemplify both the power and the limitations of ligand-controlled systems. On the one hand, excellent enantioselectivity can be achieved through carefully engineered ligands; on the other, the highest levels of performance are often contingent on scaffolds that are synthetically demanding, costly to access, and highly optimized for specific transformations.[50] As a result, while chiral-ligand strategies remain dominant, they also underscore the need for complementary approaches that introduce asymmetry through more accessible and economical means.

Alongside ligand-controlled catalysis, an alternative approach to enantioselective synthesis relies on substrate control, where stereochemical information is embedded within the reacting partners themselves. In this strategy, the stereochemical outcome is governed by a chiral auxiliary or by a stereocenter already present in the substrate, which influences the bond-forming step through steric and electronic effects. In practice, effective asymmetric induction has historically depended on placing the chiral element in close proximity to the prochiral site, so that one face is sterically or stereoelectronically shielded during the stereodetermining event.[51–54] By contrast, achieving genuine remote asymmetric induction—where the chiral information resides far from the reacting center—remains a significant challenge.[55,56] A notable example of this limitation is provided by Yu and co-workers, who reported the remote enantioselective desymmetrization of diarylmethylamines via formal reversible meta-C–H functionalization, followed by the selective reaction of one enantiomer using a chiral norbornene derivative (**43**, NBE*)(Scheme 7).[57] ù

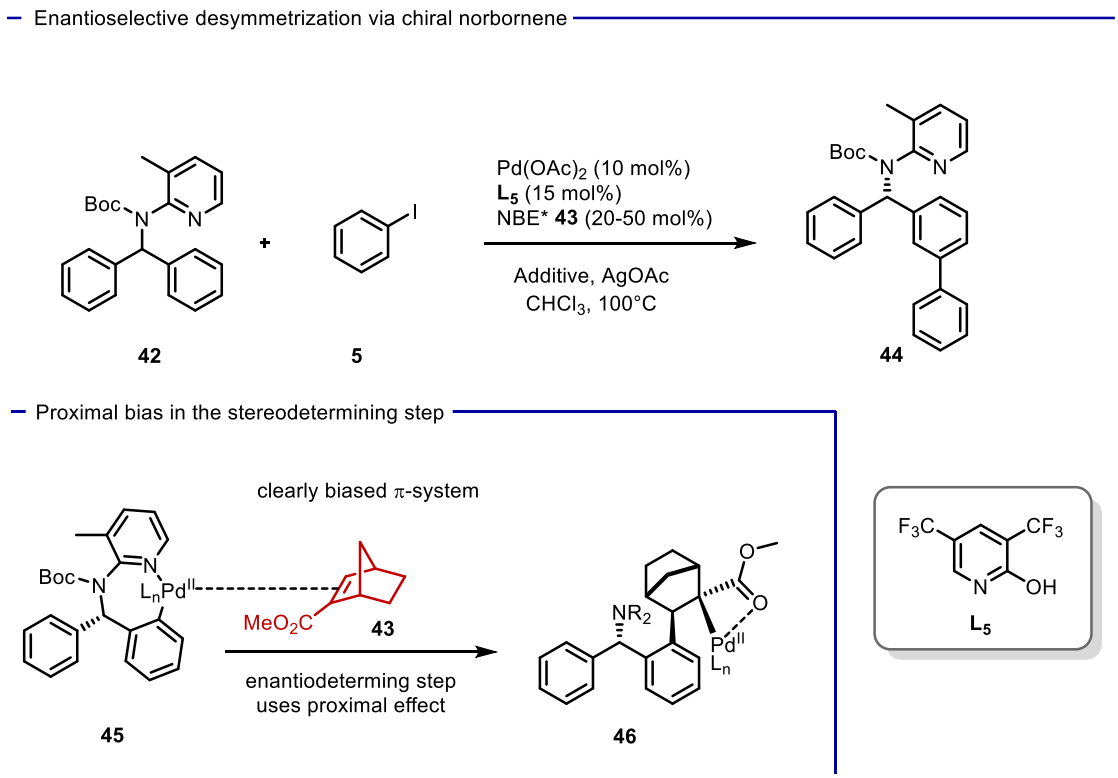

*Scheme 7. Pd-catalyzed desymmetrization of diarylmethylamines using a chiral norbornene derivative (**43**, NBE*). The ester substituent on **43** biases the π-system, so that the enantiodetermining step ultimately relies on proximal effects rather than true remote induction.*

In this case, the π-system of NBE* is biased by the presence of an ester substituent, and the enantiodetermining step ultimately relies on proximal effects rather than on a truly remote induction. Building on this background, Lautens and co-workers recently demonstrated that the stereodetermining step can proceed without relying on proximal steric interactions, thereby providing a rare example of genuine remote asymmetric induction.[58] In this work (Scheme 8), the authors introduced the concept of a "chiral acetylene equivalent," in which an enantioenriched oxabicycle serves not only as an acetylene surrogate but also as the carrier of stereochemical information. The oxabicycle engages in two sequential carbopalladation steps before undergoing retro-Diels–Alder fragmentation to release the indene product. Crucially, the enantioselectivity arises from the chiral substituents embedded within the oxabicycle itself, which remotely control the stereochemical outcome of the carbopalladations. Finally, Lautens' study also revealed that the stereochemical outcome can be finetuned by altering the structure of the chiral oxabicycle itself. Different enantiopure surrogates delivered markedly distinct yields and enantioselectivities. Strikingly, in the case of oxabicycle **47d**, the overall enantioinduction was reversed, affording the opposite enantiomer of the indene product as the major isomer. This observation shows that substrate-embedded chirality can effectively govern formal enantioselective induction and, depending on the oxabicycle employed, even alter the direction of stereochemical preference. Overall, the concept of embedding remote chirality directly within acetylene surrogates establishes a new paradigm in palladium catalysis. Chiral oxabicycles demonstrate that stereochemical information can be effectively transmitted from the substrate itself, enabling formal enantioselective transformations while simultaneously serving as acetylene equivalents. This strategy not only broadens the synthetic potential of strained bicyclic scaffolds but also opens promising avenues for future developments in remote asymmetric induction.[38,58]

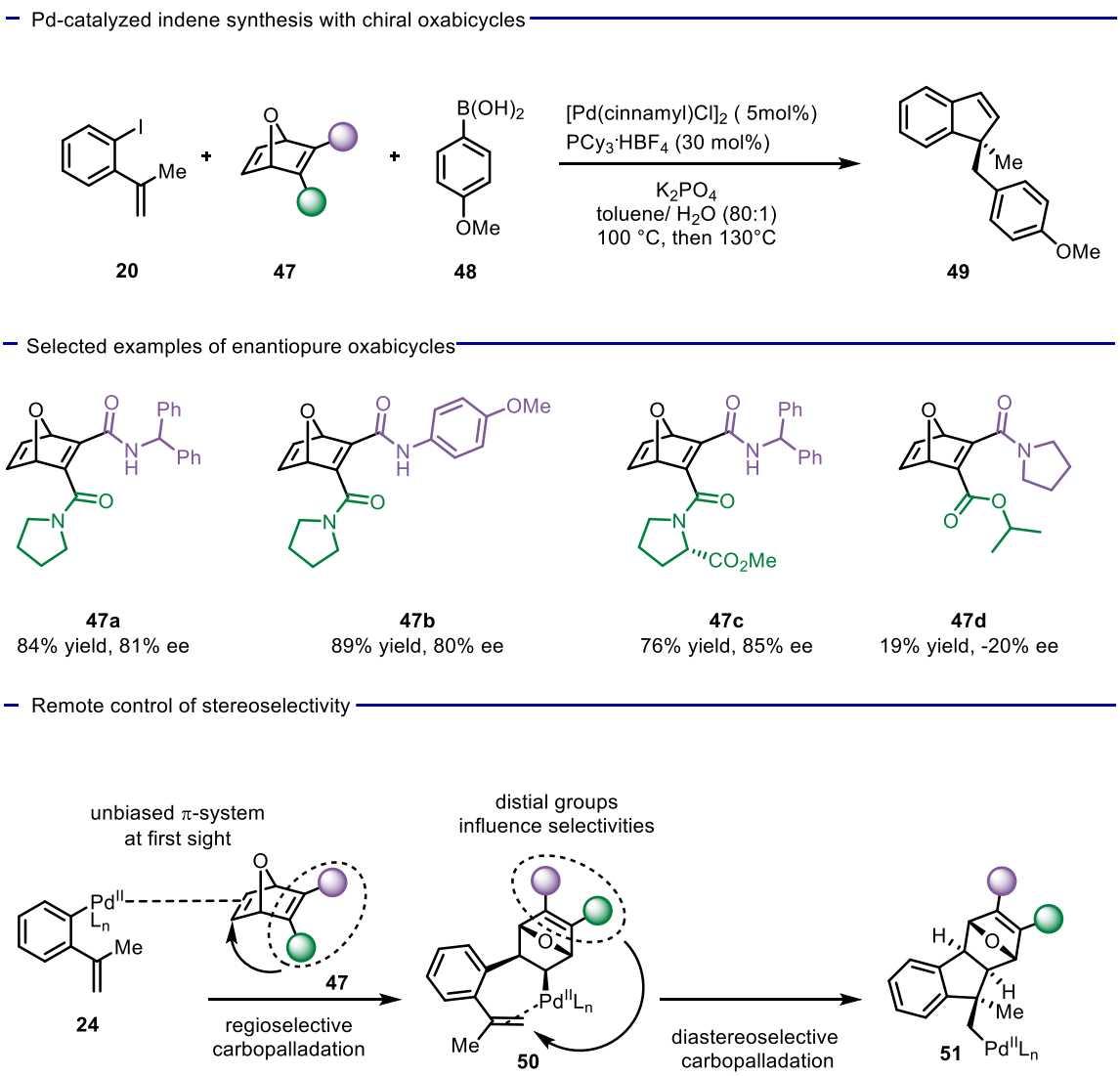

Scheme 8. Pd-catalyzed multicomponent synthesis of indenes using enantiopure oxabicycles as acetylene surrogates. Representative oxabicycle substrates enable enantioenriched indene formation, with stereocontrol arising from remote substituents that govern carbopalladation.

4.2. Aim of the project

The development of efficient strategies for constructing spirocyclic architectures remains a central goal in synthetic chemistry, as these motifs expand three-dimensional chemical space and provide access to biologically relevant scaffolds.[1,3] Among them, spiroindenes are particularly appealing, yet highly enantioselective syntheses—especially of 2,3-unsubstituted variants—are still limited.[2,24] Conventional approaches to stereocontrol rely mainly on chiral ligands, but such methods can be costly and substrate-specific.[49] An attractive alternative is the use of enantioenriched oxabicycles, which function not only as safe and practical acetylene surrogates but also as internal carriers of chirality.[58]

This project aims to establish a palladium-catalyzed domino C–H activation cascade that transforms chiral oxabicycles into spiroindenes through sequential carbopalladation, cyclization, and post-catalytic retro-Diels–Alder fragmentation.

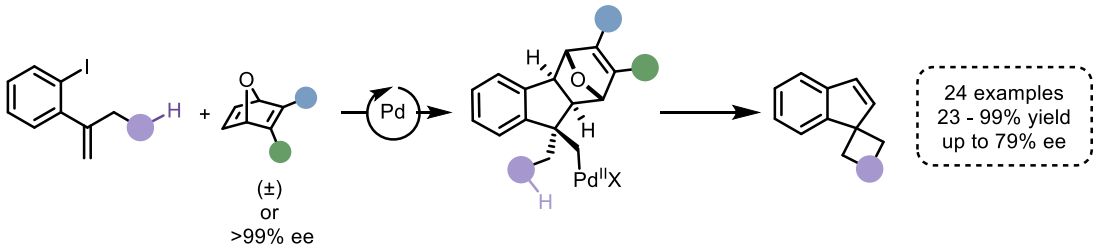

Scheme 9. General strategy for the Pd-catalyzed transformation of racemic or enantioenriched oxabicycles into indenes via sequential carbopalladation and retro-Diels–Alder fragmentation.

The dual role of the oxabicycle – both acting as an acetylene equivalent and stereoinducing agent – provides a new platform for the enantioselective synthesis of spiroindenes. In particular, the scope of this strategy was investigated with various N-heterocycle-tethered iodoarenes to elucidate the stereochemical outcome via remote induction of an intra- rather than intermolecular termination [58]and assess the potential of this method as a practical alternative to ligand-based asymmetric catalysis.

4.3. Results and discussion

4.3.1. Optimization studies

The reaction was optimized by selecting substrate **52** as the model substrate. Oxabicycle **21** was employed owing to its straightforward preparation (see Section 4.5.4), and the desired product **53** was obtained. A wide selection of palladium sources, ligands, bases, and solvents was tested to identify an effective catalytic system, with the most representative results summarized in Table 1. Among the palladium precatalysts examined, $Pd(OAc)_2$ provided the best performance, affording the highest yield under the screening conditions. The ligand screening showed that phosphines were generally the most effective, with $P(iPr)_3 \cdot HBF_4$ providing the best results for this reaction. In contrast, other ligands (entries 1–2 and 4) led to reduced efficiency. Screening of different palladium pre-catalysts was also carried out, since the nature of the precursor introduced into the reaction can significantly influence the efficiency of the active species generated under catalytic conditions. Pre-catalysts provide a well-defined and more stable entry to the active Pd(0) complex, and their use is often associated with improved reproducibility and performance in cross-coupling reactions.[59] Solvent screening indicated that 1,4-dioxane was optimal, with toluene giving comparable results (entry 9), whereas significantly lower yields were obtained in other solvents such as dimethylformamide (entry 10) and acetonitrile (entry 11). With respect to the base, cesium carbonate consistently outperformed alternatives such as potassium phosphate tribasic (entry 12), potassium carbonate (entry 13) and cesium pivalate (entry 14), enabling cleaner reactions and higher yields.

Table 1. Improving the Yield – Catalytic Conditions: Reactions were performed on a 0.1 mmol scale. Yields were determined by ^1H NMR spectroscopy analysis of crude reaction mixture using 1,3,5-trimethoxybenzene as an internal standard. (A)5 mol% Pd loading. (B)20 mol% Ligand loading. (C)100 ˚C 8 h then 120 ˚C 12 h. (D)110 ˚C 8 h then 120 ˚C 12 h

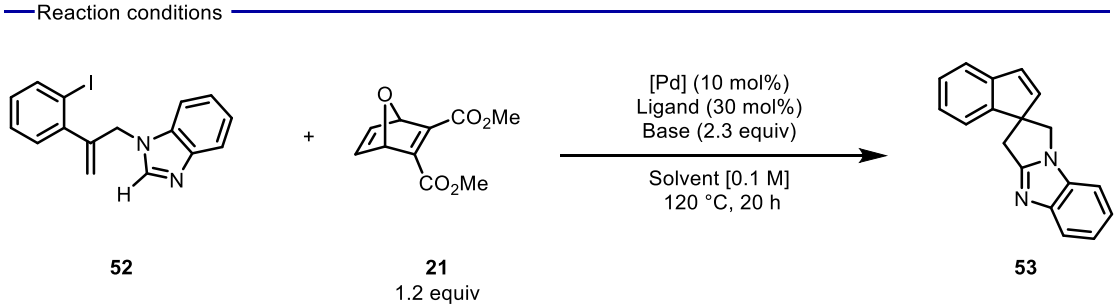

Entry	Palladium	Ligand	Base	Solvent	NMR Yield 3a (%)
1	$Pd(OAc)_2$	$P(Me)_3 \cdot HBF_4$	Cs_2CO_3	1,4-dioxane	20%
2	$Pd(OAc)_2$	$P(Et)_3 \cdot HBF_4$	Cs_2CO_3	1,4-dioxane	20%
3	**$Pd(OAc)_2$**	**$P(iPr)_3 \cdot HBF_4$**	**Cs_2CO_3**	**1,4-dioxane**	**59%**
4	$Pd(OAc)_2$	$PCy_3 \cdot HBF_4$	Cs_2CO_3	1,4-dioxane	54%
5[(A)]	$[Pd(cinnamyl)Cl]_2$	$P(iPr)_3 \cdot HBF_4$	Cs_2CO_3	1,4-dioxane	43%
6[(A)]	$[Pd(allyl)Cl]_2$	$P(iPr)_3 \cdot HBF_4$	Cs_2CO_3	1,4-dioxane	46%
7	$Pd(TFA)_2$	$P(iPr)_3 \cdot HBF_4$	Cs_2CO_3	1,4-dioxane	55%
8[(B)]	$Pd(dba)_2$	$P(iPr)_3 \cdot HBF_4$	Cs_2CO_3	1,4-dioxane	51%
9	$Pd(OAc)_2$	$PCy_3 \cdot HBF_4$	Cs_2CO_3	Toluene	53%
10	$Pd(OAc)_2$	$PCy_3 \cdot HBF_4$	Cs_2CO_3	DMF	22%
11	$Pd(OAc)_2$	$PCy_3 \cdot HBF_4$	Cs_2CO_3	MeCN	37%
12	$Pd(OAc)_2$	$PCy_3 \cdot HBF_4$	K_3PO_4	1,4-dioxane	44%
13	$Pd(OAc)_2$	$PCy_3 \cdot HBF_4$	K_2CO_3	1,4-dioxane	43%
14	$Pd(OAc)_2$	$PCy_3 \cdot HBF_4$	CsOPiv	1,4-dioxane	19%
15[(C)]	$Pd(OAc)_2$	$P(iPr)_3 \cdot HBF_4$	Cs_2CO_3	1,4-dioxane	33%
16[(D)]	$Pd(OAc)_2$	$P(iPr)_3 \cdot HBF_4$	Cs_2CO_3	1,4-dioxane	37%

Both amide- and ester-substituted oxabicycles were evaluated (Scheme 10). The best performance was obtained with the meso secondary amide derivative **47e**, which delivered a yield of 68%. In contrast, tertiary amides (like **47f**, **47h**) gave lower yields and were accompanied by increased side reactions. Oxabicycles bearing ester substituents, **47g,** also proved less efficient than their amide counterparts. Taken together, these results established secondary amide oxabicycles as the most promising surrogates for further optimization.

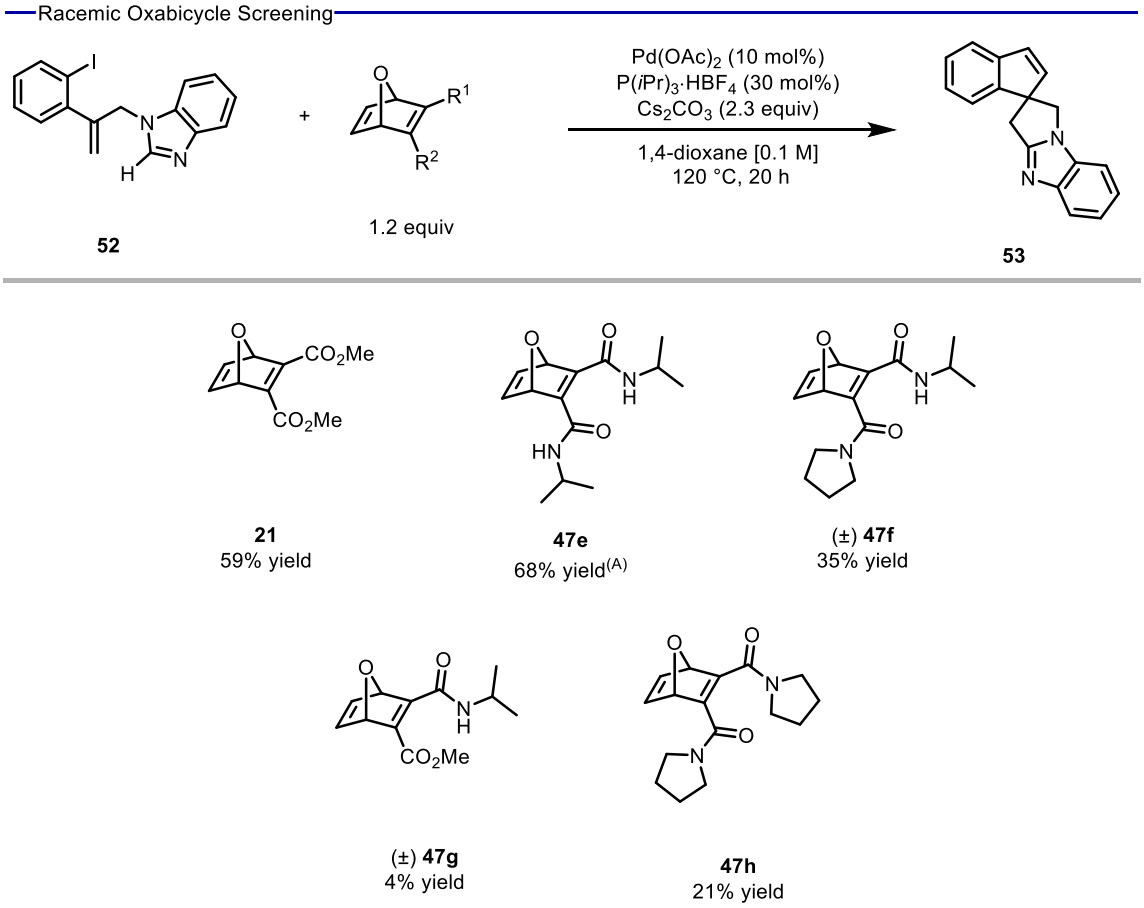

Scheme 10. Screening of racemic oxabicycles. Reactions were performed on a 0.1 mmol scale. Yields were determined by ^{1}H NMR analysis of crude mixtures using 1,3,5-trimethoxybenzene or ethylene carbonate as internal standards. (A) Reaction heated at 120 °C for 6 h, then at 150 °C for 16 h.

Further experiments investigated whether varying the amount of oxabicycle would affect the outcome (Table 2). Increasing the loading to 1.5 equiv resulted in a moderate improvement in yield (entry 2). However, reproducibility remained an issue, with yields fluctuating between 50% and 75% under ostensibly identical conditions. This variability was initially attributed to the system's sensitivity to moisture. Several attempts were therefore made to exclude water completely by performing the manipulations in a glove box, but this did not resolve the problem. To directly assess the role of water, small amounts were deliberately added to the reaction. Surprisingly, the introduction of 20 µL of water stabilized the reaction, affording reproducible yields. Under these conditions, and by employing [Pd(cinnamyl)Cl]$_2$ (entry 6) as the palladium source, the yield could be further increased to 80%.

Table 2.Improving the Yield – Variations: Reactions were performed on a 0.1 mmol scale. (A)Yields were determined by ^{1}H NMR spectroscopy analysis of crude reaction mixture using 1,3,5-trimethoxybenzene as an internal standard. (B)Addition of water to the reaction greatly improved the reproducibility and purification of the reaction. (C)5 mol% [Pd(cinnamyl)Cl]$_2$ used. (D)Isolated yield.

Reaction conditions

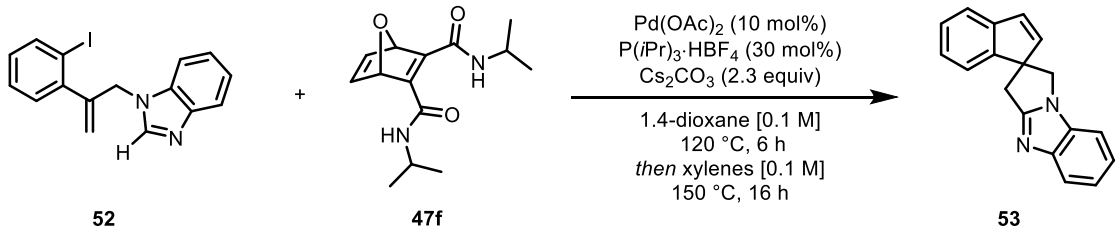

52 | **47f** 1.2 equiv | **53**

Entry	Variation	Yield 3a (%)[A]
1	-	68%
2	1.5 equiv **47f**	72%
3[(B)]	10 µL H_2O + 1.5 equiv **47f**	65%
4[(B)]	20 µL H_2O + 1.5 equiv **47f**	76%
5[(B)]	40 µL H_2O + 1.5 equiv **47f**	65%
6[(C)]	20 µL H_2O + 1.5 equiv **47f** + [Pd(cinnamyl)Cl]$_2$	80%[(D)]

With optimized conditions established, several racemic oxabicycles were re-examined (Scheme 11). The best result (83% yield) was obtained with oxabicycle **47a**, bearing a tertiary amide in combination with a secondary amide substituent. This outcome illustrates the difficulty of rationalizing the relationship between the oxabicycle structure and the observed reactivity. While earlier experiments suggested that oxabicycles bearing two secondary amides were the most promising, a higher yield was in fact achieved with a mixed tertiary/secondary amide substitution pattern.

Racemic Oxabicycle Screening

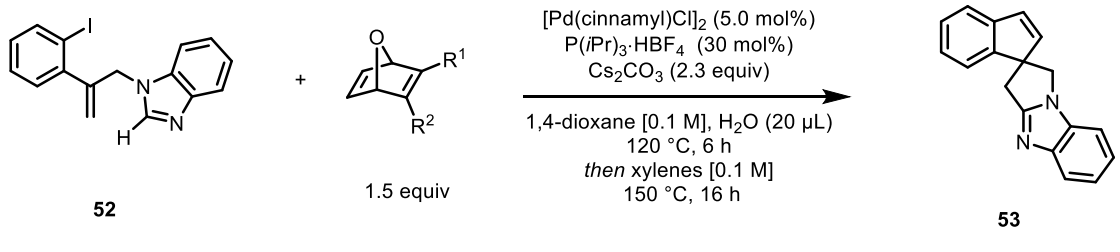

52 | 1.5 equiv | **53**

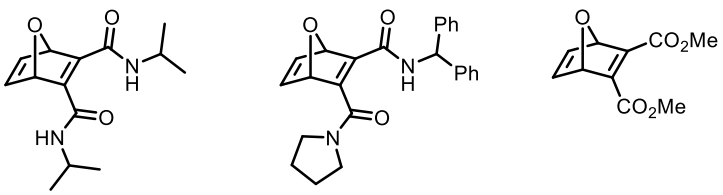

47e 80% yield **53** | (±) **47a** 83% yield **53** | **21** 60% yield[(A)] **53**

Scheme 11. Racemic oxabicycle screening under optimized conditions. Reactions were performed on a 0.1 mmol scale. Isolated yields are reported. (A) Reaction was run at 120 °C for 20 h.

Building on these results, the use of enantiopure oxabicycles was explored to determine whether the stereochemical information embedded in the surrogate could be transferred during the catalytic sequence (Scheme 12). Using enantiopure **47k**, the reaction proceeded smoothly to give spiroindene **53** in 72% yield and 77% ee. This outcome confirmed that the chirality of the oxabicycle is effectively transmitted through the catalytic cascade, and that the stereochemical bias is retained during both carbopalladation steps before retro-Diels–Alder extrusion. Interestingly, when other enantiopure oxabicycles were tested, variations in both yield and enantioselectivity were observed. These results highlight that while the oxabicycle scaffolds can indeed transfer chirality, the nature of the substituents plays a decisive, yet unpredictable role in determining both efficiency and selectivity.

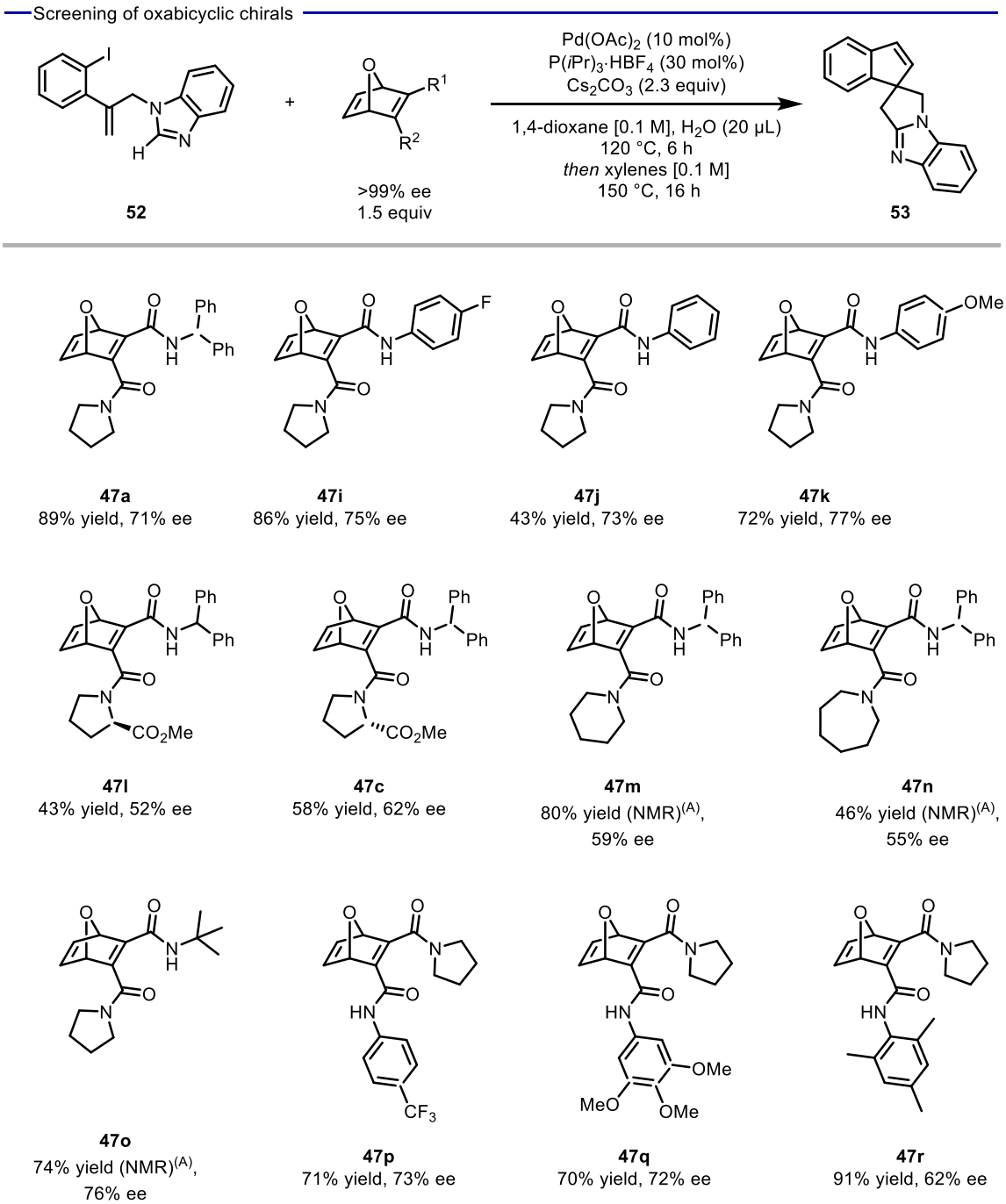

*Scheme 12. Reactions were performed on a 0.1 mmol scale. Isolated yields are reported. (A) Desired spiroindene **53** coelutes with the furan by-product; the mixture was analyzed by HPLC under standard conditions. NMR yields were determined by ^{1}H NMR spectroscopy of crude reaction mixtures using 1,3,5-trimethoxybenzene as an internal standard. Absolute configuration of **53** was not determined.*

Once these results were obtained, additional experiments were conducted to improve enantioselectivity, including temperature variations (Section 4.5.2, Table 3) and oxabicycle equivalents (Section 4.5.2, Table 4). However, none of these modifications led to better outcomes. As observed previously, the addition of a small amount of water continued to enhance reproducibility and yield. The optimized reaction conditions are shown in Scheme 13.

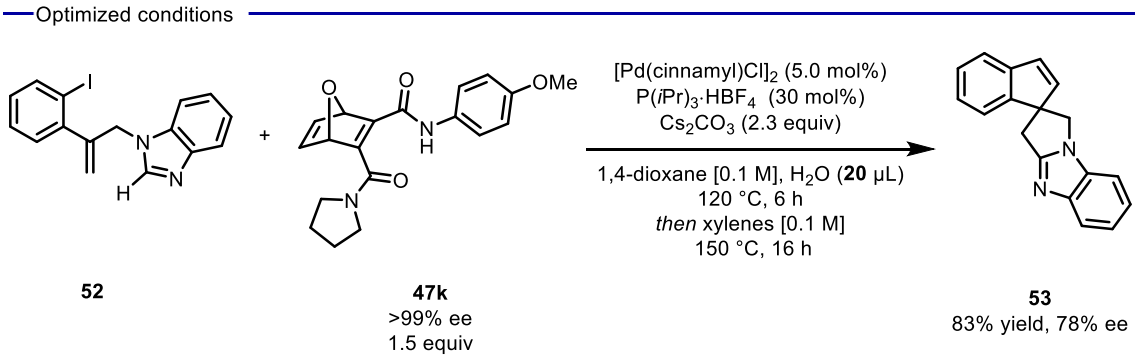

*Scheme 13. Optimized conditions for the Pd-catalyzed synthesis of spiroindene **53** using enantiopure oxabicycle **47k**. Reactions were performed on a 0.1 mmol scale.*

4.3.2. Proposed mechanism

The proposed catalytic cycle begins with oxidative addition of the in-situ formed Pd(0) catalyst into the C–I bond of iodoarene **52**, generating the arylpalladium(II) intermediate **I**. Coordination and insertion of the oxabicycle then occurs, furnishing the bicyclic palladium complex **II**. Subsequent intramolecular migratory insertion across the pendant olefin gives rise to the neopentyl palladium(II) intermediate **III**. This species undergoes base-assisted C–H activation, delivering the palladacycle IV. A reductive elimination step from **IV** forges the C–C bond and yields the pre-rDA intermediate **V**, while regenerating the Pd(0) catalyst. Finally, a post-catalytic thermal retro-Diels–Alder reaction fragments spiroindane **V** into spiroindene **53** and furan byproduct **54**.

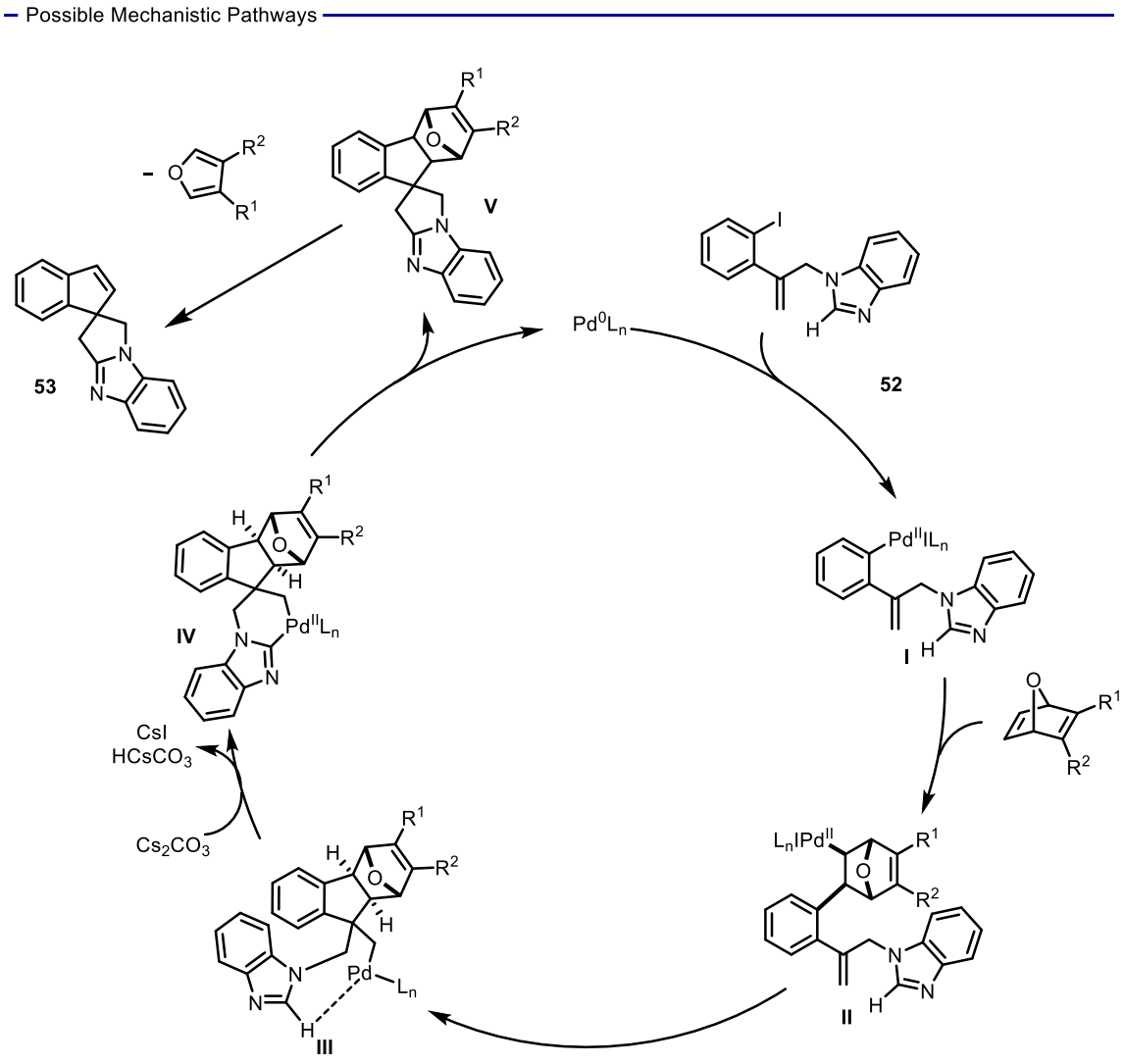

Scheme 14. Proposed catalytic cycle.

4.3.3. Scope of the reaction

With the optimized reaction conditions in hand, the substrate scope of this transformation was explored (Scheme 15). A variety of benzimidazole derivatives proved competent under the reaction conditions. The 5,6-dimethyl benzimidazole delivered the corresponding spiroindene **54** in 69% yield, while the naphthyl-substituted analogue **55** was obtained in 44% yield. Both electron-withdrawing substituents, such nitro group (**56** and **57**, 56–60% yield), and electron-donating groups, such as methoxy (**58** and **59**, 68-55% yield), were tolerated, providing the desired products in moderate to good yields. Substitution on the aryl iodide fragment was also possible, affording the methoxy- and methyl-substituted products **59** and **60** in 55% and 81% yield, respectively. Extension of the methodology to imidazole substrates was successful as well, giving product **61** in 98% yield. The robustness of the method was further demonstrated by scale-up to the millimole scale, which furnished spiroindene **53** in 73% yield. The investigation was then extended to indole and pyrrole derivatives. The standard indole substrate furnished product **62** in 79% yield, and a 1.0 mmol scale-up afforded the same product in 60% yield. The protocol was compatible with a range of functional groups, including halogens (**63** and **64**, 74–64% yield), ester (**65**, 83% yield), and cyano substituents (**66**, 76% yield), highlighting the broad tolerance of the methodology. Azaindole substrates also proved effective, with 5- and 6-azaindoles affording **67** and **68** in 95% and 63% yield, respectively. By contrast, substitution at the indole C3 position resulted in diminished reactivity, as evidenced by the formyl and acetyl derivatives **69** and **70**, which were obtained in 49% and 45% yield, respectively. Finally, the methodology was successfully extended to pyrroles, with the tetracyclic spiroindene **71** isolated in 82% yield.

Scope of the racemic reaction

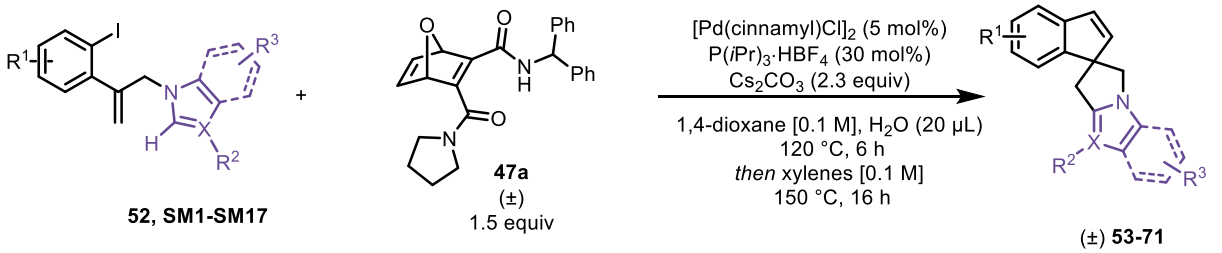

52, SM1-SM17

47a
(±)
1.5 equiv

(±) **53-71**

Benzimidazoles and Imidazoles

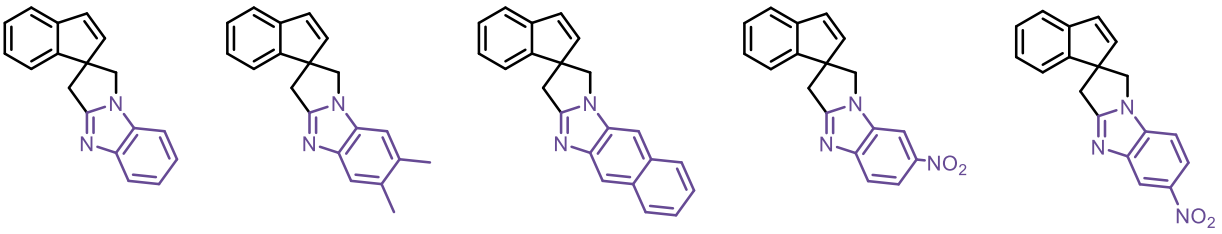

53
83% yield
Oxab **21:** 60% yield
1 mmol: 73% yield

54
69% yield

55
44% yield

56
56% yield

57
60% yield

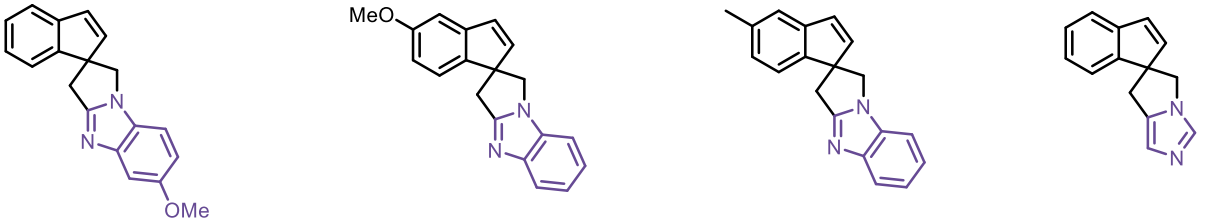

58
68% yield

59
55% yield

60
81% yield

61
98% yield

Indoles and Pyrroles

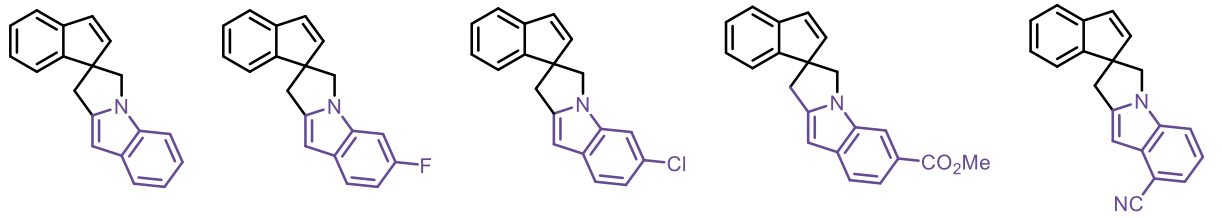

62
79% yield
1 mmol: 60% yield

63
74% yield

64
64% yield

65
83% yield

66
76% yield

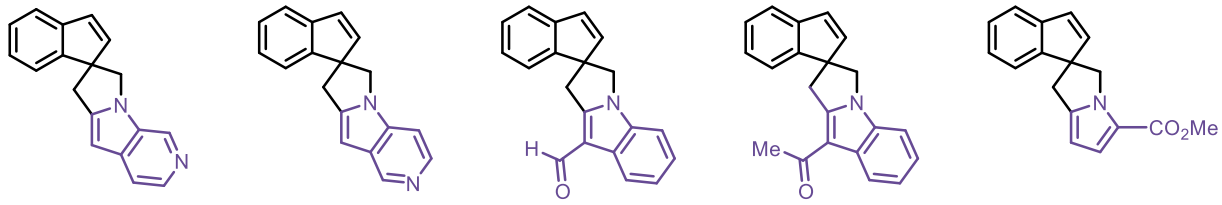

67
95% yield

68
63% yield

69
49% yield

70
45% yield

71
99% yield

Scheme 15. Evaluation of substrate scope under optimized conditions. Reactions were performed on a 0.1 mmol scale; isolated yields are reported. Selected examples were also run on 1 mmol scale.

The enantioselective conditions were further evaluated on representative substrates to probe the influence of steric and electronic factors (Scheme 16). For the indole-tethered substrate, the desired spiroindene **3j** was obtained in 65% yield and 78% ee. Comparable enantioselectivity was observed when steric bulk was increased around the C–H activation site, as illustrated by the formation of spiroindene 3r in 83% yield and 79% ee. In these cases, the use of an enantioenriched oxabicycle consistently provided better reactivity compared to its racemic counterpart. Overall, these results suggest that the identity of the pendant heterocycle exerts only a limited effect on the stereochemical outcome, while the chirality embedded in the oxabicycle remains the decisive factor in controlling enantioinduction.

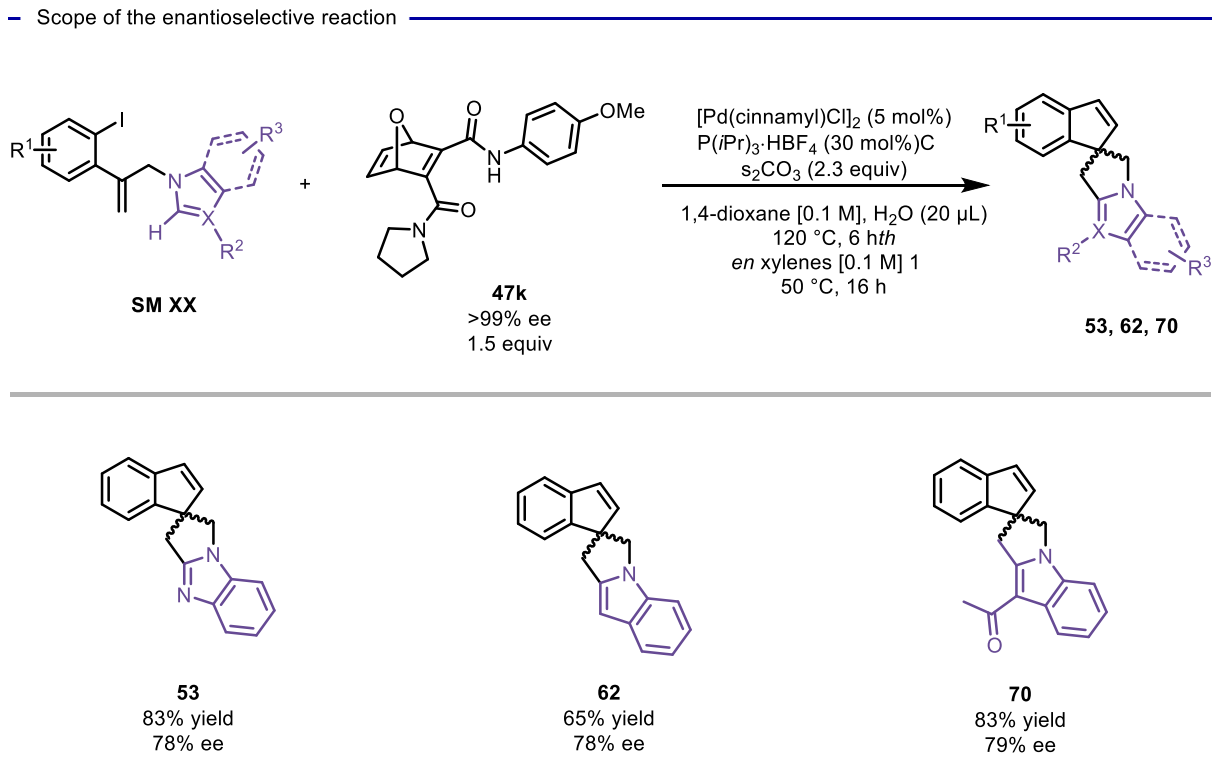

Scheme 16. Enantioselective scope with representative N-heterocycles. Reactions were performed on a 0.1 mmol scale. Isolated yields are reported. Absolute configuration of the products was not determined.

4.4. Conclusion

In conclusion, a palladium-catalyzed domino sequence has been developed for the synthesis of spiroindenes, using oxabicycles as practical acetylene surrogates. The strategy enables efficient access to diverse spirocyclic scaffolds, and preliminary enantioselective studies demonstrate that chiral oxabicycles can effectively transfer stereochemical information through the catalytic cascade. These results highlight the potential of this approach as a complementary strategy for the construction of enantioenriched spirocyclic architectures.

4.5. Experimental part

4.5.1. General considerations

Reactions were performed under argon in a dry environment unless otherwise stated. Reaction progress was monitored by thin layer chromatography (TLC) and visualized under UV light.

Dioxane was distilled over sodium/benzophenone. Palladium(π-cinnamyl) chloride dimer was purchased from Sigma Aldrich and stored in the freezer under argon atmosphere. Palladium acetate was purchased from Sigma Aldrich and stored in a desiccator. Triisoproylhexylphosphine tetrafluoroborate was purchased from Combi-Blocks and was stored in a desiccator. Cesium carbonate (anhydrous) was purchased from Sigma Aldrich and was stored in a desiccator. 1,3,5-Trimethoxybenzene was purchased from Combi-Blocks and used as received. All other commercially available starting materials and reagents were purchased from Sigma, Alfa Aesar, Fisher, Oakwood Chemical or Combi-Blocks and were used as received. Catalytic reactions were performed in 2 dram vials equipped with a Teflon-sealed cap and a stir bar (Fisher cat no. 14-513-57, 12 x 4.5 mm), with the reactions stirring at 900 rpm. An oil bath was used as the heating source for reactions requiring heat. Flash column chromatography was performed with Silicycle 46-60 μm silica gel.

^{1}H and ^{13}C NMR were obtained at 298 K on an Agilent DD2 700 equipped with a 5 mm HFCN COLD probe, an Agilent DD2 600 equipped with a 5 mm triple resonance HFX OneNMR probe, an Agilent DD2 500 equipped with a 5 mm Xsens Cold Probe, a Bruker Avance III 400 or a Varian Mercury 300 or 400. Measurements were referenced to the solvent. NMR data are referenced as chemical shift (δ ppm), multiplicity (s = singlet, d = doublet, t = triplet, q = quartet, m = multiplet, b = broad), coupling constant (Hz), integration. NMR yields were obtained by ^{1}H NMR analysis using a 10 second relaxation delay and 1,3,5-trimethoxybenzene as an internal standard.

HRMS were obtained on a JEOL AccuTOF-DART performed at the Advanced Instrumentation for Molecular Structure (AIMS) at the University of Toronto. IR spectra were acquired on a Perkin-Elmer Spectrum 100 instrument with a single-bounce diamond/ZeSe ATR accessory. Data is presented in wavenumbers (cm^{-1}). Melting point ranges were determined on a Fisher-Johns Melting Point Apparatus. Chiral HPLC was performed on Agilent 1100 or 1200 Series operated by ChemStation LC 3D software.

4.5.2. Reaction optimization

Table 3.Improving the Enantioselectivity – Temperature Screening. Reactions were performed on a 0.1 mmol scale. Isolated yields.

Temperature Screening

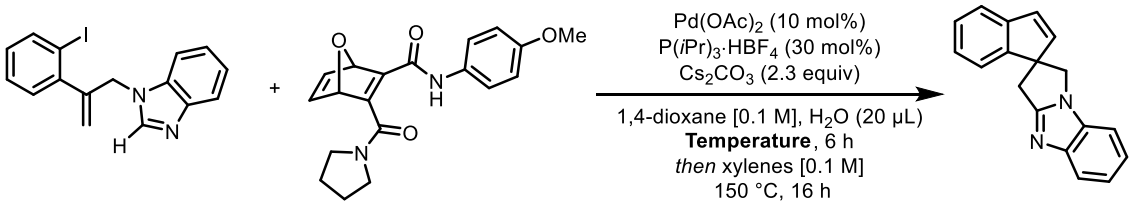

52 **47k** >99% ee 1.5 equiv **53**

Entry	Temperature	Yield 3a (%)	ee (%)
1	100 ˚C	64%	76%
2	110 ˚C	83%	73%
3	120 ˚C	72%	77%
4	130 ˚C	76%	75%

Table 4.Improving the Enantioselectivity – Oxabicycle Equivalencies. Reactions were performed on a 0.1 mmol scale. Isolated yields.

Oxabicycle Equivalencies

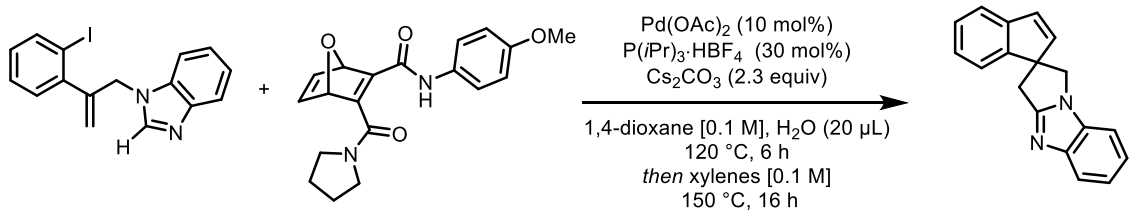

52 **47k** >99% ee **X** equiv **53**

Entry	Oxabicycle equivalencies	Yield 3a (%)	ee (%)
1	1.1	71%	70%
2	1.5	72%	77%
3	2.0	79%	63%

4.5.3. Procedures for the Synthesis of Substrates

General Procedure 1 (GP1)

Preparation of 1-(3-bromoprop-1-en-2-yl)-2-iodobenzene

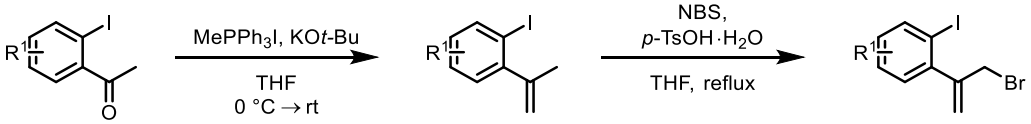

The following step is based on a literature procedure.[38] To a stirred suspension of methyltriphenylphosphonium iodide (1.5 equiv) in THF (0.3 M) at 0 °C was added potassium *tert*-butoxide. The resulting mixture was warmed to room temperature and stirred for 30 min before being cooled to 0 °C. A 1.0 M THF solution of 2′-iodoacetophenone or a derivative was added dropwise to the suspension, which was subsequently warmed to room temperature and stirred overnight. Pentanes followed by EtOAc were added to the reaction mixture, which was pushed through a pad of silica. The filtrate was concentrated under reduced pressure and the crude mixture was purified via silica gel chromatography (100% pentanes).

The following step is based on a literature procedure.[55] To a flame-dried round-bottom flask equipped with a magnetic stir bar was added NBS (recrystallized from water) (1.1 equiv), para-Toluenesulfonic acid monohydrate (0.1 equiv) and the aryl iodide. THF (0.3 M) was added via syringe, and the reaction was stirred at reflux for 4 hours. The solution was concentrated under reduced pressure and the crude mixture was purified via silica gel chromatography. When heating the reaction mixture for over 4 hours, an undesired side product is formed. The unreacted methyl styrene starting material can be recovered via column chromatography (Less polar than brominated product, 100% pentanes).

Preparation of the 2'-Iodoacetophenone derivatives

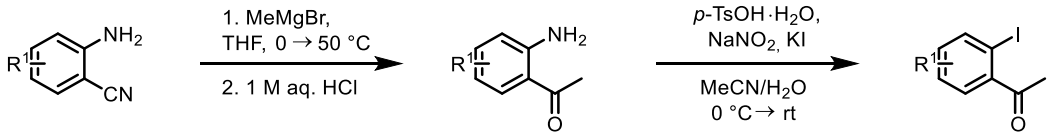

The following steps are based on a literature procedure.[38] To a flame-dried round-bottom flask equipped with a magnetic stir bar was added the corresponding 2-aminobenzonitrile derivative (1.0 equiv) in THF (0.3 M) and cooled to 0 °C. A 3M solution of methyl magnesium bromide in Et_2O (2.5 – 3.0 equiv) was added dropwise. The reaction mixture was then heated to 50 ˚C and stirred overnight, or until completion by TLC. The reaction mixture is then cooled to 0 ˚C, and a 1 M aqueous solution of HCl is slowly added to quench the mixture, and stirred at room temperature for 15 min. The reaction was diluted with brine and extracted three times with EtOAc. The organic layer was washed with brine and dried over magnesium sulfate, filtered and concentrated under reduced pressure. The crude mixture was purified via silica gel chromatography.

To a stirred solution of *p*-TsOH·H_2O (3.0 equiv) in MeCN (0.75 M) was added 2′- aminoacetophenone derivative (1.0 equiv), then cooled to 0 °C, forming a suspension. An aqueous solution of $NaNO_2$ (6.7 M, 2.0 equiv) was slowly added, followed by an aqueous solution of KI (8.3 M, 2.5 equiv). When evolution of nitrogen gas ceased, the resulting solution was warmed to room temperature and stirred for 1 h or until completion by TLC. A saturated solution of $Na_2S_2O_3$, followed by a saturated solution of $NaHCO_3$ were added. The aqueous

phase was extracted three times with EtOAc, the organic layers were combined, washed with brine, dried over magnesium sulfate, filtered and concentrated under reduced pressure. The crude mixture was purified via silica gel chromatography.

Preparation of benzimidazole, indole, imidazole and pyrazole-substituted substrates

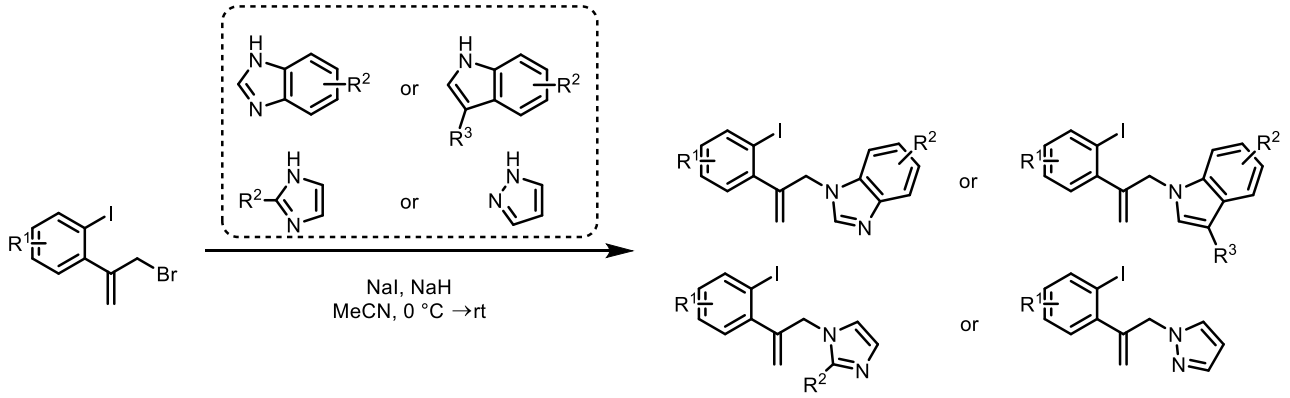

To a flame-dried round-bottom flask equipped with a magnetic stir bar was added the corresponding heterocycle (1.0 equiv) and NaI (0.3 equiv) in MeCN (0.3 M) under argon. The reaction was cooled to 0 ˚C and NaH (1.2 equiv, 60% dispersion in mineral oil) was added. The reaction was warmed to room temperature and stirred for 30 minutes. The corresponding aryl iodide (1.1 equiv) was added dropwise to the reaction mixture and the reaction was stirred at room temperature overnight. The reaction was quenched with brine and extracted three times with EtOAc, dried over magnesium sulfate and concentrated under reduced pressure. The crude mixture was purified via silica gel chromatography.

Preparation of pyrrole-substituted substrates

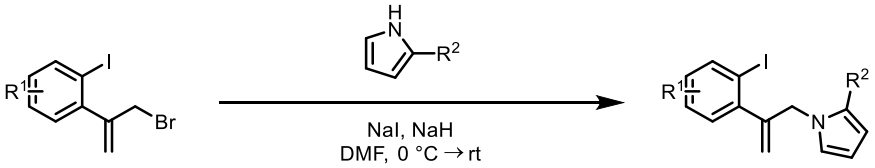

To a flame-dried round-bottom flask equipped with a magnetic stir bar was added the corresponding pyrrole (1.0 equiv) and NaI (0.3 equiv) in DMF (0.3 M) under argon. The reaction was cooled to 0 ˚C and NaH (1.2 equiv, 60% dispersion in mineral oil) was added. The reaction was warmed to room temperature and stirred for 30 minutes. The corresponding allyl-bromide intermediate (1.1 equiv) was added dropwise to the reaction mixture and the reaction was stirred at room temperature overnight. The reaction was quenched with brine and extracted three times with EtOAc, dried over magnesium sulfate and concentrated under reduced pressure. The crude mixture was purified via silica gel chromatography.

Preparation of triazole-substituted substrates

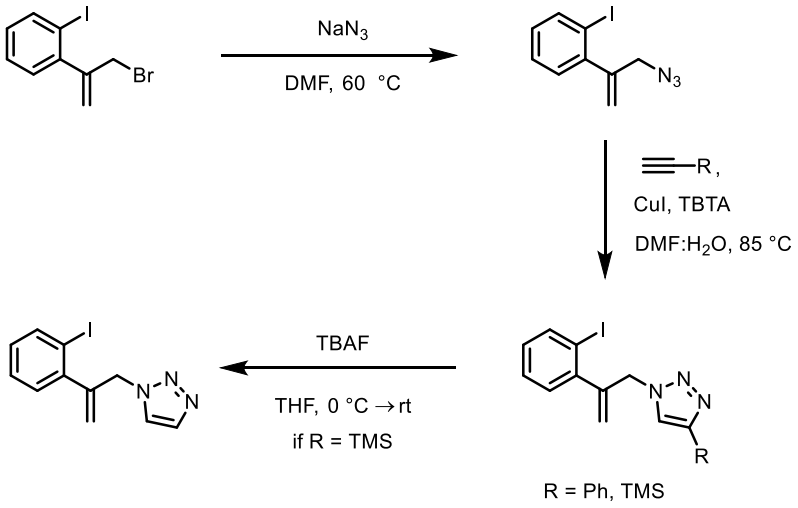

To a stirred solution of 1-(3-bromoprop-1-en-2-yl)-2-iodobenzene in DMF was added sodium azide (1.5 equiv). The reaction was stirred at 60 ˚C overnight. The crude mixture was quenched with brine and extracted five times with EtOAc, dried over magnesium sulfate and concentrated under reduced pressure. The crude mixture was purified via silica gel chromatography.

To a stirred solution of 1-(3-azidoprop-1-en-2-yl)-2-iodobenzene in 1:1 DMF:H_2O was added CuI (0.2 equiv), TBTA (0.2 equiv), and phenylacetylene (1.1 equiv). The reaction was stirred at 80 ˚C overnight. The crude mixture was diluted with EtOAc and washed five times with brine, dried over magnesium sulfate and concentrated under reduced pressure. The crude mixture was purified via silica gel chromatography.

A stirred solution of the TMS-protected triazole substrate in THF (0.5 M) was cooled to 0 ˚C. TBAF (10mL, 1M solution in THF, 2.0 equiv) was added dropwise. The reaction was allowed to warm up to room temperature and stirred overnight. The crude mixture was quenched with water and extracted five times with EtOAc, dried over magnesium sulfate and concentrated under reduced pressure. The crude mixture was purified via silica gel chromatography.

4.5.4. Procedures for the Synthesis of Oxabicycles

General Procedure 2 (GP 2)

Preparation of dimethyl 7-oxabicyclo[2.2.1]hepta-2,5-diene-2,3-dicarboxylate (**21**)

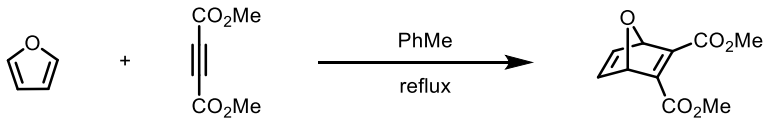

21

The following step is based on a literature procedure.[40] To a round bottom flask, dimethyl acetylene dicarboxylate (1.0 equiv) and furan (1 equiv) were dissolved in toluene (1 M) and stirred at reflux overnight. The mixture was cooled to room temperature and concentrated under reduced pressure. The crude mixture was

purified via silica gel chromatography 10→30% EtOAc/pentanes to obtain dimethyl 7-oxabicyclo[2.2.1]hepta-2,5-diene-2,3-dicarboxylate **21** as a yellow oil. Characterization was consistent with literature .[40]

Preparation of (±)-3-(methoxycarbonyl)-7-oxabicyclo[2.2.1]hepta-2,5-diene-2-carboxylic acid (**21a**)

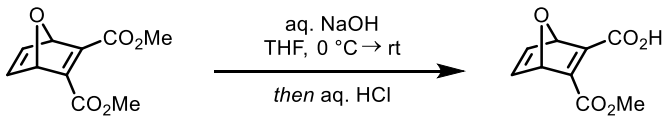

2a **21a** (±)

The following step is based on a literature procedure.[60] A stirred solution of oxabicycle **21** in THF (0.15 M) was cooled to 0 ˚C. An aqueous solution of sodium hydroxide (0.25 M, 1.2 equiv) was slowly added, and the solution was stirred at room temperature for 1 h. The reaction mixture was washed twice with EtOAc and once with pentanes. An aqueous solution of hydrochloric acid (1 M, 1.2 equiv) was added to the reaction mixture. The aqueous phase was extracted three times with EtOAc, the organic phases were combined, washed with brine, dried over magnesium sulfate, and concentrated under reduced pressure to obtain (±)-3-(methoxycarbonyl)-7-oxabicyclo[2.2.1]hepta-2,5-diene-2-carboxylic acid **21a** as a pale-yellow solid without further purification. Characterization was consistent with literature.[60]

Preparation of (1*R*,4*S*)-3-(methoxycarbonyl)-7-oxabicyclo[2.2.1]hepta-2,5-diene-2-carboxylic acid (**21a**)

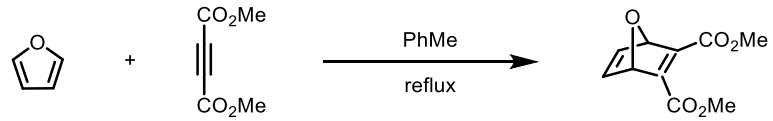

71 **72** **21**

The following step is based on a literature procedure.[58] 30 g of the dimethyl 7-oxabicyclo[2.2.1]hepta-2,5-diene-2,3-dicarboxylate **2a** was dissolved in DMSO (120 mL) and added to a 2L Kimax bottle containing 1.5 L of pH 7 buffer (prepared by dissolving 26.1 g of K_2HPO_4 in 1.5 L of deionized water and adjusting to pH 7 with H_3PO_4) and esterase BS4 (4.5 g). The mixture was stirred with a magnetic stir bar (200 rpm) and warmed on a hot plate to 30°C. After 10 h, the pH of the mixture was adjusted to 2 with H_3PO_4 and extracted 5 times with EtOAc (200 mL). The combined organic layers were washed with brine, dried over $MgSO_4$, filtered and concentrated to afford 24 g of a mixture of (1*R*,4*S*)-3-(methoxycarbonyl)-7-oxabicyclo[2.2.1]hepta-2,5-diene-2-carboxylic acid and (1*S*,4*R*)-3-(methoxycarbonyl)-7-oxabicyclo[2.2.1]hepta-2,5-diene-2- carboxylic acid **21a** as a golden oil. SFC analysis showed this material to be 84% ee.

The hydrolysed oxabicycle **21a** was dissolved in EtOAc (500 mL) and (*R*)-*N*-Benzyl α-methyl benzylamine (30.7 mL, 147 mmol) was added. The resulting slurry was warmed to reflux for 10 min, then allowed to cool slowly to ambient temperature. After 16h, the resulting slurry was filtered and the resulting cake was washed with 2 cake volumes of EtOAc. The cake was dried for 16 h in a 50 °C vacuum oven to afford (*R*)-*N*-benzyl-1-phenylethan-1-aminium (1*R*,4*S*)-3-(methoxycarbonyl)-7- oxabicyclo[2.2.1]hepta-2,5-diene-2-carboxylate salt as an off-white solid (33.5 g, 70% yield, >99% ee according to SFC analysis).

60 mL of EtOAc were added to 1.00 g of the oxabicycle salt, resulting in a cloudy solution. 40 mL of a 10% aqueous solution of H_3PO_4 was added to the solution and left to stir for 5 minutes. The organic layer was extracted and washed twice more with 20 mL of a 10% aqueous solution of H_3PO_4. The organic layers were combined, washed with brine, dried over magnesium sulfate, filtered and concentrated under reduced pressure. Obtained 509 mg of (1*R*,4*S*)-3- (methoxycarbonyl)-7-oxabicyclo[2.2.1]hepta-2,5-diene-2-carboxylic acid **21a** as a beige solid (100% yield, >99% ee).

Preparation of racemic and enantioenriched amide-amide' oxabicycles

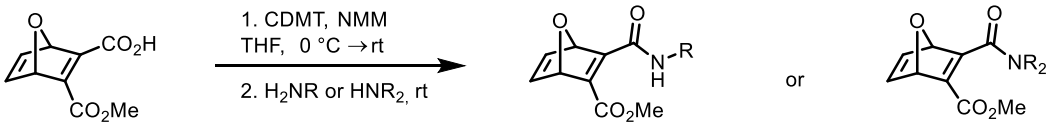

21a
(±) *or* >99% ee

(±) *or* >99% ee

(±) *or* >99% ee

The following steps are based on a literature procedure.[61] A stirred solution of (±)-3-(methoxycarbonyl)-7-oxabicyclo[2.2.1]hepta-2,5-diene-2-carboxylic acid or (1*R*,4*S*)-3-(methoxycarbonyl)-7-oxabicyclo[2.2.1]hepta-2,5-diene-2-carboxylic acid **21a** and 2-chloro-4,6-dimethoxy-1,3,5-triazine (CDMT) (1.2 equiv) in THF (0.05 M) was cooled to 0˚C. *N*-methylmorpholine (NMM) (1.2 equiv) was added dropwise and the reaction mixture was stirred at room temperature for 1 h, forming a turbid mixture. A primary or secondary amine (1.2 equiv) was added dropwise to the mixture, and the reaction was stirred for 3 h at room temperature. The reaction mixture was filtered through a pad of silica and washed with EtOAc. The filtrate was concentrated under reduced pressure and the crude mixture was purified by flash chromatography.

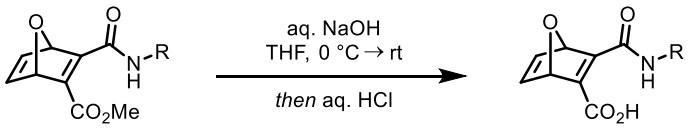

(±) *or* >99% ee

(±) *or* >99% ee

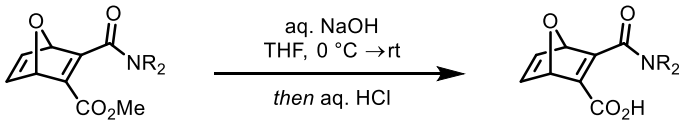

(±) *or* >99% ee

(±) *or* >99% ee

A stirred solution of "amide-ester" oxabicycle in THF (0.15 M) was cooled to 0 ˚C. An aqueous solution of sodium hydroxide (0.25 M, 1.2 equiv) was slowly added, and the solution was stirred at room temperature for 1 h. The reaction mixture was washed twice with EtOAc and once with pentanes. An aqueous solution of hydrochloric acid (1 M, 1.2 equiv) was added to the reaction mixture. The aqueous phase was extracted three times with EtOAc, the organic phases were combined, washed with brine, dried over magnesium sulfate, and concentrated under reduced pressure. The resulting "amide-acid" oxabicycle was used in the next step without further purification.

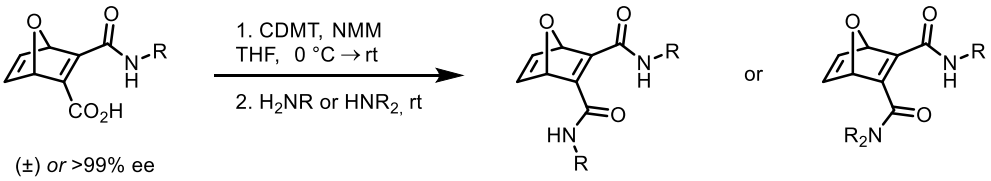

(±) *or* >99% ee

(±) *or* >99% ee

(±) *or* >99% ee

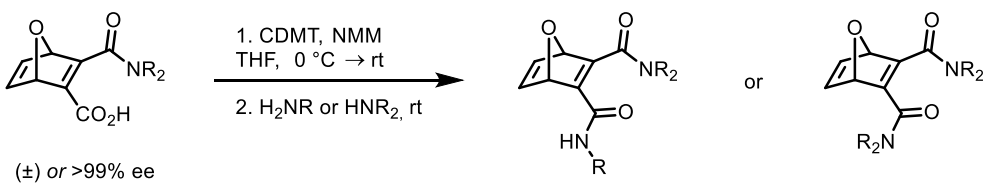

(±) *or* >99% ee

(±) *or* >99% ee

(±) *or* >99% ee

A stirred solution of "amide-acid" oxabicycle and 2-chloro-4,6-dimethoxy-1,3,5-triazine (CDMT) (1.2 equiv) in THF (0.05 M) was cooled to 0˚C. *N*-methylmorpholine (NMM) (1.2 equiv) was added dropwise and the reaction mixture was stirred at room temperature for 1 h, forming a turbid mixture. A primary or secondary amine (1.2 equiv) was added dropwise to the mixture, and the reaction was stirred for 3 h at room temperature. The reaction mixture was filtered through a pad of silica and washed with EtOAc. The filtrate was concentrated under reduced pressure and the crude mixture was purified by flash chromatography.

4.5.5. Procedures for the Catalytic Reactions

General Procedure 3 (GP3) – Standard Catalytic Conditions

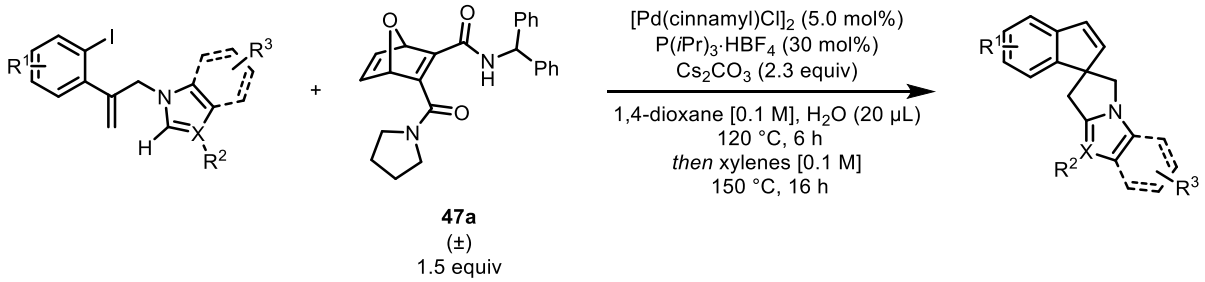

A 2 dr vial and stir bar were dried in 110 ˚C oven overnight prior to use. The vial was equipped with a stir bar and allowed to cool to room temperature under argon flow. Cesium carbonate (75 mg, 0.23 mmol, 2.3 equiv), $[Pd(cinnamyl)Cl]_2$ (2.6 mg, 0.005 mmol, 5.0 mol%), $P(iPr)_3 \cdot HBF_4$ (7.4 mg, 0.030 mmol, 30 mol%), aryl iodide (0.1 mmol, 1.0 equiv) and oxabicycle **47a** (60.1 mg, 0.15 mmol, 1.5 equiv) were added in that order to the vial. Freshly distilled dioxane (1.0 mL, 0.1 M) followed by distilled water (20 µL) were added via syringe. The vial was equipped with a Teflon-sealed cap and immediately stirred at 120 ˚C for 6 h. The reaction was concentrated under reduced pressure, and xylenes (1.0 mL, 0.1 M) was added via syringe. The reaction was then stirred at 150 ˚C for 16 h. The reaction was passed through a pad of silica washing with 90:10 ethyl acetate/methanol. The filtrate was concentrated under reduced pressure and the resulting residue purified by flash chromatography

General Procedure 4 (GP4) – Meso Oxabicycle Conditions

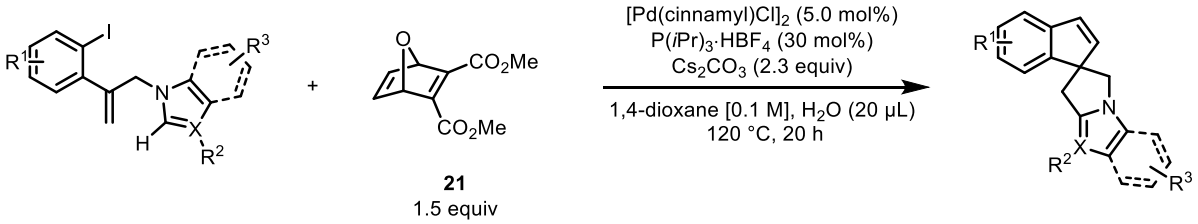

Vials and stir bars were dried in 110 ˚C oven overnight prior to use. Two 2 dr vials, one equipped with a stir bar and one without were allowed to cool to room temperature under argon flow. Cesium carbonate (75 mg, 0.23 mmol, 2.3 equiv), $[Pd(cinnamyl)Cl]_2$ (2.6 mg, 0.005 mmol, 5.0 mol%), $P(iPr)_3 \cdot HBF_4$ (7.4 mg, 0.030 mmol, 30 mol%) and aryl iodide (0.1 mmol, 1.0 equiv) were added in that order to the vial with the stir bar. Oxabicycle **21** (34.7 mg, 1.1·0.15 mmol = 0.165 mmol, 1.1·1.5 equiv = 1.65 equiv) was weighed in the empty vial. Freshly distilled dioxane (1.1·1.0 mL = 1.1 mL) was added via syringe to the oxabicycle-containing vial. 1.0 mL of the resulting solution was transferred via syringe to the first vial, followed by 20 µL of distilled

water. The vial was equipped with a Teflon-sealed cap and immediately stirred at 120 ˚C for 20 h. The reaction was passed through a pad of silica washing with 90:10 ethyl acetate/methanol. The filtrate was concentrated under reduced pressure and the resulting residue purified by flash chromatography.

General Procedure 5 (GP5) – Enantioselective Conditions

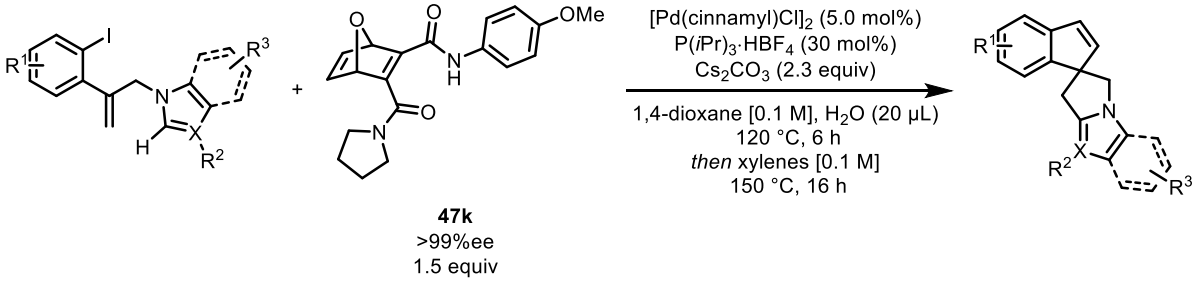

A 2 dr vial and stir bar were dried in 110 ˚C oven overnight prior to use. The vial was equipped with a stir bar and allowed to cool to room temperature under argon flow. Cesium carbonate (75 mg, 0.23 mmol, 2.3 equiv), $[Pd(cinnamyl)Cl]_2$ (2.6 mg, 0.005 mmol, 5.0 mol%), $P(iPr)_3 \cdot HBF_4$ (7.4 mg, 0.030 mmol, 30 mol%), aryl iodide (0.1 mmol, 1.0 equiv) and enantiopure oxabicycle **47k** (51.0 mg, 0.15 mmol, 1.5 equiv) were added in that order to the vial. Freshly distilled dioxane (1.0 mL, 0.1 M) followed by distilled water (20 µL) were added via syringe. The vial was equipped with a Teflon-sealed cap and immediately stirred at 120 ˚C for 6 h. The reaction was concentrated under reduced pressure, and xylenes (1.0 mL, 0.1 M) was added via syringe. The reaction was then stirred at 150 ˚C for 16 h. The reaction was passed through a pad of silica washing with 90:10 ethyl acetate/methanol. The filtrate was concentrated under reduced pressure and the resulting residue purified by flash chromatography

4.5.6. Characterization of Substrates

Benzimidazoles & Imidazoles

1-(2-(2-iodophenyl)allyl)-1H-benzo[d]imidazole (52)

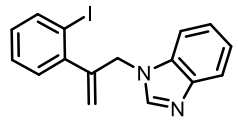

52

Prepared on 12.5 mmol scale by **GP1**, starting from 2'-Iodoacetophenone. Purified by flash column chromatography 20→ 80 % EtOAc/pentanes. Obtained 1.2 g of a white solid (26% yield over 3 steps).

^{1}H NMR (500 MHz, $CDCl_3$) δ 7.86 (dd, J = 8.0, 1.2 Hz, 1H), 7.83 (s, 1H), 7.81 – 7.79 (m, 1H), 7.50 – 7.47 (m, 1H), 7.32 – 7.26 (m, 2H), 7.21 (td, J = 7.5, 1.2 Hz, 1H), 6.98 (ddd, J = 8.0, 7.5, 1.7 Hz, 1H), 6.91 (dd, J = 7.5, 1.7 Hz, 1H), 5.17 – 5.15 (m, 2H), 5.06 (dd, J = 1.4, 1.4 Hz, 2H). **^{13}C NMR** (126 MHz, $CDCl_3$) δ 146.9, 143.9, 143.9, 143.5, 139.5, 134.1, 129.8, 129.7, 128.5, 123.2, 122.3, 120.6, 118.0, 110.3, 97.3, 49.8. **IR** (ATR) 2953, 2916, 1617, 1583, 1493, 1456, 1438, 1358, 1262, 1177, 1204. **HRMS** (DART) m/z: $[M + H]^+$ Calcd for $C_{16}H_{14}N_2I$ 361.0162; Found 361.0200. **MP** 84-87 °C.

1-(2-(2-iodophenyl)allyl)-5,6-dimethyl-1H-benzo[d]imidazole (SM1)

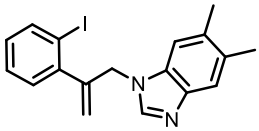

SM1

Prepared on 1.9 mmol scale by **GP1**, starting from 2'-Iodoacetophenone. Purified by flash column chromatography 20→ 100 % EtOAc/pentanes. Obtained 130 mg of a white solid (17% yield over 3 steps).

^{1}H NMR (500 MHz, $CDCl_3$) δ 7.86 (dd, *J* = 7.9, 1.2 Hz, 1H), 7.71 (s, 1H), 7.55 (s, 1H), 7.24 – 7.19 (m, 2H), 6.97 (ddd, *J* = 7.9, 7.4, 1.7 Hz, 1H), 6.93 (dd, *J* = 7.4, 1.7 Hz, 1H), 5.14 – 5.12 (m, 2H), 4.98 (t, *J* = 1.5 Hz, 2H), 2.38 (s, 3H), 2.37 (s, 3H). **^{13}C NMR** (126 MHz, $CDCl_3$) δ 146.9, 144.0, 142.7, 142.4, 139.4, 132.6, 132.3, 131.1, 129.7, 128.5, 120.5, 117.8, 110.4, 97.4, 49.6, 20.8, 20.4. **IR** (ATR) 2919, 2853, 1651, 1580, 1495, 1464, 1429, 1352, 1276, 1217. **HRMS** (DART) m/z: $[M + H]^+$ Calcd for $C_{18}H_{18}N_2I$ 389.0509; Found 389.0517. **MP** 70-73 °C.

1-(2-(2-iodophenyl)allyl)-1H-naphtho[2,3-d]imidazole (SM2)

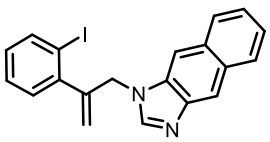

SM2

Prepared on 2.4 mmol scale by **GP1**, starting from 2'-Iodoacetophenone. Purified by flash column chromatography 10→ 100 % EtOAc/pentanes. Obtained 180 mg of a brown solid (18% yield over 3 steps).

^{1}H NMR (500 MHz, $CDCl_3$) δ 8.29 (s, 1H), 8.05 – 7.93 (m, 3H), 7.89 – 7.85 (m, 2H), 7.47 – 7.39 (m, 2H), 7.18 (td, J = 7.5, 1.2 Hz, 1H), 6.97 (ddd, J = 7.9, 7.5, 1.7 Hz, 1H), 6.90 (dd, J = 7.5, 1.7 Hz, 1H), 5.29 – 5.27 (m, 1H), 5.22 – 5.20 (m, 1H), 5.15 (dd, J = 1.4, 1.4 Hz, 2H). **^{13}C NMR** (126 MHz, $CDCl_3$) δ 147.4, 146.6, 144.0, 143.8, 139.5, 134.6, 130.7, 130.3, 129.8, 129.7, 128.7, 128.5, 127.7, 124.7, 123.7, 118.4, 117.7, 106.2, 97.3, 50.0. **IR** (ATR) 3055, 2929, 2857, 1584, 1499, 1463, 1403, 1319, 1274, 1192.

HRMS (DART) m/z: $[M + H]^+$ Calcd for $C_{20}H_{15}IN_2$ 411.0353, Found 411.0341. **MP** 120-124 °C.

1-(2-(2-iodophenyl)allyl)-5-nitro-1H-benzo[d]imidazole (SM3)

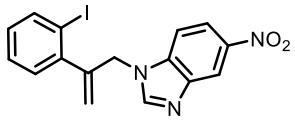

SM3

Prepared on 5.1 mmol scale by **GP1**, starting from 2'-Iodoacetophenone. Purified by flash column chromatography 30→ 80 % EtOAc/pentanes (Least polar regioisomer by TLC). Obtained 76 mg of an off-white solid (4% yield over 3 steps).

^{1}H NMR (500 MHz, $CDCl_3$) δ 8.69 (dd, J = 2.1, 0.5 Hz, 1H), 8.21 (dd, J = 8.9, 2.1 Hz, 1H), 7.99 (s, 1H), 7.85 (dd, J = 8.0, 1.1 Hz, 1H), 7.50 (dd, J = 8.9, 0.5 Hz, 1H), 7.20 (td, J = 7.5, 1.1 Hz, 1H), 6.98 (ddd, J = 8.0, 7.5, 1.7 Hz, 1H), 6.87 (dd, J = 7.6, 1.7 Hz, 1H), 5.26 – 5.24 (m, 1H), 5.23 – 5.21 (m, 1H), 5.15 (t, J = 1.3 Hz, 2H). **^{13}C NMR** (126 MHz, $CDCl_3$) δ 146.8, 146.2, 143.9, 143.1, 143.1, 139.6, 138.2, 130.1, 129.6, 128.6, 119.0, 118.9, 117.3, 110.3, 97.2, 50.3. **IR** (ATR) 2979, 2942, 1619, 1514, 1437, 1464, 1332, 1261, 1182, 1014. **HRMS** (DART) m/z: $[M + H]^+$ Calcd for $C_{16}H_{13}N_3O_2I$ 406.0047; Found 406.0044.

MP 104-109 °C.

1-(2-(2-iodophenyl)allyl)-5-methoxy-1H-benzo[d]imidazole (SM4)

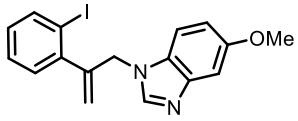

SM4

Prepared on 6.25 mmol scale by **GP1**, starting from 2'-Iodoacetophenone. Purified by flash column chromatography 50→ 70 % EtOAc/Toluene (Most polar regioisomer by TLC). Obtained 80 mg of an orange oil (3% yield over 3 steps).

^{1}H NMR (500 MHz, $CDCl_3$) δ 7.84 (dd, *J* = 7.9, 1.2 Hz, 1H), 7.77 (s, 1H), 7.34 (d, *J* = 8.8 Hz, 1H), 7.26 (s, 1H), 7.19 (td, *J* = 7.5, 1.2 Hz, 1H), 7.00 – 6.92 (m, 2H), 6.88 (dd, *J* = 7.5, 1.7 Hz, 1H), 5.18 – 5.16 (m, 1H), 5.16 – 5.13 (m, 1H), 5.01 (t, *J* = 1.4 Hz, 2H), 3.85 (s, 3H).

^{13}C NMR (126 MHz, $CDCl_3$) δ 156.3, 146.8, 144.3, 143.8, 143.5, 139.4, 129.7, 129.6, 128.5, 128.5, 118.0, 113.5, 110.7, 102.3, 97.3, 55.8, 49.9. **IR** (ATR) 2979, 2931, 2849, 1622, 1603, 1496, 1466, 1437, 1394, 1353, 1266. **HRMS** (DART) m/z: $[M + H]^+$ Calcd for $C_{17}H_{15}IN_2O$ 391.0307, Found 391.0322

1-(2-(2-iodo-4-methoxyphenyl)allyl)-1H-benzo[d]imidazole (SM5)

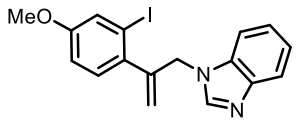

SM5

Prepared on 7.6 mmol scale by **GP1**, starting from 2-amino-4-methoxybenzonitrile. Purified by flash column chromatography 0→ 20 % MeOH/EtOAc. Obtained 196 mg of a pale orange oil (7% yield over 5 steps).

^{1}H NMR (500 MHz, $CDCl_3$) δ 7.82 – 7.75 (m, 2H), 7.50 – 7.44 (m, 1H), 7.37 (d, J = 2.5 Hz, 1H), 7.31 – 7.25 (m, 2H), 6.77 (d, J = 8.4 Hz, 1H), 6.72 (dd, J = 8.4, 2.5 Hz, 1H), 5.15 (td, J = 1.6, 0.8 Hz, 1H), 5.13 (q, J = 1.1 Hz, 1H), 5.02 (t, J = 1.4 Hz, 2H), 3.74 (s, 3H). **^{13}C NMR** (126 MHz, $CDCl_3$) δ 159.5, 146.3, 143.8, 143.5, 136.0, 134.0, 129.9, 124.6, 123.1, 122.2, 120.5, 118.3, 114.3, 110.3, 97.3, 55.6, 50.0. **IR** (ATR) 2920, 2853, 1710, 1593, 1555, 1487, 1458, 1438, 1283, 1225. **HRMS** (DART) m/z: $[M + H]^+$ Calcd for $C_{17}H_{16}N_2OI$ 391.0302; Found 391.0304.

1-(2-(2-iodo-4-methylphenyl)allyl)-1H-benzo[d]imidazole (SM6)

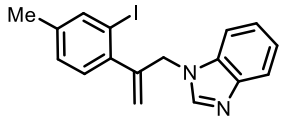

SM6

Prepared on 15 mmol scale by **GP1**, starting from 2-amino-4-methylbenzonitrile. Purified by flash column chromatography 20→ 100 % EtOAc/pentanes, then 0→ 10 % MeOH/EtOAc. Obtained 80 mg of a colourless oil (2% yield over 5 steps). **^{1}H NMR** (500 MHz, $CDCl_3$) δ 7.82 (s, 1H), 7.81 – 7.79 (m, 1H), 7.70 – 7.68 (m, 1H), 7.50 – 7.47 (m, 1H), 7.32 – 7.26 (m, 2H), 7.00 (ddd, *J* = 7.7, 1.7, 0.8 Hz, 1H), 6.77 (d, *J* = 7.7 Hz, 1H), 5.15 – 5.14 (m, 1H), 5.13 (dd, *J* = 1.1, 1.1 Hz, 1H), 5.04 (dd, *J* = 1.4, 1.4 Hz, 2H), 2.27 (s, 3H). **^{13}C NMR** (126 MHz, $CDCl_3$) δ 146.7, 143.8, 143.5, 140.9, 139.9, 139.9, 134.1, 129.3, 129.3, 123.1, 122.3, 120.5, 118.0, 110.3, 97.2, 49.9, 20.6. **IR** (ATR) 2968, 2916, 2851, 1599, 1494, 1458, 1438, 1284, 1260, 1188. **HRMS** (DART) m/z: $[M + H]^+$ Calcd for $C_{17}H_{16}N_2I$ 375.0353; Found 375.0347.

1-(2-(2-iodophenyl)allyl)-1H-imidazole (SM7)

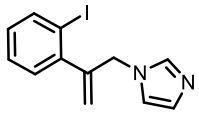

SM7

Prepared on 6.25 mmol scale by **GP1**, starting from 2'-Iodoacetophenone. Purified by flash column chromatography 20→ 100 % EtOAc/pentanes. Obtained 213 mg of a pale-yellow oil (11% yield over 3 steps). **^{1}H NMR** (500 MHz, $CDCl_3$) δ 7.86 (ddd, J = 7.8, 1.2, 0.6 Hz, 1H), 7.45 (s, 1H), 7.27 (td, J = 7.5, 1.2 Hz, 1H), 7.05 (t, J = 1.2 Hz, 1H), 7.02 – 6.97 (m, 2H), 6.94 (t, J = 1.2 Hz, 1H), 5.17 (dt, J = 2.2, 1.1 Hz, 1H), 5.14 (q, J = 1.1 Hz, 1H), 4.80 (t, J = 1.4 Hz, 2H). **^{13}C NMR** (126 MHz, $CDCl_3$) δ 148.0, 143.8, 139.4, 137.6, 129.7, 129.6, 129.3, 128.5, 119.6, 118.0, 97.5, 51.7. **IR** (ATR) 3108, 3099, 1582, 1482, 1463, 1331, 1283, 1242, 1229, 1178.
HRMS (DART) m/z: $[M + H]^+$ Calcd for $C_{12}H_{13}N_2I$ 311.0040; Found 311.0051.

Indoles & Pyrroles

1-(2-(2-iodophenyl)allyl)-1H-indole (SM8)

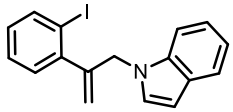

SM8

Prepared on 4.80 mmol scale by **GP1**, starting from 2'-Iodoacetophenone. Purified by flash column chromatography 0→ 30 % EtOAc/pentanes. Obtained 328 mg of a while oil (25% yield over 3 steps). **^{1}H NMR** (500 MHz, $CDCl_3$) δ 7.90 (ddd, J = 7.9, 1.2, 0.5 Hz, 1H), 7.68 (dt, J = 7.9, 1.0 Hz, 1H), 7.48 (dq, J = 8.1, 1.0 Hz, 1H), 7.26 (td, J = 7.7, 1.2 Hz, 3H), 7.16 (ddd, J = 8.1, 7.0, 1.0 Hz, 1H), 7.13 (d, J = 3.2 Hz, 1H), 7.03 – 6.98 (m, 2H), 6.55 (dd, J = 3.2, 1.0 Hz, 1H), 5.09 (q, J = 1.3 Hz, 1H), 5.02 (t, J = 1.5 Hz, 3H), 5.01 – 5.00 (m, 1H). **^{13}C NMR** (126 MHz, $CDCl_3$) δ 148.1, 144.8, 139.3, 136.5, 129.6, 129.4, 128.6, 128.5, 128.3, 121.7, 121.0, 119.6, 116.7, 109.9, 101.7, 97.6, 51.2. **IR** (ATR) 2975, 2929, 1513, 1484, 1462, 1431, 1390, 1315, 1255, 1012
HRMS (DART) m/z: $[M + H]^+$ Calcd for $C_{17}H_{15}IN$ 360.0249; Found 360.0257.

6-fluoro-1-(2-(2-iodophenyl)allyl)-1H-indole (SM9)

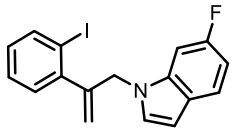

SM9

Prepared on 2.75 mmol scale by **GP1**, starting from 2'-Iodoacetophenone. Purified by flash column chromatography 0→ 10 % EtOAc/pentanes. Obtained 311 mg of a white oil (29% yield over 3 steps). **^{1}H NMR** (500 MHz, $CDCl_3$) δ 7.86 (dd, *J* = 7.9, 1.1 Hz, 1H), 7.33 (ddt, *J* = 8.9, 4.3, 0.7 Hz, 1H), 7.26 (ddd, *J* = 9.6, 2.6, 0.5 Hz, 1H), 7.22 (td, *J* = 7.5, 1.2 Hz, 1H), 7.11 (d, *J* = 3.1 Hz, 1H), 7.00 – 6.92 (m, 4H), 6.44 (dd, *J* = 3.1, 0.9 Hz, 1H), 5.08 – 5.06 (m, 1H), 4.99 – 4.96 (m, 3H). **^{13}C NMR** (126 MHz, $CDCl_3$) δ 158.00 (d, *J* = 234.0 Hz), 148.05, 144.60, 139.33, 133.09, 130.08, 129.60, 129.49, 128.89 (d, *J* = 10.1 Hz), 128.35, 116.87, 110.58 (d, *J* = 9.8 Hz), 110.15 (d, *J* = 26.4 Hz), 105.74 (d, *J* = 23.3 Hz), 101.71 (d, *J* = 4.7 Hz), 97.55, 51.57.

^{19}F NMR (377 MHz, $CDCl_3$) δ -124.84. **IR** (ATR) 2976, 2919, 1623, 1581, 1484, 1465, 1449, 1430, 1396, 1228, 1340. **HRMS** (DART) m/z: $[M + H]^+$ Calcd for $C_{17}H_{14}FIN$ 378.0155; Found 378.0154.

6-chloro-1-(2-(2-iodophenyl)allyl)-1H-indole (SM10)

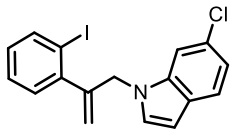

SM10

Prepared on 2.75 mmol scale by **GP1**, starting from 2'-Iodoacetophenone. Purified by flash column chromatography 10→ 40 % DCM/pentanes. Obtained 181 mg of a clear oil (17% yield over 3 steps).

^{1}H NMR (500 MHz, $CDCl_3$) δ 7.89 – 7.86 (m, 1H), 7.53 (dd, J = 8.4, 0.6 Hz, 1H), 7.43 – 7.42 (m, 1H), 7.24 (td, J = 7.5, 1.2 Hz, 1H), 7.09 (dd, J = 8.4, 1.8 Hz, 1H), 7.07 (d, J = 3.2 Hz, 1H), 7.01 – 6.97 (m, 2H), 6.47 (dd, J = 3.2, 0.9 Hz, 1H), 5.10 – 5.08 (m, 1H), 5.00 – 4.97 (m, 1H), 4.95 (dd, J = 1.6, 1.6 Hz, 2H). **^{13}C NMR** (126 MHz, $CDCl_3$) δ 147.7, 144.5, 139.3, 136.9, 129.6, 129.5, 129.2, 128.4, 127.8, 127.2, 121.9, 120.3, 117.0, 110.0, 102.0, 97.6, 51.3. **IR** (ATR) 2977, 2904, 1604, 1558, 1504, 1462, 1428, 1393, 1316, 1240, 1188. **HRMS** (DART) m/z: $[M + H]^+$ Calcd for $C_{17}H_{14}ClIN$ 393.9859; Found 393.9843.

Methyl 1-(2-(2-iodophenyl)allyl)-1H-indole-6-carboxylate (SM11)

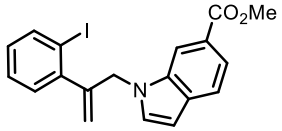

SM11

Prepared on 2.75 mmol scale by **GP1**, starting from 2'-Iodoacetophenone. Purified by flash column chromatography 10→ 50 % EtOAc/pentanes. Obtained 252 mg of a clear oil (22% yield over 3 steps).

^{1}H NMR (500 MHz, $CDCl_3$) δ 8.22 (dt, J = 1.5, 0.8 Hz, 1H), 7.88 – 7.85 (m, 1H), 7.80 (dd, J = 8.3, 1.4 Hz, 1H), 7.63 (dd, J = 8.3, 0.8 Hz, 1H), 7.25 – 7.21 (m, 2H), 7.00 – 6.96 (m, 2H), 6.52 (dd, J = 3.1, 0.8 Hz, 1H), 5.08 – 5.07 (m, 1H), 5.05 (t, J = 1.5 Hz, 2H), 4.99 – 4.97 (m, 1H), 3.94 (s, 3H). **^{13}C NMR** (126 MHz, $CDCl_3$) δ 168.4, 147.9, 144.5, 139.4, 135.9, 132.3, 131.8, 129.7, 129.5, 128.4, 123.5, 120.7, 120.6, 117.0, 112.5, 102.2, 97.6, 52.1, 51.4. **IR** (ATR) 2984, 2945, 1706, 1613, 1501, 1463, 1432, 1352, 1317, 1230. **HRMS** (DART) m/z: $[M + H]^+$ Calcd for $C_{19}H_{17}NO_2I$ 418.0299; Found 418.0301.

1-(2-(2-iodophenyl)allyl)-1H-indole-4-carbonitrile (SM12)

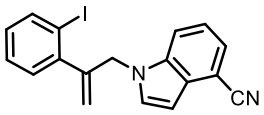

SM12

Prepared on 2.75 mmol scale by **GP1**, starting from 2'-Iodoacetophenone. Purified by flash column chromatography 0→ 80 % EtOAc/pentanes. Obtained 307 mg of a white solid (29% yield).

^{1}H NMR (500 MHz, $CDCl_3$) δ 7.86 (dd, J = 7.9, 1.0 Hz, 1H), 7.63 (dt, J = 8.3, 0.9 Hz, 1H), 7.46 (dd, J = 7.5, 1.0 Hz, 1H), 7.25 – 7.19 (m, 5H), 6.98 (ddd, J = 7.9, 7.5, 1.7 Hz, 1H), 6.89 (dd, J = 7.5, 1.4 Hz, 1H), 6.70 (dd, J = 3.2, 1.1 Hz, 1H), 5.09 (q, J = 1.1 Hz, 1H), 5.04 (t, J = 1.5 Hz, 3H), 5.02 – 5.00 (m, 1H). **^{13}C NMR** (126 MHz, $CDCl_3$) δ 147.6, 144.1, 139.4, 136.1, 131.1, 129.9, 129.7, 129.6, 128.4, 125.2, 121.4, 118.9, 117.3, 114.7, 103.4, 101.0, 97.4, 51.6. **IR** (ATR) 3089, 3047, 2223, 1604, 1507, 1466, 1434, 1346, 1134, 1012. **HRMS** (DART) m/z: $[M + H]^+$ Calcd for $C_{18}H_{14}N_2I$ 385.0196; Found 385.0186. **MP** 77-80 °C.

1-(2-(2-iodophenyl)allyl)-1H-pyrrolo[2,3-c]pyridine (SM13)

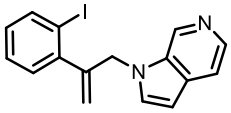

SM13

Prepared on 2.75 mmol scale by **GP1**, starting from 2'-Iodoacetophenone. Purified by flash column chromatography 20→ 100 % EtOAc/pentanes. Obtained 48 mg of a light brown solid (4.7% yield over 3 steps).

^{1}H NMR (500 MHz, $CDCl_3$) δ 8.86 (s, 1H), 8.24 (d, J = 5.5 Hz, 1H), 7.84 (dd, J = 7.9, 1.2 Hz, 1H), 7.50 (dd, J = 5.5, 1.1 Hz, 1H), 7.22 – 7.17 (m, 2H), 7.01 – 6.89 (m, 2H), 6.47 (dd, J = 3.1, 0.8 Hz, 1H), 5.11 – 5.09 (m, 1H), 5.08 (t, J = 1.5 Hz, 3H), 5.05 – 5.04 (m, 2H). **^{13}C NMR** (126 MHz, $CDCl_3$) δ 147.7, 144.1, 139.3, 138.7, 133.4, 133.4, 133.3, 132.1, 129.6, 129.5, 128.3, 117.3, 115.4, 101.2, 97.4, 51.6. **IR** (ATR) 2976, 2911, 2857, 1650, 1602, 1497, 1467, 1393, 1322, 1190. **HRMS** (DART) m/z: $[M + H]^+$ Calcd for $C_{16}H_{14}N_2I$ 361.0196; Found 361.0208. **MP** 87-89 °C.

1-(2-(2-iodophenyl)allyl)-1H-pyrrolo[3,2-c]pyridine (SM14)

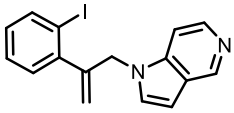

SM14

Prepared on 2.75 mmol scale by **GP1**, starting from 2'-Iodoacetophenone. Purified by flash column chromatography 20→ 100 % EtOAc/pentanes. Obtained 100 mg of an brown oil (10% yield over 3 steps)

^{1}H NMR (500 MHz, $CDCl_3$) δ 8.88 (d, J = 1.1 Hz, 1H), 8.28 (d, J = 5.8 Hz, 1H), 7.81 (dd, J = 8.0, 1.1 Hz, 1H), 7.27 (dt, J = 5.8, 1.0 Hz, 1H), 7.16 (td, J = 7.4, 1.1 Hz, 1H), 7.07 (d, J = 3.2 Hz, 1H), 6.93 (ddd, J = 8.0, 7.4, 1.7 Hz, 1H), 6.88 (dd, J = 7.4, 1.7 Hz, 1H), 6.55 (dd, J = 3.2, 1.0 Hz, 1H), 5.07 – 5.04 (m, 1H), 4.98 – 4.97 (m, 1H), 4.97 – 4.95 (m, 2H).

^{13}C NMR (126 MHz, $CDCl_3$) δ 147.5, 144.0, 143.9, 140.8, 140.0, 139.2, 129.5, 129.5, 129.3, 128.3, 125.4, 117.2, 105.2, 101.5, 97.4, 51.0. **IR** (ATR) 3148, 3088, 1242, 1229, 1178, 1152, 1079, 1048, 1013, 917. **HRMS** (DART) m/z: $[M + H]^+$ Calcd for $C_{16}H_{14}N_2I$ 361.0196; Found 361.0192.

1-(2-(2-iodophenyl)allyl)-1H-indole-3-carbaldehyde (SM15)

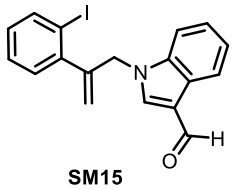
SM15

Prepared on 2.75 mmol scale by **GP1**, starting from 2'-Iodoacetophenone. Purified by flash column chromatography 0→ 30 % EtOAc/pentanes. Obtained 284 mg of an orange oil (27% yield over 3 steps).

^{1}H NMR (500 MHz, $CDCl_3$) δ 9.97 (s, 1H), 8.31 – 8.29 (m, 1H), 7.87 (dd, J = 7.9, 1.2 Hz, 1H), 7.66 (s, 1H), 7.48 – 7.45 (m, 1H), 7.36 – 7.29 (m, 2H), 7.21 (ddd, J = 7.5, 7.5, 1.2 Hz, 1H), 6.99 (ddd, J = 7.9, 7.5, 1.7 Hz, 1H), 6.90 (dd, J = 7.5, 1.7 Hz, 1H), 5.17 (td, J = 1.3, 0.6 Hz, 1H), 5.16 – 5.14 (m, 1H), 5.08 (t, J = 1.3 Hz, 2H). **^{13}C NMR** (126 MHz, $CDCl_3$) δ 184.8, 146.8, 143.8, 139.5, 139.0, 137.6, 129.8, 129.7, 128.5, 125.4, 124.3, 123.1, 122.3, 118.6, 118.1, 110.6, 97.3, 52.0. **IR** (ATR) 3051, 2977, 2819, 2761, 1653, 1614, 1579, 1530, 1464, 1432, 1399, 1385. **HRMS** (DART) m/z: $[M + H]^+$ Calcd for $C_{18}H_{15}NOI$ 388.0193; Found 388.0199.

1-(1-(2-(2-iodophenyl)allyl)-1H-indol-3-yl)ethan-1-one (SM16)

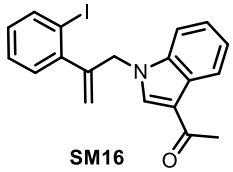
SM16

Prepared on 2.75 mmol scale by **GP1**, starting from 2'-Iodoacetophenone. Purified by flash column chromatography 0→ 40 % EtOAc/pentanes. Obtained 280mg of a white solid (25% yield over 3 steps).

^{1}H NMR (500 MHz, $CDCl_3$) δ 8.40 – 8.35 (m, 1H), 7.87 (dd, *J* = 7.9, 1.0 Hz, 1H), 7.68 (s, 1H), 7.46 – 7.42 (m, 1H), 7.32 – 7.27 (m, 2H), 7.22 (td, *J* = 7.5, 1.2 Hz, 1H), 6.99 (ddd, *J* = 7.9, 7.5, 1.7 Hz, 1H), 6.93 (dd, *J* = 7.5, 1.5 Hz, 1H), 5.16 – 5.14 (m, 1H), 5.12 – 5.10 (m, 1H), 5.04 (dd, *J* = 1.5, 1.5 Hz, 2H), 2.49 (s, 3H). **^{13}C NMR** (126 MHz, $CDCl_3$) δ 193.2, 147.0, 144.0, 139.5, 137.2, 135.3, 129.8, 129.7, 128.5, 128.5, 126.4, 123.6, 122.8, 117.9, 117.6, 110.4, 97.5, 51.8, 27.8. **IR** (ATR) 2976, 2904, 1710, 1640, 1527, 1465, 1385, 1282, 1237, 1185. **HRMS** (DART) m/z: $[M + H]^+$ Calcd for $C_{19}H_{17}NOI$ 402.0349; Found 402.0348. **MP** 125-127 °C.

Methyl 1-(2-(2-iodophenyl)allyl)-1H-pyrrole-2-carboxylate (SM17)

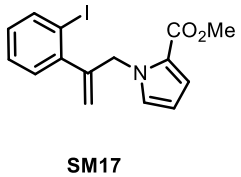
SM17

Prepared on 2.40 mmol scale by **GP1**, starting from 2'-Iodoacetophenone. Purified by flash column chromatography 0→ 80 % EtOAc/pentanes. Obtained 116 mg of a grey solid (13% yield over 3 steps).

^{1}H NMR (500 MHz, $CDCl_3$) δ 7.85 (ddd, J = 7.9, 1.2, 0.4 Hz, 1H), 7.30 (td, J = 7.5, 1.2 Hz, 1H), 7.19 (ddd, J = 7.5, 1.7, 0.4 Hz, 1H), 7.00 – 6.96 (m, 2H), 6.89 (dd, J = 2.6, 1.7 Hz, 1H), 6.15 (dd, J = 3.9, 2.6 Hz, 1H), 5.19 (t, J = 1.7 Hz, 2H), 5.03 – 4.98 (m, 1H), 4.84 – 4.82 (m, 1H), 3.81 (s, 3H). **^{13}C NMR** (126 MHz, $CDCl_3$) δ 161.4, 149.3, 144.8, 139.1, 129.7, 129.4, 129.3, 128.3, 122.0, 118.4, 115.7, 108.4, 98.0, 53.0, 51.2. **IR** (ATR) 3128,3088, 1582, 1436,1358, 1283, 1201, 1152, 1079, 1012. **HRMS** (DART) m/z: $[M + H]^+$ Calcd for $C_{15}H_{15}NO_2I$ 368.0142; Found 368.0141. **MP** 54-57 °C.

4.5.7. Failed Substrates

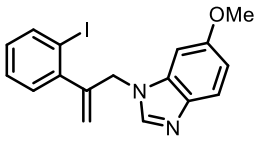

coelutes with furan by-product

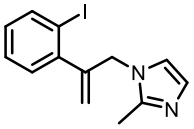

coelutes with $P{=}O(iPr)_3$

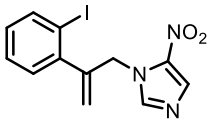

not isolable cleanly

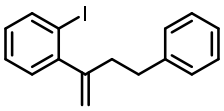

<10% yield

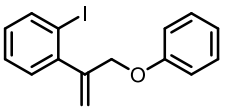

<10% yield

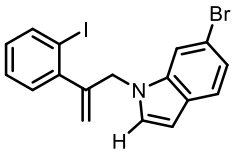

<10% yield, complex mixture

4.5.8. Characterization of Oxabicycles

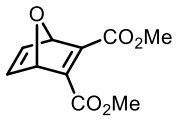

21

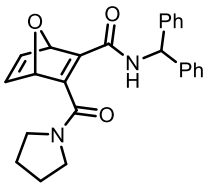

47a

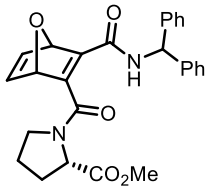

47c

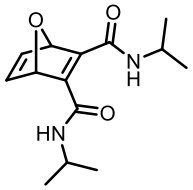

47e

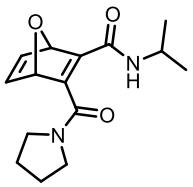

47f

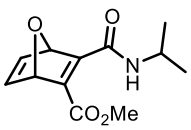

47g

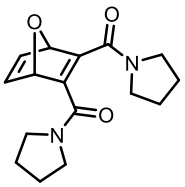

47h

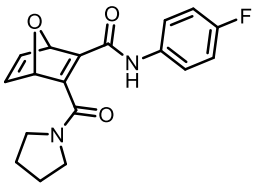

47i

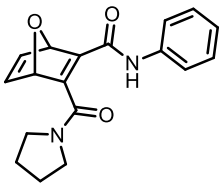

47j

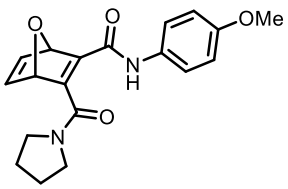

47k

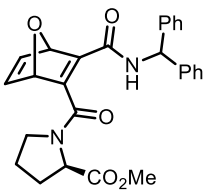

47l

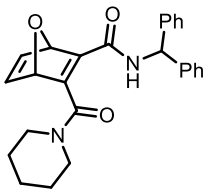

47m

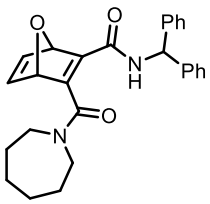

47n

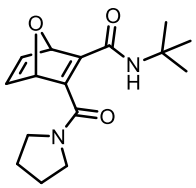

47o

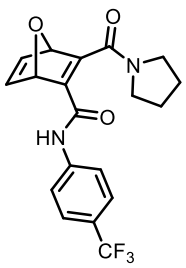

47p

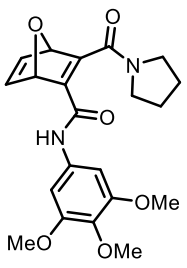

47q

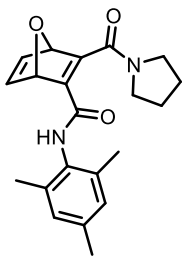

47r

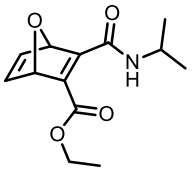

47s

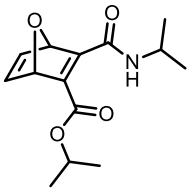

47t

Racemic and enantioenriched oxabicycles **47a-47t** were synthesized following **GP2** from oxabicycle **21**. Characterization was consistent with literature.[58]

4.5.9. Characterization of Products

Benzimidazoles & Imidazoles

1H,3H-spiro[benzo[d]pyrrolo[1,2-a]imidazole-2,1'-indene] (53)

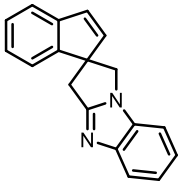

53

Prepared on 0.1 mmol scale by **GP3**. Purified by flash column chromatography 20→ 80 % EtOAc/pentanes. Obtained 21.4 mg of an off-white solid (83% yield). Also prepared on 0.1 mmol scale by **GP4.** Obtained 15.4 mg of an off-white solid (60% yield).

Also prepared on 1.0 mmol scale. Obtained 188 mg of an off-white solid (73% yield).

^{1}H NMR (500 MHz, $CDCl_3$) δ 7.81 – 7.77 (m, 1H), 7.37 (dt, *J* = 7.6, 1.0 Hz, 1H), 7.33 – 7.24 (m, 4H), 7.17 (td, *J* = 7.6, 1.2 Hz, 1H), 7.11 – 7.08 (m, 1H), 6.85 (dd, *J* = 5.5, 0.7 Hz, 1H), 6.53 (d, *J* = 5.5 Hz, 1H), 4.30 (d, *J* = 10.3 Hz, 1H), 4.23 (d, *J* = 10.3 Hz, 1H), 3.39 (d, *J* = 16.7 Hz, 1H), 3.31 (d, *J* = 16.7 Hz, 1H). **^{13}C NMR** (126 MHz, $CDCl_3$) δ 159.9, 148.9, 148.7, 142.7, 140.2, 132.8, 131.9, 128.2, 126.6, 122.3, 122.1, 121.9, 121.3, 120.1, 109.8, 61.3, 50.2, 32.9. **IR** (ATR) 2956, 2924, 2854, 1721, 1621, 1531, 1454, 1415, 1261, 1215. **HRMS** (DART) m/z: $[M + H]^+$ Calcd for $C_{18}H_{15}N_2$ 259.1230; Found 259.1225. **MP** 118-125 °C .

Enantioselective reaction: Prepared on 0.1 mmol scale by **GP5**. Purified by flash column chromatography 20→ 80 % EtOAc/pentanes. Obtained 21.4 mg of an off-white solid (83% yield).

$\boldsymbol{\alpha_D^{20}}$ (c = 0.220, CH_2Cl_2) +90.0

HPLC: IA column, 1mL/min, 8% IPA / 92% Hexanes.

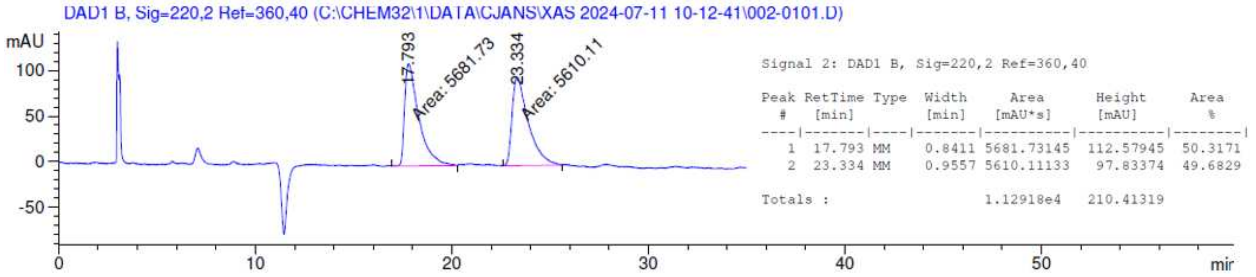

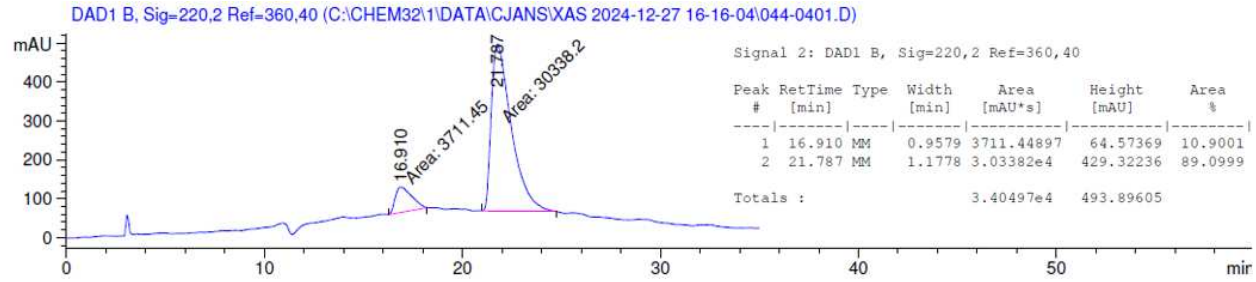

6,7-dimethyl-1H,3H-spiro[benzo[d]pyrrolo[1,2-a]imidazole-2,1'-indene] (54)

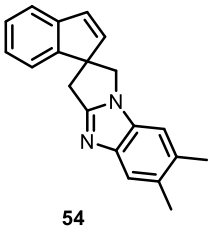

54

Prepared on 0.1 mmol scale by **GP3**. Purified by flash column chromatography 20→ 80 % EtOAc/pentanes. Obtained 19.7 mg of a light brown solid (69% yield).

^{1}H NMR (500 MHz, $CDCl_3$) δ 7.55 (s, 1H), 7.35 (d, J = 7.5 Hz, 0H), 7.29 (td, J = 7.4, 1.2 Hz, 1H), 7.14 (td, J = 7.5, 1.2 Hz, 1H), 7.10 – 7.05 (m, 2H), 6.84 (d, J = 5.5 Hz, 1H), 6.51 (d, J = 5.5 Hz, 1H), 4.24 (d, J = 10.2 Hz, 1H), 4.16 (d, J = 10.2 Hz, 1H), 3.36 (d, J = 16.7 Hz, 1H), 3.25 (d, J = 16.7 Hz, 1H), 2.40 (s, 3H), 2.38 (s, 3H). **^{13}C NMR** (126 MHz, $CDCl_3$) δ 158.9, 149.0, 146.9, 142.7, 140.2, 131.8, 131.4, 131.2, 131.0, 128.2, 126.5, 121.8, 121.3, 120.1, 110.1, 61.4, 50.2, 32.9, 20.5, 20.5. **IR** (ATR) 2975, 2922, 1692, 1530, 1457, 1358, 1317, 1248, 1140, 999. **HRMS** (DART) m/z: $[M + H]^+$ Calcd for $C_{20}H_{19}N_2$ 287.1548; Found 287.1547. **MP** 120-124°C.

1'H,3'H-spiro[indene-1,2'-naphtho[2,3-d]pyrrolo[1,2-a]imidazole] (55)

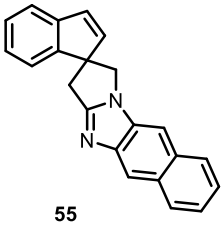

55

Prepared on 0.1 mmol scale by **GP3**. Purified by flash column chromatography 20→ 100 % EtOAc/pentanes. Obtained 13.4 mg of a light orange solid (44% yield).

^{1}H NMR (500 MHz, $CDCl_3$) δ 8.26 (s, 1H), 8.06 – 8.00 (m, 1H), 7.94 – 7.87 (m, 1H), 7.64 (s, 1H), 7.46 – 7.40 (m, 2H), 7.38 (dt, J = 7.5, 1.0 Hz, 1H), 7.31 (td, J = 7.5, 1.1 Hz, 1H), 7.15 (td, J = 7.5, 1.1 Hz, 1H), 7.08 (dq, J = 7.5, 1.0 Hz, 1H), 6.86 (d, J = 5.5 Hz, 1H), 6.52 (d, J = 5.5 Hz, 1H), 4.28 (d, J = 10.0 Hz, 1H), 4.22 (d, J = 10.0 Hz, 1H), 3.42 (d, J = 17.0 Hz, 1H), 3.33 (d, J = 17.0 Hz, 1H). **^{13}C NMR** (126 MHz, $CDCl_3$) δ 164.2, 148.9, 148.8, 142.6, 140.0, 133.4, 131.9, 130.3, 130.2, 128.6, 128.2, 127.5, 126.6, 124.5, 123.6, 121.9, 121.2, 116.7, 105.4, 61.2, 50.1, 33.1. **IR** (ATR) 2912, 2853, 1725, 1620, 1512, 1462, 1439, 1395, 1329, 1250.

HRMS (DART) m/z: $[M + H]^+$ Calcd for $C_{22}H_{17}N_2$ 309.1386; Found 309.1384. **MP** 211-213 °C.

7-nitro-1H,3H-spiro[benzo[d]pyrrolo[1,2-a]imidazole-2,1'-indene] (55)

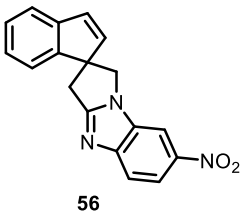

56

Prepared on 0.1 mmol scale by **GP3**. Purified by flash column chromatography 20→ 100 % EtOAc/pentanes. Obtained 17.0 mg of an off white solid (56% yield).

^{1}H NMR (400 MHz, $CDCl_3$) δ 8.29 – 8.25 (m, 1H), 8.24 – 8.18 (m, 1H), 7.81 (dd, J = 9.0, 1.6 Hz, 1H), 7.39 (d, J = 7.4 Hz, 1H), 7.33 (t, J = 7.4 Hz, 1H), 7.19 (td, J = 7.4, 1.1 Hz, 1H), 7.08 (dd, J = 7.4, 1.1 Hz, 1H), 6.89 (d, J = 5.5 Hz, 1H), 6.53 (d, J = 5.5 Hz, 1H), 4.39 (d, J = 10.5 Hz, 1H), 4.32 (d, J = 10.5 Hz, 1H), 3.46 (d, J = 17.3 Hz, 1H), 3.37 (d, J = 17.3 Hz, 1H). **^{13}C NMR** (101 MHz, $CDCl_3$) δ 165.1, 153.0, 148.2, 143.3, 142.6, 139.4, 132.5, 131.9, 128.6, 126.8, 122.2, 121.1, 119.9, 118.2, 106.7, 61.1, 50.8, 33.3. **IR** (ATR) 2925, 2853, 1331, 1283, 1242, 1200, 1152, 1102, 1080, 1040. **HRMS** (DART) m/z: $[M + H]^+$ Calcd for $C_{18}H_{14}N_3O_2$ 304.1081; Found 304.1078. **MP** 170-174 °C

6-nitro-1H,3H-spiro[benzo[d]pyrrolo[1,2-a]imidazole-2,1'-indene] (57)

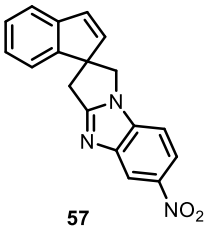

57

Prepared on 0.1 mmol scale by **GP3**. Purified by flash column chromatography 20→ 100 % EtOAc/pentanes. Obtained 18.1 mg of a yellow solid (60% yield).

^{1}H NMR (500 MHz, $CDCl_3$) δ 8.60 (d, J = 2.1 Hz, 1H), 8.15 (dd, J = 8.8, 2.1 Hz, 1H), 7.37 (dt, J = 7.6, 1.0 Hz, 1H), 7.35 – 7.30 (m, 2H), 7.18 (td, J = 7.5, 1.2 Hz, 1H), 7.09 (dd, J = 7.5, 1.0 Hz, 1H), 6.88 (d, J = 5.5 Hz, 1H), 6.53 (d, J = 5.5 Hz, 1H), 4.37 (d, J = 10.6 Hz, 1H), 4.30 (d, J = 10.5 Hz, 1H), 3.43 (d, J = 17.1 Hz, 1H), 3.35 (d, J = 17.2 Hz, 1H). **^{13}C NMR** (126 MHz, $CDCl_3$) δ 163.7, 148.1, 147.9, 143.5, 142.6, 139.4, 136.8, 132.4, 128.5, 126.7, 122.1, 121.1, 118.4, 116.5, 109.5, 61.2, 50.6, 33.0. **IR** (ATR) 2925, 2853, 1621, 1511, 1457, 1443, 1384, 1329, 1253, 1148. **HRMS** (DART) m/z: $[M + H]^+$ Calcd for $C_{18}H_{14}N_3O_2$ 304.1081; Found 304.1079. **MP** 214-215 °C.

6-methoxy-1H,3H-spiro[benzo[d]pyrrolo[1,2-a]imidazole-2,1'-indene] (58)

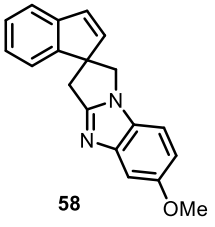

58

Prepared on 0.1 mmol scale by **GP3**. Purified by flash column chromatography 30→ 100 % EtOAc/pentanes. Obtained 19.7 mg of a brown solid (68% yield).

^{1}H NMR (500 MHz, $CDCl_3$) δ 7.35 (d, *J* = 7.4 Hz, 1H), 7.29 (q, *J* = 1.2 Hz, 2H), 7.18 (d, *J* = 8.7 Hz, 1H), 7.16 (td, *J* = 7.4, 1.3 Hz, 1H), 7.09 (d, *J* = 7.4 Hz, 1H), 6.90 (dd, *J* = 8.7, 2.4 Hz, 1H), 6.84 (d, *J* = 5.5 Hz, 1H), 6.52 (d, *J* = 5.5 Hz, 1H), 4.25 (d, *J* = 10.3 Hz, 1H), 4.18 (d, *J* = 10.3 Hz, 1H), 3.88 (s, 3H), 3.37 (d, *J* = 16.7 Hz, 1H), 3.27 (d, *J* = 16.7 Hz, 1H). **^{13}C NMR** (101 MHz, $CDCl_3$) δ 160.1, 156.2, 149.3, 148.9, 142.7, 140.2, 131.8, 128.2, 127.4, 126.5, 121.9, 121.3, 112.0, 110.0, 102.7, 61.3, 56.0, 50.4, 33.0. **IR** (ATR) 3100, 1436, 1427, 1358, 1331, 1242, 1229, 1178, 1152, 1037. **HRMS** (DART) m/z: $[M + H]^+$ Calcd for $C_{19}H_{17}N_2O$ 289.1335; Found 289.1335.

5'-methoxy-1H,3H-spiro[benzo[d]pyrrolo[1,2-a]imidazole-2,1'-indene] (59)

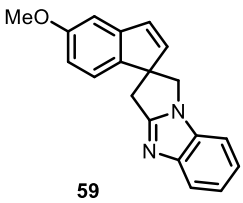

59

Prepared on 0.1 mmol scale by **GP3**. Purified by flash column chromatography 30→ 70 % EtOAc/p entanes. Obtained 15.8 mg of a waxy yellow solid (55% yield).

^{1}H NMR (500 MHz, $CDCl_3$) δ 7.82 – 7.76 (m, 1H), 7.35 – 7.22 (m, 3H), 7.00 (d, J = 8.2 Hz, 1H), 6.92 (d, J = 2.4 Hz, 1H), 6.79 (d, J = 5.5 Hz, 1H), 6.69 (dd, J = 8.2, 2.4 Hz, 1H), 6.54 (d, J = 5.5 Hz, 1H), 4.27 (d, J = 10.3 Hz, 1H), 4.21 (d, J = 10.3 Hz, 1H), 3.82 (s, 2H), 3.36 (d, J = 16.7 Hz, 1H), 3.28 (d, J = 16.7 Hz, 1H). **^{13}C NMR** (126 MHz, $CDCl_3$) δ 160.1, 144.3, 141.6, 140.7, 131.6, 128.8, 128.7, 127.6, 122.3, 122.1, 121.9, 120.0, 111.5, 109.8, 108.0, 60.8, 55.7, 50.4, 33.1. **IR** (ATR) 3130, 1201, 1178, 1152, 1102, 1079, 1024, 1011, 940, 917. **HRMS** (DART) m/z: $[M + H]^+$ Calcd for $C_{19}H_{17}N_2O$ 289.1335; Found 289.1338. **MP** 35-40 °C.

5'-methyl-1H,3H-spiro[benzo[d]pyrrolo[1,2-a]imidazole-2,1'-indene] (60)

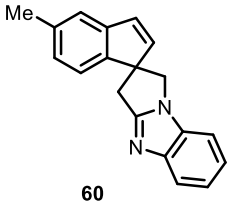

60

Prepared on 0.1 mmol scale by **GP3**. Purified by flash column chromatography 20→ 80 % EtOAc/pentanes. Obtained 22.1 mg of a white solid (81% yield).

^{1}H NMR (500 MHz, $CDCl_3$) δ 7.82 – 7.76 (m, 1H), 7.34 – 7.23 (m, 3H), 7.21 – 7.16 (m, 1H), 7.02 – 6.95 (m, 2H), 6.80 (d, J = 5.4 Hz, 1H), 6.51 (d, J = 5.4 Hz, 1H), 4.28 (d, J = 10.3 Hz, 1H), 4.21 (d, J = 10.3 Hz, 1H), 3.37 (d, J = 16.7 Hz, 1H), 3.29 (d, J = 16.7 Hz, 1H), 2.38 (s, 3H). **^{13}C NMR** (126 MHz, $CDCl_3$) δ 160.0, 148.7, 146.0, 143.0, 140.5, 138.1, 132.8, 131.8, 127.2, 122.7, 122.3, 122.1, 121.1, 120.1, 109.8, 61.0, 50.4, 33.1, 21.6. **IR** (ATR) 2975, 2924, 1620, 1531, 1477, 1451, 1406, 1378, 1329, 1214. **HRMS** (DART) m/z: $[M + H]^+$ Calcd for $C_{19}H_{17}N_2$ 273.1386; Found 273.1390. **MP** 170-173 °C.

5'H,7'H-spiro[indene-1,6'-pyrrolo[1,2-c]imidazole] (61)

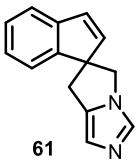

61

Prepared on 0.1 mmol scale by **GP3**. Purified by flash column chromatography 0→ 30 % MeOH/EtOAc. Obtained 20.3 mg of a white solid (98% yield)

Calculations on similar N-substituted imidazoles predict that the C5-position has a lower energy barrier for C-H activation.[62,63] Based off the difference in chemical shifts in the imidazole's H2 and H4 protons (7.62 ppm & 6.89 ppm) and their multiplicity (singlets), this regioisomer is most likely formed. NOESY and COSY analysis did not show any through-space interactions or coupling between H2 and H4. HMBC analysis was inconclusive, as the C2 and C4 imidazole positions are most likely shielded by the neighbouring N1 and N3.

^{1}H NMR (400 MHz, $CDCl_3$) δ 7.62 (s, 1H), 7.37 – 7.26 (m, 2H), 7.16 (td, J =F 7.5, 1.3 Hz, 1H), 6.98 (d, J = 7.5 Hz, 1H), 6.89 (s, 1H), 6.81 (d, J = 5.5 Hz, 1H), 6.45 (d, J = 5.5 Hz, 1H), 4.19 (d, J = 10.8 Hz, 1H), 4.06 (d, J = 10.8 Hz, 1H), 3.15 (d, J = 15.3 Hz, 1H), 3.00 (d, J = 15.3 Hz, 1H). **^{13}C NMR** (126 MHz, $CDCl_3$) δ 148.6, 142.6, 139.6, 136.1, 131.7, 131.4, 128.0, 126.4, 121.7, 121.2, 121.0, 64.4, 51.1, 30.8. **IR** (ATR) 2952, 2924, 2849, 1483, 1459, 1439, 1381, 1262, 1224, 1086. **HRMS** (DART) m/z: $[M + H]^+$ Calcd for $C_{14}H_{13}N_2$ 209.1073; Found 209.1072. **MP** 164-166 °C.

Indoles & Pyrroles

1'H,3'H-spiro[indene-1,2'-pyrrolo[1,2-a]indole] (62)

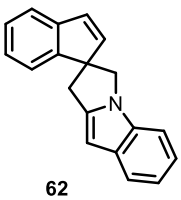

62

Prepared on 0.1 mmol scale by **GP3**. Purified by flash column chromatography 0→ 25 % EtOAc/pentanes. Obtained 20.2 mg of a white solid (79% yield).

Also prepared on 1.0 mmol scale with oxabicycles **21** and **47a**. Obtained 154 mg of a white solid (60% yield) with oxabicycle **47a**, and 124 mg of a white solid (48% yield) with oxabicycle **21**.

^{1}H NMR (500 MHz, $CDCl_3$) δ 7.65 – 7.61 (m, 1H), 7.35 (dt, J = 7.5, 1.0 Hz, 1H), 7.28 (dd, J = 7.5, 1.1 Hz, 1H), 7.24 – 7.21 (m, 1H), 7.16 (td, J = 7.1, 1.4 Hz, 1H), 7.14 – 7.09 (m, 2H), 6.95 (dq, J = 7.5, 0.7 Hz, 1H), 6.83 (dd, J = 5.5, 0.7 Hz, 1H), 6.53 (d, J = 5.5 Hz, 1H), 6.32 (dd, J = 1.1, 1.1 Hz, 1H), 4.29 (d, J = 10.0 Hz, 1H), 4.17 (d, J = 10.0 Hz, 1H), 3.36 (dd, J = 15.8, 1.2 Hz, 1H), 3.18 (dd, J = 15.8, 1.1 Hz, 1H).

^{13}C NMR (126 MHz, $CDCl_3$) δ 149.7, 143.3, 142.8, 140.8, 133.4, 133.1, 131.3, 127.8, 126.3, 121.6, 121.4, 120.8, 120.8, 119.5, 109.6, 94.3, 63.1, 50.8, 33.6. **IR** (ATR) 3059, 2967, 2917, 1613, 1554, 1479, 1455, 1377,

1337, 1304, 1220. **HRMS** (DART) m/z: $[M + H]^+$ Calcd for $C_{19}H_{16}N$ 258.1282; Found 258.1289. **MP** 144-146 °C.

Enantioselective reaction: Prepared on 0.1 mmol scale by **GP5**. Purified by flash column chromatography 0→ 25 % EtOAc/pentanes. Obtained 16.8 mg of a white solid (65% yield).

$\boldsymbol{\alpha_D^{20}}$ (c = 0.231, CH_2Cl_2) +126.4

HPLC: IB column, 1mL/min, 1% IPA / 99% Hexanes.

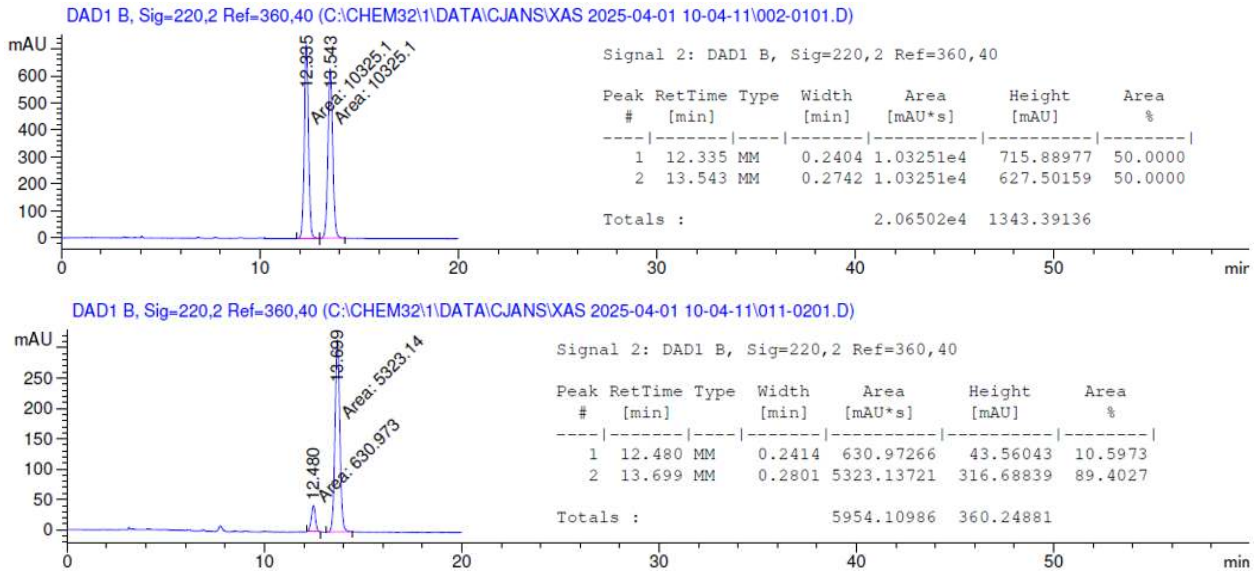

6'-fluoro-1'H,3'H-spiro[indene-1,2'-pyrrolo[1,2-a]indole] (63)

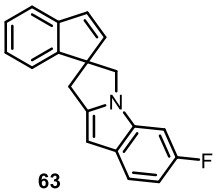

63

Prepared on 0.1 mmol scale by **GP3**. Purified by flash column chromatography 0→ 25 % EtOAc/pentanes. Obtained 20.3 mg of a yellow oil (74% yield).

^{1}H NMR (500 MHz, $CDCl_3$) δ δ 7.38 (dd, *J* = 7.4, 1.2 Hz, 1H), 7.33 – 7.27 (m, 2H), 7.16 – 7.10 (m, 2H), 6.96 (d, *J* = 7.4 Hz, 1H), 6.94 – 6.89 (m, 1H), 6.87 – 6.84 (m, 1H), 6.53 (d, *J* = 5.5 Hz, 1H), 6.30 (s, 1H), 4.28 (d, *J* = 10.0 Hz, 1H), 4.15 (d, *J* = 10.0 Hz, 1H), 3.37 (d, *J* = 15.9 Hz, 1H), 3.19 (d, *J* = 15.9 Hz, 1H). **^{19}F NMR** (377 MHz, $CDCl_3$) δ -125.22. **IR** (ATR) 2915, 2862, 1708, 1621, 1531, 1482, 1460, 1406, 1359, 1251. **HRMS** (DART) m/z: $[M + H]^+$ Calcd for $C_{19}H_{15}NF$ 276.1183; Found 276.1184.

6'-chloro-1'H,3'H-spiro[indene-1,2'-pyrrolo[1,2 -a]indole] (64)

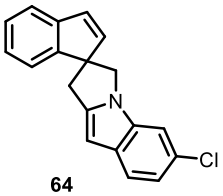

64

Prepared on 0.1 mmol scale by **GP3**. Purified by flash column chromatography 0→ 20 % EtOAc/pentanes. Obtained 18.6 mg of a yellow solid (64% yield).

^{1}H NMR (500 MHz, $CDCl_3$) δ 7.51 (d, *J* = 8.4 Hz, 1H), 7.35 (d, *J* = 7.6 Hz, 1H), 7.30 – 7.26 (m, 1H), 7.21 (d, *J* = 1.8 Hz, 1H), 7.11 (td, *J* = 7.6, 1.2 Hz, 1H), 7.08 (dd, *J* = 8.4, 1.8 Hz, 1H), 6.91 (dq, *J* = 7.4, 0.8 Hz, 1H), 6.83 (d, *J* = 5.5 Hz, 1H), 6.50 (d, *J* = 5.5 Hz, 1H), 6.30 (s, 1H), 4.25 (d, *J* = 10.0 Hz, 1H), 4.12 (d, *J* = 10.0 Hz, 1H), 3.34 (dd, *J* = 15.9, 1.1 Hz, 1H), 3.16 (dd, *J* = 15.9, 1.0 Hz, 1H). **^{13}C NMR** (126 MHz, $CDCl_3$) δ 149.4, 144.1, 142.8, 140.4, 133.7, 131.6, 131.6, 127.9, 126.7, 126.3, 121.7, 121.5, 121.3, 120.2, 109.6, 94.6, 63.0, 50.8, 33.6.

IR (ATR) 2967, 2921, 2857, 1607, 1547, 1456, 1395, 1331, 1254, 1215. **HRMS** (DART) m/z: $[M + H]^+$ Calcd for $C_{19}H_{15}NCl$ 292.0888; Found 292.0897. **MP** 141-143 °C.

Methyl 1'H,3'H-spiro[indene-1,2'-pyrrolo[1,2-a]indole]-6'-carboxylate (65)

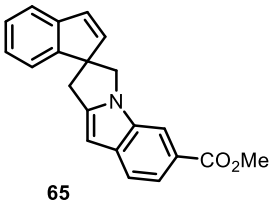

65

Prepared on 0.1 mmol scale by **GP3**. Purified by flash column chromatography 0→ 30 % EtOAc/pentanes. Obtained 26.3 mg of a pale-yellow solid (83% yield).

^{1}H NMR (500 MHz, $CDCl_3$) δ 7.98 (dt, J = 1.5, 0.8 Hz, 1H), 7.81 (dd, J = 8.4, 1.5 Hz, 1H), 7.62 (dd, J = 8.4, 0.8 Hz, 1H), 7.36 (dt, J = 7.4, 1.0 Hz, 1H), 7.28 (td, J = 7.4, 1.0 Hz, 1H), 7.11 (td, J = 7.4, 0.8 Hz, 1H), 6.91 (dq, J = 7.4, 0.8 Hz, 1H), 6.84 (dd, J = 5.5, 0.7 Hz, 1H), 6.51 (d, J = 5.5 Hz, 1H), 6.37 (dd, *J* = 1.2, 1.2 Hz, 1H), 4.35 (d, J = 10.2 Hz, 1H), 4.22 (d, J = 10.2 Hz, 1H), 3.93 (s, 3H), 3.38 (dd, J = 16.1, 1.2 Hz, 1H), 3.21 (dd, J = 16.1, 1.2 Hz, 1H). **^{13}C NMR** (126 MHz, $CDCl_3$) δ 168.3, 149.2, 147.0, 142.6, 140.2, 136.7, 132.6, 131.5, 127.8, 126.2, 122.3, 121.6, 121.1, 120.7, 120.0, 111.8, 94.9, 62.7, 51.9, 50.9, 33.7. **IR** (ATR) 2916, 2853, 1693, 1615, 1485, 1458, 1355, 1281, 1245,1191, **HRMS** (DART) m/z: $[M + H]^+$ Calcd for $C_{21}H_{18}NO_2$ 316.1332; Found 316.1332. **MP** 174-177 °C.

1'H,3'H-spiro[indene-1,2'-pyrrolo[1,2-a]indole]-8'-carbonitrile (66)

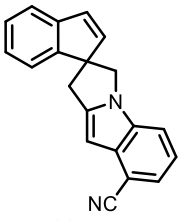

66

Prepared on 0.1 mmol scale by **GP3**. Purified by flash column chromatography 0→ 60 % EtOAc/pentanes. Obtained 21.3 mg of a yellow oil (76% yield).

^{1}H NMR (500 MHz, $CDCl_3$) δ 7.46 (dd, J = 7.5, 0.9 Hz, 1H), 7.42 (dt, J = 8.2, 0.9 Hz, 1H), 7.37 (dt, J = 7.5, 1.0 Hz, 1H), 7.30 (td, J = 7.5, 1.1 Hz, 1H), 7.18 (dd, J = 8.2, 7.5 Hz, 1H), 7.13 (td, J = 7.5, 1.2 Hz, 1H), 6.91 (dq, J = 7.5, 0.8 Hz, 1H), 6.86 (dd, J = 5.5, 0.7 Hz, 1H), 6.56 (dd, J = 1.1, 1.1 Hz, 1H), 6.51 (d, J = 5.5 Hz, 1H), 4.34 (d, J = 10.1 Hz, 1H), 4.21 (d, J = 10.1 Hz, 1H), 3.41 (dd, J = 16.2, 1.1 Hz, 1H), 3.24 (dd, J = 16.2, 1.1 Hz, 1H).

^{13}C NMR (126 MHz, $CDCl_3$) δ 149.1, 146.6, 142.7, 140.0, 134.3, 133.1, 131.9, 128.1, 126.4, 124.9, 121.8, 121.1, 120.4, 119.0, 114.2, 102.8, 93.8, 62.9, 51.1, 33.7. **IR** (ATR) 3065, 2960, 2920, 2218, 1716, 1605, 1546, 1433, 1406, 1349. **HRMS** (DART) m/z: $[M + H]^+$ Calcd for $C_{20}H_{15}N_2$ 283.1230; Found 283.1236.

6'H,8'H-spiro[indene-1,7'-pyrido[4,3-b]pyrrolizine] (67)

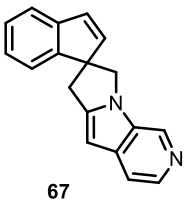

67

Prepared on 0.1 mmol scale by **GP3**. Purified by flash column chromatography 20→100 % EtOAc/pentanes, then 10% MeOH/EtOAc. Obtained 24.5 mg of a pink solid (95% yield).

^{1}H NMR (500 MHz, $CDCl_3$) δ 8.63 (s, 1H), 8.24 (d, J = 5.6 Hz, 1H), 7.52 (d, J = 5.8 Hz, 1H), 7.36 (dt, J = 7.5, 1.0 Hz, 1H), 7.29 (td, J = 7.5, 1.1 Hz, 1H), 7.12 (td, J = 7.5, 1.1 Hz, 1H), 6.90 (dd, J = 7.5, 1.0 Hz, 1H), 6.85 (dd, J = 5.5, 0.8 Hz, 1H), 6.50 (d, J = 5.5 Hz, 1H), 6.35 (d, J = 0.8 Hz, 1H), 4.38 (d, J = 10.2 Hz, 1H), 4.25 (d, J = 10.2 Hz, 1H), 3.38 (dd, J = 16.2, 1.2 Hz, 1H), 3.21 (dd, J = 16.2, 1.1 Hz, 1H). **^{13}C NMR** (126 MHz, $CDCl_3$) δ 149.1, 148.1, 142.7, 140.0, 138.6, 138.0, 132.3, 131.9, 130.7, 128.1, 126.4, 121.8, 121.2, 115.4, 94.3, 63.0, 51.2, 33.7. **IR** (ATR) 3086, 1245, 1230, 1150, 1100, 1079, 1037, 1025, 1012, 940. **HRMS** (DART) m/z: $[M + H]^+$ Calcd for $C_{18}H_{15}N_2$ 259.1230; Found 259.1229. **MP** 129-134 °C

6'H,8'H-spiro[indene-1,7'-pyrido[3,4-b]pyrrolizine] (68)

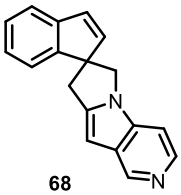

68

Prepared on 0.1 mmol scale by **GP3**. Purified by flash column chromatography 20→ 100 % EtOAc/pentanes, then 5→ 30 % MeOH/EtOAc. Obtained 16.4 mg of a brown solid (63% yield).

^{1}H NMR (500 MHz, $CDCl_3$) δ 8.90 (s, 1H), 8.28 (d, J = 5.7 Hz, 1H), 7.35 (dt, J = 7.5, 1.0 Hz, 1H), 7.28 (td, J = 7.5, 1.1 Hz, 1H), 7.14 (d, J = 5.7 Hz, 1H), 7.11 (td, J = 7.5, 1.2 Hz, 1H), 6.87 (dq, J = 7.5, 0.8 Hz, 1H), 6.84 (dd, J = 5.5, 0.7 Hz, 1H), 6.49 (d, J = 5.5 Hz, 1H), 6.41 (dd, J = 1.2, 1.2 Hz, 1H), 4.29 (d, J = 10.3 Hz, 1H), 4.16 (d, J = 10.3 Hz, 1H), 3.36 (dd, J = 16.0, 1.2 Hz, 1H), 3.18 (dd, J = 16.0, 1.2 Hz, 1H). **^{13}C NMR** (126 MHz, $CDCl_3$) δ 149.0, 144.8, 143.0, 142.7, 139.9, 139.8, 136.9, 131.9, 129.8, 128.1, 126.4, 121.8, 121.1, 105.1, 94.1, 63.0, 50.7, 33.3. **IR** (ATR) 3063, 3042, 2959, 2879, 1606, 1557, 1461, 1386, 1322, 1288. **HRMS** (DART) m/z: $[M + H]^+$ Calcd for $C_{18}H_{15}N_2$ 259.1230; Found 259.1239. **MP** 129-134 °C.

1'H,3'H-spiro[indene-1,2'-pyrrolo[1,2-a]indole]-9'-carbaldehyde (69)

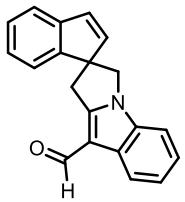

69

Prepared on 0.1 mmol scale by **GP3**. Purified by flash column chromatography 0→ 90 % EtOAc/pentanes. Obtained 14.1 mg of a light yellow solid (49% yield).

^{1}H NMR (500 MHz, $CDCl_3$) δ 10.01 (s, 1H), 8.31 (d, J = 7.5 Hz, 1H), 7.38 (d, J = 7.5 Hz, 1H), 7.36 – 7.28 (m, 3H), 7.27 – 7.24 (m, 1H), 7.16 (td, J = 7.5, 1.2 Hz, 1H), 7.02 (dd, J = 7.5, 0.9 Hz, 1H), 6.88 (d, J = 5.5 Hz, 1H), 6.52 (d, J = 5.5 Hz, 1H), 4.33 (d, J = 10.6 Hz, 1H), 4.24 (d, J = 10.6 Hz, 1H), 3.58 (d, J = 17.0 Hz, 1H), 3.47 (d, J = 17.0 Hz, 1H).

^{13}C NMR (126 MHz, $CDCl_3$) δ 183.6, 154.2, 148.7, 142.6, 139.5, 133.7, 132.2, 129.6, 128.3, 126.6, 123.4, 123.1, 121.9, 121.9, 121.1, 111.6, 110.2, 62.3, 51.5, 33.6. **IR** (ATR) 2950, 1290, 1228, 1179, 1103,1089, 1034, 1022, 1010, 988. **HRMS** (DART) m/z: $[M + H]^+$ Calcd for $C_{20}H_{16}NO$ 286.1226; Found 286.1220. **MP** 159-163 °C.

1-(1'H,3'H-spiro[indene-1,2'-pyrrolo[1,2-a]indol]-9'-yl)ethan-1-one (70)

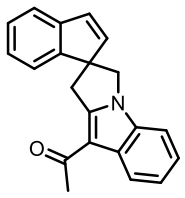

70

Prepared on 0.1 mmol scale by **GP3**. Purified by flash column chromatography 0→ 60 % EtOAc/pentanes. Obtained 13.5 mg of an off-white solid (45% yield).

^{1}H NMR (500 MHz, $CDCl_3$) δ 8.39 (d, J = 7.9 Hz, 1H), 7.38 (d, J = 7.5 Hz, 1H), 7.35 – 7.24 (m, 3H), 7.23 (dt, J = 7.9, 1.1 Hz, 1H), 7.16 (td, J = 7.5, 1.2 Hz, 1H), 7.05 (d, J = 7.9 Hz, 1H), 6.87 (d, J = 5.5 Hz, 1H), 6.54 (d, J = 5.5 Hz, 1H), 4.31 (d, J = 10.5 Hz, 1H), 4.22 (d, J = 10.5 Hz, 1H), 3.58 (d, J = 17.1 Hz, 1H), 3.48 (d, J = 17.1 Hz, 1H), 2.46 (s, 3H).

^{13}C NMR (126 MHz, $CDCl_3$) δ 192.9, 150.8, 149.0, 142.6, 139.9, 133.4, 132.0, 130.5, 128.2, 126.6, 122.8, 122.6, 122.5, 121.9, 121.2, 111.5, 110.0, 61.9, 51.2, 36.2, 29.5. **IR** (ATR) 2950,1283, 1242, 1201, 1178, 1152, 1102, 1047, 1026, 978. **HRMS** (DART) m/z: $[M + H]^+$ Calcd for $C_{21}H_{18}NO$ 300.1383; Found 300.1381.

MP 156-161°C.

Enantioselective reaction: Prepared on 0.1 mmol scale by **GP5**. Purified by flash column chromatography 0→ 60 % EtOAc/pentanes. Obtained 25.0 mg of a white solid (83% yield).

$\boldsymbol{\alpha_D^{20}}$ (c = 0.226, CH_2Cl_2) +5.3

HPLC: AD-H Column, 1mL/min, 8% IPA / 92% Hexanes.

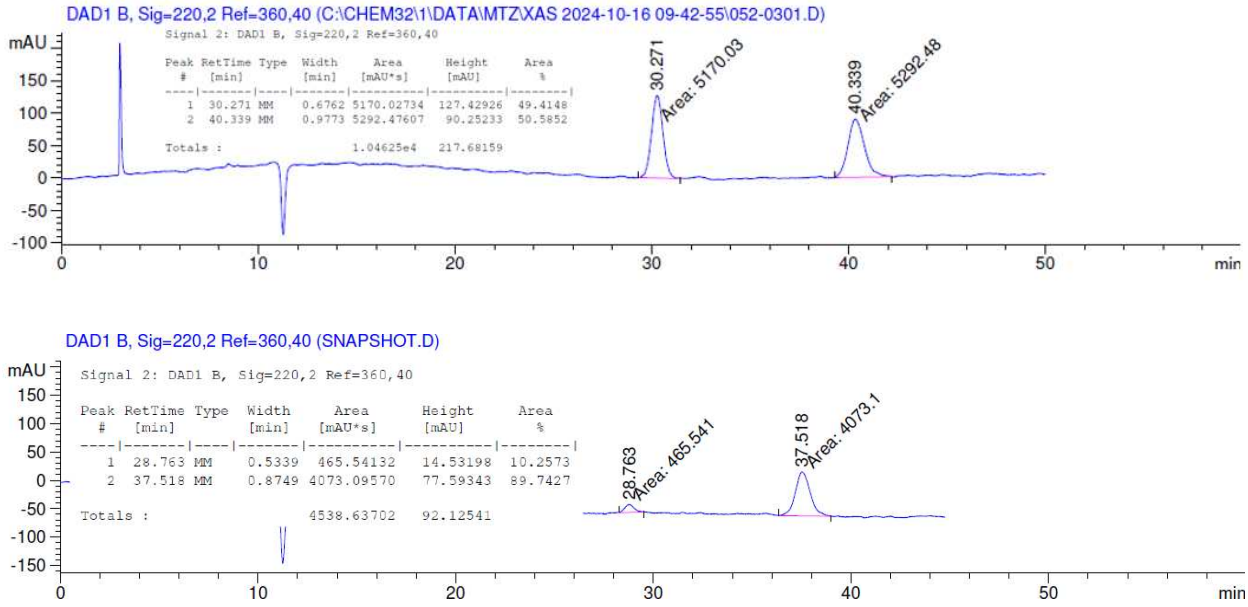

Methyl 1'H,3'H-spiro[indene-1,2'-pyrrolizine]-5'-carboxylate (71)

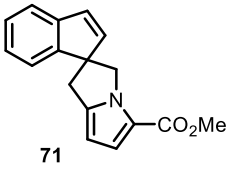

71

Prepared on 0.1 mmol scale by **GP3**. Purified by flash column chromatography 10→40 % EtOAc/pentanes. Obtained 26.5 mg of a pale orange solid (99% yield). **^{1}H NMR** (400 MHz, $CDCl_3$) δ 7.33 (dt, *J* = 7.4, 1.0 Hz, 1H), 7.27 (td, *J* = 7.4, 1.1 Hz, 1H), 7.15 (td, *J* = 7.4, 1.1 Hz, 1H), 7.04 – 6.99 (m, 2H), 6.79 (d, *J* = 5.2 Hz, 1H), 6.49 (d, *J* = 5.5 Hz, 1H), 6.01 (d, *J* = 3.8 Hz, 1H), 4.45 (d, *J* = 11.9 Hz, 1H), 4.37 (d, *J* = 11.9 Hz, 1H), 3.79 (s, 3H), 3.18 (d, *J* = 15.8 Hz, 1H), 3.03 (d, *J* = 15.8 Hz, 1H). **^{13}C NMR** (101 MHz, $CDCl_3$) δ 161.6, 149.5, 142.8, 142.6, 140.7, 131.3, 127.8, 126.3, 121.6, 121.3, 120.5, 119.1, 102.7, 62.6, 54.5, 51.2, 33.7. **IR** (ATR) 2952, 2919, 2852, 1704, 1471, 1436, 1328, 1266, 1136, 1072. **HRMS** (DART) m/z: $[M + H]^+$ Calcd for $C_{17}H_{16}NO_2$ 266.1176; Found 266.1188. **MP** 101-106 °C.

4.5.10. Procedure for Scale-up

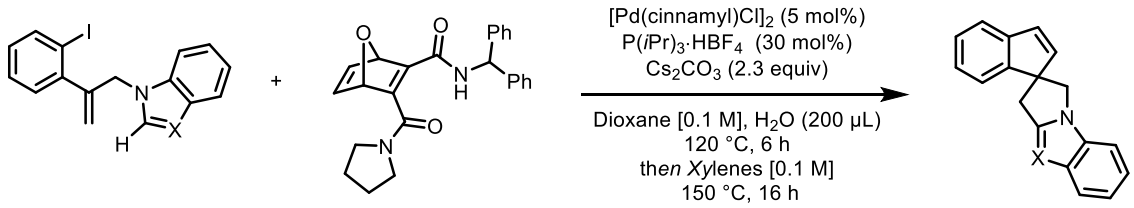

52 (X = N),
SM 8 (X = C)

47a
1.5 equiv

53 (X = N),
62 (X = C)

An oven-dried 9.5-dram vial was charged with a PTFE-coated stir bar and cooled under a positive pressure of argon. Cesium carbonate (750 mg, 2.3 mmol, 2.3 equiv), $[Pd(cinnamyl)Cl]_2$ (26 mg, 0.05 mmol, 5.0 mol%), P(*i*Pr)$_3$·HBF_4 (74 mg, 0.30 mmol, 30 mol%), aryl iodide (1.0 mmol, 1.0 equiv) and oxabicycle **47a** (601 mg, 1.5 mmol, 1.5 equiv) were added in that order to the vial. Freshly distilled dioxane (10 mL, 0.1 M) followed

by distilled water (200 μL) were added via syringe. The reaction vial was then sealed and immediately stirred at 120 ˚C for 6 h. The reaction was concentrated under reduced pressure, and xylenes (1.0 mL, 0.1 M) was added via syringe. The reaction was then stirred at 150 ˚C for 16 h. The reaction was passed through a pad of silica washing with 90:10 ethyl acetate/methanol. The filtrate was concentrated under reduced pressure and the resulting residue purified by flash chromatography.

1H,3H-spiro[benzo[d]pyrrolo[1,2-a]imidazole-2,1'-indene] (**53**): Purification by flash chromatography (20 → 80 % EtOAc/pentanes) to afford **53** as an off-white solid (188 mg, 73% yield).

1'H,3'H-spiro[indene-1,2'-pyrrolo[1,2-a]indole**]** (**62**): Purification by flash chromatography (0 → 25 % EtOAc/pentanes) to afford 62 as a white solid (154 mg, 60% yield).

4.6. References

(1) Phukon, J.; Jyoti Borah, A.; Gogoi, S. Transition-Metal-Catalyzed Synthesis of Spiro Compounds through Activation and Cleavage of C−H Bonds. *Asian J. Org. Chem.* **2022**, *11* (12). https://doi.org/10.1002/ajoc.202200581.

(2) Ding, A.; Meazza, M.; Guo, H.; Yang, J. W.; Rios, R. New Development in the Enantioselective Synthesis of Spiro Compounds. *Chem. Soc. Rev.* **2018**, *47* (15), 5946–5996. https://doi.org/10.1039/c6cs00825a.

(3) Alexandra S. Bubnova , Daria V. Vorobyeva, Ivan A. Godovikov, A. F. S. and S. N. O. Synthesis of CF3-Containing Spiro-[Indene-Proline] Derivatives via Rh(III)-Catalyzed C-H Activation/Annulation Alexandra. *Molecules* **2023**, *28* (7809). https://doi.org/10.1002/chin.200408111.

(4) Jimonet, P.; Boireau, A.; Chevé, M.; Damour, D.; Genevois-Borella, A.; Imperato, A.; Pratt, J.; Randle, J. C. R.; Ribeill, Y.; Stutzmann, J. M.; Mignani, S. Spiro-Imidazo[1,2-a]Indeno[1,2-e]Pyrazine-4-One Derivatives Are Mixed AMPA and NMDA Glycine-Site Antagonists Active in Vivo. *Bioorganic Med. Chem. Lett.* **1999**, *9* (20), 2921–2926. https://doi.org/10.1016/S0960-894X(99)00502-8.

(5) Ari J. Firestone and James K. Chen. Controlling Destiny through Chemistry: Small-Molecule Regulators of Cell Fate. *ACS Chem. Biol.* **2009**, *5* (1), 15–34. https://doi.org/10.1111/j.1743-4580.2001.00162.x.

(6) Wrobel, J.; Dietrich, A.; Woolson, S. A.; Millen, J.; McCaleb, M.; Harrison, M. C.; Hohman, T. C.; Sredy, J.; Sullivan, D. Novel Spirosuccinimides with Incorporated Isoindolone and Benzisothiazole 1,1-Dioxide Moieties as Aldose Reductase Inhibitors and Antihyperglycemic Agents. *J. Med. Chem.* **1992**, *35* (24), 4613–4627. https://doi.org/10.1021/jm00102a016.

(7) Saraswat, P.; Jeyabalan, G.; Hassan, M. Z.; Rahman, M. U.; Nyola, N. K. Review of Synthesis and Various Biological Activities of Spiro Heterocyclic Compounds Comprising Oxindole and Pyrrolidine Moities. *Synth. Commun.* **2016**, *46* (20), 1643–1664. https://doi.org/10.1080/00397911.2016.1211704.

(8) He, L.; Qu, B. Le; Xiao, M.; Yu, J. Q.; Yu, J.; Cheng, Y.; Zhang, Z.; Xiao, W. J.; Lu, L. Q. Synthesis of Chiral Spiro-Indenes via Pd-Catalyzed Asymmetric (4 + 2) Dipolar Cyclization. *Chem. Synth.* **2024**, *4* (4). https://doi.org/10.20517/cs.2024.39.

(9) Morales-García, B. C.; Pérez-González, A.; Galano, A. Spirochromene and Spiroindene Compounds as Antioxidants. *J. Mol. Struct.* **2024**, *1318* (July). https://doi.org/10.1016/j.molstruc.2024.139355.

(10) H, S. Physiological Society Symposium : Impaired Endothelial and Smooth Muscle Cell Function in Oxidative Stress Oxidative Stress : Oxidants and Antioxidants. *Exp. Physiol.* **1996**, *82*, 291–295.

(11) Bremner, I. Manifestations of Copper Excess. *Am. J. Clin. Nutr.* **1998**, *67* (5 SUPPL.), 1069S-1073S. https://doi.org/10.1093/ajcn/67.5.1069S.

(12) Kadiiska, M. B.; Hanna, P. M.; Jordan, S. J.; Mason, R. P. Electron Spin Resonance Evidence for Free Radical Generation in Copper-Treated Vitamin E- and Selenium-Deficient Rats: In Vivo Spin-Trapping Investigation. *Mol. Pharmacol.* **1993**, *44* (1), 222–227. https://doi.org/10.1016/s0026-895x(25)13157-x.

(13) Kahlon, A. K.; Negi, A. S.; Kumari, R.; Srivastava, K. K.; Kumar, S.; Darokar, M. P.; Sharma, A. Identification of 1-Chloro-2-Formyl Indenes and Tetralenes as Novel Antistaphylococcal Agents Exhibiting Sortase a Inhibition. *Appl. Microbiol. Biotechnol.* **2014**, *98* (5), 2041–2051. https://doi.org/10.1007/s00253-013-5036-1.

(14) Huffman, J. W.; Padgett, L. W. Recent Developments in the Medicinal Chemistry of Cannabimimetic Indoles, Pyrroles and Indenes. *Front. Med. Chem. - (Volume 4)* **2005**, *12*, 1395–1411. https://doi.org/10.2174/978160805207310904010661.

(15) Keylor, M. H.; Matsuura, B. S.; Stephenson, C. R. J. Chemistry and Biology of Resveratrol-Derived Natural Products. *Chem. Rev.* **2015**, *115* (17), 8976–9027. https://doi.org/10.1021/cr500689b.

(16) Zhang, Y. L.; Zhang, J.; Jiang, N.; Lu, Y. H.; Wang, L.; Xu, S. H.; Wang, W.; Zhang, G. F.; Xu, Q.; Ge, H. M.; Ma, J.; Song, Y. C.; Tan, R. X. Immunosuppressive Polyketides from Mantis-Associated Daldinia Eschscholzii. *J. Am. Chem. Soc.* **2011**, *133* (15), 5931–5940. https://doi.org/10.1021/ja110932p.

(17) Zhang, Y. L.; Ge, H. M.; Zhao, W.; Dong, H.; Xu, Q.; Li, S. H.; Li, J.; Zhang, J.; Song, Y. C.; Tan, R. X. Unprecedented Immunosuppressive Polyketides from Daldinia Eschscholzii, a Mantis-Associated Fungus. *Angew. Chemie - Int. Ed.* **2008**, *47* (31), 5823–5826. https://doi.org/10.1002/anie.200801284.

(18) Zhao, P.; Guo, Y.; Luan, X. Total Synthesis of Dalesconol A by Pd(0)/Norbornene-Catalyzed Three-Fold Domino Reaction and Pd(II)-Catalyzed Trihydroxylation. *J. Am. Chem. Soc.* **2021**, *143* (50), 21270–21274. https://doi.org/10.1021/jacs.1c12118.

(19) Das, B. G.; Chirila, A.; Tromp, M.; Reek, J. N. H.; De Bruin, B. CoIII-Carbene Radical Approach to Substituted 1H-Indenes. *J. Am. Chem. Soc.* **2016**, *138* (28), 8968–8975. https://doi.org/10.1021/jacs.6b05434.

(20) Oh, D. C.; Williams, P. G.; Kauffman, C. A.; Jensen, P. R.; Fenical, W. Cyanosporasides A and B, Chloro- and Cyano-Cyclopenta[a]Indene Glycosides from the Marine Actinomycete "Salinispora Pacifica." *Org. Lett.* **2006**, *8* (6), 1021–1024. https://doi.org/10.1021/ol052686b.

(21) Majetich, G.; Shimkus, J. M. The Taiwaniaquinoids. *J Nat Prod* **2010**, *73*, 284–298.

(22) Yang, L.; Zheng, H.; Luo, L.; Nan, J.; Liu, J.; Wang, Y.; Luan, X. Palladium-Catalyzed Dynamic Kinetic Asymmetric Transformation of Racemic Biaryls: Axial-to-Central Chirality Transfer. *J. Am. Chem. Soc.* **2015**, *137* (15), 4876–4879. https://doi.org/10.1021/jacs.5b01285.

(23) Zheng, J.; Wang, S. B.; Zheng, C.; You, S. L. Asymmetric Dearomatization of Naphthols via a Rh-Catalyzed C(Sp2)-H Functionalization/Annulation Reaction. *J. Am. Chem. Soc.* **2015**, *137* (15), 4880–4883. https://doi.org/10.1021/jacs.5b01707.

(24) Donslund, B. S.; Nielsen, R. P.; Mønsted, S. M. N.; Jørgensen, K. A. Benzofulvenes in Trienamine Catalysis: Stereoselective Spiroindene Synthesis. *Angew. Chemie - Int. Ed.* **2016**, *55* (37), 11124–11128. https://doi.org/10.1002/anie.201605079.

(25) Chai, Z.; Rainey, T. J. Pd(II)/Brønsted Acid Catalyzed Enantioselective Allylic C−H Activation for the Synthesis of Spirocyclic Rings. *J. Am. Chem. Soc.* **2012**, *134*, 3615–3618.

(26) Chang, X.; Liu, X. T.; Li, F.; Yang, Y.; Chung, L. W.; Wang, C. J. Electron-Rich Benzofulvenes as Effective Dipolarophiles in Copper(i)-Catalyzed Asymmetric 1,3-Dipolar Cycloaddition of Azomethine Ylides. *Chem. Sci.* **2023**, *14* (20), 5460–5469. https://doi.org/10.1039/d3sc00435j.

(27) Voronin, V. V.; Ledovskaya, M. S.; Bogachenkov, A. S.; Rodygin, K. S.; Ananikov, V. P. Acetylene in Organic Synthesis: Recent Progress and New Uses. *Molecules* **2018**, *23* (10), 1–84. https://doi.org/10.3390/molecules23102442.

(28) Trotuş, I. T.; Zimmermann, T.; Schüth, F. Catalytic Reactions of Acetylene: A Feedstock for the Chemical Industry Revisited. *Chem. Rev.* **2014**, *114* (3), 1761–1782. https://doi.org/10.1021/cr400357r.

(29) *SAFETY BULLETIN: Safe Use of Acetylene*.

(30) Rattanangkool, E.; Vilaivan, T.; Sukwattanasinitt, M.; Wacharasindhu, S. An Atom-Economic Approach for Vinylation of Indoles and Phenols Using Calcium Carbide as Acetylene Surrogate. *European J. Org. Chem.* **2016**, *2016* (25), 4347–4353. https://doi.org/10.1002/ejoc.201600666.

(31) Ledovskaya, M. S.; Polynski, M. V.; Ananikov, V. P. One-Pot and Two-Chamber Methodologies for Using Acetylene Surrogates in the Synthesis of Pyridazines and Their D-Labeled Derivatives. *Chem. - An Asian J.* **2021**, *16* (16), 2286–2297. https://doi.org/10.1002/asia.202100562.

(32) Doraghi, F.; Kermaninia, S.; Afaridoun, H.; Larijani, B.; Mahdavi, M. Transition Metal-Catalyzed Transformations of Oxa/Aza Bicyclic Alkenes. *Asian J. Org. Chem.* **2025**, *14* (3), 1–23. https://doi.org/10.1002/ajoc.202400617.

(33) Della Ca', N.; Maestri, G.; Malacria, M.; Derat, E.; Catellani, M. Palladium-Catalyzed Reaction of Aryl Iodides with Ortho-Bromoanilines and Norbornene/Norbornadiene: Unexpected Formation of Dibenzoazepine Derivatives. *Angew. Chemie - Int. Ed.* **2011**, *50* (51), 12257–12261. https://doi.org/10.1002/anie.201104363.

(34) Dutta, S.; Bhattacharya, T.; Werz, D. B.; Maiti, D. Transition-Metal-Catalyzed C–H Allylation Reactions. *Chem* **2021**, *7* (3), 555–605. https://doi.org/10.1016/j.chempr.2020.10.020.

(35) Thansandote, P.; Hulcoop, D. G.; Langer, M.; Lautens, M. Palladium-Catalyzed Annulation of Haloanilines and Halobenzamides Using Norbornadiene as an Acetylene Synthon: A Route to Functionalized Indolines, Isoquinolinones, and Indoles. *J. Org. Chem.* **2009**, *74* (4), 1673–1678. https://doi.org/10.1021/jo802604g.

(36) Donaldson, J. S.; Jiang, H.; Kong, D.; Li, W.; McAlpine, I. J.; Nair, S. K.; Sakata, S.; Spangler, J. E.; Sun, N.; Tran-Dubé, M. B.; Zhou, Y.; Patman, R. L. Microwave-Assisted Synthesis of Heterocycles via Rhodium(III)-Catalyzed C-H Activation: Norbornadiene as an Acetylene Equivalent. *Org. Lett.* **2025**, *27* (3), 728–733. https://doi.org/10.1021/acs.orglett.4c04334.

(37) Sun, M.; Chen, X.; Feng, Z.; Deng, G.; Yang, Y.; Liang, Y. A Catellani and: Retro -Diels-Alder Strategy to Access 1-Amino Phenanthrenes via Ortho - And Interannular C-H Activation of 2-Iodobiphenyls. *Org. Chem. Front.* **2021**, *8* (23), 6535–6540. https://doi.org/10.1039/d1qo01103k.

(38) Abel-Snape, X.; Wycich, G.; Lautens, M. Synthesis of Indenes and Benzofulvenes via a Palladium-Catalyzed Three-Component Reaction. *ACS Catal.* **2022**, *12* (6), 3291–3301. https://doi.org/10.1021/acscatal.1c06046.

(39) Zhang, Y.; Chen, Y.; Tian, Q.; Wang, B.; Cheng, G. Palladium-Catalyzed Multicomponent Assembly of (Z)-Alkenylborons via Carbopalladation/Boronation/Retro-Diels-Alder Cascade Reaction. *J. Org. Chem.* **2023**, *88* (16), 11793–11800. https://doi.org/10.1021/acs.joc.3c01084.

(40) Lv, W.; Wen, S.; Yu, J.; Cheng, G. Palladium-Catalyzed Ortho-Silylation of Aryl Iodides with Concomitant Arylsilylation of Oxanorbornadiene: Accessing Functionalized (Z)-β-Substituted Vinylsilanes and Their Analogues. *Org. Lett.* **2018**, *20* (16), 4984–4987. https://doi.org/10.1021/acs.orglett.8b02106.

(41) Abel-Snape, X.; Johnson, C. E.; Imbriaco, B.; Lautens, M. Synthesis of Spirooxindoles via Formal Acetylene Insertion into a Common Palladacycle Intermediate. *Chem. Sci.* **2023**, *14* (21), 5650–5655. https://doi.org/10.1039/d3sc01072d.

(42) Shi, B.; Maugel, N.; Zhang, Y.; Yu, J. Pd II -Catalyzed Enantioselective Activation of C(Sp 2)-H and C(Sp 3)-H Bonds Using Monoprotected Amino Acids as Chiral Ligands. *Angew. Chemie* **2008**, *120* (26), 4960–4964. https://doi.org/10.1002/ange.200801030.

(43) Lin, G. Q.; Li, Y. M.; Chan, A. S. C. *Principles and Applications of Asymmetric Synthesis*; 2001; Vol. 0.

(44) Hartwig, J. *Organotransition Metal Chemistry*; 2010.

(45) Wang, D. H.; Lam, J. K.; Shi, B. F.; Yu, J. Q. Ligand-Enabled Reactivity and Selectivity in a Synthetically Versatile Aryl C-H Olefination. *Science* **2010**, *327* (5963), 315–319. https://doi.org/10.1126/science.1182512.

(46) Shao, Q.; Wu, K.; Zhuang, Z.; Qian, S.; Yu, J. Q. From Pd(OAc)2 to Chiral Catalysts: The Discovery and Development of Bifunctional Mono-N-Protected Amino Acid Ligands for Diverse C-H Functionalization Reactions. *Acc. Chem. Res.* **2020**, *53* (4), 833–851. https://doi.org/10.1021/acs.accounts.9b00621.

(47) Bai, X. F.; Mu, Q. C.; Xu, Z.; Yang, K. F.; Li, L.; Zheng, Z. J.; Xia, C. G.; Xu, L. W. Catalytic Asymmetric Carbonylation of Prochiral Sulfonamides via C-H Desymmetrization. *ACS Catal.* **2019**, *9* (2), 1431–1436. https://doi.org/10.1021/acscatal.8b04725.

(48) Zhang, L.; Qureshi, Z.; Sonaglia, L.; Lautens, M. Sequential Rhodium/Palladium Catalysis: Enantioselective Formation of Dihydroquinolinones in the Presence of Achiral and Chiral Ligands. *Angew. Chemie - Int. Ed.* **2014**, *53* (50), 13850–13853. https://doi.org/10.1002/anie.201407400.

(49) González, J. M.; Vidal, X.; Ortuño, M. A.; Mascareñas, J. L.; Gulías, M. Chiral Ligands Based on Binaphthyl Scaffolds for Pd-Catalyzed Enantioselective C-H Activation/Cycloaddition Reactions. *J. Am. Chem. Soc.* **2022**, *144* (47), 21437–21442. https://doi.org/10.1021/jacs.2c09479.

(50) Garg, A.; Rendina, D.; Bendale, H.; Akiyama, T.; Ojima, I. Recent Advances in Catalytic Asymmetric Synthesis. *Front. Chem.* **2024**, *12* (May), 1–28. https://doi.org/10.3389/fchem.2024.1398397.

(51) Clayden, J.; Kenworthy, M. N.; Youssef, L. H.; Helliwell, M. Axial Chirality in Xanthene-4,5-Dicarboxamides: 1,9-Stereocontrol Mediated by Remote Interactions between Conformationally Constrained Amide Groups. *Tetrahedron Lett.* **2000**, *41* (27), 5171–5175. https://doi.org/10.1016/S0040-4039(00)00833-9.

(52) Clayden, J.; Lund, A.; Vallverdú, L.; Helltwell, M. Ultra-Remote Stereocontrol by Conformational Communication of Information along a Carbon Chain. *Nature* **2004**, *431* (7011), 966–971. https://doi.org/10.1038/nature02933.

(53) Hsieh, S. Y.; Tang, Y.; Crotti, S.; Stone, E. A.; Miller, S. J. Catalytic Enantioselective Pyridine N-Oxidation. *J. Am. Chem. Soc.* **2019**, *141* (46), 18624–18629. https://doi.org/10.1021/jacs.9b10414.

(54) Zhou, L.; Cheng, H. G.; Li, L.; Wu, K.; Hou, J.; Jiao, C.; Deng, S.; Liu, Z.; Yu, J. Q.; Zhou, Q. Synthesis of Planar Chiral Ferrocenes via Enantioselective Remote C–H Activation. *Nat. Chem.* **2023**, *15* (6), 815–823. https://doi.org/10.1038/s41557-023-01176-3.

(55) Magnus, P.; Linnane, P.; Magnus, N. Induction of Molecular Asymmetry by a Remote Chiral Group. *Nature* **1997**, *385*, 799–801.

(56) Li, J. J.; Zhao, J. H.; Shen, H. C.; Wu, K.; Kuang, X.; Wang, P.; Yu, J. Q. Atroposelective Remote Meta-C–H Activation. *Chem* **2023**, *9* (6), 1452–1463. https://doi.org/10.1016/j.chempr.2023.04.003.

(57) Shi, H.; Herron, A. N.; Shao, Y.; Shao, Q.; Yu, J. Enantioselective Remote Meta-C-H Arylation And. *Nature* **2018**, *558* (7711), 1–6.

(58) Abel-Snape, X.; Jans, C.; Mirabi, B.; Klischan, M. K. T.; Melder, J. J.; Peloewetse, A.; Hughes, G. J.; Lautens, M. Remote Asymmetric Induction via a Chiral Acetylene Equivalent. *ACS Catal.* **2025**, 14239–14251. https://doi.org/10.1021/acscatal.5c03724.

(59) Hazari, N.; Melvin, P. R.; Beromi, M. M. Well-Defined Nickel and Palladium Precatalysts for Cross-Coupling. *Nat. Rev. Chem.* **2017**, *1* (3), 1–17. https://doi.org/10.1038/s41570-017-0025.

(60) Van Berkel, S. S.; Dirks, A. J.; Debets, M. F.; Van Delft, F. L.; Cornelissen, J. J. L. M.; Nolte, R. J. M.; Rutjes, F. P. J. T. Metal-Free Triazole Formation as a Tool for Bioconjugation. *ChemBioChem* **2007**, *8* (13), 1504–1508. https://doi.org/10.1002/cbic.200700278.

(61) De Luca, L.; Giacomelli, G.; Taddei, M. An Easy and Convenient Synthesis of Weinreb Amides and Hydroxamates. *J. Org. Chem.* **2001**, *66* (7), 2534–2537. https://doi.org/10.1021/jo015524b.

(62) Gorelsky, S. I.; Lapointe, D.; Fagnou, K. Analysis of the Concerted Metalation-Deprotonation Mechanism in Palladium-Catalyzed Direct Arylation across a Broad Range of Aromatic Substrates. *J. Am. Chem. Soc.* **2008**, *130* (33), 10848–10849. https://doi.org/10.1021/ja802533u.

(63) Gorelsky, S. I. Tuning the Regioselectivity of Palladium-Catalyzed Direct Arylation of Azoles by Metal Coordination. **2012**, *31* (3), 794–797. https://doi.org/10.1021/om2012612.